University of Reading

Bis Aromatic Urea Hydrogen Bonding Motifs for Use in Supramolecular Materials

A thesis submitted in part fulfilment of the degree of Doctor of Philosophy

Adam David O'Donnell

Department of Chemistry

June 2022

Supervised by Professor W. Hayes, Dr A. T. Russell, and Dr I. German

Sponsored by EPSRC and Kinectrics UK Ltd

Declaration of Original Authorship

I confirm that the research described in this thesis is my own work and that the use of the materials from other sources has been properly and fully acknowledged.

Adam David O’Donnell

Acknowledgements

This thesis is dedicated to my mother, Carolyn Jane O’Donnell.

My sincere gratitude for the support of my friends and family during my PhD candidature. Furthermore, I am eternally grateful for the unwavering support from my supervisors, Wayne, particularly during this write-up phase, Andy and Ian.

As the idiom goes, ‘Give him enough rope, and he will hang himself’ - thankfully, I did not hang myself.

Alex, it has certainly been a journey to remember. I am surprised that we got out alive.

Synopsis

The design of hydrogen bonding motifs is an incredibly attractive proposition for a wide range of applications; these motifs can be integrated into polymeric materials to produce stronger, tougher, stiffer, or more elastic materials that exhibit thermo-reversible behaviour. This thesis describes the design of hydrogen bonding motifs and their successful incorporation in supramolecular materials through the formation of low molecular weight 'super' hydrogelators and elastomeric materials. Hydrogelators were chosen as they offer a unique insight into supramolecular assembly, and they remove the influence of the polymeric backbone which is often responsible for the mechanical properties of polymer networks. The objective was to understand the structure to property relationships for low molecular weight substrates and how that translated to functional materials such as hydrogels. With an appreciation of the mode of assembly of these units and an understanding of how to tailor the assembly of the hydrogen bonding motif, these motifs could then be applied to polymeric systems to generate novel supramolecular elastomers.

Chapter 1. provides a summary of molecular recognition phenomena, the application of weak non-covalent interactions and self-assembly processes in polymeric systems to create functional supramolecular materials.

Chapter 2. details the synthesis of eight low molecular weight bis-aromatic ureas which contain carboxylic acid groups such that, upon pH switching form extended networks through carboxylate-carboxylate interactions. The supramolecular assembly was tailored by introducing methyl substituents on the aromatic rings, which attenuated the assembly by providing steric bulk and forcing the urea and phenyl substituents into a non-planar arrangement, thus promoting urea-urea stacking interactions. The expectation was that forcing the urea-phenyl into a non-planar arrangement would strengthen the urea-urea interaction and, by extension improve the robustness of the hydrogelators. The strengthening of the urea-urea interaction was evident, as rather than form stable gels, the bis-ureas with the strongest urea-urea interactions were found to undergo gel to crystal transitions.

Chapter 3. outlines the synthesis and characterisation of thirteen telechelic poly(butadiene)-based elastomers whose properties were modulated by changing the assembly motif at the end of the polymer chain. The effect of the end-group was stark upon the elastomers' properties; in the absence of a nitro substituent to act as a hydrogen bonding acceptor, the polyurethanes would form exceptionally phase-separated materials that were unsuitable for extensive mechanical testing as they presented behaviour comparable to as crosslinked rubbers. Extensive mechanical property assessment revealed that in the presence of a nitro moiety, the resultant polyurethanes would behave as thermoreversible elastomers that demonstrated self-healing and reversible adherence to a range of different substrates.

Chapter 4. describes the shift in approach to supramolecular polyurethanes, in that, rather than end functionalise telechelic apolar polymer backbones, an apolar backbone, namely PTMG, was chain extended with a bis aromatic urea assembly motif to form chain extended polyurethanes. The synthesised polyurethanes exhibited a significant increase in their mechanical properties because of the addition of a supramolecular assembly within the repeat unit of the resultant polyurethanes. Additionally, the resultant supramolecular elastomers demonstrated self-healing capabilities.

The **General** and **Specific Experimental Procedures** are given at the end of each ***Chapter*** — as are the **References** relevant to a specific ***Chapter***. The thesis also features an Appendix section that contains the analytical data for **Chapters 2**–**4**.

Chapter 1 – Introduction

This chapter is based, in part, on the peer-reviewed publication: *Applications of supramolecular polymer networks*, A.D. O'Donnell, S. Salimi, L.R. Hart, T. S. Babra, B.W. Greenland and W. Hayes, *Reactive and Functional Polymers*, **2022**, *172*, 105209.

1.1 Non-covalent Interactions

Non-covalent interactions are ubiquitous and essential for life; the most elegant and famous examples are the supramolecular interactions of DNA and protein structures responsible for the function of these natural macromolecular assemblies.[1–5] Several types of supramolecular interactions have been successfully utilised to generate supramolecular polymers and gels; examples of these include ionic bonds,[6–12] metal-ligand interactions,[13–16] hydrogen bonding,[7–25] π - π stacking,[26–31] host-guest interactions,[32–40] and van der Waal forces.[41] Supramolecular interactions have become key 'tools' for synthetic chemists as they offer the opportunity to tune the mechanical properties of polymeric materials and impart reversibility through dynamic bonds.[36,42–46]

Association strength is a critical parameter when designing supramolecular polymers, and representative energy ranges for covalent and different non-covalent interactions are shown in Table 1. Although a vital parameter to be evaluated, it should be noted that bond strength is being referred to in isolation; a more representative view in a supramolecular polymer assembly will be present as a combination of multiple interactions forming a much stronger overall interaction. Furthermore, phase separation between hard and soft domains within polymer matrices has been found to be critical in bestowing improved mechanical properties to supramolecular polymer networks.[47–50]

Table 1. Isolated bond energy values for covalent and non-covalent interactions.[51–54]

Interaction	**ΔH (kJ mol^{-1})**
Covalent	100 – 942
Coulombic	100 – 350
Metal-ligand	0 – 400
Hydrogen bonding	10 – 65
π - π stacking	0 – 50
van der Waal forces	< 5

The following sections discuss the different types of non-covalent interactions in more detail. A further consideration that is often overlooked is that the dynamicity of supramolecular polymer systems, which were previously assumed to be in thermodynamic equilibrium, are in fact, undergoing minor changes in their assembly until they reach an even more stable state.[55]

1.2 Supramolecular Chemistry

Polymer chemistry has grown substantially since Staudinger proposed that polymers were made up of long chains of atoms held together by covalent bonds,[56] an insightful hypothesis that led to his award of the Nobel prize in Chemistry in 1953 for his discoveries in macromolecular chemistry. The origins of supramolecular chemistry can be traced back to 1937 when the term "Übermoleküle*"* was introduced by Wolf *et al.*[57] to label hydrogen-bonded dimers of acetic acid (see Figure 1).

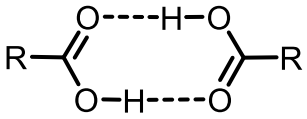

Figure 1. The dimerisation of acetic acid

However, it was not until the 1970s, when Lehn defined the field as 'the chemistry of molecular assemblies and of the intermolecular bond' or, more simplistically, as 'chemistry beyond the molecule',[58–60] that the field of supramolecular chemistry received appropriate recognition from the scientific community. The past four decades have witnessed how synthetic and materials chemists have learnt from nature, in part by trial and error and elegant design, to understand and master the use of weak non-covalent interactions and self-assembly processes in synthetic systems to realise complex multi-component assemblies that exhibit attractive functionalities. To this end, Lehn's proposal that supramolecular chemistry is a new field where the scientific focus lies on the 'chemistry beyond the molecule' is now being borne out. It has enabled the realisation of a diverse array of molecularly assembled materials and complex mechanically-interlocked systems capable of, for example, switching behaviour and even doing physical work.[61-72] The fundamentals of this field are based upon the design of intermolecular complexes created via specific non-covalent interactions (metal-ligand interactions, hydrogen bonding, π-π stacking, electrostatic interactions, van der Waals forces of attraction). A supramolecular material can be defined as a material held together by reversible non-covalent interactions.[58,73–75] In isolation, these non-covalent forces are often too weak to hold together monomers; however, it becomes possible to form supramolecular aggregates when multiple non-covalent interactions combine and reinforce the association. Supramolecular polymers are built up of multifunctional covalently bonded monomers held together by numerous weak non-covalent interactions. The field can be described as the point at which supramolecular chemistry and polymer science intertwine. Notable examples include (see Figure 2) the highly preorganised quadruple hydrogen bonding ureidopyrimidinone (UPy) moiety (**1.1**) developed by Meijer and co-workers,[76–78] the triply hydrogen-bonded assembly (**1.2**) by Lehn and co-workers,[79] and the quadruply hydrogen-bonded complex by Zimmerman and co-workers (**1.3**).[80]

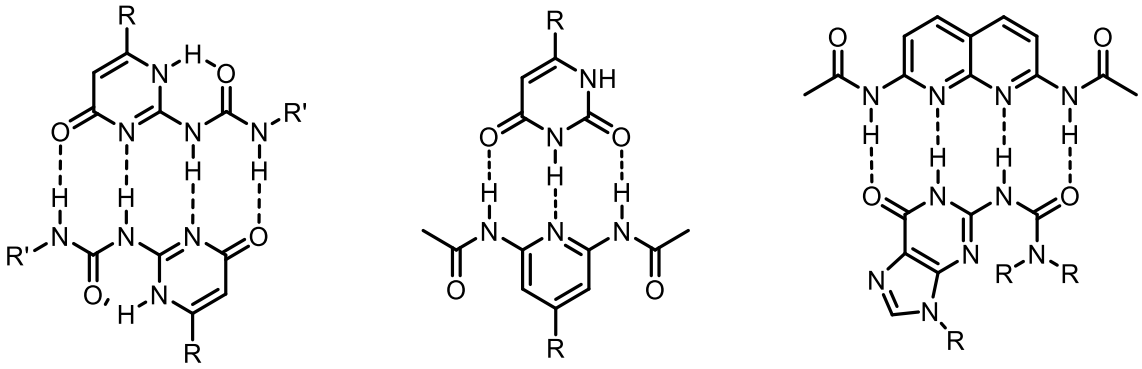

1.1 **1.2** **1.3**

Figure 2. Structures of supramolecular motifs developed by Meijer and Sijbesma (**1.1**) – ureidopyrimidinones dimerising via DDAA arrays of hydrogen bonding sites.[76–78] Lehn and co-workers developed (**1.2**) a complementary motif pair between a pyrimidine-dione and a pyridine diacetamide – using the dimerisation of an ADA with a DAD motif, and Zimmerman and co-workers established the assembly of (**1.3**) a complementary motif pair between a purinone and a naphthyridine diacetamide – dimerisation of DAAD with an ADDA motif.

Initial studies revealed that these discrete units of complementary hydrogen bonding could form a linear chain of which the length depends on the stability of the supramolecular bond and monomer concentration. The UPy moiety has been used extensively in various systems because of its strong association constant (>10^8),[78] and its versatility as it can be inserted easily into polymer systems to yield supramolecular network materials with impressive materials properties.[76,77] The binding strength of supramolecular complexes can be defined by its association constant (K_a). Meijer and co-workers quantified supramolecular polymers' effective degree of polymerisation (DP) (Equation 1).

$$DP \alpha (K_a[M])^{1/2}$$

Equation 1. Effective degree of polymerisation (DP) of supramolecular polymers. Where [M] is the concentration of the repeat unit.

Increasing the number of associating groups makes it possible to design elaborate supramolecular systems with large association constants (K_a). It may seem that it would be desirable to maximise the association constant; however, a delicate balance of enthalpy and entropy exists. If the supramolecular system has a significant association constant, it will require a large amount of energy to dissociate, and thus the strength of the supramolecular association must be considered appropriately for a given application.[81] Furthermore, as these systems can be considered dynamic, they become very environmentally dependent. For example, if the system is held together primarily through hydrogen bonding, one must consider the competing hydrogen bonding from the environment. Water can interact as both a donor and acceptor of hydrogen bonds, coordinate with metal cations and solvate ions, and, therefore, lower the binding association of these interactions when present as a competitive

medium. Dilution studies can access the association constant via nuclear magnetic resonance (NMR) or UV-vis spectroscopic analysis if a suitable chromophore is present.[82,83]

1.2 Supramolecular polymers

The overlap of supramolecular chemistry with polymer synthesis in the past thirty years has afforded a new class of materials – supramolecular polymers – that, on account of weak reversible non-covalent interactions combined with bulk phase separation processes within their assemblies, are dynamic. Seminal studies in the early 1990s by the research groups of Lehn,[79,84] Meijer,[47,85–87] and Stadler,[88] took advantage of the strength of association between complementary hydrogen bonding units to afford stable supramolecular materials. The properties of these new materials were comparable to linear polymers possessing molecular weights far greater than the self-associating oligomeric units involved in the supramolecular network formation.

Molecular recognition units have been incorporated within macromolecular structures in several different ways to afford supramolecular networks, for example, at polymer chain ends,[89] the termini of the arms of combs/brushes,[17] or within the polymer main chain. In addition, the polymer architecture and number of molecular recognition units per polymer chain (referred to as the valency)[90] have also been adjusted to afford stable and processable supramolecular materials to permit multiple association sites per polymer chain. In addition to these structural factors, phase separation between the recognition units, typically polar hard segments and apolar soft blocks, results in improved mechanical properties. Furthermore, apolar polymer blocks have been shown to aid network stability.[91,92] The physical properties and mechanical characteristics of supramolecular polymer networks have been improved by various strategies. Additionally, enhancing the number of interactions per polymer chain, increasing the association (dimerisation) constant of the recognition unit,[93,94] and controlling the recognition dynamics can lead to more strongly associated networks with enhanced mechanical properties.[95] The mixing of different polymers that feature mutually compatible recognition units has proven to be a successful route for generating stable supramolecular polymer blends.[96–101] Reinforcement of supramolecular polymer networks by using additives has also been shown to lead to property enhancement of this type of material.[102,103] These dynamic properties have been used advantageously to yield exciting materials that are, for example, stimuli-responsive and capable of autonomous repair.[104]

1.2.1 Ionic Interactions in Supramolecular Systems

Ionic interactions have been used to generate self-heal materials, relying primarily on coulombic interactions. As charged functional groups are typically water-soluble, ionic interactions have primarily been used to design supramolecular hydrogels. Early studies by Hennink and co-workers illustrated the self-gelling of oppositely charged dextran

microspheres, physically crosslinked through cationic and anionic interactions capable of breaking upon stress and reforming upon stress removal.[105]

In applying ionic interactions to self-healing polymers, research from Zwaag and Varley investigated the self-healing phenomenon of the commercially available ionomer Surlyn® 8940 a sodium carboxylate of (**1.4**), manufactured by DuPont, a poly(ethylene-*co*-methacrylic acid) (PEMA) (**1.5**), a copolymerisation of **1.6** and **1.7**, by ballistic testing (see Scheme 1). Healing depended on the shape of the impacting projectile; blunt projectiles resulted in reduced recovery compared to pointed projectiles. However, complete wound healing could not be achieved, even after heating beyond the melting temperature of the ionomer. Its resistance to puncturing and self-sealing capabilities have resulted in Surlyn® ionomers finding applications ranging from food, pharma, and medical packaging to golf ball coatings. More recently, Surlyn® has gained renewed interest, Sun and co-workers investigated the blending of PEMA with Zn^{2+}, and by varying the ratio of Zn^{2+} relative to PEMA, they were able to fabricate supramolecular elastomers through Zn^{2+} coordination to the carboxylate functional groups (see Scheme 1). Coordination with zinc produced elastomers with comparable mechanical properties to networks where the coordinating metal was sodium. Sun and co-workers reported tensile strengths of ~37 MPa, Young's modulus values of ~343 MPa, and toughness values of ~95 MJ m^{-3} for their ionomers containing 50% Zn^{2+} (**1.8**). In comparison, Dupont has a reported tensile strength at break of 33 MPa for **1.4** and a tensile strength at break of 37.2 MPa for Surlyn 8920 (60% Na^{+}) (**1.9**). However, healing experiments determined that the original mechanical properties of the polymers could be restored over multiple cycles when hot pressing the material at 100 °C with a pressure of 3 MPa.

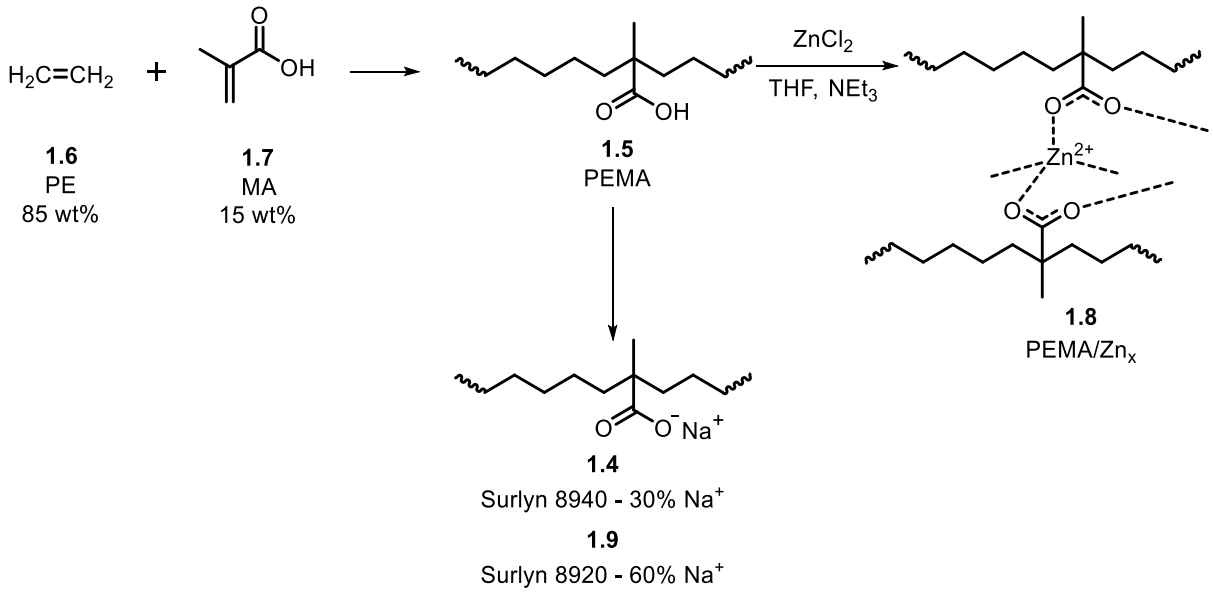

Scheme 1. PEMA ionomers – **1.4** and **1.9** are sold commercially by Dupont and were subject

to ballistic testing by Zwaag and Varley.[106] 1.8, where x denotes the wt.% ratio of Zn relative to PEMA ionomers, was investigated by Sun and co-workers.[107]

Guler and co-workers fabricated supramolecular n/p- nanowires utilising oppositely charged peptides with complementary π-electron donor-acceptor domains, namely, pyrenyl (**1.10**) and naphthalenediimide (**1.11**) moieties (see Figure 3).[108] The peptide conjugates assembled independently of one another into well-ordered nanofibers in aqueous media and, upon mixing, assembled via combinations of electrostatic interactions, charge-transfer complex formation, and hydrogen bonding.

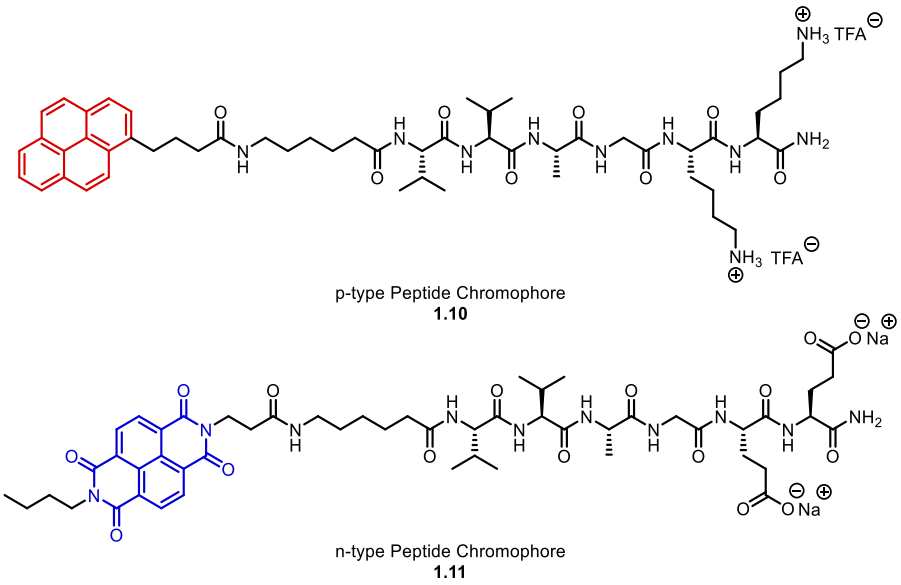

Figure 3. p-/n-type Peptide Chromophores **1.10** and **1.11**, designed by Guler and co-workers.[108]

Electrical measurements of the nanowire films showed about 2400- and 10-times higher conductivity than the individual n-type and p-type nanofiber films, respectively. Reviews on molecular electronics, including supramolecular, have been covered in detail by others and thus will not be discussed further in this introduction section.[109–112]

1.2.2 Metal-coordinated Supramolecular Systems

An alternative approach to synthesise supramolecular systems is to use metal-coordination phenomena. Several metal-coordinated supramolecular systems have been designed and synthesised.[113] These include interpenetrating networks with robust physical properties,[114] to supramolecular polymers that utilise metal coordination to induce self-assembly.[115,116] Rowan, Weder and co-workers have illustrated how tough and optically healable supramolecular polymers can be generated through reversible metal-ligand coordination chemistries.[117] A low molecular weight telechelic poly(ethylene-*co*-butylene) core was functionalised with 2,6-bis(1'-methylbenzimidazolyl) pyridine (Mebip) ligands and assembled with varying ratios of $Zn(NTf_2)_2$ or $La(NTf_2)_3$ (**1.12**) (see Figure 4). Through electron microscopy and small-angle X-ray scattering experiments, the metallosupramolecular polymer was found to possess a

microphase-separated morphology. The poly(ethylene-*co*-butylene) core formed the "soft" phase, and the metal-ligand complexes formed the "hard" phase. The microphase-separated morphology and non-covalent metal-ligand complexes responsible for network formation afforded the material interesting mechanical properties, elongation, and stress at a break of 60-85% and 15-45 MPa.

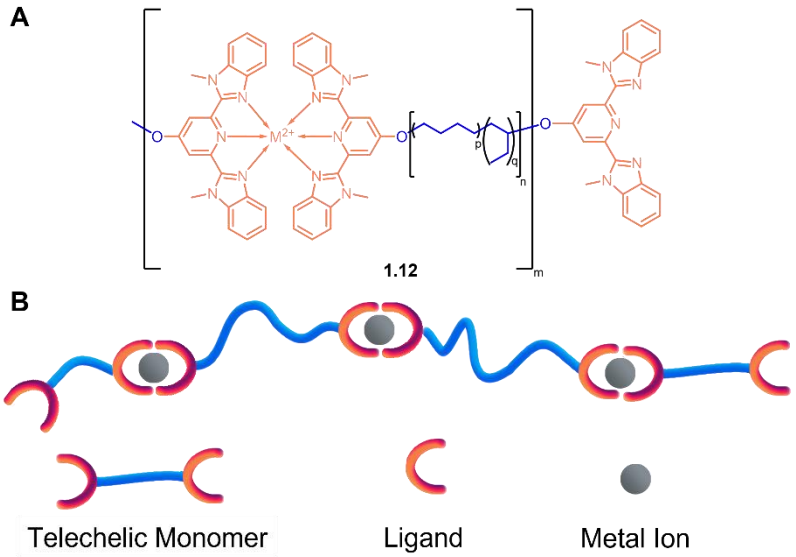

Figure 4. A) A low molecular weight telechelic poly(ethylene-*co*-butylene) core was functionalised with Mebip ligands and assembled with varying ratios of $Zn(NTf_2)_2$ or $La(NTf_2)_3$ (**1.12**). **B)** Illustrative representation of the assembly between telechelic polymer chains.

Another notable metallosupramolecular healable polymer system has been reported by Zhang and co-workers.[118] A dual network was described where Fe^{3+} ions are exploited through metal-ligand interactions and ionic coordination chemistry to impart stiffness and healing to a siloxane network. The siloxane polymer backbone had *N*-acetyl-L-cysteine to allow ionic interactions, while 2,6-pyridinedicarboxamide was introduced as a chain extender and served as the ligand. By tuning the assembly motif content, Zhang and co-worked demonstrated control over mechanical properties and the ability to heal at room temperature.[118] As a means of fabricating self-healable, flexible electronics Bao and co-workers produced a self-healing poly(dimethylsiloxane) (PDMS) elastomer **1.13** based on the concept of reversible metal-ligand coordination (see Scheme 2)[119] In this case, the elastomer featured 2,2'-bipyridine-5,5'-dicarboxylic amide ligand (bpy) in the polymer backbone that was capable of binding Zn^{2+}/Fe^{2+} metal salts. Indeed, coordination between Zn^{2+} and the labile bpy ligand allowed for the generation of supramolecular polymeric networks that presented rapid self-healing in ambient conditions (healing efficiency of 76 ± 22%). In contrast, the polymers crosslinked by Fe^{2+} salts had significantly lower healing efficiencies at ambient conditions because of strong coordination with the bpy ligand. However, upon heating to 90 °C, the Fe^{2+} crosslinked polymers exhibited complete healing. This design strategy shows promise in stretchable electronics as it has an improved dielectric constant compared to PDMS and good self-healing

properties. Interestingly, by taking advantage of a similar interaction between zinc and urea moieties, a polymer material capable of self-healing at sub-zero temperature (-20 °C) has also been reported by Wu *et al.*[120] The ability to heal at sub-zero temperatures offers value where there is an anti-icing coating demand, such as found on the leading edges of aeroplane wings and wind turbine blades, potentially increasing these precision pieces' life span and reducing the costs associated with their maintenance.

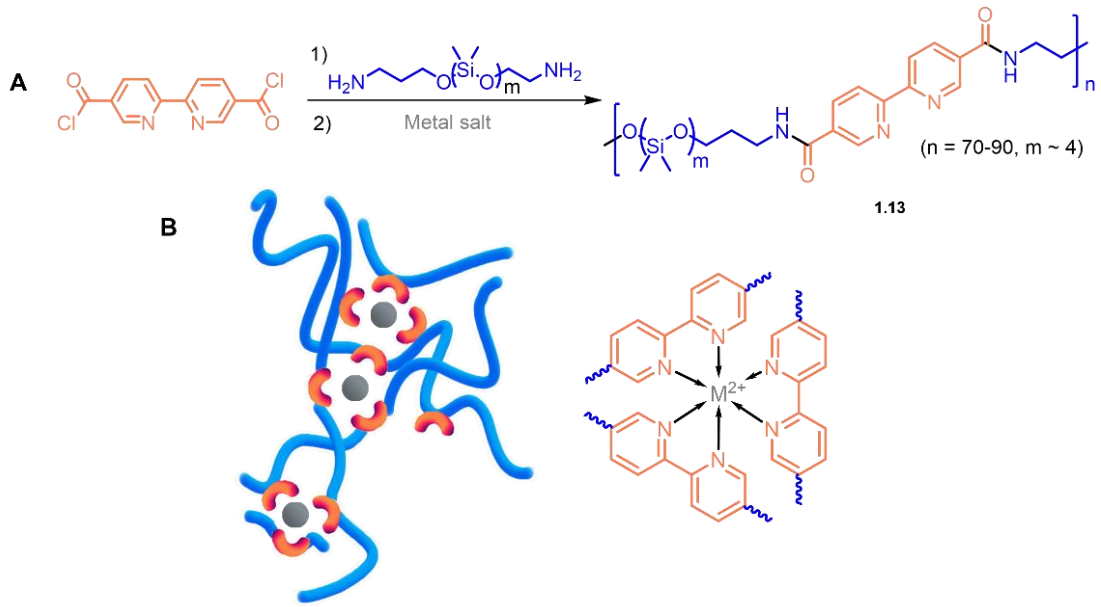

Scheme 2. A) Synthetic strategy to the PDMS-2,2'-bipyridine polymer **1.13**. **B)** Illustration of proposed dynamic interactions upon crosslinking with Fe or Zn metal salts.[119]

1.2.3 Aromatic π - π Interactions in Supramolecular Systems

Monomeric units have been found to self-assemble via aromatic electrostatic interactions. Sanders and Hunter developed a simple electrostatic model of the charge distribution in π-π interactions.[121] It was concluded that π-π interactions are not the consequence of electronic interactions but instead because of π - σ attractive interactions eclipse unfavourable electron repulsion. The significant contribution to this type of non-covalent interaction stems from electrostatic and van der Waal components. Hunter and Sanders proposed geometrical requirements for non-polarised π systems: when two aromatic systems face each other, the π-π repulsion term dominates; however, upon rotation of one of the faces towards 90°, the π – σ attractive term begins to offset the repulsion term. Furthermore, the π – σ attractive term also dominates with an offset π stacked geometry (see Figure 5).

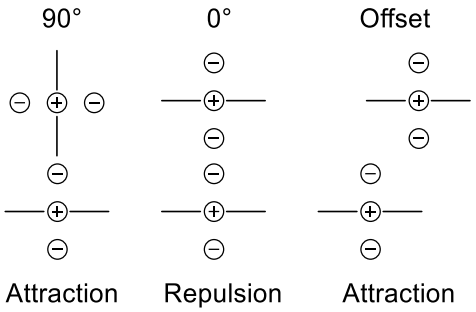

Figure 5. Interaction diagram illustrated as point charges to represent the electrostatic charge distribution for varying geometric stacking orientations.[121]

Müller, Dethlefs and Hobza dismissed the π – π theory introduced by Sanders and Hunter on account of the arbitrary use of σ and π charges.[122] Reinforced by high-level *ab initio* calculations, quadrupole-quadrupole interactions were found to determine the stacking of aromatic residues. The π-electron density on aromatic rings creates a quadrupole, with a partial positive charge found around the edge of the plane and a partial negative charge above and below the aromatic plane.[123] Therefore, the quadrupole-quadrupole term becomes repulsive when stacked in a sandwich-like pattern and attractive for both the T-shaped and offset arrangements.[124] It was since found that by polarising the electron density on an aromatic pair, there is a reversal in the direction of the quadrupole moment, i.e. one of the aromatic systems will have a central area that is relatively electron-deficient, allowing for preferential centred face-to-face stacking. Stoddart and co-workers have reported notable examples of supramolecular aromatic stacking,[28] utilising macrocyclic polyethers containing two π-electron-rich moieties as receptors for a bypridinium dication. Colquhoun and co-workers later designed and synthesised aromatic tweezer molecules as a model for chain-folding polymer blends that exploited charge transfer from π-electron-rich pyrenyl groups and π-electron-deficient diimide units. In the pursuit of a healable material, a chain-folding tweezer molecule (**1.14**) separated by a short ethylene glycol spacer was designed and synthesised with binding constants of up to 11,000 M^{-1} (see Figure 6).[29]

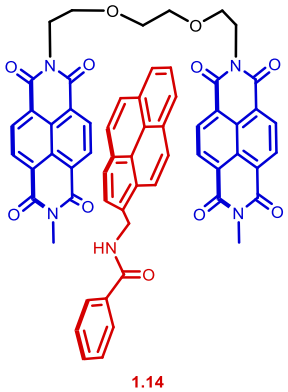

Figure 6. Schematic representation of the tweezer complex designed and synthesised by Colquhoun and co-workers.[29]

Since designing and characterising the tweezer complex, supramolecular polymer blends were designed and realised using the same association motif (see Figure 7).[125]

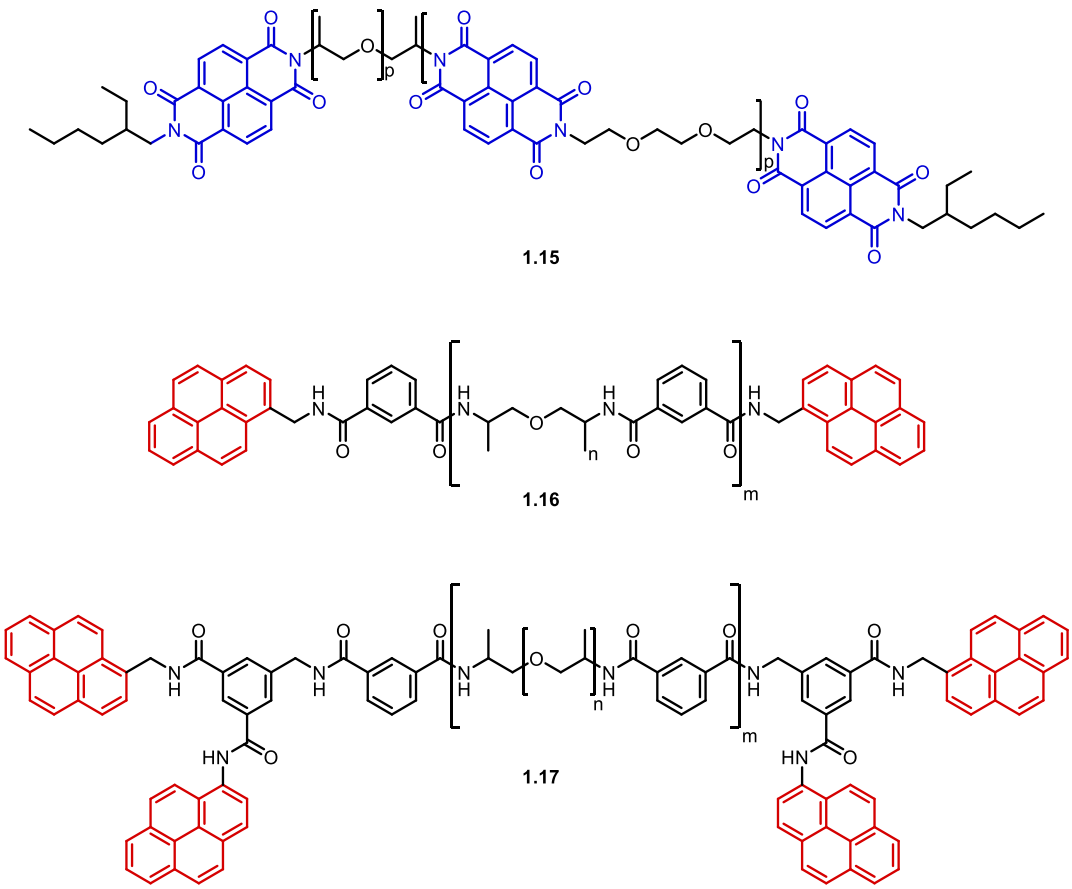

Figure 7. Structures of the healable supramolecular polymers developed by Colquhoun and co-workers. Electron-rich species are coloured in red, and electron-deficient are blue.[125]

Blending the π-electron-deficient end-capped polymer **1.15** with the π-electron-rich pyrenyl polymer **1.16** resulted in the fabrication of a thermally healable material with a healing efficiency of 100% after 5 minutes at 50 °C. The strength of the supramolecular interactions was tuned by the design of a further polymer system **1.17,** which incorporated a dipyrene moiety on the terminals of the backbone, which could act as tweezers and effectively complexed the π-electron-deficient terminals of polymer **1.15**. Blending the dipyrene end-capped polymer **1.17** with π-electron deficient polymer **1.15** generated a polymer blend that exhibited a modulus of toughness of 3×10^8 Pa, an order of magnitude greater than was previously observed for the blend of polymers **1.15** and **1.16**. However, the significant increase in mechanical properties resulted in increased healing times and required higher temperatures (140 °C for 160 minutes when compared to 50 °C for 5 minutes for supramolecular polymer blends utilising **1.15** and **1.16**) to achieve similar healing efficiencies. Thus, there is an apparent compromise for materials of this type between enhancing the mechanical properties of a supramolecular polymer and maintaining facile healing conditions that can be practically applied.

1.2.4 Host-guest Interactions in Supramolecular Systems

Another approach to afford healable supramolecular materials is to employ host-guest interactions as the critical network assembly element. Guest elements of molecules/polymers

are bound inside the host moieties of a complementary polymer (these are typically macrocyclic receptors) to form a network via the creation of multiple inclusion complexes. Exposure to certain stimuli such as changes in pH, temperature, or oxidation state, can reversibly dissociate these non-covalent host-guest complexes.[126] A wide variety of macrocyclic receptors have been reported in the literature as the host species in host-guest polymeric systems, including pillar[n]arenes,[127–132] cucurbit[n]uril (CB[n]s),[133–142] calix[n]arenes,[143–146] cyclodextrins (CD),[126] and crown ethers.[147] From these options, cucurbit[n]urils, calix[n]arenes, and cyclodextrins have been employed most successfully to date because the ease of functionalisation of these hosts allows coupling to the polymer. One of the advantages of the host-guest approach is the host's selectivity towards the guest species to permit efficient and selective network formation and allow for rapid and repeatable healing of the non-covalent network.[145,148] Harada and co-workers demonstrated the first example of a healable host-guest system by supramolecular cross-linking poly(acrylic acid)s bearing either 6βCD (pAA-6βCD) (**1.18**) or ferrocene (pAA-Fc) (**1.19**) (see Figure 8).[126] Mixing pAA-6αCD (**1.20**) and pAA-Fc in 2 wt.% solutions showed a negligible change in viscosity, whereas, mixing the larger CD (pAA-6βCD) with pAA-Fc selectively increased the viscosity of the solution to yield a hydrogel. Control over the inclusion complex of the formed hydrogel was achieved through the redox-responsive properties of the ferrocene. Altering the oxidation state of the ferrocene resulted in sol-gel transitions in the supramolecular hydrogel formed between the host and guest complexes. The hydrogel was able to heal a cut in 24 hours at room temperature, provided that the ferrocene was in its reduced form so that the 6βCD units bound it.

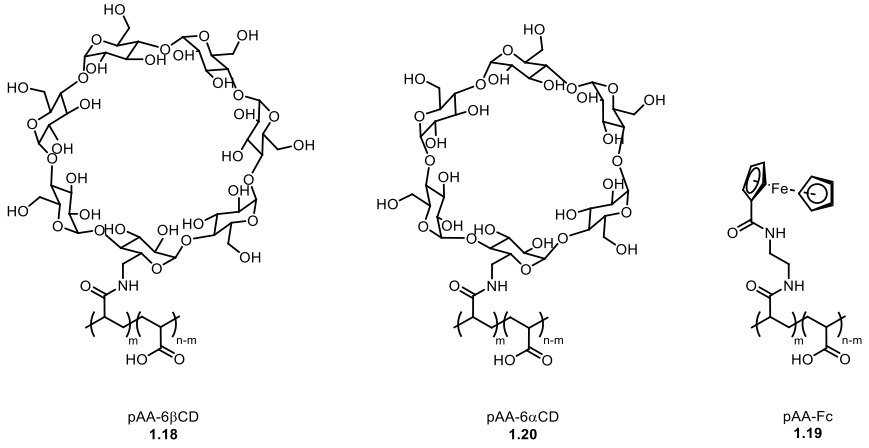

Figure 8. Structures of host pAA-6βCD (**1.18**), pAA-6αCD (**1.20**), and guest (pAA-Fc) (**1.19**) polymers investigated by Harada and co-workers, where m = 4-5% for host polymers and m = 2.7% for guest polymer.

Since this report, several groups have introduced and used different macrocycles to produce healable systems with tailored applications in specific fields or improve these systems' mechanical performance. Also, various healing methods can simultaneously be used in a single system to improve the supramolecular network's healing ability. For example, Lu and co-workers reported a healable system that takes advantage of both UPy end group for

complementary hydrogen bonding assembly and CD binding with UPy units to generate a network material that can regain >92% of the physical properties of the pristine network within 36 hours.[149]

Zhu and co-workers have reported the development of a healable injectable photonic hydrogel using host-guest and hydrogen bonding interactions.[150] Their system consists of imidazole-decorated colloidal photonic crystal balls (referred to as ''supraballs') embedded within a UV-curable gelatin-based hydrogel. The continuous hydrogel phase includes hydrogen-bonding moiety, CD receptors, and imidazole guest functionalities. Therefore, host-guest and hydrogen bonding interactions between the hydrogel backbones and hydrogel/supraballs lead to healing properties. The wavelength of the reflected light from the particles and the particles' colour could be adjusted by changing the particles' size. The light reflectance of supraballs within the hydrogel offers an efficient heat-shielding property (up to 17.4 °C compared to the pure hydrogel in 4 hours of mid-day sun exposure) which can be further developed to produce advanced healable heat-insulating materials.

1.2.5 Hydrogen-bonded Supramolecular Systems

Hydrogen bonding is an electrostatic interaction between a proton donor and an electron donor. The hydrogen atom bridges two electronegative atoms, and the strength of the hydrogen bonds are determined by the donor and acceptor structure and its relative arrangement in space.[151] The strength of a hydrogen bond allows it to be classified as strong (~40 kJ mol^{-1}), medium or weak (20 – 40 kJ mol^{-1}).[76,152] Hydrogen bonding plays a significant role in defining three-dimensional structures, and this can be seen most prominently in nature in determining the double-helical structure of DNA.[1] The nucleotide base pairs, adenine **1.21** (A), thymine **1.22** (T), cytosine **1.23** (C), and guanine **1.24** (G), assemble pairwise through hydrogen bonding interactions (Figure 9) to form a helical structure. The non-covalent hydrogen bonding interactions are crucial for DNA replication as the two complementary strands readily dissociate before replication and associate with a daughter product strand.

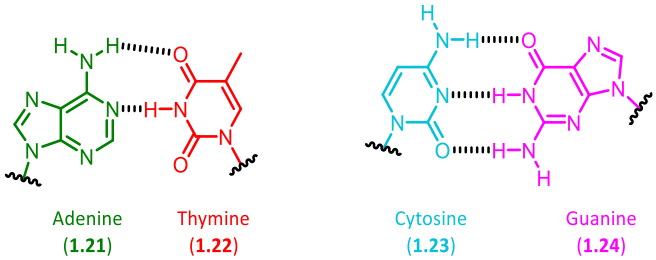

Figure 9. Watson-Crick hydrogen-bonding interactions between DNA base pairs.

Therefore, DNA base pairs have been used as hydrogen bonding motifs in supramolecular chemistry as their assembly shows thermal reversibility.[81,153–160] The ability of this interaction to be used in supramolecular aggregates depends on the quantity of hydrogen bonding sites. Additionally, the relative position of hydrogen bond acceptors/donors can dramatically impact the strength of the association; this was elucidated theoretically by Jorgensen *et al.*,[161,162] who

reported the importance of secondary interactions in triply hydrogen-bonded complexes utilising Monte Carlo simulations. The conclusions were that the arrangements of the complex's hydrogen bond donor and acceptor sites significantly impact whether the secondary interactions are attractive or repulsive. DAA-ADD arrangements are more stable than ADA-DAD arrangements as the former has a reinforcing effect from secondary interactions while the secondary repulsion interactions destabilise the latter (see Figure 10, **1.25** and **1.26** form an ADA-DAD arrangement, whereas **1.27** and **1.28** form a DAA-ADD arrangement). Murray and Zimmerman experimentally verified Jorgensen's theoretical proposal. The stability of triply hydrogen-bonded complexes was shown to be dictated by the arrangement of the hydrogen bonding sites, and that one cannot simply use the number of hydrogen bonding sites as an indicator of complex stability.[163] Furthermore, a triply hydrogen-bonding motif arranged by AAA-DDD (compounds **1.29** and **1.30**) was an order of magnitude greater strength than the DAA-ADD arrangement.

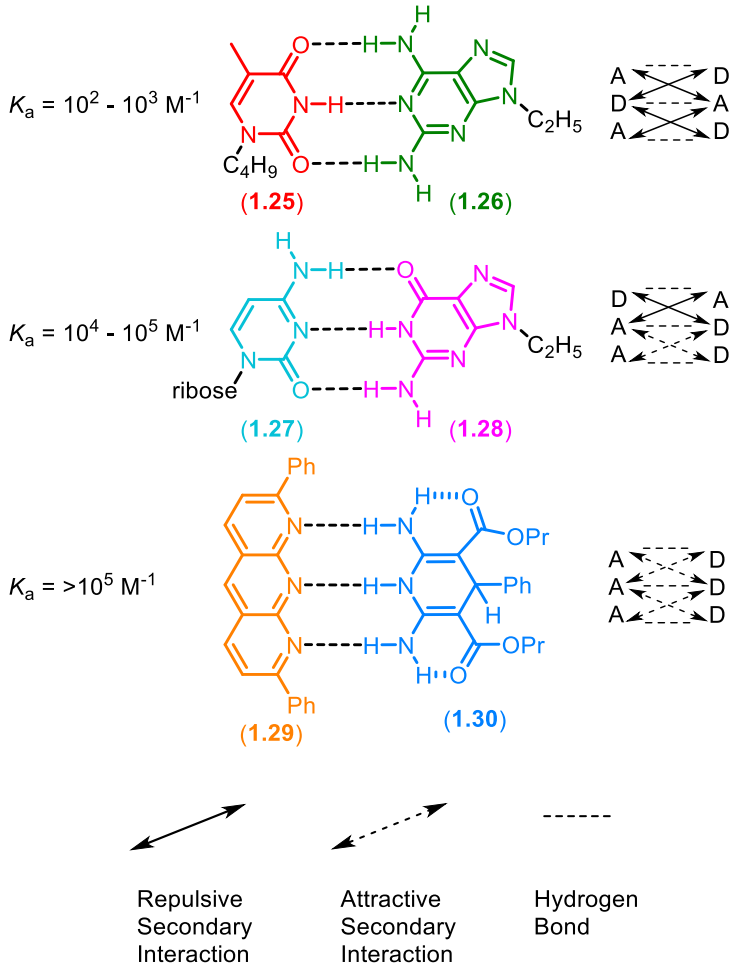

Figure 10. Examples of hydrogen-bonding motifs and their association constants (**1.25-1.30**).[76,164]

A further consideration is the ability of the hydrogen bonding receptors to form tautomers that disrupt or reinforce the association, as shown by Meijer and co-workers,[78,165] and more recently by Sanjayan *et al.*[166] The receptor UPy **1.31** is preorganised by an intramolecular hydrogen bond (see **1.32**) that holds the DDAA motif in a linear conformation thus favouring dimerisation (see **1.31**-**1.35** in Scheme 3).

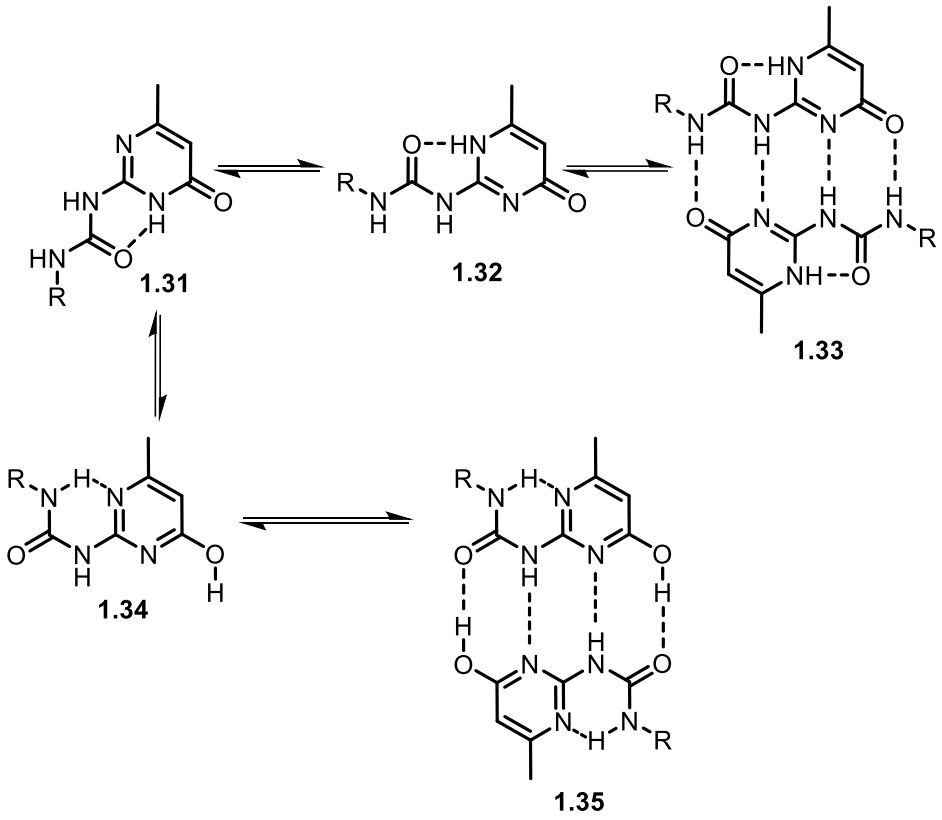

Scheme 3. Tautomer equilibria expressed between UPy monomer and dimer structures.[167]

Utilising the preorganisation/directionality of hydrogen bonding sites in synthon design, it becomes possible to imagine/realise complex supramolecular networks that exploit both the strengths and weaknesses of hydrogen bonding. Its reversibility and relative weakness, compared to covalent bonds, can be employed to present “weak spots” which, upon deformation or impact on the material, will be the first to break, absorb and dissipate the impact energy while the majority covalent network remains still intact. Therefore, allowing the reversibility of the hydrogen bonds to reform a three-dimensional network and recover the net bulk properties of the pristine material. In 2008, Leibler and co-workers published the first use of primarily hydrogen bonding interactions to generate a supramolecular network capable of self-healing.[25] The elastomer, commercialised subsequently by Arkema under the name Reverlink^{TM}, utilised a mixture of diacids and tri-acids, which were reacted in sequence with an excess of diethylenetriamine and then reacted further with urea to produce a mixture of oligomers with hydrogen bonding receptors (see Scheme 4).[168–173]

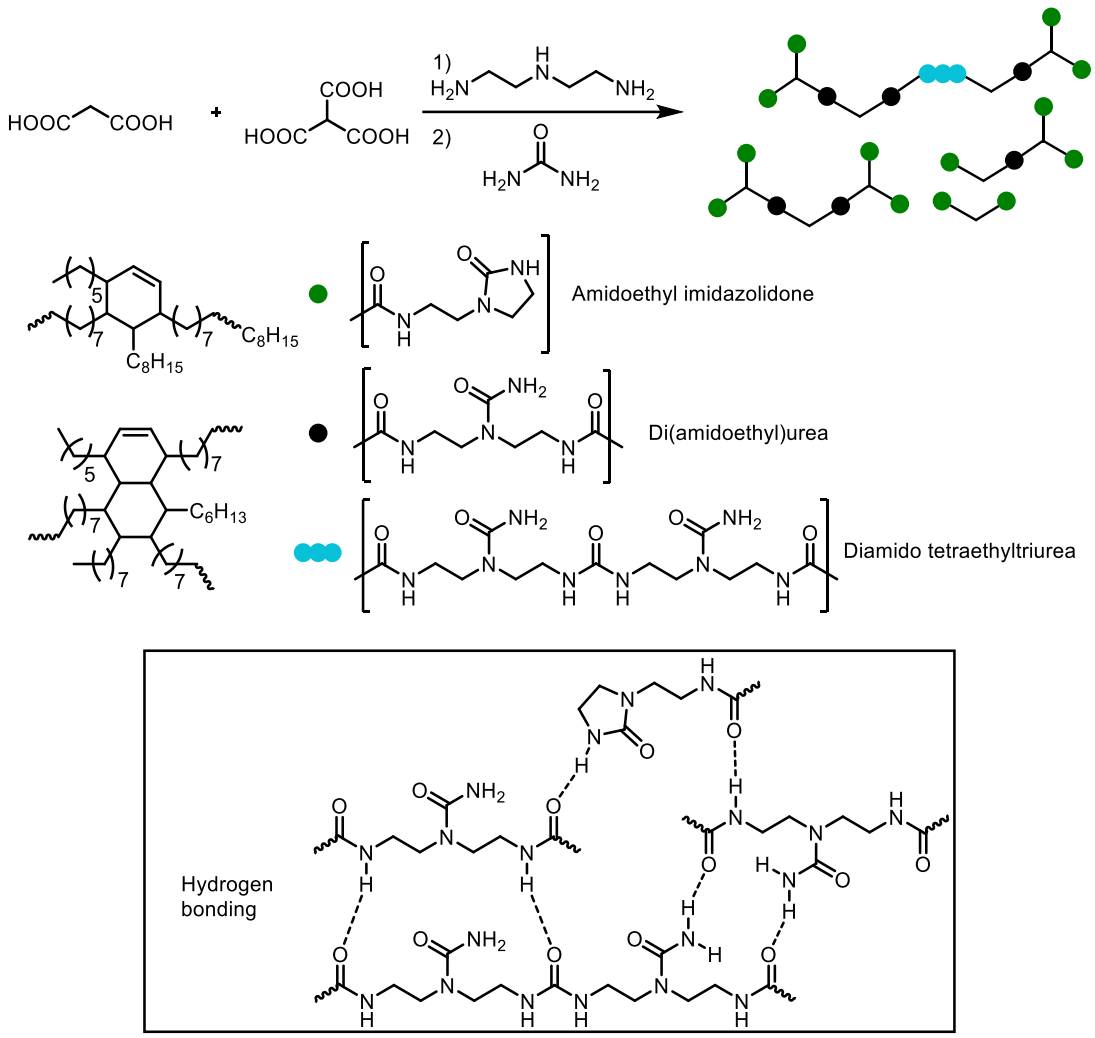

Scheme 4. Schematic representation of the synthesis of Reverlink™,[174] a dispersed mixture of oligomers responsible for its unique mechanical properties and capability to heal through hydrogen bonding motifs.

The amidoethyl imidazolidone, di(amido ethyl)urea, and diamido tetraethyl triurea functional groups behaved as the hydrogen bonding sites within the disperse product to facilitate the formation of a network. Upon heating the material to 90 °C (above the glass transition temperature, T_g = 28 °C), the network material showed soft elastomeric properties with a strain at breaking of 350% (when plasticised with dodecane, *vide infra*). Additionally, complete elastic recovery was obtained up to 100% strain, and at temperatures above 160 °C, the material behaves as a viscoelastic liquid and can be extruded. The glass transition temperature was lowered (T_g = 8 °C) using a plasticiser to obtain a material that behaved as an elastomer at room temperature. Using low molecular weight oligomers that self-assemble is a unique pathway toward self-healing supramolecular polymer networks. It was found that healing efficiency dropped significantly after two faces were kept apart (3 hours), and this was rationalized by the dissociated hydrogen bonding sites migrating into the bulk of the polymer. Thus, when the two surfaces were put together, the supramolecular motifs at the surface could not find a partner in the opposite cut surface. Reverlink™ has since found application in the fabrication of self-healing stretchable wires.[175] In this use, the elastomer was heated to 60 °C and poured into a mould containing a single copper wire. The mould was then cured at 120 °C

for 48 hours, and the copper wire was removed to produce a microchannel. This microchannel was later injected with a liquid alloy eutectic gallium-indium (EGaIn) to create a conducting wire that can be cut and rapidly self-heal at ambient temperatures.

Mono and bis end functionalised supramolecular poly(isobutylene)s (PIBs) featuring either a Hamilton wedge receptor (**1.36**) or barbituric acid (**1.37**)[176] were designed and synthesised by Binder and co-workers (see Scheme 5). Solution mixing of the PIBs allowed for the effect of end-group clustering to be investigated. Viscosity measurements of the barbituric acid monofunctionalised PIBs *vs* temperature showed a significant increase in viscosity (by a factor of *ca.* 18 at 20 °C) compared to the reference monofunctional PIBs (azide functionalized). Terminal flow of the barbituric acid functionalized polymer was only achieved at temperatures above 100 °C; the material behaved as a brittle rubber below 100 °C. Polymer chains associated with end-to-end interactions of the A-A type would expect an increase in viscosity by a factor of 2. Thus, the viscosity change was attributed to larger aggregates, not just the dimerisation of two polymer chains. Mixing the Hamilton wedge receptor functionalized PIBs with the barbituric acid-functionalised PIBs resulted in a significant decrease in the viscosity of the blend because of an A-B interaction which disturbed the A-A clusters of the barbituric acid, and an equimolar mixture of the two exhibited terminal flow at only 40 °C. This ability to disaggregate the clusters formed by the barbituric acid resulted in the ability to tune the mechanical properties of the blended material.

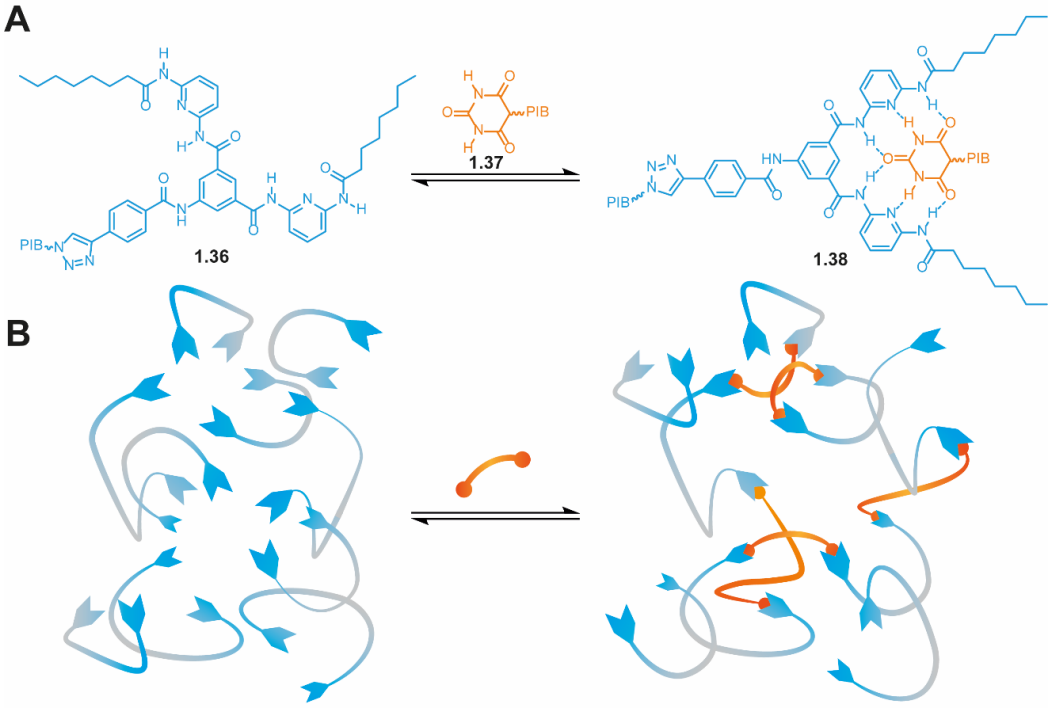

Scheme 5. End-capped PIB with a hydrogen bonding assembly between a Hamilton wedge (**1.36**) and barbituric acid (**1.37**) to form a self-healable supramolecular polymer network (**1.38**) developed by Binder and co-workers.[177]

Yanagisawa *et al.* reported a series of mechanically robust amorphous poly(ether-thiourea)s (**1.39)** based on the reaction of diamino-ethylene glycols (**1.40**) with di(1*H*-imidazol-

1yl)methanethione (**1.41**). They found that although the polymers contained many hydrogen bonding units, the material would remain amorphous because of the non-linear thiourea arrays (Scheme 6A).[178] In contrast, it was found that the analogous urea polymers were semi-crystalline (see Scheme 6B and 6C). The less ordered thiourea arrays do not crystallise and, in combination with low molecular weight polymer chains, thereby easing chain motion, led to the development of a polymeric material capable of self-healing with compression in the absence of heating.

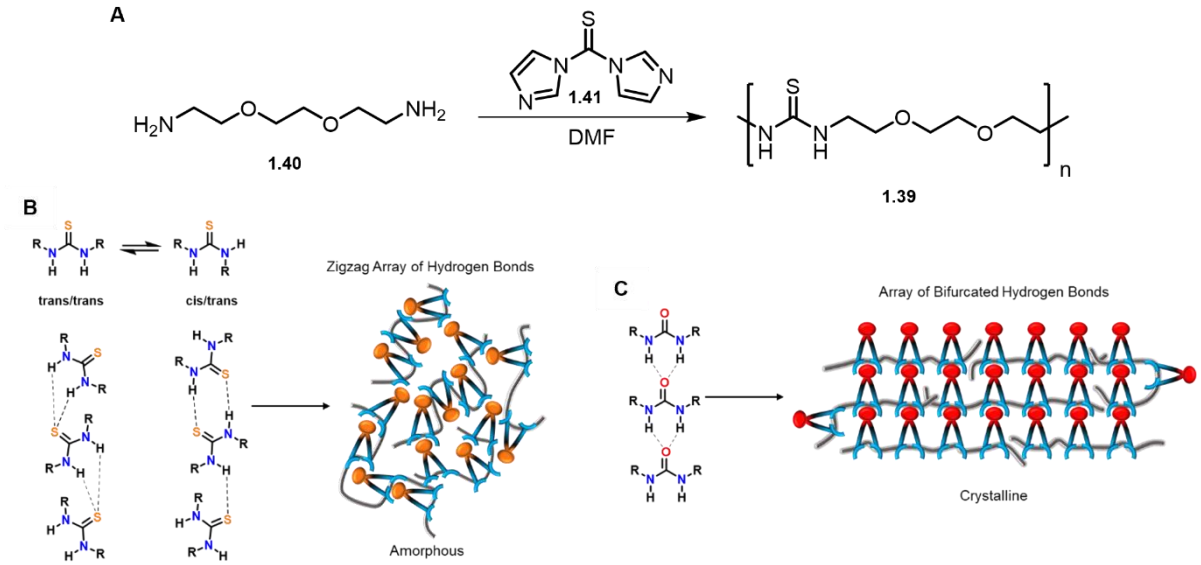

Scheme 6. A) The synthetic strategy to yield poly(ether-thiourea)s (**1.39**) employed by Yanagisawa *et al.*[178] Schematic representation of the assembly modes of **B)** zigzag array of hydrogen bonds in thiourea stacks and **C)** a crystalline array of bifurcated ureas stacks.

Stable supramolecular assemblies form because of strong complementary non-covalent interactions and controlling these associations' strength is critical when designing dynamic and responsive polymeric materials. Meijer, Sijbesma and co-workers modified telechelic polymers such as polysiloxanes,[89] and poly(ethylene-*co*-butylene),[179] with ureidopyrimidones (UPy), and the introduction of the UPy end-cap to telechelic polymers has resulted in the manufacturing of commercial, thermoreversible, supramolecular polymer materials by SupraPolix BV.[180–189] Meijer and Palmans and co-workers recently illustrated the significance of association strength by functionalising a poly(dimethylsiloxane) (PDMS) polymer backbone with three different supramolecular moieties that vary in association strength (see Figure 11).[190] A dinitrohydrazone (hydz) (**1.42**) moiety was chosen as it associates through weak supramolecular interactions such as π - π stacking, afforded a viscous material at room temperature. In contrast, when more robust self-associating motifs were used, e.g., benzene-1,3,5-carboxamides (BTA) (**1.43**) and UPy (**1.44**), which can assemble via more potent triple and quadruple hydrogen bonding, materials with vastly different physical properties were produced. A thermoplastic elastomer was generated in the case of the BTA functionalised PDMS, and functionalising PDMS with UPy units afforded a very brittle material such that high-

temperature compression moulding (130 °C, 100 bar, 20 minutes) was needed to reprocess the material. The dynamic properties of the polymers were probed through stress relaxation experiments. In the cases of the hydz- (**1.42**) and the BTA-functionalized PDMS polymers (**1.43**), complete stress relaxation was achieved in 160 and 210 seconds, respectively. However, for the UPy grafted polymer (**1.44**), more than 8 hours were needed to obtain total stress relaxation. This study elegantly highlights the importance of understanding and controlling the association strength of the supramolecular receptor. Efficient stress relaxation is a function of the supramolecular network's reversibility and the relaxation of the polymeric chains that have undergone stress. Supramolecular interactions, having dynamic behaviour and potentially functional reversible properties, allowed the materials generated to be reprocessed without loss in mechanical properties. In contrast, in covalently crosslinked materials, if the covalent bonds are broken because of mechanical damage, then recovery of the original mechanical properties requires an external healing agent.

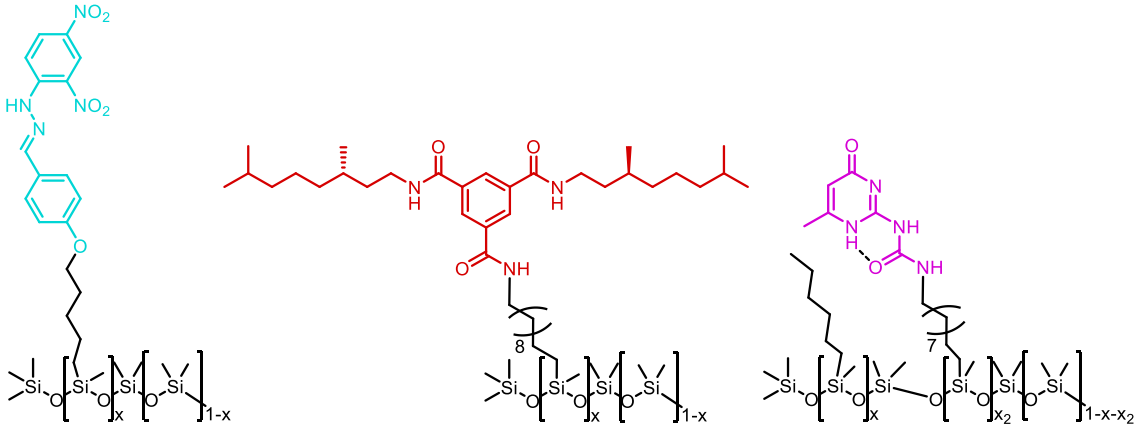

Figure 11. The structures of the supramolecular polymers **1.42**, **1.43** and **1.44** were reported by Meijer, Palmans and co-workers.[190] PDMS-g-UPy contains an intramolecular hydrogen bond between the pyrimidinone ring and the urea carbonyl.

The inverse relationship between temperature and strength of supramolecular bonds has been well-studied in the solution state. Indeed, the structural manipulation of supramolecular receptors on telechelic polymers to tailor their association constants has been demonstrated to dramatically affect the viscosity of the materials as a function of temperature in a broad range of supramolecular systems.[191] The reduction of viscosity of polymers with heat has been used extensively in the adhesive industry to produce polyurethane hot-melt adhesives, which flow sufficiently to be applied at elevated temperature, then cool and solidify to form the bond.[192] In these systems, no new covalent bonds have been formed during the heating and cooling process, enabling the polymers to be reheated to facilitate debonding of the substrates.

Long and co-workers exemplified the thermal debonding of supramolecular adhesives, synthesising a series of ureidopyrimidone (UPy) functionalised comb-like polyacrylates, which

showed adhesion to glass substrates (see Figure 12A).[193] Higher loadings of the UPy group were found to afford stronger adhesion to a range of substrates. Similarly, the same group also developed adenine and thymine functionalised two-pot polyacrylate adhesives (see Figure 12B), which showed thermal reversibility of adhesion at 80 °C.[154,155] Using related functionality on a siloxane polymer backbone, Bosman and co-workers synthesised a UPy terminated siloxane that adhered to glass at 120 °C and held a 1 kg weight for 24 hours without breaking.[194] If fractured, the adhesive could be re-adhered at 120 °C and exhibited the same adhesive properties as the pristine bond (see Figure 12C).

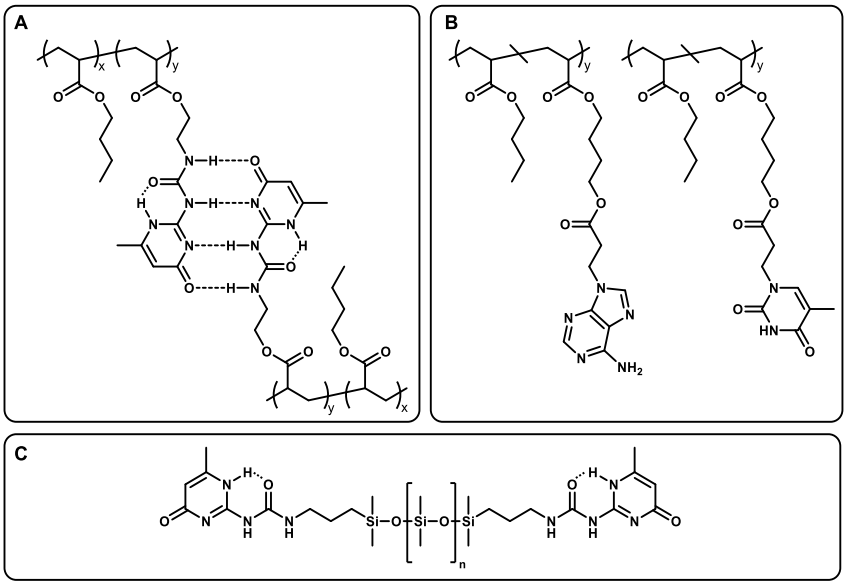

Figure 12. The hydrogen-bonded supramolecular adhesives of (**A**) UPy functionalised and (**B**) adenine-thymine functionalised polymethacrylate co-polymerised with poly(butylacrylate) developed by Long and co-workers.[154,155,193] (**C**) UPy functionalised poly(siloxane) used as an adhesive that is thermally reversible at 120 °C.[194]

1.3 Healable materials

A polymeric material's ability to heal any damage in either an autonomous way or via a mild stimulus is a desirable proposition. The global focus on environmentally friendly uses of polymeric materials has meant that minimising maintenance costs, reducing environmental waste, and extending a material's lifespan by learning how to make polymers healable are sufficient reasons to justify the extensive research on this topic over the past decade. Prototype healable polymer systems have found applications in areas ranging from the healthcare industry[195] to anti-corrosion coatings[196] and flexible/wearable electronics.[118,197–200]

A principal area of interest in supramolecular polymer networks has been dedicated to healable materials.[43] Several different methodologies have been explored to deliver healable supramolecular polymer networks, and the mechanism for healing can be divided into two general categories: intrinsic and extrinsic. In intrinsically healable materials, physical assembly motifs are exploited within the polymer chains, and therefore the healing process is reversible. In the case of extrinsically healable materials, the healing agent is typically encapsulated and dispersed within the polymer, and once ruptured, a reaction occurs, and this process is not reversible. The first instance of an extrinsic approach was reported by Dry and collaborators

in 1996, who encapsulated a two-part epoxy adhesive in 100 μL glass pipette tubes within a clear epoxy matrix.[201] In 2001, White and co-workers,[202] taking advantage of a catalysed ring-opening metathesis polymerisation of dicyclopentadiene, encapsulated dicyclopentadiene and mixed them with an epoxy resin and a Grubb's catalyst to afford a self-healing material. Recovery experiments showed a 75% recovery in toughness, and since then, the concept has been applied to several various substrates such as polydimethylsiloxane (PDMS),[203] glycidyl methacrylate,[204] and tung oil.[205]

An inherent difficulty with extrinsically healed materials is the need for effective healing agent dispersion upon a damage event. Healing events cannot occur if the healing agent is not dispersed at the damaged event's location. Likewise, healing cannot occur when the supply of the healing agent is exhausted. An alternative approach relies on the temporary disassembly of covalent bonds, lowering the polymer's molecular weight to induce material flow through increased chain mobility. The dissembled polymer can then fill the defects before reforming its network. These materials have been shown to heal and do not require additional healing agents. The first example of this was illustrated using Diels-Alder chemistry.[206] The polymer network's cross-link density could be temporarily reduced by heating the polymer to induce a retro-Diels-Alder reaction. Since then, many different dynamic covalent bonds have been applied to make Dynamers, examples of which include imines,[207,208] oximes,[209–212] acylhydrazones,[213–216] hydrazones,[217] disulfides,[218–226] trithiocarbonates,[227,228] boroxines,[229] and alkoxyamine radicals (see Figure 13).[230–232]

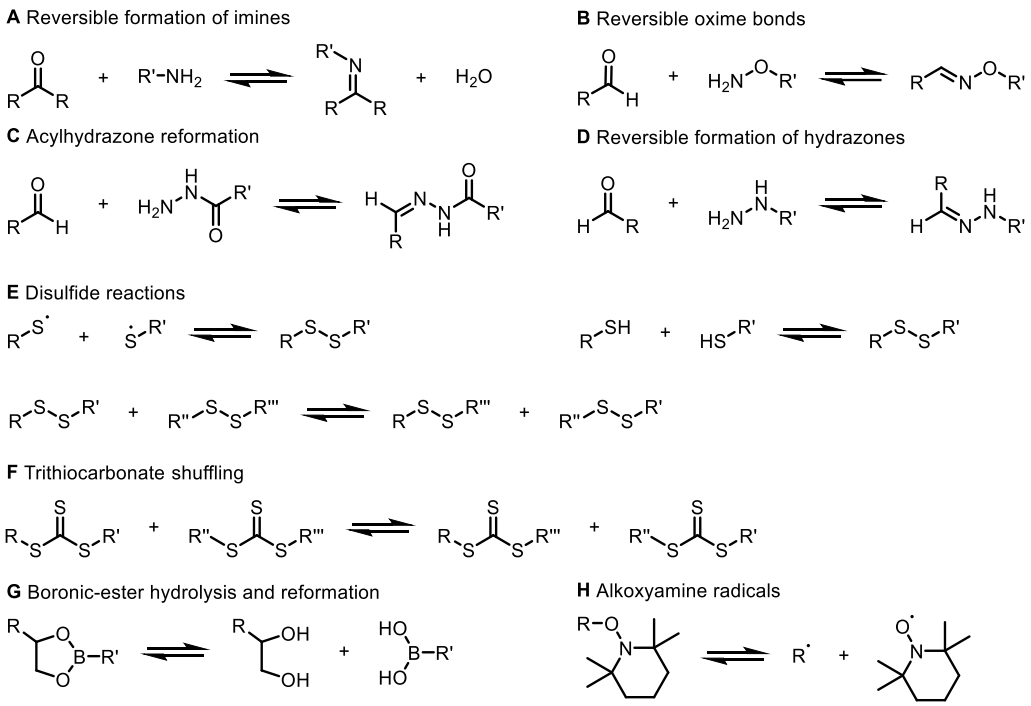

Figure 13. Reversible covalent bonds are used in the synthesis of Dynamers.

The introduction of supramolecular interactions in polymer chemistry allows for the generation of *pseudo*-high molecular weight polymers, and as such, they can display mechanical

properties like those of high molecular weight polymers. Supramolecular interactions allow the polymer network to be temporarily broken into shorter polymer chains upon exposure to suitable stimuli and ease intrinsic healing mechanisms through increased chain mobility through dynamic bonding. The opportunity to tune the mechanical properties of polymeric materials and the reversibility of dynamic bonds has led to self-healing materials finding their way into real-world applications, such as in energy storage devices,[10,233–235] and flexible electronics.[236,237]

Understanding the mechanism of healing in polymer systems is non-trivial. Building on the seminal work of De Gennes, who coined the term and concept of polymer reptation,[238] and Edwards,[239] Wool and O'Connor developed a theoretical framework to understand crack healing of thermoplastic polymers,[240] they proposed that at the reptation time τ_{rep} an entire chain escapes its original tube and can diffuse across the polymer-polymer interface. Therefore, the equilibrium healing time τ_{eq} is approximately equal to the reptation time for a polymer chain. Wool and Kim later proposed that healing at the polymer-polymer interface in amorphous polymers by heating above the T_g involves multiple processes: firstly, surface rearrangement and approach, followed by wetting, diffusion, and re-entanglement of the polymer chains. When two similar bulk polymer surfaces contact one another at a temperature above the T_g, the interface between the surfaces gradually disappears primarily due to chain diffusion across the interface.[241,242] However, more recently, molecular dynamic (MD) simulations of polymer welding by Ge *et al.* investigated the process of bringing two polymer surfaces in close contact above the T_g, showing that restoration of interfacial mechanical strength to that of the bulk polymer occurs much more rapidly than the time taken for a polymer chain to diffuse by their radius of gyration.[243] Subsequently, Ge *et al.* probed the healing process of polymer-polymer interfaces with MD simulations.[244] Pre-cut symmetrical surfaces were simulated with polydispersity. The damage process results in the polymer chains' chain scission, thus increasing the low molecular weight fraction at the interface. Increased chain mobility of the low molecular weight fraction resulted in rapid diffusion away from the interface, which was found to be randomly distributed by the model's simulation after a short period of time. Employing the same rationale, larger, less mobile polymer chains were found in increasing quantities at the interface because of enhanced diffusion times. Overall, this study found that the recovery of bulk mechanical strength depends on the diffusion of the entangled chains into the bulk of the material, away from the interface and not the rapid diffusion of the low molecular weight fraction diffusing into the bulk.

Rubinstein and co-workers developed a theoretical model to understand self-healing in unentangled supramolecular polymer systems. Rubinstein and co-workers suggested that the τ_{eq} was dependent on many variables, such as the waiting time, bond lifetime and relaxation time for the reversible bond at the interface of the polymer materials.[245] More recently, Hornat and Urban, through chain extension of PTMG (M_n = 250) (**1.45**) with IPDI (**1.46**), produced

thermoplastic polyurethanes of varied M_w (22, 32, 45, 72 and 180 kDa by varying the stoichiometry of the feed) (**1.47**) and investigated the two proposed self-healing mechanisms (see Scheme 7).

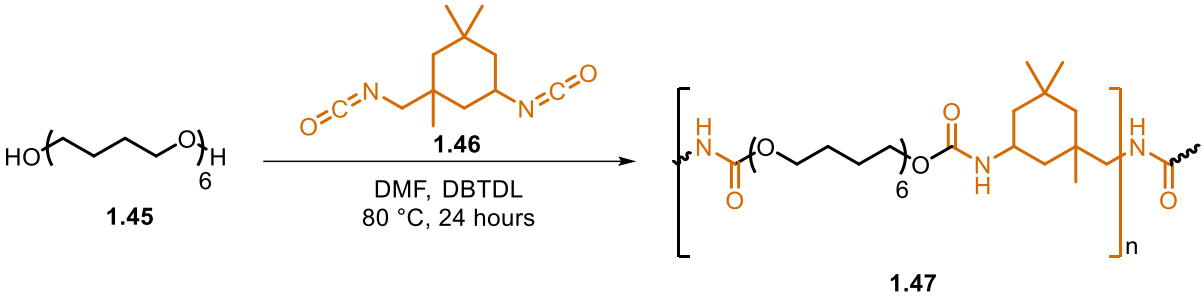

Scheme 7. The synthetic strategy employed by Hornat and co-workers to access thermoplastic polyurethanes.[246]

The first mechanism to be investigated was viscoelastic shape memory (VESM), which is driven by the conformational entropy stored during the mechanical damage, and the other process assessed was the excess surface tension from the mechanical damage. Unfortunately, the fundamental experimental study by Hornat and Urban did not consider polydispersity as a factor in either of the above-mentioned healing processes and although GPC analysis was performed to determine the M_w of the resultant polymers, chromatographic data was not provided; however, it is a fair assumption that the polydispersity of the polymers analysed was similar given the same reagents and reaction conditions were used.[246] They found that the TPU fibres with an Mw of 72 kDa completely recovered their mechanical properties compared to lower molecular weight TPU fibres with an M_w of 45 kDa, which showed a significant decrease in tenacity and strain at failure relative to the pristine material. This would appear counter-intuitive, as it might be expected that a TPU with fibres comprised of a lower molecular weight material would be more mobile and more likely to diffuse across the polymer interface. This phenomenon suggests that the healing mechanism for the lower molecular weight polymer network with an M_w of 45 kDa differs significantly from the TPU material with an M_w of 72 kDa. The proposed healing mechanism for the TPU (M_w of 72 kDa) is derived from an entropically driven process. However, the pattern appears reversed for the polymers with M_w of 22, 33 and 45 kDa, whereby the lowest molecular weight polymer repairs the fastest as determined by optical microscopy. Thus, it is suggested that the healing mechanism is a consequence of excess surface energy from the damage event, which acts to reduce the newly generated surface by the interfacial flow of the material (see Figure 14).

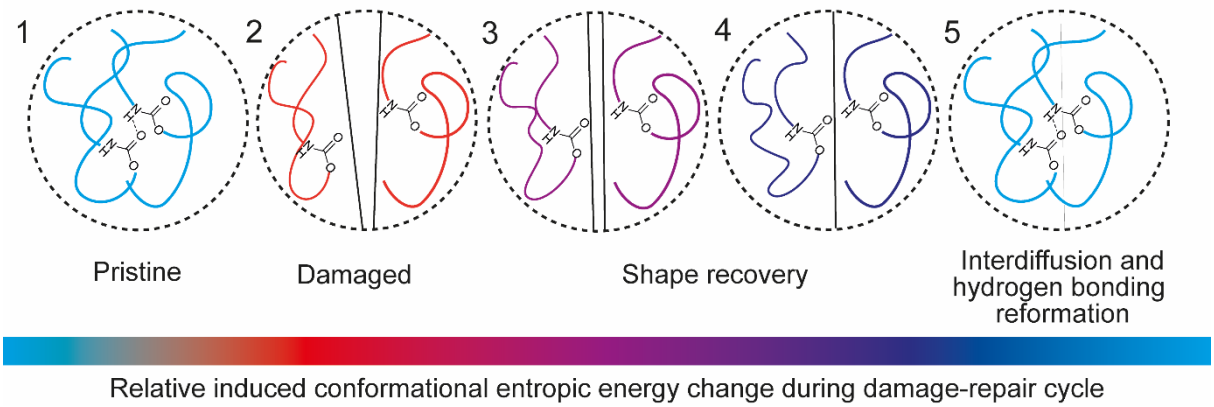

Figure 14. Pictorial representation of molecular and macroscopic events during an entropy-driven self-repair mechanism. Illustrating conformational changes, breaking, and forming of hydrogen bonds and the disentanglement and re-entanglement process of chains during and after a damage event. A qualitative description of entropic energy change is illustrated by the colour of the polymer chains, from low energy (blue) to high energy shortly after a damage event (red), followed by a period of shape recovery (purple) and interdiffusion of polymer chains and ultimately reformation of hydrogen bonds (blue). The figure is inspired by a scheme from the paper published by Hornat and Urban.[246]

Different models have been devised to consider molecular weight dependence during healing events, and it is generally accepted that there is an inversely proportional relationship between molecular weight and chain diffusion and re-entanglement. In the theoretical model, various assumptions are made, which do not always apply to practical polymer systems used as materials. For example, Wool and Kim assumed that all chains have the same length,[240,241] and in practice, polyurethane networks are typically synthesised by the uncontrolled reaction of a diisocyanate, and a chain extender has a typical polydispersity range from 1.50 to 2.5. Furthermore, side reactions are common with biuret, allophanate and uretidione linkages being generated (see Figure 15).

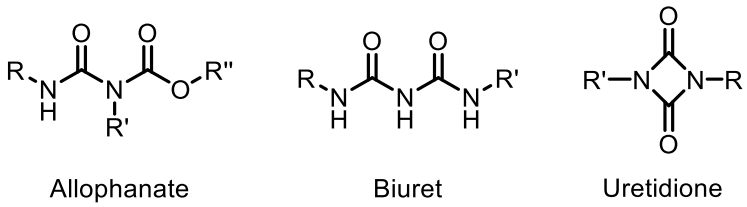

Figure 15. Chemical structures of allophanate, biuret and uretidione units.

Thus, the theory may not necessarily apply to real-world polymer networks that exhibit polydispersity, and modelling the influence of polydispersity on healing mechanisms is not one that has been explored extensively until more recently by Ge *et al.*[244]

Through MD simulations, Li and co-workers systematically studied the self-adhesion of both unentangled and entangled polymer networks. It was found that the recovery of macroscopic interfacial strength depends almost linearly on the microscopic molecular formations at the interface. Complete recovery of interfacial strength was attributed to polymer chains diffusing

successfully across the fractured interface and that the polymer chains had reassociated through the reversible bond formation and entanglement.[247]

The Reverlink™ polymer networks developed by Liebler and co-workers that exhibit self-healing ability employs dodecane as a plasticiser and, by doing so, increases the free volume, thus decreasing the T_g of the polymer architecture by allowing the chain segments to move and rotate more freely. Therefore, there is justification for using low molecular weight telechelic polymers, which intrinsically are more mobile and can diffuse more rapidly. Indeed, this hypothesis is employed by many working in the field of healable supramolecular polymers to justify their deployment of low-molecular-weight polymer chains that are interlocked by non-covalent interactions or thermally reversible covalent bonds. At face value, the approach appears valid; however, in practice, the materials generated by this approach typically lack the mechanical robustness afforded to chain-extended polymers or covalently crosslinked networks. Low molecular weight polymers that can heal under ambient conditions without external stimuli are prone to viscoelastic creep; [248] this process was acknowledged by Liebler and co-workers in the development of Reverlink™, and thus there is a conflict between mechanical robustness and dynamic association. If conventional chain-extended polymer networks can undergo healing mechanisms through polymer scission, reversible dissociation of non-covalent interactions, VESM and surface tension effects, then the drive to use low-molecular-weight polymer chains is reduced as chain-extended systems will naturally show increased mechanical properties. For example, the relatively simple system by Hornat and Urban,[246] (see Scheme 7) is proposed to be the strongest and stiffest self-healing polymer that can repair under ambient conditions without intervention and is a chain-extended PTMG with IPDI to molecular weights ranging from 22 kDa to 180 kDa.

A range of approaches has been applied to designing and synthesising healable materials. Xu and co-workers synthesised a fluorescence-responsive self-healing hydrogel that consisted of a mixed gel network of chitosan, agarose, PVA, borax, and glycerol. Relying on the hydrogen bonding interactions of chitosan-agarose, chitosan-PVA, and agarose-PVA, combined with interactions between PVA-borax and PVA-glycerol, quantum dots were dispersed within the hydrogel to obtain a fluorescent self-healing hydrogel.[249] This extensive array of hydrogen bonding interactions was justified as the properties of the hydrogels produced could be tailored between the elongation of break of almost thirteen times the original length with a tensile strength of 2 MPa to elongation at break of nearly nine times the original length and tensile strength of 6.5 MPa. Multiple hydrogen bonding interactions were rationalised as the hydrogen bonding interactions between the chitosan-agarose-PVA chains are much stronger than the weaker and more prone to fission PVA-borax and PVA glycerol interactions. Thus, the weak reversible hydrogen bonding interactions break upon external forces, and the stronger interactions prevent complete material failure.

Shape memory polymers are stimuli-responsive polymers that can interchangeably switch from a temporarily fixed geometry to a previously programmed geometry upon applying an appropriate external stimulus.[250,251] This previously programmed geometry can be programmed in various ways, most commonly through permanent covalent cross-links and thermal transitions such as the polymer network's glass or melting transition temperature. Supramolecular polymers have been shown to exhibit shape memory effects utilising dynamic bonds, delivering tunability to mechanical properties and self-healing capabilities.[252] Ma and co-workers have developed a self-healing supramolecular bioelastomer capable of rapid shape memory recovery utilising a poly(glycerol sebacate) (PGS) backbone and UPy grafted via the hydroxy in the repeat unit.[253] Utilising UPy as a physical crosslink, the ability of the supramolecular polymer to heal was evaluated. Three temperatures were chosen for healing (37, 55 and 75 °C, respectively), and as anticipated, the healing efficiency increased with prolonged heating (12 hours) and at higher temperatures (75 °C). However, complete recovery of the mechanical properties was not achieved; in the case of the supramolecular polymer containing ~23 wt % UPy-HDI, a healing efficiency of 85% in terms of tensile strength and 60% for strain recovery was achieved when held at 55 °C for 12 hours in comparison to 40% and 25%, respectively, when exposed to the same temperature for only 30 minutes. At higher wt% values of UPy-HDI, similar healing efficiencies were observed, but relatively weak mechanical properties were recovered when exposed to 37 °C – healing required exposure to 55 °C and 75 °C for the mechanical properties to be regained effectively. Similarly, photo-crosslinked metallo-supramolecular polymers have been used to access shape-memory polymers, utilising light, heat, and or chemicals to disrupt the metal-ligand interactions to recover back to their permanent shape. Rowan and co-workers used a low molecular weight poly(butadiene) (**1.48**) end-capped with 4-hydroxy-2,6-bis(10-methylbenzimidazoyl)pyridine (HOMebip) (**1.49**) to deliver **1.50** and subsequently covalently crosslinked with a tetrathiol (**1.51**) in the presence of either a Zn or Eu metal salt (see Scheme 8).[254] Metal-ligand complexation acted as the hard phase and, as such, was used to fix a temporary shape. Upon breaking these metal-ligand interactions, the polymer material returned to its permanent shape. The cross-link density of the polymer was also investigated, and regardless of the number of cross-links per chain, excellent shape memory properties were observed.

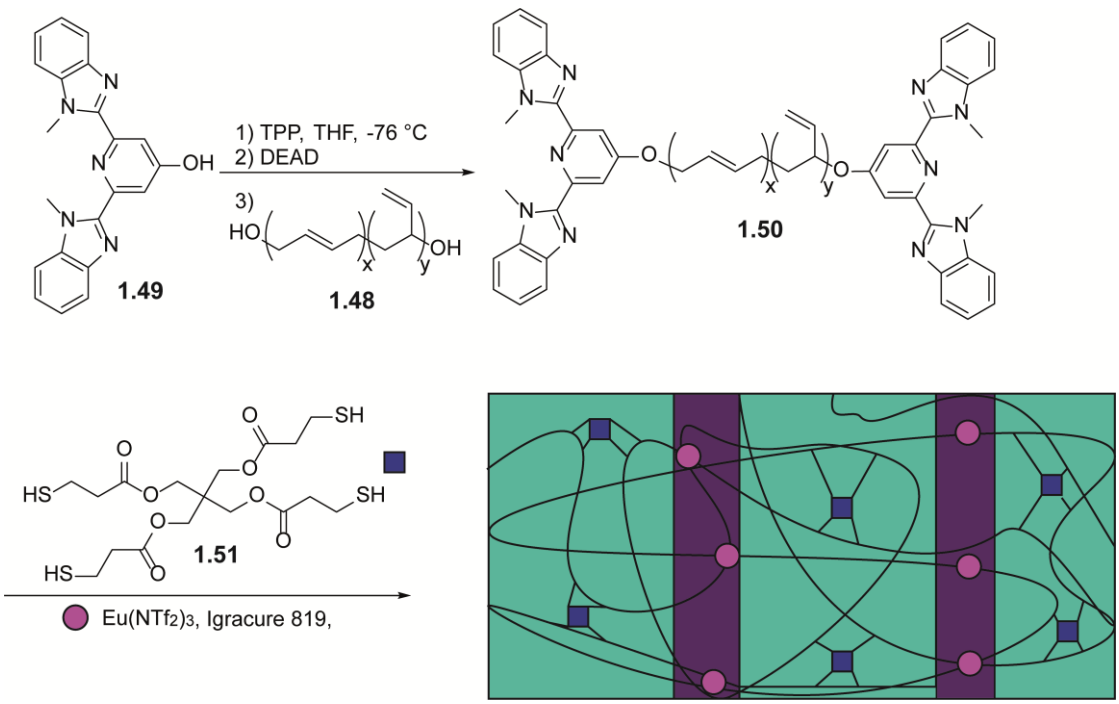

Scheme 8. Synthesis devised by Rowan and co-workers.[254] A metal-chelating ligand (**1.49**) end functionalised a poly(butadiene) core (**1.48**) to deliver a metallosupramolecular polymer (**1.50**) which was then covalently crosslinked with a tetrathiol crosslinker (**1.51**) and photoinitiator (Igracure 819).

Fu and co-workers designed self-healing polyurethane ureas, which were found to heal at 60 °C in 24 hours with healing efficiencies > 98.5%.[255] A commercially available polypropylene diisocyanate (PPGTD, M_n = 2300) was chain extended with three different diamines, and it was found that optimal self-healing was found when chain extending with a hindered aliphatic diamine, namely, isophorone diamine (IDA) to produce PPGTD-IDA (**1.52)**. Chain extending with a linear aliphatic hexane diamine (HDA) was found to produce a "poor self-healing" polyurethane urea (PPGTD-HDA **1.53**) and had a much higher polymer relaxation time (1.57 hours) in comparison to 390.1 seconds for PPGTD-IDA, as determined by the reciprocal of the crossover frequency determined by rheological measurements at a reference temperature of 26 °C (see Figure 16). No self-healing behaviour was observed when the chain was extended with an aromatic diamine, 1,4-phenylenediamine (PDA) (see **1.54**), and crossover events were not evident in rheological measurements up to 156 °C. Often the determinant self-healing behaviour is a result of chain mobility and rigidity, and a balancing act is required to produce materials that are sufficiently robust and possess self-healing capabilities.

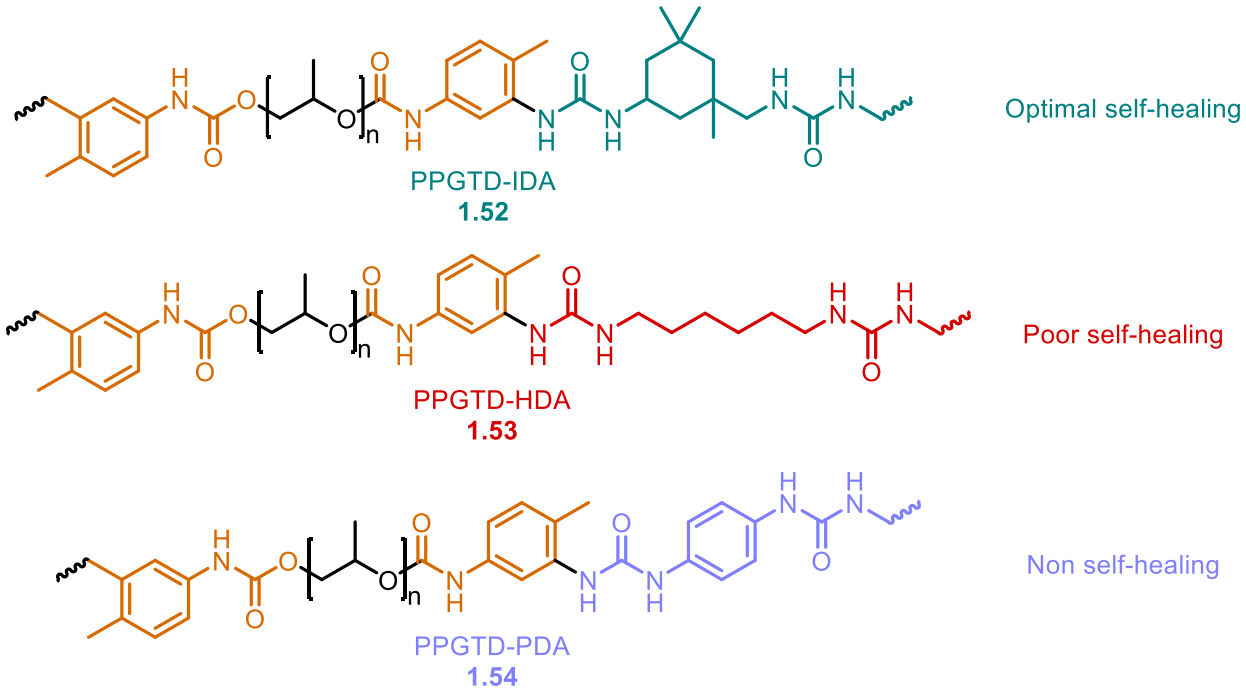

Figure 16. The chemical structures of PPGTD-IDA (**1.52**), PPGTD-HAD (**1.53**) and PPGTD-PDA (**1.54**).[255]

The result is not surprising, considering multiple bodies of work show that for effective self-healing of polymer networks, the relaxation time of the network at a given temperature should be in the range of 0.1 to 100 seconds and not on the order of multiple hours.[256–261]

Tong and co-workers designed a shape memory polyampholyte hydrogel (**1.55**) by the copolymerisation of a combination of weak, 2-(dimethylamino)-ethyl methacrylate (DMAEMA) (**1.56**), and strong, [3-(methacryloylamino)propyl]trimethylammonium chloride (MPTC) (**1.57**), cationic monomers, with stoichiometric equivalents of the anionic monomer *p*-styrene sulfonate hydrate (NaSS) (**1.58**) and covalently crosslinked with N,N'-methylenediacrylamide (BIS) (**1.59**) (see Scheme 9).[262] The geometry of the hydrogel could be temporarily fixed by protonation of DMAEMA in HCl solution; recovery of the original geometry could be achieved by subsequent deprotonation in NaOH solution. The hydrogel's tensile strength increased by 10-fold after cycling immersion of the hydrogel network in HCl and NaOH five times. Furthermore, the material was reported to be self-healing, with a healing percentage of 70% after being in contact with itself for 5 minutes.

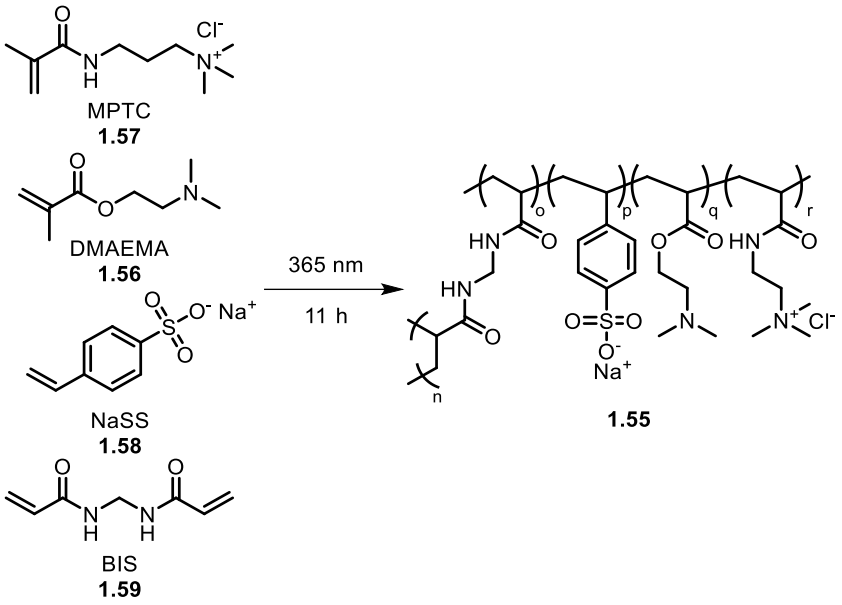

Scheme 9. The macromolecular design used by Tong and co-workers to develop self-healing polyampholyte hydrogels (**1.55**).[262]

Guo and co-workers prepared a highly transparent (optically transparency determined to be 93%), elastic, healable, and conductive supramolecular ionogel (**1.60**) that could be 3D-printed or used as a robust adhesive.[263] First reported in 2017,[264] an interesting synthetic procedure is used, in which a significant excess of isophorone diisocyanate (**1.61**) is converted to the respective amine by adding water *in situ* and allowed to react further (see Scheme 10). A similar approach is used to make polyurethane foams.[265] However, the CO_2 is trapped to deliver a cross-linked foam in the latter. In this instance, Guo and co-workers produce chain-extended poly(urethane-urea) with an elongation at break of 1500-2500%, depending on the ionic liquid content (20 to 50 wt.%). Similarly, an ultimate tensile strength between 16.81 – 1.85 MPa was achieved.

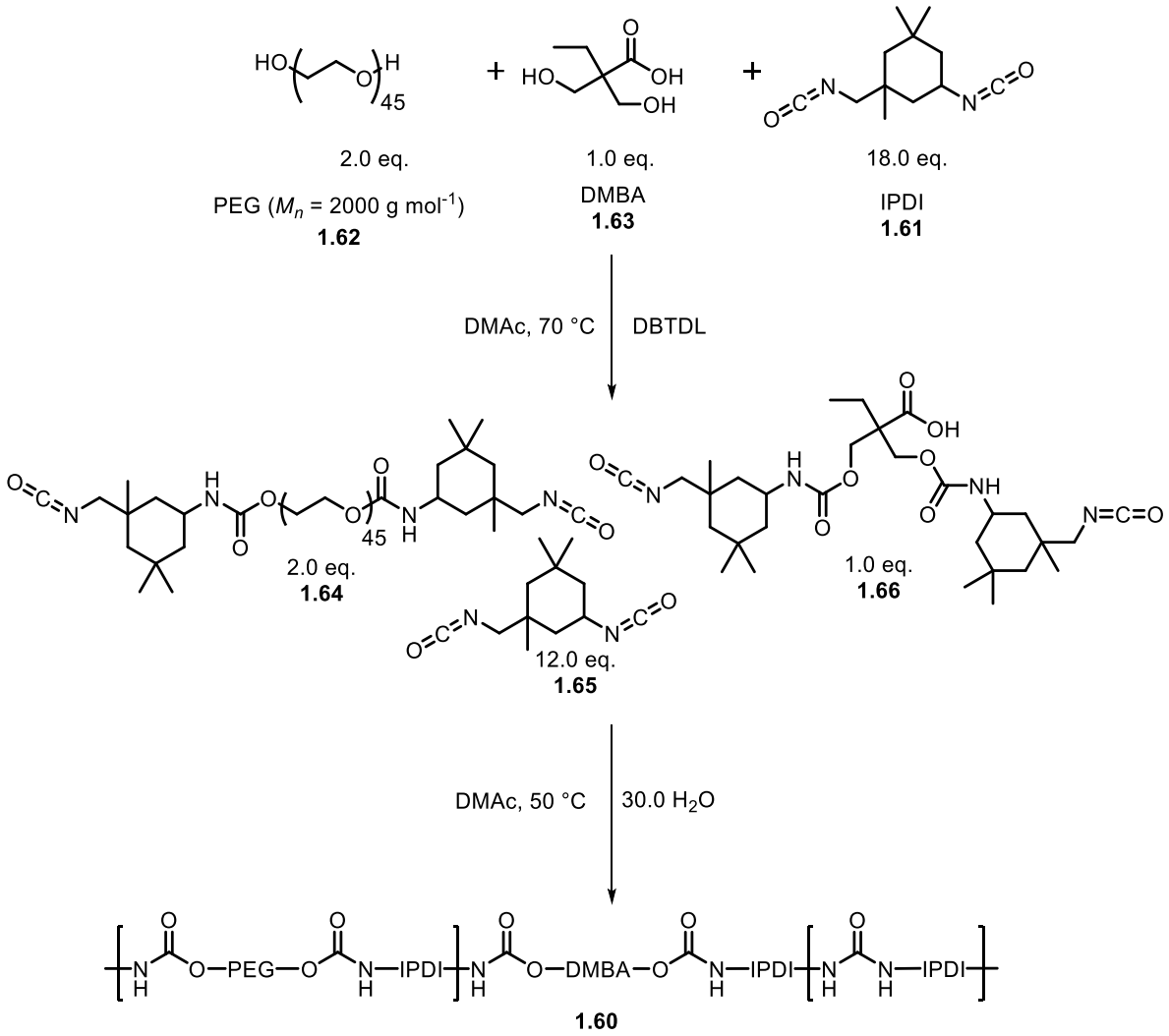

Scheme 10. Schematic for the synthesis of ionogels (**1.60**) developed by Guo and co-workers.[263]

Bouteiller and co-workers imparted self-healing properties to a PDMS thermoplastic elastomer by blending *n*-alkylated urea additives that can effectively soften the hard domains by accelerating the chain dynamics and disrupting bifurcated urea-urea stacking.[266] Meijer, Sijbesma and co-workers functionalised telechelic polymers, such as poly(ethylene-*co*-butylene)s,[179] and polysiloxanes,[89] with ureidopyrimidones (UPy) to deliver thermoreversible supramolecular materials. Anthamatten and co-workers integrated UPy side groups into linear and cross-linked siloxanes and realised biocompatible PDMS elastomers with control over variable stiffness and viscoelastic relaxation.[267] Wilson and co-workers examined hydrogen-bonding motifs and created self-sorting networks.[268,269]

Another use of healable supramolecular polymers for energy applications is their deployment in batteries. Organic cathode materials are promising candidates for a new generation of green batteries since they have low toxicity and can be produced from renewable resources. Deng and co-workers have built on the studies of Meijer and Sijbesma by applying their quadruple hydrogen-bonding motif,[89,179] ureidopyrimidinone,[85] to develop a healable supramolecular comb-polymer binder for high-performance silicone anodes for lithium-ion batteries.[270] Silicone

undergoes significant volume changes during charge and discharge cycles leading to loss of capacity and reduced life cycles. The healable polymer network comprising poly(acrylic acid) and ureidopyrimidinone (PAA-UPy) exhibited strong binding between the silicon particles. Furthermore, it was shown to effectively withstand the significant volume change of the silicon anode upon lithiation and delithiation through the reorganisation of the polymer network. The electrochemical properties of the PAA-UPy polymer binder were explored extensively, and an initial discharge capacity of 4194 mAh g^{-1} measured at a current density of 210 mA g^{-1} was achieved from the composite, whilst a relatively high capacity of 2638 mAh g^{-1} was achieved after 110 cycles, revealing reasonable long-term cycling stability. A favourable Columbic efficiency of 86.4% was superior to Si anodes using poly(acrylic acid), carboxymethyl cellulose, and polyvinylidene difluoride as binders. Furthermore, the anode with the dynamic polymer matrix showed the highest reversible capacity (3592 mAh g^{-1}) of all materials explored. In light of the reversible characteristics of the anode's polymer matrix, capacity retention of 2662 mAh g^{-1} was achieved, even at a high current density. This gave rise to an excellent performance rate compared to the control materials, with only a tiny impedance increase. The substantial enhancement in electrochemical performance of the PAA-UPy was attributed to the supramolecular network formed and the dynamic nature of the polymer matrix. It was proposed that the self-assembly of the polymer matrix may enable the development of stable silicone electrodes which high capacities and long-life cycles for use in commercial lithium-ion batteries.[270] A similar concept was also employed by Kwon *et al.*[271]. A host-guest system containing β-cyclodextrin recognition motifs on a polymer backbone blended with dendritic gallic acid crosslinkers containing adamantane was prepared for high-capacity silicon anodes. The dynamic network allowed for intimate and spontaneous interactions between complementary motifs, with an association constant of 104 M^{-1}, giving rise to a structurally stable electrode gel. Additionally, the polymeric network afforded possessed adhesive capabilities to silicone anodes. Fortuitously, the polymer could self-heal and be used to restore broken electrode contacts during the volume changes experienced during charge and discharge cycles. Furthermore, galvanostatic measurements with Li half-cells were performed to understand the effect of host-guest interactions on the electrochemical performance of silicon anodes. The highest capacity retention (90% after 150 cycles) was found in a 1:05 (CD:AD) stoichiometry, a significant improvement on conventional linear binders, which only achieved 30.5% after 150 cycles. Finally, SEM analysis was used to inspect the morphology of the silicon nanoparticles coated with β-cyclodextrin containing polymers. Even after 150 cycles, the material maintained well-defined morphologies without micro-cracks, suggesting that the dynamic crosslinking enabled stability throughout the large volume changes experienced in multiple charges and discharge cycles.

Matsumi and co-workers improved the performance of silicon anodes in lithium-ion batteries using a self-healing composite polymer binder for the silicon particles.[273] The binder was a

blend of an n-type conducting polymer, poly(bisiminoacenaphthenequinone) (BIAN-*p*-phenylene) (**1.67**) and a carboxylate-containing polymer poly(acrylic acid) (PAA) (**1.68**) which are postulated to interact through hydrogen bonding interactions (see Figure 17). The composite blend prevents the silicon particles from disintegrating over multiple charging cycles, and the hydrogen bonding between the polymer blend permits the material's self-repair. Thus, the n-doping effect of the BIAN-p-phenylene layer improves the conductivity of the anode and maintains a thin solid-electrolyte interphase (SEI). Si anodes were stabilised for greater than 600 cycles of charge-discharge, and a reversible capacity of 2100 mAh g^{-1}, ~95% capacity retention, and >99% Coulombic efficiency was achieved.

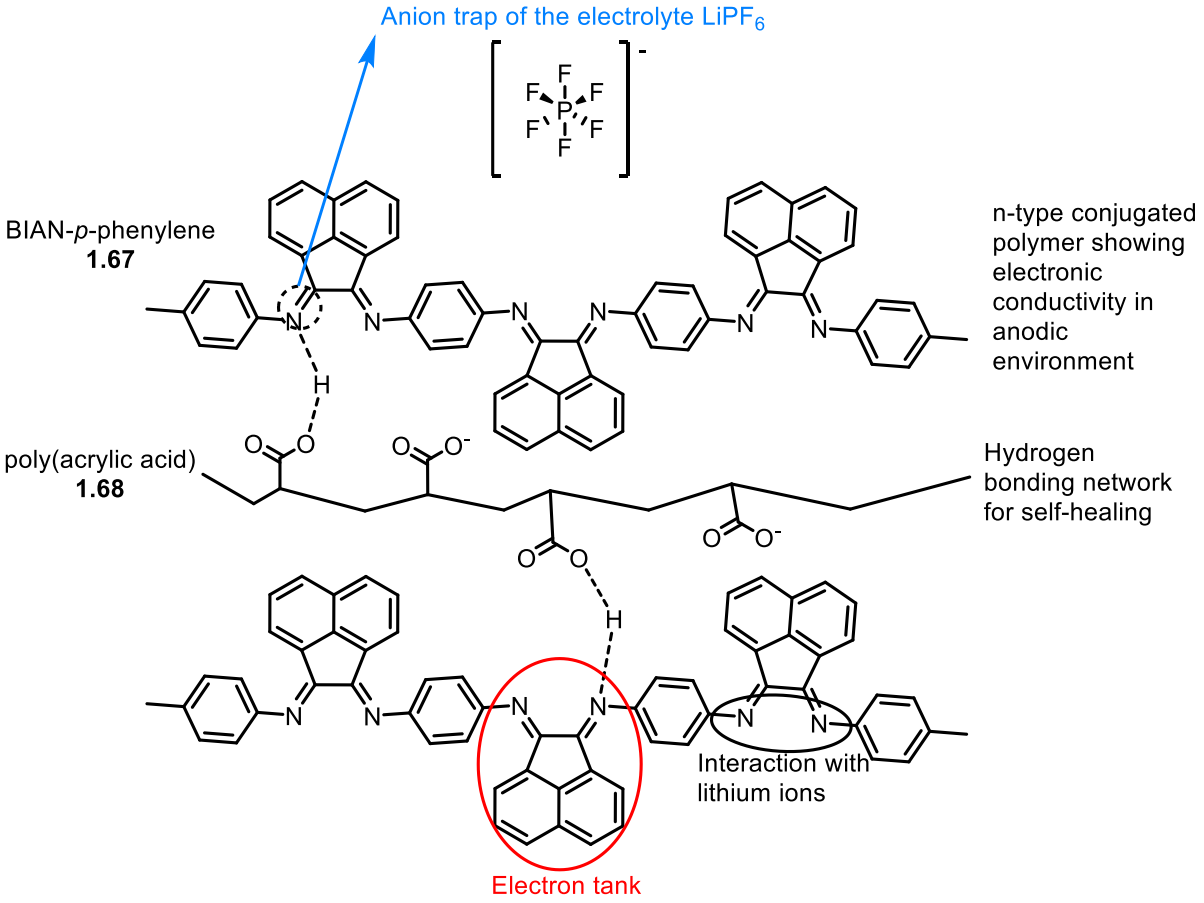

Figure 17. Schematic of the BIAN-*p*-phenylene/PAA composite blend devised by Matsumi and co-workers.[273]

Nicoud and co-workers investigated nitrophenyl urea crystal structures and found that the nitro oxygen acts as a competitive acceptor for acidic urea hydrogen donors and disrupts urea-urea interactions.[274] Gale and co-workers established that by applying nitrophenyl urea motifs to gelators, the main differences in gelation resulted from perturbation of the urea tape motif by strong nitro-urea interactions and not because of changes in the relative acidity of the urea protons.[275] Llansola *et al.* studied a meta-nitrophenyl urea hydrogelator and found it assembled into ribbons by intermolecular hydrogen bonding between carboxylic acid functional groups and carboxylic acid-nitro interactions.[276] Wood *et al.* later crystallised a para-nitro derivative

and found that it had an extended urea-urea tape structure that increased the ability of the hydrogelator to intercalate an aromatic dye.[277] Baker *et al.* demonstrated these aromatic nitro-urea receptors' utility and self-assembly capability by attaching a nitrophenyl urea group to a series of bi- and tri- armed poly(ethylene glycols) (PEGs).[278] By blending the bi- and tri-functionalised PEGs, polymer films capable of self-repair at room temperature were realised. Furthermore, the mechanical properties of the polymer blend could be tailored by altering the ratio of bi- to tri-functionalised PEG in the polymer film. A key advantage of utilising a polar PEG backbone was that the polymer film would swell and seal post-damage by exposure to water. However, the polar mid-block did not afford polymer films that were robust enough for tensile testing. Further developments by Baker *et al.* involved changing the polymer backbone to poly(propylene glycol) and adding a tripodal linker to afford a healable, mechanically robust supramolecular network made up of branched oligomer units capable of self-assembly through a nitrophenyl urea moiety (see Scheme 11).[22]

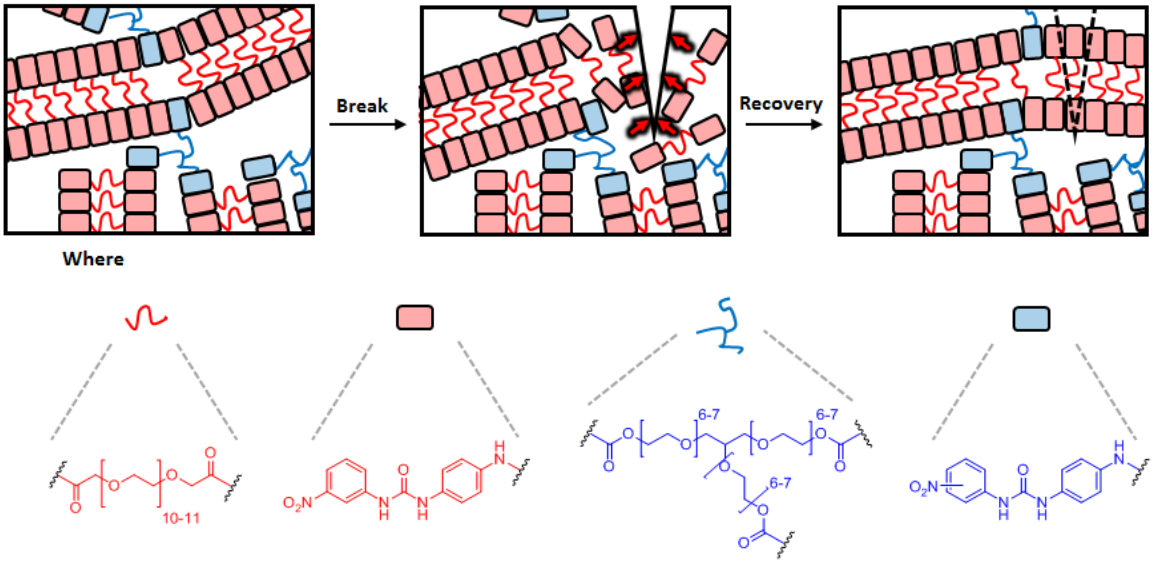

Scheme 11. A schematic representation of the nitro-aryl urea motif developed by Baker *et al.* end functionalising bi and tri-armed PEG units delivering a supramolecular network which upon a damage event can repair because of low molecular weight oligomers flowing and reassociating in the damaged region leading to bulk mechanical property recovery.[22]

Bouteiller and co-workers have subsequently illustrated the effects of conformation control of aromatic bis-urea systems through viscometry measurements with ortho-methyl substituents found to enforce a non-coplanar conformation between the urea and the phenyl moiety, in turn enhancing hydrogen bonding.[279]

1.4 Project Aims and Objectives

The field of healable materials is a rapidly developing field, and the number of publications has grown tremendously over the past decade. This thesis's focus has been exploring structure to property relationships in self-assembled systems to generate new healable materials suitable for use in cable coatings. Inspired by the studies of Baker *et al.* (who devised a bis-aromatic

urea assembly motif) and Bouteiller and co-workers, Chapter 2 describes a study of low molecular weight systems to explore how conformational control of assembly motifs can be utilised to realise a family of bis-aromatic urea hydrogelators. In the light of the results reported in Chapter 2, Chapter 3 details the investigation of the structure-property relationships between conformationally restricted nitro-aryl urea end groups and their ability to act as supramolecular synthons through the synthesis, characterisation, and mechanical testing of thirteen telechelic supramolecular poly(ethylene-*co*-butylene)s. Intrigued by studies reported by Long and co-workers[193] a change of strategy in terms of polymer structure was investigated; Chapter 4 describes the synthesis of chain-extended polyurethanes and incorporates a bis aromatic urea assembly motif into the repeat unit of the polymer network to tune mechanical properties. The intention is that by increasing the bis aromatic urea content, the mechanical properties of the resultant supramolecular polymer network could be tailored for self-healing applications. Chapter 5 provides an overarching summary of the studies described in this thesis and maps out scope for future studies on supramolecular materials of the type reported.

1.5 References

(1) Watson, J. D.; Crick, F. H. C. Molecular Structure of Nucleic Acids: A Structure for Deoxyribose Nucleic Acid. *Nature* **1953**, *171* (4356), 737–738. https://doi.org/10.1038/171737a0.

(2) Varshney, D.; Spiegel, J.; Zyner, K.; Tannahill, D.; Balasubramanian, S. The Regulation and Functions of DNA and RNA G-Quadruplexes. *Nat. Rev. Mol. Cell Biol.* **2020**, *21* (8), 459–474. https://doi.org/10.1038/s41580-020-0236-x.

(3) Mullis, K. B. The Polymerase Chain Reaction (Nobel Lecture). *Angew. Chemie Int. Ed. English* **1994**, *33* (12), 1209–1213. https://doi.org/10.1002/anie.199412091.

(4) Smith, M. Synthetic DNA and Biology (Nobel Lecture). *Angew. Chemie Int. Ed. English* **1994**, *33* (12), 1214–1221. https://doi.org/10.1002/anie.199412141.

(5) Steitz, T. A. From the Structure and Function of the Ribosome to New Antibiotics (Nobel Lecture). *Angew. Chemie - Int. Ed.* **2010**, *49* (26), 4381–4398. https://doi.org/10.1002/anie.201000708.

(6) Guo, P.; Zhang, H.; Liu, X.; Sun, J. Counteranion-Mediated Intrinsic Healing of Poly(Ionic Liquid) Copolymers. *ACS Appl. Mater. Interfaces* **2018**, *10* (2), 2105–2113. https://doi.org/10.1021/acsami.7b16880.

(7) Lei, Z.; Wu, P. A Supramolecular Biomimetic Skin Combining a Wide Spectrum of Mechanical Properties and Multiple Sensory Capabilities. *Nat. Commun.* **2018**, *9* (1), 1134. https://doi.org/10.1038/s41467-018-03456-w.

(8) Lei, Z.; Wu, P. A Highly Transparent and Ultra-Stretchable Conductor with Stable

Conductivity during Large Deformation. *Nat. Commun.* **2019**, *10* (1), 3429. https://doi.org/10.1038/s41467-019-11364-w.

(9) Fang, X.; Sun, J. One-Step Synthesis of Healable Weak-Polyelectrolyte-Based Hydrogels with High Mechanical Strength, Toughness, and Excellent Self-Recovery. *ACS Macro Lett.* **2019**, 500–505. https://doi.org/10.1021/acsmacrolett.9b00189.

(10) D'Angelo, A. J.; Panzer, M. J. Design of Stretchable and Self-Healing Gel Electrolytes via Fully Zwitterionic Polymer Networks in Solvate Ionic Liquids for Li-Based Batteries. *Chem. Mater.* **2019**, *31* (8), 2913–2922. https://doi.org/10.1021/acs.chemmater.9b00172.

(11) Stein, S.; Mordvinkin, A.; Voit, B.; Komber, H.; Saalwächter, K.; Böhme, F. Self-Healing and Reprocessable Bromo Butylrubber Based on Combined Ionic Cluster Formation and Hydrogen Bonding. *Polym. Chem.* **2020**, *11* (6), 1188–1197. https://doi.org/10.1039/c9py01630a.

(12) Kalista, S. J.; Ward, T. C. Thermal Characteristics of the Self-Healing Response in Poly(Ethylene-Co-Methacrylic Acid) Copolymers. *J. R. Soc. Interface* **2007**, *4* (13), 405–411. https://doi.org/10.1098/rsif.2006.0169.

(13) Mozhdehi, D.; Ayala, S.; Cromwell, O. R.; Guan, Z. Self-Healing Multiphase Polymers via Dynamic Metal–Ligand Interactions. *J. Am. Chem. Soc.* **2014**, *136* (46), 16128–16131. https://doi.org/10.1021/ja5097094.

(14) Li, C.-H.; Wang, C.; Keplinger, C.; Zuo, J.-L.; Jin, L.; Sun, Y.; Zheng, P.; Cao, Y.; Lissel, F.; Linder, C.; You, X.-Z.; Bao, Z. A Highly Stretchable Autonomous Self-Healing Elastomer. *Nat. Chem.* **2016**, *8* (6), 618–624. https://doi.org/10.1038/nchem.2492.

(15) Lai, J. C.; Li, L.; Wang, D. P.; Zhang, M. H.; Mo, S. R.; Wang, X.; Zeng, K. Y.; Li, C. H.; Jiang, Q.; You, X. Z.; Zuo, J. L. A Rigid and Healable Polymer Cross-Linked by Weak but Abundant Zn(II)-Carboxylate Interactions. *Nat. Commun.* **2018**, *9* (1). https://doi.org/10.1038/s41467-018-05285-3.

(16) Zhang, Q.; Niu, S.; Wang, L.; Lopez, J.; Chen, S.; Cai, Y.; Du, R.; Liu, Y.; Lai, J.-C. C.; Liu, L.; Li, C.-H. H.; Yan, X.; Liu, C.; Tok, J. B. H.; Jia, X.; Bao, Z. An Elastic Autonomous Self-Healing Capacitive Sensor Based on a Dynamic Dual Crosslinked Chemical System. *Adv. Mater.* **2018**, *30* (33), 1801435. https://doi.org/10.1002/adma.201801435.

(17) Chen, Y.; Kushner, A. M.; Williams, G. A.; Guan, Z. Multiphase Design of Autonomic Self-Healing Thermoplastic Elastomers. *Nat. Chem.* **2012**, *4* (6), 467–472. https://doi.org/10.1038/nchem.1314.

(18) Song, Y.; Liu, Y.; Qi, T.; Li, G. L. Towards Dynamic but Supertough Healable Polymers through Biomimetic Hierarchical Hydrogen-Bonding Interactions. *Angew. Chemie - Int.*

Ed. **2018**, *57* (42), 13838–13842. https://doi.org/10.1002/anie.201807622.

(19) Xu, J.; Chen, J.; Zhang, Y.; Liu, T.; Fu, J. A Fast Room-Temperature Self-Healing Glassy Polyurethane. *Angew. Chemie Int. Ed.* **2021**, *60* (14), 7947–7955. https://doi.org/10.1002/anie.202017303.

(20) Yan, X.; Liu, Z.; Zhang, Q.; Lopez, J.; Wang, H.; Wu, H.-C. C.; Niu, S.; Yan, H.; Wang, S.; Lei, T.; Li, J.; Qi, D.; Huang, P.; Huang, J.; Zhang, Y.; Wang, Y.; Li, G.; Tok, J. B. H.; Chen, X.; Bao, Z. Quadruple H-Bonding Cross-Linked Supramolecular Polymeric Materials as Substrates for Stretchable, Antitearing, and Self-Healable Thin Film Electrodes. *J. Am. Chem. Soc.* **2018**, *140* (15), 5280–5289. https://doi.org/10.1021/jacs.8b01682.

(21) Tamate, R.; Hashimoto, K.; Horii, T.; Hirasawa, M.; Li, X.; Shibayama, M.; Watanabe, M. Self-Healing Micellar Ion Gels Based on Multiple Hydrogen Bonding. *Adv. Mater.* **2018**, *30* (36), 1802792. https://doi.org/10.1002/adma.201802792.

(22) Baker, B. C.; German, I. M.; Stevens, G. C.; Colquhoun, H. M.; Hayes, W. Synthesis and Analysis of a Healable, Poly(Propylene Glycol)-Based Supramolecular Network. *Prog. Org. Coatings* **2019**, *127*, 260–265. https://doi.org/10.1016/j.porgcoat.2018.11.029.

(23) Zhang, Z. P.; Rong, M. Z.; Zhang, M. Q. Mechanically Robust, Self-Healable, and Highly Stretchable “Living” Crosslinked Polyurethane Based on a Reversible C–C Bond. *Adv. Funct. Mater.* **2018**, *28* (11), 1706050. https://doi.org/10.1002/adfm.201706050.

(24) Montarnal, D.; Tournilhac, F.; Hidalgo, M.; Couturier, J.-L. L.; Leibler, L. Versatile One-Pot Synthesis of Supramolecular Plastics and Self-Healing Rubbers. *J. Am. Chem. Soc.* **2009**, *131* (23), 7966–7967. https://doi.org/10.1021/ja903080c.

(25) Cordier, P.; Tournilhac, F.; Soulié-Ziakovic, C.; Leibler, L. Self-Healing and Thermoreversible Rubber from Supramolecular Assembly. *Nature* **2008**, *451* (7181), 977–980. https://doi.org/10.1038/nature06669.

(26) Zimmerman, S. C. A Journey in Bioinspired Supramolecular Chemistry: From Molecular Tweezers to Small Molecules That Target Myotonic Dystrophy. *Beilstein J. Org. Chem.* **2016**, *12*, 125–138. https://doi.org/10.3762/bjoc.12.14.

(27) Yang, K.; He, T.; Chen, X.; Cheng, S. Z. D.; Zhu, Y. Patternable Conjugated Polymers with Latent Hydrogen-Bonding on the Main Chain. *Macromolecules* **2014**, *47* (24), 8479–8486. https://doi.org/10.1021/ma501960t.

(28) Claessens, C. G.; Stoddart, J. F. π - π Interactions in Self-Assembly. *J. Phys. Org. Chem.* **1997**, *10* (5), 254–272. https://doi.org/10.1002/(SICI)1099-1395(199705)10:5<254::AID-POC875>3.0.CO;2-3.

(29) Greenland, B. W.; Burattini, S.; Hayes, W.; Colquhoun, H. M. Design, Synthesis and Computational Modelling of Aromatic Tweezer-Molecules as Models for Chain-Folding Polymer Blends. *Tetrahedron* **2008**, *64* (36), 8346–8354. https://doi.org/10.1016/j.tet.2008.05.077.

(30) Lee, J.; Jang, M.; Myeon Lee, S.; Yoo, D.; Shin, T. J.; Oh, J. H.; Yang, C. Fluorinated Benzothiadiazole (BT) Groups as a Powerful Unit for High-Performance Electron-Transporting Polymers. *ACS Appl. Mater. Interfaces* **2014**, *6* (22), 20390–20399. https://doi.org/10.1021/am505925w.

(31) Burattini, S.; Colquhoun, H. M.; Fox, J. D.; Friedmann, D.; Greenland, B. W.; Harris, P. J. F.; Hayes, W.; MacKay, M. E.; Rowan, S. J. A Self-Repairing, Supramolecular Polymer System: Healability as a Consequence of Donor-Acceptor π-π Stacking Interactions. *Chem. Commun.* **2009**, No. 44, 6717–6719. https://doi.org/10.1039/b910648k.

(32) Liu, J.; Tan, C. S. Y.; Yu, Z.; Li, N.; Abell, C.; Scherman, O. A. Tough Supramolecular Polymer Networks with Extreme Stretchability and Fast Room-Temperature Self-Healing. *Adv. Mater.* **2017**, *29* (22), 1605325. https://doi.org/10.1002/adma.201605325.

(33) Liu, J.; Tan, C. S. Y.; Scherman, O. A. Dynamic Interfacial Adhesion through Cucurbit[n]Uril Molecular Recognition. *Angew. Chemie - Int. Ed.* **2018**, *57* (29), 8854–8858. https://doi.org/10.1002/anie.201800775.

(34) McKee, J. R.; Appel, E. A.; Seitsonen, J.; Kontturi, E.; Scherman, O. A.; Ikkala, O. Healable, Stable and Stiff Hydrogels: Combining Conflicting Properties Using Dynamic and Selective Three-Component Recognition with Reinforcing Cellulose Nanorods. *Adv. Funct. Mater.* **2014**, *24* (18), 2706–2713. https://doi.org/10.1002/adfm.201303699.

(35) Appel, E. A.; Biedermann, F.; Rauwald, U.; Jones, S. T.; Zayed, J. M.; Scherman, O. A. Supramolecular Cross-Linked Networks via Host-Guest Complexation with Cucurbit[8]Uril. *J. Am. Chem. Soc.* **2010**, *132* (40), 14251–14260. https://doi.org/10.1021/ja106362w.

(36) Appel, E. A.; Del Barrio, J.; Loh, X. J.; Scherman, O. A. Supramolecular Polymeric Hydrogels. *Chem. Soc. Rev.* **2012**, *41* (18), 6195–6214. https://doi.org/10.1039/c2cs35264h.

(37) Zhang, Z.; Cheng, L.; Zhao, J.; Wang, L.; Liu, K.; Yu, W.; Yan, X. Synergistic Covalent and Supramolecular Polymers for Mechanically Robust but Dynamic Materials. *Angew. Chemie Int. Ed.* **2020**, *59* (29), 12139–12146. https://doi.org/10.1002/anie.202004152.

(38) Wang, Z.; Ren, Y.; Zhu, Y.; Hao, L.; Chen, Y.; An, G.; Wu, H.; Shi, X.; Mao, C. A Rapidly Self-Healing Host-Guest Supramolecular Hydrogel with High Mechanical Strength and

Excellent Biocompatibility. *Angew. Chemie* **2018**, *130* (29), 9146–9150. https://doi.org/10.1002/ange.201804400.

(39) Nakahata, M.; Mori, S.; Takashima, Y.; Yamaguchi, H.; Harada, A. Self-Healing Materials Formed by Cross-Linked Polyrotaxanes with Reversible Bonds. *Chem* **2016**, *1* (5), 766–775. https://doi.org/10.1016/j.chempr.2016.09.013.

(40) Lu, C.; Zhang, M.; Tang, D.; Yan, X.; Zhang, Z.; Zhou, Z.; Song, B.; Wang, H.; Li, X.; Yin, S.; Sepehrpour, H.; Stang, P. J. Fluorescent Metallacage-Core Supramolecular Polymer Gel Formed by Orthogonal Metal Coordination and Host–Guest Interactions. *J. Am. Chem. Soc.* **2018**, *140* (24), 7674–7680. https://doi.org/10.1021/jacs.8b03781.

(41) Urban, M. W.; Davydovich, D.; Yang, Y.; Demir, T.; Zhang, Y.; Casabianca, L. Key-and-Lock Commodity Self-Healing Copolymers. *Science (80-.).* **2018**, *362* (6411), 220–225. https://doi.org/10.1126/science.aat2975.

(42) Burattini, S.; Greenland, B. W.; Chappell, D.; Colquhoun, H. M.; Hayes, W. Healable Polymeric Materials: A Tutorial Review. *Chem. Soc. Rev.* **2010**, *39* (6), 1973–1985. https://doi.org/10.1039/b904502n.

(43) Hart, L. R.; Harries, J. L.; Greenland, B. W.; Colquhoun, H. M.; Hayes, W. Healable Supramolecular Polymers. *Polym. Chem.* **2013**, *4* (18), 4860–4870. https://doi.org/10.1039/c3py00081h.

(44) Fiore, G. L.; Rowan, S. J.; Weder, C. Optically Healable Polymers. *Chem. Soc. Rev.* **2013**, *42* (17), 7278–7288. https://doi.org/10.1039/c3cs35471g.

(45) Binder, W. H. *Self-Healing Polymers: From Principles to Applications*; Wiley-VCH, 2013. https://doi.org/10.1002/9783527670185.

(46) Thomas, S.; Surendran, A. *Self-Healing Polymer-Based Systems*; Elsevier, 2020.

(47) Lange, R. F. M.; Van Gurp, M.; Meijer, E. W. Hydrogen-Bonded Supramolecular Polymer Networks. *J. Polym. Sci. Part A Polym. Chem.* **1999**, *37* (19), 3657–3670. https://doi.org/10.1002/(SICI)1099-0518(19991001)37:19<3657::AID-POLA1>3.0.CO;2-6.

(48) Merino, D. H.; Feula, A.; Melia, K.; Slark, A. T.; Giannakopoulos, I.; Siviour, C. R.; Buckley, C. P.; Greenland, B. W.; Liu, D.; Gan, Y.; Harris, P. J.; Chippindale, A. M.; Hamley, I. W.; Hayes, W. A Systematic Study of the Effect of the Hard End-Group Composition on the Microphase Separation, Thermal and Mechanical Properties of Supramolecular Polyurethanes. *Polymer (Guildf).* **2016**, *107*, 368–378. https://doi.org/10.1016/j.polymer.2016.07.029.

(49) Yilgor, I.; Yilgor, E.; Guler, I. G.; Ward, T. C.; Wilkes, G. L. FTIR Investigation of the

Influence of Diisocyanate Symmetry on the Morphology Development in Model Segmented Polyurethanes. *Polymer (Guildf).* **2006**, *47* (11), 4105–4114. https://doi.org/10.1016/j.polymer.2006.02.027.

(50) Colquhoun, H. M. Self-Repairing Polymers: Materials That Heal Themselves. *Nat. Chem.* **2012**, *4* (6), 435–436. https://doi.org/10.1038/nchem.1357.

(51) Martín, N.; Nierengarten, J. F. *Supramolecular Chemistry of Fullerenes*; John Wiley & Sons Ltd, 2006; Vol. 62. https://doi.org/10.1016/j.tet.2005.12.050.

(52) Hoeben, F. J. M.; Jonkheijm, P.; Meijer, E. W.; Schenning, A. P. H. J. About Supramolecular Assemblies of π-Conjugated Systems. *Chem. Rev.* **2005**, *105* (4), 1491–1546. https://doi.org/10.1021/cr030070z.

(53) Faul, C. F. J.; Antonietti, M. Ionic Self-Assembly: Facile Synthesis of Supramolecular Materials. *Adv. Mater.* **2003**, *15* (9), 673–683. https://doi.org/10.1002/adma.200300379.

(54) Schalley, C. *Analytical Methods in Supramolecular Chemistry*; Schalley, C., Ed.; Wiley, 2007. https://doi.org/10.1002/9783527610273.

(55) Schoenmakers, S. M. C.; Spiering, A. J. H.; Herziger, S.; Böttcher, C.; Haag, R.; Palmans, A. R. A.; Meijer, E. W. Structure and Dynamics of Supramolecular Polymers: Wait and See. *ACS Macro Lett.* **2022**, *11* (5), 711–715. https://doi.org/10.1021/acsmacrolett.2c00223.

(56) Staudinger, H. Über Polymerisation. *Ber. Dtsch. Chem. Ges* **1920**, *53* (6), 1073–1085. https://doi.org/10.1002/cber.19200530627.

(57) Wolf, K. L.; Prahm, H.; Harms, H. Über Den Ordnungszustand Der Moleküle in Flüssigkeiten. *Zeitschrift für Phys. Chemie* **2017**, *36B* (1), 237–287. https://doi.org/10.1515/zpch-1937-3618.

(58) Lehn, J. -M. Supramolecular Chemistry—Scope and Perspectives Molecules, Supermolecules, and Molecular Devices (Nobel Lecture). *Angew. Chemie Int. Ed. English* **1988**, *27* (1), 89–112. https://doi.org/10.1002/anie.198800891.

(59) Lehn, J. M. Supramolecular Chemistry: Where from? Where To? *Chem. Soc. Rev.* **2017**, *46* (9), 2378–2379. https://doi.org/10.1039/c7cs00115k.

(60) Lehn, J. M. Cryptates: Inclusion Complexes of Macropolycyclic Receptor Molecules. *Pure Appl. Chem.* **1978**, *50* (9–10), 871–892. https://doi.org/10.1351/pac197850090871.

(61) Ashton, P. R.; Goodnow, T. T.; Kaifer, A. E.; Reddington, M. V.; Slawin, A. M. Z.; Spencer, N.; Stoddart, J. F.; Vicent, C.; Williams, D. J. A [2] Catenane Made to Order. *Angew. Chemie Int. Ed. English* **1989**, *28* (10), 1396–1399.

https://doi.org/10.1002/anie.198913961.

(62) Sauvage, J. P. Transition Metal-Containing Rotaxanes and Catenanes in Motion: Toward Molecular Machines and Motors. *Acc. Chem. Res.* **1998**, *31* (10), 611–619. https://doi.org/10.1021/ar960263r.

(63) Balzani, V.; Credi, A.; Raymo, F. M.; Stoddart, J. F. Artificial Molecular Machines. *Angew. Chemie* **2000**, *39* (19), 3348–3391. https://doi.org/10.1002/1521-3773(20001002)39:19<3348::AID-ANIE3348>3.0.CO;2-X.

(64) Collier, C. P.; Wong, E. W.; Belohradský, M.; Raymo, F. M.; Stoddart, J. F.; Kuekes, P. J.; Williams, R. S.; Heath, J. R. Electronically Configurable Molecular-Based Logic Gates. *Science (80-.).* **1999**, *285* (5426), 391–394. https://doi.org/10.1126/science.285.5426.391.

(65) Philp, D.; Stoddart, J. F. Self-Assembly in Natural and Unnatural Systems. *Angew. Chemie Int. Ed. English* **1996**, *35* (11), 1154–1196. https://doi.org/10.1002/anie.199611541.

(66) Rowan, S. J.; Cantrill, S. J.; Cousins, G. R. L.; Sanders, J. K. M.; Stoddart, J. F. Dynamic Covalent Chemistry. *Angew. Chemie Int. Ed.* **2002**, *41* (6), 898–952. https://doi.org/10.1002/1521-3773(20020315)41:6<898::AID-ANIE898>3.0.CO;2-E.

(67) Amabilino, D. B.; Stoddart, J. F. Interlocked and Intertwined Structures and Superstructures. *Chem. Rev.* **1995**, *95* (8), 2725–2828. https://doi.org/10.1021/cr00040a005.

(68) Collins, B. S. L.; Kistemaker, J. C. M.; Otten, E.; Feringa, B. L. A Chemically Powered Unidirectional Rotary Molecular Motor Based on a Palladium Redox Cycle. *Nat. Chem.* **2016**, *8* (9), 860–866. https://doi.org/10.1038/nchem.2543.

(69) Cheng, C.; McGonigal, P. R.; Schneebeli, S. T.; Li, H.; Vermeulen, N. A.; Ke, C.; Stoddart, J. F. An Artificial Molecular Pump. *Nat. Nanotechnol.* **2015**, *10* (6), 547–553. https://doi.org/10.1038/nnano.2015.96.

(70) Feringa, B. L. The Art of Building Small: From Molecular Switches to Motors (Nobel Lecture). *Angew. Chemie - Int. Ed.* **2017**, *56* (37), 11060–11078. https://doi.org/10.1002/anie.201702979.

(71) Stoddart, J. F. Mechanically Interlocked Molecules (MIMs)—Molecular Shuttles, Switches, and Machines (Nobel Lecture). *Angew. Chemie - Int. Ed.* **2017**, *56* (37), 11094–11125. https://doi.org/10.1002/anie.201703216.

(72) Sauvage, J. P. From Chemical Topology to Molecular Machines (Nobel Lecture). *Angew. Chemie - Int. Ed.* **2017**, *56* (37), 11080–11093.

https://doi.org/10.1002/anie.201702992.

(73) Lehn, J.-M. Perspectives in Supramolecular Chemistry—From Molecular Recognition towards Molecular Information Processing and Self-Organization. *Angew. Chemie Int. Ed. English* **1990**, *29* (11), 1304–1319. https://doi.org/10.1002/anie.199013041.

(74) Lehn, J.-M. Perspectives in Chemistry-Aspects of Adaptive Chemistry and Materials. *Angew. Chemie Int. Ed.* **2015**, *54* (11), 3276–3289. https://doi.org/10.1002/anie.201409399.

(75) Lehn, J. M. Dynamic Combinatorial Chemistry and Virtual Combinatorial Libraries. *Chem. - A Eur. J.* **1999**, *5* (9), 2455–2463. https://doi.org/10.1002/(sici)1521-3765(19990903)5:9<2455::aid-chem2455>3.0.co;2-h.

(76) Brunsveld, L.; Folmer, B. J. B.; Meijer, E. W.; Sijbesma, R. P. Supramolecular Polymers. *Chem. Rev.* **2001**, *101* (12), 4071–4097. https://doi.org/10.1021/cr990125q.

(77) De Greef, T. F. A.; Smulders, M. M. J.; Wolffs, M.; Schenning, A. P. H. J.; Sijbesma, R. P.; Meijer, E. W. Supramolecular Polymerization. *Chem. Rev.* **2009**, *109* (11), 5687–5754. https://doi.org/10.1021/cr900181u.

(78) Beijer, F. H.; Sijbesma, R. P.; Kooijman, H.; Spek, A. L.; Meijer, E. W. Strong Dimerization of Ureidopyrimidones via Quadruple Hydrogen Bonding. *J. Am. Chem. Soc.* **1998**, *120* (27), 6761–6769. https://doi.org/10.1021/ja974112a.

(79) Fouquey, C.; Lehn, J. -M; Levelut, A. -M. Molecular Recognition Directed Self-assembly of Supramolecular Liquid Crystalline Polymers from Complementary Chiral Components. *Adv. Mater.* **1990**, *2* (5), 254–257. https://doi.org/10.1002/adma.19900020506.

(80) Park, T.; Todd, E. M.; Nakashima, S.; Zimmerman, S. C. A Quadruply Hydrogen Bonded Heterocomplex Displaying High-Fidelity Recognition. *J. Am. Chem. Soc.* **2005**, *127* (51), 18133–18142. https://doi.org/10.1021/ja0545517.

(81) Sivakova, S.; Bohnsack, D. A.; Mackay, M. E.; Suwanmala, P.; Rowan, S. J. Utilization of a Combination of Weak Hydrogen-Bonding Interactions and Phase Segregation to Yield Highly Thermosensitive Supramolecular Polymers. *J. Am. Chem. Soc.* **2005**, *127* (51), 18202–18211. https://doi.org/10.1021/ja055245w.

(82) Nielsen, M. B.; Jeppesen, J. O.; Laut, J.; Lomholt, C.; Damgaard, D.; Jacobsen, J. P.; Becher, J.; Stoddart, J. F. Binding Studies between Tetrathiafulvalene Derivatives and Cyclobis(Paraquat-p-Phenylene). *J. Org. Chem.* **2001**, *66* (10), 3559–3563. https://doi.org/10.1021/jo010173m.

(83) Connors, K. A. Binding Constants: The Measurement of Molecular Complex Stability.

Eur. J. Med. Chem. **1987**, *22* (4), 373. https://doi.org/10.1016/0223-5234(87)90280-7.

(84) Kotera, M.; Lehn, J.-M.; Vigneron, J.-P. Design and Synthesis of Complementary Components for the Formation of Self-Assembled Supramolecular Rigid Rods. *Tetrahedron* **1995**, *51* (7), 1953–1972. https://doi.org/10.1016/0040-4020(94)01076-C.

(85) Sijbesma, R. P.; Beijer, F. H.; Brunsveld, L.; Folmer, B. J. B.; Hirschberg, J. H. K. K.; Lange, R. F. M.; Lowe, J. K. L.; Meijer, E. W. Reversible Polymers Formed from Self-Complementary Monomers Using Quadruple Hydrogen Bonding. *Science (80-.).* **1997**, *278* (5343), 1601–1604. https://doi.org/10.1126/science.278.5343.1601.

(86) Folmer, B. J. B.; Sijbesma, R. P.; Kooijman, H.; Spek, A. L.; Meijer, E. W. Cooperative Dynamics in Duplexes of Stacked Hydrogen-Bonded Moieties. *J. Am. Chem. Soc.* **1999**, *121* (39), 9001–9007. https://doi.org/10.1021/ja991409v.

(87) Lange, R. F. M.; Meijer, E. W. Supramolecular Polymer Interactions Based on the Alternating Copolymer of Styrene and Maleimide. *Macromolecules* **1995**, *28* (3), 782–783. https://doi.org/10.1021/ma00107a016.

(88) Müller, M.; Dardin, A.; Seidel, U.; Balsamo, V.; Iván, B.; Spiess, H. W.; Stadler, R. Junction Dynamics in Telechelic Hydrogen Bonded Polyisobutylene Networks. *Macromolecules* **1996**, *29* (7), 2577–2583. https://doi.org/10.1021/ma950984q.

(89) Hirschberg, J. H. K. K.; Beijer, F. H.; van Aert, H. A.; Magusin, P. C. M. M.; Sijbesma, R. P.; Meijer, E. W. Supramolecular Polymers from Linear Telechelic Siloxanes with Quadruple-Hydrogen-Bonded Units. *Macromolecules* **1999**, *32* (8), 2696–2705. https://doi.org/10.1021/ma981950w.

(90) Hart, L. R.; Hunter, J. H.; Nguyen, N. A.; Harries, J. L.; Greenland, B. W.; Mackay, M. E.; Colquhoun, H. M.; Hayes, W. Multivalency in Healable Supramolecular Polymers: The Effect of Supramolecular Cross-Link Density on the Mechanical Properties and Healing of Non-Covalent Polymer Networks. *Polym. Chem.* **2014**, *5* (11), 3680–3688. https://doi.org/10.1039/c4py00292j.

(91) Merino, D. H.; Slark, A. T.; Colquhoun, H. M.; Hayes, W.; Hamley, I. W. Thermo-Responsive Microphase Separated Supramolecular Polyurethanes. *Polym. Chem.* **2010**, *1* (8), 1263–1271. https://doi.org/10.1039/c0py00122h.

(92) Kumpfer, J. R.; Rowan, S. J. Thermo-, Photo-, and Chemo-Responsive Shape-Memory Properties from Photo-Cross-Linked Metallo-Supramolecular Polymers. *J. Am. Chem. Soc.* **2011**, *133* (32), 12866–12874. https://doi.org/10.1021/ja205332w.

(93) De Greef, T. F. A.; Nieuwenhuizen, M. M. L.; Sijbesma, R. P.; Meijer, E. W. Competitive Intramolecular Hydrogen Bonding in Oligo(Ethylene Oxide) Substituted Quadruple Hydrogen Bonded Systems. *J. Org. Chem.* **2010**, *75* (3), 598–610.

https://doi.org/10.1021/jo902053t.

(94) Brassinne, J.; Cadix, A.; Wilson, J.; Ruymbeke, E. Van. Dissociating Sticker Dynamics from Chain Relaxation in Supramolecular Polymer Networks — The Importance of Free Partner ! **2017**, *1123*, 1122–1134.

(95) Appel, E. A.; Forster, R. A.; Rowland, M. J.; Scherman, O. A. The Control of Cargo Release from Physically Crosslinked Hydrogels by Crosslink Dynamics. *Biomaterials* **2014**, *35* (37), 9897–9903. https://doi.org/10.1016/j.biomaterials.2014.08.001.

(96) Xu, Z.; Kramer, E. J.; Edgecombe, B. D.; Fréchet, J. M. J. Strengthening Polymer Phase Boundaries with Hydrogen-Bonding Random Copolymers. *Macromolecules* **1997**, *30* (25), 7958–7963. https://doi.org/10.1021/ma9609590.

(97) Edgecombe, B. D.; Stein, J. A.; Fréchet, J. M. J.; Xu, Z.; Kramer, E. J. The Role of Polymer Architecture in Strengthening Polymer-Polymer Interfaces: A Comparison of Graft, Block, and Random Copolymers Containing Hydrogen-Bonding Moieties. *Macromolecules* **1998**, *31* (4), 1292–1304. https://doi.org/10.1021/ma970832q.

(98) Vaiyapuri, R.; Greenland, B. W.; Rowan, S. J.; Colquhoun, H. M.; Elliott, J. M.; Hayes, W. Thermoresponsive Supramolecular Polymer Network Comprising Pyrene-Functionalized Gold Nanoparticles and a Chain-Folding Polydiimide. *Macromolecules* **2012**, *45* (13), 5567–5574. https://doi.org/10.1021/ma300796w.

(99) Vaiyapuri, R.; Greenland, B. W.; Colquhoun, H. M.; Elliott, J. M.; Hayes, W. Molecular Recognition between Functionalized Gold Nanoparticles and Healable, Supramolecular Polymer Blends-a Route to Property Enhancement. *Polym. Chem.* **2013**, *4* (18), 4902–4909. https://doi.org/10.1039/c3py00086a.

(100) Kim, S. H.; Seo, H.; Kang, J.; Hong, J.; Seong, D.; Kim, H.-J.; Kim, J.; Mun, J.; Youn, I.; Kim, J.; Kim, Y.-C.; Seok, H.-K.; Lee, C.; Tok, J. B. H.; Bao, Z.; Son, D. An Ultrastretchable and Self-Healable Nanocomposite Conductor Enabled by Autonomously Percolative Electrical Pathways. *ACS Nano* **2019**, *13* (6), 6531–6539. https://doi.org/10.1021/acsnano.9b00160.

(101) Tee, B. C. K.; Wang, C.; Allen, R.; Bao, Z. An Electrically and Mechanically Self-Healing Composite with Pressure- and Flexion-Sensitive Properties for Electronic Skin Applications. *Nat. Nanotechnol.* **2012**, *7* (12), 825–832. https://doi.org/10.1038/nnano.2012.192.

(102) Biyani, M. V.; Foster, E. J.; Weder, C. Light-Healable Supramolecular Nanocomposites Based on Modified Cellulose Nanocrystals. *ACS Macro Lett.* **2013**, *2* (3), 236–240. https://doi.org/10.1021/mz400059w.

(103) Fox, J.; Wie, J. J.; Greenland, B. W.; Burattini, S.; Hayes, W.; Colquhoun, H. M.;

MacKay, M. E.; Rowan, S. J. High-Strength, Healable, Supramolecular Polymer Nanocomposites. *J. Am. Chem. Soc.* **2012**, *134* (11), 5362–5368. https://doi.org/10.1021/ja300050x.

(104) Huo, Y.; He, Z.; Wang, C.; Zhang, L.; Xuan, Q.; Wei, S.; Wang, Y.; Pan, D.; Dong, B.; Wei, R.; Naik, N.; Guo, Z. The Recent Progress of Synergistic Supramolecular Polymers: Preparation, Properties and Applications. *Chem. Commun.* **2021**, *57* (12), 1413–1429. https://doi.org/10.1039/d0cc07247h.

(105) van Tomme, S. R.; van Steenbergen, M. J.; de Smedt, S. C.; van Nostrum, C. F.; Hennink, W. E. Self-Gelling Hydrogels Based on Oppositely Charged Dextran Microspheres. *Biomaterials* **2005**, *26* (14), 2129–2135. https://doi.org/10.1016/j.biomaterials.2004.05.035.

(106) Varley, R. J.; van der Zwaag, S. Towards an Understanding of Thermally Activated Self-Healing of an Ionomer System during Ballistic Penetration. *Acta Mater.* **2008**, *56* (19), 5737–5750. https://doi.org/10.1016/j.actamat.2008.08.008.

(107) Zhan, S.; Wang, X.; Sun, J. Rediscovering Surlyn: A Supramolecular Thermoset Capable of Healing and Recycling. *Macromol. Rapid Commun.* **2020**, *41* (24), 2000097. https://doi.org/10.1002/marc.202000097.

(108) Khalily, M. A.; Bakan, G.; Kucukoz, B.; Topal, A. E.; Karatay, A.; Yaglioglu, H. G.; Dana, A.; Guler, M. O. Fabrication of Supramolecular n/p-Nanowires via Coassembly of Oppositely Charged Peptide-Chromophore Systems in Aqueous Media. *ACS Nano* **2017**, *11* (7), 6881–6892. https://doi.org/10.1021/acsnano.7b02025.

(109) Schenning, A. P. H. J.; Meijer, E. W. Supramolecular Electronics; Nanowires from Self-Assembled π-Conjugated Systems. *Chem. Commun.* **2005**, No. 26, 3245–3258. https://doi.org/10.1039/b501804h.

(110) Carroll, R. L.; Gorman, C. B. The Genesis of Molecular Electronics. *Angew. Chemie Int. Ed.* **2002**, *41* (23), 4378–4400. https://doi.org/10.1002/1521-3773(20021202)41:23<4378::AID-ANIE4378>3.0.CO;2-A.

(111) Joachim, C.; Gimzewski, J. K.; Aviram, A. Electronics Using Hybrid-Molecular and Mono-Molecular Devices. *Nature* **2000**, *408* (6812), 541–548. https://doi.org/10.1038/35046000.

(112) Bronstein, H.; Nielsen, C. B.; Schroeder, B. C.; McCulloch, I. The Role of Chemical Design in the Performance of Organic Semiconductors. *Nat. Rev. Chem.* **2020**, *4* (2), 66–77. https://doi.org/10.1038/s41570-019-0152-9.

(113) Whittell, G. R.; Hager, M. D.; Schubert, U. S.; Manners, I. Functional Soft Materials from Metallopolymers and Metallosupramolecular Polymers. *Nat. Mater.* **2011**, *10* (3), 176–

188. https://doi.org/10.1038/nmat2966.

(114) Batten, S. R.; Robson, R. Interpenetrating Nets: Ordered, Periodic Entanglement. *Angew. Chemie - Int. Ed.* **1998**, *37* (11), 1460–1494. https://doi.org/10.1002/(SICI)1521-3773(19980619)37:11<1460::AID-ANIE1460>3.0.CO;2-Z.

(115) Hagrman, P. J.; Hagrman, D.; Zubieta, J. Organic-Inorganic Hybrid Materials: From “simple” Coordination Polymers to Organodiamine-Templated Molybdenum Oxides. *Angew. Chemie - Int. Ed.* **1999**, *38* (18), 2638–2684. https://doi.org/10.1002/(SICI)1521-3773(19990917)38:18<2638::AID-ANIE2638>3.0.CO;2-4.

(116) Lehn, J.-M. Toward Self-Organization and Complex Matter. *Science (80-.).* **2002**, *295* (5564), 2400–2403. https://doi.org/10.1126/science.1071063.

(117) Burnworth, M.; Tang, L.; Kumpfer, J. R.; Duncan, A. J.; Beyer, F. L.; Fiore, G. L.; Rowan, S. J.; Weder, C. Optically Healable Supramolecular Polymers. *Nature* **2011**, *472* (7343), 334–337. https://doi.org/10.1038/nature09963.

(118) Tian, M.; Tian, M.; Tian, M.; Zuo, H.; Wang, J.; Ning, N.; Ning, N.; Ning, N.; Yu, B.; Yu, B.; Yu, B.; Zhang, L.; Zhang, L.; Zhang, L. A Silicone Elastomer with Optimized and Tunable Mechanical Strength and Self-Healing Ability Based on Strong and Weak Coordination Bonds. *Polym. Chem.* **2020**, *11* (24), 4047–4057. https://doi.org/10.1039/d0py00434k.

(119) Rao, Y. L.; Chortos, A.; Pfattner, R.; Lissel, F.; Chiu, Y. C.; Feig, V.; Xu, J.; Kurosawa, T.; Gu, X.; Wang, C.; He, M.; Chung, J. W.; Bao, Z. Stretchable Self-Healing Polymeric Dielectrics Cross-Linked through Metal-Ligand Coordination. *J. Am. Chem. Soc.* **2016**, *138* (18), 6020–6027. https://doi.org/10.1021/jacs.6b02428.

(120) Wu, X.; Luo, R.; Li, Z.; Wang, J.; Yang, S. Readily Self-Healing Polymers at Subzero Temperature Enabled by Dual Cooperative Crosslink Strategy for Smart Paint. *Chem. Eng. J.* **2020**, *398* (November 2019), 125593. https://doi.org/10.1016/j.cej.2020.125593.

(121) Hunter, C. A.; Sanders, J. K. M. The Nature of π-π Interactions. *J. Am. Chem. Soc.* **1990**, *112* (14), 5525–5534. https://doi.org/10.1021/ja00170a016.

(122) Müller-Dethlefs, K.; Hobza, P. Noncovalent Interactions: A Challenge for Experiment and Theory. *Chem. Rev.* **2000**, *100* (1), 143–167. https://doi.org/10.1021/cr9900331.

(123) Martinez, C. R.; Iverson, B. L. Rethinking the Term “Pi-Stacking.” *Chem. Sci.* **2012**, *3* (7), 2191. https://doi.org/10.1039/c2sc20045g.

(124) Hobza, P.; Selzle, H. L.; Schlag, E. W. Potential Energy Surface for the Benzene Dimer. Results of *Ab Initio* CCSD(T) Calculations Show Two Nearly Isoenergetic Structures: T-Shaped and Parallel-Displaced. *J. Phys. Chem.* **1996**, *100* (48), 18790–18794.

https://doi.org/10.1021/jp961239y.

(125) Burattini, S.; Greenland, B. W.; Merino, D. H.; Weng, W.; Seppala, J.; Colquhoun, H. M.; Hayes, W.; MacKay, M. E.; Hamley, I. W.; Rowan, S. J. A Healable Supramolecular Polymer Blend Based on Aromatic π-π Stacking and Hydrogen-Bonding Interactions. *J. Am. Chem. Soc.* **2010**, *132* (34), 12051–12058. https://doi.org/10.1021/ja104446r.

(126) Nakahata, M.; Takashima, Y.; Yamaguchi, H.; Harada, A. Redox-Responsive Self-Healing Materials Formed from Host–Guest Polymers. *Nat. Commun.* **2011**, *2* (1), 511. https://doi.org/10.1038/ncomms1521.

(127) Yu, G.; Han, C.; Zhang, Z.; Chen, J.; Yan, X.; Zheng, B.; Liu, S.; Huang, F. Pillar[6]Arene-Based Photoresponsive Host-Guest Complexation. *J. Am. Chem. Soc.* **2012**, *134* (20), 8711–8717. https://doi.org/10.1021/ja302998q.

(128) Xue, M.; Yang, Y.; Chi, X.; Zhang, Z.; Huang, F. Pillararenes, a New Class of Macrocycles for Supramolecular Chemistry. *Acc. Chem. Res.* **2012**, *45* (8), 1294–1308. https://doi.org/10.1021/ar2003418.

(129) Shao, L.; Yang, J.; Hua, B. A Dual-Responsive Cross-Linked Supramolecular Polymer Network Gel: Hierarchical Supramolecular Self-Assembly Driven by Pillararene-Based Molecular Recognition and Metal-Ligand Interactions. *Polym. Chem.* **2018**, *9* (11), 1293–1297. https://doi.org/10.1039/c8py00057c.

(130) Ogoshi, T.; Yamagishi, T. A. Pillararenes: Versatile Synthetic Receptors for Supramolecular Chemistry. *European J. Org. Chem.* **2013**, No. 15, 2961–2975. https://doi.org/10.1002/ejoc.201300079.

(131) Kakuta, T.; Yamagishi, T. A.; Ogoshi, T. Stimuli-Responsive Supramolecular Assemblies Constructed from Pillar[n]Arenes. *Acc. Chem. Res.* **2018**, *51* (7), 1656–1666. https://doi.org/10.1021/acs.accounts.8b00157.

(132) Ogoshi, T. Synthesis of Novel Pillar-Shaped Cavitands “Pillar[5]Arenes” and Their Application for Supramolecular Materials. *J. Incl. Phenom. Macrocycl. Chem.* **2012**, *72* (3–4), 247–262. https://doi.org/10.1007/s10847-011-0027-2.

(133) Wang, Z.; Shui, M.; Wyman, I. W.; Zhang, Q. W.; Wang, R. Cucurbit[8]Uril-Based Supramolecular Hydrogels for Biomedical Applications. *RSC Med. Chem.* **2021**, *12* (5), 722–729. https://doi.org/10.1039/d1md00019e.

(134) Gao, R. H.; Huang, Y.; Chen, K.; Tao, Z. Cucurbit[n]Uril/Metal Ion Complex-Based Frameworks and Their Potential Applications. *Coord. Chem. Rev.* **2021**, *437*, 213741. https://doi.org/10.1016/j.ccr.2020.213741.

(135) Biedermann, F.; Uzunova, V. D.; Scherman, O. A.; Nau, W. M.; De Simone, A. Release

of High-Energy Water as an Essential Driving Force for the High-Affinity Binding of Cucurbit[n]Urils. *J. Am. Chem. Soc.* **2012**, *134* (37), 15318–15323. https://doi.org/10.1021/ja303309e.

(136) Isaacs, L. Stimuli Responsive Systems Constructed Using Cucurbit[n]Uril-Type Molecular Containers. *Acc. Chem. Res.* **2014**, *47* (7), 2052–2062. https://doi.org/10.1021/ar500075g.

(137) Jon, S. Y.; Selvapalam, N.; Oh, D. H.; Kang, J. K.; Kim, S. Y.; Jeon, Y. J.; Lee, J. W.; Kim, K. Facile Synthesis of Cucurbit[n]Uril Derivatives via Direct Functionalization: Expanding Utilization of Cucurbit[n]Uril. *J. Am. Chem. Soc.* **2003**, *125* (34), 10186–10187. https://doi.org/10.1021/ja036536c.

(138) Liu, S.; Ruspic, C.; Mukhopadhyay, P.; Chakrabarti, S.; Zavalij, P. Y.; Isaacs, L. The Cucurbit[n]Uril Family: Prime Components for Self-Sorting Systems. *J. Am. Chem. Soc.* **2005**, *127* (45), 15959–15967. https://doi.org/10.1021/ja055013x.

(139) Masson, E.; Ling, X.; Joseph, R.; Kyeremeh-Mensah, L.; Lu, X. *Cucurbituril Chemistry: A Tale of Supramolecular Success*. Vol. 2. *RSC Adv.*, **2012**, *2*, 1213-1247. https://doi.org/10.1039/c1ra00768h.

(140) Kim, K.; Selvapalam, N.; Ho Ko, Y.; Min Park, K.; Kim, D.; Kim, J. Functionalized Cucurbiturils and Their Applications. *Chem. Soc. Rev.* **2007**, *36* (2), 267–279. https://doi.org/10.1039/b603088m.

(141) Lagona, J.; Mukhopadhyay, P.; Chakrabarti, S.; Isaacs, L. The Cucurbit[n]Uril Family. *Angew. Chemie - Int. Ed.* **2005**, *44* (31), 4844–4870. https://doi.org/10.1002/anie.200460675.

(142) Lee, J. W.; Samal, S.; Selvapalam, N.; Kim, H. J.; Kim, K. Cucurbituril Homologues and Derivatives: New Opportunities in Supramolecular Chemistry. *Acc. Chem. Res.* **2003**, *36* (8), 621–630. https://doi.org/10.1021/ar020254k.

(143) Ovsyannikov, A.; Solovieva, S.; Antipin, I.; Ferlay, S. Coordination Polymers Based on Calixarene Derivatives: Structures and Properties. *Coord. Chem. Rev.* **2017**, *352*, 151–186. https://doi.org/10.1016/j.ccr.2017.09.004.

(144) Arora, V.; Chawla, H. M.; Singh, S. P. Calixarenes as Sensor Materials for Recognition and Separation of Metal Ions. *Arkivoc* **2007**, *2007* (2), 172–200. https://doi.org/10.3998/ark.5550190.0008.205.

(145) Yang, X.; Yu, H.; Wang, L.; Tong, R.; Akram, M.; Chen, Y.; Zhai, X. Self-Healing Polymer Materials Constructed by Macrocycle-Based Host-Guest Interactions. *Soft Matter* **2015**, *11* (7), 1242–1252. https://doi.org/10.1039/c4sm02372b.

(146) Zadmard, R.; Hokmabadi, F.; Jalali, M. R.; Akbarzadeh, A. Recent Progress to Construct Calixarene-Based Polymers Using Covalent Bonds: Synthesis and Applications. *RSC Adv.* **2020**, *10* (54), 32690–32722. https://doi.org/10.1039/d0ra05707j.

(147) Zheng, B.; Wang, F.; Dong, S.; Huang, F. Supramolecular Polymers Constructed by Crown Ether-Based Molecular Recognition. *Chem. Soc. Rev.* **2012**, *41* (5), 1621–1636. https://doi.org/10.1039/c1cs15220c.

(148) Sinawang, G.; Osaki, M.; Takashima, Y.; Yamaguchi, H.; Harada, A. Supramolecular Self-Healing Materials from Non-Covalent Cross-Linking Host-Guest Interactions. *Chem. Commun.* **2020**, *56* (32), 4381–4395. https://doi.org/10.1039/d0cc00672f.

(149) Xiao, L.; Shi, J.; Wu, K.; Lu, M. Self-Healing Supramolecular Waterborne Polyurethane Based on Host–Guest Interactions and Multiple Hydrogen Bonds. *React. Funct. Polym.* **2020**, *148* (January), 104482. https://doi.org/10.1016/j.reactfunctpolym.2020.104482.

(150) Zhu, Z.; Liu, J. D.; Liu, C.; Wu, X.; Li, Q.; Chen, S.; Zhao, X.; Weitz, D. A. Microfluidics-Assisted Assembly of Injectable Photonic Hydrogels toward Reflective Cooling. *Small* **2020**, *16* (9), 1903939. https://doi.org/10.1002/smll.201903939.

(151) Huggins, M. L. The Hydrogen Bond (Pimentel, George C.; McClellan, Aubrey L.). *J. Chem. Educ.* **1960**, *37* (11), A754. https://doi.org/10.1021/ed037pa754.

(152) Jeffrey, G. A.; Saenger, W. *Hydrogen Bonding in Biological Structures*; Springer, Berlin Heidelberg, 1991. https://doi.org/10.1007/978-3-642-85135-3.

(153) Ishikawa, N.; Furutani, M.; Arimitsu, K. Adhesive Materials Utilizing a Thymine–Adenine Interaction and Thymine Photodimerization. *ACS Macro Lett.* **2015**, *4* (7), 741–744. https://doi.org/10.1021/acsmacrolett.5b00359.

(154) Zhang, K.; Aiba, M.; Fahs, G. B.; Hudson, A. G.; Chiang, W. D.; Moore, R. B.; Ueda, M.; Long, T. E. Nucleobase-Functionalized Acrylic ABA Triblock Copolymers and Supramolecular Blends. *Polym. Chem.* **2015**, *6* (13), 2434–2444. https://doi.org/10.1039/c4py01798f.

(155) Cheng, S.; Zhang, M.; Dixit, N.; Moore, R. B.; Long, T. E. Nucleobase Self-Assembly in Supramolecular Adhesives. *Macromolecules* **2012**, *45* (2), 805–812. https://doi.org/10.1021/ma202122r.

(156) Cortese, J.; Soulié-Ziakovic, C.; Leibler, L. Binding and Supramolecular Organization of Homo- and Heterotelechelic Oligomers in Solutions. *Polym. Chem.* **2014**, *5* (1), 116–125. https://doi.org/10.1039/c3py00638g.

(157) Rudkevich, D. M.; Shivanyuk, A. N.; Brzozka, Z.; Verboom, W.; Reinhoudt, D. N. A Self-

Assembled Bifunctional Receptor. *Angew. Chemie Int. Ed. English* **1995**, *34* (19), 2124–2126. https://doi.org/10.1002/anie.199521241.

(158) Fogleman, E. A.; Yount, W. C.; Xu, J.; Craig, S. L. Modular, Well-Behaved Reversible Polymers from DNA-Based Monomers. *Angew. Chemie Int. Ed.* **2002**, *41* (21), 4026–4028. https://doi.org/10.1002/1521-3773(20021104)41:21<4026::AID-ANIE4026>3.0.CO;2-E.

(159) Xu, J.; Fogleman, E. A.; Craig, S. L. Structure and Properties of DNA-Based Reversible Polymers. *Macromolecules* **2004**, *37* (5), 1863–1870. https://doi.org/10.1021/ma035546v.

(160) Kim, J.; Liu, Y.; Ahn, S. J.; Zauscher, S.; Karty, J. M.; Yamanaka, Y.; Craig, S. L. Self-Assembly and Properties of Main-Chain Reversible Polymer Brushes. *Adv. Mater.* **2005**, *17* (14), 1749–1753. https://doi.org/10.1002/adma.200401355.

(161) Jorgensen, W. L.; Pranata, J. Importance of Secondary Interactions in Triply Hydrogen Bonded Complexes: Guanine-Cytosine vs Uracil-2,6-Diaminopyndine. *J. Am. Chem. Soc.* **1990**, *112* (5), 2008–2010. https://doi.org/10.1021/ja00161a061.

(162) Pranata, J.; Wierschke, S. G.; Jorgensen, W. L. OPLS Potential Functions for Nucleotide Bases. Relative Association Constants of Hydrogen-Bonded Base Pairs in Chloroform. *J. Am. Chem. Soc.* **1991**, *113* (8), 2810–2819. https://doi.org/10.1021/ja00008a002.

(163) Murray, T. J.; Zimmerman, S. C. New Triply Hydrogen Bonded Complexes with Highly Variable Stabilities. *J. Am. Chem. Soc.* **1992**, *114* (10), 4010–4011. https://doi.org/10.1021/ja00036a079.

(164) Corbin, P. S.; Zimmerman, S. C. Self-Association without Regard to Prototropy. A Heterocycle That Forms Extremely Stable Quadruply Hydrogen-Bonded Dimers. *J. Am. Chem. Soc.* **1998**, *120* (37), 9710–9711. https://doi.org/10.1021/ja981884d.

(165) Beijer, F. H.; Sijbesma, R. P.; Vekemans, J. A. J. M.; Meijer, E. W.; Kooijman, H.; Spek, A. L. Hydrogen-Bonded Complexes of Diaminopyridines and Diaminotriazines: Opposite Effect of Acylation on Complex Stabilities. *J. Org. Chem.* **1996**, *61* (18), 6371–6380. https://doi.org/10.1021/jo960612v.

(166) Prabhakaran, P.; Puranik, V. G.; Sanjayan, G. J. Preorganizing Linear (Self-Complementary) Quadruple Hydrogen-Bonding Arrays Using Intramolecular Hydrogen Bonding as the Sole Force. *J. Org. Chem.* **2005**, *70* (24), 10067–10072. https://doi.org/10.1021/jo051768a.

(167) Sijbesma, R. P.; Meijer, E. W. Quadruple Hydrogen Bonded Systems. *Chem. Commun.* **2003**, No. 1, 5–16. https://doi.org/10.1039/b205873c.

(168) Tournilhac, F.; Ludwik, L.; Philippe, C.; Corinne, S. Elastic Materials. US 8188293 B2, 2012.

(169) Tournilhac, F.; Hidalgo, M.; Leibler, L. Material Formed From Dendritic Molecules Containing Associative Groups. US 9301912 B2, 2009.

(170) Leibler, L.; Tournilhac, F.; Capelot, M.; Agnaou, R.; Pineau, Q. Supramolecular Materials Made Of Oligoamides. WO 2014/128426 A1, 2014.

(171) Tournilhac, F.; Hidalgo, M.; Leibler, L. Method For Preparing A Material Formed From Arborescent-Branched Molecules Comprising Associative Groups. US 8530671 B2, 2013.

(172) Grimaldi, S.; Gillet, J.; Hidalgo, M.; Tournilhac, F.; Cordier, P.; Leibler, L. Semi-Crystalline Supramolecular Polymers. US 2010/0135940 A1, 2010.

(173) Tournilhac, F.; Leibler, L.; Cordier, P.; Soulie-ziakovic, C.; Linnemann, A.; Hidalgo, M. Polymer Material Containing Chains Bearing Imidazolidone Functions. EP 2157106 A1, 2008.

(174) Cordier, P.; Tournilhac, F.; Soulié-Ziakovic, C.; Leibler, L. Self-Healing and Thermoreversible Rubber from Supramolecular Assembly. *Nature* **2008**, *451* (7181), 977–980. https://doi.org/10.1038/nature06669.

(175) Palleau, E.; Reece, S.; Desai, S. C.; Smith, M. E.; Dickey, M. D. Self-Healing Stretchable Wires for Reconfigurable Circuit Wiring and 3D Microfluidics. *Adv. Mater.* **2013**, *25* (11), 1589–1592. https://doi.org/10.1002/adma.201203921.

(176) Chang, S. K.; Hamilton, A. D. Molecular Recognition of Biologically Interesting Substrates: Synthesis of an Artificial Receptor for Barbiturates Employing Six Hydrogen Bonds. *J. Am. Chem. Soc.* **1988**, *110* (4), 1318–1319. https://doi.org/10.1021/ja00212a065.

(177) Herbst, F.; Seiffert, S.; Binder, W. H. Dynamic Supramolecular Poly(Isobutylene)s for Self-Healing Materials. *Polym. Chem.* **2012**, *3* (11), 3084–3092. https://doi.org/10.1039/c2py20265d.

(178) Yanagisawa, Y.; Nan, Y.; Okuro, K.; Aida, T. Mechanically Robust, Readily Repairable Polymers via Tailored Noncovalent Cross-Linking. *Science (80-.).* **2018**, *359* (6371), 72–76. https://doi.org/10.1126/science.aam7588.

(179) Folmer, B. J. B.; Sijbesma, R. P.; Versteegen, R. M.; van der Rijt, J. A. J.; Meijer, E. W. Supramolecular Polymer Materials: Chain Extension of Telechelic Polymers Using a Reactive Hydrogen-Bonding Synthon. *Adv. Mater.* **2000**, *12* (12), 874–878. https://doi.org/10.1002/1521-4095(200006)12:12<874::AID-ADMA874>3.0.CO;2-C.

(180) Beijer, F. H.; Brunsveld, L.; Meijer, E. W.; Sijbesma, R. P. Supramolecular Polymer. EP 0929597 B1, 2003.

(181) Bosman, A. W.; Jassen, H. M.; Meijer, E. W.; Van Gemert, G. M. L. Preparation Of Supramolecular Polymer Containing Quadruple Hydrogen Bonding Units In The Polymer Backbone. US 2007/0093639 A1, 2007.

(182) Bosman, A. W.; Janssen, H. M.; Meijer, E. W.; Van Gemert, G. M. L.; Versteegen, R. M. Supramolecular Ionomers. US 2009/0111930 A1, 2009.

(183) Bosman, A. W.; Janssen, H. M.; Meijer, E. W.; Sijbesma, R. P.; van Gemert, G. M. L.; Versteegen, R. M. Siloxane Polymers With Quadruple Hydrogen Bonding Units. EP 1569984 B1, 2009.

(184) Bosman, A. W.; Chodorowski-Kimmes, S.; Hoorne-Van Gemert, G. M. L.; Janssen, H. M.; Meijer, E. W. High Flow Supramolecular Compounds. WO 2010/002262 A1, 2014.

(185) Bosman, A. W.; Janssen, H. M.; Meijer, E. W.; Sijbesma, R. P.; Ten Cate, A. T.; Van Beek, D. J. M.; Van Gemert, G. M. L. Monomers Capable Of Forming Four Hydrogen Bridges And Supramolecular Polymers Formed By Copolymerization Of These Monomers With Regular Monomers. WO 2004/016598 A1, 2005.

(186) Bosman, A. W.; Janssen, H. M.; Meijer, E. W.; van Gemert, G. M. L. Supramolecular Polymers From Low-Melting, Easily Processable Building Blocks. US 9006364 B2, 2009.

(187) Bosman, A. W.; Janssen, H. M.; Meijer, E. W.; Hoorne-Van Gemert, G. M. L. Hydrogen Bonded Hydrogels. US 8246990 B2, 2011.

(188) Bosman, A. W.; Dankers, P. Y. W.; Janssen, H. M.; Meijer, E. W.; Van Gemert, G. M. L. Modular Bioresorbable Or Biomedical, Biologically Active Supramolecular Materials. US 9907637 B2, 2016.

(189) Baughman, T. W.; Bosman, A. W.; Hoorne-Van Gemert, G. M. L.; Janssen, H. M.; Meijer, E. W. Strong Reversible Hydrogels. EP 2343342 B1, 2008.

(190) Lamers, B. A. G.; Ślęczkowski, M. L.; Wouters, F.; Engels, T. A. P.; Meijer, E. W.; Palmans, A. R. A. Tuning Polymer Properties of Non-Covalent Crosslinked PDMS by Varying Supramolecular Interaction Strength. *Polym. Chem.* **2020**, *11* (16), 2847–2854. https://doi.org/10.1039/d0py00139b.

(191) Bosman, A. W.; Sijbesma, R. P.; Meijer, E. W. Supramolecular Polymers at Work. *Mater. Today* **2004**, *7* (4), 34–39. https://doi.org/10.1016/S1369-7021(04)00187-7.

(192) Li, W.; Bouzidi, L.; Narine, S. S. Current Research and Development Status and Prospect of Hot-Melt Adhesives: A Review. *Ind. Eng. Chem. Res.* **2008**, *47* (20), 7524–

7532. https://doi.org/10.1021/ie800189b.

(193) Yamauchi, K.; Lizotte, J. R.; Long, T. E. Thermoreversible Poly(Alkyl Acrylates) Consisting of Self-Complementary Multiple Hydrogen Bonding. *Macromolecules* **2003**, *36* (4), 1083–1088. https://doi.org/10.1021/ma0212801.

(194) Van Gemert, G. M. L.; Peeters, J. W.; Söntjens, S. H. M.; Janssen, H. M.; Bosman, A. W. Self-Healing Supramolecular Polymers in Action. *Macromol. Chem. Phys.* **2012**, *213* (2), 234–242. https://doi.org/10.1002/macp.201100559.

(195) Hemmelgarn, C. D.; Wood, T.; Margraf; Havens, D. E.; Reed, J. L.; Snyder, L. W.; Louderbough, A.; Dietsch, B. A. Composite Self-Healing System. US 9180632 B2, 2015.

(196) Yang, J.; Huang, M. Microencapsulation of Reactive Diisocyanates and the Application To Self-Healing Anticorrosion Coatings. US 8993066 B2, 2013.

(197) Jeong, Y. R.; Oh, S. Y.; Kim, J. W.; Jin, S. W.; Ha, J. S. A Highly Conductive and Electromechanically Self-Healable Gold Nanosheet Electrode for Stretchable Electronics. *Chem. Eng. J.* **2020**, *384* (November 2019), 123336. https://doi.org/10.1016/j.cej.2019.123336.

(198) Chen, T.; Lu, F.; Xiang, K.; Wang, Y.; Deng, L. A Conductive Composite Enabled by Graphene-Cyclodextrin-Azobenzene Host-Guest Complex and Its Potential Application in Healable Soft Sensor. *Mater. Lett.* **2019**, *254*, 348–352. https://doi.org/10.1016/j.matlet.2019.07.114.

(199) Guo, K.; Zhang, D. L.; Zhang, X. M.; Zhang, J.; Ding, L. S.; Li, B. J.; Zhang, S. Conductive Elastomers with Autonomic Self-Healing Properties. *Angew. Chemie - Int. Ed.* **2015**, *54* (41), 12127–12133. https://doi.org/10.1002/anie.201505790.

(200) Bai, S.; Sun, C.; Yan, H.; Sun, X.; Zhang, H.; Luo, L.; Lei, X.; Wan, P.; Chen, X. Healable, Transparent, Room-Temperature Electronic Sensors Based on Carbon Nanotube Network-Coated Polyelectrolyte Multilayers. *Small* **2015**, *11* (43), 5807–5813. https://doi.org/10.1002/smll.201502169.

(201) Dry, C. Procedures Developed for Self-Repair of Polymer Matrix Composite Materials. *Compos. Struct.* **1996**, *35* (3), 263–269. https://doi.org/10.1016/0263-8223(96)00033-5.

(202) White, S. R.; Sottos, N. R.; Geubelle, P. H.; Moore, J. S.; Kessler, M. R.; Sriram, S. R.; Brown, E. N.; Viswanathan, S. Autonomic Healing of Polymer Composites. *Nature* **2001**, *409* (6822), 794–797. https://doi.org/10.1038/35057232.

(203) Cho, S. H.; Andersson, H. M.; White, S. R.; Sottos, N. R.; Braun, P. V. Polydiniethylsiloxane-Based Self-Healing Materials. *Adv. Mater.* **2006**, *18* (8), 997–1000. https://doi.org/10.1002/adma.200501814.

(204) Wang, H. P.; Yuan, Y. C.; Rong, M. Z.; Zhang, M. Q. Self-Healing of Thermoplastics via Living Polymerization. *Macromolecules* **2010**, *43* (2), 595–598. https://doi.org/10.1021/ma902021v.

(205) Li, H.; Cui, Y.; Wang, H.; Zhu, Y.; Wang, B. Preparation and Application of Polysulfone Microcapsules Containing Tung Oil in Self-Healing and Self-Lubricating Epoxy Coating. *Colloids Surfaces A Physicochem. Eng. Asp.* **2017**, *518*, 181–187. https://doi.org/10.1016/j.colsurfa.2017.01.046.

(206) Chen, X.; Dam, M. A.; Ono, K.; Mal, A.; Shen, H.; Nutt, S. R.; Sheran, K.; Wudl, F. A Thermally Re-Mendable Cross-Linked Polymeric Material. *Science (80-.).* **2002**, *295* (5560), 1698–1702. https://doi.org/10.1126/science.1065879.

(207) Tseng, T.; Tao, L.; Hsieh, F.; Wei, Y.; Chiu, I.; Hsu, S. An Injectable, Self-Healing Hydrogel to Repair the Central Nervous System. *Adv. Mater.* **2015**, *27* (23), 3518–3524. https://doi.org/10.1002/adma.201500762.

(208) Hu, J.; Mo, R.; Sheng, X.; Zhang, X. A Self-Healing Polyurethane Elastomer with Excellent Mechanical Properties Based on Phase-Locked Dynamic Imine Bonds. *Polym. Chem.* **2020**, *11* (14), 2585–2594. https://doi.org/10.1039/D0PY00151A.

(209) Liu, W. X.; Zhang, C.; Zhang, H.; Zhao, N.; Yu, Z. X.; Xu, J. Oxime-Based and Catalyst-Free Dynamic Covalent Polyurethanes. *J. Am. Chem. Soc.* **2017**, *139* (25), 8678–8684. https://doi.org/10.1021/jacs.7b03967.

(210) Kuhl, N.; Abend, M.; Bode, S.; Schubert, U. S.; Hager, M. D. Oxime Crosslinked Polymer Networks: Is Every Reversible Covalent Bond Suitable to Create Self-Healing Polymers? *J. Appl. Polym. Sci.* **2016**, *133* (44), 44168. https://doi.org/10.1002/app.44168.

(211) Mukherjee, S.; Hill, M. R.; Sumerlin, B. S. Self-Healing Hydrogels Containing Reversible Oxime Crosslinks. *Soft Matter* **2015**, *11* (30), 6152–6161. https://doi.org/10.1039/c5sm00865d.

(212) Mukherjee, S.; Bapat, A. P.; Hill, M. R.; Sumerlin, B. S. Oximes as Reversible Links in Polymer Chemistry: Dynamic Macromolecular Stars. *Polym. Chem.* **2014**, *5* (24), 6923–6931. https://doi.org/10.1039/c4py01282h.

(213) Kuhl, N.; Bode, S.; Bose, R. K.; Vitz, J.; Seifert, A.; Hoeppener, S.; Garcia, S. J.; Spange, S.; Van Der Zwaag, S.; Hager, M. D.; Schubert, U. S. Acylhydrazones as Reversible Covalent Crosslinkers for Self-Healing Polymers. *Adv. Funct. Mater.* **2015**, *25* (22), 3295–3301. https://doi.org/10.1002/adfm.201501117.

(214) Yang, X.; Liu, G.; Peng, L.; Guo, J.; Tao, L.; Yuan, J.; Chang, C.; Wei, Y.; Zhang, L. Highly Efficient Self-Healable and Dual Responsive Cellulose-Based Hydrogels for

Controlled Release and 3D Cell Culture. *Adv. Funct. Mater.* **2017**, *27* (40), 1703174. https://doi.org/10.1002/adfm.201703174.

(215) Deng, G.; Li, F.; Yu, H.; Liu, F.; Liu, C.; Sun, W.; Jiang, H.; Chen, Y. Dynamic Hydrogels with an Environmental Adaptive Self-Healing Ability and Dual Responsive Sol-Gel Transitions. *ACS Macro Lett.* **2012**, *1* (2), 275–279. https://doi.org/10.1021/mz200195n.

(216) Wang, P.; Deng, G.; Zhou, L.; Li, Z.; Chen, Y. Ultrastretchable, Self-Healable Hydrogels Based on Dynamic Covalent Bonding and Triblock Copolymer Micellization. *ACS Macro Lett.* **2017**, *6* (8), 881–886. https://doi.org/10.1021/acsmacrolett.7b00519.

(217) Tatum, L. A.; Su, X.; Aprahamian, I. Simple Hydrazone Building Blocks for Complicated Functional Materials. *Acc. Chem. Res.* **2014**, *47* (7), 2141–2149. https://doi.org/10.1021/ar500111f.

(218) Pepels, M.; Filot, I.; Klumperman, B.; Goossens, H. Self-Healing Systems Based on Disulfide-Thiol Exchange Reactions. *Polym. Chem.* **2013**, *4* (18), 4955–4965. https://doi.org/10.1039/c3py00087g.

(219) Gao, W.; Bie, M.; Liu, F.; Chang, P.; Quan, Y. Self-Healable and Reprocessable Polysulfide Sealants Prepared from Liquid Polysulfide Oligomer and Epoxy Resin. *ACS Appl. Mater. Interfaces* **2017**, *9* (18), 15798–15808. https://doi.org/10.1021/acsami.7b05285.

(220) Amamoto, Y.; Otsuka, H.; Takahara, A.; Matyjaszewski, K. Self-Healing of Covalently Cross-Linked Polymers by Reshuffling Thiuram Disulfide Moieties in Air under Visible Light. *Adv. Mater.* **2012**, *24* (29), 3975–3980. https://doi.org/10.1002/adma.201201928.

(221) Lei, Z. Q.; Xiang, H. P.; Yuan, Y. J.; Rong, M. Z.; Zhang, M. Q. Room-Temperature Self-Healable and Remoldable Cross-Linked Polymer Based on the Dynamic Exchange of Disulfide Bonds. *Chem. Mater.* **2014**, *26* (6), 2038–2046. https://doi.org/10.1021/cm4040616.

(222) Lei, Z. Q.; Xie, P.; Rong, M. Z.; Zhang, M. Q. Catalyst-Free Dynamic Exchange of Aromatic Schiff Base Bonds and Its Application to Self-Healing and Remolding of Crosslinked Polymers. *J. Mater. Chem. A* **2015**, *3* (39), 19662–19668. https://doi.org/10.1039/c5ta05788d.

(223) Li, X.; Yu, R.; He, Y.; Zhang, Y.; Yang, X.; Zhao, X.; Huang, W. Self-Healing Polyurethane Elastomers Based on a Disulfide Bond by Digital Light Processing 3D Printing. *ACS Macro Lett.* **2019**, *8* (11), 1511–1516. https://doi.org/10.1021/acsmacrolett.9b00766.

(224) Rekondo, A.; Martin, R.; Ruiz De Luzuriaga, A.; Cabañero, G.; Grande, H. J.; Odriozola, I. Catalyst-Free Room-Temperature Self-Healing Elastomers Based on Aromatic

Disulfide Metathesis. *Mater. Horizons* **2014**, *1* (2), 237–240. https://doi.org/10.1039/c3mh00061c.

(225) Lai, Y.; Kuang, X.; Zhu, P.; Huang, M.; Dong, X.; Wang, D. Colorless, Transparent, Robust, and Fast Scratch-Self-Healing Elastomers via a Phase-Locked Dynamic Bonds Design. *Adv. Mater.* **2018**, *30* (38), 1802556. https://doi.org/10.1002/adma.201802556.

(226) Kim, S. M.; Jeon, H.; Shin, S. H.; Park, S. A.; Jegal, J.; Hwang, S. Y.; Oh, D. X.; Park, J. Superior Toughness and Fast Self-Healing at Room Temperature Engineered by Transparent Elastomers. *Adv. Mater.* **2018**, *30* (1), 1705145. https://doi.org/10.1002/adma.201705145.

(227) Amamoto, Y.; Kamada, J.; Otsuka, H.; Takahara, A.; Matyjaszewski, K. Repeatable Photoinduced Self-Healing of Covalently Cross-Linked Polymers through Reshuffling of Trithiocarbonate Units. *Angew. Chemie - Int. Ed.* **2011**, *50* (7), 1660–1663. https://doi.org/10.1002/anie.201003888.

(228) Nicolaÿ, R.; Kamada, J.; Van Wassen, A.; Matyjaszewski, K. Responsive Gels Based on a Dynamic Covalent Trithiocarbonate Cross-Linker. *Macromolecules* **2010**, *43* (9), 4355–4361. https://doi.org/10.1021/ma100378r.

(229) Lai, J.-C.; Mei, J.-F.; Jia, X.-Y.; Li, C.-H.; You, X.-Z.; Bao, Z. A Stiff and Healable Polymer Based on Dynamic-Covalent Boroxine Bonds. *Adv. Mater.* **2016**, *28* (37), 8277–8282. https://doi.org/10.1002/adma.201602332.

(230) Yuan, C.; Rong, M. Z.; Zhang, M. Q.; Zhang, Z. P.; Yuan, Y. C. Self-Healing of Polymers via Synchronous Covalent Bond Fission/Radical Recombination. *Chem. Mater.* **2011**, *23* (22), 5076–5081. https://doi.org/10.1021/cm202635w.

(231) Zhang, Z. P.; Rong, M. Z.; Zhang, M. Q.; Yuan, C. Alkoxyamine with Reduced Homolysis Temperature and Its Application in Repeated Autonomous Self-Healing of Stiff Polymers. *Polym. Chem.* **2013**, *4* (17), 4648–4654. https://doi.org/10.1039/c3py00679d.

(232) Yuan, C.; Zhang, M. Q.; Rong, M. Z. Application of Alkoxyamine in Self-Healing of Epoxy. *J. Mater. Chem. A* **2014**, *2* (18), 6558–6566. https://doi.org/10.1039/c4ta00130c.

(233) Cheng, X.; Pan, J.; Zhao, Y.; Liao, M.; Peng, H. Gel Polymer Electrolytes for Electrochemical Energy Storage. *Adv. Energy Mater.* **2018**, *8* (7), 1702184. https://doi.org/10.1002/aenm.201702184.

(234) Wang, Z.; Tao, F.; Pan, Q. A Self-Healable Polyvinyl Alcohol-Based Hydrogel Electrolyte for Smart Electrochemical Capacitors. *J. Mater. Chem. A* **2016**, *4* (45), 17732–17739. https://doi.org/10.1039/C6TA08018A.

(235) Wang, Z.; Pan, Q. An Omni-Healable Supercapacitor Integrated in Dynamically Cross-Linked Polymer Networks. *Adv. Funct. Mater.* **2017**, *27* (24), 1700690. https://doi.org/10.1002/adfm.201700690.

(236) Benight, S. J.; Wang, C.; Tok, J. B. H.; Bao, Z. Stretchable and Self-Healing Polymers and Devices for Electronic Skin. *Prog. Polym. Sci.* **2013**, *38* (12), 1961–1977. https://doi.org/10.1016/j.progpolymsci.2013.08.001.

(237) Kang, J.; Tok, J. B. H.; Bao, Z. Self-Healing Soft Electronics. *Nat. Electron.* **2019**, *2* (4), 144–150. https://doi.org/10.1038/s41928-019-0235-0.

(238) De Gennes, P. G. Reptation of a Polymer Chain in the Presence of Fixed Obstacles. *J. Chem. Phys.* **1971**, *55* (2), 572–579. https://doi.org/10.1063/1.1675789.

(239) Edwards, S. F. The Statistical Mechanics of Polymerized Material. *Proc. Phys. Soc.* **1967**, *92* (1), 9–16. https://doi.org/10.1088/0370-1328/92/1/303.

(240) Wool, R. P.; O'Connor, K. M. A Theory of Crack Healing in Polymers. *J. Appl. Phys.* **1981**, *52* (10), 5953–5963. https://doi.org/10.1063/1.328526.

(241) Kim, Y. H.; Wool, R. P. A Theory of Healing at a Polymer Polymer Interface. *Macromolecules* **1983**, *16* (7), 1115–1120. https://doi.org/10.1021/ma00241a013.

(242) Wool, R. P. Self-Healing Materials: A Review. *Soft Matter* **2008**, *4* (3), 400–418. https://doi.org/10.1039/b711716g.

(243) Ge, T.; Pierce, F.; Perahia, D.; Grest, G. S.; Robbins, M. O. Molecular Dynamics Simulations of Polymer Welding: Strength from Interfacial Entanglements. *Phys. Rev. Lett.* **2013**, *110* (9), 1–5. https://doi.org/10.1103/PhysRevLett.110.098301.

(244) Ge, T.; Robbins, M. O.; Perahia, D.; Grest, G. S. Healing of Polymer Interfaces: Interfacial Dynamics, Entanglements, and Strength. *Phys. Rev. E - Stat. Nonlinear, Soft Matter Phys.* **2014**, *90* (1), 1–15. https://doi.org/10.1103/PhysRevE.90.012602.

(245) Stukalin, E. B.; Cai, L. H.; Kumar, N. A.; Leibler, L.; Rubinstein, M. Self-Healing of Unentangled Polymer Networks with Reversible Bonds. *Macromolecules* **2013**, *46* (18), 7525–7541. https://doi.org/10.1021/ma401111n.

(246) Hornat, C. C.; Urban, M. W. Entropy and Interfacial Energy Driven Self-Healable Polymers. *Nat. Commun.* **2020**, *11* (1), 1028. https://doi.org/10.1038/s41467-020-14911-y.

(247) Shen, Z.; Ye, H.; Wang, Q.; Kröger, M.; Li, Y. Sticky Rouse Time Features the Self-Adhesion of Supramolecular Polymer Networks. *Macromolecules* **2021**, *54* (11), 5053–5064. https://doi.org/10.1021/acs.macromol.1c00335.

(248) Heinzmann, C.; Weder, C.; De Espinosa, L. M. Supramolecular Polymer Adhesives: Advanced Materials Inspired by Nature. *Chem. Soc. Rev.* **2016**, *45* (2), 342–358. https://doi.org/10.1039/c5cs00477b.

(249) Li, M.; Li, W.; Cai, W.; Zhang, X.; Wang, Z.; Street, J.; Ong, W. J.; Xia, Z.; Xu, Q. A Self-Healing Hydrogel with Pressure Sensitive Photoluminescence for Remote Force Measurement and Healing Assessment. *Mater. Horizons* **2019**, *6* (4), 703–710. https://doi.org/10.1039/c8mh01441h.

(250) Liu, C.; Qin, H.; Mather, P. T. Review of Progress in Shape-Memory Polymers. *J. Mater. Chem.* **2007**, *17* (16), 1543–1558. https://doi.org/10.1039/b615954k.

(251) Rousseau, I. A. Challenges of Shape Memory Polymers: A Review of the Progress toward Overcoming SMP's Limitations. *Polym. Eng. Sci.* **2008**, *48* (11), 2075–2089. https://doi.org/10.1002/pen.21213.

(252) Jiang, Z.-C.; Xiao, Y.-Y.; Kang, Y.; Pan, M.; Li, B.-J.; Zhang, S. Shape Memory Polymers Based on Supramolecular Interactions. *ACS Appl. Mater. Interfaces* **2017**, *9* (24), 20276–20293. https://doi.org/10.1021/acsami.7b03624.

(253) Wu, Y.; Wang, L.; Zhao, X.; Hou, S.; Guo, B.; Ma, P. X. Self-Healing Supramolecular Bioelastomers with Shape Memory Property as a Multifunctional Platform for Biomedical Applications via Modular Assembly. *Biomaterials* **2016**, *104*, 18–31. https://doi.org/10.1016/j.biomaterials.2016.07.011.

(254) Kumpfer, J. R.; Rowan, S. J. Thermo-, Photo-, and Chemo-Responsive Shape-Memory Properties from Photo-Cross-Linked Metallo-Supramolecular Polymers. *J. Am. Chem. Soc.* **2011**, *133* (32), 12866–12874. https://doi.org/10.1021/ja205332w.

(255) Wang, D.; Xu, J. H.; Chen, J. Y.; Hu, P.; Wang, Y.; Jiang, W.; Fu, J. J. Transparent, Mechanically Strong, Extremely Tough, Self-Recoverable, Healable Supramolecular Elastomers Facilely Fabricated via Dynamic Hard Domains Design for Multifunctional Applications. *Adv. Funct. Mater.* **2020**, *30* (3), 1907109. https://doi.org/10.1002/adfm.201907109.

(256) Aida, T.; Meijer, E. W.; Stupp, S. I. Functional Supramolecular Polymers. *Science (80-.).* **2012**, *335* (6070), 813–817. https://doi.org/10.1126/science.1205962.

(257) Campanella, A.; Döhler, D.; Binder, W. H. Self-Healing in Supramolecular Polymers. *Macromol. Rapid Commun.* **2018**, *39* (17), 1700739. https://doi.org/10.1002/marc.201700739.

(258) Döhler, D.; Peterlik, H.; Binder, W. H. A Dual Crosslinked Self-Healing System: Supramolecular and Covalent Network Formation of Four-Arm Star Polymers. *Polymer (Guildf).* **2015**, *69*, 264–273. https://doi.org/10.1016/j.polymer.2015.01.073.

(259) Chen, S.; Döhler, D.; Binder, W. H. Rheology of Hydrogen-Bonded Dendritic Supramolecular Polymer Networks in the Melt State. *Polymer (Guildf).* **2016**, *107*, 466–473. https://doi.org/10.1016/j.polymer.2016.08.046.

(260) Bode, S.; Enke, M.; Bose, R. K.; Schacher, F. H.; Garcia, S. J.; van der Zwaag, S.; Hager, M. D.; Schubert, U. S. Correlation between Scratch Healing and Rheological Behavior for Terpyridine Complex Based Metallopolymers. *J. Mater. Chem. A* **2015**, *3* (44), 22145–22153. https://doi.org/10.1039/c5ta05545h.

(261) Bose, R. K.; Hohlbein, N.; Garcia, S. J.; Schmidt, A. M.; Van Der Zwaag, S. Connecting Supramolecular Bond Lifetime and Network Mobility for Scratch Healing in Poly(Butyl Acrylate) Ionomers Containing Sodium, Zinc and Cobalt. *Phys. Chem. Chem. Phys.* **2015**, *17* (3), 1697–1704. https://doi.org/10.1039/c4cp04015e.

(262) Zhang, Y.; Hu, Q.; Yang, S.; Wang, T.; Sun, W.; Tong, Z. Unique Self-Reinforcing and Rapid Self-Healing Polyampholyte Hydrogels with a PH-Induced Shape Memory Effect. *Macromolecules* **2021**, *54* (11), 5218–5228. https://doi.org/10.1021/acs.macromol.0c02657.

(263) Chen, L.; Guo, M. Highly Transparent, Stretchable, and Conductive Supramolecular Ionogels Integrated with Three-Dimensional Printable, Adhesive, Healable, and Recyclable Character. *ACS Appl. Mater. Interfaces* **2021**. https://doi.org/10.1021/acsami.1c04255.

(264) Yang, N.; Yang, H.; Shao, Z.; Guo, M. Ultrastrong and Tough Supramolecular Hydrogels from Multiurea Linkage Segmented Copolymers with Tractable Processability and Recyclability. *Macromol. Rapid Commun.* **2017**, *38* (17), 1700275. https://doi.org/10.1002/marc.201700275.

(265) Randall, D.; Lee, S. The Polyurethanes Book. Wiley, 2002, p 477.

(266) Simonin, L.; Falco, G.; Pensec, S.; Dalmas, F.; Chenal, J. M.; Ganachaud, F.; Marcellan, A.; Chazeau, L.; Bouteiller, L. Macromolecular Additives to Turn a Thermoplastic Elastomer into a Self-Healing Material. *Macromolecules* **2021**, *54* (2), 888–895. https://doi.org/10.1021/acs.macromol.0c02352.

(267) Meng, Y.; Xu, W.; Newman, M. R.; Benoit, D. S. W.; Anthamatten, M. Thermoreversible Siloxane Networks: Soft Biomaterials with Widely Tunable Viscoelasticity. *Adv. Funct. Mater.* **2019**, *29* (38), 1903721. https://doi.org/10.1002/adfm.201903721.

(268) Pellizzaro, M. L.; Houton, K. A.; Wilson, A. J. Sequential and Phototriggered Supramolecular Self-Sorting Cascades Using Hydrogen-Bonded Motifs. *Chem. Sci.* **2013**, *4* (4), 1825–1829. https://doi.org/10.1039/c3sc22194f.

(269) Coubrough, H. M.; van der Lubbe, S. C. C.; Hetherington, K.; Minard, A.; Pask, C.;

Howard, M. J.; Fonseca Guerra, C.; Wilson, A. J. Supramolecular Self-Sorting Networks Using Hydrogen-Bonding Motifs. *Chem. - A Eur. J.* **2019**, *25* (3), 785–795. https://doi.org/10.1002/chem.201804791.

(270) Zhang, G.; Yang, Y.; Chen, Y.; Huang, J.; Zhang, T.; Zeng, H.; Wang, C.; Liu, G.; Deng, Y. A Quadruple-Hydrogen-Bonded Supramolecular Binder for High-Performance Silicon Anodes in Lithium-Ion Batteries. *Small* **2018**, *14* (29), 1801189. https://doi.org/10.1002/smll.201801189.

(271) Kwon, T. W.; Jeong, Y. K.; Deniz, E.; Alqaradawi, S. Y.; Choi, J. W.; Coskun, A. Dynamic Cross-Linking of Polymeric Binders Based on Host-Guest Interactions for Silicon Anodes in Lithium Ion Batteries. *ACS Nano* **2015**, *9* (11), 11317–11324. https://doi.org/10.1021/acsnano.5b05030.

(272) Nishikawa, Y.; Yamamoto, H. Iron-Catalyzed Asymmetric Epoxidation of β,β-Disubstituted Enones. *J. Am. Chem. Soc.* **2011**, *133* (22), 8432–8435. https://doi.org/10.1021/ja201873d.

(273) Gupta, A.; Badam, R.; Matsumi, N. Heavy-Duty Performance from Silicon Anodes Using Poly(BIAN)/Poly(Acrylic Acid)-Based Self-Healing Composite Binder in Lithium-Ion Secondary Batteries. *ACS Appl. Energy Mater.* **2022**. https://doi.org/10.1021/acsaem.2c00278.

(274) George, S.; Nangia, A.; Lam, C. K.; Mak, T. C. W.; Nicoud, J. F. Crystal Engineering of Urea α-Network via I···O_2N Synthon and Design of SHG Active Crystal N-4-Iodophenyl-N′-4′-Nitrophenylurea. *Chem. Commun.* **2004**, *4* (10), 1202–1203. https://doi.org/10.1039/b402050b.

(275) Piana, F.; Case, D. H.; Ramalhete, S. M.; Pileio, G.; Facciotti, M.; Day, G. M.; Khimyak, Y. Z.; Angulo, J.; Brown, R. C. D.; Gale, P. A. Substituent Interference on Supramolecular Assembly in Urea Gelators: Synthesis, Structure Prediction and NMR. *Soft Matter* **2016**, *12* (17), 4034–4043. https://doi.org/10.1039/c6sm00607h.

(276) Rodríguez-Llansola, F.; Escuder, B.; Miravet, J. F.; Hermida-Merino, D.; Hamley, I. W.; Cardin, C. J.; Hayes, W. Selective and Highly Efficient Dye Scavenging by a PH-Responsive Molecular Hydrogelator. *Chem. Commun.* **2010**, *46* (42), 7960–7962. https://doi.org/10.1039/c0cc02338h.

(277) Wood, D. M.; Greenland, B. W.; Acton, A. L.; Rodríguez-Llansola, F.; Murray, C. A.; Cardin, C. J.; Miravet, J. F.; Escuder, B.; Hamley, I. W.; Hayes, W. PH-Tunable Hydrogelators for Water Purification: Structural Optimisation and Evaluation. *Chem. - A Eur. J.* **2012**, *18* (9), 2692–2699. https://doi.org/10.1002/chem.201102137.

(278) Baker, B. C.; German, I. M.; Chippindale, A. M.; McEwan, C. E. A. A.; Stevens, G. C.;

Colquhoun, H. M.; Hayes, W. Nitroarylurea-Terminated Supramolecular Polymers That Exhibit Facile Thermal Repair and Aqueous Swelling-Induced Sealing of Defects. *Polymer.* **2018**, *140*, 1–9. https://doi.org/10.1016/j.polymer.2018.02.029.

(279) Isare, B.; Pembouong, G.; Boué, F.; Bouteiller, L. Conformational Control of Hydrogen-Bonded Aromatic Bis-Ureas. *Langmuir* **2012**, *28* (19), 7535–7541. https://doi.org/10.1021/la300887p.

Chapter 2 – Conformational control of self-assembled supramolecular pH switchable low-molecular-weight hydrogelators

This Chapter has, in part, been published by the author as a research article entitled “Conformational control of bis-urea self-assembled supramolecular pH switchable low-molecular-weight hydrogelators, Adam D. O'Donnell, Alexander G. Gavriel, William Christie, Ann M. Chippindale, Ian M. German, and Wayne Hayes, *Arkivoc*, **2021**, https://doi.org/10.24820/ark.5550190.p011.581.

This chapter reports the synthesis and investigation into the structure-property relationships of eight different low molecular weight hydrogelators based on a bisaromatic urea core unit, all of which form gels as the pH of the solution is lowered. The low molecular weight hydrogelators are functionalised with carboxylic acid moieties on one aromatic ring, and the other aromatic ring features a nitro functional group either in the *meta*- or *para*-position relative to the urea linkage. *Ortho*-methyl substituents were installed on the aromatic rings to enforce a non-coplanar arrangement between the phenyl and urea moieties. Gel formation was triggered by adding a mineral acid or the ring-opening hydrolysis of glucono-δ-lactone. The low molecular weight hydrogelators were studied by various analytical techniques, including NMR spectroscopy and rheology. In addition, their ability to uptake a dye, methylene blue, was determined by UV-vis spectroscopy.

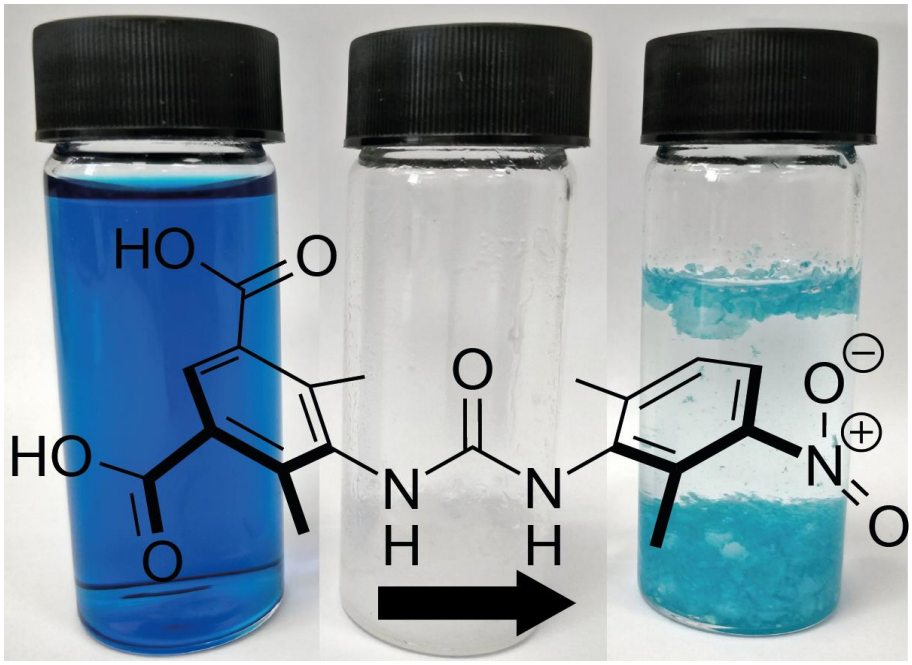

Figure 1. Methylene blue dye extraction through the addition of a hydrogelator.

2.1 Introduction

A wide range of complex biological assemblies are formed through non-covalent interactions that enable the construction of functional supramolecular structures from low molecular weight building blocks. As such, biomimicry and understanding the subtleties of non-covalent interactions are at the forefront of supramolecular self-assembly.[1–6] It is well-known that conformational control is critical in the self-assembly of lipids, folding polypeptides into proteins, and folding nucleic acids into their helical tertiary structure. Aromatic urea systems are ever-present in supramolecular chemistry because of their strong self-assembly through self-complementary hydrogen bonding and π-π stacking interactions.[7–10] Their synthetic accessibility and strong association characteristics have been exploited to synthesise self-assembled organogelators,[11–14] hydrogelators,[15–17] liquid crystals,[18] self-assembled monolayers,[19–21] hydrogen-bonded molecular capsules,[22–25] tunable hydrogen bond-donating catalysts,[26–29] and supramolecular polymers,[30–38] as well as in anion complexation,[39–43] and crystal engineering.[10,44,45]

In 2012, Bouteiller and co-workers reported the effects of conformation control of aromatic bis-urea systems through viscometry measurements with *ortho*-methyl substituents found to enforce a non-coplanar conformation between the urea and the phenyl moiety, in turn enhancing hydrogen bonding.[46] Substitution of the *ortho*-position of the benzene unit adjacent to the urea group with methyl groups was shown to be more effective at increasing the viscosity of the solution than larger functional groups (see Figure 2), resulting from reduced steric hindrance allowing for rotation.

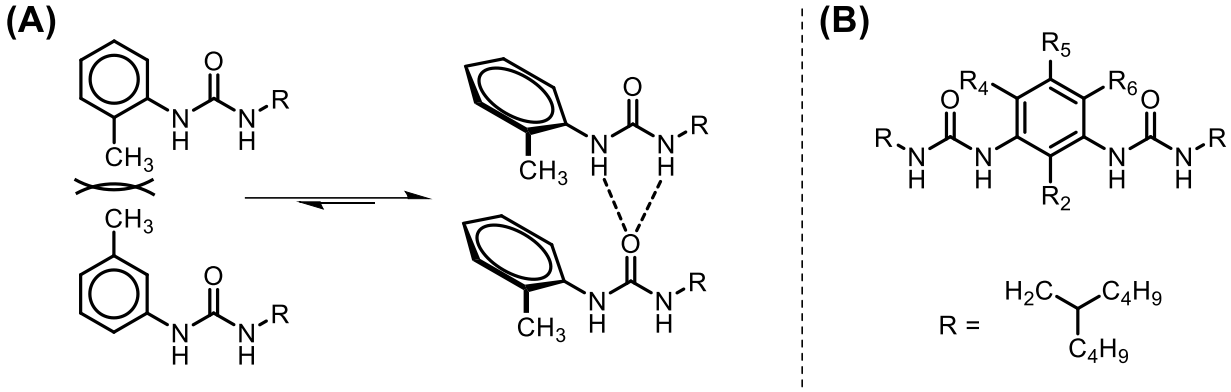

Figure 2. A) Schematic illustrating the design of Bouteiller's bis-urea compounds.[46] **B)** Model compounds synthesised where R_4, R_5 and R_6 are protons, methyl, or ethyl substituents.

Low molecular weight gelators (LMWG) have been investigated for several reasons; they offer a unique opportunity to design soft materials with controllable assembly through structural modification of the associating groups and have found applications ranging from biomedical injectable gelators designed to release a drug molecule at its desired location,[47–49] to removing pollutants from wastewater or organic solvents.[50–54] Adams and co-workers analysed a Fmoc-dipeptide LMWG and found that the mechanical properties of the gels prepared were

dependent on the volume fraction of the co-solvent and the temperature cycle used to generate the gel.[55] Smith and co-workers developed a hybrid gel by combining two supramolecular gelators, one of which enabled the controlled release of an active pharmaceutical ingredient and the other provided enhanced mechanical stability.[56] Ulijn and co-workers investigated the significance of the Fmoc moiety in aromatic peptide amphiphile hydrogelators and concluded that the Fmoc moiety provided a rigid linker of sufficient length to allow for effective assembly.[57]

Baker *et al.* synthesised a series of hydrogelators (see Figure 3A and Figure 3B).[15] The gelators seen in Figure 3A all formed stable hydrogels upon pH switching. However, in the absence of the aromatic unit flanking the urea substituent, the gelator seen in Figure 3B, the proposed gelator, preferred to precipitate from the solution. This was postulated to be a consequence of the amide linking units attenuating the self-assembly of the urea group. Wood *et al*. reported the synthesis and characterisation of a series of hydrogelators, one of which is seen in Figure 3C. It was found that the gelator with a nitro substituent in the -ortho position had a critical gelation concentration an order of magnitude greater than when the nitro substituent was positioned in either the *-meta* or *-para* position.

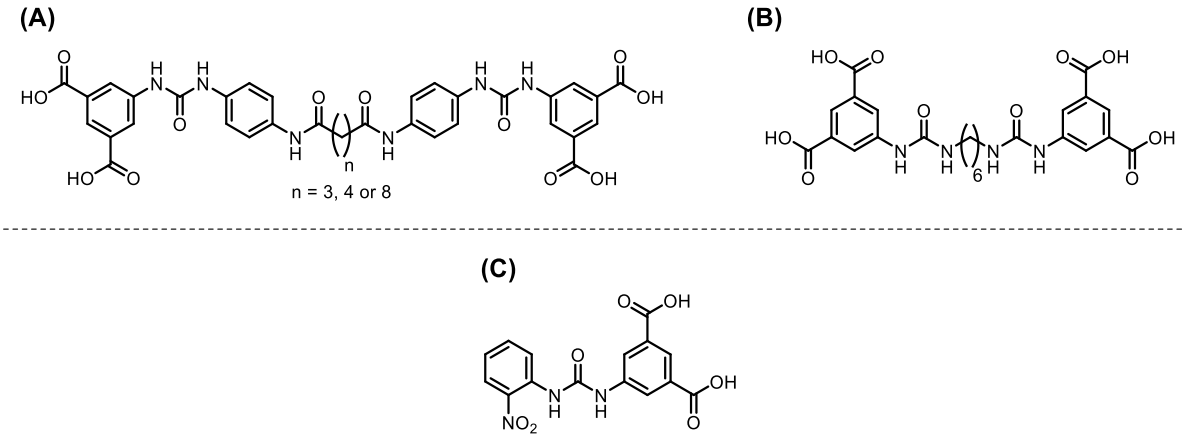

Figure 3. A) Gelator systems developed by Baker *et al*. and **B)** proposed aromatic urea gelator system featuring alkyl spacer units.[15] **C**) *o*-nitro hydrogelator reported by Wood *et al*.[17]

Inspired by the establishment of detailed structure-property relationships and the desire to understand their use in developing functional materials such as low molecular weight gelator systems, this chapter will synthesise eight bisaromatic ureas and investigate the structure-property relationships of these low molecular weight hydrogelators.

2.2 Results and Discussion

A series of potential low molecular weight aromatic urea hydrogelators were designed and synthesised (see **2.1 – 2.8** in Figure 4) in which substituents were introduced systematically onto the *-ortho* positions of the benzene rings relative to the urea recognition group in order to establish the effect on the properties of the materials.

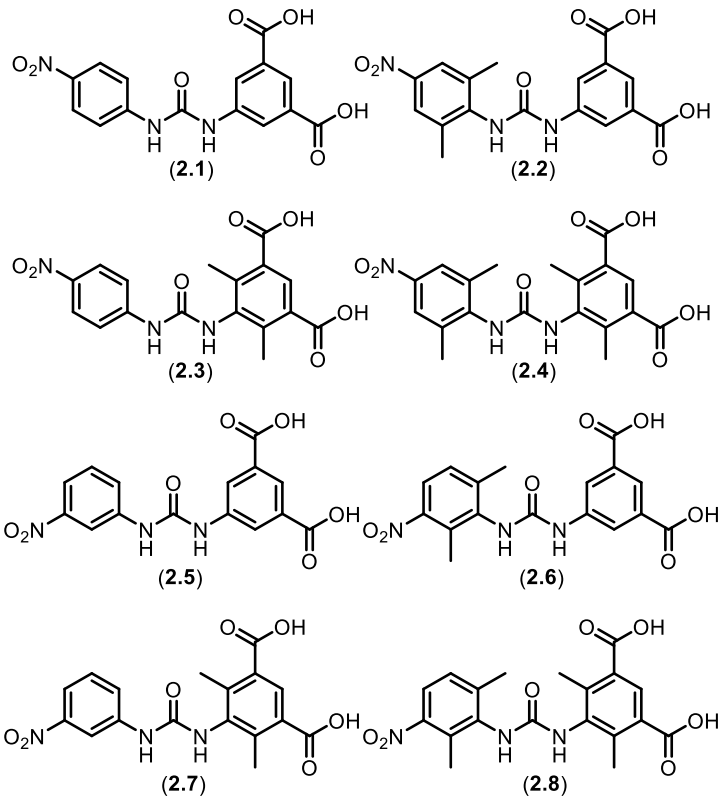

Figure 4. The bisaromatic ureas (**2.1 – 2.8**) that were designed, synthesised, and investigated in this study. Note, the bisaromatic ureas **2.1** and **2.5** have previously been reported by Wood *et al*. [17]

2.3 Synthesis and Characterisation

The synthesis of bisaromatic ureas featuring *ortho*-methyl substituents shown in Figure 4 required the generation of the corresponding aniline precursors. For example, in the case of bisaromatic ureas **2.4** and **2.8**, the generation of the desired aniline **2.9** involved chloromethylation of *meta*-xylene with HCl and paraformaldehyde in the presence of acetic acid to afford 1,5-bis(chloromethyl)-2-4-dimethylbenzene **2.10** (Scheme 1, see also the Appendix 1, Figures 1 – 40 for the characterisation data of the bisaromatic ureas and their precursors **2.9 – 2.20**).[58] A modified procedure from Hopff *et al.*[59] was used to nitrate selectively *ortho*- to the methyl substituents (to yield **2.11**, see the solid-state structure in Appendix 1, Figure 41) and then oxidise the chloromethyl substituents to carboxylic acids (**2.12**). ^{1}H NMR spectroscopic analysis of the diacid **2.12** revealed the disappearance of the methylene resonance at δ_H 4.86 ppm and the appearance of a broad singlet at δ_H 13.56 ppm corresponding to the carboxylic acid protons (see Appendix 1, Figure 23). Furthermore, Fourier-transform infrared (FTIR) spectroscopic analysis of **2.12** revealed a strong absorbance band at 1668 cm^{-1} corresponding to the aromatic carboxylic acid stretch. Esterification with thionyl chloride and methanol yielded the desired dimethyl isophthalate **2.13** in excellent yield (see the solid-state structure in Appendix 1, Figure 25). Selective reduction of the nitro functional group with hydrogen and Pd/C in MeOH to an arylamine (**2.14**) was confirmed by ^{1}H NMR spectroscopic analysis (see Appendix 1, Figure 27), which featured a broad singlet at

δ_H 5.09 ppm. Subsequent ester hydrolysis was achieved with NaOH and monitored by thin-layer chromatography (TLC); after completion, the solvent was removed, and the aminoisophthalic acid 2.9 was isolated by acidification with acidification HCl until pH = 4, at which point the desired amine hydrochloride precipitated.

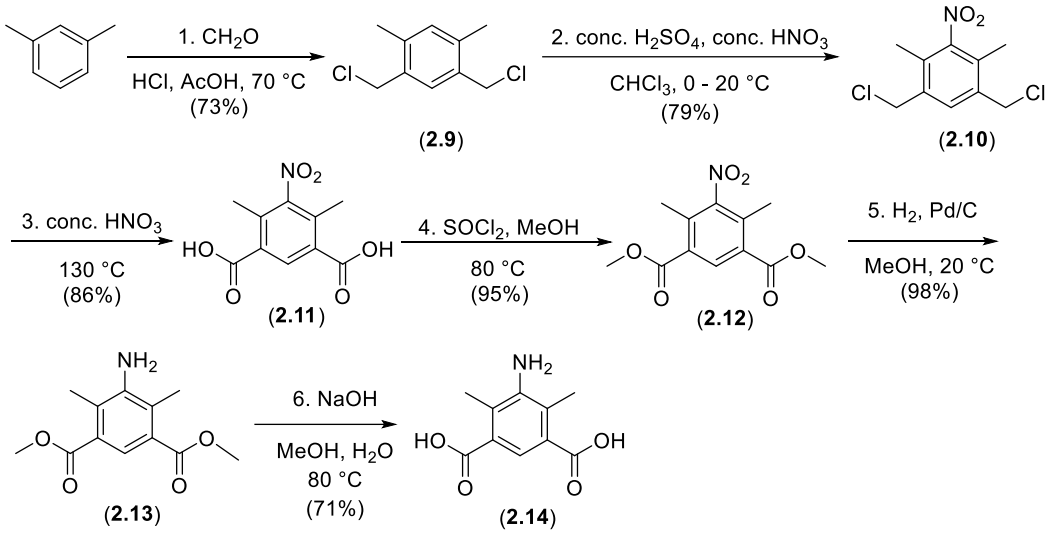

Scheme 12. Synthesis of 5-amino-4,6-dimethylisophthalic acid (**2.14**).

The *ortho*-methyl-substituted isocyanates **2.15** and **2.16** were synthesised from their respective amines **2.17** and **2.18** using phosgene in toluene and isolated in excellent yields (> 99%) (see Scheme 2). In the case of the isocyanate **2.15** featuring a nitro group *meta* to the reactive isocyanate unit, this was synthesised from 2,6-dimethylaniline. Nitration of 2,6-dimethylaniline afforded the desired 2,6-dimethyl-3-nitroaniline **2.17** in 83%. A more complex approach was required to generate the *para*-nitro substituted isocyanate **2.16**. 2,6-Dimethylaniline was first converted to the corresponding toluenesulfonamide **2.19** to direct nitration -*para*, yielding **2.20**. Treatment of the *para*-nitro-toluenesulfonamide **2.20** with sulfuric acid afforded the desired *para*-nitroaniline **2.18** in 81%. A strong absorbance band confirmed isocyanate generation at 2272 and 2263 cm^{-1} in the IR spectra of **2.15** and **2.16**, respectively, and by the $^{13}C\{H\}$ NMR spectra (broad quaternary carbon resonances were evident at δ_C 124.8 and 125.7 ppm, respectively).

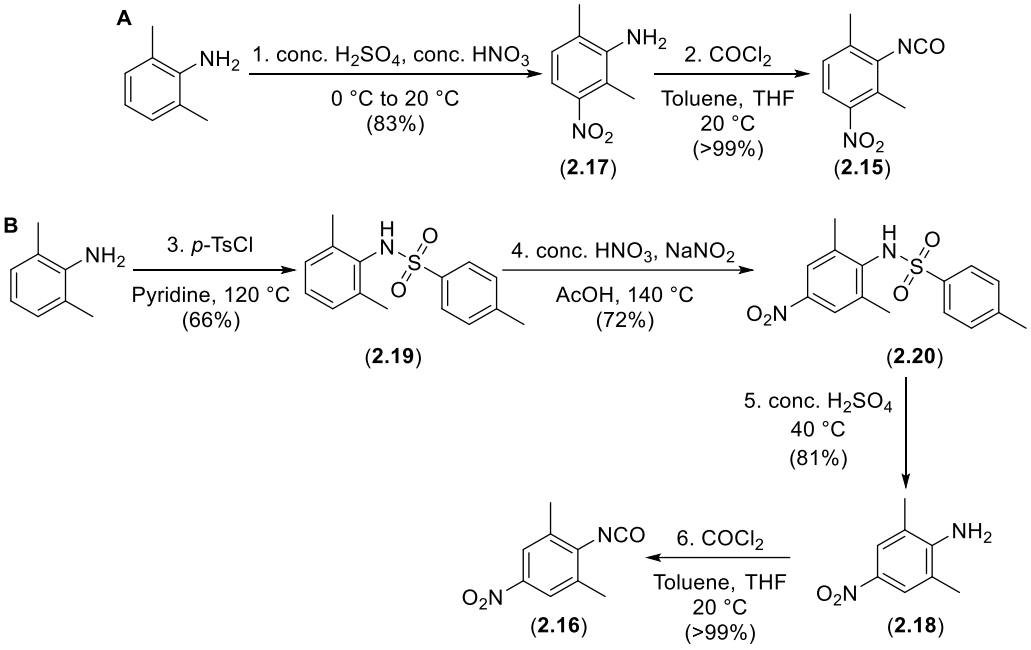

Scheme 13. The synthesis of the isocyanates **2.15** and **2.16**.

Ureas, **2.1** – **2.8** were then synthesised by reacting the respective amine 5-aminoisophthalic acid (**2.21**) or **2.14** with the appropriate isocyanate 3-nitrophenylisocyanate (**2.22**) or 4-nitrophenylisocyanate (**2.23**) (see Scheme 3). The reactions were monitored with FTIR spectroscopy to study the consumption of the isocyanate group and conversion to the corresponding urea.

2.15, **2.16**, **2.22**, **2.23** **2.14**, **2.21** **2.1 - 2.8**

2.14: $R_5 = R_6 = CH_3$
2.15: $R_1 = R_2 = CH_3$, $R_3 = NO_2$, $R_4 = H$
2.16: $R_1 = R_2 = CH_3$, $R_3 = H$, $R_4 = NO_2$
2.21: $R_5 = R_6 = H$
2.22: $R_1 = R_2 = H$, $R_3 = NO_2$, $R_4 = H$
2.23: $R_1 = R_2 = H$, $R_3 = H$, $R_4 = NO_2$

2.1: $R_1 = R_2 = R_3 = H$, $R_4 = NO_2$, $R_5 = R_6 = H$
2.2: $R_1 = R_2 = CH_3$, $R_3 = H$, $R_4 = NO_2$, $R_5 = R_6 = H$
2.3: $R_1 = R_1 = R_2 = R_3 = H$, $R_4 = NO_2$, $R_5 = R_6 = CH_3$
2.4: $R_1 = R_2 = CH_3$, $R_3 = H$, $R_4 = NO_2$, $R_5 = R_6 = CH_3$
2.5: $R_1 = R_2 = H$, $R_3 = NO_2$, $R_4 = R_5 = R_6 = H$
2.6: $R_1 = R_2 = CH_3$, $R_3 = NO_2$, $R_4 = R_5 = R_6 = H$
2.7: $R_1 = R_2 = H$, $R_3 = NO_2$, $R_4 = H$, $R_5 = R_6 = CH_3$
2.8: $R_1 = R_2 = CH_3$, $R_3 = NO_2$, $R_4 = H$, $R_5 = R_6 = CH_3$

Scheme 14. The general synthetic protocol used to afford the bisaromatic ureas **2.1** – **2.8**.

See the Appendix, Figures 1 – 40 for the characterisation data of these compounds and their precursors **2.9 – 2.20**. ^{1}H NMR spectroscopic analysis was employed to confirm the successful synthesis of the hydrogelator systems (see Figure 5).

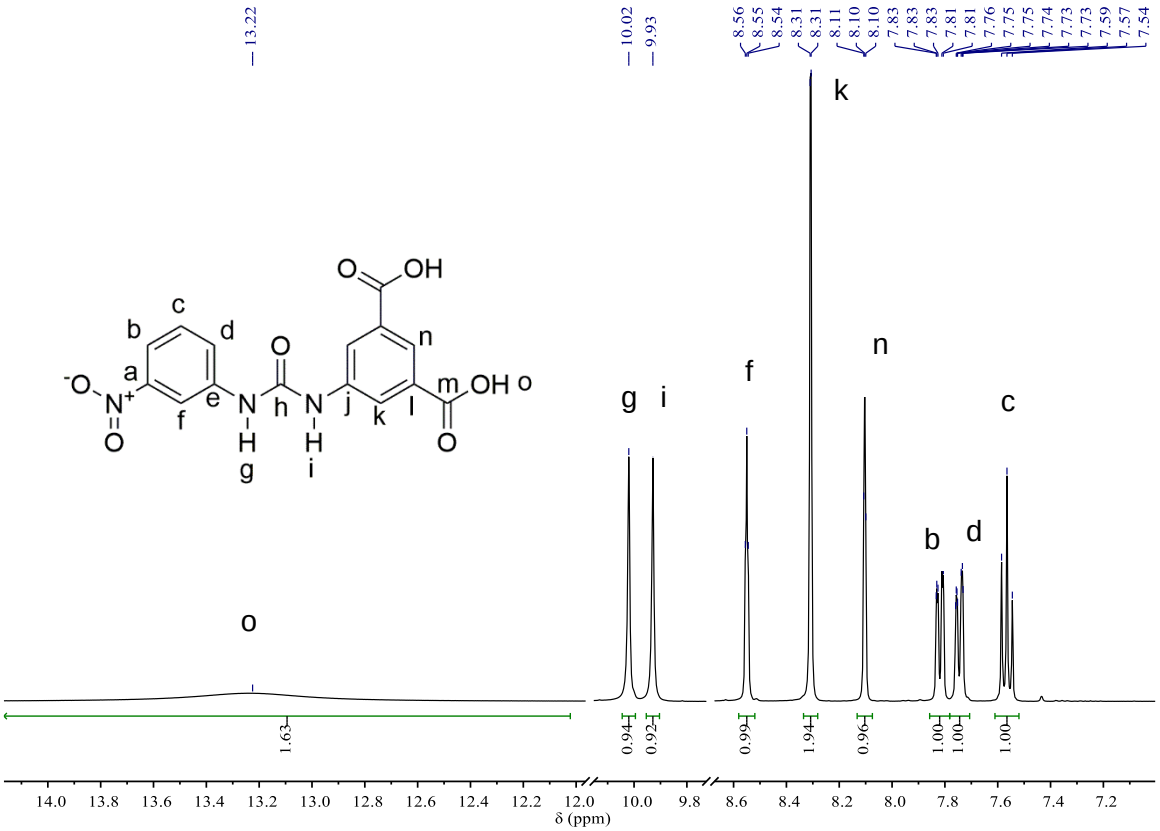

Figure 5. ^{1}H NMR spectra of bisaromatic urea **2.5** (400 MHz, DMSO-d_6, 298 K). The spectrum has been truncated for clarity; the full spectrum can be found in Appendix 1, Figure 9.

2.4 Critical gelation concentration discussion

The gel-forming potential of the bisaromatic ureas was assessed initially using vial inversion and the HCl pH switching methods (see Figure 6 and Appendix 1, Figures 43 – 46). All eight gelators were soluble in basic solution (NaOH, 0.1M) and, upon acidification, either formed a free-standing gel or failed to be self-supporting (see Figure 6).

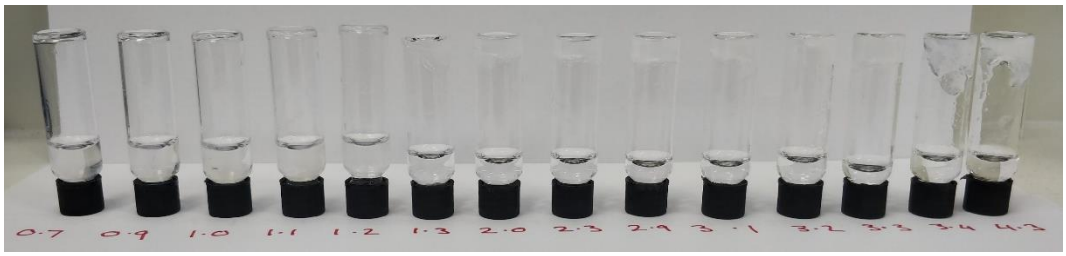

Figure 6. CGC determination via vial inversion of gelator **2.8**. The mass of the gelator in mg is written below each vial.

The bisaromatic ureas **2.1** and **2.5** each exhibited the same critical gelation concentrations (CGC) as reported previously (see Table 1).[17] Unexpectedly, **2.2** did not produce a free-standing gel upon pH switching and instead yielded a weak gel that did not pass the vial inversion test up to a gelator concentration of 20 mM (see Appendix 1, Figure 43). Gelator **2.3** did not pass the vial inversion test and instead formed a granular precipitate upon pH switching over the tested concentrations (see Appendix 1, Figure 43). The only structural difference

between the bisaromatic ureas **2.1**, **2.2,** and **2.3** is the presence of the two *ortho*-methyl substituents on **2.2** and **2.3**. The precipitation of bisaromatic urea **2.3** indicates increased structural order and phase separation from the solvent. Previously it has been observed in a structurally related bisaromatic urea series that precipitation also occurs for structures where the nitro group is not present, highlighting its importance in mediating hydrogen bond formation and fibril assembly in the gel state.[17] Solid-state analysis has shown that hydrogelator **2.1** assembles as a regular array of ribbons with planar molecules connected via urea to nitro hydrogen bonds and dimerisation of the carboxylic acid functional groups.[16] It is evident from the comparison of bisaromatic ureas **2.1 – 2.3** that the addition of *ortho*-methyl substituents to the aromatic units on either side of the urea has had a disruptive effect on the gel assembly process, probably by twisting the aromatic rings perpendicular to the urea and preventing co-planar assembly. Upon comparing the infrared spectroscopic data, the absorption band associated with the urea carbonyl was shifted to higher wavenumbers, 1645 and 1641 cm^{-1} for **2.2** and **2.3**, respectively, corresponding to the disordered urea carbonyl, in comparison to **2.1** (1600 cm^{-1}), indicative of an ordered hydrogen-bonded urea carbonyl. The nitro group in **2.1** is a hydrogen bond acceptor and able to effectively disrupt urea-urea hydrogen bonding in preference for urea-nitro interactions and form a regular array of ribbons;[7] however, in **2.2** and **2.3**, urea-urea interactions are now promoted as a result of the conformational control exerted by the *ortho*-methyl substituents.[46] This mismatch of intramolecular interactions is the likely reason for the inability of both **2.2** and **2.3** to form robust gel networks under comparable conditions to the bisaromatic urea **2.1**. This mismatch of intramolecular interactions was also evident for bisaromatic urea **2.4**; however, there is now an increased preference for urea-urea interactions as the urea is fixed into its perpendicular conformation. As a result, the urea carbonyl stretch was observed at 1614 cm^{-1} and weak gels could be formed (CGC of 3.3 mM). By employing the HCl pH switching procedure, the CGC values were established between 0.9 and 6.5 mM for the six gel-forming bisaromatic ureas (**2.1, 2.4 – 2.8**) (see Appendix 1, Figures 43 – 46). As a result of the low molecular weights of these compounds and their ability to form stable gels below 1% wt %, all six can be categorised as “super gelators”.[60]

Table 2. CGC values for hydrogelators synthesized in this study as determined by pH switching with HCl.

Compound	(**2.1**)	(**2.2**)	(**2.3**)	(**2.4**)	(**2.5**)	(**2.6**)	(**2.7**)	(**2.8**)
CGC (**mM**)	0.9	Not observed	Not observed	3.3	4.5	6.5	2.4	3.3

2.5 Rheological Studies

Rheological measurements were conducted at a constant gelator concentration (20.0 mM) to examine the viscoelastic properties of the self-assembled hydrogels. Gelation kinetics were

initially assessed by oscillatory time sweep experiments using the robust glucono-δ-lactone protocol introduced by Adams *et al.* to slowly switch the pH of the solution whilst simultaneously measuring storage and loss modulus as a function of time (Figure 7A).[61] As the pH was lowered, fibres formed, and eventually, network formation became apparent, entrapping the water medium. After equilibrating for twelve hours, the most stable hydrogelators (**2.1**, **2.4**, **2.6**, **2.7**) were subjected to amplitude (Figure 7A) and frequency sweep experiments (Figure 7B).

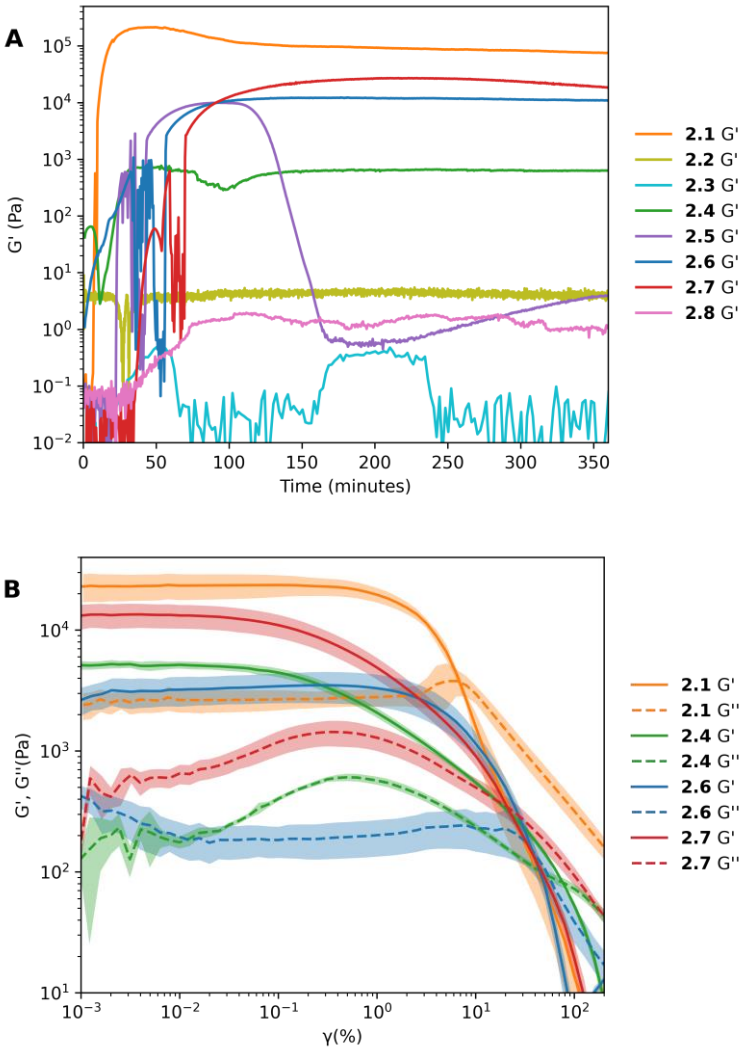

Figure 7. A) Storage modulus *vs* time graphs for hydrogels formed from gelators **2.1 – 2.8** as the pH was slowly switched using glucono-δ-lactone. **B**) Strain-controlled oscillatory amplitude sweeps of hydrogelators (**2.1**, **2.4**, **2.6**, and **2.7**), from 0.001% to 100% shear strain, shaded regions are standard deviation error bars calculated from three separate measurements.

Hydrogelator **2.1** proved to be the most robust gelator network in all of these tests, and its maximum storage modulus was observed within an hour of the addition of glucono-δ-lactone (Figure 7A). The appearance of a plateau, followed by a slight drop, indicates an equilibration period, after which the storage modulus remains approximately constant. The storage modulus of the hydrogelator **2.5** reached its maximum 100 minutes after the addition of glucono-δ-lactone. At this point, a gel to crystal transition was observed, resulting in a steep drop in the gel's storage modulus and syneresis of the entrapped water. A similar gel to crystal transition

was observed for **2.7**; however, the steep drop in storage modulus was not observed, and the partial gel phase is seen to be stable in oscillatory time sweep measurements. Hydrogelator **2.6** exhibited a very visually similar gel phase to that of **2.1**; a transparent gel is formed, which does not appear to undergo the same gel-to-crystal transition seen in **2.5** and **2.7**. The position of the *ortho*-substituents has a significant impact on the gel assembly. Hydrogelator **2.4** went through a gel to crystal transition within 12 hours of pH switching and remained stable after that. Hydrogelator **2.8** underwent a shallow increase in storage modulus as the solution became more acidic. The hydrogel formed from **2.8** is several orders of magnitude weaker than the other hydrogelators, and the gel robustness was thus not evaluated in greater detail. Both the bisaromatic ureas **2.2** and **2.3** failed to form gel networks and preferred to precipitate upon pH switching with glucono-δ-lactone. Oscillatory amplitude sweep experiments were performed to determine the yield stress, yield strain, and yield strain at the inversion of G' and G'' (Table 2). Frequency sweep experiments were performed under a constant strain of ($\gamma = 0.1\%$), and it was observed that the storage modulus (G') is almost independent of angular frequency within the tested frequency range and that the storage modulus (G') is approximately an order of magnitude greater than the loss modulus (G''), confirming the presence of the gel phase (Figure 8B).

Table 3. Rheological properties of hydrogelators.

	(2.1)	**(2.4)**	**(2.6)**	**(2.7)**
G'[a] (Pa)	1.780E+004	2.135E+003	4.653E+003	4.935E+003
G''[a] (Pa)	2.085E+003	211.9	206.8	228.5
γ_y%[b]	6.77±1.48	77.14±2.60	41.02±11.15	22.56±6.88
σ_y (Pa)[c]	373.40±28.17	72.65±4.87	118.35±57.60	92.21±32.69
γ_y%[c]	3.71±0.70	40.61±1.63	11.36±2.96	9.85±2.17

a = observed after equilibrating for 12 hours, measured at 1Hz and 0.1% shear strain, b = determined as the % strain at the inversion of G' and G'', c = determined from peak analysis of elastic stress *vs* shear strain data.

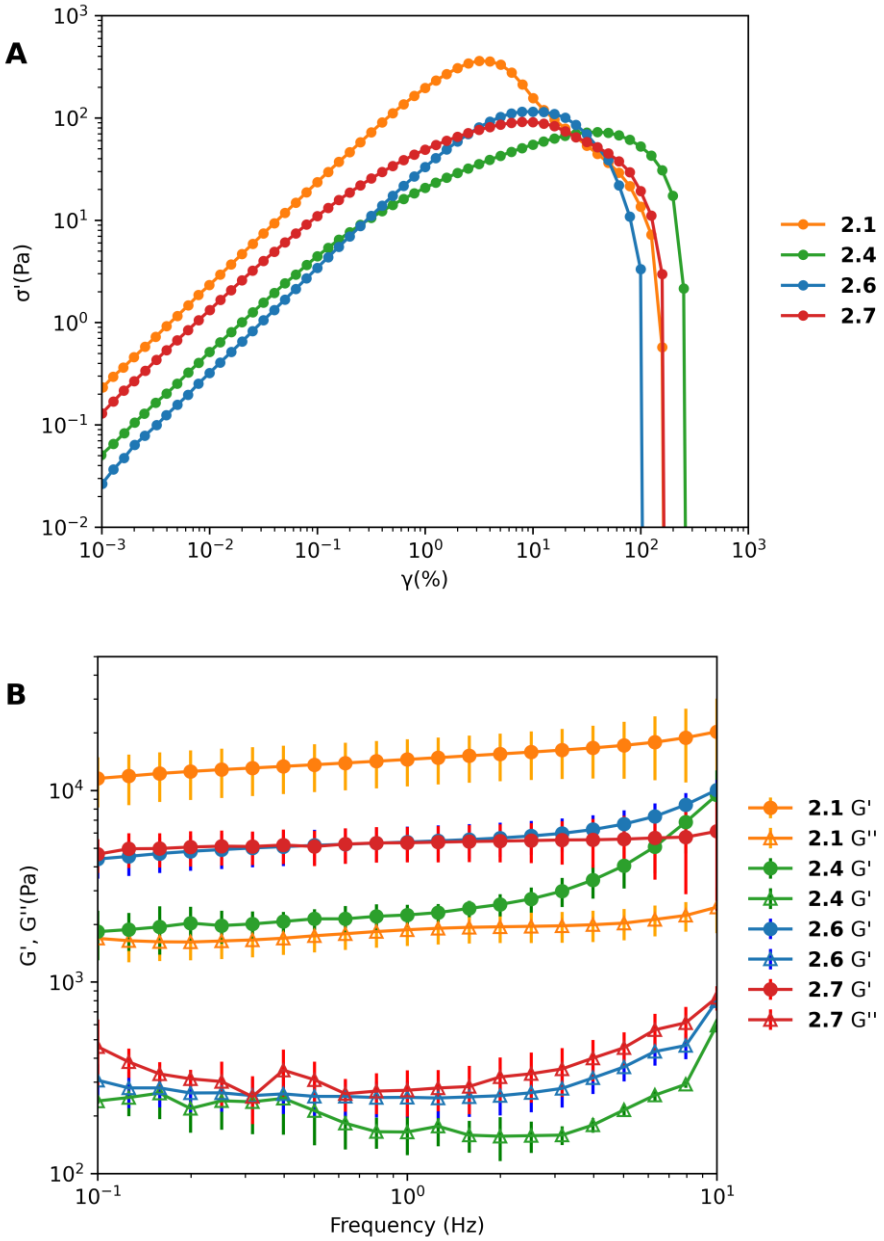

Figure 8. A) Strain-controlled oscillatory amplitude sweeps to measure elastic stress as a function of applied strain for hydrogels **2.1**, **2.4**, **2.6**, and **2.7**. **B**) Frequency sweep experiments showing the parallel dependence of G' and G'', standard deviation error bars were calculated from three separate measurements.

Microscopic self-healing behaviour was probed for the urea-based hydrogelator networks via rheological step strain measurements.[62–69] Mesoscale ruptures are induced at high shear strain, a critical parameter for the processing and injection of soft materials. As shown in Figure 9, a high-strain oscillatory shear strain sweep (γ = 250%, frequency = 1 Hz, 250 s) resulted in a quasi-liquid structure (G">G') because of the structural breakdown of the gel induced at high shear and the hydrogel material can thus flow. Upon removing the subjected high shear strain and applying a low magnitude strain sweep (γ = 0.1%, frequency = 1 Hz, 250 s), the network reforms, and G' recovers its initial value to form a quasi-solid state following the stress-induced flow. The rate and extent to which **2.1**, **2.4**, and **2.7** recovered their initial state were effectively identical over several cycles of breaking and reforming the network, highlighting the reversible

and robust nature of these dynamically cross-linked networks. Reversible dissociation and re-association of the network can effectively retard network failure, prolonging the material's lifespan. Most interestingly, the hydrogel network formed from gelator **2.6** did not recover its initial state upon returning to a low shear strain (γ = 0.1%) and formed a gel network an order of magnitude less robust than the initial gel. Upon closer inspection, when applying a high shear strain, mesoscale ruptures result in network destruction. Almost immediately, a gel network was reformed within this high shear domain where G' exceeds G'' by an order of magnitude. This resulted in slower network formation upon removal of the shear strain, evidenced by the steep gradient of G' and G'' and by a reduction in G' by a factor of 31 relative to that recorded before the high-shear exposure.

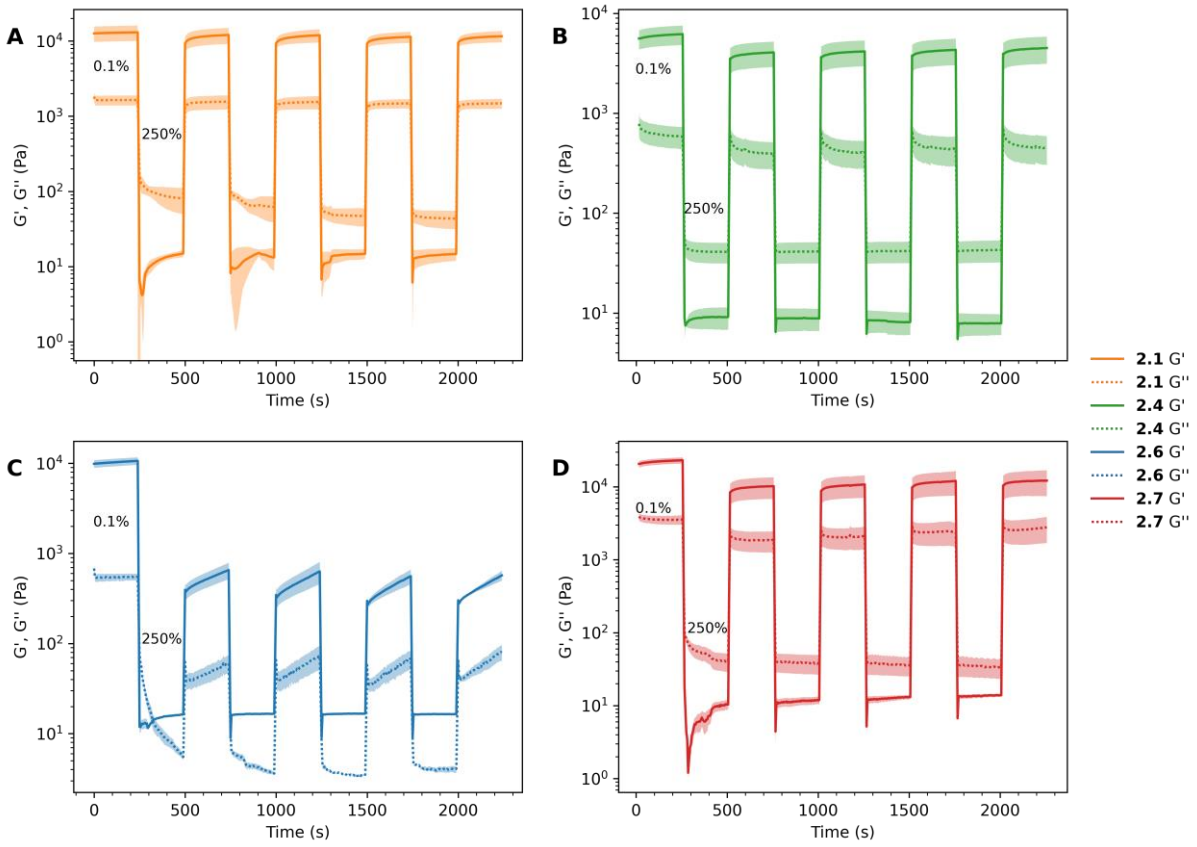

Figure 9. Continuous step-strain measurements of **A**) **2.1**, **B**) **2.4**, **C**) **2.6**, and **D**) **2.7** hydrogelator networks at 25 °C (high-amplitude oscillatory parameters: strain γ = 250%, frequency = 1 Hz, low-amplitude oscillatory parameters: strain γ = 0.1%, frequency = 1 Hz). Shaded regions are standard deviation error bars calculated from three separate measurements.

Intrigued by this phenomenon, further rheological studies were conducted, and hydrogelator **2.6** recovered its initial G' property following an extended low shear recovery period of 1200 s (See Figure 10).

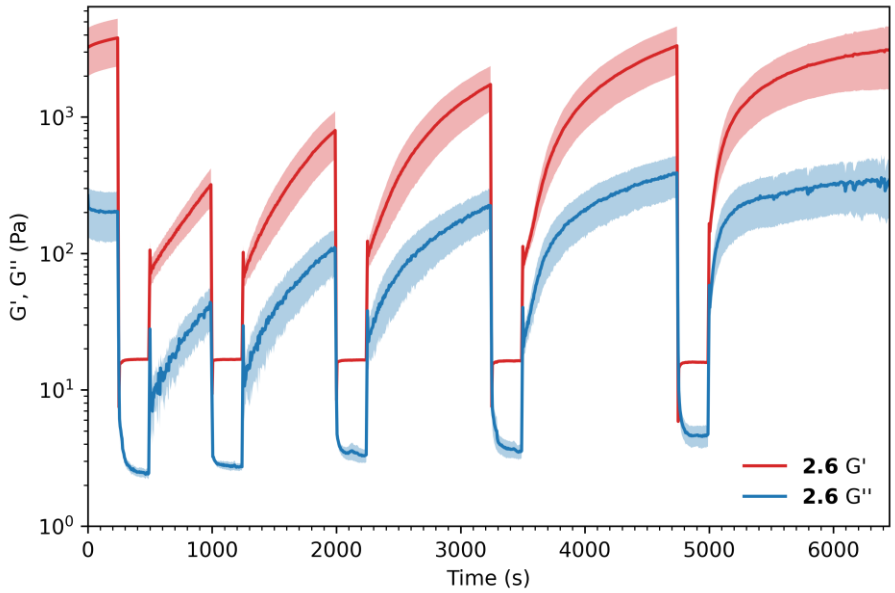

Figure 10. Continuous step-strain measurements of **2.6** at 25 °C (high-amplitude oscillatory parameters: strain γ = 250%, frequency = 1 Hz, low-amplitude oscillatory parameters: strain γ = 0.1%, frequency = 1 Hz) with increasing low shear interval until complete network recovery.

2.6 NMR Spectroscopic Kinetic Studies

The gel assembly kinetics were also probed by ^{1}H NMR spectroscopy.[70–72] Before gel assembly, the gelator molecules are sufficiently mobile to be detected on the NMR timescale;[73,74] they have suitable relaxation times for NMR spectroscopic analysis. As the pH is switched, gel formation occurs, and the non-mobile gel fibres become invisible to the spectrometer because of their molecular size and slow diffusion characteristics. Monomeric and oligomeric units can be quantified against an internal standard, in this case, dimethylsulfoxide (DMSO), by integrating the regions associated with the mobile phase. Kinetic information can be obtained by monitoring the changes in the ^{1}H NMR spectrum over time following the addition of glucono-δ-lactone. By plotting the concentration of gelator molecules

in the mobile phase against time, it was evident that there was a rapid initial drop in concentration in the first 20-30 minutes after addition (see Figure 11).

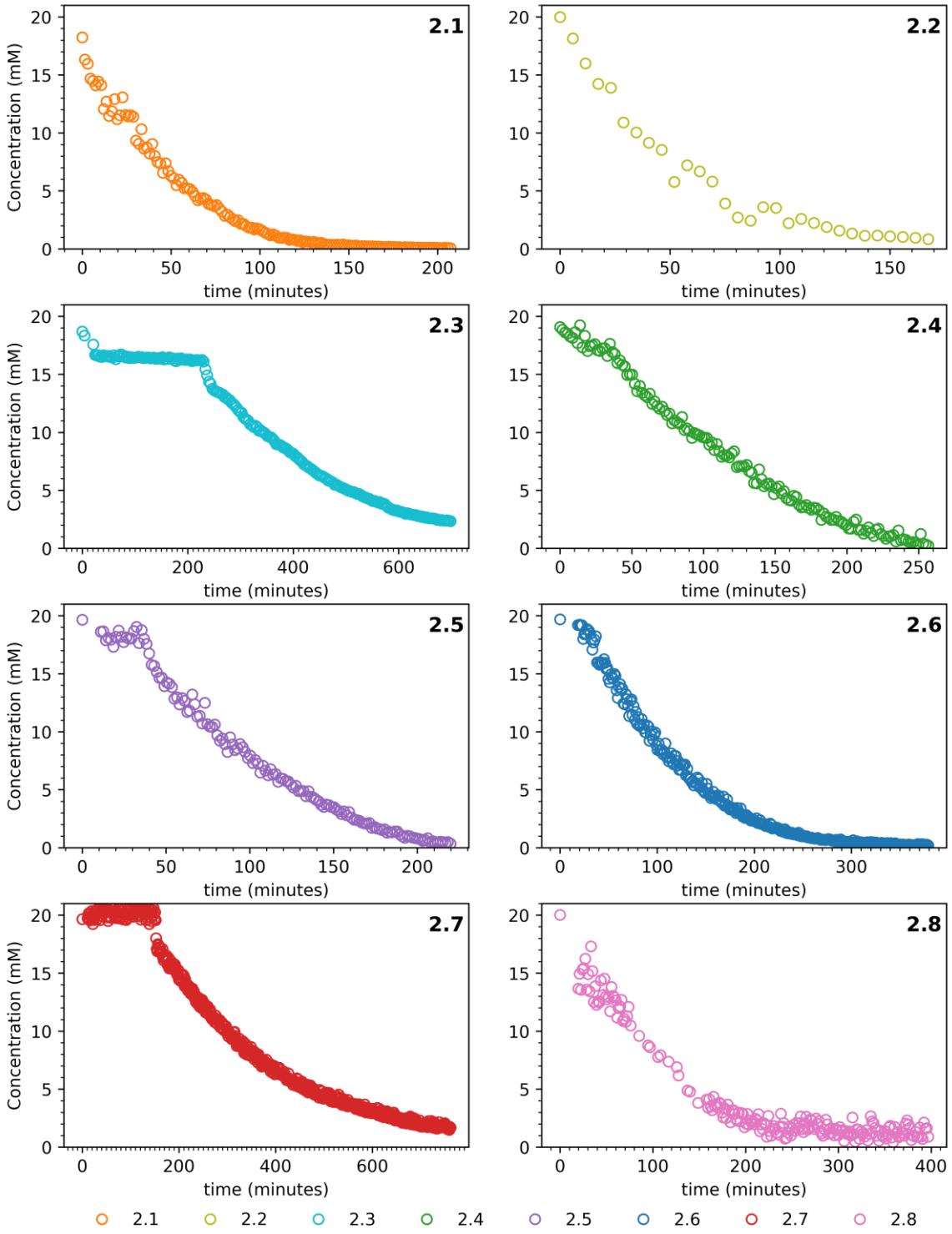

Figure 11. Kinetics of formation of gelator networks **2.1** – **2.8** as monitored by ^{1}H NMR spectroscopy.

This can be attributed to the rapid conversion of glucono-δ-lactone into gluconic acid by residual NaOH, rapidly lowering the pH of the solution. Afterwards, there is a buffering period as the pH gradually lowers to the pK_a of the gelator; this can be seen as a plateau in the

concentration *vs* time plot (see Figure 11). Once the pH is equivalent to the pK_a of the gelator, assembly of the LMWG network proceeds over several hours. The presence of methyl groups *ortho* to the carboxylic acids of the hydrogelators lowers their pKa, illustrated in a series of regioisomers by the increased buffering period of **2.3** and **2.7** relative to **2.2** and **2.6,** respectively. Thus, hydrogelators **2.3** and **2.7** took up to 750 minutes to convert to the less mobile phase compared to less than 250 minutes for both **2.2** and **2.6**. Intriguingly, the influence of the *ortho*-methyl substituents on the pK_a of carboxylic acids of **2.4** and **2.8** is not reflected as significantly in the buffering period. Rationalising this difference is not trivial, as the apparent pK_a of gelator molecules depends on the self-assembly step and can effectively change the pK_a from what might be expected for the non-assembled small molecule.[75] As such, this decreased buffering period was attributed to increased order within the gel network, imposed by the conformation control of the urea phenyl torsion predicted to accommodate two methyl groups *ortho* to the urea on each aryl ring. It is proposed that the urea-urea interactions dominate and consequently increase the apparent pK_a of **2.4** and **2.8**.

To further understand the nature of the assembly, the data were then fitted to Avrami's kinetic model,[76–78] where *n* is the Avrami exponent and reflects the growth of the hydrogelator network (see Figure 12). Exponent values close to 1.0 are associated with 1-dimensional growth with little branching, whereas values of 2 or higher are associated with 3-dimensional growth and branching. The effect is demonstrated elegantly by hydrogelators **2.2** and **2.8**, which have exponents of 1.0, and in the case of **2.2** a stable gel network could not be formed when pH switching with glucono-δ-lactone; similarly, **2.8** formed one of the weakest gel networks as determined by rheological testing. Hydrogelator **2.3** exhibited the most 3-dimensional growth, and an Avrami exponent value of 2.28 was determined for this compound, indicating significant branching and eventual precipitation from solution rather than gel formation. Gelators **2.4**, **2.5,** and **2.7** all have exponents between 1.6 and 1.9, suggesting branching, and tended to undergo gel to crystal transitions over time as the extended network formed. Hydrogelators **2.1** and **2.6** had exponents between 1.33-1.38, suggesting some degree of branching, exhibited metastability,[79,80] and did not undergo observable gel-to-crystal transitions for periods greater than one month, illustrating the requirement for understanding the delicate balance in network growth when designing gelator molecules.

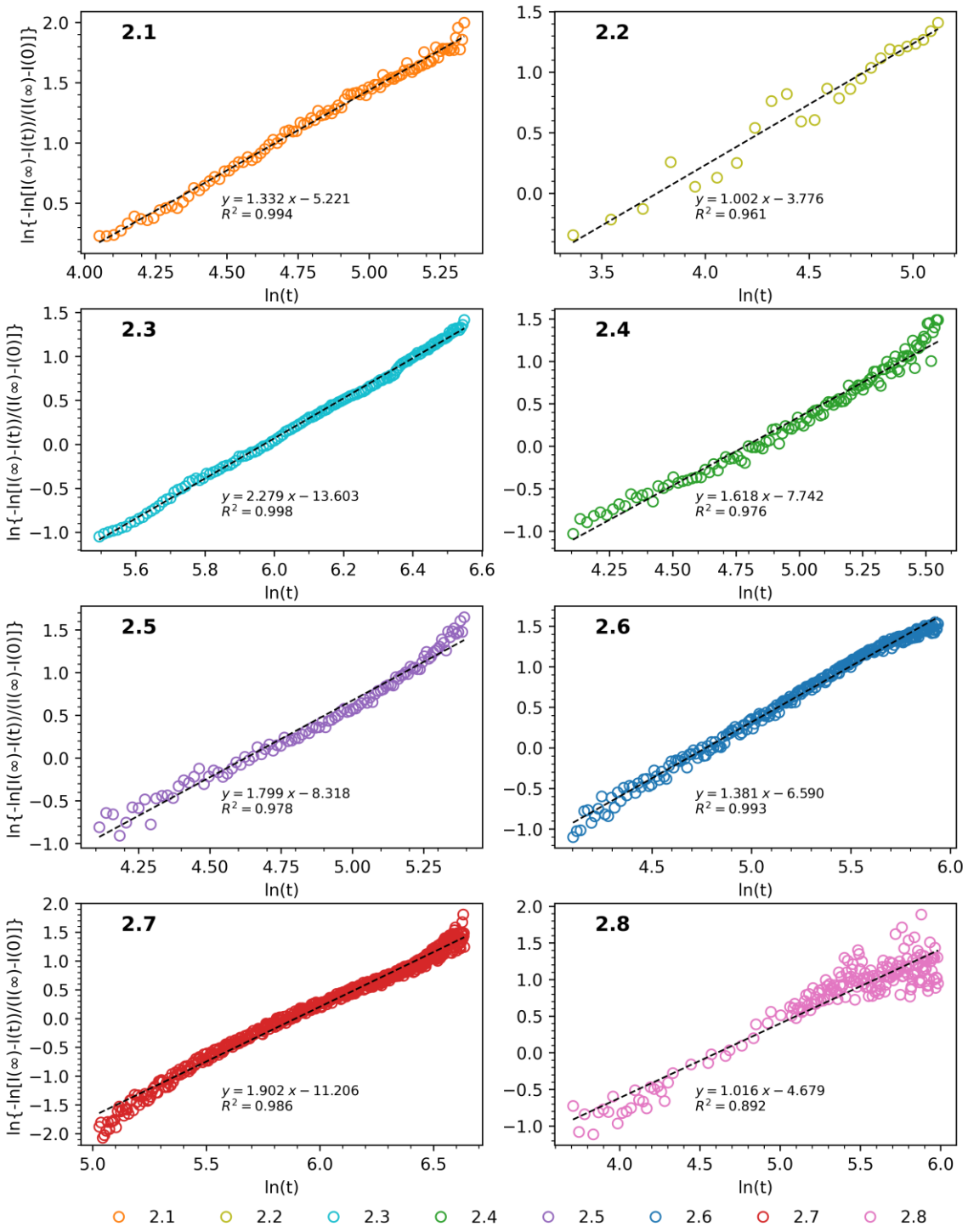

Figure 12. Avrami plot for the network formation of gelators **2.1 – 2.8** (20 mM) as monitored by ^{1}H NMR spectroscopy, where the Avrami exponent, *n*, is the gradient of the line of best fit.

2.7 Dye uptake experiments

Organic dyes such as methylene blue have been used as model organic pollutants because of their characteristic UV-vis absorbance bands to predict contaminant removal capability from water sources.[17] Previous studies have shown that the hydrogel formed from bisaromatic urea **2.1** is an effective scavenger of methylene blue, methylene green, and Rhodamine B.[17] In this study, it was decided to reduce the quantity of hydrogelator used from 1.00 mL of gel

(concentration: 20 mM) to 0.25 mL (with a concentration of 10 mM) to conduct dye uptake studies within a cuvette. The gelators were pH switched using HCl with the resultant solution left to stand without agitation, thus removing the influence of mixing. The dye, in this case, methylene blue (3.00 mL, 4.0 mgL^{-1}), was pipetted gently onto the gel surface, allowing dye sequestering. Interestingly, it was found that four of the eight hydrogelators (**2.1**, **2.5**, **2.6**, and **2.8**) were able to effectively sequester the planar cationic dye from the solution (see Figures 13 and 14), evident by the significant drop in absorbance (Figures 13 and 14).

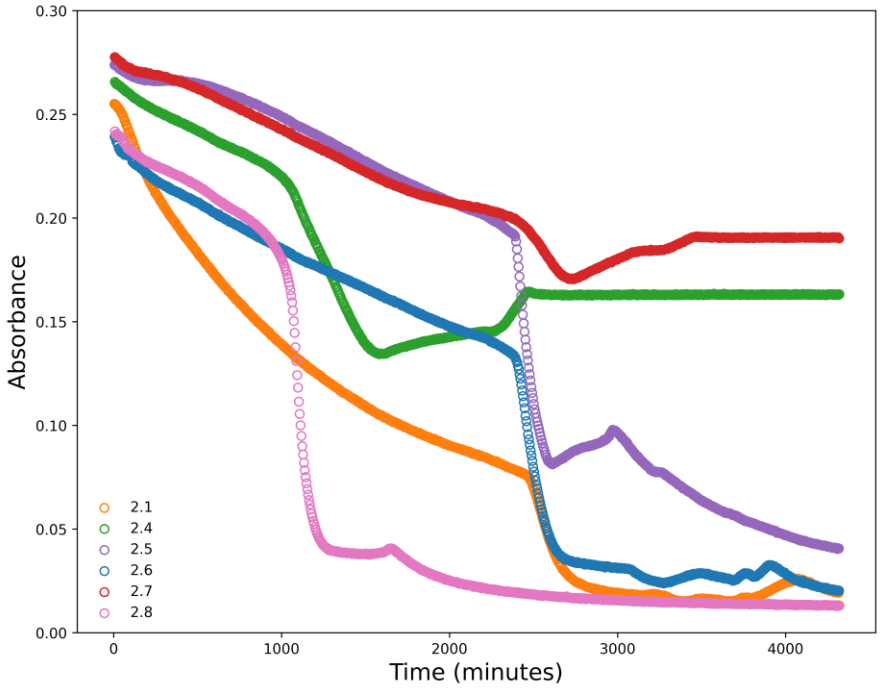

Figure 13. Absorbance maxima of methylene blue (664 nm) *vs* time for hydrogelators **2.1**, **2.4**, **2.5**, **2.6**, **2.7** and **2.8**.

Hydrogelators **2.2** and **2.3** showed poor dye sequestering ability and did not form stable gels when pH switched with glucono-δ-lactone. Hydrogelator **2.5** precipitated after pH switching with HCl, and although it showed impressive extraction capabilities (88%), it was not suitable for effective dye extraction. Hydrogelator **2.6** proved to be more stable than **2.5** and **2.7**; it had a similar dye extraction capability (94%) to **2.1** (95%) and **2.8** (96%). Hydrogelators **2.4** and **2.7** showed a reduced proficiency at removing methylene blue from solution, with only 54% and 46% of the methylene blue removed, respectively (see Figure 14A and B). The asymmetry of the aromatic rings in **2.7** compared to **2.8** may result in a less planar network, potentially presenting a barrier to methylene blue intercalation and reducing its extraction from solution.

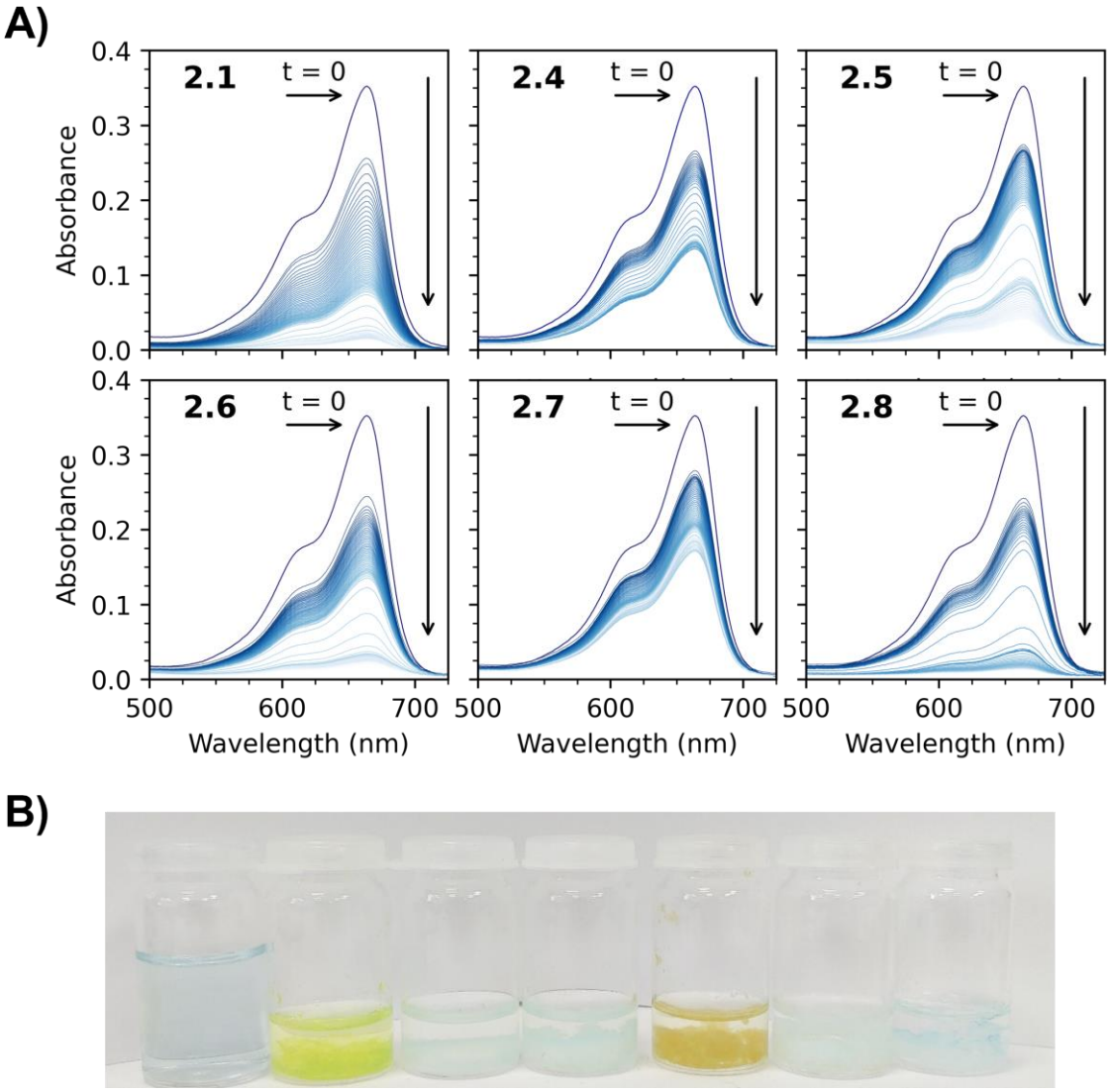

Figure 14. A) Plot of methylene blue absorption for hydrogelators **2.1**, **2.4**, **2.5**, **2.6**, **2.7**, and **2.8**; each line represents a measurement taken every hour. **B)** From left to right: methylene blue solution (3 mL, 4 mgL^{-1}) without gelator, gelators **2.1**, **2.4**, **2.5**, **2.6**, **2.7**, **2.8** (10 mM), gelled with HCl, within 12 hours after addition of methylene blue solution (3 mL, 4 mgL^{-1}).

2.8 Conclusions

A library of structurally similar bisaromatic ureas (**2.1 – 2.8**) were synthesised and characterised. The gelation of these behaviour compounds was investigated in aqueous media by acidifying a basic solution of the hydrogelator by either adding HCl or by the slow hydrolysis of glucono-δ-lactone. Gel assembly kinetics were monitored using rheology by ^{1}H NMR spectroscopic analysis; rheological measurements also assessed the gel's ability to form stable networks and reform after experiencing destructive oscillatory shear. The bisaromatic ureas **2.1**, **2.6** and **2.8** were more effective at extracting methylene blue from the solution. This was attributed to intermolecular urea to nitro interactions promoting the formation of a 1-dimensional network (as determined by Avrami plots), thus allowing for the intercalation of

the planar cationic dye. In contrast, the bisaromatic ureas **2.4** (54%) and **2.7** (46%), which featured *ortho*-methyl groups, formed weak gel networks and were not suitable for dye sequestering - the result of the domination of urea-urea associations as an interaction mode for those structures. In addition, although bisaromatic urea **2.5** exhibited excellent dye extraction capabilities (88%), it underwent a gel to crystal transition if left for more than twelve hours and therefore is not practical for dye extraction. The structure-property relationships developed in this study will contribute to improvements in the targeted design of materials for highly effective water purification systems.

2.9 Experimental Section

General. Dry dimethylformamide (DMF) (Sigma Aldrich) was used as supplied. Tetrahydrofuran (THF) was distilled from benzophenone and sodium before use. All other reagents were purchased from Sigma Aldrich and used as received. Thin-layer chromatography (TLC) was conducted using TLC silica gel 60 F254 aluminium-backed sheets (Sigma Aldrich) and visualised with ultraviolet light, ninhydrin, or potassium permanganate staining. ^{1}H NMR and ^{13}C{H} NMR spectra were recorded on either a Bruker Nanobay 400 or a Bruker DPX 400 spectrometer operating at 400 MHz for ^{1}H NMR or 100 MHz ^{13}C{H} NMR, respectively. The data were processed using MestReNova Version 11.0.3-18688. Samples for NMR spectroscopic analysis were prepared in $CDCl_3$ or DMSO-d_6, and dissolution was aided with brief heating. Chemical shifts (δ) are reported in ppm relative to tetramethylsilane (δ 0.00 ppm) for $CDCl_3$ and the residual solvent resonance (δ 2.50 ppm) for d_6-DMSO in ^{1}H NMR. Infrared (IR) spectroscopic analysis was carried out using a Perkin Elmer 100 FT-IR (Fourier Transform Infrared) instrument with a diamond-ATR sampling accessory. Ultraviolet-visible spectra were measured with a Varian Cary 300 spectrophotometer, using 1 cm^2 quartz cuvettes, in the wavelength range of 500–750 nm. Mass spectrometry was conducted using ThermoFisher Scientific Orbitrap XL LCMS. The sample was introduced by liquid chromatography, and sample ionisation was achieved by electrospray ionisation (ESI). Melting points were recorded using a Stuart MP10 melting point apparatus and are uncorrected. Elemental microanalyses of **2.3**, **2.8**, **2.9, 2.10**, **2.14**, **2.15** and **2.16** were performed by MEDAC Ltd.

2.10 Dye adsorption studies

Dye uptake was measured using 1 cm^2 quartz cuvettes with a 20 mM solution of each hydrogelator in a 0.1 M NaOH solution. 125 μL of this solution was then pipetted into the base of a cuvette, to which HCl (125 μL, 0.2 M) was added to switch the pH and initiate gelation. A stock solution of methylene blue (3.00 mL, 4.0 mgL^{-1}) was then pipetted carefully on top of the gel. Scans were performed once a minute with the spectrometer operating in kinetic mode.

2.11 pH switching procedures

The bisaromatic ureas were subject to two different pH-switching methodologies. In both cases, the dried hydrogelator was dissolved in 0.1 M NaOH solution and briefly sonicated to ensure complete dissolution. The pH of the solution was then switched using either aliquots of 0.2 M HCl (left momentarily to equilibrate), or two equivalents of glucono-δ-lactone were added as a solid and vortexed until complete dissolution had occurred.

2.12 Critical gelation concentration determination

Critical Gelation Concentration (CGC) determination was carried out in a 2 mL screw**-**top glass vial. The minimum gelator mass was determined to the nearest milligram and varied every 0.2 mg to obtain an accurate CGC value.

2.13 NMR gelation kinetic measurements

The gelation kinetics can be measured using the glucono-δ-lactone pH switching procedure, which induces a controlled change in the solution's pH.[61] The gel-phase is invisible to the spectrometer, and the concentration of the sol-phase can be measured against an internal standard, in this case, non-deuterated DMSO.[70] Fitting Avrami's kinetic model to the concentration *vs* time data,[76–78] the Avrami exponent of n was determined. This analysis was performed on all bisaromatic ureas (**2.1 – 2.8**).

2.14 Rheology measurements

Rheological measurements were performed on a Malvern Kinexus Lab+ rheometer using a 40 mm diameter 4° cone and plate geometry configuration or a 20 mm parallel plate geometry and analysed using RSpace Kinexus v1.75.2326 software. Oscillatory time sweep measurements involved casting 1000 µL of 20 mM solutions of **2.1 – 2.8** prepared according to the gel pH switching method described above onto the stainless-steel plate and then lowering the cone to the measurement position (0.15 mm). Oscillatory time sweep gelation measurements commenced immediately after that, but otherwise, the solution was left to form a gel for 12 hours. A temperature of 25 °C was used for the oscillatory time sweep study, frequency, and amplitude sweeps. Oscillatory time sweep experiments were performed at 1 rad/s and constant strain (γ) = 0.1%. Frequency sweeps were performed with a log ramp frequency (f) = 0.01 – 10 Hz and constant strain (γ) = 0.1%. Amplitude sweeps were performed with constant frequency (f) = 1 Hz and log ramp strain (γ) = 0.1 – 100%. Thixotropy measurements were performed alternating between low strain (f = 1 Hz, γ = 0.1%, 250 s) and high strain (f = 1 Hz, γ = 250%, 250 s).

2.15 X-ray crystallographic analysis

Crystals of **2.10** and **2.12** were mounted under Paratone-N oil and flash cooled to 100 K under nitrogen in an Oxford Cryosystems Cryostream. Single-crystal X-ray intensity data were

collected using a Rigaku XtaLAB Synergy diffractometer (Cu Kα radiation (λ = 1.54180 Å)). The data were reduced within the CrysAlisPro software.[81] The structures were solved using the program Superflip[82] and all non-hydrogen atoms located. Least-squares refinement against *F* was carried out using the *CRYSTALS* suite of programs.[83] The non-hydrogen atoms were refined anisotropically. All the hydrogen atoms were located in difference Fourier maps, then placed geometrically with a C-H distance of 0.95 Å and a U_{iso} of ~1.2 times the value of U_{eq} of the parent C atom. The hydrogen atoms were then refined with riding constraints.

Synthesis of compounds 2.1 – 2.8. The aromatic isocyanate (3 mmol), amine (3.05 mmol), THF (30 mL), and DMF (3 mL) were mixed under an argon atmosphere. The reaction mixture was stirred at 20 °C for 16 hours. The solution was concentrated *in vacuo,* and the residue was dissolved in the 1M NaOH (100 mL) solution and filtered to remove any insoluble material. The bisaromatic ureas were then isolated by inducing gelation by adding conc. HCl and filtering. The resulting gels **2.1** (0.96 g, 94%), **2.2** (0.97 g, 87%), **2.3** (0.80 g, 72%), **2.4** (1.02 g, 85%), **2.5** (0.95 g, 92%), **2.6** (0.90 g, 81%), **2.7** (0.78 g, 70%), **2.8** (0.89 g, 74%) were then washed with deionised water until neutral and dried under vacuum.

5-(3-(4-Nitrophenyl)ureido)isophthalic acid[16] **(2.1).** Mp = 281 – 283 °C (lit. 296 – 297 °C);[16] FTIR ATR: 3366 (νN-H), 3329 (νN-H), 3120 (νC-$H_{aromatic}$), 2972 (νC-H_{alkyl}), 1720 (νC=O_{acid}), 1703 (νC=O_{acid}), 1600 (νC=O_{urea}), 1538 (νN-$O_{asymmetric}$), 1320 (νN-$O_{symmetric}$); ^{1}H NMR: (400 MHz, DMSO-d_6) δ 10.40 (s, 1H, H_e), 10.17 (s, 1H, H_g), 8.31 (d, J = 1.5 Hz, 2H, H_i), 8.19 (AA'XX', 2H, H_b), 8.11 (t, J = 1.5 Hz, 1H, H_k), 7.72 (AA'XX', 2H, H_c); ^{13}C{H} NMR: (100 MHz, DMSO-d_6) δ 166.5 (C_i), 152.3 (C_f), 146.3 (C_d), 141.2 (C_a), 140.0 (C_h), 131.9 (C_j), 125.2 (C_b), 123.7 (C_k), 122.6 (C_i), 117.5 (C_c); HRMS (ESI, m/z): calcd for $C_{15}H_{12}O_7N_3$ ($[M+H]^+$) 346.0670, found 346.0668.

5-(3-(2,6-Dimethyl-4-nitrophenyl)ureido)isophthalic acid (2.2). Mp = 285 – 287 °C; FTIR ATR: 3346 (νN-H), 3200 (νN-H), 3073 (νC-$H_{aromatic}$), 2973 (νC-H_{alkyl}), 1714 (νC=O_{acid}), 1691 (νC=O_{acid}) 1645 (νC=O_{urea}), 1562 (νN-$O_{asymmetric}$), 1338 (νN-$O_{symmetric}$) cm^{-1}; ^{1}H NMR: (400 MHz, DMSO-d_6) δ 13.19 (s, 2H, H_n), 9.53 (s, 1H, H_h), 8.43 (s, 1H, H_f), 8.29 (d, J = 1.5 Hz, 2H, H_j), 8.07 (t, J = 1.6 Hz, 1H, H_l), 8.02 (s, 2 H, H_b), 2.34 (s, 6 H, H_d); ^{13}C{H} NMR: (100 MHz, DMSO-d_6) δ 166.6 (C_m), 152.3 (C_g), 144.7 (C_a), 142.0 (C_i), 140.6 (C_e), 137.0 (C_c), 131.2 (C_k), 123.2 (C_l), 122.60 (C_j), 122.58 (C_b), 18.9 (C_d); HRMS (ESI, m/z): calcd for $C_{17}H_{16}O_7N_3$ ($[M+H]^+$) 374.0983, found 374.0982.

4,6-Dimethyl-5-(3-(4-nitrophenyl)ureido)isophthalic acid (2.3). Mp = 286 – 288 °C; 3538 (νN-H), 3258 (νN-H), 3195(νN-H), 3053 (νC-$H_{aromatic}$), 2973 (νC-H_{alkyl}), 1691 (νC=O_{acid}), 1641 (νC=O_{urea}), 1543 (νN-$O_{asymmetric}$),1327 (νN-$O_{symmetric}$); ^{1}H NMR: (400 MHz, DMSO-d_6) δ 13.07 (s, 2H, H_m), 10.37 (s, 1H, $H_{e/g}$), 8.72 (s, 1H, $H_{e/g}$), 8.21 – 8.13 (m, 3H, H_b + H_n), 7.69 (AA'XX', 2H, H_c), 2.46 (s, 6H, H_j); ^{13}C{H} NMR: (100 MHz, DMSO-d_6) δ 168.2 (C_l), 152.8(C_f), 146.9 (C_a),

140.8 ($C_d + C_k$), 137.3(C_h), 129.7(C_i), 129.3 (C_n), 125.2 (C_b), 117.1 (C_c), 16.1 (C_j); Anal. Calcd. For $C_{17}H_{15}N_3O_7$: C, 54.69; H, 4.05; N, 11.25. Found C, 54.56; H, 4.03; N, 11.21.

5-(3-(2,6-Dimethyl-4-nitrophenyl)ureido)-4,6-dimethylisophthalic acid (2.4). Mp = 322 – 324 °C; FTIR ATR: 3250 (νN-H), 2926 (νC-$H_{aromatic}$), 1689 (νC=O_{acid}), 1614 (νC=O_{urea}), 1528 (νN-$O_{asymmetric}$), 1468 (νC-C), 1436 (νC-C), 1399 (νC-C), 1347 (νN-$O_{symmetric}$), cm^{-1}; ^{1}H NMR: (400 MHz, DMSO-d_6) δ 13.05 (s, 2H, H_n), 8.57 (s, 1H, $H_{f/h}$), 8.26 (s, 1H, $H_{f/h}$), 8.12 (s, 1H, H_o), 7.98 (s, 2H, H_b), 2.48 (s, 6H, H_k), 2.36 (s, 6H, H_d); ^{13}C{H} NMR: (100 MHz, DMSO-d_6) δ 168.3 (C_m), 153.1 (C_g), 144.5 (C_a), 142.7 (C_e), 140.9 (C_l), 138.0 (C_i), 136.8 (C_c), 129.5 (C_j), 129.3 (C_o), 122.6 (C_b), 18.5 (C_d), 16.1 (C_k); HRMS (ESI, m/z): calcd for $C_{19}H_{20}O_7N_3$ ($[M+H]^+$) 402.1296, found 402.1294.

5-(3-(3-Nitrophenyl)ureido)isophthalic acid[17] **(2.5).** Mp = 283 – 285 °C; FTIR ATR: 3374 (νN-H), 3088 (νC-$H_{aromatic}$), 2831 (νC-H_{alkyl}), 1727 (νC=O_{acid}), 1688 (νC=O_{acid}), 1602 (νC=O_{urea}), 1521 (νN-$O_{asymmetric}$), 1440 (νC-C), 1405 (νC-C), 1333 (νN-$O_{symmetric}$) cm^{-1}; ^{1}H NMR: (400 MHz, DMSO-d_6) δ 13.22 (s, 2H, H_o), 10.02 (s, 1H, H_g), 9.93 (s, 1H, H_i), 8.55 (appt. t, 1H, H_f), 8.31 (d, J = 1.5 Hz, 2H, H_k), 8.10 (t, J = 1.5 Hz, 1H, H_n), 7.82 (appt. dd, 1H, H_b), 7.75 (appt. dd, 1H, H_d), 7.57 (appt. t, J = 8.2 Hz, 1H, H_c); ^{13}C{H} NMR: (100 MHz, DMSO-d_6) δ 166.5 (C_m), 152.6 (C_g), 148.2 (C_a), 140.9 (C_e), 140.2 (C_j), 131.8 (C_l), 130.1 (C_c), 124.2 (C_d), 123.5 (C_n), 122.6 (C_k), 116.4 (C_b), 112.0 (C_f); HRMS (ESI, m/z): calcd for $C_{15}H_{12}O_7N_3$ ($[M+H]^+$) 346.0670, found 346.0668.

5-(3-(2,6-Dimethyl-3-nitrophenyl)ureido)isophthalic acid (2.6). Mp = 269 – 271 °C; FTIR ATR: 3260 (νN-H), 3086 (νC-$H_{aromatic}$), 2932 (νC-H_{alkyl}), 1695 (νC=O_{acid}), 1646 (νC=O_{urea}), 1518 (νN-$O_{asymmetric}$), 1439 (νC-C), 1342 (νN-$O_{symmetric}$) cm^{-1}; ^{1}H NMR: (400 MHz, DMSO-d_6) δ 9.66 (1H, s, H_p), 8.41 (s, 1H, $H_{i/k}$), 8.30 (d, J = 1.5 Hz, 2H, H_m), 8.08 (t, J = 1.5 Hz, 1 H, H_q), 7.75 (d, J = 8.4 Hz, 1H, H_b), 7.35 (d, J = 8.4 Hz, 1H, H_c), 2.33 (s, 3H, H_h), 2.32 (s, 3 H, H_e); ^{13}C{H} NMR: (100 MHz, DMSO-d_6) δ 166.7 (C_n), 153.1 (C_i), 148.7 (C_a), 142.1 (C_g), 140.8 (C_l), 137.0 (C_f), 131.7 (C_n), 130.6 (C_d), 128.1 (C_c), 123.2 (C_q), 122.6 (C_m), 121.9 (C_b), 18.8 (C_e), 14.6 (C_h); HRMS (ESI, m/z): calcd for $C_{17}H_{16}O_7N_3$ ($[M+H]^+$) 374.0983, found 374.0981.

4,6-Dimethyl-5-(3-(3-nitrophenyl)ureido)isophthalic acid (2.7). Mp = 285 – 286 °C; FTIR ATR: 3276 (νN-H), 3087 (νC-$H_{aromatic}$), 2980, (νC-H_{alkyl}), 2929 (νC-H_{alkyl}), 2860 (νC-H_{alkyl}), 1681 (νC=O_{acid}), 1642 (νC=O_{urea}), 1528 (νN-$O_{asymmetric}$), 1464 (νC-C), 1434 (νC-C), 1378 (νC-C), 1350 (νN-$O_{symmetric}$) cm^{-1}; ^{1}H NMR: (400 MHz, DMSO-d_6) δ 13.07 (s, 2H, H_o), 9.66 (s, 1H, $H_{g/i}$), 8.54 (s, 1H, H_f), 8.21 (s, 1H, $H_{g/i}$), 8.17 (s, 1H, H_p), 7.82 – 7.69 (m, 2H, H_b + H_d), 7.59 – 7.50 (m, 1H, H_c), 2.47 (s, 6H, H_l). ^{13}C{H} NMR: (100 MHz, DMSO-d_6) δ 168.2 (C_n), 153.2 (C_a), 148.1 (C_h), 141.5 (C_m), 141.0(Ce), 137.4 (C_j), 130.0 (C_c), 129.7 (C_p), 129.3 (C_k), 124.1 (C_d), 116.0 (C_b), 111.9 (C_f), 16.1 (C_l). HRMS (ESI, m/z): calcd for $C_{17}H_{16}O_7N_3$ ($[M+H]^+$) 374.0983, found 374.0980.

5-(3-(2,6-Dimethyl-3-nitrophenyl)ureido)-4,6-dimethylisophthalic acid (2.8). Mp =312 – 314 °C; FTIR ATR: 3239 (νN-H), 3085 (νC-$H_{aromatic}$), 2980 (νC-H_{alkyl}), 2926 (νC-H_{alkyl}), 1691 (νC=O_{acid}), 1619 (νC=O_{urea}), 1522 (νN-$O_{asymmetric}$), 1469 (νC-C), 1423 (νC-C), 1379 (νN-$O_{asymmetric}$) cm^{-1}; ^{1}H NMR: (400 MHz, DMSO-d_6) δ 13.05 (s, 2H, H_f), 8.33 (s, 1H, $H_{i/k}$), 8.20 (s, 1H, $H_{i/k}$), 8.13 (s, 1H, H_q), 7.72 (d, J = 8.4 Hz, 1H, H_b), 7.33 (d, J = 8.4 Hz, 1H, H_c), 2.49 (s, 6H, H_l), 2.37 (s, 3H, H_h), 2.35 (s, 3H, H_e). $^{13}C\{H\}$ NMR: (100 MHz, DMSO-d_6) 168.3 (C_p), 153.8 (C_j), 148.7 (C_a), 142.1 (C_d), 141.0 (C_o), 138.1 (C_f), 137.6 (C_m), 130.6 (C_g), 129.5 (C_q), 129.2 (C_n), 128.0 (C_c), 121.7 (C_b), 18.7 (C_e), 16.1 (C_l), 14.5 (C_h). Anal. Calcd. For $C_{19}H_{19}N_3O_7$: C, 56.86; H, 4.77; N, 10.46. Found C, 56.56; H, 4.64; N, 10.21.

1,5-Bis(chloromethyl)-2,4-dimethylbenzene[58] **(2.9).** *m*-Xylene (86.0 g, 810.0 mmol), paraformaldehyde (55.9 g, 1.86 mol) were suspended in conc. HCl (800 mL) and glacial acetic acid (200 mL) and heated to 70 °C for 96 hours, over which time the reaction mixture turned clear, and large colourless crystals started to form. The reaction mixture was cooled to 20 °C and extracted with dichloromethane (5 × 200 mL). The combined organic phases were washed with $NaHCO_3$ solution (3 × 200 mL), water (3 × 200 mL), and brine (3 × 200 mL). The organic phase was then dried over $MgSO_4$, filtered, and evaporated to dryness to yield a white crystalline solid, which was subsequently purified by crystallisation from hexane (120.4 g, 73%). Mp = 95 – 96 °C (lit. 95 °C);[58] FTIR ATR: 3011 (νC-$H_{aromatic}$), 2974 (νC-H_{alkyl}), 2925 (νC-H_{alkyl}), 2864 (νC-H_{alkyl}), 1618 (νC-C), 1507 (νC-C), 1450 (νC-C) cm^{-1}; ^{1}H NMR: (400 MHz, DMSO-d_6) δ 7.38 (s, 1H, H_f), 7.09 (s, 1H, H_e), 4.74 (s, 4H, H_a), 2.33 (s, 6H, H_d); $^{13}C\{H\}$ NMR: (100 MHz, DMSO-d_6) δ 137.8 (C_b), 133.4 (C_c), 132.7 (C_e), 131.5 (C_f), 44.6 (C_a), 17.9 (C_d); Anal. Calcd. For $C_{10}H_{12}Cl_2$: C, 59.14; H, 5.95. Found: C, 59.33; H, 5.95.

1,5-Bis(chloromethyl)-2,4-dimethyl-3-nitrobenzene[59] **(2.10). 2.9** (10.0 g, 49.2 mmol) was added to $CHCl_3$ (80 mL) at 0 °C and conc. H_2SO_4 (75 mL) was added slowly to the vigorously stirring solution, conc. HNO_3 (14.3 mL, ρ = 1.4) was then added dropwise over 30 minutes. The reaction mixture was immediately separated, and the H_2SO_4 layer was then back extracted with $CHCl_3$ (80 mL × 1). The combined organic phases were washed with deionised water (200 mL), Na_2CO_3 solution (2M, 3 × 200 mL), and brine (3 × 200 mL). The organic phase was then dried over $MgSO_4$, filtered, and evaporated to dryness to yield a white crystalline solid, which was subsequently purified by crystallisation from MeOH (9.7 g, 79%). Mp = 143 – 144 °C (lit. 140 – 141 °C);[59] FTIR ATR: 3036 (νC-$H_{aromatic}$), 3009 (νC-$H_{aromatic}$), 2971 (νC-H_{alkyl}), 2893 (νC-H_{alkyl}), 1518 (νN-$O_{asymmetric}$), 1452 (νC-C), 1373 (νN-$O_{symmetric}$) cm^{-1}; ^{1}H NMR: (400 MHz, DMSO-d_6) δ 7.72 (s, 1H, H_f), 4.86 (s, 4H, H_e), 2.25 (s, 6H, H_c); $^{13}C\{H\}$ NMR: (100 MHz, DMSO-d_6) δ 153.2 (C_a), 135.7 (C_b), 132.9 (C_f), 128.4 (C_d), 43.6 (C_e), 13.0 (C_c); Anal. Calcd. For $C_{10}H_{11}NO_2Cl_2$: C, 48.41; H, 4.47; N, 5.65. Found: C, 48.25; H, 4.39; N, 5.63.

4,6-Dimethyl-5-nitroisophthalic acid[59] **(2.11). 2.10** (8.00 g, 34.24 mmol) was added to conc. HNO_3 (200 mL, ρ = 1.4) and heated to 130 °C for 24h. **2.11** precipitated as a white crystalline

mass upon cooling to 20 °C and was filtered, washed with cold deionised water (3 × 10 mL), and then dried (6.67 g, 86%). Mp = 314 – 315 °C (lit. 294 °C);[59] FTIR ATR: 2992 (νC-H_{alkyl}), 2884(νC-H_{alkyl}), 1688 (νC=O_{acid}), 1530 (νN-$O_{asymmetric}$), 1484 (νC-C), 1421 (νC-C), 1394 (νN-$O_{symmetric}$) cm^{-1}; ^{1}H NMR: (400 MHz, DMSO-d_6) δ 13.56 (s, 2H, H_f), 8.39 (s, 1H, H_g), 2.41 (s, 6H, H_c); ^{13}C{H} NMR: (100 MHz, DMSO-d_6) δ 166.6 (C_e), 154.4 (C_a), 133.13 (C_g), 133.05 (C_d), 130.1(C_b), 15.1 (C_c). HRMS (ESI, m/z): calcd for $C_{10}H_9NO_6$ ($[M-H]^+$) 238.0352, found 238.0344.

Dimethyl 4,6-dimethyl-5-nitroisophthalate[59] **(2.12).** Thionyl chloride (6.8 mL, 94.1 mmol) was added dropwise to a stirred suspension of **2.11** (4.5 g, 18.8 mmol) in MeOH (100 mL) at 0 °C under argon. The reaction mixture was stirred at 20 °C and monitored by TLC (4:1, EtOAc: n-hexane) analysis. The solvent was removed *in vacuo* after completion of the reaction to yield **12** as a crystalline solid (4.80 g, 95%). Mp = 143 – 144 °C (lit. 143.5 – 144.5 °C);[59] FTIR ATR: 2962 (νC-H_{alkyl}), 1723 (νC=O_{ester}), 1532 (νN-$O_{asymmetric}$), 1446 (νC-C), 1435 (νC-C), 1294 (νN-$O_{symmetric}$) cm^{-1}; ^{1}H NMR: (400 MHz, DMSO-d_6) δ 8.40 (s, 1H, H_d), 3.89 (s, 6H, H_a), 2.44 (s, 6H, H_g); ^{13}C{H} NMR: (100 MHz, DMSO-d_6) δ 165.1 (C_b), 154.2 (C_e), 133.5 (C_c), 132.7 (C_d), 129.2 (C_f), 52.7 (C_a), 15.0 (C_g); HRMS (ESI, *m/z*): calcd for $C_{12}H_{13}NO_6Na$ ($[M+Na]^+$) 290.0635, found 290.0641.

Dimethyl 5-amino-4,6-dimethylisophthalate[59] **(2.13).** Pd/C (10 wt. %, 300 mg) and **2.12** (3.0 g, 11.2 mmol) were suspended in MeOH (30 mL) under a hydrogen atmosphere. The suspension was stirred for 3 hours at 20 °C, filtered through a bed of celite and the solvent removed *in vacuo* to isolate the desired target material as a white solid (2.60 g, 98%). Mp = 95 – 96 °C (lit. 95.5 – 97 °C);[85] FTIR ATR: 3454 (νN-H), 3378 (νN-H), 3004 (νC-$H_{aromatic}$), 2952 (νC-H_{alkyl}), 2842 (νC-H_{alkyl}), 1712 (νC=O_{ester}), 1432 (νC-C), 1403 (νC-C) cm^{-1}; ^{1}H NMR: (400 MHz, DMSO-d_6) δ 7.37 (s, 1H, H_d), 5.09 (s, 2H, H_h), 3.80 (s, 6H, H_a), 2.29 (s, 6H, H_g); ^{13}C{H} NMR: (100 MHz, DMSO-d_6) δ 167.9 (C_b), 146.4 (C_e), 128.1(C_f), 124.2 (C_c), 118.4(C_d), 51.9 (C_a), 14.6 (C_g); HRMS (ESI, m/z): calcd for $C_{12}H_{15}NO_4$ ($[M+H]^+$) 238.1074, found 238.1070.

5-Amino-4,6-dimethylisophthalic acid[85] **(2.14).** NaOH (1.28 g, 32.0 mmol) was added to a stirred solution of **2.13** (3.45 g, 14.5 mmol) in MeOH (50 mL) and water (10 mL). The reaction mixture was maintained under reflux for 3 hours under argon. The reaction mixture was monitored by TLC (9:1, EtOAc:MeOH) analysis and upon completion, was cooled to 20 °C and acidified with 6M HCl, at pH 4 a large volume of white precipitate is formed, filtered, and dried *in vacuo* (2.17 g, 71%). Mp = 308 – 310 °C (lit. 305 – 306 °C);[85] FTIR ATR: 3495 (νN-H), 3413 (νN-H), 2869 (νC-H_{alkyl}), 2815 (νC-H_{alkyl}), 1671 (νC=O_{acid}), 1488 (νC-C), 1442 (νC-C), 1427 (νC-C), 1410 (νC-C) cm^{-1}; ^{1}H NMR: (400 MHz, DMSO-d_6) δ 12.65 (s, 2H, H_a), 7.39 (s, 1H, H_d), 4.95 (s, 2H, H_h), 2.30 (s, 6H, H_g); ^{13}C{H} NMR: (100 MHz, DMSO-d_6)

δ 169.4 (C_b), 146.2 (C_e), 129.1 (C_f), 123.8 (C_c), 118.8 (C_d), 14.66 (C_g); Anal. Calcd. For $C_{10}H_{11}NO_4$: C, 57.41; H, 5.30; N, 6.69. Found C, 57.26; H, 5.28; N, 6.65.

2-Isocyanato-1,3-dimethyl-4-nitrobenzene (2.15) To a solution of phosgene (47.2 mL, 66.2 mmol, 15 wt. % in toluene) at 0 °C, a solution of **2.17** (5.0 g, 30.1 mmol) in anhydrous THF was added dropwise over the course of 1 hour at 0 – 10 °C and allowed to react for a further 24 hours. The volatiles were removed *in vacuo,* and the yellow crystalline solid was stored at -10 °C under an argon atmosphere (5.78 g, >99%). Mp = 45 – 46 °C; FTIR ATR: 3092 (νC-$H_{aromatic}$), 2990 (νC-H_{alkyl}), 2955 (νC-H_{alkyl}), 2928 (νC-H_{alkyl}), 2862 (νC-H_{alkyl}), 2272 (νNCO), 1506 (νN-$O_{asymmetric}$), 1455 (νC-C), 1443 (νC-C), 1346 (νN-$O_{symmetric}$) cm^{-1}; ^{1}H NMR: (400 MHz, $CDCl_3$) δ 7.64 (d, *J* = 8.4 Hz, 1H, H_b), 7.18 (d, *J* = 8.4 Hz, 1H, H_c), 2.52 (s, 3H, H_i), 2.43 (s, 3H, H_e); ^{13}C{H} NMR: (100 MHz, $CDCl_3$) δ 149.0 (C_a), 138.8 (C_h), 133.4 (C_f), 128.1 (C_d), 128.1 (C_c), 124.8 (C_g), 121.3 (C_b), 19.4 (C_e), 15.2 (C_i); Anal. Calcd. For $C_9H_8N_2O_3$: C, 56.25; H, 4.20; N, 14.57. Found C, 56.16; H, 4.16; N, 14.50.

2-Isocyanato-1,3-dimethyl-5-nitrobenzene (2.16). To a solution of phosgene (42.5 mL, 59.6 mmol, 15 wt. % in toluene) at 0 °C, a solution of **2.18** (4.5 g, 27.1 mmol) dissolved in anhydrous THF was added dropwise over the course of 1 hour at 0 – 10 °C and allowed to react for a further 24 hours. The volatiles were removed *in vacuo,* and the yellow crystalline solid was stored at -10 °C under an argon atmosphere (5.20 g, > 99%). Mp = 90 – 91 °C; FTIR ATR: 3083 (νC-$H_{aromatic}$), 2964 (νC-H_{alkyl}), 2928 (νC-H_{alkyl}), 2852 (νC-H_{alkyl}), 2263 (νNCO), 1512 (νN-$O_{asymmetric}$), 1457 (νC-C), 1442(νC-C), 1425 (νC-C), 1342 (νN-$O_{symmetric}$) cm^{-1}; ^{1}H NMR: (400 MHz, DMSO-d_6) δ 7.9 (s, 2H, H_b), 2.4 (s, 6H, H_d); ^{13}C{H} NMR: (100 MHz, DMSO-d_6) δ 144.6 (C_a), 137.6 (C_e), 134.4 (C_c), 125.7 (C_f), 123.3 (C_b), 19.0 (C_d); Anal. Calcd. For $C_9H_8N_2O_3$: C, 56.25; H, 4.20; N, 14.57. Found C, 56.07; H, 4.24; N, 14.28.

2,6-Dimethyl-3-nitroaniline[86] **(2.17).** 2,6-Dimethylaniline (10.0 g, 82.5 mmol) was dissolved in conc. H_2SO_4 (80 mL), conc. HNO_3 (4.1 mL, ρ = 1.4) was added dropwise, keeping the temperature at 10 – 15 °C. The reaction mixture was stirred for 1 hour, poured into ice water, and made basic (pH 10) with 6M NaOH solution without the temperature exceeding 25 °C. The yellow precipitate was collected and recrystallized from methanol to give yellow crystals (11.4 g, 83%). Mp = 81 – 82 °C (lit. 81 – 82 °C);[87] FTIR ATR: 3422 (νN-H), 3350 (νN-H), 3100 (νC-$H_{aromatic}$), 2982 (νC-H_{alkyl}), 2951 (νC-H_{alkyl}), 2919 (νC-H_{alkyl}), 2851 (νC-H_{alkyl}), 1635 (νN-H_{bend}), 1601 (νC-C), 1514 (νN-$O_{asymmetric}$), 1481 (νC-C), 1460 (νC-C), 1434 (νC-C), 1423 (νC-C), 1349 (νN-$O_{symmetric}$), 1322 (νC-N) cm^{-1}; ^{1}H NMR: (400 MHz, DMSO-d_6) δ 6.98 (d, *J* = 8.2 Hz, 1H, H_i), 6.93 (d, *J* = 8.2 Hz, 1H, H_h), 5.22 (s, 2H, H_e), 2.15 (appt. s, 6H, $H_{c/g}$); ^{13}C{H} NMR: (100 MHz, DMSO-d_6) δ 149.6 (C_a), 146.0 (C_d), 127.4 (C_i), 125.7 (C_f), 113.3(C_b), 110.6 (C_h), 18.3 ($C_{c/g}$), 13.0 ($C_{c/g}$); HRMS (ESI, m/z): $C_8H_{11}N_2O_2$ ($[M+H]^+$) 167.0815, found 167.0812.

2,6-Dimethyl-4-nitroaniline[88] **(2.18). 2.20** (10.0 g, 31.2 mmol), conc. H_2SO_4 (100 mL) and deionised water (10 mL) were mixed together and stirred for 24 hours, after which the reaction mixture was diluted with water (250 mL) and made basic with NH_4OH (30% NH_3) solution and filtered. The yellow precipitate was then recrystallized from ethanol:water 50:50 to give yellow crystals (4.20 g, 81%). Mp = 162 – 163 °C (lit. 163.5 – 164.5 °C);[88] FTIR ATR: 3492 (νN-H), 3390 (νN-H), 2984 (νC-H_{alkyl}), 2940 (νC-H_{alkyl}), 2915 (νC-H_{alkyl}), 2852 (νC-H_{alkyl}), 1626 (νN-H_{bend}), 1595 (νC-C), 1486 (νN-$O_{asymmetric}$), 1463 (νC-C), 1324 (νN-$O_{symmetric}$) cm^{-1}; ^{1}H NMR: (400 MHz, DMSO-d_6) δ 7.77 (s, 2H, H_b), 6.13 (s, 2H, H_f), 2.15 (s, 6H, H_d); ^{13}C{H} NMR: (100 MHz, DMSO-d_6) δ 152.0 (C_a), 135.2 (C_e), 124.1 (C_b), 120.0 (C_c), 17.7 (C_d); HRMS (ESI, m/z): calcd for $C_8H_{11}N_2O_2$ ($[M+H]^+$) 167.0815, found 167.0814.

N-(2,6-Dimethylphenyl)-4-methylbenzenesulfonamide[88] **(2.19).** 2,6-Dimethylaniline (20.00 g, 165.04 mmol), *p*-toluenesulfonyl chloride (34.61 g, 181.54 mmol) were suspended in pyridine (75 mL) and heated to 120 °C for 4 hours. The reaction mixture was cooled to 20 °C, poured into 2M HCl (750 mL) and extracted with ethyl acetate (3 × 200 mL). The combined organic phases were washed with water (3 × 200 mL) and brine (3 × 200 mL). The organic phase was then dried over $MgSO_4$, filtered, and evaporated to dryness to yield an off-white solid, which was subsequently purified by crystallisation from ethanol (30.10 g, 66%). Mp = 135 – 137 °C (lit. 136.5 – 137.5 °C);[88] FTIR ATR: 3281 (νN-H), 3038 (νC-$H_{aromatic}$), 2971 (νC-H_{alkyl}), 2925 (νC-H_{alkyl}), 2859 (νC-H_{alkyl}), 1597 (νC-C), 1472 (νSO_2), 1154 (νSO_2) cm^{-1}; ^{1}H NMR: (400 MHz, DMSO-d_6) 9.25 (s, 1H, H_f), 7.58 – 7.51 (AA'XX', 2H, H_h), 7.39 – 7.32 (AA'XX', 2 H, H_i), 7.05 (dd, J = 8.7, 6.0 Hz, 1H, H_d), 7.01 – 6.97 (m, 2H, H_c), 2.38 (s, 3H, H_k), 1.94 (s, 6H, H_a); ^{13}C{H} NMR: (100 MHz, DMSO-d_6) δ 142.8 (C_j), 139.2 (C_g), 137.7 (C_b), 133.4 (C_e), 129.6 (C_i), 128.4 (C_c), 127.2 (C_d), 126.4 (C_i), 21.0 (C_k), 18.5 (C_a); HRMS (ESI, m/z): calcd for $C_{15}H_{17}NO_2S$ ($[M+H]^+$) 276.1053, found 276.1051.

N-(2,6-Dimethyl-4-nitrophenyl)-4-methylbenzenesulfonamide[88] **(2.20).** To a solution of conc. HNO_3 (20.0 mL, ρ = 1.52 gmL^{-1}) and deionised water (150 mL) was added **2.19** (20.0 g, 72.6 mmol), glacial acetic acid (150 mL) and $NaNO_2$ (501 mg, 7.3 mmol). The suspension was heated to 140 °C for 2 hours, over which time the reaction mixture turned clear, and after some time, large colourless crystals started to form. The reaction mixture was cooled to 20 °C, and deionised water (300 mL) was added to precipitate the desired product, which was subsequently purified by crystallisation from ethanol (16.8 g, 72%). Mp = 165 – 167 °C (lit. 167 – 168 °C);[88] FTIR ATR: 3265 (νN-H), 3081 (νC-$H_{aromatic}$), 2929 (νC-H_{alkyl}), 2857 (νC-H_{alkyl}), 1597 (νC-C), 1589 (νC-C), 1510 (νN-$O_{asymmetric}$), 1494 (νSO_2), 1294 (νN-$O_{symmetric}$), 1155 (νSO_2), cm^{-1}; ^{1}H NMR: (400 MHz, DMSO-d_6) δ 9.73 (s, 1H, H_f), 7.92 (s, 2H, H_c), 7.57 (AA'XX', 2H, H_h), 7.39 (AA'XX', 2H, H_i), 2.39 (s, 3H, H_k), 2.07 (s, 6H, H_a);^{13}C{H} NMR: (100 MHz, DMSO-d_6) δ 145.5 (C_d), 143.4 (C_j), 139.9 (C_e), 139.7 (C_b), 138.7 (C_g), 129.9 (C_i), 126.4 (C_h), 123.0 (C_c),

21.0 (C_k), 18.6 (C_a); HRMS (ESI, m/z): calcd for $C_{15}H_{16}N_2O_4S$ ($[M-H]^+$) 319.0758, found 319.0744.

2.16 References

(1) Fischer, L.; Guichard, G. Folding and Self-Assembly of Aromatic and Aliphatic Urea Oligomers: Towards Connecting Structure and Function. *Org. Biomol. Chem.* **2010**, *8* (14), 3101. https://doi.org/10.1039/c001090a.

(2) Lehn, J.-M. Perspectives in Supramolecular Chemistry—From Molecular Recognition towards Molecular Information Processing and Self-Organization. *Angew. Chemie Int. Ed. English* **1990**, *29* (11), 1304–1319. https://doi.org/10.1002/anie.199013041.

(3) Lehn, J.-M. Perspectives in Chemistry-Aspects of Adaptive Chemistry and Materials. *Angew. Chemie Int. Ed.* **2015**, *54* (11), 3276–3289. https://doi.org/10.1002/anie.201409399.

(4) Lehn, J.-M. Toward Self-Organisation and Complex Matter. *Science (80-.).* **2002**, *295* (5564), 2400–2403. https://doi.org/10.1126/science.1071063.

(5) Lehn, J. M. Dynamers: Dynamic Molecular and Supramolecular Polymers. *Aust. J. Chem.* **2010**, *63* (4), 611–623. https://doi.org/10.1071/CH10035.

(6) Müller-Dethlefs, K.; Hobza, P. Noncovalent Interactions: A Challenge for Experiment and Theory. *Chem. Rev.* **2000**, *100* (1), 143–167. https://doi.org/10.1021/cr9900331.

(7) Zhang, A.; Han, Y.; Yamato, K.; Zeng, X. C.; Gong, B. Aromatic Oligoureas: Enforced Folding and Assisted Cyclization. *Org. Lett.* **2006**, *8* (5), 803–806. https://doi.org/10.1021/ol0526322.

(8) van Gorp, J. J.; Vekemans, J. A. J. M.; Meijer, E. W. Facile Synthesis of a Chiral Polymeric Helix; Folding by Intramolecular Hydrogen Bonding. *Chem. Commun.* **2004**, *4* (1), 60–61. https://doi.org/10.1039/b312407j.

(9) Etter, M. C.; Panunto, T. W. 1,3-Bis(m-Nitrophenyl)Urea: An Exceptionally Good Complexing Agent for Proton Acceptors. *J. Am. Chem. Soc.* **1988**, *110* (17), 5896–5897. https://doi.org/10.1021/ja00225a049.

(10) Etter, M. C.; Zia-Ebrahimi, M.; Urbañczyk-Lipkowska, Z.; Panunto, T. W. Hydrogen Bond Directed Cocrystallization and Molecular Recognition Properties of Diarylureas. *J. Am. Chem. Soc.* **1990**, *112* (23), 8415–8426. https://doi.org/10.1021/ja00179a028.

(11) van Esch, J.; Schoonbeek, F.; de Loos, M.; Kooijman, H.; Spek, A. L.; Kellogg, R. M.; Feringa, B. L. Cyclic Bis-Urea Compounds as Gelators for Organic Solvents. *Chem. - A Eur. J.* **1999**, *5* (3), 937–950. https://doi.org/10.1002/(sici)1521-3765(19990301)5:3<937::aid-chem937>3.3.co;2-s.

(12) van der Laan, S.; Feringa, B. L.; Kellogg, R. M.; van Esch, J. Remarkable Polymorphism in Gels of New Azobenzene Bis-Urea Gelators. *Langmuir* **2002**, *18* (19), 7136–7140. https://doi.org/10.1021/la025561d.

(13) Mohmeyer, N.; Schmidt, H. W. A New Class of Low-Molecular-Weight Amphiphilic Gelators. *Chem. - A Eur. J.* **2005**, *11* (3), 863–872. https://doi.org/10.1002/chem.200400716.

(14) Mohmeyer, N.; Schmidt, H. W. Synthesis and Structure-Property Relationships of Amphiphilic Organogelators. *Chem. - A Eur. J.* **2007**, *13* (16), 4499–4509. https://doi.org/10.1002/chem.200601154.

(15) Baker, B. C.; Acton, A. L.; Stevens, G. C.; Hayes, W. Bis Amide-Aromatic-Ureas - Highly Effective Hydro- and Organogelator Systems. *Tetrahedron* **2014**, *70* (44), 8303–8311. https://doi.org/10.1016/j.tet.2014.09.017.

(16) Rodríguez-Llansola, F.; Escuder, B.; Miravet, J. F.; Hermida-Merino, D.; Hamley, I. W.; Cardin, C. J.; Hayes, W. Selective and Highly Efficient Dye Scavenging by a pH-Responsive Molecular Hydrogelator. *Chem. Commun.* **2010**, *46* (42), 7960–7962. https://doi.org/10.1039/c0cc02338h.

(17) Wood, D. M.; Greenland, B. W.; Acton, A. L.; Rodríguez-Llansola, F.; Murray, C. A.; Cardin, C. J.; Miravet, J. F.; Escuder, B.; Hamley, I. W.; Hayes, W. pH-Tunable Hydrogelators for Water Purification: Structural Optimisation and Evaluation. *Chem. - A Eur. J.* **2012**, *18* (9), 2692–2699. https://doi.org/10.1002/chem.201102137.

(18) Kishikawa, K.; Nakahara, S.; Nishikawa, Y.; Kohmoto, S.; Yamamoto, M. A Ferroelectrically Switchable Columnar Liquid Crystal Phase with Achiral Molecules: Superstructures and Properties of Liquid Crystalline Ureas. *J. Am. Chem. Soc.* **2005**, *127* (8), 2565–2571. https://doi.org/10.1021/ja046100c.

(19) Vonau, F.; Suhr, D.; Aubel, D.; Bouteiller, L.; Reiter, G.; Simon, L. Evolution of Multilevel Order in Supramolecular Assemblies. *Phys. Rev. Lett.* **2005**, *94* (6), 1–4. https://doi.org/10.1103/PhysRevLett.94.066103.

(20) Vonau, F.; Aubel, D.; Bouteiller, L.; Reiter, G.; Simon, L. Cooperative Rearrangements Leading to Long Range Order in Monolayers of Supramolecular Polymers. *Phys. Rev. Lett.* **2007**, *99* (8), 1–4. https://doi.org/10.1103/PhysRevLett.99.086103.

(21) Vonau, F.; Linares, M.; Isare, B.; Aubel, D.; Habar, M.; Bouteiller, L.; Reiter, G.; Geskin, V.; Zerbetto, F.; Lazzaroni, R.; Simon, L. Branched Substituents Generate Improved Supramolecular Ordering in Physisorbed Molecular Assemblies. *J. Phys. Chem. C* **2009**, *113* (12), 4955–4959. https://doi.org/10.1021/jp809552j.

(22) Moon, K.; Kaifer, A. E. Dimeric Molecular Capsules under Redox Control. *J. Am. Chem.*

Soc. **2004**, *126* (46), 15016–15017. https://doi.org/10.1021/ja045587m.

(23) Alajarín, M.; Pastor, A.; Orenes, R. Á.; Steed, J. W.; Arakawa, R. Self-Assembly of Tris,(2-Ureidobenzyl)Amines: A New Type of Capped, Capsule-Like Dimeric Aggregates Derived from a Highly Flexible Skeleton. *Chem. - A Eur. J.* **2004**, *10* (6), 1383–1397. https://doi.org/10.1002/chem.200305559.

(24) Alajarín, M.; Pastor, A.; Orenes, R. Á.; Steed, J. W. Dimeric Self-Assembling Capsules Derived from the Highly Flexible Tribenzylamine Skeleton. *J. Org. Chem.* **2002**, *67* (20), 7091–7095. https://doi.org/10.1021/jo025852r.

(25) Rudzevich, Y.; Rudzevich, V.; Böhmer, V. Fine-Tuning the Dimerization of Tetraureacalix [4] Arenes. *Chem. - A Eur. J.* **2010**, *16* (15), 4541–4549. https://doi.org/10.1002/chem.201000024.

(26) Zhu, C.; Tang, H.; Yang, K.; Wu, X.; Luo, Y.; Wang, J.; Li, Y. A Urea-Containing Metal-Organic Framework as a Multifunctional Heterogeneous Hydrogen Bond-Donating Catalyst. *Catal. Commun.* **2020**, *135*, 105837. https://doi.org/10.1016/j.catcom.2019.105837.

(27) Pothupitiya, J. U.; Hewawasam, R. S.; Kiesewetter, M. K. Urea and Thiourea H-Bond Donating Catalysts for Ring-Opening Polymerization: Mechanistic Insights via (Non)Linear Free Energy Relationships. *Macromolecules* **2018**, *51* (8), 3203–3211. https://doi.org/10.1021/acs.macromol.8b00321.

(28) Nickerson, D. M.; Angeles, V. V.; Auvil, T. J.; So, S. S.; Mattson, A. E. Internal Lewis Acid Assisted Ureas: Tunable Hydrogen Bond Donor Catalysts. *Chem. Commun.* **2013**, *49* (39), 4289–4291. https://doi.org/10.1039/c2cc37073e.

(29) Sigman, M. S.; Vachal, P.; Jacobsen, E. N. A General Catalyst for the Asymmetric Strecker Reaction. *Angew. Chemie - Int. Ed.* **2000**, *39* (7), 1279–1281. https://doi.org/10.1002/(SICI)1521-3773(20000403)39:7<1279::AID-ANIE1279>3.0.CO;2-U.

(30) Boileau, S.; Bouteiller, L.; Laupretre, F.; Lortie, F. Soluble Supramolecular Polymers Based on Urea Compounds. *New J. Chem.* **2000**, *24* (11), 845–848. https://doi.org/10.1039/b006742n.

(31) van Gorp, J. J.; Vekemans, J. A. J. M. J. M.; Meijer, E. W. C3-Symmetrical Supramolecular Architectures: Fibers and Organic Gels from Discotic Trisamides and Trisureas. *J. Am. Chem. Soc.* **2002**, *124* (49), 14759–14769. https://doi.org/10.1021/ja020984n.

(32) Simic, V.; Bouteiller, L.; Jalabert, M. Highly Cooperative Formation of Bis-Urea Based Supramolecular Polymers. *J. Am. Chem. Soc.* **2003**, *125* (43), 13148–13154.

https://doi.org/10.1021/ja037589x.

(33) Colombani, O.; Bouteiller, L. Selective Synthesis of Non-Symmetrical Bis-Ureas and Their Self-Assembly. *New J. Chem.* **2004**, *28* (11), 1373–1382. https://doi.org/10.1039/b316913h.

(34) Cazacu, A.; Tong, C.; van der Lee, A.; Fyles, T. M.; Barboiu, M. Columnar Self-Assembled Ureido Crown Ethers: An Example of Ion-Channel Organization in Lipid Bilayers. *J. Am. Chem. Soc.* **2006**, *128* (29), 9541–9548. https://doi.org/10.1021/ja061861w.

(35) Lortie, F.; Boileau, S.; Bouteiller, L.; Chassenieux, C.; Lauprêtre, F. Chain Stopper-Assisted Characterization of Supramolecular Polymers. *Macromolecules* **2005**, *38* (12), 5283–5287. https://doi.org/10.1021/ma050168a.

(36) Obert, E.; Bellot, M.; Bouteiller, L.; Andrioletti, F.; Lehen-Ferrenbach, C.; Boué, F. Both Water- and Organo-Soluble Supramolecular Polymer Stabilized by Hydrogen-Bonding and Hydrophobic Interactions. *J. Am. Chem. Soc.* **2007**, *129* (50), 15601–15605. https://doi.org/10.1021/ja074296l.

(37) Sabadini, E.; Francisco, K. R.; Bouteiller, L. Bis-Urea-Based Supramolecular Polymer: The First Self-Assembled Drag Reducer for Hydrocarbon Solvents. *Langmuir* **2010**, *26* (3), 1482–1486. https://doi.org/10.1021/la903683e.

(38) Colombani, O.; Barioz, C.; Bouteiller, L.; Chanéac, C.; Fompérie, L.; Lortie, F.; Montés, H. Attempt toward 1D Cross-Linked Thermoplastic Elastomers: Structure and Mechanical Properties of a New System. *Macromolecules* **2005**, *38* (5), 1752–1759. https://doi.org/10.1021/ma048006m.

(39) Brooks, S. J.; Edwards, P. R.; Gale, P. A.; Light, M. E. Carboxylate Complexation by a Family of Easy-to-Make Ortho-Phenylenediamine Based Bis-Ureas: Studies in Solution and the Solid State. *New J. Chem.* **2006**, *30* (1), 65–70. https://doi.org/10.1039/b511963d.

(40) Pinault, T.; Cannizzo, C.; Andrioletti, B.; Ducouret, G.; Lequeux, F.; Bouteiller, L. Anions as Efficient Chain Stoppers for Hydrogen-Bonded Supramolecular Polymers. *Langmuir* **2009**, *25* (15), 8404–8407. https://doi.org/10.1021/la804138u.

(41) Barišić, D.; Cindro, N.; Kulcsár, M. J.; Tireli, M.; Užarević, K.; Bregović, N.; Tomišić, V. Protonation and Anion Binding Properties of Aromatic Bis-Urea Derivatives—Comprehending the Proton Transfer. *Chem. - A Eur. J.* **2019**, *25* (18), 4695–4706. https://doi.org/10.1002/chem.201805633.

(42) Dos Santos, C. M. G.; McCabe, T.; Watson, G. W.; Kruger, P. E.; Gunnlaugsson, T. The Recognition and Sensing of Anions through “Positive Allosteric Effects” Using Simple

Urea-Amide Receptors. *J. Org. Chem.* **2008**, *73* (23), 9235–9244. https://doi.org/10.1021/jo8014424.

(43) Raatikainen, K.; Beyeh, N. K.; Rissanen, K. Tri- and Tetraurea Piperazine Cyclophanes: Synthesis and Complexation Studies of Preorganized and Folded Receptor Molecules. *Chem. - A Eur. J.* **2010**, *16* (48), 14554–14564. https://doi.org/10.1002/chem.201001695.

(44) Custelcean, R. Crystal Engineering with Urea and Thiourea Hydrogen-Bonding Groups. *Chem. Commun.* **2008**, 295–307. https://doi.org/10.1039/b708921j.

(45) Yang, J.; Dewal, M. B.; Sobransingh, D.; Smith, M. D.; Xu, Y.; Shimizu, L. S. Examination of the Structural Features That Favor the Columnar Self-Assembly of Bis-Urea Macrocycles. *J. Org. Chem.* **2009**, *74* (1), 102–110. https://doi.org/10.1021/jo801717w.

(46) Isare, B.; Pembouong, G.; Boué, F.; Bouteiller, L. Conformational Control of Hydrogen-Bonded Aromatic Bis-Ureas. *Langmuir* **2012**, *28* (19), 7535–7541. https://doi.org/10.1021/la300887p.

(47) Norouzi, M.; Nazari, B.; Miller, D. W. Injectable Hydrogel-Based Drug Delivery Systems for Local Cancer Therapy. *Drug Discov. Today* **2016**, *21* (11), 1835–1849. https://doi.org/10.1016/j.drudis.2016.07.006.

(48) Pertici, V.; Pin-Barre, C.; Rivera, C.; Pellegrino, C.; Laurin, J.; Gigmes, D.; Trimaille, T. Degradable and Injectable Hydrogel for Drug Delivery in Soft Tissues. *Biomacromolecules* **2019**, *20* (1), 149–163. https://doi.org/10.1021/acs.biomac.8b01242.

(49) Aliaghaei, M.; Mirzadeh, H.; Dashtimoghadam, E.; Taranejoo, S. Investigation of Gelation Mechanism of an Injectable Hydrogel Based on Chitosan by Rheological Measurements for a Drug Delivery Application. *Soft Matter* **2012**, *8* (27), 7128–7137. https://doi.org/10.1039/c2sm25254f.

(50) Bhattacharya, S.; Krishnan-Ghosh, Y. First Report of Phase Selective Gelation of Oil from Oil/Water Mixtures. Possible Implications toward Containing Oil Spills. *Chem. Commun.* **2001**, 185–186. https://doi.org/10.1039/b007848o.

(51) Adhikari, B.; Palui, G.; Banerjee, A. Self-Assembling Tripeptide Based Hydrogels and Their Use in Removal of Dyes from Waste-Water. *Soft Matter* **2009**, *5* (18), 3452–3460. https://doi.org/10.1039/b905985g.

(52) Wang, J.; Wang, H.; Song, Z.; Kong, D.; Chen, X.; Yang, Z. A Hybrid Hydrogel for Efficient Removal of Methyl Violet from Aqueous Solutions. *Colloids Surfaces B Biointerfaces* **2010**, *80* (2), 155–160. https://doi.org/10.1016/j.colsurfb.2010.05.042.

(53) Baker, B. C.; Higgins, C. L.; Ravishankar, D.; Colquhoun, H. M.; Stevens, G. C.; Greco, F.; Greenland, B. W.; Hayes, W. Multifunctional, Biocompatible, Non-Peptidic Hydrogels: From Water Purification to Drug Delivery. *ChemistrySelect* **2016**, *1* (8), 1641–1649. https://doi.org/10.1002/slct.201600249.

(54) Okesola, B. O.; Smith, D. K. Applying Low-Molecular Weight Supramolecular Gelators in an Environmental Setting-Self-Assembled Gels as Smart Materials for Pollutant Removal. *Chem. Soc. Rev.* **2016**, *45* (15), 4226–4251. https://doi.org/10.1039/c6cs00124f.

(55) Chen, L.; Raeburn, J.; Sutton, S.; Spiller, D. G.; Williams, J.; Sharp, J. S.; Griffiths, P. C.; Heenan, R. K.; King, S. M.; Paul, A.; Furzeland, S.; Atkins, D.; Adams, D. J. Tuneable Mechanical Properties in Low Molecular Weight Gels. *Soft Matter* **2011**, *7* (20), 9721. https://doi.org/10.1039/c1sm05827d.

(56) Patterson, A. K.; Smith, D. K. Two-Component Supramolecular Hydrogel for Controlled Drug Release. *Chem. Commun.* **2020**, *56* (75), 11046–11049. https://doi.org/10.1039/D0CC03962D.

(57) Fleming, S.; Debnath, S.; Frederix, P. W. J. M.; Tuttle, T.; Ulijn, R. V. Aromatic Peptide Amphiphiles: Significance of the Fmoc Moiety. *Chem. Commun.* **2013**, *49* (90), 10587–10589. https://doi.org/10.1039/c3cc45822a.

(58) Gerisch, M.; Krumper, J. R.; Bergman, R. G.; Tilley, T. D. Novel Bis(Oxazoline) Pincer Ligands: Formation of Mononuclear Rhodium(II) Complexes. *J. Am. Chem. Soc.* **2001**, *123* (24), 5818–5819. https://doi.org/10.1021/ja005857a.

(59) Hopff, H.; Maggi, A.; Manukian, B. K. Über Pyromellitsäure- Und Cumidinsäure-Derivate. III. Teil. *Helv. Chim. Acta* **1961**, *44* (2), 367–379. https://doi.org/10.1002/hlca.19610440205.

(60) Murata, K.; Aoki, M.; Suzuki, T.; Harada, T.; Kawabata, H.; Komori, T.; Ofaseto, F.; Ueda, K.; Shinkai, S. Thermal and Light Control of the Sol-Gel Phase Transition in Cholesterol-Based Organic Gels. Novel Helical Aggregation Modes As Detected by Circular Dichroism and Electron Microscopic Observation. *J. Am. Chem. Soc.* **1994**, *116* (15), 6664–6676. https://doi.org/10.1021/ja00094a023.

(61) Adams, D. J.; Butler, M. F.; Frith, W. J.; Kirkland, M.; Mullen, L.; Sanderson, P. A New Method for Maintaining Homogeneity during Liquid–Hydrogel Transitions Using Low Molecular Weight Hydrogelators. *Soft Matter* **2009**, *5* (9), 1856–1862. https://doi.org/10.1039/b901556f.

(62) Rutgeerts, L. A. J.; Soultan, A. H.; Subramani, R.; Toprakhisar, B.; Ramon, H.; Paderes, M. C.; De Borggraeve, W. M.; Patterson, J. Robust Scalable Synthesis of a Bis-Urea

Derivative Forming Thixotropic and Cytocompatible Supramolecular Hydrogels. *Chem. Commun.* **2019**, *55* (51), 7323–7326. https://doi.org/10.1039/C9CC02927C.

(63) Talebian, S.; Mehrali, M.; Taebnia, N.; Pennisi, C. P.; Kadumudi, F. B.; Foroughi, J.; Hasany, M.; Nikkhah, M.; Akbari, M.; Orive, G.; Dolatshahi-Pirouz, A. Self-Healing Hydrogels: The Next Paradigm Shift in Tissue Engineering? *Adv. Sci.* **2019**, *6* (16), 1801664. https://doi.org/10.1002/advs.201801664.

(64) Wang, H.; Biswas, S. K.; Zhu, S.; Lu, Y.; Yue, Y.; Han, J.; Xu, X.; Wu, Q.; Xiao, H. Self-Healable Electro-Conductive Hydrogels Based on Core-Shell Structured Nanocellulose/Carbon Nanotubes Hybrids for Use as Flexible Supercapacitors. *Nanomaterials* **2020**, *10* (1), 112. https://doi.org/10.3390/nano10010112.

(65) Han, J.; Wang, H.; Yue, Y.; Mei, C.; Chen, J.; Huang, C.; Wu, Q.; Xu, X. A Self-Healable and Highly Flexible Supercapacitor Integrated by Dynamically Cross-Linked Electro-Conductive Hydrogels Based on Nanocellulose-Templated Carbon Nanotubes Embedded in a Viscoelastic Polymer Network. *Carbon N. Y.* **2019**, *149*, 1–18. https://doi.org/10.1016/j.carbon.2019.04.029.

(66) Liao, H.; Guo, X.; Wan, P.; Yu, G. Conductive MXene Nanocomposite Organohydrogel for Flexible, Healable, Low-Temperature Tolerant Strain Sensors. *Adv. Funct. Mater.* **2019**, *29* (39), 1904507. https://doi.org/10.1002/adfm.201904507.

(67) Wang, P.; Deng, G.; Zhou, L.; Li, Z.; Chen, Y. Ultrastretchable, Self-Healable Hydrogels Based on Dynamic Covalent Bonding and Triblock Copolymer Micellization. *ACS Macro Lett.* **2017**, *6* (8), 881–886. https://doi.org/10.1021/acsmacrolett.7b00519.

(68) Li, H.; Lv, T.; Sun, H.; Qian, G.; Li, N.; Yao, Y.; Chen, T. Ultrastretchable and Superior Healable Supercapacitors Based on a Double Cross-Linked Hydrogel Electrolyte. *Nat. Commun.* **2019**, *10* (1), 536. https://doi.org/10.1038/s41467-019-08320-z.

(69) Gao, G.; Du, G.; Sun, Y.; Fu, J. Self-Healable, Tough, and Ultrastretchable Nanocomposite Hydrogels Based on Reversible Polyacrylamide/Montmorillonite Adsorption. *ACS Appl. Mater. Interfaces* **2015**, *7* (8), 5029–5037. https://doi.org/10.1021/acsami.5b00704.

(70) Nebot, V. J.; Smith, D. K. CHAPTER 2. Techniques for the Characterisation of Molecular Gels. In *Functional Molecular Gels*; Beatriu Escuder, Miravet, J. F., Eds.; Royal Society of Chemistry, Cambridge, 2013; pp 30–66. https://doi.org/10.1039/9781849737371-00030.

(71) Escuder, B.; LLusar, M.; Miravet, J. F. Insight on the NMR Study of Supramolecular Gels and Its Application to Monitor Molecular Recognition on Self-Assembled Fibers. *J. Org. Chem.* **2006**, *71* (20), 7747–7752. https://doi.org/10.1021/jo0612731.

(72) Hirst, A. R.; Coates, I. A.; Boucheteau, T. R.; Miravet, J. F.; Escuder, B.; Castelletto, V.; Hamley, I. W.; Smith, D. K. Low-Molecular-Weight Gelators: Elucidating the Principles of Gelation Based on Gelator Solubility and a Cooperative Self-Assembly Model. *J. Am. Chem. Soc.* **2008**, *130* (28), 9113–9121. https://doi.org/10.1021/ja801804c.

(73) Nonappa; Šaman, D.; Kolehmainen, E. Studies on Supramolecular Gel Formation Using DOSY NMR. *Magn. Reson. Chem.* **2015**, *53* (4), 256–260. https://doi.org/10.1002/mrc.4185.

(74) Iqbal, S.; Rodríguez-Llansola, F.; Escuder, B.; Miravet, J. F.; Verbruggen, I.; Willem, R. HRMAS ^{1}H NMR as a Tool for the Study of Supramolecular Gels. *Soft Matter* **2010**, *6* (9), 1875–1878. https://doi.org/10.1039/b926785a.

(75) Tang, C.; Smith, A. M.; Collins, R. F.; Ulijn, R. V.; Saiani, A. Fmoc-Diphenylalanine Self-Assembly Mechanism Induces Apparent pKa Shifts. *Langmuir* **2009**, *25* (16), 9447–9453. https://doi.org/10.1021/la900653q.

(76) Avrami, M. Kinetics of Phase Change. I General Theory. *J. Chem. Phys.* **1939**, *7* (12), 1103–1112. https://doi.org/10.1063/1.1750380.

(77) Avrami, M. Kinetics of Phase Change. II Transformation-Time Relations for Random Distribution of Nuclei. *J. Chem. Phys.* **1940**, *8* (2), 212–224. https://doi.org/10.1063/1.1750631.

(78) Avrami, M. Granulation, Phase Change, and Microstructure Kinetics of Phase Change. III. *J. Chem. Phys.* **1941**, *9* (2), 177–184. https://doi.org/10.1063/1.1750872.

(79) Moffat, J. R.; Smith, D. K. Metastable Two-Component Gel—Exploring the Gel–Crystal Interface. *Chem. Commun.* **2008**, *44* (19), 2248. https://doi.org/10.1039/b801913d.

(80) Adams, D. J.; Morris, K.; Chen, L.; Serpell, L. C.; Bacsa, J.; Day, G. M. The Delicate Balance between Gelation and Crystallisation: Structural and Computational Investigations. *Soft Matter* **2010**, *6* (17), 4144. https://doi.org/10.1039/c0sm00409j.

(81) *CrysAlis PRO. Rigaku OD (2019). Rigaku Oxford Diffraction Ltd, Yarnton, Oxfordshire, England.*

(82) Palatinus, L.; Chapuis, G. SUPERFLIP - A Computer Program for the Solution of Crystal Structures by Charge Flipping in Arbitrary Dimensions. *J. Appl. Crystallogr.* **2007**, *40* (4), 786–790. https://doi.org/10.1107/S0021889807029238.

(83) Betteridge, P. W.; Carruthers, J. R.; Cooper, R. I.; Prout, K.; Watkin, D. J. CRYSTALS Version 12: Software for Guided Crystal Structure Analysis. *J. Appl. Crystallogr.* **2003**, *36* (6), 1487–1487. https://doi.org/10.1107/s0021889803021800.

(84) Beijer, F. H.; Brunsveld, L.; Meijer, E. W.; Sijbesma, R. P. Supramolecular Polymer. EP

0929597 B1, 2003.

(85) de Diesbach, H.; Chardonnens, L. Les Dibenzoyl-Xylènes et Les Dinaphtanthracène-Diquinones II. *Helv. Chim. Acta* **1924**, *7* (1), 614–618. https://doi.org/10.1002/hlca.19240070175.

(86) Bergman, J.; Sand, P. Synthesis of Indoles via Ring Closure of 2-Alkylnitroaniline Derivatives. *Tetrahedron* **1990**, *46* (17), 6085–6112. https://doi.org/10.1016/S0040-4020(01)87932-1.

(87) Suzuki, H.; Maruyama, K.; Goto, R. The Synthesis of Four Isomeric Diiodo- m -Xylenes. Their Isomerisation in Sulfuric and Polyphosphoric Acids. *Bull. Chem. Soc. Jpn.* **1965**, *38* (10), 1590–1595. https://doi.org/10.1246/bcsj.38.1590.

(88) Wepster, B. M. Steric Effects on Mesomerism: XIII. Preparation of 2,6-Dimethyl-4-Nitroaniline. *Recl. des Trav. Chim. des Pays-Bas* **1954**, *73* (10), 809–818. https://doi.org/10.1002/recl.19540731004.

Chapter 3 – Tailoring Viscoelastic Properties of Dynamic Supramolecular Poly(butadiene)-Based Elastomers

This chapter has, in part, been published by the author as a research article entitled “Tailoring Viscoelastic Properties of Dynamic Supramolecular Poly(butadiene)-Based Elastomers, Matthew Hyder, Adam D. O'Donnell, Ann M. Chippindale, Ian M. German, Josephine L. Harries, Olga Shebanova, Ian W. Hamley and Wayne Hayes, *Materials Today Chemistry*, **2022**, doi.org/10.1016/j.mtchem.2022.101008.

In this Chapter is reported the discovery and development of new adhesive materials critical for real-world applications of polymeric composite materials. Herein, we report the design and synthesis of a library of structurally related phase-separated supramolecular polyurethanes whose mechanical properties and adhesive characteristics can be enhanced through minor structural modifications of the polymer end-group. The interplay between phase separation of the hard domain polar end-groups and soft polybutadiene domains, coupled with tuneable self-assembly afforded by the polar end-groups, gives rise to a class of materials with tuneable mechanical properties. Exceptionally strong supramolecular adhesives and mechanically robust self-healing elastomers were identified. The mechanical properties were investigated through tensile testing. Finally, rheological analysis of the supramolecular materials was used to identify suitable healing and adhesive temperatures in addition to elucidate the supramolecular polyurethanes' thermal-responsive nature.

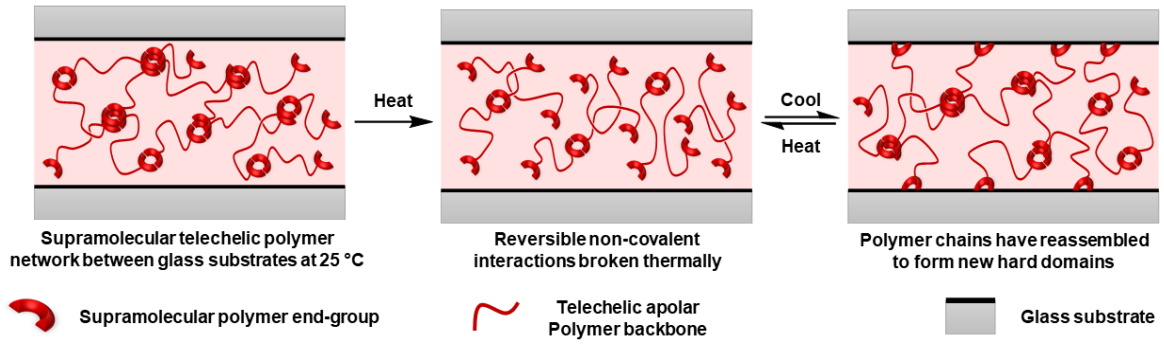

Figure 1. Schematic representation of supramolecular interactions between a polymer network and a glass substrate. Initially, the supramolecular polymer network is sandwiched between two glass substrates and has little to no interactions with the glass surface. Upon heating the substrate above a set temperature, the supramolecular interactions break and, upon cooling, can reassemble, forming new hard domains and interact with the functional groups on the silica surface, thus forming a non-covalent bond to the substrate.

3.1 Introduction

Supramolecular materials offer many attractive properties, particularly durability, robustness, and performance. Many strategies have been employed to deliver supramolecular materials, ranging from host-guest interactions to complex supramolecular networks combining multiple orthogonal interactions.[1–3] In recent years, numerous polymers have been reported capable of

self-healing upon exposure to a suitable stimulus.[4–7] Subsequently, supramolecular materials have seen application in adhesives,[8–10] healable materials,[11–16] inkjet and 3D printing,[17,18] and biomedical applications.[19–21]

Rowan, Weder and co-workers generated a tough, optically healable supramolecular polymer through the functionalisation of a soft telechelic poly(ethylene-*co*-butylene) with hard 2,6-bis(1'-methylbenzimidazolyl) pyridine ligands that assembled with varying ratios of $Zn(NTf_2)_2$ or $La(NTf_2)_3$.[15] The mechanical properties of the supramolecular polymer were attributed to phase separation between the hard and soft domains. To tailor the mechanical properties of supramolecular polymers, Schrettl and Weder combined two metallosupramolecular polymers, a rigid low molecular weight tri-functional semicrystalline polymer and a soft elastic telechelic polymer. Utilising the same metal-ligand complex as a binding motif, they found that by varying the ratio of the two constituents, they realised materials higher in ultimate tensile strength (UTS), modulus of toughness and elasticity than either supramolecular network in isolation.[22] Bouteiller and co-workers imparted self-healing properties to a PDMS thermoplastic elastomer by blending *n*-alkylated urea additives that can effectively soften the hard domains by accelerating the chain dynamics and disrupting bifurcated urea-urea stacking.[23] Meijer, Sijbesma and co-workers functionalised telechelic polymers, such as poly(ethylene-*co*-butylene)s,[24] and polysiloxanes,[25] with ureidopyrimidones (UPy) to deliver thermoreversible supramolecular materials. Anthamatten and co-workers integrated UPy side groups into linear and cross-linked siloxanes and realised biocompatible PDMS elastomers with control over variable stiffness and viscoelastic relaxation.[26] Wilson and co-workers have also examined hydrogen-bonding motifs and created self-sorting networks.[27,28]

Nitrophenyl urea motifs have found applications as supramolecular gelators, assembling through both urea-urea and urea-nitro interactions.[29] We have previously reported hydrogelator systems based on this motif,[30,31] and their utility in creating polymer films capable of self-repair upon swelling.[32] Viscometry measurements performed by Bouteiller and co-workers highlighted the ability to enhance the hydrogen bonding capability of urea-based supramolecular systems by enforcing a non-coplanar conformation between the urea and the phenyl moiety, in turn enhancing hydrogen bonding.[33] Furthermore, we have recently demonstrated the influence of enhancing non-coplanar conformation between the urea and the phenyl moieties on hydrogelators systems.[34]

This chapter reports the synthesis of a series of supramolecular polyurethanes (SPUs) in which attenuation of the assembly capabilities of the urea end-groups by conformational restriction, enforced by the presence of *ortho* substituents, has led to the ability to adjust the bulk properties of these materials. Through a better understanding of the urea-urea assembly and the disruptive capability of the nitro substituents, SPU materials with valuable properties, such as adhesion and healability, were afforded.

3.2 Results and Discussion

The SPUs were designed to take advantage of multiple complementary supramolecular interactions (see Figure 2). π-π stacking interactions derive from the choice of isocyanate, namely, methylene diphenyl diisocyanate (MDI). Other interactions result from urea bifurcated hydrogen bonds on the chain end, urethane hydrogen bonding in the polymer mid-block and urea-nitro hydrogen bonds between polymer chains. The position of the nitro-substituent was varied between the *-meta* and *-para* position, as previously it has been shown that the two regioisomers behave very differently [31,32] and provide scope for optimisation of mechanical properties of SPUs. Furthermore, the influence of steric bulk was investigated by employing methyl substituents placed at strategic substitution patterns probing the effect of conformationally controlling the end group to tailor the mechanical properties of the resultant SPU.

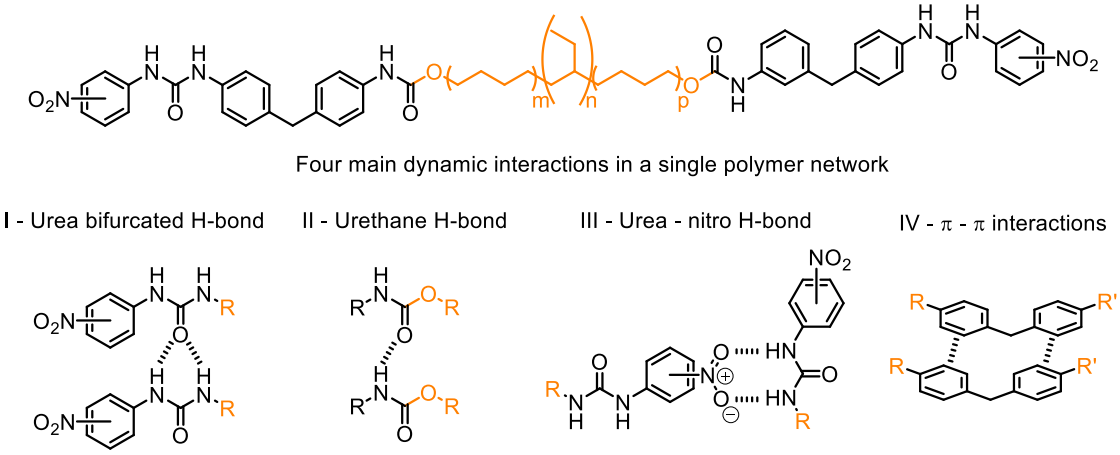

Figure 2. Chemical structure and the four main dynamic bonds present in the SPUs synthesised in this study.

A series of 13 aniline-derived end-cap groups were selected, incorporating *meta-*/*para*-nitro substitution and varying degrees of steric hindrance from methyl substituents on the aromatic ring. The synthetic routes used to access the four anilines not available commercially are shown in Scheme 1. In the case of anilines **3.1**, **3.2**, and **3.3**, which feature a nitro residue -*meta* to the amine unit, these were synthesised via the nitration of 2,6-xylidine,[34] 2,4,6-trimethylaniline,[35] and *p*-toluidine, respectively, to afford the desired compounds in good yield (83%, 94%, and 89%, respectively). More complex approaches were required to synthesise the *para*-nitro substituted **3.4**,[34] and **3.5**. 2,6-Xylidine was first converted to the corresponding toluenesulfonamide **3.6** to promote nitration at the *para* position, and the resulting *para*-nitro-toluenesulfonamide **3.7** was then treated with sulfuric acid to generate the desired 2,6-dimethyl-4-nitroaniline **3.4** in 81% yield. In the case of aniline **3.5**, 1,2,4,5-tetramethylbenzene was nitrated twice to form 1,2,4,5-tetramethyl-3,6-dinitrobenzene **3.7,** which was then selectively reduced by treatment with sodium disulfide to yield 2,3,5,6-

tetramethyl-4-nitroaniline, **3.5**, in 68% yield.[36] The analytical data for **3.1**-**3.21** are provided in Appendix 2 (see Figures 1–68).

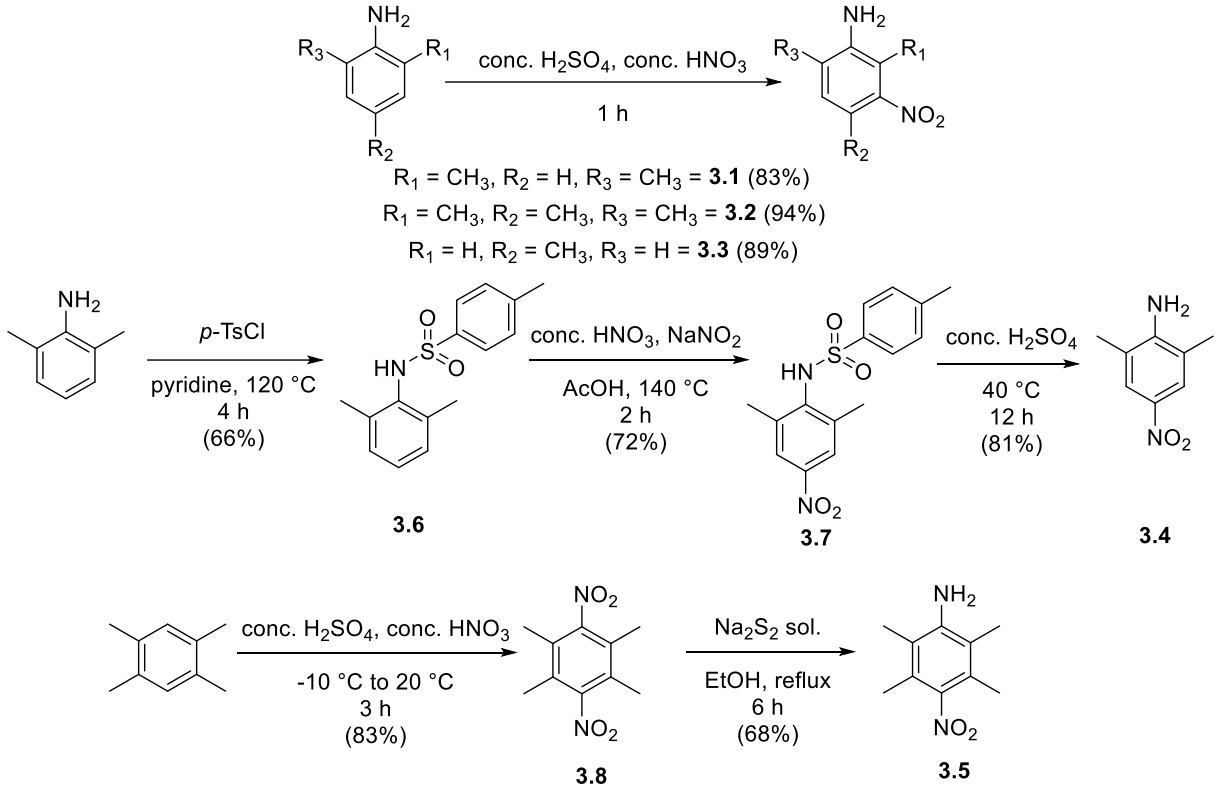

Scheme 15. The synthetic protocol for the synthesis of compounds **3.1–3.8** to afford the desired aniline derivatives: 2,6-dimethyl-3-nitroaniline **3.1**, 2,4,6-trimethyl-3-nitroaniline **3.2**, 4-methyl-3-nitroaniline **3.3**, 2,6-dimethyl-4-nitroaniline **3.4**, and 2,3,5,6-tetramethyl-4-nitroaniline **3.5**.[34,36,37]

To understand how the spatial assembly of the supramolecular end-caps of **SPU1–SPU13** within the hard domains is affected by the presence of *ortho*-methyl substituents adjacent to the urea and nitro moieties, a series of model bisaromatic ureas were synthesised, **3.9–3.21**. Ureas **3.9–3.21** were synthesised by reacting the respective aniline with phenyl isocyanate (see Scheme 2). The reactions were monitored by FTIR spectroscopy to observe the consumption of the isocyanate group, $\nu N{=}C{=}O_{(stretch)}$ 2275–2250 cm^{-1}, and the formation of the corresponding urea, $\nu C{=}O_{(stretch)}$ *ca*. 1640 cm^{-1}. The solid-state geometries of the bisaromatic ureas and their hydrogen bonding patterns provide valuable insight into the assembly of **SPU1–SPU13**. Single crystals of the ureas **3.9**, **3.11**-**3.16**, **3.19** and **3.21** were grown via vapour diffusion or slow evaporation and studied by X-ray crystallography.

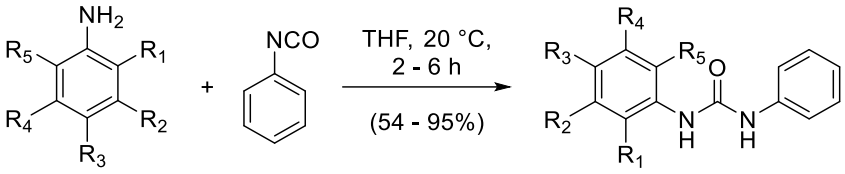

3.9 - 3.21

3.9 $R_1 = R_2 = R_3 = R_4 = R_5 = H$
3.10 $R_1 = H, R_2 = NO_2, R_3 = R_4 = R_5 = H$
3.11 $R_1 = R_2 = H, R_3 = NO_2, R_4 = R_5 = H$
3.12 $R_1 = CH_3, R_2 = R_3 = R_4 = R_5 = H$
3.13 $R_1 = CH_3, R_2 = NO_2, R_3 = R_4 = R_5 = H$
3.14 $R_1 = CH_3, R_2 = H, R_3 = NO_2, R_4 = R_5 = H$
3.15 $R_1 = CH_3, R_2 = R_3 = H, R_4 = NO_2, R_5 = H$
3.16 $R_1 = H, R_2 = NO_2, R_3 = CH_3, R_4 = H, R_5 = H$
3.17 $R_1 = CH_3, R_2 = R_3 = R_4 = H, R_5 = CH_3$
3.18 $R_1 = CH_3, R_2 = NO_2, R_3 = R_4 = H, R_5 = CH_3$
3.19 $R_1 = CH_3, R_2 = H, R_3 = NO_2, R_4 = H, R_5 = CH_3$
3.20 $R_1 = CH_3, R_2 = NO_2, R_3 = CH_3, R_4 = H, R_5 = CH_3$
3.21 $R_1 = R_2 = CH_3, R_3 = NO_2, R_4 = R_5 = CH_3$

Scheme 2. The general synthetic protocol used to afford the bisaromatic ureas **3.9**–**3.21**.[38–41]

The key intermolecular interactions established from the X-ray crystallographic analysis of the single crystals of ureas **3.9**, **3.11**-**3.16**, **3.19**, and **3.21** are shown in Figure 3 (for the crystallographic data and detailed atom assignments, see Appendix Tables 1–18 and Figures 69–77). The solid-state structures of compounds **3.9**, **3.11**-**3.16**, **3.19**, and **3.21** all reveal bifurcated hydrogen bonding between the urea carbonyl and the urea protons of an adjacent molecule (Figure 3A), with the singly methyl-substituted **3.12**, the *para*-nitro substituted **3.11**, **3.19**, and **3.21** and the *meta*-nitro substituted **3.13**, **3.15**, and **3.16**, exhibiting ordered 1-dimensional growth through this hydrogen-bonding motif. Urea **3.9,** which does not feature a nitro group,[38] shows the strongest urea-urea hydrogen bonding with the shortest hydrogen bond lengths (O1 · · H-N3: 2.131(18) Å; O1 · · H-N10: 1.919(18) Å). On comparing **3.9** and **3.12**, the introduction of a single *ortho*-methyl substituent increases the torsion angles from -38.1(2) ° and 43.0(2) ° (for C2-N3-C4-C9 and C2-N10-C11-C12, respectively in **3.9**) to -45.7(2) ° and 50.0(2) ° (for C2-N3-C4-C9 and C2-N10-C11-C16, respectively in **3.12**), with the latter torsion angle for **12** involving the *ortho*-methyl substituted ring. As observed in **3.12**, the presence of *ortho*-methyl substituents in **3.13**, **3.14** and **3.15** results in the substituted phenyl ring being twisted out of the plane to a greater degree compared to unsubstituted **3.11**, increasing the torsion angle of C2-N10-C11-C16 from -28.3(3) ° (**3.11**) to -45.0(2) ° (**3.14**) and 50.3(2) ° (**3.15**) and the C2-N3-C4-C5 torsion angle in **3.13** to 62.9(4) °. The introduction of two *ortho*-methyl substituents in **3.19** and **3.21** further twist the substituted phenyl ring out of the plane of the urea compared to the single *ortho*-methyl substituted **3.14**, increasing the torsion angle to -62.3(2) ° (C2-N3-C4-C12, **3.19**) and -78.1(4) ° (C2-N3-C4-C5, **3.21**). This twist results in stronger urea-urea hydrogen bonding in **3.13**, **3.14**, **3.15**, **3.19**, and **3.21,** as evidenced by their shorter hydrogen-bond lengths (O1 · · H-N3: 2.082(44) Å; O1 · · H-N14: 2.121(43) Å, **3.13**), (O1 · · H-N3: 2.029(18) Å; O1 · · H-N10: 2.167(18) Å, **3.14**), (O1 · · H-N3: 2.151(20) Å; O1 · · H-N10: 2.067(18) Å, **3.15**), (O1 · · H-N3: 2.014(20) Å; O1 · · H-N15: 2.087(20) Å, **3.19**), and (O1 · · H-N3: 1.965(37) Å; O1 · · H-N17: 2.051(39) Å, **3.21**), compared to those in **3.11** (O1 · · H-N3: 2.045(20) Å; O1 · · H-N10: 2.302(20) Å). As observed with the urea moiety, the incorporation of two methyl substituents *ortho* to the nitro, **3.21**, result in the

nitro being twisted out of the plane of the substituted aryl ring, evident in the increase of the torsion angles of C11-C7-N8-O9 and C11-C7-N8-O10 from 179.3(2) ° and 0.0(3) ° (**3.11**), 170.6(1) ° and -8.7(2) ° (**3.14**), and -175.2(1) ° and 4.7(2) ° (**3.19**) to 105.5(4) and -76.2(4) (**3.21**) respectively. This phenomena is also observed to a lesser extent with **3.13** and **3.16**, which only have a single methyl substituent *ortho* to the nitro, with an increase in torsion angles from 176.8(1) ° and -3.1(2) ° (C14-C15-N17-O18 and C14-C15-N17-O19, respectively, **3.15**) to -31.4(5) ° and 149.1(3) ° (C5-C6-N7-O8 and C5-C6-N7-O9, respectively, **3.13**), and -24.6(3) ° and 150.5(2) ° (C7-C8-N10-O11 and C7-C8-N10-O12, respectively, **3.16**). Moving the methyl substituent from the *ortho*, **3.13**, to the *para* position, **3.16**, removes the steric hindrance experienced by the urea increasing the urea-urea hydrogen bond strength, evident in the shorter bond distances (O1 · · H-N3: 2.082(44) Å; O1 · · H-N14: 2.121(43) Å, **3.13**) and (O1 · · H-N3: 2.091(21) Å; O1 · · H-N14: 2.082(26) Å, **3.16**).

Additional, weaker intermolecular hydrogen bonds are observed in **3.11**, **3.13**-**3.16**, **3.19**, and **3.21**, with the nitro substituents as the acceptor moieties, as shown in Figure 3. Hydrogen bonding mediated by the nitro group in **3.11**, as depicted in Figure 3**B**, comprises one of the oxygen atoms of nitro behaving as an acceptor for both the NH donor and *ortho*-Ph hydrogen donor of the same molecule (O18 · · H-N10: 2.65(2) Å; O18 · · H-C12: 2.402(2) Å) and the other oxygen atom as an acceptor for a *para*-Ph hydrogen donor of an adjacent molecule (O19 · · H-C7: 2.696(3) Å). A symmetrical hydrogen bonding arrangement in **3.13** (Figure 3**C**) is observed between O9 of the nitro moiety and the *para*-Ph hydrogen donor on the substituted aryl ring of an adjacent molecule (O9 · · H-C10: 2.667(4) Å). Furthermore, the O9 atom of the nitro group acts as an acceptor for the *meta*-Ph hydrogen donor on the non-substituted aryl ring of an adjacent molecule (O8 · · H-C19: 2.528(4) Å). The hydrogen bonding motif of the nitro group in **3.14** (Figure 3**D**) consists of one oxygen atom behaving as the acceptor for the *ortho*-Ph hydrogen donor and the other oxygen as the acceptor for the *meta*-Ph hydrogen donor of the same molecule (O18 · · H-C16: 2.583(2) Å and O19 · · H-C15: 2.582(2) Å, respectively). The urea oxygen in **3.14** also acts as a weak acceptor for the *meta*-Ph hydrogen donor on the non-substituted phenyl ring (O1 · · H-C8: 2.674(2) Å) (not shown). In **3.15** (Figure 3**E**), one oxygen of the nitro moiety, O19, acts as an acceptor for the *para*-Ph hydrogen donor of an adjacent molecule. Furthermore, the O19 atom of the nitro group of this adjacent molecule is an acceptor for the *para*-Ph hydrogen donor in the original molecule to form a symmetrical arrangement (O19 · · H-C14: 2.535(2) Å). The second oxygen of the nitro group acts as an acceptor for the *para*-Ph hydrogen donor of the non-substituted phenyl ring of a separate molecule (O18 · · H-C7: 2.585(2) Å). The nitro hydrogen bonding in **3.16** (Figure 3**F**) consists of O12 acting as an acceptor for two *para*-methyl donors on separate molecules (O12 · · H-C13: 2.599(3) Å; O12 · · H-C13: 2.562(3) Å), as well as an acceptor for the meta-Ph donor on the unsubstituted aryl ring of a third molecule (O12 · · H-C17: 2.689(2) Å). The hydrogen

bonding in **3.19** (Figure 3**G**) consists of two symmetrical arrangements, the first of which consists of O10 of the nitro moiety acting as an acceptor for the *meta*-Ph hydrogen donor and *ortho*-methyl hydrogen donor of an adjacent molecule which in turn forms a symmetrical arrangement (O10 · · H-C11: 2.486(2) Å and O10 · · H-C13: 2.690(2) Å). The second oxygen, O9, of the nitro group acts as an acceptor for the *ortho*-methyl hydrogen donor of a separate molecule forming a second symmetrical arrangement (O9 · · H-C14: 2.651(2) Å).[42] In **3.21** (Figure 3**H**), one oxygen of the nitro moiety, O10, acts as an acceptor for the *para*-Ph hydrogen donor of the non-substituted phenyl ring of a separate molecule (O10 · · H-C21: 2.597(4) Å). The second oxygen of the nitro moiety, O9, acts as an acceptor for two methyl hydrogen donors on separate molecules, one *ortho*-methyl and one *meta*-methyl (O9 · · H-C13: 2.704(4) Å and O9 · · H-C14: 2.586(5) Å, respectively). All the solid-state structures revealed π-π interactions, with T-shaped interactions exhibited in compounds **3.9**, **3.11**, **3.16**, and **3.21** and displaced parallel π-π interactions exhibited in **3.11**, **3.12**, **3.13**, **3.14**, **3.15**, **3.19**, and **3.21**.

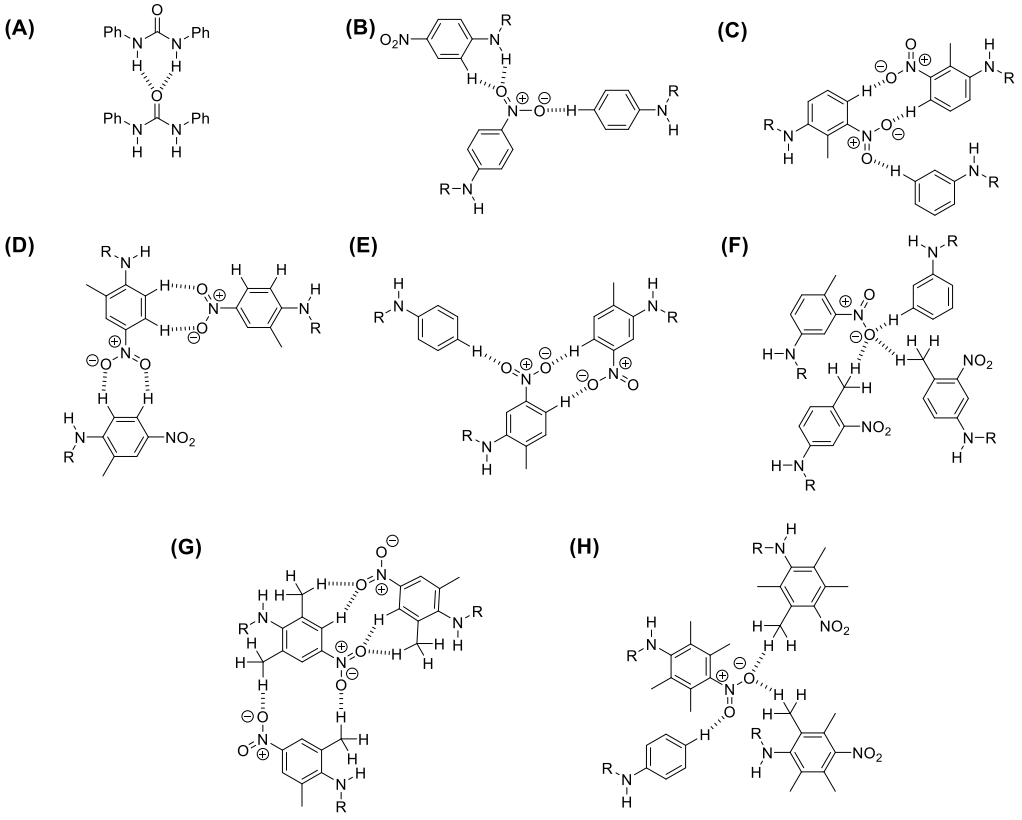

Figure 3. Schematic representation of some of the hydrogen bonding motifs observed within the crystal structures of compounds **3.9**, **3.11**, **3.12**, **3.13**, **3.14**, **3.15**, **3.16**, **3.19**, and **3.21**. **(A)** Bifurcated urea-urea hydrogen bonding was observed in **3.9**, **3.11**, **3.12**, **3.13**, **3.14**, **3.15**, **3.16**, **3.19**, and **3.21**; **(B)** hydrogen bonding involving the nitro group observed in **3.11**; **(C)** hydrogen bonding of the nitro group observed in **3.13**; **(D)** hydrogen bonding observed in **3.14**; **(E)** hydrogen bonding involving the nitro group observed in **3.15**; **(F)** hydrogen bonding involving the nitro group observed in **3.16; (G)** hydrogen bonding involving the nitro group observed in **19**; **(H)** hydrogen bonding involving the nitro group observed in **3.21**. CCDC cif deposition numbers: (**3.9**, 2131759), (**3.11**, 2131884), (**3.12**, 2157688), (**3.13**, 2173628), (**3.14**, 2131885), (**3.15**, 2131760), (**3.16**, 2173818), (**3.19**, 2172066), (**3.21**, 2172071).

The SPUs, **SPU1**–**SPU13,** were synthesised using the two-step process[43] (see Figure 4A) that had been used previously to generate supramolecular materials capable of healing at body temperature.[44] Briefly, Krasol™ HLBH-P2000 was reacted in bulk with 2.05 equivalents of MDI at 80 °C for three hours to afford an isocyanate-terminated prepolymer. Each reaction vessel was then cooled to room temperature, solvated with THF, and 2.05 equivalents of end-cap were added before being brought to and maintained under reflux to furnish dynamic supramolecular materials (**SPU1**–**SPU13**). Each reaction was monitored by FTIR spectroscopy, and upon the disappearance of the isocyanate band, the polymers were then purified by repeated precipitations.

Unwanted chain extension of the polyurethanes was minimal, and ^{1}H NMR spectroscopic analysis revealed a ratio of 1:1 for the resonances associated with the urethanes and urea end-groups, which is consistent with the feed ratios (see the NMR spectroscopic data in Appendix 2, Figures 43–68). The synthesis of the SPUs was first confirmed by ^{1}H NMR spectroscopy, which revealed resonances *ca.* 8.50 ppm and *ca.* 7.80 ppm, corresponding to the urethane protons in the prepolymer core and the urea protons of the aniline derivative end-caps, respectively. ^{13}C NMR spectroscopy was also used to confirm the formation of the urethane and urea linkages, *ca.* 153 and 155 ppm, respectively. FTIR spectroscopic analysis of the polymers revealed the complete consumption of isocyanate functionalities, as noted by the disappearance of the isocyanate stretching absorption at 2250–2275 cm^{-1}. Additionally, the new absorbances observed at 1640–1680 cm^{-1} and 1710–1740 cm^{-1} were attributed to the newly formed urea/urethane moieties. GPC analysis of the polymers (see Appendix 2, Figures 78–90 and Table 19) was employed to confirm the degree of chain extension in the polyurethane, with an average of 3.5 hydrogenated poly(butadiene) residues per supramolecular polymer (M_n = 8700 g mol^{-1}).

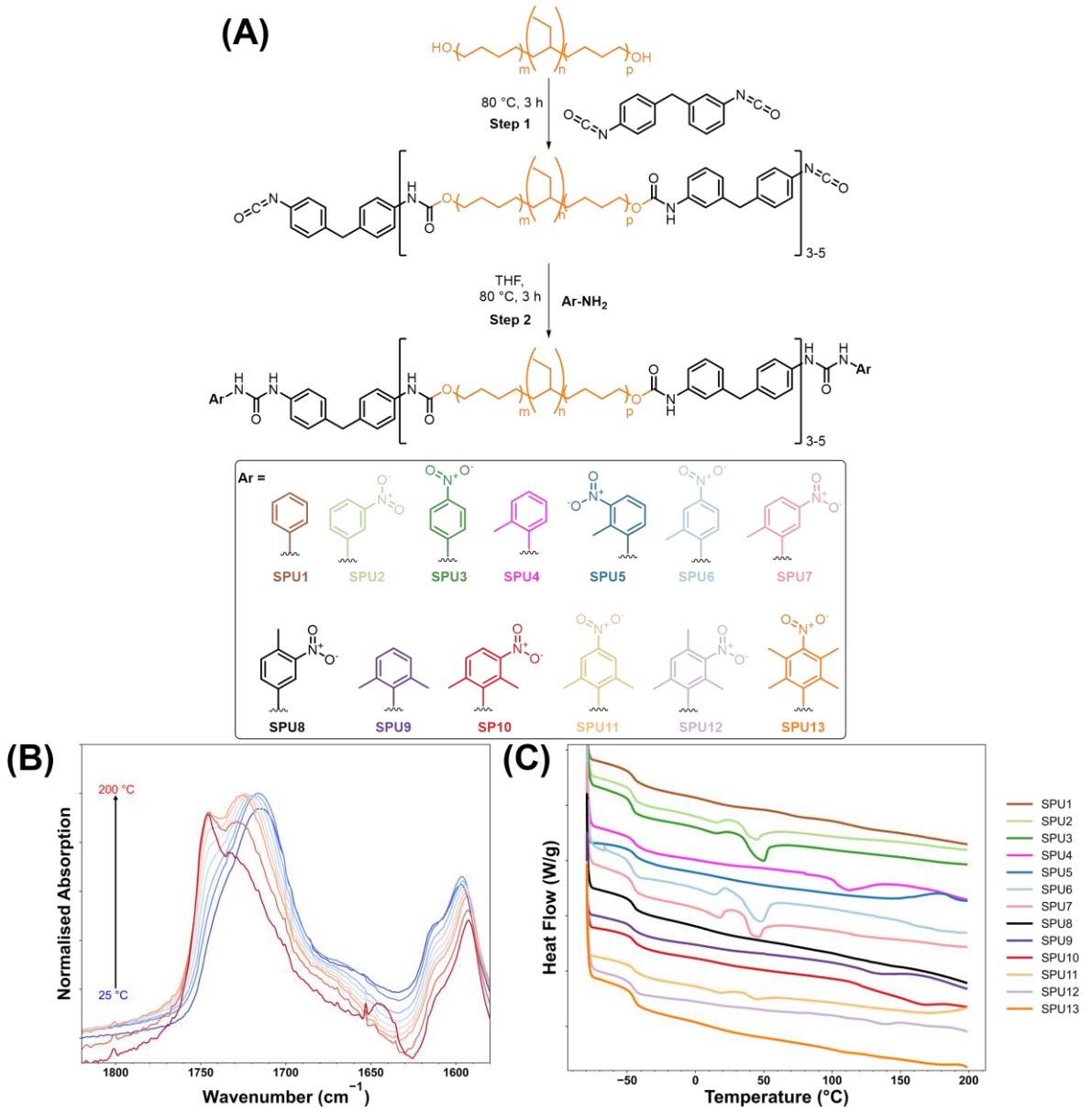

Figure 4. (A) The synthetic strategy employed to synthesise supramolecular polymer networks **SPU1**–**SPU13**; **(B)** *In situ* VTIR spectra of **SPU5** upon heating from 25 °C to 200 °C; **(C)** Stacked DSC plot of **SPU1**–**SPU13** from the 2nd heating cycle.

Quantitative analysis of both urethane and urea stretching vibrations observed in the FTIR spectra of **SPU1**–**SPU13** was conducted (Figure 4B) to calculate the degree of hydrogen bonding,[45] and illustrate the effects of each end-cap on their respective polymer's supramolecular hydrogen-bonding network at 20 °C. The carbonyl stretching vibrations for hydrogen-bonded (1710 cm^{-1}) and free (1740 cm^{-1}) urethane groups were observed for all polymers, **SPU1**–**SPU13**, arising from the urethane linker bonds within the polymer core.[45] The observation of the urea carbonyl stretching vibrations associated with the ordered hydrogen-bonded (1640 cm^{-1}), disordered hydrogen-bonded (1656–1680 cm^{-1}), and free (1692 cm^{-1}) urea groups varied for polymers **SPU1**–**SPU13**;[46] these stretching vibrations arise from the urea linker bonds formed by the polymer end-groups. The degree of hydrogen bonding within the supramolecular polymer networks was calculated by deconvoluting the carbonyl absorption

bands from the FT-IR spectroscopic data (see Table 1 and Appendix 2, Figures 91–104).[25] Deconvolution of the urethane absorbances for the free and hydrogen-bonded carbonyls (see Figure 5) of **SPU1**–**SPU13** show a range of percentage hydrogen bonding, with **SPU1** exhibiting the lowest percentage of hydrogen bonding (64 ± 2%) and **SPU8** exhibiting the highest (89 ± 6%), respectively.

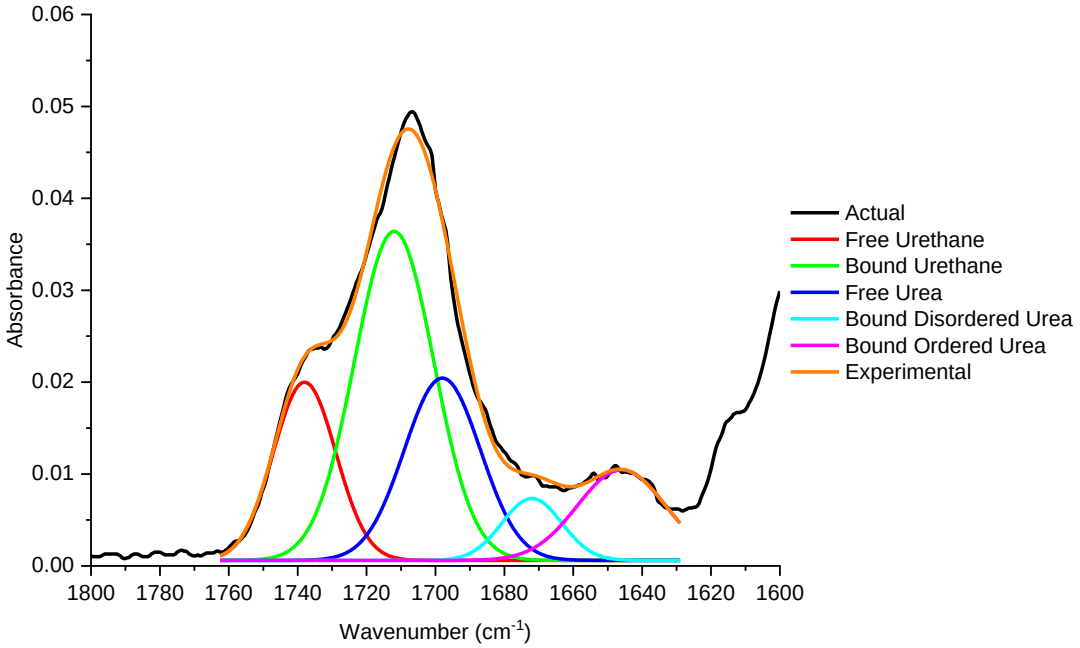

Figure 5. Example of the deconvolution of IR spectroscopic data; shown for **SPU10** at 25 °C in the carbonyl region 1800-1600 cm^{-1}. OriginLab was used for peak deconvolution.

Unsurprisingly, changing the end-group had little discernible influence on the percentages of bound and unbound urethane carbonyls (see Appendix 2, Figures 91–99). However, the deconvolution of the urea-bound and unbound carbonyl absorbances provided vital insights into the supramolecular assembly in the solid state. Deconvolution of the carbonyl bands in their respective infrared spectra provided critical insight into the supramolecular assembly of the end-group (see Appendix 2, Figures 91–105).[33,47,48] In the absence of the nitro substituent, the influence of increasing the conformational restraint of the urea carbonyl into a non-coplanar arrangement with the aryl ring can be assessed. The *ortho*-methyl substituents on **SPU9** and **SPU4** increased the hydrogen-bonded urea, ordered and disordered, from 81 ± 3% in **SPU1** to 85 ± 2% and 92 ± 3%, respectively. Interestingly, **SPU1,** which has no conformational restraint, was found to have 81 ± 3% hydrogen-bonded urea, only 50 ± 2% of which is ordered, the remaining 31 ± 4% being disordered hydrogen bonding. **SPU9** and **SPU4** possessed 71 ± 2% and 78 ± 2% ordered hydrogen-bonded urea. Therefore, imparting the non-coplanar arrangement increases the ordered hydrogen bonding of the urea carbonyl and, as a result, encourages the π-π stacking of the aryl moiety.[33] Interestingly, the *ortho*-dimethyl substituted **SPU9** has fewer ordered hydrogen-bonded and overall hydrogen-bonded urea carbonyl groups than the *ortho*-methyl substituted **SPU4**, suggesting the increased steric hindrance

around the urea moiety negatively affects the urea carbonyl group's ability to form ordered hydrogen bonds. The presence of a nitro moiety, either -*meta* (**SPU2**, **SPU5**, **SPU7**, **SPU8 SPU10,** and **SPU12**) or -*para* (**SPU3**, **SPU6**, **SPU11,** and **SPU13**) to the urea on the aryl substituent has a dramatic influence on the degree and order of the urea-carbonyl hydrogen bonding, because of the introduction of a competitive hydrogen-bond acceptor which effectively disrupts urea-urea hydrogen bonding interactions in favour of urea-nitro interactions.[49] It is known that introducing nitro substitution of aryl ureas at either the *meta* or *para* position can drastically alter the 3-dimensional supramolecular assembly.[31,50] The introduction of the competitive nitro hydrogen bonding acceptors in **SPU2** and **SPU3**, where the nitro is *meta* and *para*, respectively, results in the absence of any ordered hydrogen-bonded urea carbonyl and a significant decrease in the percentage of hydrogen-bonded urea to 42 ± 4% and 27 ± 4%, respectively, when compared to **SPU1**. Contrary to that observed with **SPU4**, imparting conformational restraint of the urea to force a non-coplanar conformation of the urea and aryl groups with the presence of a single *ortho*-methyl moiety while keeping the nitro in the same plane as the aryl ring, decreases the percentage of hydrogen-bonded urea for **SPU6** and **SPU7**. Increased steric hindrance experienced by the urea carbonyl further promotes the urea-nitro hydrogen bonding over urea-urea hydrogen bonding.[33] The *ortho*-methyl substituent adjacent to the urea and nitro moieties in **SPU5** forces a non-coplanar conformation of both the urea and nitro with respect to the benzene ring. This non-coplanar conformation inhibits its resonance forms [36,51], inhibiting its efficacy as a hydrogen-bond acceptor. This, along with the steric hindrance experienced by the nitro from the *ortho*-methyl, translates to 49 ± 2% ordered hydrogen-bonded urea in **SPU5**. As observed with **SPU9**, the increase in the steric hindrance of the urea moiety the *ortho*-dimethyl substituted **SPU10** experiences compared to **SPU5** results in a decrease in overall hydrogen-bonded urea and ordered hydrogen-bonded urea. The opposite trend was observed when the nitro group was located in the *para* position and not hindered by an *ortho*-methyl substituent: in **SPU11**, an increase in both overall hydrogen-bonded urea and ordered hydrogen-bonded urea was observed, 46 ± 8% and 31 ± 8%, respectively when compared to **SPU6**. The *para*-methyl substituent adjacent to the nitro moiety in **SPU8** forces a non-coplanar conformation of the nitro with the aryl ring without influencing the geometry between the urea and aryl ring. Inhibition of the resonance experienced by the nitro moiety translates to a significant increase in both overall hydrogen-bonded urea and ordered hydrogen-bonded urea, 84 ± 2% and 71 ± 2%, respectively. Inducing full conformational restraint of both the urea and nitro when in *meta*-nitro substituted, **SPU12**, and *para*-nitro substituted, **SPU13**, results in the highest percentage of hydrogen-bound urea when the urea is in the presence of *ortho*-methyl substituents, 77 ± 4%, and 76 ± 3%, respectively, and percentage of ordered hydrogen-bonded urea, 49 ± 4%, and 56 ± 2%, respectively. This promotion of urea-urea hydrogen bonding over urea-nitro hydrogen bonding results from the combined effect of the non-coplanar conformation adopted by the urea and aryl groups and the increased steric hindrance experienced by the nitro

moieties from the *ortho*-methyl substituents, which in turn inhibits resonance from the induced nitro-aryl non-coplanar conformation.

Table 4. Normalised percentage integrals of the urethane and urea absorbances of **SPU1–SPU13** from their respective FT-IR spectra, where the total bound urea equals the sum of the ordered bound urea and disordered bound urea.

End-group	Bound Urethane (%)	Free Urethane (%)	Ordered Bound Urea (%)	Disordered Bound Urea (%)	Total Bound Urea (%)	Free Urea (%)
SPU1	64 ± 2	36 ± 6	50 ± 2	31 ± 4	81 ± 3	19 ± 5
SPU2	86 ± 3	14 ± 5	-	42 ± 4	42 ± 4	58 ± 3
SPU3	76 ± 2	25 ± 4	-	27 ± 4	27 ± 4	73 ± 2
SPU4	76 ± 3	25 ± 6	78 ± 2	14 ± 7	92 ± 3	8 ± 6
SPU5	80 ± 2	21 ± 3	49 ± 2	18 ± 6	67 ± 3	33 ± 5
SPU6	74 ± 2	26 ± 4	-	17 ± 6	17 ± 6	83 ± 3
SPU7	70 ± 2	30 ± 3	-	23 ± 5	23 ± 5	77 ± 2
SPU8	89 ± 6	11 ± 6	71 ± 2	13 ± 3	84 ± 2	16 ± 6
SPU9	78 ± 6	22 ± 4	71 ± 2	13 ± 5	85 ± 2	15 ± 5
SPU10	65 ± 2	35 ± 4	21 ± 5	26 ± 8	47 ± 7	53 ± 3
SPU11	70 ± 2	30 ± 5	31 ± 8	15 ± 8	46 ± 8	54 ± 5
SPU12	70 ± 2	30 ± 8	49 ± 4	27 ± 4	77 ± 4	23 ± 7
SPU13	81 ± 2	19 ± 4	56 ± 2	20 ± 6	76 ± 3	24 ± 6

It has previously been illustrated the value of utilising VT-IR spectra to assess the reversibility of hydrogen-bonding functional groups in supramolecular polyurethanes.[45] To further understand the reversible processes in **SPU5**, VT-IR spectroscopic analysis was recorded from 25 °C to 200 °C, monitoring the relative absorbances of the urea and urethane carbonyl groups to understand the thermal stability of the hydrogen-bonded supramolecular networks of the urethane and urea moieties (see Figure 4B). **SPU5** was prepared as a KBr disc with a loading of 0.1% wt. to ensure homogeneity throughout the beam path over the temperature range. Dissociation of the hydrogen-bonding networks within the SPU was assessed by deconvolution of the urea and urethane absorbances as a function of temperature (see Appendix 2, Figures 106–109). Variation between the deconvoluted FT-IR and VT-IR spectra of **SPU5** was attributed to measurement differences: the room temperature FT-IR spectra were obtained from a polymer film on an ATR accessory, whereas the variable-temperature measurements used KBr discs. Upon increasing temperature, a shift to longer wavenumbers was observed for the urethane and urea carbonyls moving from a bound to an unbound state. A qualitative comparison of the deconvoluted absorbances assigned to the bound and unbound urethane carbonyl groups throughout the heating cycle has revealed two thermal regions of interest. The first was evident from 40 °C to 80 °C, where an initial decrease in the

percentage bound urethane was clear, with a second decrease from 100 °C to 140 °C. The deconvolution of the urea carbonyl has also revealed two thermal regions of interest, 40 °C to 60 °C and 80 °C to 120 °C. The first is associated with a transition from ordered bound urea to disordered bound urea, and the second region is attributed to a transition of the disordered bound urea to free urea. However, the complete dissociation of the hydrogen-bonded carbonyls was not evident up to 200 °C. Polymer films were subsequently solvent cast from a concentrated solution of THF (see Figure 6), and the influence of modifying the end-group of the supramolecular polyurethane could then be assessed through mechanical property testing.

Figure 6. Representative homogeneous cast translucent film of **SPU11** in 10 cm × 10 cm aluminium mould.

The thermal properties of **SPU1**–**SPU13** were assessed by DSC analysis (see Figure 4**C** and Table 2). In the second heating cycle, all the SPUs exhibited a T_g *ca*. -45 °C associated with the glass transition of the poly(ethylene-*co*-butylene) soft domain. **SPU5** displayed the thermal characteristics of a typical amorphous polymer in that only a single glass transition was evident. Interestingly, the SPUs which contained a nitro functional group that lay in-plane with the aryl ring, such as **SPU6**, exhibited two distinct melting transitions in the second heating run, 13.4 °C and 36.0 °C, and a cold crystallisation (a transition from a crystalline state to an amorphous state, followed by chain reorganisation resulting in crystallisation prior to melting again) between these melting transitions at around 16 °C. Cold crystallisation was also evident in the first cooling cycle at 23.1 °C. Apart from **SPU12**, which features an elevated melting temperature of 124.0 °C, this data indicates that when the nitro substituent of the end-group is

twisted orthogonal to the aryl ring by an ortho methyl substituent, the remaining SPUs do not have melting transitions that are discernible by DSC analysis. This trend was evident in the SPUs synthesised herein. As **SPU1**–**SPU13** all have similar molecular weights and polydispersity (see Appendix 2, Table 19), the differences in thermal transitions originate purely from the aggregation and crystallisation of the end-group in the hard domains. The melting and crystallisation of the hard domains are proposed to be a consequence of nanofiber formation, which Appel *et al*. have previously reported for ureidopyrimidinone supramolecular thermoplastic elastomers.[52] SAXS/WAXS experiments were therefore performed on the supramolecular polyurethane networks to further investigate the crystallinity within the hard domain in more detail.

Table 5. Thermal properties of the supramolecular polymers SPU1–SPU13.

	T_g (°C)[b]	T_m (°C)[a]	T_m (°C)[b]	T_c (°C)[c]	T_c (°C)[b,d]
SPU1	-45.7	98.9	-	-	-
SPU2	-45.6	41.0	13.7; 33.0	16.8	17.1
SPU3	-46.1	41.1	13.3; 34.2	22.8	16.5
SPU4	-44.5	56.1	-	-	-
SPU5	-45.0	-	-	-	-
SPU6	-46.1	40.7	13.4; 36.0	23.1	15.9
SPU7	-45.7	42.0	14.1; 35.7	22.1	18.9
SPU8	-45.5	-	-	-	-
SPU9	-46.3	-	15.0; 36.8	11.3	20.0
SPU10	-45.3	-	-	-	-
SPU11	-44.9	40.0	8.6; 36.3	16.2	19.6
SPU12	-45.9	42.3	124.0	-	-
SPU13	-44.6	-	-	-	-

[a] First heating run, 10 °C min^{-1}. [b] Second heating run, 10 °C min^{-1}. [c] First cooling run, 10 °C min^{-1}. [d] Cold crystallisation

TGA analysis was employed to ascertain the maximum processing temperature, whereby samples were heated from 20 °C to 550 °C at a rate of 10 °C min^{-1} under a nitrogen atmosphere. **SPU13** exhibited the lowest temperature for the onset of degradation at 237 °C, and all the SPUs degraded fully by 475 °C (see Appendix 2 Figures 110–115).

The properties of thermoplastic supramolecular polyurethanes are dependent on their microphase-separated morphology.[53–55] SAXS has thus been used to investigate the microphase separation in these materials.[11,45,56] At room temperature, **SPU2**, **SPU3**, **SPU6,** and **SPU10** exhibit broad Bragg peaks at 95.1 Å, 84.0 Å, 87.0 Å, and 82.7 Å, respectively, implying a microphase-separated morphology arising from the immiscibility of the hard hydrogen-bonding end-groups with the soft poly(butadiene) backbone.[43,45,56,57] In the cases of **SPU3** and **SPU6**, an -*ortho*-methyl substituent on the end-groups resulted in a clear shift to

longer interdomain spacings from 84.0 Å to 87.0 Å. The most notable change, however, was observed in the case of **SPU2** and **SPU10**; in the absence of -*ortho*-methyl substituents, the interdomain spacing (**SPU2**) was 95.1 Å, and upon constraining the conformation of the end-cap through the addition of two -*ortho* methyl substituents, a significant shift to 82.7 Å was evident (see Figure 7**A**). In the case of **SPU5**, where only one methyl substituent is *ortho* to the urea, and the nitro substituent is twisted out of plane relative to the aryl substituent, a broad Bragg peak was observed at 62.8 Å, indicating a reduced degree of microphase separation between the polymer backbone and the end-group. Compared to previously reported supramolecular poly(butadiene)s, which featured chiral end-groups, broad reflections were observed with domain spacings of 101.3 Å and were associated with the nanophase separation.[45] **SPU1**, **SPU4,** and **SPU9** are end-capped with an aniline that does not feature the nitro hydrogen-bonding acceptor group and the difference in the SAXS data between these SPUs and those SPUs where the end groups possess a nitro moiety is dramatic. Bragg peaks associated with microphase separation are significantly less intense and are shifted to larger domain spacings, implying reduced microphase separation between the polar end groups and the apolar polymer backbone. Furthermore, **SPU9** exhibited a second-order peak suggesting a lamellar structure.

WAXS was also performed to investigate the ordering within the hard domains (see Figure 7B). Several reflections were observed (*ca.* 14.6 Å, 9.8 Å, 7.4 Å, 5.5 Å, 4.7 Å, 4.2 Å, 3.5 Å and 3.1 Å). All the SPUs in this study exhibited well-ordered packing with reflections (*ca.* 4.7 Å to 4.2 Å) corresponding to ordering within the urea based hard domains.[58] Furthermore, reflections (*ca.* 3.5 Å), characteristic of π–π stacking assemblies, can be seen.[59] **SPU4** and **SPU9**, which do not contain a nitro substituent, feature sharp reflections, especially *ca.* 4.7 to 4.2 Å, corresponding to urea-urea hydrogen-bonding interactions. Deconvolution of FTIR spectroscopic data revealed that these SPUs had the highest ordered urea hydrogen-bonding content (see Table 1).

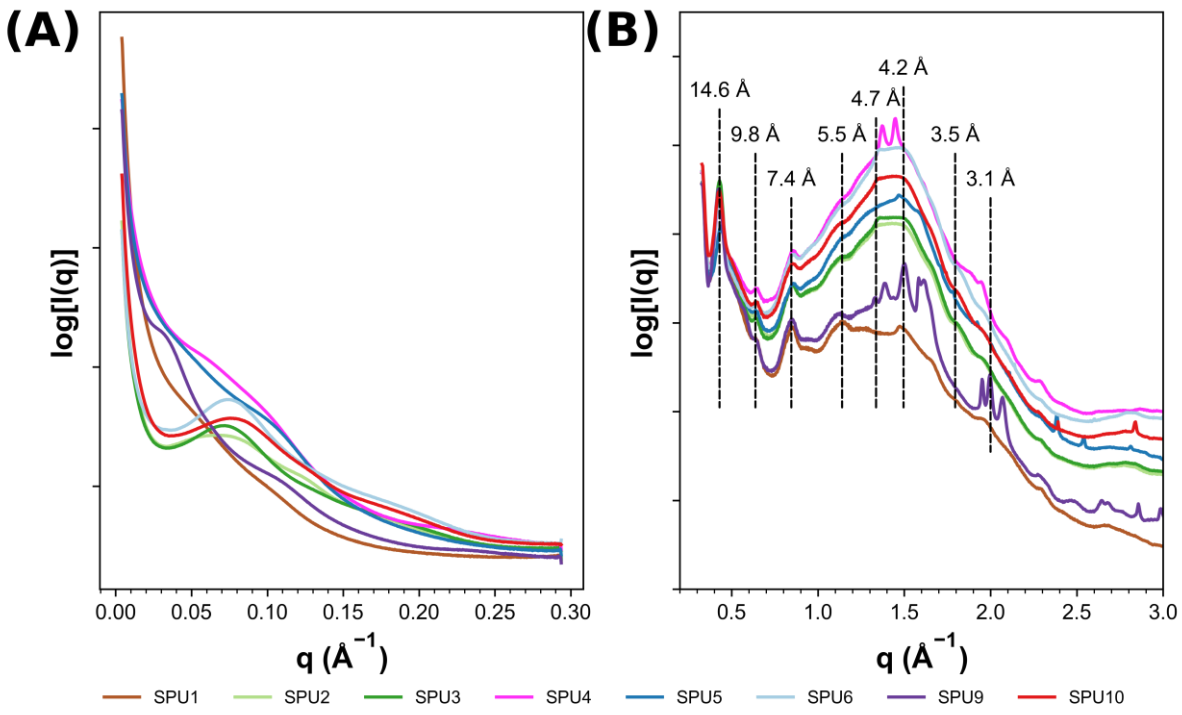

Figure 7. (A) SAXS intensity profiles of the SPUs **(B)** WAXS intensity profiles of the SPUs. Data were acquired at room temperature.

Visual inspection of the polymer films provided critical insight into the assembly of the end group. **SPU1**, **SPU4**, and **SPU9**, which did not feature a nitro substituent, did not form homogeneous films and instead appeared significantly phase-separated (see Figure 8).

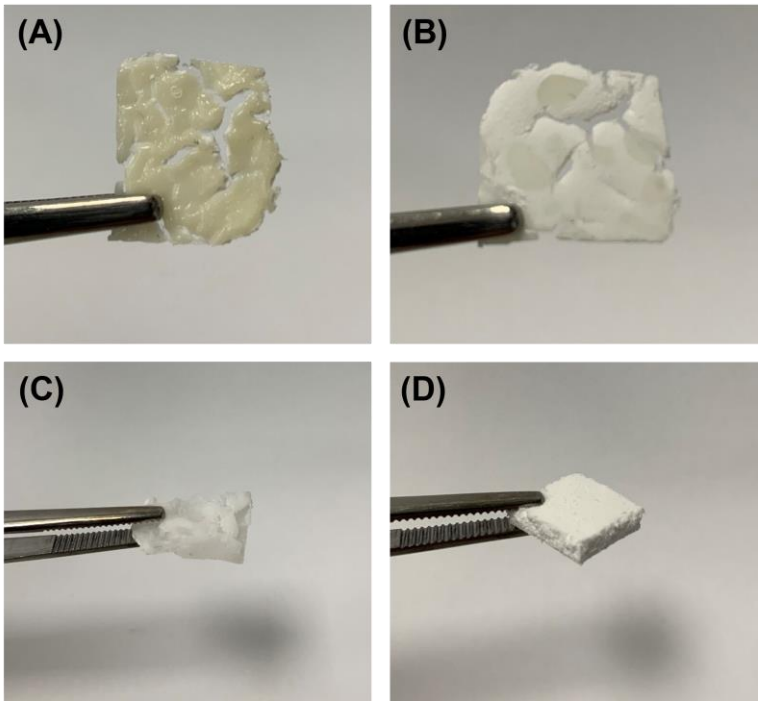

Figure 8. Cast polymer films of **(A) SPU1** top face, **(B) SPU1** bottom face, **(C) SPU4** and **(D) SPU9**. **SPU1**, **SPU4**, and **SPU9** do not feature a nitro moiety.

The viscoelastic properties of **SPU1**–**SPU13** were assessed with dynamic rheological testing (see Figures 9A and 9B). The storage modulus (G') dominates, and **SPU1**–**SPU13** behave as viscoelastic solids in the low-temperature regime. At elevated temperatures, the differences between **SPU1**–**SPU13** became apparent, and the dissociation and association of supramolecular polymer networks could be compared. The strong association of the hard domains in **SPU1**, **SPU4** and **SPU9** and the lack of nitro substituent resulted in no meaningful change in the storage modulus up to 100 °C. This data reinforces the concept that the nitro substituent on the polymer end-group attenuates the interchain hydrogen bonding. A similar observation was made by Nicoud and co-workers, who investigated nitrophenyl urea crystal structures and found that the nitro oxygen acts as a competitive acceptor for acidic urea hydrogen donors and disrupts urea-urea interactions.[60] In the case of **SPU1**, a gradual relaxation mechanism was observed, yet the polymer did not transition into the viscous state (see Figure 9B).

SPU4 and **SPU9**, which feature ortho-methyl substituents, resist this relaxation mechanism, presumably because of the hard domains' increased association and crystallinity and hence increased order within the domain. Furthermore, their high level of ordered urea (as determined by FTIR) indicates a more extended assembly. **SPU2**, **SPU3**, **SPU6** and **SPU7** exhibited terminal flow below 60 °C and a crossover between G' and the loss modulus (G") was observed. The common feature of these SPUs is that they all possess a nitro functional group and in the case of **SPU6** and **SPU7**, a single methyl substituent situated ortho to the urea moiety. Therefore, these SPUs were investigated for their potential as low-temperature adhesives and healable materials to exploit their reversible dissociation. Interestingly, SPU5, which also features a nitro substituent and an ortho-methyl substituent (to both the nitro and urea groups), exhibited exceptional resistance to temperature and no terminal flow nor significant relaxation event was observed up to 150 °C. In this case, the ortho-methyl substituent can twist the nitro group out of the plane of the aryl ring and disrupt its ability to act as a hydrogen-bond acceptor and thus, SPU5 exhibits similar rheological characteristics to **SPU1**, **SPU4** and **SPU9**. SPUs: **SPU10**, **SPU11**, **SPU12** and **SPU13**, which contained two ortho-methyl substituents and therefore more organised hard domains, because of the forced non-coplanar assembly, also did not exhibit dramatic changes in their rheological properties with increasing temperature. **SPU11**, however, is the exception, as in this case, the nitro substituent is in the para position and thus able to act as an uninhibited hydrogen-bonding acceptor, and a noticeable relaxation event is observed around 40 °C (see Figure 9), presumably softening of the hard domains, however, a new rubbery plateau is found. The supramolecular network can resist terminal flow up to 140 °C, where the onset of terminal flow is observed. As observed with **SPU11**, **SPU8**, which contains a *para*-methyl adjacent to the nitro moiety, experiences a significant relaxation event around 40 °C with a new rubbery plateau being found after, resisting terminal flow up to 120 °C.

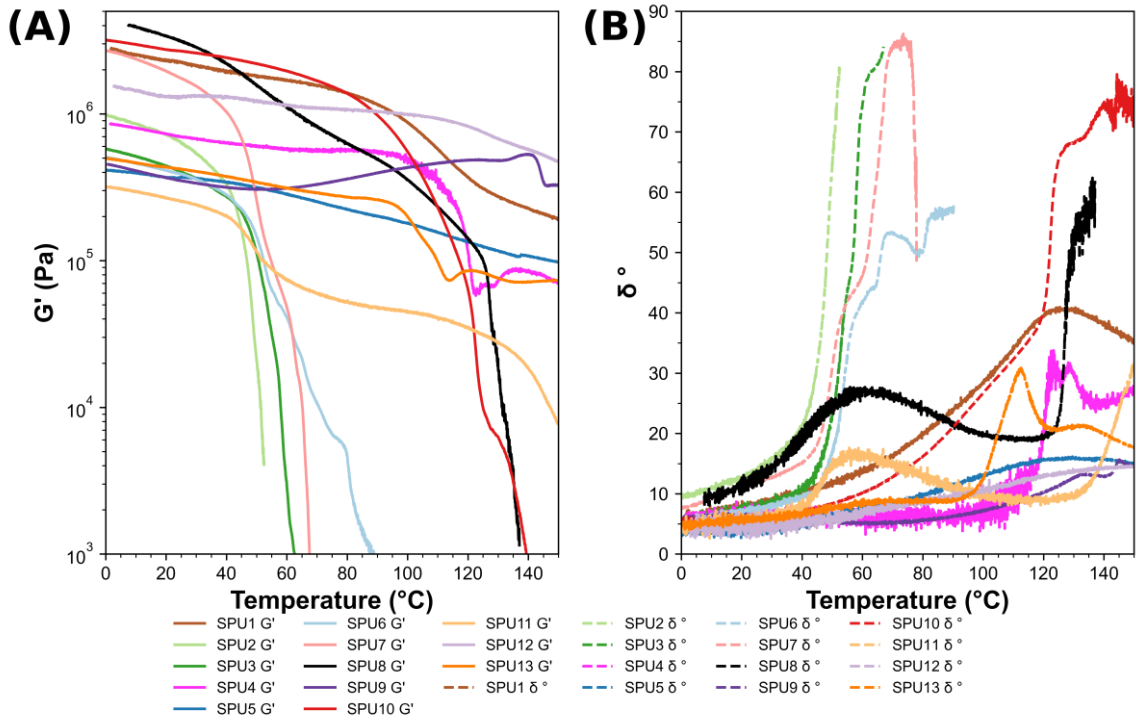

Figure 9. Temperature sweep analysis of **SPU1–SPU13** over a temperature regime of 0 °C to 150 °C, using a normal force of 1 N and a frequency of 1 Hz. **(A)** G' against temperature, **(B)** phase shift (δ) against temperature.

Master curves of G' and G'' for **SPU2**, **SPU3**, **SPU5–SPU8** and **SPU10–SPU13** were attempted using the time-temperature superposition (TTS) principle; however, the frequency curves could not be fitted with only horizontal shift factors (see Figure 10 and Appendix 2, Figures 131–140). The principle of TTS can sometimes fail in systems when there is more than one assembly mode with distinctly different temperature dependencies, which is observed commonly in immiscible polymer blends.[61] In this case, it is postulated that the four main dynamic hydrogen-bonding interactions involving these end groups had distinctly different temperature dependencies, and as such, we could not apply TTS for all of the SPUs tested. van Gurp-Palmen plots were used to confirm this (see Figure 11 and Appendix 2, Figures 141–150).

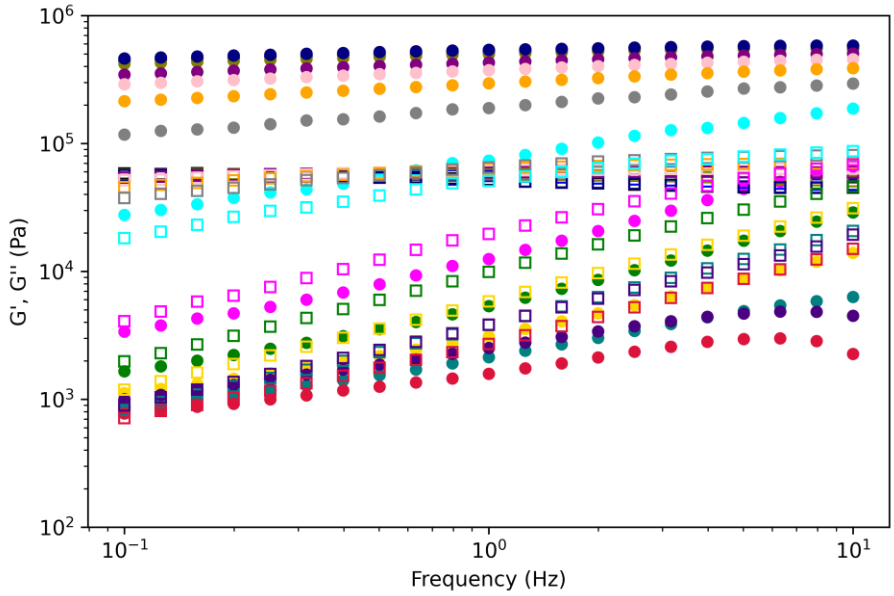

Figure 10. Frequency sweep rheological analysis of **SPU2** at 0 (black), 5 (red), 10 (blue), 15 (olive), 20 (navy), 25 (purple), 30 (pink), 35 (orange), 40 (gray), 45 (cyan), 50 (magenta), 55 (green), 60 (gold), 65 (teal), 70 (crimson), 75 °C (indigo). G' closed symbols and G'' open symbols frequency sweeps were performed between 0.1 to 10 Hz at an applied strain of 0.1%.

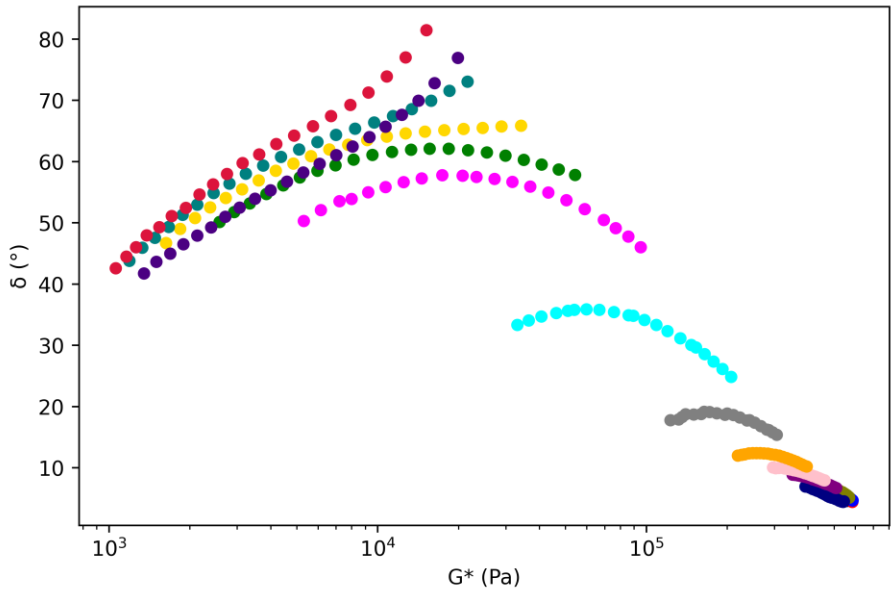

Figure 11. van Gurp-Palmen plot of **SPU2** at 0 (black), 5 (red), 10 (blue), 15 (olive), 20 (navy), 25 (purple), 30 (pink), 35 (orange), 40 (gray), 45 (cyan), 50 (magenta), 55 (green), 60 (gold), 65 (teal), 70 (crimson), 75 °C (indigo). Frequency sweeps were performed between 0.1 to 10 Hz at an applied strain of 0.1%.

Previous studies have shown that the supramolecular assembly of nitro-aryl urea hydrogelators can be controlled by conformationally forcing the urea and aryl substituents into a non-coplanar arrangement.[34] Changing the end-group of the supramolecular polymer networks synthesised in this study significantly affected mechanical properties by changing the

supramolecular-assembly mode. The binding interactions in the polar hard domains (e.g. proposed to comprise the chain end groups predominantly) dictate the extent and strength of the supramolecular assembly and, thus, the mechanical properties of the polymer network. Tensile stress-strain measurements probed the mechanical properties of the supramolecular elastomers at a rate of 10 mm min^{-1} (Figure 12).

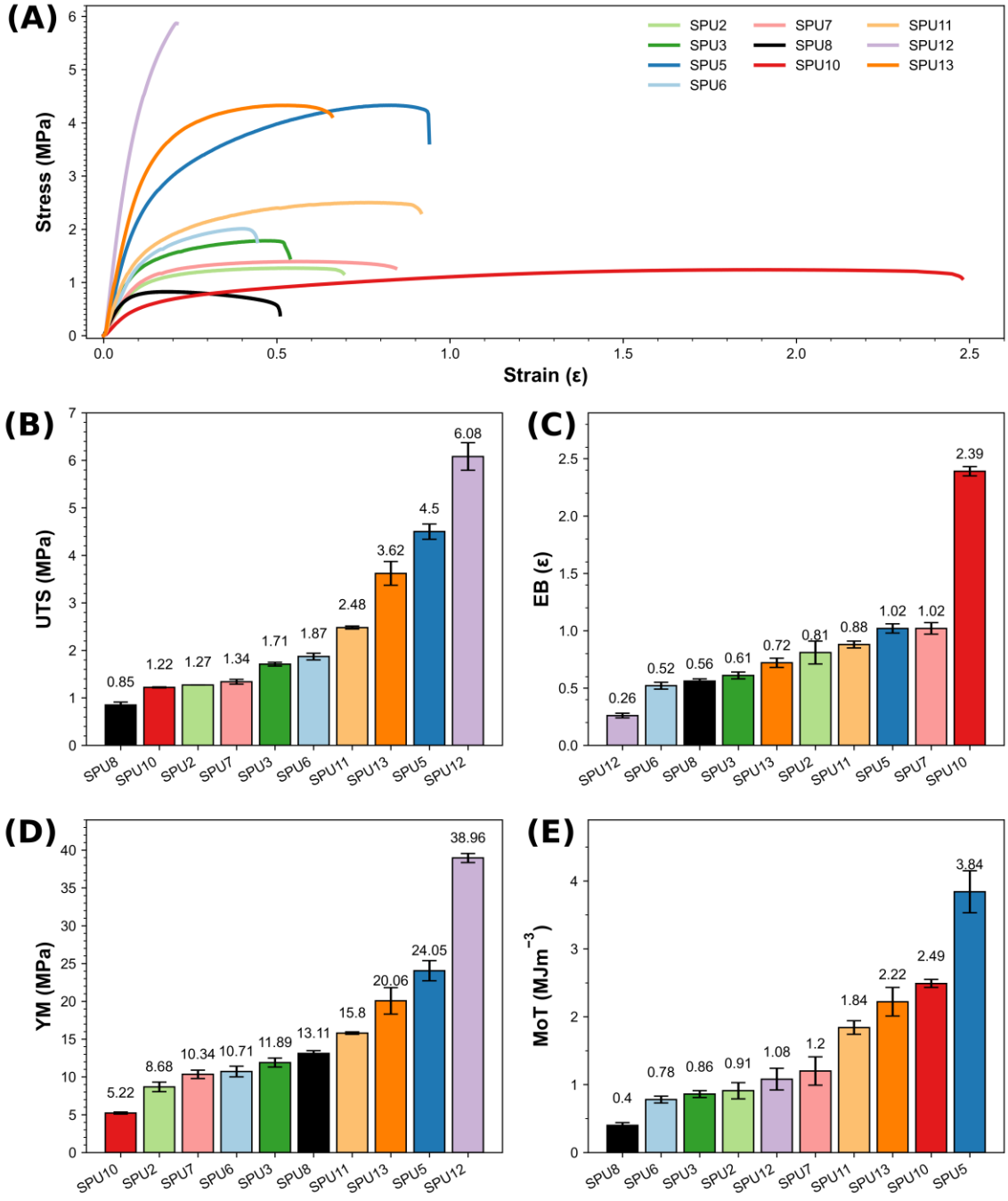

Figure 12. (A) Representative stress-strain curves of supramolecular elastomers, **SPU2**, **SPU3**, **SPU5–SPU7** and **SPU10–SPU13**. Comparison of **(B)** ultimate tensile strength (UTS), **(C)** elongation at break (EB), **(D)** Young's modulus, and **(E)** Modulus of toughness (MoT). The error shown is the standard deviation between the three repeats for each sample.

The general structure of supramolecular polyurethanes and the four primary dynamic interactions give rise to their unique mechanical properties (see Figure 2 and Appendix Figures 151-165). It is helpful to evaluate the -*meta* and -*para*-nitro supramolecular polyurethanes separately to assess and effectively discuss the differences in mechanical properties. The SPUs featuring each regioisomer behave differently, and the influence of the pattern of substituents surrounding the nitro substituent was critical. Assessing first the *meta*-nitro substituted supramolecular polyurethanes (**SPU2**, **SPU5**, **SPU8**, **SPU10**, and **SPU12**), a drastic increase in both ultimate tensile strength (UTS) and Young's modulus was obtained in **SPU11**. In **SPU12**, where the end-group was 2,4,6-trimethyl-3-nitroaniline, a UTS of 6.08 ± 0.29 MPa and Young's modulus of 38.96 ± 0.60 MPa was achieved. This result contrasted with that obtained for **SPU10** (2,6-dimethyl-3-nitroaniline), which had the second-lowest UTS value in this study of 1.22 ± 0.01 MPa and the second-lowest Young's modulus at 5.22 ± 0.14 MPa. The only primary structural difference between these two supramolecular elastomers is the addition of a single methyl substituent that flanks the nitro substituent position, enforcing non-coplanarity between the nitro and the aryl ring. In contrast, when the end-group was 3-nitroaniline (**SPU2**), a UTS value of 1.27 ± 0.00 MPa and Young's modulus of 8.68 ± 0.63 MPa was determined comparable in value to **SPU10**. However, **SPU10** proved to be the most elastic supramolecular polymer in this study, with an elongation at break (EB) of 2.39 ± 0.04. **SPU5** offers a unique insight into how adding a single -*ortho*-methyl substituent adjacent to the urea and nitro moieties resulted in more than doubling the UTS compared to the cases of **SPU2**, **SPU7**, and **SPU10**. Rationalising this outcome is non-trivial, and the influence of the methyl substituent appears to be two-fold; when located *ortho* to the urea, the plane of the aryl unit is twisted into a non-coplanar arrangement; this effect is also magnified when two methyl substituents flank the urea group. Secondly, when a methyl substituent is situated -*ortho* to the nitro substituent, the nitro acceptor unit can twist out-of-plane and act as a hydrogen bonding acceptor to adjacent polymer chains perpendicular to the main chain. To our surprise, having two methyl substituents flanking the urea (in the case of the end-group of **SPU9**) serves to affect the UTS of the SPU negatively. Thus, the enforced non-planar arrangement of the aryl and urea has a detrimental influence on the assembly of the hard domain. Evaluating the -*para* regioisomer (**SPU3**, **SPU6**, **SPU11**, and **SPU13**) and removing the influence of the -*ortho* methyl substituent, a trend appears for all parameters tested. The difference between **SPU6** and **SPU3** is negligible, suggesting that adding a single methyl substituent *ortho* to the urea has no significant effect on the hard domain. This correlates to the urea carbonyl's absence of ordered hydrogen bonding within the FT-IR spectroscopic analysis (see Table 1). However, in the case of **SPU11**, where two methyl substituents flank the urea and force non-coplanarity between the urea and the aryl substituent, marked increases in UTS, EB, Young's modulus, and modulus of toughness were observed (Figure 12**B**-**E**). **SPU13** exemplifies this observation further, with the largest UTS, Young's modulus and modulus of toughness compared to the other *para*-nitro substituted SPUs (Table 3). These observations correlate to the introduction

of ordered hydrogen-bonded urea carbonyls in the cases of **SPU11** and **SPU13**, with **SPU13** featuring the highest percentage of ordered and total hydrogen-bonded urea carbonyl within the *para*-nitro substituted SPUs (see Table 1).

Table 6. Effect of end-group on the mechanical properties of the SPUs; the recorded are averages of three separate samples of each SPU. The error shown is the standard deviation between the three repeats for each sample.

End-group	UTS[a] (MPa)	EB[b] (ε)	Young's Modulus[a] (MPa)	Modulus of Toughness[a] (MJm^{-3})
SPU2	1.27 ± 0.00	0.81 ± 0.10	8.68 ± 0.63	0.91 ± 0.12
SPU3	1.71 ± 0.04	0.61 ± 0.03	11.89 ± 0.60	0.86 ± 0.05
SPU5	4.50 ± 0.16	1.02 ± 0.04	24.05 ± 1.33	3.84 ± 0.31
SPU6	1.87 ± 0.07	0.52 ± 0.03	10.71 ± 0.70	0.78 ± 0.05
SPU7	1.34 ± 0.05	1.02 ± 0.15	10.34 ± 0.55	1.20 ± 0.21
SPU8	0.85 ± 0.06	0.56 ± 0.02	13.11 ± 0.35	0.41 ± 0.04
SPU10	1.22 ± 0.01	2.39 ± 0.04	5.22 ± 0.14	2.49 ± 0.06
SPU11	2.48 ± 0.03	0.88 ± 0.03	15.80 ± 0.16	1.84 ± 0.10
SPU12	6.08 ± 0.29	0.26 ± 0.02	38.96 ± 0.60	1.08 ± 0.16
SPU13	3.62 ± 0.25	0.72 ± 0.04	20.06 ± 1.75	2.22 ± 0.21

[a]UTS, ultimate tensile strength; [b]EB, elongation at break.

Adhesion between two substrates requires strong interfacial interactions and is a non-trivial challenge. We envisaged that by taking advantage of the tuneable supramolecular assembly through end-group design, our supramolecular networks could more efficiently dissipate mechanical load by breaking physical (non-covalent) interactions and therefore reduce adhesive and cohesive failure. These non-covalent interactions will reform after breaking and restore the polymer adhesive's mechanical properties with sufficient time and temperature.[22,62,63] Advantageously, our relatively low molecular weight supramolecular polymer adhesives have the advantage of reversibility and derive their mechanical properties from non-covalent interactions. Consequently, they do not suffer the same mechanical property loss as polymer systems that rely on chain scission for energy dissipation. We tested the hot-melt adhesion properties of the supramolecular polymer networks through triplicate lap-shear experiments. The adhesion of the supramolecular polymers was assessed at two different bonding temperatures, 70 °C and 120 °C, to understand the bulk viscoelastic properties in more detail. Four substrates, namely, glass, aluminium, high-density polyethylene (HDPE) and polypropylene (PP), were assessed (Figure 13**A**). Unsurprisingly, strong adhesion was achieved with glass (see Appendix 2, Figure 155) and aluminium substrates, as the supramolecular polyurethanes can interact with the substrate through non-covalent interactions.[64,65] **SPU12** exhibited exceptional shear strength in adhering to glass (5.70 ± 0.10 MPa) and aluminium (3.59 ± 0.23 MPa). To put this data into context, Feringa, Tian, and co-

workers explored a thioctic acid copolymer with a maximum lap shear strength of 2.5 MPa when adhering glass, making it comparable to 3M instant adhesive at 2.25 MPa.[47] Similarly, Weder and co-workers reported an optically responsive supramolecular polymer glass that took advantage of the self-assembly characteristics of UPy units. The adhesion of two glass slides bonded together by the supramolecular polymer glass yielded a lap shear strength of approximately 1.2 MPa.[66] To demonstrate the reusability of these SPUs as adhesives, re-adhesion of **SPU12** between glass substrates was conducted and exhibited no fatigue after 5 cycles (Figure 13**B**). This observation is owing to the dynamic nature of supramolecular materials. In contrast, adhesion to HDPE and PP proved challenging, as these substrates do not have surface structural motifs that can cooperatively interact with the supramolecular polyurethanes. Hydrogen-bonding interactions are highly directional and must be within 5 Å of each other and be orientated cooperatively throughout the bulk material to be effective.[67] Thus, we anticipated controlling this bulk orientation through effective end-group modulation. Interestingly an inverse relationship was observed for **SPU7**, whereby it was found to be the strongest adherent to PP with a UTS of 1.43 ± 0.14 MPa and, surprisingly, the weakest to HDPE (0.58 ± 0.03 MPa).

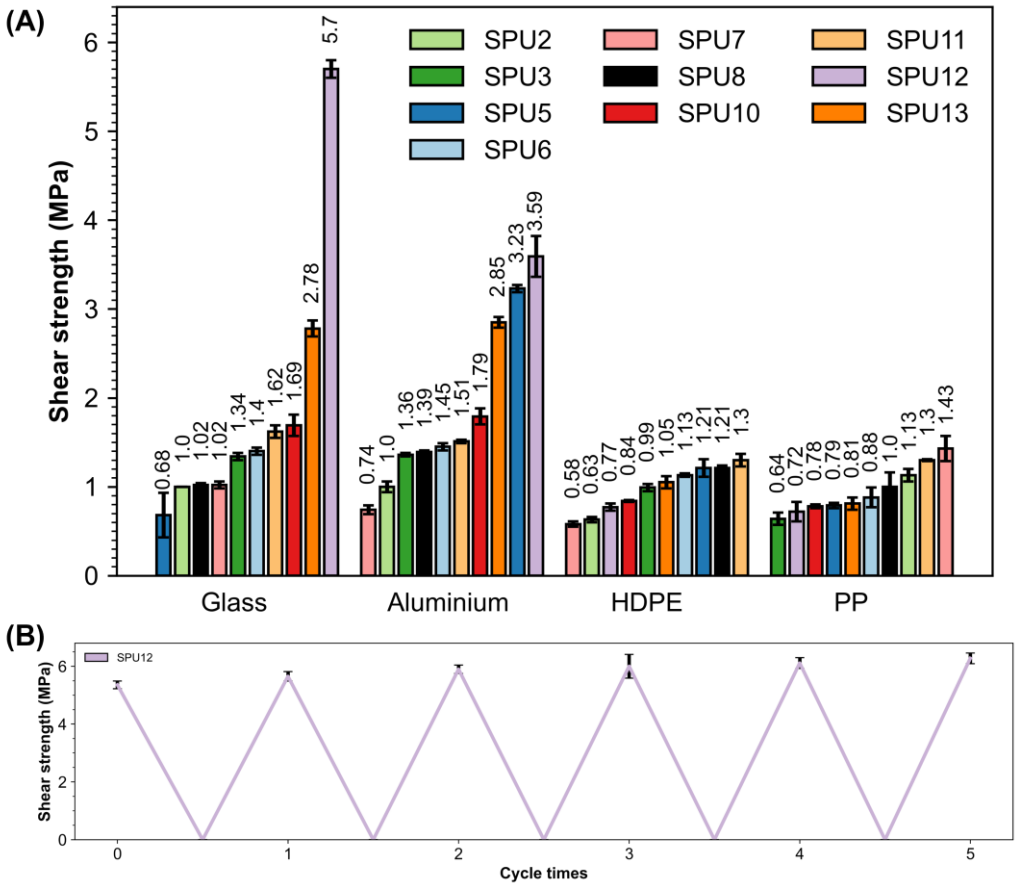

Figure 13. A) Shear strength of supramolecular networks as determined by tensile lap-shear experiments. **B)** Shear strength of SPU after cycling 5 times through the cycling experiments.

The polymer healing tests were conducted by first cutting the polymer tensile strips in half with a scalpel, and the edges were butted together on a PTFE plate.[44] The strips were then

transferred into a preheated oven for 1 hour at an appropriate temperature derived from the rheological data for each SPU before allowing to cool to room temperature for 30 minutes and carefully peeling from the PTFE plate (see Figure 14).[68] It has been previously reported that for a strong self-healing response, the relaxation time of the polymer film should range from 0.1 seconds to 100 seconds.[69] For this to occur, G' and G" need to crossover at the determined healing temperature. **SPU5** and **SPU11–SPU13** do not exhibit crossover between G', and G" at temperatures below 150 °C, as evident in the temperature sweep analysis (see Figure 11) and TTS analysis (see Appendix 2, Figure 131–150). As a result of the absence of material flow for these SPUs, poor recovery of mechanical properties was observed, and healing was not observed for **SPU12**. **SPU3**, **SPU6** and **SPU7** exhibited modest recoveries, 53%, 53% and 39%, respectively, in terms of UTS and increases in their EB relative to the pristine material, 249%, 167% and 137% (see Table 4). **SPU2** and **SPU10** saw an increase in their UTS (134% and 220%) and a modest recovery in EB (37% and 54%). Healing recoveries greater than 100% have been observed previously for other elastomer systems described by Bao, Binder, and co-workers, presumably, a consequence of the preparation conditions used to afford the pristine material not permitting the supramolecular networks in question to reach their energetic minimum.[69]

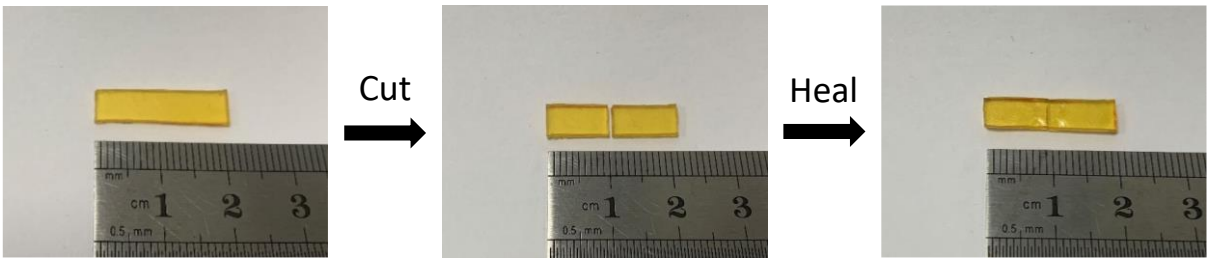

Figure 14. Images of the healing process for SPU **SPU10**

Table 7. Healing data for the SPUs; the order of data in the table for each entry is as follows:– pristine SPU; healed SPU; % healing.

Polymer	Healed UTS (MPa)	Healed EB (ε)	Healed Young's Modulus (MPa)	Healed Modulus of Toughness (MJm^{-3})
SPU2	1.27 ± 0.00	0.81 ± 0.10	8.68 ± 0.63	0.91 ± 0.12
	1.70 ± 0.15	0.30 ± 0.04	13.68 ± 0.81	0.39 ± 0.09
	134%	37%	158%	43%
SPU3	1.71 ± 0.04	0.61 ± 0.03	11.89 ± 0.60	0.86 ± 0.05
	0.90 ± 0.06	1.52 ± 0.24	6.99 ± 0.95	1.17 ± 0.23
	53%	249%	59%	136%
SPU5	4.50 ± 0.16	1.02 ± 0.04	24.05 ± 1.33	3.84 ± 0.31
	1.36 ± 0.32	0.07 ± 0.02	28.50 ± 3.99	0.08 ± 0.03
	30%	7%	119%	2%
SPU6	1.87 ± 0.07	0.52 ± 0.03	10.71 ± 0.70	0.78 ± 0.05
	1.00 ± 0.06	0.87 ± 0.14	8.69 ± 0.57	0.67 ± 0.12
	53%	167%	81%	86%
SPU7	1.34 ± 0.05	1.02 ± 0.15	10.34 ± 0.55	1.20 ± 0.21
	0.52 ± 0.04	1.40 ± 0.32	4.84 ± 0.10	0.61 ± 0.16
	39%	137%	47%	51%
SPU8	0.85 ± 0.06	0.56 ± 0.02	13.11 ± 0.35	0.41 ± 0.04
	0.58 ± 0.00	0.41 ± 0.00	10.49 ± 1.63	0.19 ± 0.00
	68%	72%	80%	47%
SPU10	1.22 ± 0.01	2.39 ± 0.04	5.22 ± 0.14	2.49 ± 0.06
	2.68 ± 0.13	1.28 ± 0.14	9.94 ± 0.06	2.49 ± 0.42
	220%	54%	190%	100%
SPU11	2.48 ± 0.03	0.88 ± 0.03	15.80 ± 0.16	1.84 ± 0.10
	0.94 ± 0.09	0.47 ± 0.04	6.43 ± 0.42	0.32 ± 0.07
	38%	53%	41%	17%
SPU12	6.08 ± 0.29	0.26 ± 0.02	38.96 ± 0.60	1.08 ± 0.16
	-	-	-	-
	-	-	-	-
SPU13	3.62 ± 0.25	0.72 ± 0.04	20.06 ± 1.75	2.22 ± 0.21
	1.38 ± 0.40	0.24 ± 0.05	12.96 ± 1.89	0.22 ± 0.10
	38%	33%	65%	10%

3.3 Conclusions

A series of novel SPUs that feature polar end groups were synthesised, and their physical properties were assessed with respect to their end groups. End-groups that did not feature a nitro moiety were too brittle and phase-separated because of increased crystallinity in the hard domain. Upon attenuating this assembly with a nitro substituent, which acted as a competitive hydrogen-bonding group for urea-urea associations, the mechanical properties of the resultant SPUs could be tailored, and adhesion to glass, aluminium, PP and HDPE was assessed. Furthermore, promisingly these SPU derivatives were also found to be elastomeric and self-healing. SAXS/WAXS analysis revealed a microphase-separated morphology which was attributed to the improved mechanical properties of the SPUs. DSC analysis showed that SPUs with unhindered nitro substituents exhibited melt transitions around 36 °C. Temperature sweep rheological analysis of the SPUs revealed key insights, into the reversibility of the supramolecular networks, in the absence of a nitro substituent, a crossover between G' and

G'' was not observed, and the material behaved as a covalently crosslinked rubber. This was also the case when the nitro substituent was twisted out of plane relative to the aryl ring and unable to act as a competitive hydrogen bonding acceptor.

3.4 Experimental Section

General. Total Cray Valley kindly provided Krasol™ HLBH-P2000 for this study. Tetrahydrofuran (THF) was distilled from benzophenone and sodium before use. All other reagents were purchased from Sigma Aldrich and used as received.

Analysis. The analytical data for compounds **3.1–3.21** plus **SPU1**–**SPU13** are reported in Appendix 2. Analytical techniques used to characterise the compounds and polymers reported in this Chapter are described in Section 2.9 unless specified below. Samples for NMR spectroscopic analysis were prepared in $CDCl_3$, d_6-DMSO and d_8-THF, and dissolution of the sample was aided with gentle heating. Variable temperature IR (VT-IR) spectroscopic analysis was carried out using a Perkin Elmer 100 FT-IR spectrometer with a Specac variable temperature cell holder and Temperature Controller. The temperature was measured locally with a thermocouple embedded inside the solid cell frame. An Agilent Technologies 1260 Infinity system obtained gel permeation chromatography (GPC) analysis in HPLC-grade THF at a flow rate of 1.0 mL min^{-1}, calibration was achieved using a series of near monodisperse polystyrene standards, and samples were prepared at a concentration of 1 mg mL^{-1}. Differential scanning calorimetry measurements were performed on a TA Instruments DSC Q2000 adapted with a TA Refrigerated Cooling System 90, using aluminium TA Tzero pans and lids from -80 °C to 200 °C with a heating and cooling rate of 10 °C min^{-1}. Thermogravimetric analysis (TGA) was carried out on TA Instruments TGA Q50 instrument with aluminium Tzero pans. The sample was heated from 20 °C to 550 °C at 10 °C min^{-1} under nitrogen gas at a flow rate of 100 mL min^{-1}. Rheological measurements were performed on a Malvern Panalytical Kinexus Lab+ instrument fitted with a Peltier plate cartridge and 8 mm parallel plate geometry and analysed using rSpace Kinexus v1.76.2398 software. Tensile tests were carried out using a Thümler Z3-X1200 tensometer at a rate of 10 mm min^{-1} with a 1 KN load cell and THSSD-2019 software. The modulus of toughness was calculated by integrating the recorded plot to give the area under the curve. The trapezium rule was applied to calculate the area between zero strain to strain at break for each sample. The error reported is the standard deviation between the three repeats for each sample.

Small-angle X-ray scattering (SAXS) and Wide-angle X-ray scattering (WAXS) experiments were performed on beamline I22 at Diamond Light Source (Harwell, UK).[70] Samples were mounted in modified DSC pans in a Linkam 600 DSC stage for temperature control. SAXS data were collected with a Pilatus 2M detector, and WAXS data with a Pilatus P3-2M detector. SAXS data were reduced using the software DAWN.[71]

Crystals of **3.8**, **3.10**, **3.11**, **3.13** and **3.14** were mounted under Paratone-N oil and flash cooled to 100 K under nitrogen in an Oxford Cryosystems Cryostream. Single-crystal X-ray intensity data were collected using a Rigaku XtaLAB Synergy diffractometer (Cu Kα radiation (λ = 1.54184 Å)). The data were reduced within the CrysAlisPro software.[72] The structures were solved using the program Superflip,[73] and all non-hydrogen atoms were located. Least-squares refinement against *F* was carried out using the *CRYSTALS* suite of programs.[74] The non-hydrogen atoms were refined anisotropically. All the hydrogen atoms were located in difference Fourier maps. The positions of the hydrogen atoms attached to nitrogen were refined with a U_{iso} of ~1.2-1.5 times the value of U_{eq} of the parent N atom. The hydrogen atoms attached to carbon were placed geometrically with a C-H distance of 0.95 Å and a U_{iso} of ~1.2–1.5 times the value of U_{eq} of the parent C atom, and the positions refined with riding constraints.

The casting of the SPUs was performed as follows: the precipitated polymer was dissolved in a minimum volume of THF (approximately 3 mL per 1 g of polymer) at 40 °C whilst stirring. Once fully dissolved, the polymer solution was poured into a 15 cm × 15 cm mould with a PTFE base. The solvent was allowed to evaporate slowly over 24 hours at room temperature and pressure. The mould was placed into a vacuum oven at 60 °C for 24 hours, then under partial vacuum (approximately 800 mbar) at 60 °C for 24 hours. The polymer film was then allowed to reach room temperature before removal from the mould.

Synthesis

2,6-Dimethyl-3-nitroaniline (3.1). 2,6-Dimethyl-3-nitroaniline was synthesised according to the protocol described in Chapter 2, and the analytical data obtained are in accordance with those reported. 2,6-Dimethyl-3-nitroaniline was obtained as yellow crystals (11.4 g, 83%) from 2,6-xylidine (10.00 g, 82.52 mmol); Mp 79-80 °C (lit.[34] 81-82 °C); ^{1}H NMR (400 MHz, DMSO-d_6) δ 6.99 (d, J = 8.2 Hz, 1H, H_d), 6.93 (d, J = 8.2 Hz, 1H, H_c), 5.21 (s, 2H, H_a), 2.15 (s, 6H, H_b and H_e).

2,4,6-Trimethyl-3-nitroaniline (3.2). 2,4,6-Trimethylaniline was synthesised according to the protocol described by Harnying and co-workers.[35] 2,4,6-Trimethylaniline was obtained as yellow crystals (15.02 g, 94%) from 2,4,6-trimethylaniline (12.05 g, 89.12 mmol); Mp 65-67 °C (lit.[35] 73-74 °C); FTIR ATR (cm^{-1}): 3415 (νN-H), 3347 (νN-H), 3000 (νC-$H_{aromatic}$), 2932 (νC-H_{alkyl}), 2864 (νC-H_{alkyl}), 1635 (νN-H), 1510 (νN-$O_{asymmetric}$), 1357 (νN-$O_{symmetric}$); ^{1}H NMR (400 MHz, DMSO-d_6) δ 6.85 (s, 1H, H_d), 4.98 (s, 2H, H_a), 2.09 (s, 3H, H_e), 2.04 (s, 3H, H_c), 1.95 (s, 3H, H_b); ^{13}C NMR (100 MHz, DMSO-d_6) δ 150.7, 143.4, 129.5, 123.2, 114.1, 111.1, 17.8, 15.9, 12.4; FTMS (ESI) *m/z* [M + H$^+$] calculated for $C_9H_{13}O_2N_2$ = 181.0972, found = 181.0967.

4-Methyl-3-nitroaniline (**3.3**)

p-toluidine (15.05 g, 140.45 mmol, 1.0 equiv.) was dissolved in conc. H_2SO_4 (75 mL), conc. HNO_3 (9.8 mL, ρ = 1.4, 1.1 equiv.) was added dropwise, keeping the temperature below 0 °C.

The reaction mixture was stirred for 1 hour at 0 °C, poured over ice, and made basic (pH 10) with 6M NaOH solution without the reaction mixture's temperature exceeding 25 °C. The orange precipitate was collected, washed with water, and then recrystallised from ethanol to give dark orange crystals (19.06 g, 89%). Mp 78-79 °C (lit.[75] 78 °C); FTIR ATR (cm^{-1}): 3480 (νN-H), 3450 (νN-H), 3080 (νC-$H_{aromatic}$), 3065 (νC-$H_{aromatic}$), 2930 (νC-H_{alkyl}), 1625 (νN-H), 1517 (νN-$O_{asymmetric}$), 1346 (νN-$O_{symmetric}$); ^{1}H NMR (400 MHz, DMSO-d_6) δ 7.15 (d, J = 2.4 Hz, 1H, H_b), 7.09 (d, J = 8.3, 1H, H_d), 6.80 (dd, J = 8.2, 2.4 Hz, 1H, H_e), 5.53 (s, 2H, H_a), 2.31 (s, 3H, H_c); ^{13}C NMR (101 MHz, DMSO-d_6) δ 149.2, 147.9, 133.0, 119.0, 118.5, 108.2, 18.8; FTMS (ESI) *m/z* [M + H^+] calculated for $C_7H_9O_2N_2$ = 153.0659, found = 153.0658.

2,6-Dimethyl-4-nitroaniline (**3.4**) 2,6-dimethyl-4-nitroaniline was synthesised according to the protocol described in Chapter 2, and the analytical data are in accordance with those reported. 2,6-Dimethyl-4-nitroaniline was obtained as yellow crystals (4.20 g, 81%) from **3.3** (10.00 g, 31.21 mmol); Mp 161-162 °C (lit.[34] 162-163 °C); ^{1}H NMR (400 MHz, DMSO-d_6) δ 7.77 (s, 2H, H_c), 6.13 (s, 2H, H_a), 2.15 (s, 6H, H_b).

2,3,5,6-Tetramethyl-4-nitroaniline (**3.5**) 2,3,5,6-tetramethyl-4-nitroaniline was synthesised according to the protocol described by Ingham and Hampson.[36] 2,3,5,6-Tetramethyl-4-nitroaniline was obtained as an orange powder (2.68 g, 68 %) from **3.8** (5.00 g, 22.30 mmol); Mp 160-161 °C (lit.[51] 156-158 °C); FTIR ATR (cm^{-1}): 3479 (νN-H), 3398 (νN-H), 2995 (νC-$H_{aromatic}$), 2920 (νC-H_{alkyl}), 2868 (νC-H_{alkyl}), 1636 (νN-H), 1499 (νN-$O_{asymmetric}$), 1362 (νN-$O_{symmetric}$); ^{1}H NMR (400 MHz, DMSO-d_6) δ 5.11 (s, 2H, H_a), 2.04 (s, 6H, H_b), 2.03 (s, 6H, H_c); ^{13}C NMR (100 MHz, DMSO-d_6) δ 146.0, 143.8, 124.4, 117.1, 14.8, 13.5; FTMS (ESI) *m/z* [M + H^+] calculated for $C_{10}H_{15}O_2N_2$ = 195.1128, found = 195.1122.

***N*-(2,6-Dimethylphenyl)-4-methylbenzenesulfonamide** (**3.6**) 2,6-Dimethylaniline was synthesised according to the protocol described in chapter 2, and the analytical data obtained are in accordance with those reported. 2,6-Dimethylaniline was obtained as an off-white solid (30.10 g, 66%) from 2,6-xylidine (20.00 g, 165.04 mmol); Mp 133-135 °C (lit.[34] 135-137 °C); ^{1}H NMR (400 MHz, DMSO-d_6) δ 9.25 (s, 2H, H_f), 7.55 (AA'XX', 2H, H_e), 7.36 (AA'XX', 2H, H_f), 7.05 (dd, J 8.7, 6.0 Hz, 1H, H_d), 7.01-6.97 (m, 2H, H_c), 2.38 (s, 3H, H_g), 1.94 (6, s, H_b).

***N*-(2,6-Dimethyl-4-nitrophenyl)-4-methylbenzenesulfonamide** (**3.7**) was synthesised according to the protocol described in chapter 2, and the analytical data are in accordance with those reported. *N*-(2,6-Dimethyl-4-nitrophenyl)-4-methylbenzenesulfonamide was obtained as colourless crystals (16.8 g, 72%) from **3.6** (20.00 g, 72.63 mmol; Mp 166-168 °C (lit.[34] 165-167 °C); ^{1}H NMR (400 MHz, DMSO-d_6) δ 9.72 (s, 1H, H_a), 7.92 (s, 2H, H_c), 7.57 (AA'XX', 2H, H_d), 7.39 (AA'XX', 2H, H_e), 2.39 (s, 3H, H_f), 2.07 (s, 6H, H_b).

1,2,4,5-Tetramethyl-3,6-dinitrobenzene (**3.8**) 1,2,4,5-Tetramethylbenzene (10.0 g, 74.5 mmol) was dissolved in conc. H_2SO_4 (80 mL), conc. HNO_3 (4.0 mL, ρ = 1.4) was added

dropwise, keeping the temperature at – 10 °C. The reaction mixture was stirred for 3 hours, poured into ice water, and made basic (pH 10) with 6M NaOH solution without the temperature exceeding 25 °C. The yellow precipitate was collected and recrystallised from methanol to give colourless crystals (11.4 g, 83%); Mp 209-211 °C (lit.[76] 206-208 °C); FTIR ATR (cm^{-1}): 3000 ($\nu C\text{-}H_{aromatic}$), 2944 ($\nu C\text{-}H_{alkyl}$), 2898 ($\nu C\text{-}H_{alkyl}$), 1524 ($\nu N\text{-}O_{asymmetric}$), 1366 ($\nu N\text{-}O_{symmetric}$); ^{1}H NMR (400 MHz, $CDCl_3$) δ 2.19 (s, 12H, H_a); ^{13}C NMR (100 MHz, $CDCl_3$) δ 153.1, 127.0, 14.7.

General synthesis of low molecular weight ureas (**3.9**–**3.21**)

The aniline derivative (1 equiv.) was dissolved in distilled THF (10 mL), to which phenyl isocyanate (1 equiv.) was added dropwise at room temperature under an argon atmosphere. The progress of the reaction was monitored via IR spectroscopy, and once the isocyanate absorbance band at 2275-2250 cm^{-1} ($\nu N{=}C{=}O_{stretch}$) was not evident, the reaction was deemed to have reached completion. The solution was concentrated *in vacuo,* and the crude product was triturated using $CHCl_3$ and then dried under vacuum to afford the desired product.

1,3-Diphenylurea (**3.9**) was synthesised according to the general synthetic protocol described above for low molecular weight ureas, and the analytical data are in accord with those reported in the literature. 1,3-Diphenylurea was obtained as a colourless crystalline solid (10.85 g, 95 %) from aniline (5.01 g, 53.80 mmol); Mp 242-243 °C (lit.[77] 240-241 °C); ^{1}H NMR (400 MHz, DMSO-d_6) δ 8.65 (s, 2H, H_d), 7.45 (AA'MM'X, 4H, H_c), 7.28 (AA'MM'X, 4H, H_b), 6.96 (AA'MM'X, 2H, H_a).

1-(3-Nitrophenyl)-3-phenylurea (**3.10**) was synthesised according to the general synthetic protocol described above for low molecular weight ureas, and the analytical data are in accord with those reported in the literature. 1-(3-Nitrophenyl)-3-phenylurea was obtained as a cream solid (1.12 g, 79 %) from 3-nitroaniline (0.76 g, 5.50 mmol); Mp 209-210 °C (lit.[78] 209.3 °C); ^{1}H NMR (400 MHz, DMSO-d_6) δ 9.24 (s, 1H, H_e), 8.86 (s, 1H, H_f), 8.56 (t, J = 2.3 Hz, 1H, H_a), 7.82 (dt, J = 8.1, 2.3 Hz, 1H, H_d), 7.71 (dd, J = 8.1, 2.3 Hz, 1H, H_b), 7.57 (t, J = 8.1 Hz, 1H, H_c), 7.47 (AA'MM'X, 2H, H_g), 7.30 (AA'MM'X, 2H, H_h), 7.00 (AA'MM'X, 1H, H_i).

1-(4-Nitrophenyl)-3-phenylurea (**3.11**) was synthesised according to the general synthetic protocol described above for low molecular weight ureas, and the analytical data are in accord with those reported in the literature.[78] 1-(4-Nitrophenyl)-3-phenylurea was obtained as a light-brown solid (5.13 g, 92 %) from 4-nitroaniline (3.00 g, 27.72 mmol); Mp 222-223 °C (lit.[7877] 221.2 °C); ^{1}H NMR (400 MHz, DMSO-d_6) δ 9.42 (s, 1H, H_c), 8.91 (s, 1H, H_d), 8.19 (AA'XX', 2H, H_b), 7.69 (AA'XX', 2H, H_a), 7.48 (AA'MM'X, 2H, H_e), 7.31 (AA'MM'X, 2H, H_f), 7.02 (AA'MM'X, 1H, H_g).

1-Phenyl-3-(*o*-tolyl)urea (**3.12**) was synthesised according to the general synthetic protocol described above for low molecular weight ureas, and the analytical data are in accord with those reported in the literature. 1-Phenyl-3-(*o*-tolyl)urea was obtained as a colourless solid

(5.73 g, 25.32 mmol, 94 %) from *o*-toluidine (2.90 g, 27.06 mmol); Mp 203-205 °C (lit.[79] 203-205 °C); ^{1}H NMR (400 MHz, DMSO-d_6) δ 9.00 (s, 1H, H_g), 7.91 (s, 1H, H_f), 7.83 (dd, J = 8.1, 1.2 Hz, 1H, H_e), 7.46 (AA'MM'X, 2H, H_h), 7.28 (AA'MM'X, 2H, H_i), 7.19-7.11 (m, 2H, H_b + H_d), 6.99-6.91 (m, 2H, H_c + H_j), 2.24 (s, 3H, H_a).

1-(2-Methyl-3-nitrophenyl)-3-phenylurea (**3.13**) was synthesised according to the general synthetic protocol described above for low molecular weight ureas. 1-(2-Methyl-3-nitrophenyl)-3-phenylurea was obtained as a cream solid (1.52 g, 85 %) from 2-methyl-3-nitroaniline (1.00 g, 6.57 mmol); Mp 208-210 °C; FTIR ATR (cm^{-1}): 3279 (νN-H), 3187 (νN-H), 3089 (νC-$H_{aromatic}$), 3041 (νC-$H_{aromatic}$), 2945 (νC-H_{alkyl}), 1633 (νC=O_{urea}), 1521 (νN-$O_{asymmetic}$), 1312 (νN-$O_{symmetic}$); ^{1}H NMR (400 MHz, DMSO-d_6) δ 9.10 (s, 1H, H_f), 8.32 (s, 1H, H_e), 8.06 (dd, J = 8.1, 1.1 Hz, 1H, H_b), 7.55 (dd, J = 8.1, 1.1 Hz, 1H, H_d), 7.46 (AA'MM'X, 2H, H_g), 7.40 (t, J = 8.1 Hz, 1H, H_c), 7.29 (AA'MM'X, 2H, H_h), 6.99 (AA'MM'X, 1H, H_i), 2.29 (s, 3H, H_a); ^{13}C NMR (100 MHz, DMSO-d_6) δ 152.6, 151.1, 139.5, 139.2, 128.9, 126.7, 126.1, 122.5, 122.1, 118.3, 118.2, 13.5; FTMS (ESI) *m/z* [M + H$^+$] calculated for $C_{14}H_{14}O_3N_3$ = 272.1030, found = 272.1025.

1-(2-Methyl-4-nitrophenyl)-3-phenylurea (**3.14**) was synthesised according to the general synthetic protocol described above for low molecular weight ureas. 1-(2-Methyl-4-nitrophenyl)-3-phenylurea was obtained as a pale-yellow solid (1.68 g, 81 %) from 2-methyl-4-nitroaniline (1.16 g, 7.62 mmol); Mp 220-223 °C; FTIR ATR: 3351 (νN-H), 3275 (νN-H), 3140 (νC-$H_{aromatic}$), 3091 (νC-$H_{aromatic}$), 3036 (νC-$H_{aromatic}$), 1647 (νC=O_{urea}), 1533 (νN-$O_{asymmetic}$), 1315 (νN-$O_{symmetic}$); ^{1}H NMR (400 MHz, DMSO-d_6) δ 9.38 (s, 1H, H_f), 8.36 (d, J = 9.1 Hz, 1H, H_d and H_e), 8.10 (d, J = 2.8 Hz, 1H, H_b), 8.06 (dd, J = 9.1, 2.8 Hz, 1H, H_c), 7.48 (AA'MM'X, 2H, H_g), 7.32 (AA'MM'X, 2H, H_h), 7.02 (AA'MM'X, 1H, H_i), 2.36 (s, 3H, H_a); ^{13}C NMR (100 MHz, DMSO-d_6) δ 151.9, 144.5, 140.9, 139.1, 129.0, 126.6, 125.5, 122.6, 122.5, 118.4, 118.1, 17.8; FTMS (ESI) *m/z* [M + H$^+$] calculated for $C_{14}H_{14}O_3N_3$ = 272.1030, found = 272.1025.

1-(2-Methyl-5-nitrophenyl)-3-phenylurea (**3.15**) was synthesised according to the general synthetic protocol described above for low molecular weight ureas. 1-(2-Methyl-5-nitrophenyl)-3-phenylurea was obtained as a cream solid (1.37, 80 %) from 2-methyl-5-nitroaniline (0.96 g, 6.31 mmol); Mp 243-244 °C; FTIR ATR (cm^{-1}): 3308 (νN-H), 3278 (νN-H), 3104 (νC-$H_{aromatic}$), 3087 (νC-$H_{aromatic}$), 1642 (νC=O_{urea}), 1556 (νN-$O_{asymmetic}$), 1314 (νN-$O_{symmetic}$); ^{1}H NMR (400 MHz, DMSO-d_6) δ 9.25 (s, 1H, H_e), 8.95 (d, J = 2.4 Hz, 1H, H_d), 8.27 (s, 1H, H_f), 7.80 (dd, J = 8.4, 2.4 Hz, 1H, H_c), 7.52 – 7.43 (m, 3H, H_b + H_g), 7.31 (AA'MM'X, 2H, H_h), 7.01 (AA'MM'X, 1H, H_i), 2.37 (s, 3H, H_a); ^{13}C NMR (100 MHz, DMSO-d_6) δ 152.4, 146.1, 139.3, 138.6, 134.4, 131.1, 128.9, 122.2, 118.3, 116.6, 113.5, 18.1; FTMS (ESI) *m/z* [M + H$^+$] calculated for $C_{14}H_{14}O_3N_3$ = 272.1030, found = 272.1025.

1-(4-Methyl-3-nitrophenyl)-3-phenylurea (**3.16**)

1-(4-methyl-3-nitrophenyl)-3-phenylurea was synthesised according to the general procedure described above for low molecular weight ureas. 1-(4-Methyl-3-nitrophenyl)-3-phenylurea was

obtained as a pale-yellow solid (3.12 g, 88 %) from **3** (2.00 g, 13.14 mmol); Mp 215-216 °C (lit.[80] 218-219 °C); FTIR ATR (cm^{-1}): 3292 (νN-H), 3275 (νN-H), 3073 (νC-$H_{aromatic}$), 2985 (νC-H_{alkyl}), 1620 (νC=O_{urea}), 1557 (νN-$O_{asymmetic}$), 1349 (νN-$O_{symmetic}$); ^{1}H NMR (400 MHz, DMSO-d_6) δ 9.03 (s, 1H, H_e), 8.77 (s, 1H, H_f), 8.29 (d, *J* = 2.3 Hz, 1H, H_a), 7.55 (dd, *J* = 8.3, 2.3 Hz, 1H, H_d), 7.46 (AA'XX'M, 2H, H_g), 7.39 (d, *J* = 8.3, 1H, H_c), 7.29 (AA'XX'M, 2H, H_h), 6.99 (AA'XX'M, 1H, H_i), 2.45 (s, 3H, H_b); ^{13}C NMR (101 MHz, DMSO-d_6) δ 152.5, 148.8, 139.3, 138.8, 133.0, 128.8, 125.5, 122.92, 122.2, 118.5, 113.2, 19.0; FTMS (ESI) m/z [M + H] calculated for $C_{14}H_{14}O_3N_3$ = 272.1030, found = 272.1026.

1-(2,6-Dimethylphenyl)-3-phenylurea (**3.17**) was synthesised according to the general synthetic protocol described above for low molecular weight ureas, and the analytical data are in accord with those reported in the literature.[79] 1-(2,6-Dimethylphenyl)-3-phenylurea was obtained as a crystalline solid (8.52 g, 89 %) from 2,6-xylidine (4.82 g, 39.72 mmol); Mp 235-236 °C (lit.[79] 245-247 °C); ^{1}H NMR (400 MHz, DMSO-d_6) δ 8.73 (s, 1H, H_e), 7.71 (s, 1H, H_d), 7.44 (AA'MM'X, 2H, H_f), 7.24 (AA'MM'X, 2H, H_g), 7.10 – 7.02 (m, 3H, H_b + H_c), 6.92 (AA'MM'X, 1H, H_h), 2.20 (s, 6H, H_a).

1-(2,6-Dimethyl-3-nitrophenyl)-3-phenylurea (**3.18**) was synthesised according to the general synthetic protocol described above for low molecular weight ureas. 1-(2,6-dimethyl-3-nitrophenyl)-3-phenylurea was obtained as a pale-orange solid (3.58 g, 88 %) from **3.1** (2.36 g, 14.20 mmol); Mp 233-235 °C; FTIR ATR (cm^{-1}): 3288 (νN-H), 3102 (νC-$H_{aromatic}$), 3040 (νC-$H_{aromatic}$), 2984 (νC-H_{alkyl}), 1635 (νC=O_{urea}), 1558 (νN-$O_{asymmetic}$), 1340 (νN-$O_{symmetic}$); ^{1}H NMR (400 MHz, DMSO-d_6) δ 8.91 (s, 1H, H_f), 8.05 (s, 1H, H_e), 7.74 (d, *J* = 8.3 Hz, 1H, H_b), 7.45 (AA'MM'X, 2H, H_b), 7.34 (d, *J* = 8.3 Hz, 1H, H_c), 7.26 (AA'MM'X, 2H, H_h), 6.95 (AA'MM'X, 1H, H_i), 2.32 (s, 3H, H_a), 2.30 (s, 3H, H_d); ^{13}C NMR (100 MHz, DMSO-d_6) δ 153.0, 148.7, 141.9, 134.0, 137.3, 130.5, 128.8, 128.1, 121.8, 121.7, 118.2, 18.8, 14.5; FTMS (ESI) *m/z* [M + H^+] calculated for $C_{15}H_{16}O_3N_3$ = 286.1186, found = 286.1182.

1-(2,6-Dimethyl-4-nitrophenyl)-3-phenylurea (**3.19**)

1-(2,6-Dimethyl-4-nitrophenyl)-3-phenylurea was synthesised according to the general synthetic protocol described above for low molecular weight ureas. 1-(2,6-dimethyl-4-nitrophenyl)-3-phenylurea was obtained as a colourless solid (1.14 g, 89 %) from **3.4** (0.75 g, 4.51 mmol); Mp 276-278 °C; FTIR ATR (cm^{-1}): 3301 (νN-H), 3265 (νN-H), 3088 (νC-$H_{aromatic}$), 3040 (νC-$H_{aromatic}$), 2936 (νC-H_{alkyl}), 1637 (νC=O_{urea}), 1551 (νN-$O_{asymmetic}$), 1345 (νN-$O_{symmetic}$); ^{1}H NMR (400 MHz, DMSO-d_6) δ 8.89 (s, 1H, H_d), 8.17 (s, 1H, H_c), 8.00 (s, 2H, H_b), 7.45 (AA'MM'X, 2H, H_e), 7.27 (AA'MM'X, 2H, H_f), 6.96 (AA'MM'X, 1H, H_g), 2.33 (s, 6H, H_a); ^{13}C NMR (100 MHz, DMSO-d_6) δ 152.2, 144.4, 142.3, 139.8, 136.6, 128.8, 122.6, 121.8, 118.1, 18.5; FTMS (ESI) *m/z* [M + H^+] calculated for $C_{15}H_{16}O_3N_3$ = 286.1186, found = 286.1183.

1-Phenyl-3-(2,4,6-trimethyl-3-nitrophenyl)urea (**3.20**)

1-Phenyl-3-(2,4,6-trimethyl-3-nitrophenyl)urea was synthesised according to the general synthetic protocol described above for low molecular weight ureas. 1-Phenyl-3-(2,4,6-trimethyl-3-nitrophenyl)urea was obtained as a colourless fibrous solid (0.67 g, 54 %) from **3.5** (0.75 g, 4.16 mmol); Mp 122-124 °C; FTIR ATR (cm^{-1}): 3306 (νN-H), 3275 (νN-H), 3168 (νC-$H_{aromatic}$), 2929 (νC-H_{alkyl}), 1628 (νC=O_{urea}), 1558 (νN-$O_{asymmetic}$), 1362 (νN-$O_{symmetic}$); ^{1}H NMR (400 MHz, DMSO-d_6) δ 8.86 (s, 1H, H_f), 7.93 (s, 1H, H_e), 7.44 (AA'MM'X, 2H, H_g), 7.25 (AA'MM'X, 2H, H_h), 7.20 (s, 1H, H_c), 6.94 (AA'MM'X, 1H, H_i), 2.23 (s, 3H, H_b), 2.22 (s, 3H, H_d), 2.10 (s, 3H, H_a); ^{13}C NMR (100 MHz, DMSO-d_6) δ 153.0, 150.1, 140.0, 138.7, 134.5, 130.0, 128.7, 127.2, 126.1, 121.7, 118.1, 18.2, 16.5, 13.3; FTMS (ESI) *m/z* [M + H^+] calculated for $C_{16}H_{18}O_3N_3$ = 300.1343, found = 300.1338.

1-Phenyl-3-(2,3,5,6-tetramethyl-4-nitrophenyl)urea (**3.21**)

1-Phenyl-3-(2,3,5,6-tetramethyl-4-nitrophenyl)urea was synthesised according to the general synthetic protocol described above for low molecular weight ureas. 1-Phenyl-3-(2,3,5,6-tetramethyl-4-nitrophenyl)urea was obtained as a pale-yellow solid (0.92 g, 70 %) from **3.7** (0.81 g, 4.17 mmol); Mp 281-282 °C; FTIR ATR (cm^{-1}): 3300 (νN-H), 3276 (νN-H), 3030 (νC-$H_{aromatic}$), 2927 (νC-H_{alkyl}), 1637 (νC=O_{urea}), 1558 (νN-$O_{asymmetic}$), 1375 (νN-$O_{symmetic}$); ^{1}H NMR (400 MHz, DMSO-d_6) δ 8.84 (s, 1H, H_d), 8.01 (s, 1H, H_c), 7.44 (AA'MM'X, 2H, H_e), 7.25 (AA'MM'X, 2H, H_f), 6.94 (AA'MM'X, 1H, H_g), 2.17 (s, 6H, H_a), 2.10 (s, 6H, H_b); ^{13}C NMR (100 MHz, DMSO-d_6) δ 153.2, 150.8, 140.1, 136.6, 134.1, 128.7, 124.0, 121.6, 118.0, 15.1, 14.5; FTMS (ESI) *m/z* [M + H^+] calculated for $C_{17}H_{20}O_3N_3$ = 314.1499, found = 314.1494.

General synthetic protocol for SPUs (**SPU1**- **SPU12**)

Hydrogenated poly(butadiene) (Krasol HLBH-P 2000), molecular weight as supplied (M_n = 2100 g/mol), was dried under vacuum at 80 °C for 2 hours. In the bulk, Krasol HLBH-P 2000 (1.0 equiv.) was mixed with 4,4'-methylenebis(phenyl isocyanate) (4,4'-MDI) (2.05 equiv.) at 80 °C under argon for 3 hours with gentle stirring. The colourless pre-polymer obtained was dissolved in dry THF (40 mL), and the aniline derivative (2.05 equiv.) was then added to the solution, which was then brought to and maintained under reflux for 3 hours under argon. The supramolecular polymer solution was precipitated into ice-cold methanol (3 × 1000 mL), and the solid material was filtered off and then dried *in vacuo*.

SPU1

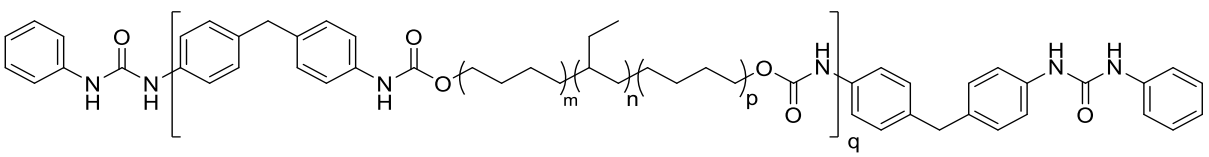

The synthesis was carried out according to the general synthetic protocol described above for the SPUs. The polymer was isolated as a powdery colourless opaque solid (11.88 g, 88 %)

from Krasol HLBH-P 2000 (10.11 g, 4.81 mmol); T_g = -45.7 °C, T_m = 123.8 °C; FTIR ATR (cm^{-1}): 3320 (νN-$H_{stretch}$), 2955 (νC-$H_{aromatic}$), 2920 (νC-H_{alkyl}), 2850 (νC-H_{alkyl}), 1740 (νC=$O_{urethane}$), 1710 (νC=$O_{urethane}$), 1645 (νC=O_{urea}), 1610 (νC=O_{urea}), 1230 (νC-$N_{stretch}$); ^{1}H NMR (400 MHz, THF-d_8) δ 8.54 (s, 3H), 7.77 (d, J = 6.4 Hz, 4H), 7.46 (AA'MM'X, 4H), 7.37 (AA'XX', 11H), 7.18 (AA'MM'X, 4H), 7.03 (AA'XX', 11H), 6.88 (AA'MM'X, 2H), 4.17 – 4.02 (m, 8H), 3.83 (s, 6H), 2.10 – 1.82 (m, 10H), 1.68 – 0.64 (m, 644H); ^{13}C NMR (100 MHz, THF-d_8) δ 154.5, 153.2, 141.5, 139.3, 138.8, 136.5, 136.1, 129.9, 129.9, 129.5, 122.5, 119.3, 119.1, 65.22, 63.6, 41.5, 40.3, 40.1, 39.7, 39.5, 39.0, 37.4, 34.6, 34.4, 31.8, 31.3, 30.9, 30.3, 27.9, 27.7, 27.5, 27.1, 26.9, 11.4, 11.2, 11.1, 11.0; GPC (THF) M_n = 8500 g mol^{-1}, M_w = 12600 g mol^{-1}, Đ = 1.49.

SPU2

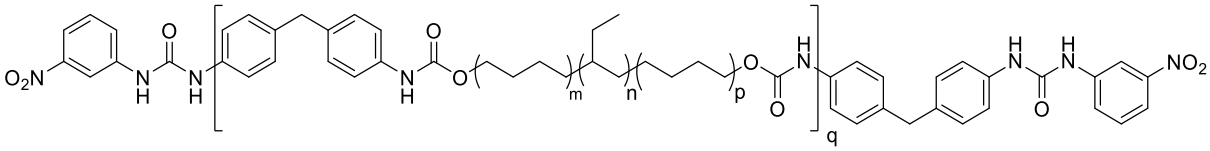

The synthesis was carried out according to the general synthetic protocol described above for the SPUs. The polymer was isolated as an transparent yellow elastomeric solid (12.62 g, 98 %) from Krasol HLBH-P 2000 (9.34 g, 4.44 mmol); T_g = -45.6 °C, T_m = 45.9 °C; FTIR ATR (cm^{-1}): 3337 (νN-$H_{stretch}$), 2962 (νC-H_{alkyl}), 2923 (νC-H_{alkyl}), 2875 (νC-H_{alkyl}), 2854 (νC-H_{alkyl}), 1739 (νC=$O_{urethane}$), 1708 (νC=$O_{urethane}$), 1600 (νC=O_{urea}), 1534 (νN-$O_{stretch}$); ^{1}H NMR (400 MHz, THF-d_8) δ 8.64 – 8.47 (m, 22H), 8.39 (t, J = 2.2 Hz, 2H), 8.32 (s, 2H), 7.89 (dd, J = 8.1, 2.2 Hz, 2H), 7.78 (dd, J = 8.1, 2.2 Hz, 2H), 7.48 – 7.29 (m, 53H), 7.11 – 6.99 (m, 48H), 4.19 – 4.02 (m, 34H), 3.85 (s, 5H), 3.65 (s, 18H), 2.10 – 1.87 (m, 42H), 1.69 – 0.77 (m, 2908H); ^{13}C NMR (100 MHz, THF-d_8) δ 154.7, 154.4, 138.7, 138.6, 136.4, 136.3, 130.3, 129.9, 129.8, 129.8, 119.5, 118.9, 116.9, 113.3, 65.1, 63.4, 51.8, 41.3, 40.0, 39.5, 39.4, 38.9, 37.2, 34.5, 34.2, 31.6, 31.2, 30.8, 30.2, 27.7, 27.6, 27.4, 27.0, 26.8, 11.3, 11.10, 11.0, 10.8, 10.7; GPC (THF) M_n = 8400 g mol^{-1}, M_w = 13500 g mol^{-1}, Đ = 1.61.

SPU3

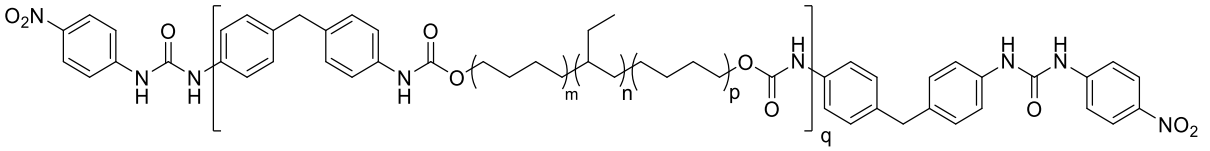

The synthesis was carried out according to the general synthetic protocol described above for the SPUs. The polymer was isolated as a transparent yellow elastomeric solid (14.41 g, 91 %) from Krasol HLBH-P 2000 (11.48 g, 5.47 mmol); T_g = -46.1 °C, T_m = 49.9 °C; FTIR ATR (cm^{-1}): 3335 (νN-$H_{stretch}$), 2962 (νC-H_{alkyl}), 2922 (νC-H_{alkyl}), 2874 (νC-H_{alkyl}), 2854 (νC-H_{alkyl}), 1738 (νC=$O_{urethane}$), 1700 (νC=$O_{urethane}$), 1601 (νC=O_{urea}), 1535 (νN-$O_{stretch}$); ^{1}H NMR (400 MHz, THF-d_8) δ 8.65 – 8.47 (m, 10H), 7.37 (AA'XX', 21H), 7.26 – 7.13 (m, 2H), 7.04 (AA'XX', 21H), 5.45 – 4.63 (m, 5H), 4.22 – 4.04 (m, 14H), 3.83 (s, 11H), 3.65 (s, 10H), 2.14 – 1.84 (m, 18H), 1.69

– 0.77 (m, 1232H); ^{13}C NMR (100 MHz, THF-d_8) δ 154.7, 154.4, 138.7, 138.6, 136.4, 136.3, 129.8, 118.9, 65.1, 63.4, 51.8, 41.3, 40.2, 40.0, 39.5, 39.4, 38.9, 37.2, 34.5, 34.2, 31.6, 31.2, 30.8, 30.2, 27.7, 27.6, 27.4, 27.2, 27.0, 26.8, 11.3, 11.1, 11.1, 11.0, 11.0, 10.9; GPC (THF) M_n = 8100 g mol^{-1}, M_w = 12400 g mol^{-1}, Đ = 1.53.

SPU4

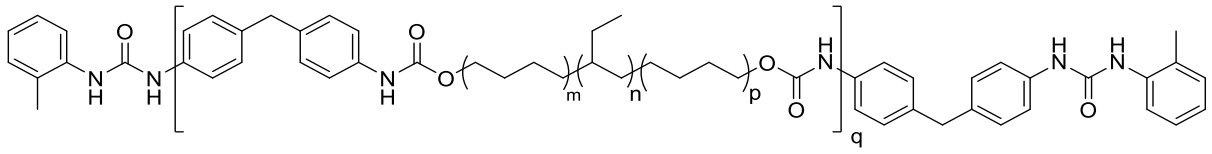

The synthesis was carried out according to the general synthetic protocol described above for the SPUs. The polymer was isolated as a powdery colourless opaque solid (10.44 g, 93 %) from Krasol HLBH-P 2000 (8.31 g, 3.96 mmol); T_g = -44.5 °C, T_m = 113.6 °C; FTIR ATR (cm^{-1}): 2990 (νC-H$_{aromatic}$), 2962 (νC-H$_{alkyl}$), 2923 (νC-H$_{alkyl}$), 2854 (νC-H$_{alkyl}$), 1738 (νC=O$_{urethane}$), 1712 (νC=O$_{urethane}$), 1638 (νC=O$_{urea}$), 1608 (νC=O$_{urea}$), 1590 (νN-O$_{stretch}$); ^{1}H NMR (400 MHz, THF-d_8) δ 8.64 – 8.46 (m, 4H), 8.14 (s, 2H), 8.00 (d, J = 8.1 Hz, 2H), 7.47 – 7.31 (m, 12H), 7.24 (s, 2H), 7.13 – 7.00 (m, 17H), 6.86 (t, J = 7.4 Hz, 2H), 4.18 – 4.01 (m, 8H), 3.83 (s, 6H), 3.65 (s, 1H), 2.23 (s, 7H), 2.10 – 1.83 (m, 10H), 1.68 – 0.65 (m, 671H); ^{13}C NMR (100 MHz, THF-d_8) δ 154.4, 153.2, 139.4, 139.0, 138.7, 136.4, 136.3, 135.8, 130.7, 129.8, 129.8, 127.6, 127.1, 123.2, 121.8, 119.1, 118.9, 65.1, 63.4, 41.3, 40.2, 40.0, 39.5, 39.4, 38.9, 37.2, 34.5, 34.2, 31.6, 31.2, 30.8, 30.2, 27.74, 27.6, 27.4, 27.1, 27.0, 26.8, 18.0, 11.31, 11.14, 11.10, 11.01, 10.82, 10.69; GPC (THF) M_n = 6800 g mol^{-1}, M_w = 9800 g mol^{-1}, Đ = 1.44.

SPU5

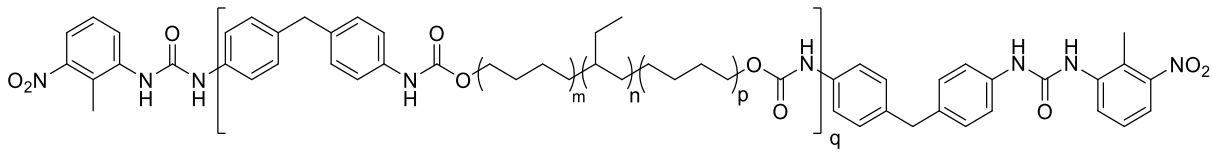

The synthesis was carried out according to the general synthetic protocol described above for the SPUs. The polymer was isolated as an transparent yellow elastomeric solid (19.73 g, 92 %) from Krasol HLBH-P 2000 (15.37 g, 7.32 mmol); T_g = -45.0 °C; FTIR ATR (cm^{-1}): 3317 (νN-H$_{stretch}$), 2962 (νC-H$_{alkyl}$), 2922 (νC-H$_{alkyl}$), 2874 (νC-H$_{alkyl}$), 2854 (νC-H$_{alkyl}$), 1739 (νC=O$_{urethane}$), 1715 (νC=O$_{urethane}$), 1640 (νC=O$_{urea}$), 1597 (νC=O$_{urea}$), 1558 (νN-O$_{stretch}$), 1527 (νN-O$_{stretch}$); ^{1}H NMR (400 MHz, THF-d_8) δ 8.59 – 8.50 (m, 10H), 8.36 – 8.13 (m, 5H), 7.67 – 7.61 (m, 5H), 7.48 (d, J = 8.0 Hz, 2H), 7.45 – 7.24 (m, 56H), 7.10 – 7.00 (m, 37H), 6.91 (s, 2H), 4.18 – 4.04 (m, 23H), 4.01 – 3.91 (m, 3H), 3.83 (d, J = 5.7 Hz, 18H), 2.87 (s, 60H), 2.35 (s, 8H), 2.31 (s, 20H), 2.20 (s, 3H), 2.13 – 1.85 (m, 25H), 1.69 – 0.63 (m, 1944H); ^{13}C NMR (100 MHz, THF-d_8) δ 154.4, 152.5, 140.9, 140.4, 138.9, 138.7, 136.4, 136.3, 129.9, 129.8, 127.3, 127.2, 126.7, 125.9, 119.3, 119.2, 118.9, 118.5, 41.3, 40.0, 39.4, 38.9, 37.2, 35.1, 34.5,

34.2, 31.6, 31.2, 30.8, 30.8, 30.2, 27.7, 27.6, 27.4, 27.0, 26.8, 13.5, 13.3, 12.8, 11.3, 11.1, 11.0, 10.8; GPC (THF) M_n = 12300 g mol^{-1}, M_w = 26500 g mol^{-1}, Đ = 2.14.

SPU6

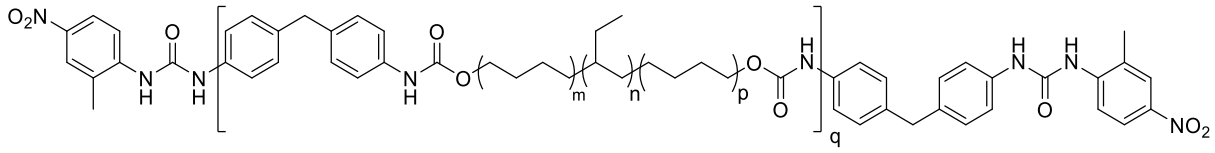

The synthesis was carried out according to the general synthetic protocol described above for the SPUs. The polymer was isolated as a transparent yellow elastomeric solid (14.15 g, 93 %) from Krasol HLBH-P 2000 (10.92 g, 5.20 mmol); T_g = -46.1 °C, T_m = 48.0 °C; FTIR ATR (cm^{-1}): 3341 (νN-H$_{stretch}$), 2962 (νC-H$_{alkyl}$), 2923 (νC-H$_{alkyl}$), 2875 (νC-H$_{alkyl}$), 2854 (νC-H$_{alkyl}$), 1740 (νC=O$_{urethane}$), 1707 (νC=O$_{urethane}$), 1601 (νC=O$_{urea}$), 1537 (νN-O$_{stretch}$); ^{1}H NMR (400 MHz, THF-d_8) δ 8.59 (s, 4H), 8.56 – 8.50 (m, 8H), 7.72 (s, 1H), 7.46 – 7.25 (m, 28H), 7.26 – 7.13 (m, 1H), 7.12 – 6.99 (m, 29H), 5.43 – 4.70 (m, 7H), 4.20 – 4.02 (m, 18H), 3.83 (s, 14H), 3.65 (s, 13H), 2.11 – 1.85 (m, 22H), 1.69 – 0.63 (m, 1482H); ^{13}C NMR (100 MHz, THF-d_8) δ 154.7, 154.4, 138.7, 138.6, 136.4, 136.3, 129.8, 129.8, 119.1, 118.9, 65.1, 63.4, 51.8, 41.3, 34.0, 39.5, 39.4, 38.9, 37.2, 34.5, 34.2, 31.6, 31.2, 31.0, 30.8, 30.2, 27.7, 27.6, 27.4, 27.2, 27.0, 26.8, 11.3, 11.1, 11.1, 11.0, 10.9, 10.7; GPC (THF) M_n = 7700 g mol^{-1}, M_w = 11900 g mol^{-1}, Đ = 1.55.

SPU7

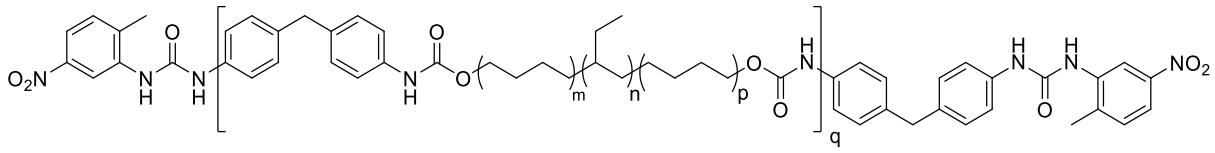

The synthesis was carried out according to the general synthetic protocol described above for the SPUs. The polymer was isolated as an transparent yellow elastomeric solid (14.62 g, 96 %) from Krasol HLBH-P 2000 (10.95 g, 5.21 mmol); T_g = -45.7 °C, T_m = 46.4 °C; FTIR ATR (cm^{-1}): 3337 (νN-H$_{stretch}$), 2962 (νC-H$_{alkyl}$), 2923 (νC-H$_{alkyl}$), 2875 (νC-H$_{alkyl}$), 2855 (νC-H$_{alkyl}$), 1739 (νC=O$_{urethane}$), 1707 (νC=O$_{urethane}$), 1599 (νC=O$_{urea}$), 1536 (νN-O$_{stretch}$); ^{1}H NMR (400 MHz, THF-d_8) δ 9.11 (d, J = 2.4 Hz, 1H), 8.73 – 8.46 (m, 27H), 8.38 (s, 1H), 7.86 – 7.66 (m, 2H), 7.60 (s, 2H), 7.46 – 7.27 (m, 62H), 7.12 – 6.97 (m, 58H), 4.19 – 4.02 (m, 40H), 3.83 (s, 28H), 3.65 (s, 27H), 2.34 (s, 3H), 2.11 – 1.86 (m, 48H), 1.69 – 0.66 (m, 3348H); ^{13}C NMR (100 MHz, THF-d_8) δ 154.7, 154.4, 138.7, 138.6, 136.4, 136.3, 129.9, 129.8, 129.8, 119.2, 118.9, 65.1, 63.4, 51.8, 41.3, 40.0, 39.5, 39.4, 38.9, 37.2, 36.9, 34.5, 34.2, 31.6, 31.2, 30.8, 30.2, 27.7, 27.6, 27.4, 27.0, 26.8, 11.3, 11.1, 11.0, 10.8, 10.7; GPC (THF) M_n = 7900 g mol^{-1}, M_w = 12400 g mol^{-1}, Đ = 1.57.

SPU8

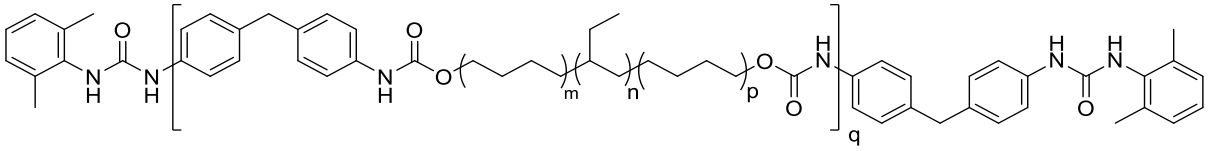

The synthesis was carried out according to the general synthetic protocol described above for the SPUs. The polymer was isolated as a powdery colourless opaque solid (11.81 g, 91 %) from Krasol HLBH-P 2000 (9.52 g, 4.53 mmol); T_g = -46.3 °C; FTIR ATR (cm^{-1}): 3303 (νN-$H_{stretch}$), 2962 (νC-H_{alkyl}), 2922 (νC-H_{alkyl}), 2853 (νC-H_{alkyl}), 1738 (νC=$O_{urethane}$), 1712 (νC=$O_{urethane}$), 1640 (νC=O_{urea}), 1596 (νN-$O_{stretch}$); ^{1}H NMR (400 MHz, THF-d_8) δ 8.61 – 8.47 (m, 4H), 7.69 (s, 2H), 7.36 (AA'XX', 13H), 7.19 – 6.87 (m, 21H), 5.44 – 4.67 (m, 3H), 4.18 – 4.02 (m, 9H), 3.86 – 3.78 (m, 7H), 2.25 (s, 12H), 2.10 – 1.87 (m, 11H), 1.69 – 0.65 (m, 717H); ^{13}C NMR (100 MHz, THF-d_8) δ 154.4, 153.8, 139.6, 138.7, 136.8, 136.6, 136.3, 135.6, 129.8, 129.8, 129.7, 128.7, 126.9, 119.1, 118.9, 65.1, 63.4, 41.3, 40.0, 39.4, 38.9, 37.2, 34.5, 34.2, 31.6, 31.2, 30.8, 27.7, 27.6, 27.4, 27.0, 26.8, 18.8, 11.3, 11.1, 11.0, 10.8; GPC (THF) M_n = 7500 g mol^{-1}, M_w = 11300 g mol^{-1}, Đ = 1.50.

SPU9

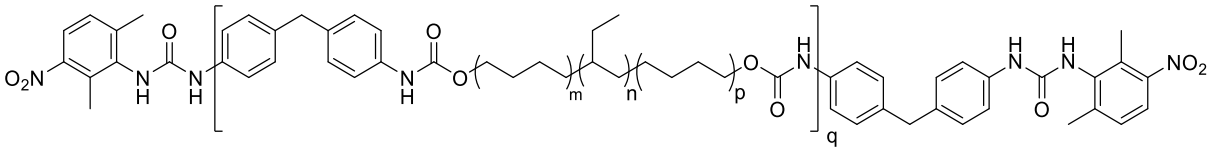

The synthesis was carried out according to the general synthetic protocol described above for the SPUs. The polymer was isolated as a transparent yellow elastomeric solid (16.81 g, 93 %) from Krasol HLBH-P 2000 (12.98 g, 6.18 mmol); T_g = -45.3 °C; FTIR ATR (cm^{-1}): 3337 (νN-$H_{stretch}$), 2961 (νC-H_{alkyl}), 2922 (νC-H_{alkyl}), 2874 (νC-H_{alkyl}), 2854 (νC-H_{alkyl}), 1740 (νC=$O_{urethane}$), 1707 (νC=$O_{urethane}$), 1600 (νC=O_{urea}), 1534 (νN-$O_{stretch}$); ^{1}H NMR (400 MHz, THF-d_8) δ 8.62 – 8.47 (m, 15H), 8.00 (s, 5H), 7.93 (d, J = 8.4 Hz, 2H), 7.66 (d, J = 8.3 Hz, 5H), 7.45 – 7.25 (m, 57H), 7.22 (d, J = 8.4 Hz, 5H), 7.09 (d, J = 8.2 Hz, 7H), 7.03 (AA'XX', 42H), 4.18 – 4.02 (m, 31H), 3.87 – 3.80 (m, 27H), 2.44 (s, 4H), 2.40 (s, 15H), 2.34 (s, 20H), 2.11 – 1.83 (m, 38H), 1.69 – 0.65 (m, 2376H); ^{13}C NMR (100 MHz, THF-d_8) δ 154.4, 150.3, 142.8, 139.2, 138.7, 138.5, 136.3, 131.9, 129.8, 129.8, 129.8, 128.6, 122.6, 119.3, 118.9, 65.1, 63.4, 41.3, 40.0, 39.4, 38.9, 37.2, 34.5, 34.2, 31.6, 31.2, 30.8, 30.2, 27.7, 27.6, 27.4, 27.0, 26.8, 19.2, 15.0, 11.3, 11.1, 11.0; GPC (THF) M_n = 10900 g mol^{-1}, M_w = 21900 g mol^{-1}, Đ = 2.01.

SPU10

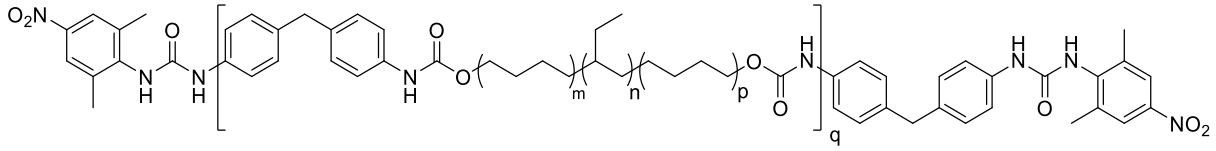

The synthesis was carried out according to the general synthetic protocol described above for the SPUs. The polymer was isolated as an orange transparent solid (12.49 g, 89 %) from Krasol HLBH-P 2000 (9.97 g, 4.74 mmol); T_g = -44.9 °C, T_m = 45.4 °C; FTIR ATR (cm^{-1}): 3329 (νN-$H_{stretch}$), 2961 (νC-H_{alkyl}), 2919 (νC-H_{alkyl}), 2875 (νC-H_{alkyl}), 2854 (νC-H_{alkyl}), 1738 (νC=$O_{urethane}$), 1709 (νC=$O_{urethane}$), 1646 (νC=O_{urea}), 1599 (νC=O_{urea}), 1535 (νN-$O_{stretch}$); ^{1}H NMR (400 MHz, THF-d_8) δ 8.60 (s, 4H), 8.57 – 8.50 (m, 8H), 7.73 (s, 3H), 7.47 – 7.26 (m, 32H), 7.17 – 6.98 (m, 34H), 5.44 – 4.70 (m, 7H), 4.20 – 4.03 (m, 19H), 4.00 – 3.91 (m, 1H), 3.83 (s, 16H), 3.65 (s, 13H), 2.12 – 1.85 (m, 20H), 1.69 – 0.78 (m, 1581H); ^{13}C NMR (100 MHz, THF-d_8) δ 154.7, 154.4, 139.3, 138.7, 138.6, 136.4, 136.3, 135.8, 129.8, 129.8, 119.1, 118.9, 65.1, 63.4, 51.8, 41.3, 40.2, 40.0, 39.4, 38.9, 37.2, 34.5, 34.2, 31.6, 31.2, 31.0, 30.8, 30.2, 27.7, 27.6, 27.4, 27.2, 27.0, 26.8, 11.3, 11.1, 11.0, 10.8; GPC (THF) M_n = 8800 g mol^{-1}, M_w = 14700 g mol^{-1}, Đ = 1.68.

SPU11

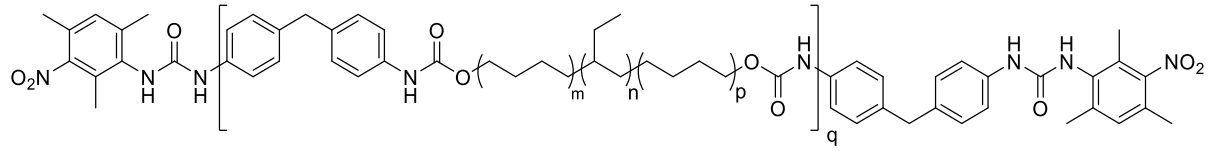

The synthesis was carried out according to the general synthetic protocol described above for the SPUs. The polymer was isolated as a waxy yellow transparent solid (13.02 g, 89 %) from Krasol HLBH-P 2000 (10.25 g, 4.88 mmol); T_g = -45.9 °C; FTIR ATR (cm^{-1}): 3289 (νN-$H_{stretch}$), 2962 (νC-H_{alkyl}), 2923 (νC-H_{alkyl}), 2876 (νC-H_{alkyl}), 2855 (νC-H_{alkyl}), 1741 (νC=$O_{urethane}$), 1714 (νC=$O_{urethane}$), 1639 (νC=O_{urea}), 1599 (νC=O_{urea}), 1526 (νN-$O_{stretch}$); ^{1}H NMR (400 MHz, THF-d_8) δ 8.63 – 8.46 (m, 12H), 7.93 (s, 7H), 7.47 – 7.28 (m, 48H), 7.25 (s, 1H), 7.18 (s, 7H), 7.09 (d, J = 7.9 Hz, 4H), 7.07 – 6.96 (m, 49H), 4.17 – 4.03 (m, 28H), 3.87 – 3.80 (m, 23H), 2.33 – 2.13 (m, 76H), 2.08 – 1.87 (m, 29H), 1.69 – 0.77 (m, 2410H); ^{13}C NMR (100 MHz, THF-d_8) δ 154.4, 153.6, 151.9, 139.5, 138.7, 136.4, 136.1, 135.7, 130.8, 129.8, 129.8, 128.5, 127.4, 119.3, 118.9, 65.1, 63.4, 41.3, 40.0, 39.4, 38.9, 37.2, 34.5, 34.2, 31.6, 31.2, 30.8, 30.2, 27.7, 27.6, 27.4, 27.0, 26.8, 18.7, 17.1, 13.7, 11.3, 11.1, 11.0; GPC (THF) M_n = 9600 g mol^{-1}, M_w = 16000 g mol^{-1}, Đ = 1.67.

SPU12

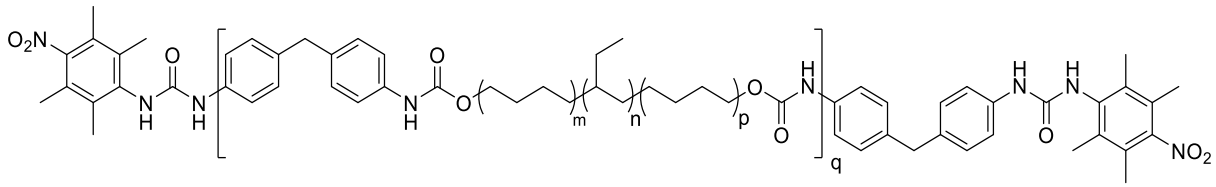

The synthesis was carried out according to the general synthetic protocol described above for the SPUs. The polymer was isolated as a waxy yellow translucent solid (14.03 g, 96 %) from Krasol HLBH-P 2000 (9.84 g, 4.69 mmol); T_g = -44.6 °C; FTIR ATR (cm^{-1}): 3308 (νN-$H_{stretch}$), 2962 (νC-H_{alkyl}), 2920 (νC-H_{alkyl}), 2875 (νC-H_{alkyl}), 2854 (νC-H_{alkyl}), 1738 (νC=$O_{urethane}$), 1705 (νC=$O_{urethane}$), 1639 (νC=O_{urea}), 1600 (νC=O_{urea}), 1528 (νN-$O_{stretch}$); ^{1}H NMR (400 MHz, THF-d_8) δ 8.60 (s, 1H), 8.58 – 8.47 (m, 8H), 7.95 – 7.51 (m, 4H), 7.45 – 7.27 (m, 27H), 7.26 – 7.07 (m, 5H), 7.07 – 6.96 (m, 27H), 5.45 – 4.68 (m, 6H), 4.20 – 4.01 (m, 18H), 3.88 – 3.75 (m, 14H), 3.65 (s, 4H), 2.23 (s, 18H), 2.13 (s, 18H), 2.08 – 1.91 (m, 17H), 1.68 – 0.75 (m, 1538H); ^{13}C NMR (100 MHz, THF-d_8) δ 154.4, 153.8, 139.4, 138.7, 136.4, 136.3, 136.0, 129.8, 129.8, 125.3, 119.3, 118.9, 65.1, 63.4, 51.8, 41.3, 40.0, 39.5, 39.4, 38.9, 37.2, 34.5, 34.2, 31.6, 31.2, 30.8, 30.2, 27.7, 27.6, 27.4, 27.0, 26.8, 22.6, 15.3, 14.9, 11.3, 11.1, 11.1, 11.0, 10.8; GPC (THF) M_n = 8400 g mol^{-1}, M_w = 13400 g mol^{-1}, Đ = 1.59.

SPU13

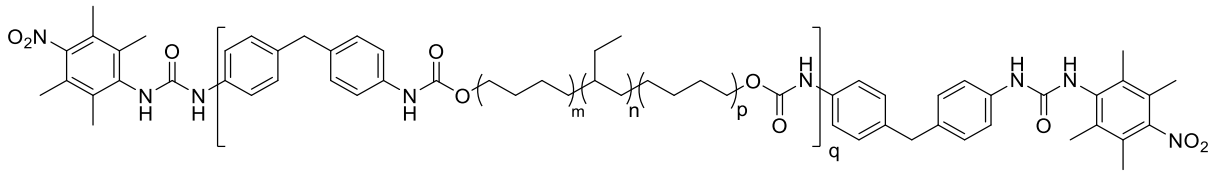

The synthesis was carried out according to the general synthetic protocol described above for the SPUs. The polymer was isolated as a waxy yellow translucent solid (14.03 g, 96 %) from Krasol HLBH-P 2000 (9.84 g, 4.69 mmol); T_g = -44.6 °C; FTIR ATR (cm^{-1}): 3308 (νN-$H_{stretch}$), 2962 (νC-H_{alkyl}), 2920 (νC-H_{alkyl}), 2875 (νC-H_{alkyl}), 2854 (νC-H_{alkyl}), 1738 (νC=$O_{urethane}$), 1705 (νC=$O_{urethane}$), 1639 (νC=O_{urea}), 1600 (νC=O_{urea}), 1528 (νN-$O_{stretch}$); ^{1}H NMR (400 MHz, THF-d_8) δ 8.60 (s, 1H), 8.58 – 8.47 (m, 8H), 7.95 – 7.51 (m, 4H), 7.45 – 7.27 (m, 27H), 7.26 – 7.07 (m, 5H), 7.07 – 6.96 (m, 27H), 5.45 – 4.68 (m, 6H), 4.20 – 4.01 (m, 18H), 3.88 – 3.75 (m, 14H), 3.65 (s, 4H), 2.23 (s, 18H), 2.13 (s, 18H), 2.08 – 1.91 (m, 17H), 1.68 – 0.75 (m, 1538H); ^{13}C NMR (100 MHz, THF-d_8) δ 154.4, 153.8, 139.4, 138.7, 136.4, 136.3, 136.0, 129.8, 129.8, 125.3, 119.3, 118.9, 65.1, 63.4, 51.8, 41.3, 40.0, 39.5, 39.4, 38.9, 37.2, 34.5, 34.2, 31.6, 31.2, 30.8, 30.2, 27.7, 27.6, 27.4, 27.0, 26.8, 22.6, 15.3, 14.9, 11.3, 11.1, 11.1, 11.0, 10.8; GPC (THF) M_n = 8400 g mol^{-1}, M_w = 13400 g mol^{-1}, Đ = 1.59.

3.5 References

(1) de Greef, T. F. A.; Meijer, E. W. Supramolecular Polymers. *Nature* **2008**, *453* (7192), 171–173. https://doi.org/10.1038/453171a.

(2) Lehn, J.-M. Perspectives in Chemistry-Aspects of Adaptive Chemistry and Materials. *Angew. Chemie Int. Ed.* **2015**, *54* (11), 3276–3289. https://doi.org/10.1002/anie.201409399.

(3) Huang, F.; Scherman, O. A. Supramolecular Polymers. *Chem. Soc. Rev.* **2012**, *41* (18), 5879–5880. https://doi.org/10.1039/c2cs90071h.

(4) Urban, M. W. Stratification, Stimuli-Responsiveness, Self-Healing, and Signaling in Polymer Networks. *Prog. Polym. Sci.* **2009**, *34* (8), 679–687. https://doi.org/10.1016/j.progpolymsci.2009.03.004.

(5) Li, J.; Viveros, J. A.; Wrue, M. H.; Anthamatten, M. Shape-Memory Effects in Polymer Networks Containing Reversibly Associating Side-Groups. *Adv. Mater.* **2007**, *19* (19), 2851–2855. https://doi.org/10.1002/adma.200602260.

(6) Kim, J. T.; Kim, B. K.; Kim, E. Y.; Kwon, S. H.; Jeong, H. M. Synthesis and Properties of near IR Induced Self-Healable Polyurethane/Graphene Nanocomposites. *Eur. Polym. J.* **2013**, *49* (12), 3889–3896. https://doi.org/10.1016/j.eurpolymj.2013.10.009.

(7) Heinzmann, C.; Coulibaly, S.; Roulin, A.; Fiore, G. L.; Weder, C. Light-Induced Bonding and Debonding with Supramolecular Adhesives. *ACS Appl. Mater. Interfaces* **2014**, *6* (7), 4713–4719. https://doi.org/10.1021/am405302z.

(8) Ji, X.; Ahmed, M.; Long, L.; Khashab, N. M.; Huang, F.; Sessler, J. L. Adhesive Supramolecular Polymeric Materials Constructed from Macrocycle-Based Host-Guest Interactions. *Chem. Soc. Rev.* **2019**, *48* (10), 2682–2697. https://doi.org/10.1039/c8cs00955d.

(9) Courtois, J.; Baroudi, I.; Nouvel, N.; Degrandi, E.; Pensec, S.; Ducouret, G.; Chanéac, C.; Bouteiller, L.; Creton, C. Supramolecular Soft Adhesive Materials. *Adv. Funct. Mater.* **2010**, *20* (11), 1803–1811. https://doi.org/10.1002/adfm.200901903.

(10) Liu, J.; Tan, C. S. Y.; Scherman, O. A. Dynamic Interfacial Adhesion through Cucurbit[n]Uril Molecular Recognition. *Angew. Chemie - Int. Ed.* **2018**, *57* (29), 8854–8858. https://doi.org/10.1002/anie.201800775.

(11) Burattini, S.; Greenland, B. W.; Merino, D. H.; Weng, W.; Seppala, J.; Colquhoun, H. M.; Hayes, W.; MacKay, M. E.; Hamley, I. W.; Rowan, S. J. A Healable Supramolecular Polymer Blend Based on Aromatic π-π Stacking and Hydrogen-Bonding Interactions. *J. Am. Chem. Soc.* **2010**, *132* (34), 12051–12058. https://doi.org/10.1021/ja104446r.

(12) Hart, L. R.; Harries, J. L.; Greenland, B. W.; Colquhoun, H. M.; Hayes, W. Healable Supramolecular Polymers. *Polym. Chem.* **2013**, *4* (18), 4860–4870. https://doi.org/10.1039/c3py00081h.

(13) Hart, L. R.; Hunter, J. H.; Nguyen, N. A.; Harries, J. L.; Greenland, B. W.; Mackay, M. E.; Colquhoun, H. M.; Hayes, W. Multivalency in Healable Supramolecular Polymers: The Effect of Supramolecular Cross-Link Density on the Mechanical Properties and Healing of Non-Covalent Polymer Networks. *Polym. Chem.* **2014**, *5* (11), 3680–3688. https://doi.org/10.1039/c4py00292j.

(14) Coulibaly, S.; Roulin, A.; Balog, S.; Biyani, M. V.; Foster, E. J.; Rowan, S. J.; Fiore, G. L.; Weder, C. Reinforcement of Optically Healable Supramolecular Polymers with Cellulose Nanocrystals. *Macromolecules* **2014**, *47* (1), 152–160. https://doi.org/10.1021/ma402143c.

(15) Burnworth, M.; Tang, L.; Kumpfer, J. R.; Duncan, A. J.; Beyer, F. L.; Fiore, G. L.; Rowan, S. J.; Weder, C. Optically Healable Supramolecular Polymers. *Nature* **2011**, *472* (7343), 334–337. https://doi.org/10.1038/nature09963.

(16) Cordier, P.; Tournilhac, F.; Soulié-Ziakovic, C.; Leibler, L. Self-Healing and Thermoreversible Rubber from Supramolecular Assembly. *Nature* **2008**, *451* (7181), 977–980. https://doi.org/10.1038/nature06669.

(17) Hart, L. R.; Harries, J. L.; Greenland, B. W.; Colquhoun, H. M.; Hayes, W. Molecular Design of a Discrete Chain-Folding Polyimide for Controlled Inkjet Deposition of Supramolecular Polymers. *Polym. Chem.* **2015**, *6* (41), 7342–7352. https://doi.org/10.1039/c5py00622h.

(18) Hart, L. R.; Li, S.; Sturgess, C.; Wildman, R.; Jones, J. R.; Hayes, W. 3D Printing of Biocompatible Supramolecular Polymers and Their Composites. *ACS Appl. Mater. Interfaces* **2016**, *8* (5), 3115–3122. https://doi.org/10.1021/acsami.5b10471.

(19) Wang, Z.; Shui, M.; Wyman, I. W.; Zhang, Q. W.; Wang, R. Cucurbit[8]Uril-Based Supramolecular Hydrogels for Biomedical Applications. *RSC Med. Chem.* **2021**, *12* (5), 722–729. https://doi.org/10.1039/d1md00019e.

(20) Jin, H.; Huang, W.; Zhu, X.; Zhou, Y.; Yan, D. Biocompatible or Biodegradable Hyperbranched Polymers: From Self-Assembly to Cytomimetic Applications. *Chem. Soc. Rev.* **2012**, *41* (18), 5986–5997. https://doi.org/10.1039/c2cs35130g.

(21) Bosman, A. W.; Dankers, P. Y. W.; Janssen, H. M.; Meijer, E. W.; van Gemert, G. M. L. Modular Supramolecular Materials For Biomedical Uses. WO 2007/058539 A2, 2008.

(22) Sautaux, J.; Marx, F.; Gunkel, I.; Weder, C.; Schrettl, S. Mechanically Robust Supramolecular Polymer Co-Assemblies. *Nat. Commun.* **2022**, *13*, 356.

https://doi.org/10.1038/s41467-022-28017-0.

(23) Simonin, L.; Falco, G.; Pensec, S.; Dalmas, F.; Chenal, J. M.; Ganachaud, F.; Marcellan, A.; Chazeau, L.; Bouteiller, L. Macromolecular Additives to Turn a Thermoplastic Elastomer into a Self-Healing Material. *Macromolecules* **2021**, *54* (2), 888–895. https://doi.org/10.1021/acs.macromol.0c02352.

(24) Folmer, B. J. B.; Sijbesma, R. P.; Versteegen, R. M.; van der Rijt, J. A. J.; Meijer, E. W. Supramolecular Polymer Materials: Chain Extension of Telechelic Polymers Using a Reactive Hydrogen-Bonding Synthon. *Adv. Mater.* **2000**, *12* (12), 874–878. https://doi.org/10.1002/1521-4095(200006)12:12<874::AID-ADMA874>3.0.CO;2-C.

(25) Hirschberg, J. H. K. K.; Beijer, F. H.; van Aert, H. A.; Magusin, P. C. M. M.; Sijbesma, R. P.; Meijer, E. W. Supramolecular Polymers from Linear Telechelic Siloxanes with Quadruple-Hydrogen-Bonded Units. *Macromolecules* **1999**, *32* (8), 2696–2705. https://doi.org/10.1021/ma981950w.

(26) Meng, Y.; Xu, W.; Newman, M. R.; Benoit, D. S. W.; Anthamatten, M. Thermoreversible Siloxane Networks: Soft Biomaterials with Widely Tunable Viscoelasticity. *Adv. Funct. Mater.* **2019**, *29* (38), 1903721. https://doi.org/10.1002/adfm.201903721.

(27) Pellizzaro, M. L.; Houton, K. A.; Wilson, A. J. Sequential and Phototriggered Supramolecular Self-Sorting Cascades Using Hydrogen-Bonded Motifs. *Chem. Sci.* **2013**, *4* (4), 1825–1829. https://doi.org/10.1039/c3sc22194f.

(28) Coubrough, H. M.; van der Lubbe, S. C. C.; Hetherington, K.; Minard, A.; Pask, C.; Howard, M. J.; Fonseca Guerra, C.; Wilson, A. J. Supramolecular Self-Sorting Networks Using Hydrogen-Bonding Motifs. *Chem. - A Eur. J.* **2019**, *25* (3), 785–795. https://doi.org/10.1002/chem.201804791.

(29) Piana, F.; Case, D. H.; Ramalhete, S. M.; Pileio, G.; Facciotti, M.; Day, G. M.; Khimyak, Y. Z.; Angulo, J.; Brown, R. C. D.; Gale, P. A. Substituent Interference on Supramolecular Assembly in Urea Gelators: Synthesis, Structure Prediction and NMR. *Soft Matter* **2016**, *12* (17), 4034–4043. https://doi.org/10.1039/c6sm00607h.

(30) Rodríguez-Llansola, F.; Escuder, B.; Miravet, J. F.; Hermida-Merino, D.; Hamley, I. W.; Cardin, C. J.; Hayes, W. Selective and Highly Efficient Dye Scavenging by a PH-Responsive Molecular Hydrogelator. *Chem. Commun.* **2010**, *46* (42), 7960–7962. https://doi.org/10.1039/c0cc02338h.

(31) Wood, D. M.; Greenland, B. W.; Acton, A. L.; Rodríguez-Llansola, F.; Murray, C. A.; Cardin, C. J.; Miravet, J. F.; Escuder, B.; Hamley, I. W.; Hayes, W. PH-Tunable Hydrogelators for Water Purification: Structural Optimisation and Evaluation. *Chem. - A Eur. J.* **2012**, *18* (9), 2692–2699. https://doi.org/10.1002/chem.201102137.

(32) Baker, B. C.; German, I. M.; Chippindale, A. M.; McEwan, C. E. A. A.; Stevens, G. C.; Colquhoun, H. M.; Hayes, W. Nitroarylurea-Terminated Supramolecular Polymers That Exhibit Facile Thermal Repair and Aqueous Swelling-Induced Sealing of Defects. *Polymer.* **2018**, *140*, 1–9. https://doi.org/10.1016/j.polymer.2018.02.029.

(33) Isare, B.; Pembouong, G.; Boué, F.; Bouteiller, L. Conformational Control of Hydrogen-Bonded Aromatic Bis-Ureas. *Langmuir* **2012**, *28* (19), 7535–7541. https://doi.org/10.1021/la300887p.

(34) ODonnell, A. D.; Gavriel, A. G.; Christie, W.; Chippindale, A. M.; German, I. M.; Hayes, W. Conformational Control of Bis-Urea Self-Assembled Supramolecular PH Switchable Low-Molecular-Weight Hydrogelators. *Arkivoc* **2021**, *2021* (6), 222–241. https://doi.org/10.24820/ark.5550190.p011.581.

(35) Harnying, W.; Neudörfl, J. M.; Berkessel, A. Enantiospecific Synthesis of Nepetalactones by One-Step Oxidative NHC Catalysis. *Org. Lett.* **2020**, *22* (2), 386–390. https://doi.org/10.1021/acs.orglett.9b04034.

(36) Ingham, C. E.; Hampson, G. C. 209. An Investigation of Steric Influences on the Phenomenon of Resonance. Part II. *J. Chem. Soc.* **1939**, 981. https://doi.org/10.1039/jr9390000981.

(37) Gavriel, A. G.; Leroux, F.; Khurana, G. S.; Lewis, V. G.; Chippindale, A. M.; Sambrook, M. R.; Hayes, W.; Russell, A. T. Self-Immolative System for Disclosure of Reactive Electrophilic Alkylating Agents: Understanding the Role of the Reporter Group. *J. Org. Chem.* **2021**, *86* (15), 10263–10279. https://doi.org/10.1021/acs.joc.1c00996.

(38) Snape, H. L. LXXVI.—Action of Phenyl Cyanate on Polyhydric and Certain Monohydric Alcohols and Phenols. *J. Chem. Soc., Trans.* **1885**, *47* (770), 770–779. https://doi.org/10.1039/CT8854700770.

(39) Leuthardt, F.; Brunner, R. Réaction Entre l'acétyl-Acétanilide et Les Amines Primaires. *Helv. Chim. Acta* **1947**, *30* (4), 958–964. https://doi.org/10.1002/hlca.19470300405.

(40) Michael, A.; Cobb, P. H. Phenylisocyanat Als Reagens Zur Feststellung Der Constitution Merotroper Verbindungen. *Justus Liebig's Ann. der Chemie* **1908**, *363* (1), 64–93. https://doi.org/10.1002/jlac.19083630105.

(41) Beaver, D. J.; Roman, D. P.; Stoffel, P. J. The Preparation and Bacteriostatic Activity of Substituted M-Nitrocarbanilides. *J. Org. Chem.* **1959**, *24* (11), 1676–1678. https://doi.org/10.1021/jo01093a012.

(42) Ellena, J.; Goeta, A. E.; Howard, J. A. K.; Punte, G. Role of the Hydrogen Bonds in Nitroanilines Aggregation: Charge Density Study of 2-Methyl-5-Nitroaniline. *J. Phys. Chem. A* **2001**, *105* (38), 8696–8708. https://doi.org/10.1021/jp010688h.

(43) Woodward, P.; Merino, D. H.; Hamley, I. W.; Slark, A. T.; Hayes, W. Thermally Responsive Elastomeric Supramolecular Polymers Featuring Flexible Aliphatic Hydrogen-Bonding End-Groups. *Aust. J. Chem.* **2009**, *62* (8), 790–793. https://doi.org/10.1071/CH09088.

(44) Feula, A.; Tang, X.; Giannakopoulos, I.; Chippindale, A. M.; Hamley, I. W.; Greco, F.; Paul Buckley, C.; Siviour, C. R.; Hayes, W. An Adhesive Elastomeric Supramolecular Polyurethane Healable at Body Temperature. *Chem. Sci.* **2016**, *7* (7), 4291–4300. https://doi.org/10.1039/c5sc04864h.

(45) Hermida-Merino, D.; Hart, L. R.; Harris, P. J.; Slark, A. T.; Hamley, I. W.; Hayes, W. The Effect of Chiral End Groups on the Assembly of Supramolecular Polyurethanes. *Polym. Chem.* **2021**, *12* (31), 4488–4500. https://doi.org/10.1039/d1py00714a.

(46) Chen, M.; Inglefield, D. L.; Zhang, K.; Hudson, A. G.; Talley, S. J.; Moore, R. B.; Long, T. E. Synthesis of Urea-Containing ABA Triblock Copolymers: Influence of Pendant Hydrogen Bonding on Morphology and Thermomechanical Properties. *J. Polym. Sci. Part A Polym. Chem.* **2018**, *56* (16), 1844–1852. https://doi.org/10.1002/pola.29066.

(47) Zhang, Q.; Shi, C. Y.; Qu, D. H.; Long, Y. T.; Feringa, B. L.; Tian, H. Exploring a Naturally Tailored Small Molecule for Stretchable, Self-Healing, and Adhesive Supramolecular Polymers. *Sci. Adv.* **2018**, *4* (7), 1–8. https://doi.org/10.1126/sciadv.aat8192.

(48) Gao, S.; Ma, G.; Ye, J.; He, L.; Guo, L.; Li, X.; Qiu, T.; Tuo, X. The Tough, Fluorescent and Adhesive Elastomer in Aqueous Dispersion: The Contribution of Aromatic Amide-Urea Segments. *Mater. Today Commun.* **2021**, *29*, 102880. https://doi.org/10.1016/j.mtcomm.2021.102880.

(49) Baker, B. C.; Acton, A. L.; Stevens, G. C.; Hayes, W. Bis Amide-Aromatic-Ureas - Highly Effective Hydro- and Organogelator Systems. *Tetrahedron* **2014**, *70* (44), 8303–8311. https://doi.org/10.1016/j.tet.2014.09.017.

(50) Baker, B. C.; Higgins, C. L.; Ravishankar, D.; Colquhoun, H. M.; Stevens, G. C.; Greco, F.; Greenland, B. W.; Hayes, W. Multifunctional, Biocompatible, Non-Peptidic Hydrogels: From Water Purification to Drug Delivery. *ChemistrySelect* **2016**, *1* (8), 1641–1649. https://doi.org/10.1002/slct.201600249.

(51) Birtles, R. H.; Hampson, G. C. 3. An Investigation of Steric Influences on the Phenomenon of Mesomerism. *J. Chem. Soc.* **1937**, 10. https://doi.org/10.1039/jr9370000010.

(52) Appel, W. P. J.; Portale, G.; Wisse, E.; Dankers, P. Y. W.; Meijer, E. W. Aggregation of Ureido-Pyrimidinone Supramolecular Thermoplastic Elastomers into Nanofibers: A Kinetic Analysis. *Macromolecules* **2011**, *44* (17), 6776–6784.

https://doi.org/10.1021/ma201303s.

(53) Chen, Y.; Kushner, A. M.; Williams, G. A.; Guan, Z. Multiphase Design of Autonomic Self-Healing Thermoplastic Elastomers. *Nat. Chem.* **2012**, *4* (6), 467–472. https://doi.org/10.1038/nchem.1314.

(54) Lai, Y.; Kuang, X.; Zhu, P.; Huang, M.; Dong, X.; Wang, D. Colorless, Transparent, Robust, and Fast Scratch-Self-Healing Elastomers via a Phase-Locked Dynamic Bonds Design. *Adv. Mater.* **2018**, *30* (38), 1802556. https://doi.org/10.1002/adma.201802556.

(55) Merino, D. H.; Feula, A.; Melia, K.; Slark, A. T.; Giannakopoulos, I.; Siviour, C. R.; Buckley, C. P.; Greenland, B. W.; Liu, D.; Gan, Y.; Harris, P. J.; Chippindale, A. M.; Hamley, I. W.; Hayes, W. A Systematic Study of the Effect of the Hard End-Group Composition on the Microphase Separation, Thermal and Mechanical Properties of Supramolecular Polyurethanes. *Polymer (Guildf).* **2016**, *107*, 368–378. https://doi.org/10.1016/j.polymer.2016.07.029.

(56) Tang, X.; Feula, A.; Baker, B. C.; Melia, K.; Hermida Merino, D.; Hamley, I. W.; Buckley, C. P.; Hayes, W.; Siviour, C. R. A Dynamic Supramolecular Polyurethane Network Whose Mechanical Properties Are Kinetically Controlled. *Polymer (Guildf).* **2017**, *133*, 143–150. https://doi.org/10.1016/j.polymer.2017.11.005.

(57) Woodward, P. J.; Merino, D. H.; Greenland, B. W.; Hamley, I. W.; Light, Z.; Slark, A. T.; Hayes, W. Hydrogen Bonded Supramolecular Elastomers: Correlating Hydrogen Bonding Strength with Morphology and Rheology. *Macromolecules* **2010**, *43* (5), 2512–2517. https://doi.org/10.1021/ma9027646.

(58) Kaushiva, B. D.; McCartney, S. R.; Rossmy, G. R.; Wilkes, G. L. Surfactant Level Influences on Structure and Properties of Flexible Slabstock Polyurethane Foams. *Polymer (Guildf).* **2000**, *41* (1), 285–310. https://doi.org/10.1016/S0032-3861(99)00135-4.

(59) Sivakova, S.; Bohnsack, D. A.; Mackay, M. E.; Suwanmala, P.; Rowan, S. J. Utilization of a Combination of Weak Hydrogen-Bonding Interactions and Phase Segregation to Yield Highly Thermosensitive Supramolecular Polymers. *J. Am. Chem. Soc.* **2005**, *127* (51), 18202–18211. https://doi.org/10.1021/ja055245w.

(60) George, S.; Nangia, A.; Lam, C. K.; Mak, T. C. W.; Nicoud, J. F. Crystal Engineering of Urea α-Network via I···O2N Synthon and Design of SHG Active Crystal N-4-Iodophenyl-N′-4′-Nitrophenylurea. *Chem. Commun.* **2004**, *4* (10), 1202–1203. https://doi.org/10.1039/b402050b.

(61) Cui, G.; Boudara, V. A. H.; Huang, Q.; Baeza, G. P.; Wilson, A. J.; Hassager, O.; Read, D. J.; Mattsson, J. Linear Shear and Nonlinear Extensional Rheology of Unentangled

Supramolecular Side-Chain Polymers. *J. Rheol. (N. Y. N. Y).* **2018**, *62* (5), 1155–1174. https://doi.org/10.1122/1.5012349.

(62) Herbst, F.; Seiffert, S.; Binder, W. H. Dynamic Supramolecular Poly(Isobutylene)s for Self-Healing Materials. *Polym. Chem.* **2012**, *3* (11), 3084–3092. https://doi.org/10.1039/c2py20265d.

(63) Neumann, L. N.; Oveisi, E.; Petzold, A.; Style, R. W.; Thurn-Albrecht, T.; Weder, C.; Schrettl, S. Dynamics and Healing Behavior of Metallosupramolecular Polymers. *Sci. Adv.* **2021**, *7* (18), 1–8 https://doi.org/10.1126/sciadv.abe4154.

(64) Dalsin, J. L.; Hu, B. H.; Lee, B. P.; Messersmith, P. B. Mussel Adhesive Protein Mimetic Polymers for the Preparation of Nonfouling Surfaces. *J. Am. Chem. Soc.* **2003**, *125* (14), 4253–4258. https://doi.org/10.1021/ja0284963.

(65) Brubaker, C. E.; Messersmith, P. B. The Present and Future of Biologically Inspired Adhesive Interfaces and Materials. *Langmuir* **2012**, *28* (4), 2200–2205. https://doi.org/10.1021/la300044v.

(66) Balkenende, D. W. R.; Monnier, C. A.; Fiore, G. L.; Weder, C. Optically Responsive Supramolecular Polymer Glasses. *Nat. Commun.* **2016**, *7*, 10995. https://doi.org/10.1038/ncomms10995.

(67) Raos, G.; Zappone, B. Polymer Adhesion: Seeking New Solutions for an Old Problem. *Macromolecules* **2021**, *54* (23), 10617–10644. https://doi.org/10.1021/acs.macromol.1c01182.

(68) Salimi, S.; Hart, L. R.; Feula, A.; Hermida-Merino, D.; Touré, A. B. R.; Kabova, E. A.; Ruiz-Cantu, L.; Irvine, D. J.; Wildman, R.; Shankland, K.; Hayes, W. Property Enhancement of Healable Supramolecular Polyurethanes. *Eur. Polym. J.* **2019**, *118* (May), 88–96. https://doi.org/10.1016/j.eurpolymj.2019.05.042.

(69) Döhler, D.; Kang, J.; Cooper, C. B.; Tok, J. B. H.; Rupp, H.; Binder, W. H.; Bao, Z. Tuning the Self-Healing Response of Poly(Dimethylsiloxane)-Based Elastomers. *ACS Appl. Polym. Mater.* **2020**, *2* (9), 4127–4139. https://doi.org/10.1021/acsapm.0c00755.

(70) Smith, A. J.; Alcock, S. G.; Davidson, L. S.; Emmins, J. H.; Hiller Bardsley, J. C.; Holloway, P.; Malfois, M.; Marshall, A. R.; Pizzey, C. L.; Rogers, S. E.; Shebanova, O.; Snow, T.; Sutter, J. P.; Williams, E. P.; Terrill, N. J. I22: SAXS/WAXS Beamline at Diamond Light Source – an Overview of 10 Years Operation. *J. Synchrotron Radiat.* **2021**, *28* (3), 939–947. https://doi.org/10.1107/S1600577521002113.

(71) Filik, J.; Ashton, A. W.; Chang, P. C. Y.; Chater, P. A.; Day, S. J.; Drakopoulos, M.; Gerring, M. W.; Hart, M. L.; Magdysyuk, O. V.; Michalik, S.; Smith, A.; Tang, C. C.; Terrill, N. J.; Wharmby, M. T.; Wilhelm, H. Processing Two-Dimensional X-Ray

Diffraction and Small-Angle Scattering Data in DAWN 2. *J. Appl. Crystallogr.* **2017**, *50* (3), 959–966. https://doi.org/10.1107/S1600576717004708.

(72) *CrysAlis PRO. Rigaku OD (2019). Rigaku Oxford Diffraction Ltd, Yarnton, Oxfordshire, England.*

(73) Palatinus, L.; Chapuis, G. SUPERFLIP - A Computer Program for the Solution of Crystal Structures by Charge Flipping in Arbitrary Dimensions. *J. Appl. Crystallogr.* **2007**, *40* (4), 786–790. https://doi.org/10.1107/S0021889807029238.

(74) Betteridge, P. W.; Carruthers, J. R.; Cooper, R. I.; Prout, K.; Watkin, D. J. CRYSTALS Version 12: Software for Guided Crystal Structure Analysis . *J. Appl. Crystallogr.* **2003**, *36* (6), 1487–1487. https://doi.org/10.1107/s0021889803021800.

(75) Sura, T. P.; Ramana, M. M. V.; Kudav, N. A. Urea Nitrate: A Reagent for Regioselective Nitration of Aromatic Amines. *Synth. Commun.* **1988**, *18* (16–17), 2161–2165. https://doi.org/10.1080/00397918808068287.

(76) Evans, D. H.; Hu, K. Inverted Potentials in Two-Electron Processes in Organic Electrochemistry. *J. Chem. Soc. Faraday Trans.* **1996**, *92* (20), 3983. https://doi.org/10.1039/ft9969203983.

(77) Guan, Z. H.; Lei, H.; Chen, M.; Ren, Z. H.; Bai, Y.; Wang, Y. Y. Palladium-Catalyzed Carbonylation of Amines: Switchable Approaches to Carbamates and N,N′-Disubstituted Ureas. *Adv. Synth. Catal.* **2012**, *354* (2–3), 489–496. https://doi.org/10.1002/adsc.201100545.

(78) Kadam, S. A.; Haav, K.; Toom, L.; Haljasorg, T.; Leito, I. NMR Method for Simultaneous Host-Guest Binding Constant Measurement. *J. Org. Chem.* **2014**, *79* (6), 2501–2513. https://doi.org/10.1021/jo4027963.

(79) Zhu, X.; Xu, M.; Sun, J.; Guo, D.; Zhang, Y.; Zhou, S.; Wang, S. Hydroamination and Hydrophosphination of Isocyanates/Isothiocyanates under Catalyst-Free Conditions. *European J. Org. Chem.* **2021**, *2021* (37), 5213–5218. https://doi.org/10.1002/ejoc.202100932.

(80) Simons, D. M.; Arnold, R. G. Relative Reactivity of the Isocyanate Groups in Toluene-2,4-Diisocyanate. *J. Am. Chem. Soc.* **1956**, *78* (8), 1658–1659. https://doi.org/10.1021/ja01589a044.

Chapter 4 – Self-assembled Supramolecular Polyurethane Elastomers Using Bis-aromatic Urea Hydrogen Bonded Arrays

This chapter describes the characterisation, synthesis, and supramolecular assembly of polyurethane elastomers. Bis-aromatic urea hydrogen bonding motifs are used to promote the self-assembly of the material. The materials described comprise a soft block, namely polytetramethylene ether glycol (PTMG) as a telechelic diol and hard crystalline domains that feature a bis-aromatic urea hydrogen bonding motif as chain extenders. Two diols were polymerised (one featuring the bis-aromatic urea hydrogen bonding motif) with a PTMG diisocyanate prepolymer to yield supramolecular polyurethanes with molecular weights *ca*. 185000 with polydispersities *ca*. 2.0. The mechanical properties and processing temperature of the polyurethanes was tuned by controlling the feed ratio of the supramolecular chain extender.

4.1 Introduction

Supramolecular polymers are dynamic systems that utilize non-covalent interactions to assemble and deliver properties that can be comparable to those exhibited by covalently bonded polymers.[1–4] The advantage of using supramolecular assembly to tailor mechanical properties stems from their stimuli-responsive nature, which is not typically observed in conventional covalently bonded polymers, especially cross-linked systems. Stimuli, such as temperature and light, have successfully been used to modify polymer properties, and as such supramolecular polymers are an intriguing proposition when selecting a material for a specific application. They have found application in adhesives,[5–8] coatings,[9–11] biomedical devices,[12–14] and healable materials.[15–20] Bao and co-workers reported the synthesis and mechanical property enhancement of a series of poly(siloxane) elastomers (PDMS).[21] By varying the chosen isocyanate and thus the strength of the hydrogen-bonding interaction in the hard domains, self-healing PDMS elastomers with tunable elasticity and toughness were synthesized.[21] The Young's moduli of these elastomers ranged from 0.4 to 13 MPa depending on the molecular weight of the PDMS prepolymer and the chosen isocyanate. Fu and co-workers described the synthesis of a chain-extended self-healing PTMG elastomer **4.1** (see Scheme 1, from PTMG **4.2** plus isophorone diisocyanate **4.3** to afford an intermediate diisocyanate prepolymer **4.4** that was then reacted with a pyridine-based diol **4.5**) with tensile strength, toughness, and fracture energy values of 29.0 MPa, 121.8 MJm^{-3} and 104.1 kJ m^{-2}.[22]

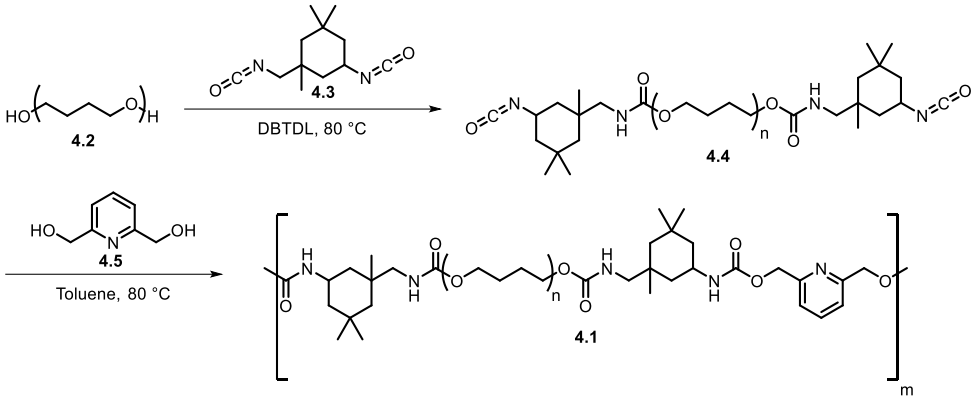

Scheme 16. Fu and co-workers' chain extended PTMG with a pyridyl diol.[22]

Similarly, Park and co-workers designed a self-healing elastomer (**4.6**, see Scheme 2) with a PTMG backbone. PTMG **4.2** was first reacted with isophorone diisocyanate **4.3** to afford an intermediate diisocyanate prepolymer **4.4** that was then reacted with a bis(4-hydroxylphenyl) disulfide (**4.7**) to form a chain extended polyurethane elastomer (**4.6**).[23] Healing was achieved by taking advantage of aromatic disulfide metathesis within the hard segments. Isophorone units were the chosen isocyanate as the asymmetric alicyclic structure was found to be more effective at providing optimal metathesis efficiency for the embedded aromatic disulphides whilst maintaining exceptional mechanical properties.

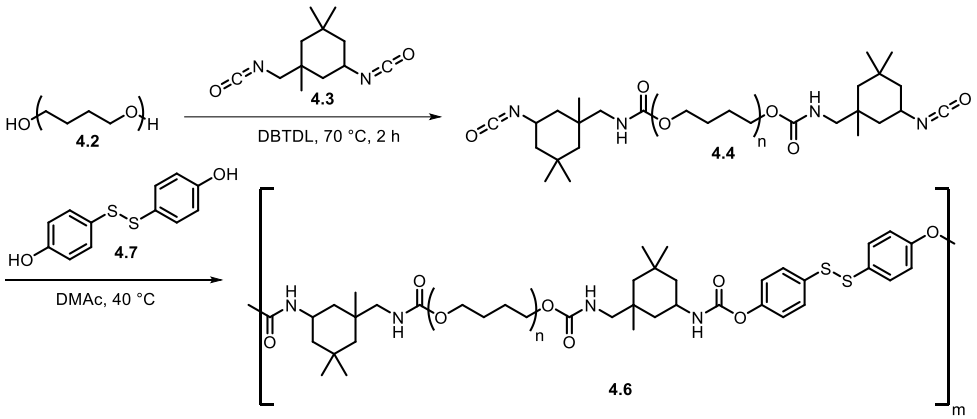

Scheme 17. Park and co-workers' chain extended PTMG with bis(4-hydroxyphenyl) disulfide.

Random comb copolymers of butyl acrylate **4.8** and a UPy functionalized methacrylate **4.9** delivered a series of thermoreversible supramolecular polymers **4.10** (see Scheme 3A).[24] Long and co-workers demonstrated the utility of incorporating a supramolecular assembly unit into a commonly used commercially available acrylate as they were able to tune the glass transition of the resultant supramolecular polymer from -50 °C (where y = 0 mol%) to -23 °C (where y = 10 mol%) and thus significantly change the physical characteristics of the resultant supramolecular polymer. Furthermore, the copolymers were found to strongly aggregate (see Scheme 3B) in non-polar solvents such as toluene and complete dissociation of the UPy groups was observed at 80 °C through VT-NMR spectroscopic experiments whereby the resonances associated with the urea proton shifted up field with respect to temperature and

then remained unchanged above 80 °C. Rheological assessment of the supramolecular polyacrylates were found to be in agreement with the VT-NMR spectroscopic experiments. The adhesive properties of the polyacrylates aptly describes the supramolecular interactions. When y = 3 mol%, the 90° peel strength test was three times higher than the parent poly(butyl acrylate) on standard glass substrates.

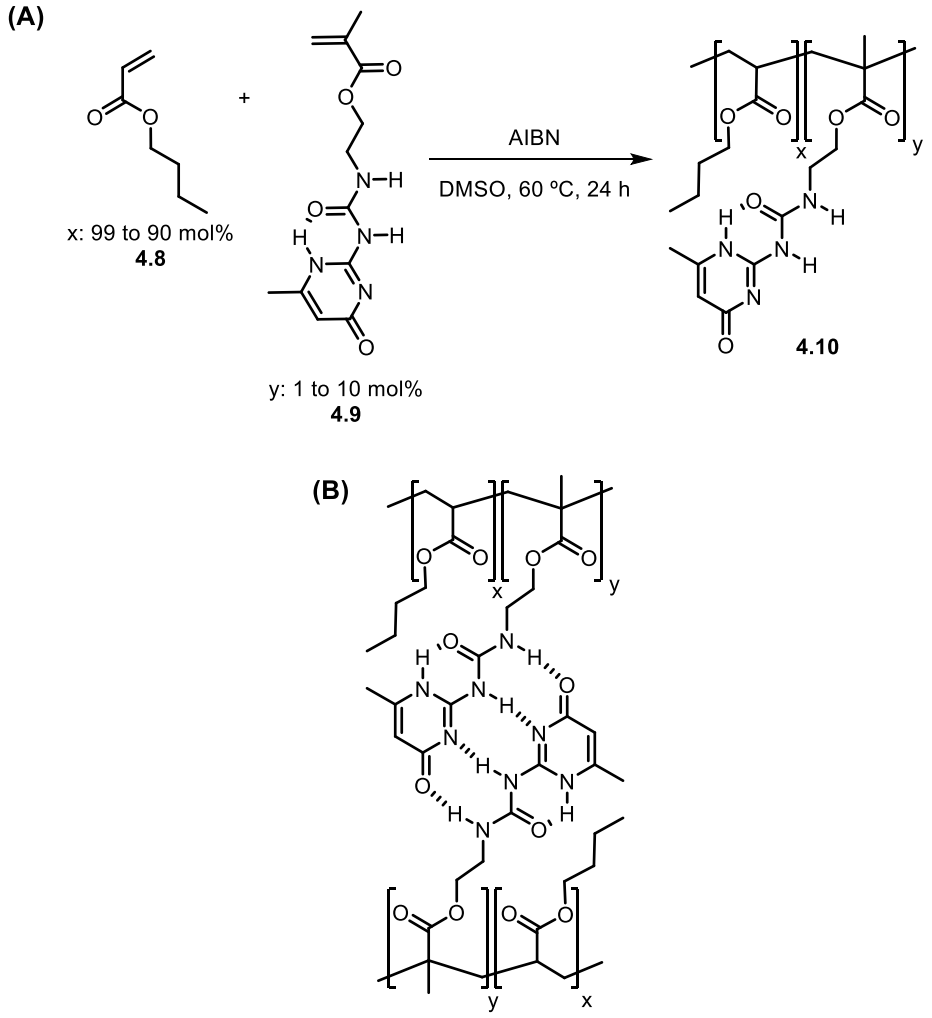

Scheme 18. A) Synthetic strategy to deliver thermoreversible poly(alkyl acrylates) (**4.10**) featuring a pendant UPy group (**4.9**) designed and synthesized by Long and co-workers. **B)** Proposed supramolecular interactions between the polymer chains through the dimerisation of UPy.[24]

In this Chapter is reported the design, and preparation of a series of supramolecular polymer elastomers (SPEs), **SPE1-12**, wherein various loadings of hydrogen bonding bis aromatic ureas with nitro moieties located in either the *meta* or *para* position and weaker π-π stacking interactions are introduced as pendant groups to physically cross-link and tune the mechanical properties of the resultant supramolecular polymer elastomer. Polyurethanes were chosen as a polymer class as they are widely used as protective films[23] and because their mechanical properties can be fine-tuned to deliver materials with desirable mechanical properties.

4.2 Results and Discussion

Elastomeric materials are under ever-increasing demands, as more strenuous applications demand greater elasticity, greater tensile strength, resilience, and increased lifespan.[25] To meet these demands, in-depth material understanding is required, and as such, a series of supramolecular elastomers (**SPE1**-**12**) have been designed and synthesised in which the density of the supramolecular crosslinks has been increased (0 to 15 mol%) via a condensation polymerisation, in which a PTMG (M_n = 2000 g/mol), a telechelic diol, was first reacted with 2.05 equivalents of 4,4′-methylenebis(cyclohexyl isocyanate) (HMDI) and a catalytic quantity of dibutyltin dilaurate (DBTDL), followed by chain extension using 1,3-benzenedimethanol (**4.11**) and 1-(3,5-bis(hydroxymethyl)phenyl)-3-(4-nitrophenyl)urea (**4.12**), or **4.11** and 1-(3,5-bis(hydroxymethyl)phenyl)-3-(3-nitrophenyl)urea (**4.13**). The bisaromatic urea motif was chosen because it can be used in a range of functional materials, from hydrogelators to other supramolecular polymer systems.[26–30] Furthermore, it was anticipated that the self-assembly of the motif would not disrupt the association of the PTMG soft domains and therefore yield soft thermoplastic elastomers capable of self-healing.

Synthesis of the nitro-aryl urea chain extender is facile, firstly 5-aminoisophthalic acid (**2.21**) is reacted with the appropriate isocyanate 3-nitrophenylisocyanate (**2.22**), or 4-nitrophenylisocyanate (**2.23**) (see Scheme 4). The reactions were monitored with FTIR spectroscopy to study the consumption of the isocyanate group and conversion to the corresponding urea. Purification of **2.1** and **2.5** was achieved through pH switching and trituration of the resultant gel material.

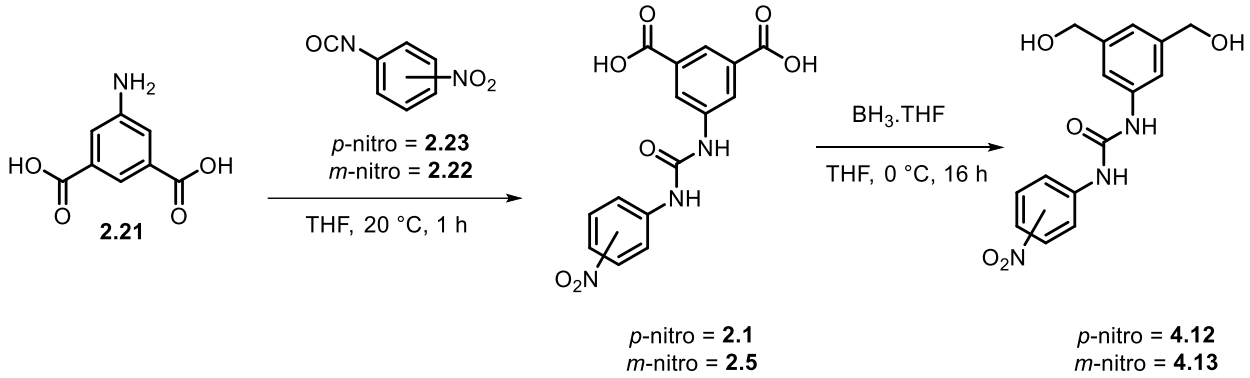

Scheme 19. General synthetic route to diol chain extenders (**4.12** and **4.13)**.

^{1}H NMR spectroscopic analysis was employed to confirm the successful synthesis of the **2.1** and **2.5,** and with the bis aromatic urea in hand, selective borane reduction[31] of two carboxylic acid functional groups yielded the respective primary alcohols. ^{1}H NMR spectroscopic analysis of **4.12** and **4.13** confirmed the selective reduction through the disappearance of the resonances associated with the carboxylic acids (4.0-5.0 ppm) and the appearance of two new proton resonances at 5.20 and 4.47 ppm that were assigned to the primary alcohol and the benzylic groups, respectively (see Figure 1). Furthermore, high-resolution mass spectrometry

was utilised to characterise **4.12** and **4.13,** and a mass ion of 318.1084 was detected corresponding to the desired compounds (see Appendix 3, Figure 10).

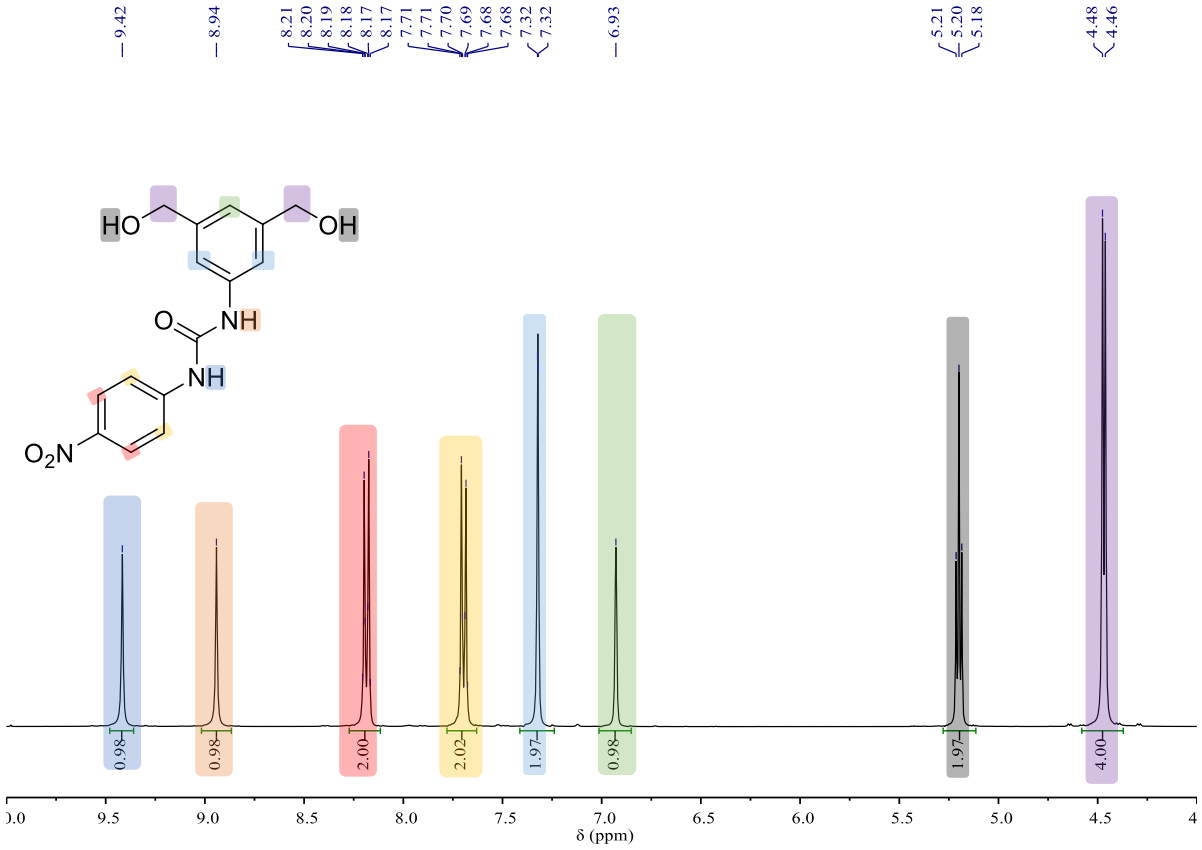

Figure 18. The ^{1}H NMR spectrum of nitro-aryl urea chain extender **4.12** (400 MHz, DMSO-d_6, 298 K).

To understand the intermolecular interactions in the hard domains of the resultant SPEs, crystals of nitro-aryl urea chain and **4.13** (see Figure 2A) were grown by slow evaporation and studied by X-ray crystallography. Key intermolecular interactions established by X-ray crystallographic analysis of the crystals of **4.13** are shown in Figure 2B. Hydrogen bond lengths were 2.22(2) and 2.07(3) Å (see Table 1) for the nitro oxygen acceptor and the urea carbonyl, respectively. Indicating that the urea carbonyl forms shorter, stronger hydrogen bonds compared to the nitro moiety. Interestingly, no urea-urea bifurcation was observed in the crystal structure, presumably because of the nitro substituent disrupting the bifurcation.

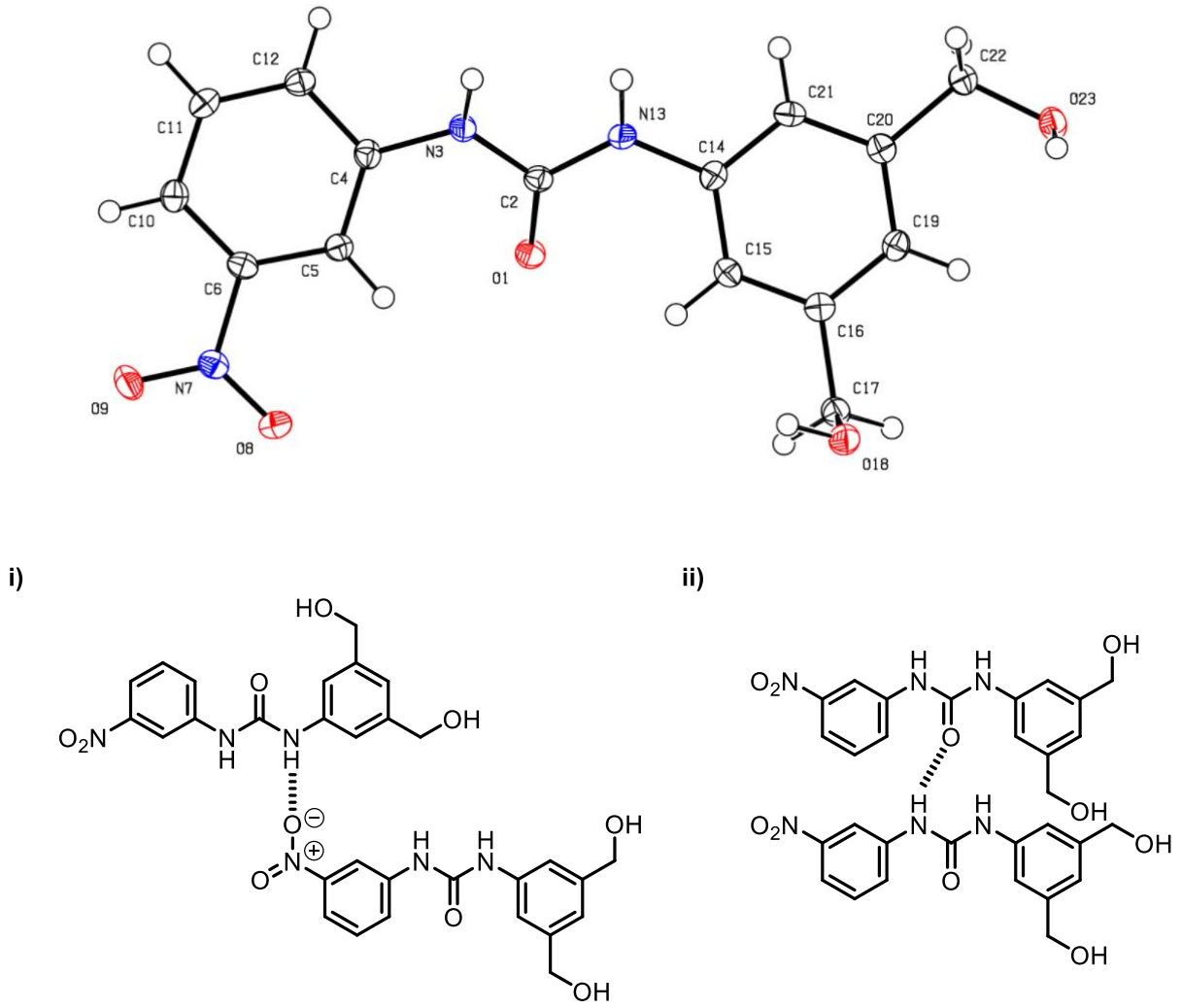

Figure 19. A) The asymmetric unit of **4.13** with ellipsoids drawn at 50% probability; **B)** Schematic representation of the hydrogen bonding motifs observed within the crystal structure of compound **4.13**. **i)** Hydrogen bonding of a nitro moiety acting as an acceptor for the urea NH of an adjacent molecule. **ii)** Off-set hydrogen bonding between two urea moieties.

Table 8. Hydrogen-bond geometry (Å, °) for **4.13**.

D – H•••A	*D* – H	H•••*A*	*D* •••*A*	*D* – H•••*A*
N(13) – H(131)•••O(8)^{i}	0.82(2)	2.22(2)	2.992 (2)	158.9(19)
N(3) – H(31)•••O(1)^{i}	0.86(3)	2.07(3)	2.836(2)	148(2)

Symmetry Codes: (i) 1+*x*, 1+*y*, *z*; (ii) *x*, *y* – 1, *z*; (iii) 2– *x*, 1/2+*y*, 1/2 – *z*.

A two-step prepolymer synthesis was performed whereby PTMG (M_n = 2000 g/mol) was first reacted with a slight excess of HMDI (2.05 eq.) in the presence of a catalytic quantity of DBTDL to form a reactive diisocyanate prepolymer in the bulk (see Scheme 5). This intermediate was diluted with anhydrous DMAc, and chain extended with **4.11**, **4.12** or **4.13**. The SPEs generated from this synthetic methodology were named **SPE1**-**12** whereby, **SPE1**-**6** feature a nitro substituent in the *-meta* position relative to the urea and the mol% of **4.13** ranges from 2.5 mol% (**SPE1**) to 15 mol% (**SPE6**) (see Table 1). Similarly, **SPE7**-**12** feature a nitro substituent in the *-para* position relative to the urea and the mol% of **4.12** ranges from 2.5 mol% (**SPE7**) to 15 mol% (**SPE12**) (see Table 2).

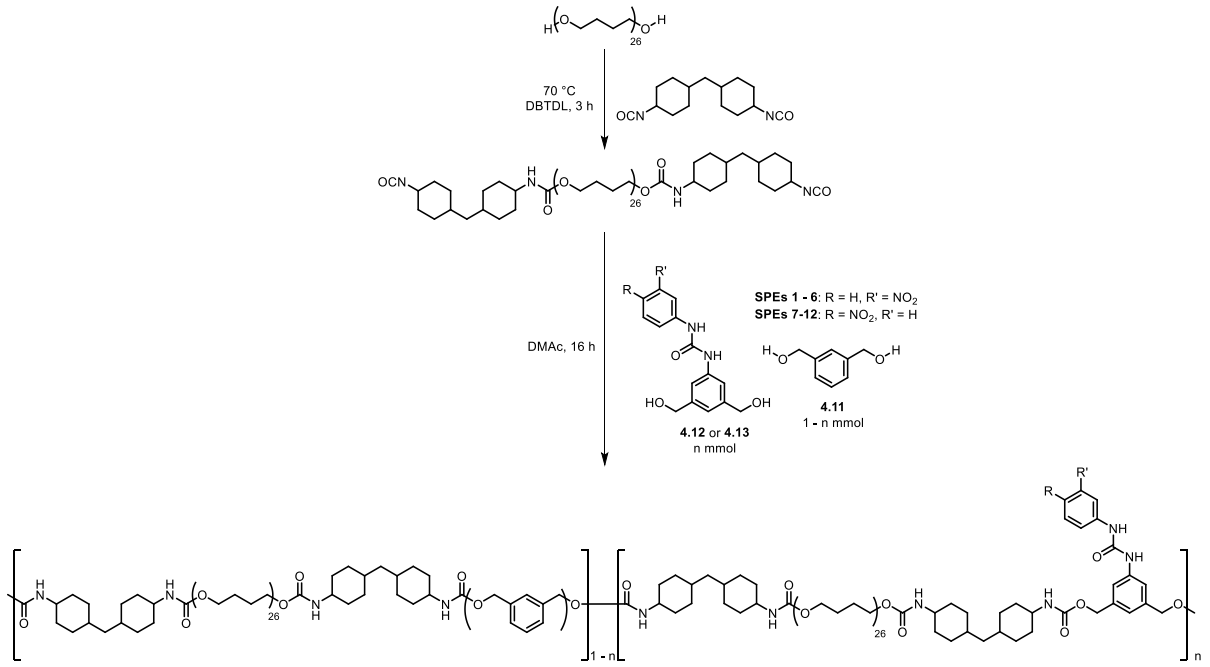

Scheme 20. General synthesis strategy employed to synthesise **SPE1**-**12**, a prepolymer is first formed by reacting PTMG with HMDI and subsequently chain extended with **4.11** and either **4.12** or **4.13**.

Table 9. Table outlining the mol% urea diol for **SPE1**-**12, SPE1**-**6** incorporate diol **4.13,** and **SPE7**-**12** incorporate diol **4.12**.

SPE	mol% urea diol
SPE1	2.5
SPE2	5.0
SPE3	7.5
SPE4	10
SPE5	12.5
SPE6	15
SPE7	2.5
SPE8	5.0
SPE9	7.5
SPE10	10
SPE11	12.5
SPE12	15

4.3 Material Characterisation

^{1}H NMR spectroscopic analysis revealed the successful preparation of the desired SPEs as determined by the key resonances associated with the PTMG backbone, HMDI and the chain extenders. As evident from Appendix 3 Figures 13-31, the proton resonances of the PTMG backbone dominate the spectra, however, the successful incorporation of the aromatic chain extenders was confirmed by the aromatic resonances observed at 7.33 ppm as well as the urethane resonances at 8.19 and 7.84 ppm. Furthermore, FTIR confirmed the complete consumption of the isocyanate residues of the prepolymer (observed typically at ~2250 cm^{-1}) in the chain extension reaction prior to polymer isolation. All of the SPEs were obtained with comparable number-average molecular weight (M_n) in the range of 83000-185000 (see the GPC eluogram of **SPE1** in Figure 3 and Table 3) and relatively narrow polydispersity indexes (<1.5-2.21) (Đ, calculated by M_w/M_n) as measured by gel permeation chromatography (GPC) utilising *N*,*N*-dimethylformamide (DMF) as the eluent and poly(styrene) (PS) as the calibrants (see Appendix 3, Figures 32-43).

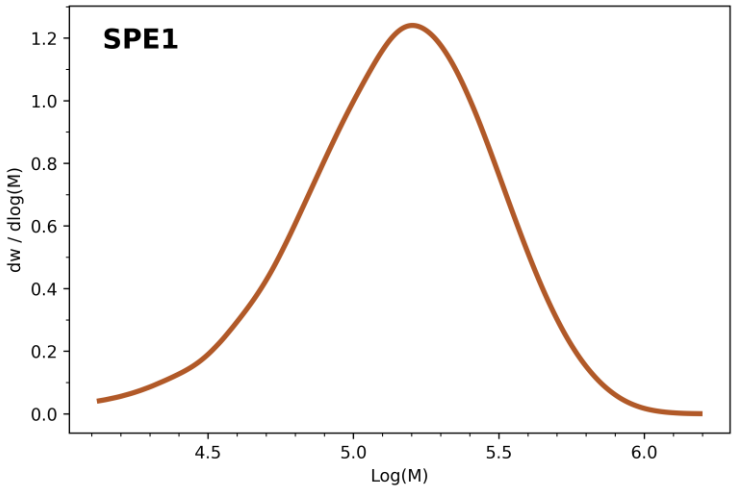

Figure 20. GPC Eluogram of **SPE1** (DMF, room temperature).

Table 10. Summary of the GPC data for SPEs **1**-**12**

SPE	M_n	M_w	Đ
SPE1	103200	184000	1.78
SPE2	82800	176000	2.13
SPE3	122200	232200	1.90
SPE4	101900	187800	1.84
SPE5	184500	408500	2.21
SPE6	101200	179000	1.76
SPE7	85400	150300	1.76
SPE8	91100	176300	1.94
SPE9	125800	236900	1.88
SPE10	92800	165300	1.78
SPE11	123800	242800	1.96
SPE12	82600	149300	1.81

The degree of hydrogen bonding within the supramolecular polymer networks was calculated by deconvolution of the carbonyl absorbance bands from the FT-IR spectroscopic data (see Table 4). The deconvolution analysis was carried out successfully on the urea and urethane carbonyl bands (see Figure 4). Assessing the percentages of free (1692 cm^{-1}), disordered hydrogen-bonded (1656–1680 cm^{-1}), and ordered hydrogen-bonded (1640 cm^{-1}) urea groups provides a key insight into the assembly of the SPEs; these stretching vibrations arise from the urea-urea interactions of the aromatic nitro-urea moieties pendant from the polymer backbone.[32]

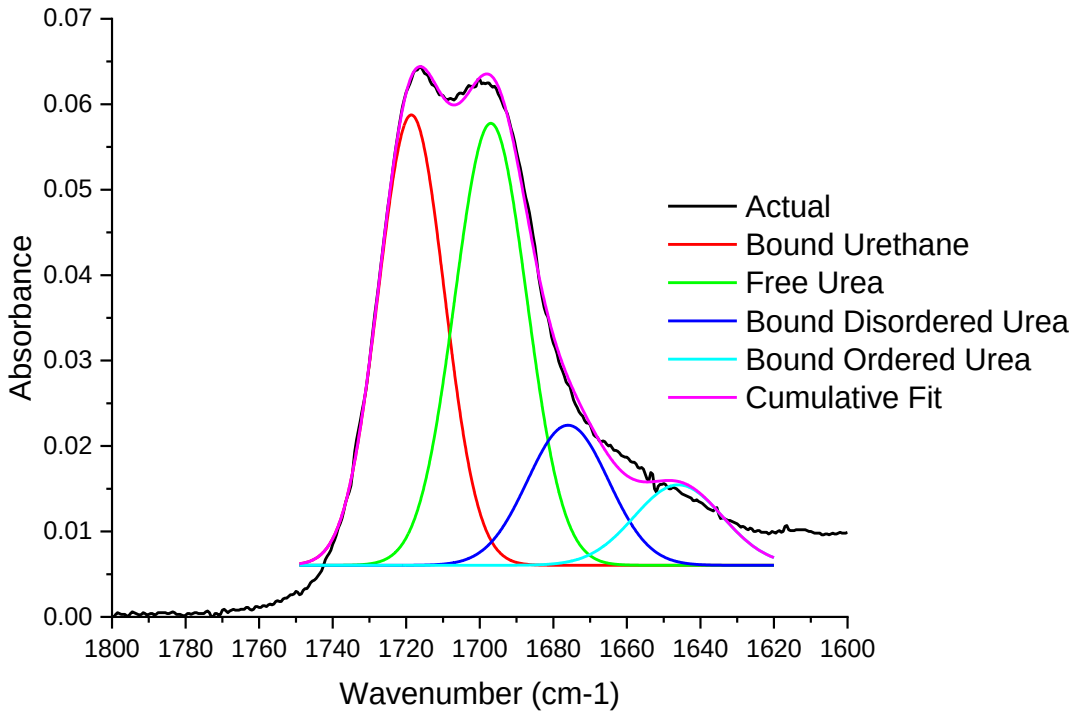

Figure 21. Example of the deconvolution analysis of IR spectroscopic data; shown for **SPE12** at 25 °C in the carbonyl region 1800-1600 cm^{-1}.

For both the -*para* and -*meta* nitro substituted functionalized SPEs, as the concentration of self-assembly units increased, so did the percentage of hydrogen-bonded urea, thus further validating the successful incorporation of the self-assembly units pendant from the polymeric backbone. Furthermore, the degree of hydrogen-bonded urea was found to be independent of the position of the nitro substituent on the aromatic ring. This result contrasts related studies that involved the chain end-functionalisation of a poly(butadiene) backbone.[33] In this study, analogous deconvolution of the IR spectroscopic data of the poly(butadiene) derivative did not reveal the contribution to the carbonyl absorption envelope from a free urethane stretch (see Chapter 3). As a result, the incorporation of the assembly unit pendant to the main chain of the polymer was not found to disrupt the urethane-urethane interactions along the polymeric backbone (see Table 4).

Table 11. Normalised percentage integrals of the urethane and urea absorbances of **SPE1**–**SPE12** from their respective FT-IR spectra, where the total bound urea equals the sum of the ordered bound urea and disordered bound urea.

SPE	Bound Urethane (%)	Free Urethane (%)	Ordered Bound Urea (%)	Disordered Bound Urea (%)	Total Bound Urea (%)	Free Urea (%)
SPE1	100 ± 1.4	-	2.8 ± 0.17	14 ± 0.22	17 ± 0.27	83 ± 0.81
SPE2	100 ± 2.0	-	3.9 ± 0.22	15 ± 0.36	19 ± 0.42	81 ± 1.2
SPE3	100 ± 1.6	-	4.9 ± 0.24	18 ± 0.35	22 ± 0.43	78 ± 1.2
SPE4	100 ± 1.9	-	10 ± 0.27	18 ± 0.33	28 ± 0.42	72 ± 1.0
SPE5	100 ± 3.3	-	15 ± 0.44	18 ± 0.51	33 ± 0.67	67 ± 1.7
SPE6	100 ± 2.3	-	16 ± 0.39	22 ± 0.48	38 ± 0.62	62 ± 1.4
SPE7	100 ± 1.8	-	3.1 ± 0.14	12 ± 0.23	15 ± 0.27	85 ± 1.1
SPE8	100 ± 2.1	-	4.5 ± 0.23	15 ± 0.33	20 ± 0.41	80 ± 1.2
SPE9	100 ± 3.0	-	8.1 ± 0.36	19 ± 0.57	27 ± 0.67	73 ± 1.7
SPE10	100 ± 3.7	-	9.9 ± 0.43	21 ± 0.73	31 ± 0.85	69 ± 1.9
SPE11	100 ± 3.2	-	12 ± 0.48	22 ± 0.65	34 ± 0.80	66 ± 1.8
SPE12	100 ± 3.3	-	14 ± 0.51	23 ± 0.65	37 ± 0.83	63 ± 1.9

Differential scanning calorimetry (DSC) determined that the glass transition temperatures (T_g) for SPEs **1**-**12** were outside the range of the instrumentation available; PTMG has an expected T_g between -80 to -90 °C, as reported by Pissis and coworkers.[34] These findings indicate that the introduction of the hard segments has had negligible influence on the T_g of the soft domain, a requirement for soft elastomeric materials. The mechanical properties of thermoplastic supramolecular polyurethanes have been shown to be dependent on their phase-separated morphology.[35–37] Small-angle X-ray scattering (SAXS) analysis has thus been used to investigate the phase separation in these materials.[18,38,39] At room temperature, SAXS analysis of the bulk SPEs displayed broad Bragg scattering peaks indicative of nanophase separation between the immiscibility of the hard hydrogen-bonded chain extender and the soft PTMG

backbone on the order of 157 Å. Furthermore, broad scattering peaks were also observed at 24 and 18 Å (see Figure 5).

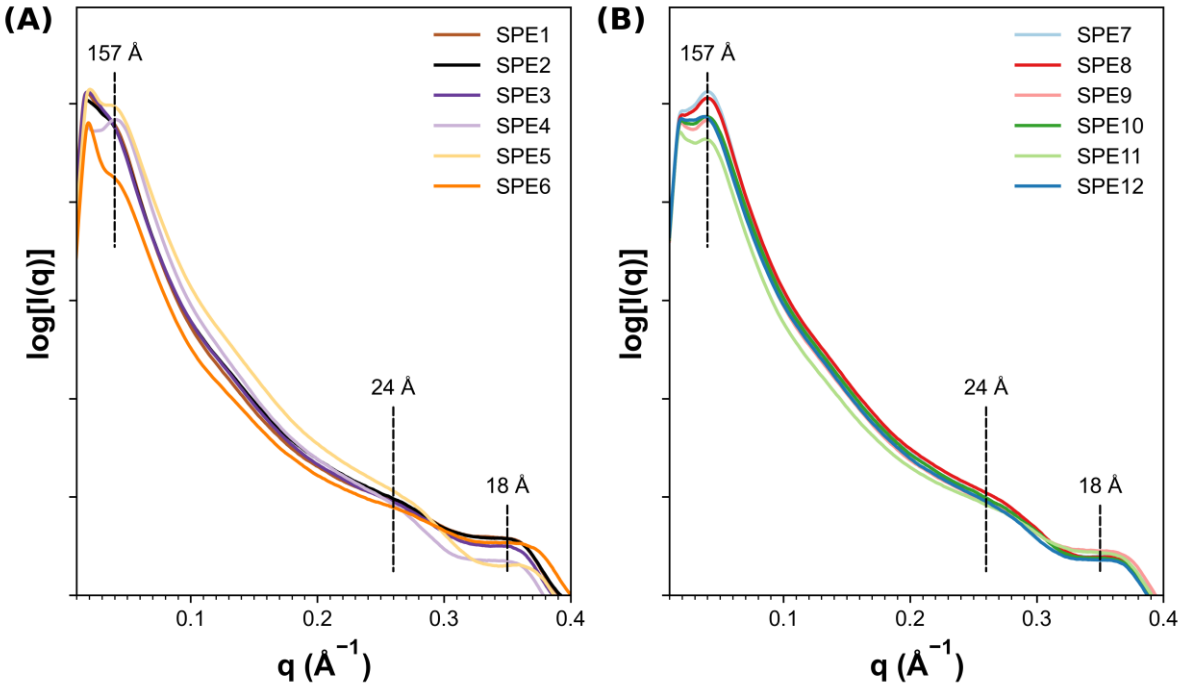

Figure 22. A) SAXS intensity profiles of the **SPE1-6 (B)** SAXS intensity profiles of the **SPE7-12.** The datasets were acquired at room temperature.

Further insight into the assembly of the hard domains was determined by wide-angle X-ray scattering (WAXS), which showed broad reflections at *ca.* 15.7 Å. Furthermore, reflections (*ca.* 3.6 Å), characteristic of π–π stacking assemblies, were also evident (see Figure 6).[40]

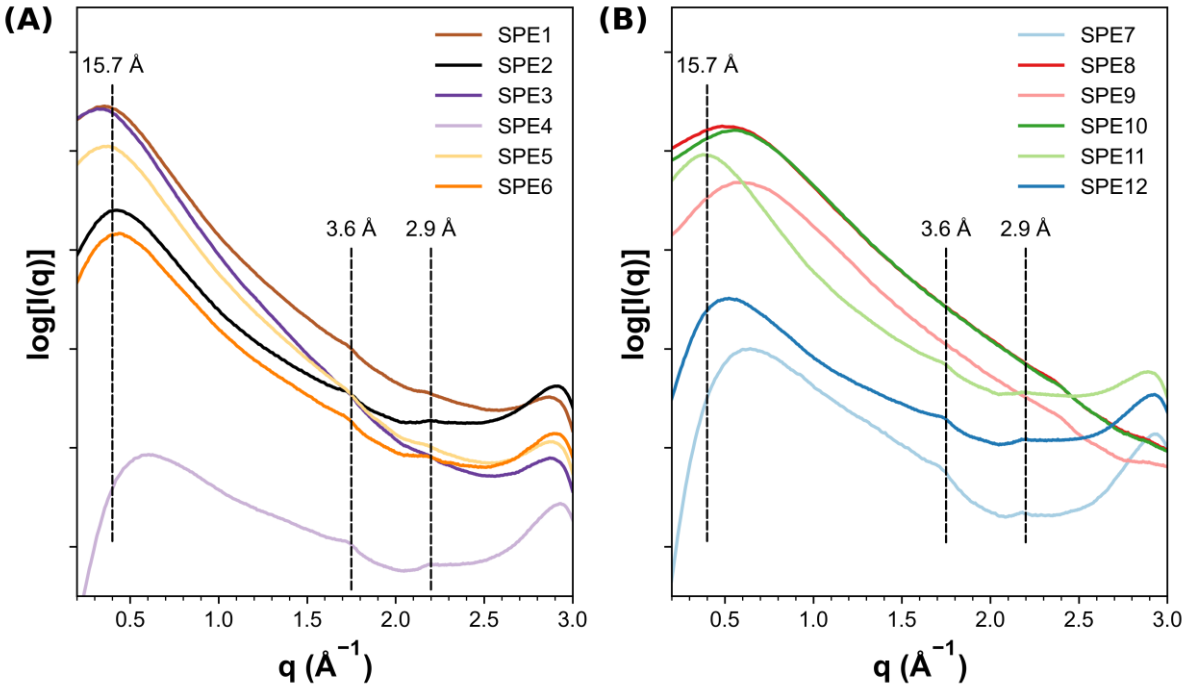

Figure 23. A) WAXS intensity profiles of the **SPE1**-**6 (B)** WAXS intensity profiles of the **SPE7**-**12** The datasets were acquired at room temperature.

Small amplitude oscillatory shear experiments were carried out to gain a more detailed understanding of the bulk material properties of the SPEs. Oscillatory frequency sweeps were conducted between 0 and 150 °C, and time-temperature superpositions (TTS) were performed (see Figure 7, shown for **SPE12**). All the SPEs exhibited a crossover frequency with an inversion of storage (G') and loss modulus (G''). At frequencies above the crossover, G' was dominant, and the materials behaved as elastomers. Increasing the density of hydrogen bonding motifs **4.12** and **4.13** with respect to **4.11** led to an elongated rubbery plateau and longer terminal relaxation times, which is estimated as the reciprocal of the crossover frequency. Evaluation of the relaxation times of the PUs for their flow transition at different temperatures was performed through frequency sweep experiments every 10 °C from 0 – 150 °C (see Figure 7 and see Appendix 3 Figures 44-55).

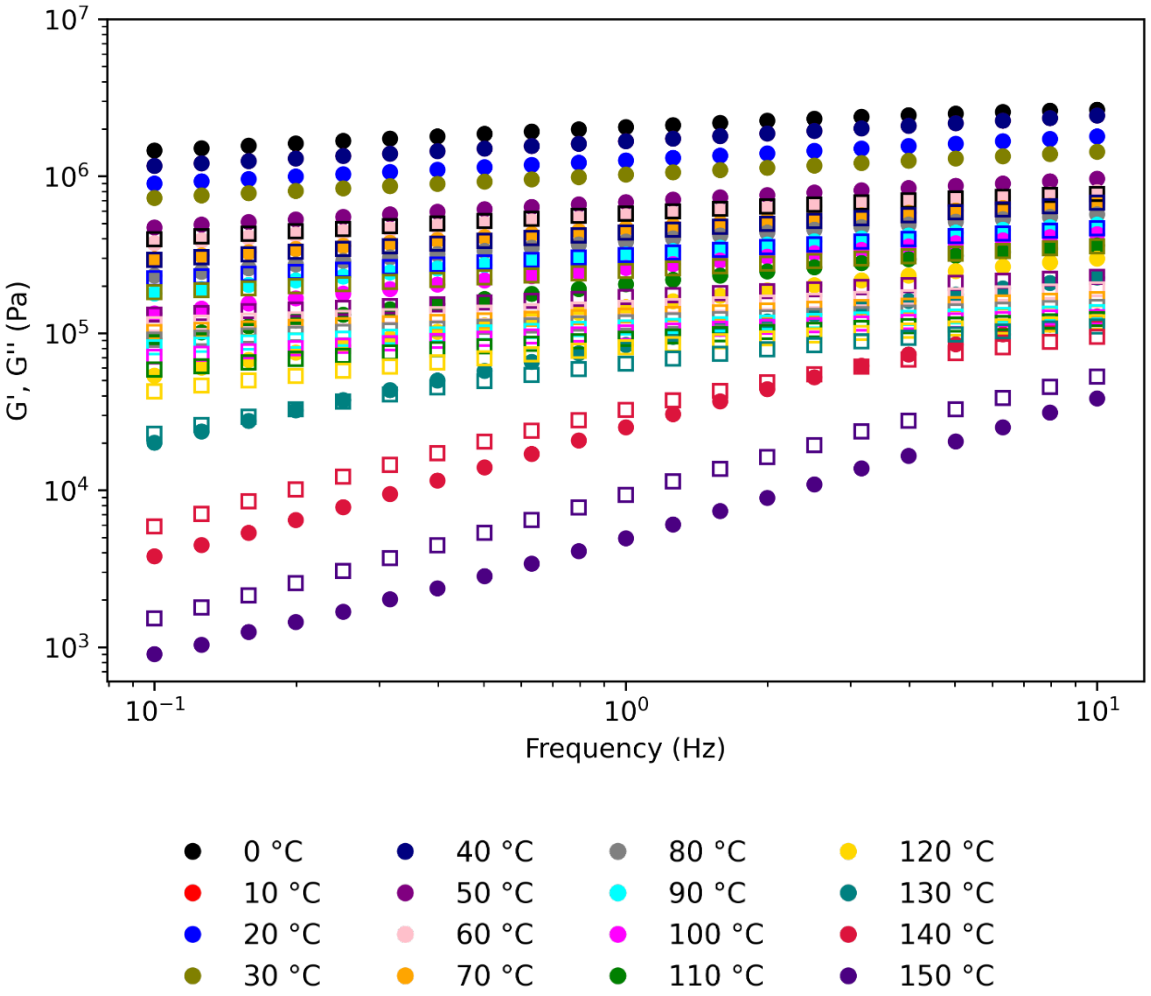

Figure 7. Frequency sweeps of **SPE12** at 0 (black), 10 (red), 20 (blue), 30 (olive), 40 (navy), 50 (purple), 60 (pink), 70 (orange), 80 (gray), 90 (cyan), 100 (magenta), 110 (green), 120 (gold), 130 (teal), 140 (crimson), 150 °C (indigo). G' closed symbols and G'' open symbols frequency sweeps were performed between 0.1 to 10 Hz at an applied strain of 0.1%.

The shear strain tolerance of the SPEs tested herein was determined by oscillatory amplitude sweeps at 1Hz, and all subsequent frequency sweep experiments were therefore conducted at 0.1% shear strain. van-Gurp Palmen plots were utilized to confirm the validity of performing a time-temperature superposition (see Appendix 3 Figures 56-67). Time-temperature

superposition (TTS) was performed for all the SPEs, and the curves were shifted to different reference temperatures (0, 50, 100 and 150 °C), see Figure 8).

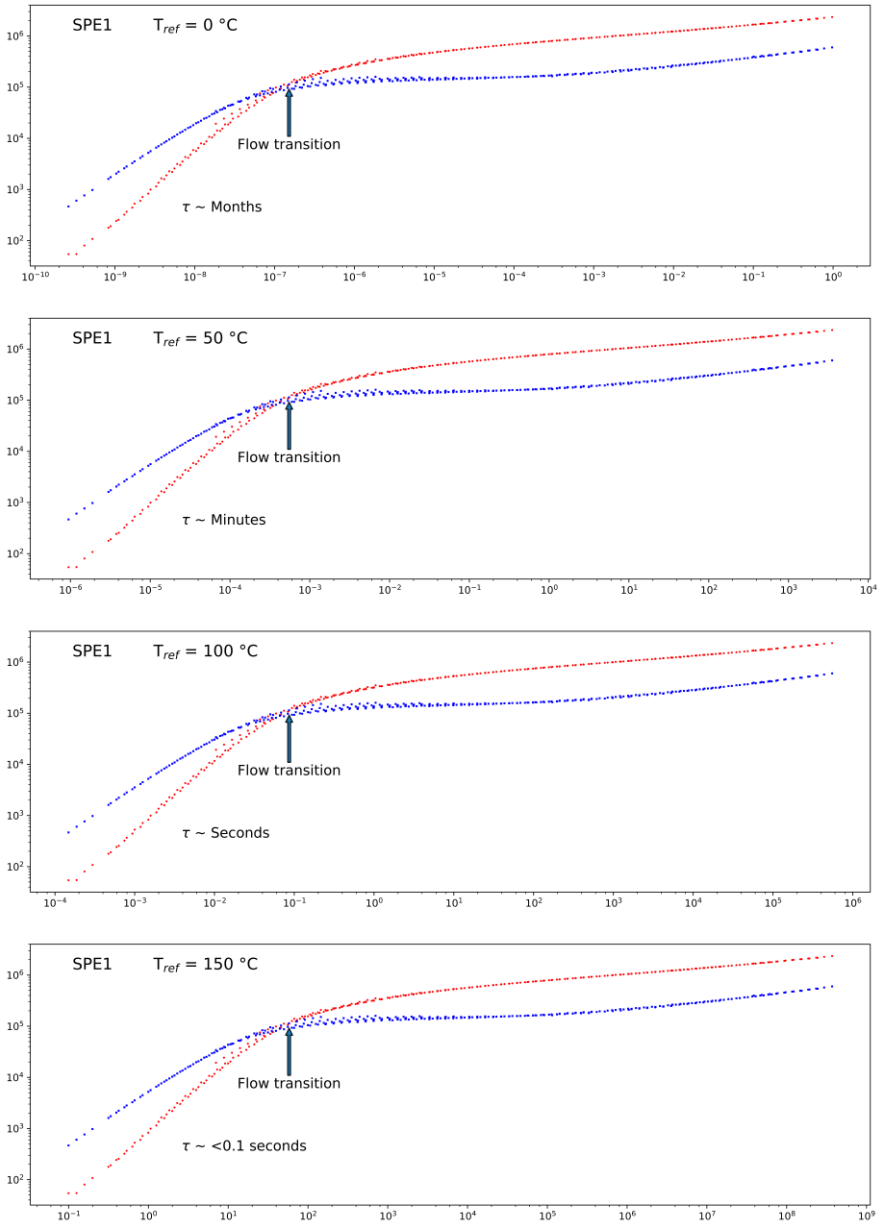

Figure 8. Master curves of **SPE1** at a reference temperature (T_{ref}) of 0, 50, 100, and 150 °C, prepared by the TTS for G' and G'' values obtained from frequency sweeps at 10 °C intervals from 0 to 150 °C, frequency sweeps were performed between 0.1 to 10 Hz at an applied strain of 0.1%.

The relaxation time of the SPEs was determined by taking the reciprocal of frequency (ω) at the point of inversion of G' (red) and G'' (blue) (see Table 5) according to $\tau = 2\pi/\omega$.[41,42] The crossover point of both G' and G'' is a generally accepted method to indirectly determine the average bond lifetime, τ, of supramolecular networks.[21,43] As anticipated, the viscoelastic properties of the SPEs were found to be temperature-dependent. For example, at temperatures below 30 °C, the SPEs were found to have a relaxation time on the order of days to weeks; however, upon heating to 40 °C, the relaxation time of the SPEs were found to

decrease hours. It has been shown that a bond lifetime ranging from 0.1 to 100 s is beneficial for optimum self-healing.[41,44–48] As expected, it was found that the supramolecular bond lifetime, τ, could be tuned across both the *-para* and *-meta* nitro series of SPEs. It was found that as the concentration of the pendant supramolecular assembly moiety increased, as did the length of the rubbery plateau, this extension of the rubbery plateau is an expected consequence of increasing the strength of the interactions between polymer chains through a combination of π-π stacking interactions, and urea to nitro, urea to urea hydrogen bonds from the pendant assembly motif. Interrogating the plateau moduli, no significant trend in change was observed; however, a clear trend emerges in terms of supramolecular bond lifetimes (see Table 5). As the concentration of **4.12** or **4.13** increases, so does the supramolecular bond lifetime, a direct consequence of the interactions from the pendant assembly units. This effect is pronounced, and at 2.5 mol% loading (**SPE1**), a supramolecular bond lifetime of 1800 s is observed, and an almost exponential trend becomes apparent as there are two orders of magnitude increase between **SPE1** and **SPE6**. Furthermore, there are three orders of magnitude differences between **SPE7** and **SPE12**. Evaluation of the apparent activation energies (E_a) for polymer chain slippage was estimated by applying an Arrhenius fit to the TTS data (see Table 5),[49] it was found that as the percentage of supramolecular motif increased, as did the apparent activation energy required to induce polymer slippage. For example, Arrhenius activation energies of 13.9 and 12.7 kJ mol^{-1} were estimated from the TTS data for **SPE1** and **SPE6**, respectively, compared to **SPE7** and **SPE12** which required 21.6 and 21.8 kJ mol^{-1}, respectively. This observation is rationalised by increasing the concentration of the sticker pendant to the polymer backbone as more sites are available for self-assembly, and therefore more energy is required to induce chain slippage.

Table 12. Plateau moduli (G_p), supramolecular bond lifetimes (τ) of supramolecular polymer networks at 50 °C (rounded to nearest 100 s).

SPE	G_p (× 10^5 Pa)[a]	τ (s)	E_a (× 10^4) (kJ mol^{-1})
SPE1	9.16	1800	13.9
SPE2	1.99	1200	13.6
SPE3	2.02	5500	16.7
SPE4	1.13	6087	18.7
SPE5	1.29	238000	17.9
SPE6	8.88	246100	21.6
SPE7	8.62	600	12.7
SPE8	8.68	1900	13.7
SPE9	9.63	9300	14.3
SPE10	2.02	72400	17.5
SPE11	5.07	116000	16.6
SPE12	2.01	279300	21.8

[a] G_p is equal to the storage modulus at the minimum of the loss tangent.[50]

4.4 Mechanical properties

The mechanical properties of the SPEs prepared in this study varied widely depending on the different amounts of hydrogen bonding motifs pendant to the polymeric backbones (see Figure 11). As shown in the stress-strain curves in Figure 9, increasing the amount of the aromatic nitro-urea assembly motif improved mechanical properties, such as elongation at break and ultimate tensile strength. Increasing the concentration of the self-assembly unit from 2.5mol% (**SPE1**) to 15mol% (**SPE6**) led to a significant increase in UTS from 7.57 to 17.93 MPa. Generally, the -meta nitro substituted pendant groups provided SPEs with greater UTS at the same loading as the -para regioisomers (excluding **SPE11**), and the elongation at break shows the reverse trend (excluding **SPE2**). Furthermore, where there is usually a significant trade-off between elasticity and ultimate tensile strength in elastomeric materials, the same trend could not be applied to the comparison of **SPE1** to **SPE6,** which had comparable elongation at break values of 10.9 and 11.1, respectively. The same trend is observed for the *-para* nitro series, **SPE7** to **SPE12**. The exceptional tensile strength of the polymers in this study could be attributed to the strong, highly directional assembly of the bis-aromatic urea motif pendant to the polymeric backbones.[51] Previous studies reported by Bao and co-workers on telechelic polymer crosslinked by metal-ligand interactions showed enhanced elasticity and tensile strength and associated it with the reversible formation of intramolecular loops within the same chain and intermolecular loops between chains.[52] A similar effect could be seen here as the

aromatic nitro-urea hydrogen bonding units self-assemble. In an unstrained state, the intrachain loops result in the folding of the polymer backbone.[52–54]

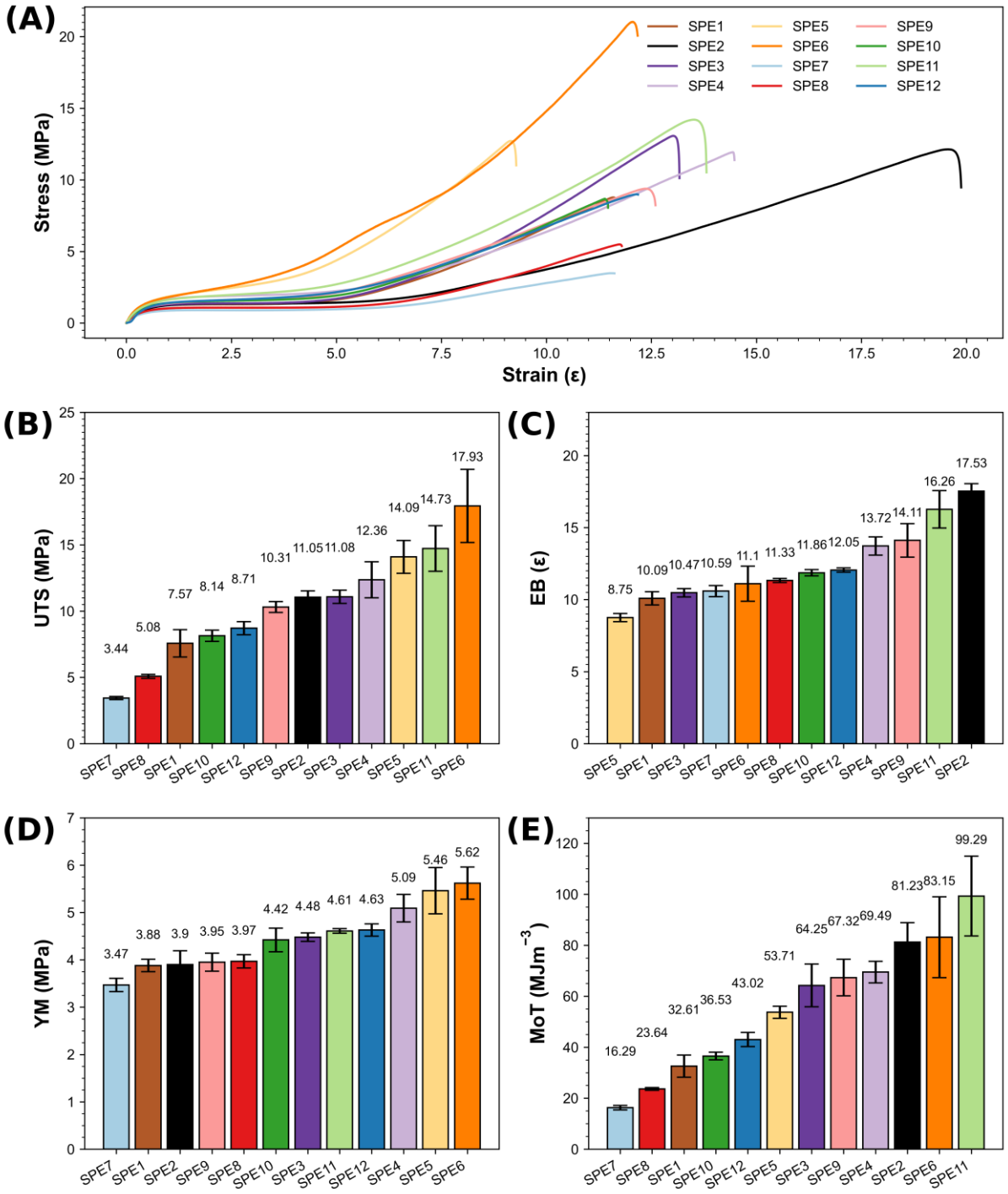

Figure 9. (A) Representative stress-strain curves of supramolecular elastomers, **SPE1–SPE12**. Comparison of **(B)** ultimate tensile strength (UTS), **(C)** elongation at break (EB), **(D)** Young's modulus (YM), and **(E)** modulus of toughness (MoT). The error shown is the standard deviation between the three repeats for each sample.

4.5 Self-healing properties

Supramolecular elastomers, which rely on non-covalent interactions such as hydrogen bonding for their mechanical properties, can be processed similarly to conventional thermoplastics as the non-covalent interactions are temperature dependent, applying heat to the polymer allows for the dissociation and reassociation of the supramolecular motifs. The proficiency of the SPEs to heal after being cut into two separate pieces was assessed by tensile testing. Rectangular specimens were cut in half with a scalpel, immediately butted together, and placed in an oven at 90 °C for two hours. The samples were removed from the oven and allowed to cool to room temperature over five hours before being assessed by tensile testing. Upon comparing the pristine tensile data to the tensile data for the samples which were cut in half and healed, it was found that healing efficiencies were, on average greater than 90% for the SPEs chain extended with **4.15** (nitro substituent in the *-para* position) and in some cases even exceeded 100% (see Table 6).

Healing efficiencies greater than 100% are a well-known phenomenon observed in self-healing hydrogen-bonded materials and is usually a case of the material not reaching an energetic minimum prior to pristine testing.[55–57] Assessing first *-meta* nitro series of SPEs (**SPE1**-**6**), modest recoveries were observed in terms of UTS, ranging from 64 to 84% recovery of tensile strength. In terms of elongation at break, **SPE1** recovered 120% of the pristine elasticity, and the remaining SPEs ranged from 60 to 114% in terms of recovery. Assessing the *-para* nitro series, at only 2.5 mol% loading (**SPE7**) - healing efficiencies for UTS, EB, YM and MoT ranged from 89% to 95%, and at higher loading ranged from 99% to 111% in terms of recovery of mechanical properties. Gratifyingly when the loading of the supramolecular motif was 15 mol% (**SPE12**), an appreciable drop off in healing efficiency was not observed because of the rigidity imposed by a higher density of pendant hydrogen bond motifs.[58]

Table 13. Healing data for the SPEs; the order of data in the table for each entry is as follows:– pristine SPE; healed SPE; % healing.

End-group	Healed UTS (MPa)	Healed EB (ε)	Healed Young's Modulus (MPa)	Healed Modulus of Toughness (MJm^{-3})
SPE1	7.57 ± 1.03	10.09 ± 0.46	3.88 ± 0.13	32.61 ± 4.34
	5.38 ± 0.14	12.09 ± 0.23	3.68 ± 0.28	23.66 ± 0.27
	71%	120%	95%	73%
SPE2	11.05 ± 0.48	17.53 ± 0.52	3.90 ± 0.29	81.23 ± 7.65
	8.22 ± 0.28	10.57 ± 0.77	4.31 ± 0.05	33.70 ± 3.40
	74%	60%	111%	41%
SPE3	11.08 ± 0.50	10.47 ± 0.29	4.48 ± 0.09	64.25 ± 8.39
	9.34 ± 0.53	11.98 ± 0.28	4.19 ± 0.06	39.98 ± 2.84
	84%	114%	94%	65%
SPE4	12.36 ± 1.36	13.72 ± 0.63	5.09 ± 0.29	69.49 ± 4.24
	7.88 ± 0.52	13.87 ± 0.85	3.69 ± 0.10	41.35 ± 4.68
	64%	101%	73%	60%
SPE5	14.09 ± 1.24	8.75 ± 0.28	5.46 ± 0.49	53.71 ± 2.37
	9.13 ± 0.89	8.30 ± 0.42	5.13 ± 0.07	31.49 ± 4.46
	65%	95%	94%	59%
SPE6	17.93 ± 2.76	11.10 ± 1.22	5.63 ± 0.34	83.15 ± 15.84
	12.68 ± 0.50	9.15 ± 0.15	6.01 ± 0.42	45.29 ± 2.74
	71%	82%	107%	54%
SPE7	3.44 ± 0.12	10.39 ± 0.27	3.47 ± 0.14	16.29 ± 0.88
	3.25 ± 0.09	9.58 ± 0.18	3.30 ± 0.11	14.43 ± 0.40
	94%	92%	95%	89%
SPE8	5.08 ± 0.15	10.16 ± 0.23	3.97 ± 0.14	23.64 ± 0.53
	5.11 ± 0.43	10.62 ± 0.34	3.47 ± 0.13	22.06 ± 2.22
	101%	105%	87%	93%
SPE9	9.50 ± 0.77	14.11 ± 1.16	3.95 ± 0.19	59.50 ± 8.66
	10.87 ± 0.78	13.03 ± 0.49	3.75 ± 0.07	56.24 ± 5.84
	115%	92%	95%	95%
SPE10	7.81 ± 0.43	10.69 ± 0.33	4.49 ± 0.20	33.96 ± 2.49
	8.69 ± 0.40	12.28 ± 0.51	3.84 ± 0.02	41.71 ± 3.11
	111%	115%	85%	123%
SPE11	14.73 ± 1.72	14.56 ± 0.58	4.68 ± 0.07	99.29 ± 15.66
	8.29 ± 0.33	10.09 ± 0.30	4.85 ± 0.09	36.28 ± 1.28
	56%	69%	104%	37%
SPE12	8.71 ± 0.50	10.82 ± 0.00	4.41 ± 0.22	43.02 ± 2.78
	9.57 ± 0.43	10.73 ± 0.21	4.90 ± 0.13	43.19 ± 2.50
	110%	99%	111%	100%

Variable temperature optical microscopy was utilised to visualise the healing process in real-time (see Figure 10). **SPE1** was divided into four pieces by cutting a cross into the polymer film before placing it onto the hot stage microscope stage. The hot stage was rapidly brought up to a temperature of 90 °C, and almost immediately (t = 1 minute), the supramolecular elastomer began to flow and fill the void space between the cut component. Between 3 and 12 minutes, the polymeric material started to 'zipper' up, and at ~24 minutes, the polymeric material was almost completely healed. After 40 minutes, a faint scratch remains where the elastomer was previously cut into four pieces, consistent with other healing studies involving supramolecular polyurethanes.[59]

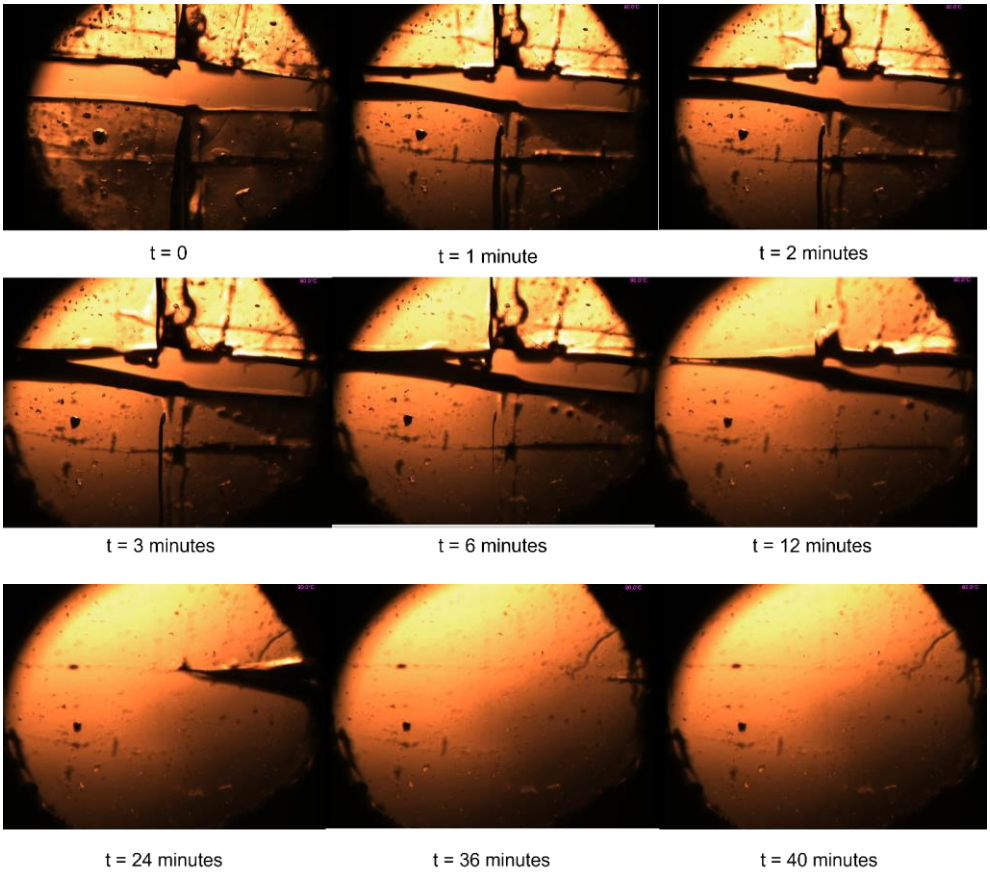

Figure 10. Variable temperature hot stage microscopy of **SPE1**. At t = 0, a crosscut was applied with a scalpel, the hot stage was then heated to 90 °C, and almost complete disappearance of the cut was observed within 40 minutes, with only a faint score mark observable on the surface.

4.6 Conclusions

In conclusion, this Chapter has described a rational approach to increasing the hydrogen bonding density within a supramolecular elastomer material by successfully incorporating two supramolecular motifs along and pendant to the backbone of PTMG polyurethane through a two-step polyurethane synthesis process. Detailed rheological analysis revealed that the average supramolecular bond lifetime could be tuned over three orders of magnitude by increasing the concentration of the supramolecular motif from 2.5 mol% to 15 mol%. Furthermore, polymer chain slippage was evaluated, and the required energy, as determined by Arrhenius plots, increased with the increasing concentration of pendant assembly moieties. Remarkably different mechanical properties were achieved by tuning the strength of the non-covalent assembly. The mechanical properties were easily attenuated by increasing the percentage of the pendant supramolecular motif relative to a non-functionalised chain extender. The Young's moduli of the materials synthesised were found to increase in a somewhat linear fashion with respect to the increasing percentage of the strongly associated bis-aryl urea pendant chains because of the formation of more hydrogen bonding interactions. The UTS of the *-para* nitro series increased from 3.44 ± 0.12 at 2.5 mol% loading to 9.50 ± 0.77 MPa at 7.5 mol%, and at higher loading, there appeared to be diminishing returns, and at

15 mol% an UTS of 8.71 ± 0.50 was achieved. Typically, there is a trade-off between UTS and elongation at break in supramolecular elastomers; however, in these studies, it was found that regardless of the percentage loading of the pendant supramolecular motif, the elastomers exhibited an elongation at break ranging between 10.16 ± 0.23 to 14.56 ± 0.58 times its original length. Furthermore, the ability of the supramolecular elastomers to heal was assessed, and at only 2.5 mol% loading - healing efficiencies ranged from 89% to 95%, and at higher loading ranged from 99% to 111%, recovery of mechanical properties. Comparing both regioisomers at the same loading, a trend emerges; to create materials with higher UTS, *-meta* nitro substitution is preferred; however, if elasticity is the desired mechanical property, then *-para* nitro substitution delivers materials with greater elongation at break.

4.7 Experimental Section

General. Tetrahydrofuran (THF) was distilled from benzophenone and sodium before use. Dry dimethylacetamide (DMAc) (Sigma Aldrich) was used as supplied. Tetrahydrofuran All other reagents were purchased from Sigma Aldrich and used as received.

Analysis. The analytical data for compounds **4.12** and **4.13** plus **SPE1**–**SPE12** are reported in Appendix 3. Analytical techniques used to characterise the compounds and polymers reported in this Chapter are described in Sections 2.9 and 3.4 unless specified below.

The casting of the SPEs was performed as follows: the dried polymer was dissolved in a minimum volume of THF (approximately 3 mL per 1 g of polymer) at 40 °C whilst stirring. Once fully dissolved, the polymer solution was poured into a 10 cm × 10 cm mould with a PTFE base. The solvent was allowed to evaporate slowly over 24 hours at room temperature and pressure. The mould was placed into a vacuum oven at 60 °C for 24 hours, then under partial vacuum (approximately 800 mbar) at 60 °C for 24 hours, and finally at 10 mbar for 24 hours. The polymer film was then allowed to reach room temperature before removal from the mould.

Synthesis. The synthesis and analytical data of compounds **2.1** and **2.5** is reported in *Chapter 2*.

Synthesis of bis-benzylic alcohols 4.12 and 4.13.

Briefly, the appropriate isocyanate was reacted with 5-aminoisophthalic acid and purified through pH switching and trituration. Synthesis of **4.12** and **4.13** was achieved by suspending **2.5** (5.0 g, 14.48 mmol) or **4.1** (5.0 g, 14.48 mmol), respectively, in THF (60 mL) and cooling the solution down to 0 °C. Borane tetrahydrofuran complex solution (58 mL, 1M in THF) was then added dropwise at 0 °C. The reaction mixture was then stirred at 20 °C for 16 hours. The mixture was cooled to 0 °C, and MeOH was added until hydrogen evolution ceased. The reaction mixture was evaporated in *vacuo,* redissolved in MeOH (150 mL), evaporated to dryness and further purified by gradient flash column chromatography (5-50% EtOH: hexane) to yield diols **4.12** (3.81 g, 83%), and **4.13** (3.31 g, 72%), respectively.

1-(3,5-bis(hydroxymethyl)phenyl)-3-(4-nitrophenyl)urea (**4.12**). Mp 225-227 °C; FTIR ATR (cm^{-1}): 3344 (νN-H), 3308 (νN-H), 3221 (νO-H), 2995 (νC-$H_{aromatic}$), 2923 (νC-H_{alkyl}), 2872 (νC-H_{alkyl}), 1717 (νC=O), 1707 (νC=O), 1689(νC=O), 1601(νN-H), 1612 (νN-H), 1548 (νN-$O_{asymmetric}$), 1294 (νN-$O_{symmetric}$); ^{1}H NMR δ $_{H}$ (400 MHz, DMSO-d_6) 9.42 (1 H, s), 8.94 (1 H, s), 8.23 – 8.14 (2 H, AA'XX'), 7.76 – 7.65 (2 H, AA'XX'), 7.32 (2 H, s), 6.93 (1 H, s), 5.20 (2 H, t, *J* = 5.7 Hz), 4.47 (4 H, d, *J* = 5.7 Hz). ^{13}C NMR (100 MHz, DMSO-d_6) δ 151.9, 146.5, 143.1, 140.9, 138.7, 125.2, 118.7, 117.4, 115.0, 62.9. HRMS (ESI, m/z): calcd for $C_{15}H_{16}N_3O_5$ ($[M+H]^+$) 318.1084, found 318.1083.

1-(3,5-bis(hydroxymethyl)phenyl)-3-(3-nitrophenyl)urea (**4.13**). Mp 201-203 °C; FTIR ATR (cm^{-1}): 3373 (νN-H), 3301 (νN-H), 3259 (νO-H), 2995 (νC-$H_{aromatic}$), 2934 (νC-H_{alkyl}), 2851 (νC-H_{alkyl}), 1670 (νC=O), 1611 (νN-H), 1596 (νN-H), 1547 (νN-$O_{asymmetric}$), 1343 (νN-$O_{symmetric}$); ^{1}H NMR δ $_{H}$ (400 MHz, DMSO-d_6) 9.18 (1 H, s), 8.84 (1 H, s), 8.60 (1 H, t, *J* = 2.2 Hz), 7.81 (1 H, dd, *J* = 8.2, 2.3 Hz), 7.73 – 7.63 (1 H, dd, *J* = 8.2, 2.3 Hz), 7.55 (1 H, t, *J* = 8.2), 7.33 (2 H, s), 6.92 (1 H, s), 4.96 (2 H, br. s) 4.47 (4 H, appt. s). ^{13}C NMR (100 MHz, DMSO-d_6) δ 152.4, 148.2, 143.1, 141.1, 138.9, 130.1, 124.2, 118.5, 116.2, 114.9, 112.0, 63.0. HRMS (ESI, m/z): calcd for $C_{15}H_{16}N_3O_5$ ($[M+H]^+$) 318.1084, found 318.1083.

General synthesis of SPEs

Poly(tetramethylene ether) glycol (PTMG) (M_n = 2000 g/mol) was dried under vacuum at 80 °C for 2 hours. In the bulk, PTMG was mixed with 2.05 equivalents of 4,4′-methylenebis(cyclohexyl isocyanate) (HMDI) and a catalytic quantity of dibutyltin dilaurate (DBTDL) (0.01 eq.) at 70 °C for 3 hours with gentle stirring. The colourless pre-polymer was cooled to 20 °C and dissolved in anhydrous DMAc (100 mL). **4.11**, and either **4.15** or **4.16** were then dissolved in DMAc (10 mL) in the correct stoichiometry (see Table 1) and added in one portion. The reaction mixture was then stirred at 20 °C for 4 hours, at which point the infrared stretch associated with the isocyanate terminals was no longer present. A further portion of DMAc (100 mL) was then added, and the reaction mixture was heated to 60 °C to decrease the viscosity of the polymer solution, which was then precipitated into water (1500 mL), the resultant polymer was redissolved in THF (100 mL) and precipitated into water (3 × 1000 mL) to remove excess DMAc. The polymeric material was then dried in *vacuo.*

SPE1-12

The synthesis was carried out according to the general synthetic protocol described above for the SPEs. The polymer was isolated as a yellow elastomeric material.

SPE 1

FTIR ATR (cm^{-1}): 3325 ($\nu N\text{-}H_{stretch}$), 2935 ($\nu C\text{-}H_{aromatic}$), 2853 ($\nu C\text{-}H_{alkyl}$), 2797 ($\nu C\text{-}H_{alkyl}$), 1720 ($\nu C{=}O_{urethane}$), 1700 ($\nu C{=}O_{urethane}$), 1660 ($\nu C{=}O_{urea}$), 1226 ($\nu C\text{-}N_{stretch}$); ^{1}H NMR δ_{H} (400 MHz, $CDCl_3$) 8.08 (1 H, m), 7.92 – 7.69 (1 H, m), 7.26 (297 H, m), 6.95 (4 H, m), 4.98 (343 H, m), 4.68 (171 H, m), 4.38 (19 H, m), 4.00 (196 H, m), 3.75 (143 H, m), 3.37 (5803 H, m), 2.14 (140 H, m), 1.93 (240 H, m), 1.57 (7184 H, m), 1.06 (1310 H, H, m). ^{13}C NMR (100 MHz, $CDCl_3$) δ 156.0, 155.6, 137.0, 128.8, 70.6, 70.3, 66.3, 64.4, 50.5, 50.3, 47.1, 44.1, 43.0, 33.8, 33.6, 33.4, 32.7, 32.5, 32.1, 30.1, 29.7, 29.3, 28.2, 28.1, 26.5, 26.3, 25.9. GPC (DMF) M_n = 184000 g mol^{-1}, M_w = 103200 g mol^{-1}, Đ = 1.78.

SPE 2

FTIR ATR (cm^{-1}): 3328 ($\nu N\text{-}H_{stretch}$), 2931 ($\nu C\text{-}H_{aromatic}$), 2854 ($\nu C\text{-}H_{alkyl}$), 2801 ($\nu C\text{-}H_{alkyl}$), 1720 ($\nu C{=}O_{urethane}$), 1700 ($\nu C{=}O_{urethane}$), 1660 ($\nu C{=}O_{urea}$), 1226 ($\nu C\text{-}N_{stretch}$); ^{1}H NMR δ_{H} (400 MHz, $CDCl_3$) 8.26 (1 H, m), 7.85 (1 H, m), 7.32 (152 H, m), 6.98 (5 H, m), 5.06 (117 H, m), 4.71 (110 H, m), 4.03 (87 H, m), 3.77 (63 H, m), 3.40 (2479 H, m), 1.97 (104 H, m), 1.86 (98 H, m), 1.73 – 1.45 (2963 H, m), 1.32 (293 H, m), 1.13 – 0.74 (465 H, m). ^{13}C NMR (100 MHz, $CDCl_3$) δ 156.0, 155.6, 137.1, 128.9, 127.9, 70.8, 70.7, 70.4, 66.4, 64.5, 50.4, 47.2, 43.1, 33.8, 33.7, 33.5, 32.8, 32.1, 30.4, 29.8, 29.4, 28.1, 26.6, 26.3, 26.0. GPC (DMF) M_n = 82800 g mol^{-1}, M_w = 176000 g mol^{-1}, Đ = 2.13

SPE 3

FTIR ATR (cm^{-1}): 3318 ($\nu N\text{-}H_{stretch}$), 2934 ($\nu C\text{-}H_{aromatic}$), 2854 ($\nu C\text{-}H_{alkyl}$), 280 ($\nu C\text{-}H_{alkyl}$), 1717 ($\nu C{=}O_{urethane}$), 1700 ($\nu C{=}O_{urethane}$), 1660 ($\nu C{=}O_{urea}$), 1226 ($\nu C\text{-}N_{stretch}$); ^{1}H NMR δ_{H} (400 MHz, $CDCl_3$) 8.18 (1 H, m), 7.95 – 7.73 (2 H, m), 7.30 (60 H, m), 6.98 (1 H, m), 5.06 (48 H, m), 4.97 – 4.41 (43 H, m), 4.03 (34 H, m), 3.77 (25 H, m), 3.39 (998 H, m), 2.07 – 1.80 (78 H, m), 1.60 (1185 H, m), 1.41 (51 H, s), 1.23 (48 H, m), 1.15 – 0.77 (187 H, m). ^{13}C NMR (100 MHz, $CDCl_3$) δ 156.0, 155.6, 137.1, 128.9, 127.9, 77.5, 77.4, 77.2, 77.0, 76.8, 70.8, 70.7, 70.4, 64.5, 50.4, 47.2, 43.0, 33.8, 33.7, 33.7, 33.5, 32.1, 29.8, 28.1, 26.8, 26.6, 26.3, 26.0. GPC (DMF) M_n = 122200 g mol^{-1}, M_w = 232200 g mol^{-1}, Đ = 1.90

SPE 4

FTIR ATR (cm^{-1}): 3338 ($\nu N\text{-}H_{stretch}$), 2935 ($\nu C\text{-}H_{aromatic}$), 2853 ($\nu C\text{-}H_{alkyl}$), 2802 ($\nu C\text{-}H_{alkyl}$), 1717 ($\nu C{=}O_{urethane}$), 1700 ($\nu C{=}O_{urethane}$), 1660 ($\nu C{=}O_{urea}$), 1227 ($\nu C\text{-}N_{stretch}$); ^{1}H NMR δ_{H} (400 MHz, $CDCl_3$) 8.18 (1 H, m), 7.84 (2 H, m), 7.47 – 7.10 (54 H, m), 6.98 (2 H, m), 5.06 (44 H, s), 4.98 – 4.39 (43 H, m), 4.03 (35 H, s), 3.78 (24 H, s), 3.40 (947 H, s), 2.10 – 1.89 (40 H, m), 1.61 (1224 H, d, J 5.3), 1.31 – 0.80 (233 H, m). ^{13}C NMR (100 MHz, $CDCl_3$) δ 156.0, 155.6, 137.1, 128.9, 127.9, 70.8, 70.7, 70.4, 66.4, 64.6, 47.2, 33.9, 33.8, 33.6, 32.8, 32.2, 29.8, 29.4, 28.2, 26.6, 26.4, 26.0. GPC (DMF) M_n = 101900 g mol^{-1}, M_w = 187800 g mol^{-1}, Đ = 1.84

SPE 5

FTIR ATR (cm^{-1}): 3326 ($\nu N\text{-}H_{stretch}$), 2925 ($\nu C\text{-}H_{aromatic}$), 2853 ($\nu C\text{-}H_{alkyl}$), 2797 ($\nu C\text{-}H_{alkyl}$), 1717 ($\nu C{=}O_{urethane}$), 1702 ($\nu C{=}O_{urethane}$), 1660 ($\nu C{=}O_{urea}$), 1226 ($\nu C\text{-}N_{stretch}$); ^{1}H NMR δ_{H} (400 MHz, $CDCl_3$) 8.18 (1 H, s), 7.85 (2 H, m), 7.47 – 7.07 (116 H, m), 6.98 (4 H, m), 5.33 (2 H, m), 5.06 (88 H, s), 4.98 – 4.38 (89 H, m), 4.03 (67 H, s), 3.77 (47 H, s), 3.40 (2025 H, s), 1.97 (92 H, s), 1.86 (100 H, s), 1.60 (2576 H, s), 1.32 – 0.69 (699 H, m). ^{13}C NMR (100 MHz, $CDCl_3$) δ 155.9, 155.5, 137.0, 128.8, 70.6, 70.3, 66.3, 64.4, 50.5, 50.3, 47.1, 33.6, 33.4, 32.5, 32.0, 30.3, 30.1, 29.7, 29.5, 29.3, 29.3, 28.0, 26.5, 26.2, 25.9, 25.5, 22.7, 14.1, 13.6. GPC (DMF) M_n = 184500 g mol^{-1}, M_w = 408500 g mol^{-1}, Đ = 2.21

SPE 6

FTIR ATR (cm^{-1}): 3322 ($\nu N\text{-}H_{stretch}$), 2939 ($\nu C\text{-}H_{aromatic}$), 2853 ($\nu C\text{-}H_{alkyl}$), 2797 ($\nu C\text{-}H_{alkyl}$), 1717 ($\nu C{=}O_{urethane}$), 1700 ($\nu C{=}O_{urethane}$), 1660 ($\nu C{=}O_{urea}$), 1226 ($\nu C\text{-}N_{stretch}$); ^{1}H NMR δ_{H} (400 MHz, $CDCl_3$) 8.19 (1 H, s), 7.84 (1 H, s), 7.46 – 7.21 (23 H, m), 5.07 (15 H, s), 4.97 – 4.44 (16 H, m), 4.04 (12 H, s), 3.79 (10 H, s), 3.41 (286 H, s), 1.98 (17 H, s), 1.61 (378 H, s), 1.46 – 0.65 (142 H, m). ^{13}C NMR (100 MHz, $CDCl_3$) δ 156.3, 155.5, 137.0, 128.8, 127.9, 127.8, 127.7, 121.7, 111.7, 70.6, 70.3, 66.2, 64.4, 50.3, 47.1, 33.7, 33.4, 32.0, 29.7, 28.0, 26.5, 26.2, 25.9, 22.7, 14.1, 1.0. GPC (DMF) M_n = 101200 g mol^{-1}, M_w = 179000 g mol^{-1}, Đ = 1.76

SPE 7

FTIR ATR (cm^{-1}): 3327 ($\nu N\text{-}H_{stretch}$), 2931 ($\nu C\text{-}H_{aromatic}$), 2853 ($\nu C\text{-}H_{alkyl}$), 2799 ($\nu C\text{-}H_{alkyl}$), 1717 ($\nu C{=}O_{urethane}$), 1700 ($\nu C{=}O_{urethane}$), 1660 ($\nu C{=}O_{urea}$), 1226 ($\nu C\text{-}N_{stretch}$); ^{1}H NMR δ_{H} (400 MHz, $CDCl_3$) 8.63 (1 H, s), 8.10 (1 H, m), 7.52 (2 H, s), 7.28 (249 H, m), 6.97 (5 H, d, J 23.8), 5.03 (197 H, s), 4.98 – 4.44 (202 H, m), 4.01 (149 H, s), 3.75 (106 H, s), 3.37 (4547 H, s), 2.10 (106 H, s), 1.93 (189 H, s), 1.58 (5484 H, s), 1.43 – 1.19 (461 H, m), 1.18 – 0.71 (929 H, m). ^{13}C NMR (100 MHz, $CDCl_3$) δ 156.0, 155.6, 137.1, 137.0, 137.0, 128.8, 127.8, 127.7, 127.7, 125.5, 70.8, 70.7, 70.6, 70.5, 70.3, 66.4, 64.4, 50.5, 50.3, 47.1, 47.0, 44.1, 43.9, 43.0, 41.7, 33.8, 33.7, 33.5, 33.4, 32.7, 32.6, 32.1, 31.9, 30.4, 30.1, 29.7, 29.6, 29.5, 29.3, 28.1, 26.7, 26.5, 26.3, 26.0, 25.9. GPC (DMF) M_n = 85400 g mol^{-1}, M_w = 150300 g mol^{-1}, Đ = 1.76

SPE 8

FTIR ATR (cm^{-1}): 3327 ($\nu N\text{-}H_{stretch}$), 2929 ($\nu C\text{-}H_{aromatic}$), 2853 ($\nu C\text{-}H_{alkyl}$), 2800 ($\nu C\text{-}H_{alkyl}$), 1717 ($\nu C{=}O_{urethane}$), 1700 ($\nu C{=}O_{urethane}$), 1660 ($\nu C{=}O_{urea}$), 1226 ($\nu C\text{-}N_{stretch}$); ^{1}H NMR δ_{H} (400 MHz, $CDCl_3$) 8.59 (1 H, s), 8.18 – 7.93 (3 H, m), 7.52 (164 H, m), 6.97 (5 H, m), 5.04 (135 H, s), 4.95 – 4.47 (124 H, m), 4.01 (104 H, s), 3.75 (69 H, s), 3.38 (2906 H, s), 2.09 (65 H, s), 1.94 (129 H, s), 1.58 (3474 H, s), 1.39 (140 H, s), 1.22 (185 H, s), 1.14 – 0.75 (552 H, m). ^{13}C NMR (100 MHz, $CDCl_3$) δ 156.0, 155.6, 137.0, 128.8, 127.9, 127.5, 126.3, 70.9, 70.9, 70.8, 70.7, 70.5, 70.3, 66.3, 64.4, 50.5, 50.3, 47.1, 44.1, 43.0, 41.7, 33.8, 33.7, 33.5, 32.7, 32.6, 32.1, 30.4,

30.1, 29.7, 29.5, 29.3, 28.1, 26.7, 26.6, 26.3, 26.1, 26.0, 25.5, 22.7. GPC (DMF) M_n = 91100 g mol^{-1}, M_w = 176300 g mol^{-1}, Đ = 1.94

SPE 9

FTIR ATR (cm^{-1}): 3327 (νN-H$_{stretch}$), 2931 (νC-H$_{aromatic}$), 2853 (νC-H$_{alkyl}$), 2802 (νC-H$_{alkyl}$), 1717 (νC=O$_{urethane}$), 1700 (νC=O$_{urethane}$), 1660 (νC=O$_{urea}$), 1226 (νC-N$_{stretch}$); ^{1}H NMR δ $_H$ (400 MHz, $CDCl_3$) 8.14 (1 H, s), 7.53 (1 H, m), 7.39 – 7.15 (31 H, m), 7.07 – 6.88 (1 H, m), 5.07 (26 H, s), 4.97 – 4.44 (23 H, m), 4.03 (19 H, s), 3.78 (13 H, s), 3.40 (528 H, s), 1.96 (27 H, s), 1.61 (688 H, s), 1.34 – 0.84 (131 H, m). ^{13}C NMR (100 MHz, $CDCl_3$) δ 156.1, 155.6, 137.1, 128.9, 127.9, 70.7, 70.4, 66.4, 64.5, 50.4, 47.2, 33.8, 33.7, 33.6, 32.1, 29.8, 28.1, 26.6, 26.3, 26.0. GPC (DMF) M_n = 125800 g mol^{-1}, M_w = 236900 g mol^{-1}, Đ = 1.88

SPE 10

FTIR ATR (cm^{-1}): 3327 (νN-H$_{stretch}$), 2931 (νC-H$_{aromatic}$), 2853 (νC-H$_{alkyl}$), 2801 (νC-H$_{alkyl}$), 1717 (νC=O$_{urethane}$), 1700 (νC=O$_{urethane}$), 1660 (νC=O$_{urea}$), 1227 (νC-N$_{stretch}$); ^{1}H NMR δ $_H$ (400 MHz, $CDCl_3$) 8.38 (1 H, s), 8.13 (1 H, s), 7.86 (1 H, s), 7.66 – 7.05 (37 H, m), 7.08 – 6.88 (2 H, m), 5.06 (27 H, s), 4.97 – 4.37 (27 H, m), 4.04 (23 H, s), 3.78 (19 H, s), 3.40 (555 H, s), 2.11 – 1.89 (30 H, m), 1.60 (704 H, s), 1.09 (134 H, m). ^{13}C NMR (100 MHz, $CDCl_3$) δ 156.1, 155.6, 137.1, 128.9, 127.9, 70.7, 70.4, 66.4, 64.6, 50.6, 50.4, 47.2, 44.2, 43.1, 33.9, 33.8, 33.6, 33.6, 32.8, 32.7, 32.2, 32.1, 29.8, 29.8, 28.2, 28.1, 28.0, 26.8, 26.6, 26.5, 26.3, 26.2, 26.0. GPC (DMF) M_n = 92800 g mol^{-1}, M_w = 165300 g mol^{-1}, Đ = 1.78

SPE 11

FTIR ATR (cm^{-1}): 3326 (νN-H$_{stretch}$), 2928 (νC-H$_{aromatic}$), 2853 (νC-H$_{alkyl}$), 2801 (νC-H$_{alkyl}$), 1716 (νC=O$_{urethane}$), 1700 (νC=O$_{urethane}$), 1660 (νC=O$_{urea}$), 1227 (νC-N$_{stretch}$); ^{1}H NMR δ $_H$ (400 MHz, $CDCl_3$) 8.15 (1 H, s), 7.54 (1 H, m), 7.46 – 7.18 (20 H, m), 7.10 – 6.84 (2 H, m), 5.07 (11 H, s), 4.97 – 4.31 (13 H, m), 4.04 (9 H, s), 3.78 (6 H, s), 3.63 (2 H, s), 3.41 (221 H, s), 2.05 – 1.89 (10 H, m), 1.82 – 1.44 (305 H, m), 1.43 – 1.02 (63 H, m), 1.03 – 0.77 (20 H, m). ^{13}C NMR (100 MHz, $CDCl_3$) δ 156.1, 155.6, 137.1, 128.9, 70.7, 70.4, 66.4, 64.5, 33.8, 33.6, 32.1, 29.8, 28.1, 26.6, 26.3, 26.0, 22.8. GPC (DMF) M_n = 123800 g mol^{-1}, M_w = 242800 g mol^{-1}, Đ = 1.96

SPE 12

FTIR ATR (cm^{-1}): 3327 (νN-H$_{stretch}$), 2930 (νC-H$_{aromatic}$), 2853 (νC-H$_{alkyl}$), 2801 (νC-H$_{alkyl}$), 1716 (νC=O$_{urethane}$), 1700 (νC=O$_{urethane}$), 1660 (νC=O$_{urea}$), 1227 (νC-N$_{stretch}$); ^{1}H NMR δ $_H$ (400 MHz, $CDCl_3$) 8.39 (1 H, s), 8.13 (2 H, s), 7.82 (1 H, s), 7.66 – 6.88 (30 H, m), 5.07 (23 H, s), 4.95 – 4.34 (20 H, m), 4.03 (16 H, s), 3.78 (11 H, s), 3.40 (440 H, s), 1.96 (20 H, s), 1.61 (575 H, s), 1.32 – 0.65 (116 H, m). ^{13}C NMR (100 MHz, $CDCl_3$) δ 155.9, 155.9, 137.0, 137.0, 128.8, 128.8, 127.9, 70.6, 70.2, 66.3, 64.4, 50.3, 47.1, 33.6, 33.4, 32.0, 29.7, 29.7, 28.0, 26.5, 26.5, 26.2, 25.9. GPC (DMF) M_n = 82600 g mol^{-1}, M_w = 149300 g mol^{-1}, Đ = 1.81

4.8 References

(1) Cordier, P.; Tournilhac, F.; Soulié-Ziakovic, C.; Leibler, L. Self-Healing and Thermoreversible Rubber from Supramolecular Assembly. *Nature* **2008**, *451* (7181), 977–980. https://doi.org/10.1038/nature06669.

(2) de Greef, T. F. A.; Meijer, E. W. Supramolecular Polymers. *Nature* **2008**, *453* (7192), 171–173. https://doi.org/10.1038/453171a.

(3) Sijbesma, R. P.; Beijer, F. H.; Brunsveld, L.; Folmer, B. J. B.; Hirschberg, J. H. K. K.; Lange, R. F. M.; Lowe, J. K. L.; Meijer, E. W. Reversible Polymers Formed from Self-Complementary Monomers Using Quadruple Hydrogen Bonding. *Science (80-.).* **1997**, *278* (5343), 1601–1604. https://doi.org/10.1126/science.278.5343.1601.

(4) Brunsveld, L.; Folmer, B. J. B.; Meijer, E. W.; Sijbesma, R. P. Supramolecular Polymers. *Chem. Rev.* **2001**, *101* (12), 4071–4097. https://doi.org/10.1021/cr990125q.

(5) Tan, M. W. M.; Thangavel, G.; Lee, P. S. Rugged Soft Robots Using Tough, Stretchable, and Self-Healable Adhesive Elastomers. *Adv. Funct. Mater.* **2021**, *31* (34), 1–12. https://doi.org/10.1002/adfm.202103097.

(6) Liu, J.; Tan, C. S. Y.; Scherman, O. A. Dynamic Interfacial Adhesion through Cucurbit[n]Uril Molecular Recognition. *Angew. Chemie - Int. Ed.* **2018**, *57* (29), 8854–8858. https://doi.org/10.1002/anie.201800775.

(7) Shi, C.; Zhang, Q.; Tian, H.; Qu, D. Supramolecular Adhesive Materials from Small-molecule Self-assembly. *SmartMat* **2020**, *1* (1), 1–19. https://doi.org/10.1002/smm2.1012.

(8) Courtois, J.; Baroudi, I.; Nouvel, N.; Degrandi, E.; Pensec, S.; Ducouret, G.; Chanéac, C.; Bouteiller, L.; Creton, C. Supramolecular Soft Adhesive Materials. *Adv. Funct. Mater.* **2010**, *20* (11), 1803–1811. https://doi.org/10.1002/adfm.200901903.

(9) Du, R.; Xu, Z.; Zhu, C.; Jiang, Y.; Yan, H.; Wu, H. C.; Vardoulis, O.; Cai, Y.; Zhu, X.; Bao, Z.; Zhang, Q.; Jia, X. A Highly Stretchable and Self-Healing Supramolecular Elastomer Based on Sliding Crosslinks and Hydrogen Bonds. *Adv. Funct. Mater.* **2020**, *30* (7), 1–9. https://doi.org/10.1002/adfm.201907139.

(10) Wei, Q.; Schlaich, C.; Prévost, S.; Schulz, A.; Böttcher, C.; Gradzielski, M.; Qi, Z.; Haag, R.; Schalley, C. A. Supramolecular Polymers as Surface Coatings: Rapid Fabrication of Healable Superhydrophobic and Slippery Surfaces. *Adv. Mater.* **2014**, *26* (43), 7358–7364. https://doi.org/10.1002/adma.201401366.

(11) Goor, O. J. G. M.; Brouns, J. E. P.; Dankers, P. Y. W. Introduction of Anti-Fouling Coatings at the Surface of Supramolecular Elastomeric Materials: Via Post-Modification of Reactive Supramolecular Additives. *Polym. Chem.* **2017**, *8* (34), 5228–5238. https://doi.org/10.1039/c7py00801e.

(12) Bosman, A. W.; Dankers, P. Y. W.; Janssen, H. M.; Meijer, E. W.; Van Gemert, G. M. L. Modular Bioresorbable Or Biomedical, Biologically Active Supramolecular Materials. US 9907637 B2, 2016.

(13) Wu, Y.; Wang, L.; Zhao, X.; Hou, S.; Guo, B.; Ma, P. X. Self-Healing Supramolecular Bioelastomers with Shape Memory Property as a Multifunctional Platform for Biomedical Applications via Modular Assembly. *Biomaterials* **2016**, *104*, 18–31. https://doi.org/10.1016/j.biomaterials.2016.07.011.

(14) Bosman, A. W.; Dankers, P. Y. W.; Janssen, H. M.; Meijer, E. W.; van Gemert, G. M. L. Modular Supramolecular Materials For Biomedical Uses. WO 2007/058539 A2, 2008.

(15) Kang, J.; Son, D.; Wang, G. J. N.; Liu, Y.; Lopez, J.; Kim, Y.; Oh, J. Y.; Katsumata, T.; Mun, J.; Lee, Y.; Jin, L.; Tok, J. B. H.; Bao, Z. Tough and Water-Insensitive Self-Healing Elastomer for Robust Electronic Skin. *Adv. Mater.* **2018**, *30* (13), 1–8. https://doi.org/10.1002/adma.201706846.

(16) Park, S.; Thangavel, G.; Parida, K.; Li, S.; Lee, P. S. A Stretchable and Self-Healing Energy Storage Device Based on Mechanically and Electrically Restorative Liquid-Metal Particles and Carboxylated Polyurethane Composites. *Adv. Mater.* **2019**, *31* (1), 1–10. https://doi.org/10.1002/adma.201805536.

(17) Hart, L. R.; Harries, J. L.; Greenland, B. W.; Colquhoun, H. M.; Hayes, W. Healable Supramolecular Polymers. *Polym. Chem.* **2013**, *4* (18), 4860–4870. https://doi.org/10.1039/c3py00081h.

(18) Tang, X.; Feula, A.; Baker, B. C.; Melia, K.; Hermida Merino, D.; Hamley, I. W.; Buckley, C. P.; Hayes, W.; Siviour, C. R. A Dynamic Supramolecular Polyurethane Network Whose Mechanical Properties Are Kinetically Controlled. *Polymer (Guildf).* **2017**, *133*, 143–150. https://doi.org/10.1016/j.polymer.2017.11.005.

(19) Fox, J.; Wie, J. J.; Greenland, B. W.; Burattini, S.; Hayes, W.; Colquhoun, H. M.; MacKay, M. E.; Rowan, S. J. High-Strength, Healable, Supramolecular Polymer Nanocomposites. *J. Am. Chem. Soc.* **2012**, *134* (11), 5362–5368. https://doi.org/10.1021/ja300050x.

(20) Burattini, S.; Colquhoun, H. M.; Fox, J. D.; Friedmann, D.; Greenland, B. W.; Harris, P. J. F.; Hayes, W.; MacKay, M. E.; Rowan, S. J. A Self-Repairing, Supramolecular Polymer System: Healability as a Consequence of Donor-Acceptor π-π Stacking Interactions. *Chem. Commun.* **2009**, No. 44, 6717–6719. https://doi.org/10.1039/b910648k.

(21) Döhler, D.; Kang, J.; Cooper, C. B.; Tok, J. B. H.; Rupp, H.; Binder, W. H.; Bao, Z. Tuning the Self-Healing Response of Poly(Dimethylsiloxane)-Based Elastomers. *ACS Appl. Polym. Mater.* **2020**, *2* (9), 4127–4139. https://doi.org/10.1021/acsapm.0c00755.

(22) Li, Y.; Li, W.; Sun, A.; Jing, M.; Liu, X.; Wei, L.; Wu, K.; Fu, Q. A Self-Reinforcing and Self-Healing Elastomer with High Strength, Unprecedented Toughness and Room-Temperature Reparability. *Mater. Horizons* **2021**, *8* (1), 267–275. https://doi.org/10.1039/d0mh01447h.

(23) Kim, S. M.; Jeon, H.; Shin, S. H.; Park, S. A.; Jegal, J.; Hwang, S. Y.; Oh, D. X.; Park, J. Superior Toughness and Fast Self-Healing at Room Temperature Engineered by

Transparent Elastomers. *Adv. Mater.* **2018**, *30* (1), 1–8. https://doi.org/10.1002/adma.201705145.

(24) Yamauchi, K.; Lizotte, J. R.; Long, T. E. Thermoreversible Poly(Alkyl Acrylates) Consisting of Self-Complementary Multiple Hydrogen Bonding. *Macromolecules* **2003**, *36* (4), 1083–1088. https://doi.org/10.1021/ma0212801.

(25) O'Donnell, A. D.; Salimi, S.; Hart, L. R.; Babra, T. S.; Greenland, B. W.; Hayes, W. Applications of Supramolecular Polymer Networks. *React. Funct. Polym.* **2022**, *172* (February), 105209. https://doi.org/10.1016/j.reactfunctpolym.2022.105209.

(26) Baker, B. C.; German, I. M.; Chippindale, A. M.; McEwan, C. E. A. A.; Stevens, G. C.; Colquhoun, H. M.; Hayes, W. Nitroarylurea-Terminated Supramolecular Polymers That Exhibit Facile Thermal Repair and Aqueous Swelling-Induced Sealing of Defects. *Polymer (Guildf).* **2018**, *140*, 1–9. https://doi.org/10.1016/j.polymer.2018.02.029.

(27) Baker, B. C.; Acton, A. L.; Stevens, G. C.; Hayes, W. Bis Amide-Aromatic-Ureas - Highly Effective Hydro- and Organogelator Systems. *Tetrahedron* **2014**, *70* (44), 8303–8311. https://doi.org/10.1016/j.tet.2014.09.017.

(28) Baker, B. C.; German, I.; Stevens, G. C.; Colquhoun, H. M.; Hayes, W. Inducing Hardening and Healability in Poly(Ethylene-Co-Acrylic Acid) via Blending with Complementary Low Molecular Weight Additives. *RSC Adv.* **2018**, *8* (72), 41445–41453. https://doi.org/10.1039/c8ra09597c.

(29) Wood, D. M.; Acton, A. L.; Rodríguez-llansola, F.; Murray, C. A.; Cardin, C. J.; Miravet, J. F.; Escuder, B.; Hamley, I. W.; Hayes, W.; Greenland, B. W.; Acton, A. L.; Rodríguez-llansola, F.; Murray, C. A.; Cardin, C. J.; Miravet, J. F.; Escuder, B.; Hamley, I. W.; Hayes, W. PH-Tunable Hydrogelators for Water Purification: Structural Optimisation and Evaluation. *Chem. - A Eur. J.* **2012**, *18* (9), 2692–2699. https://doi.org/10.1002/chem.201102137.

(30) ODonnell, A. D.; Gavriel, A. G.; Christie, W.; Chippindale, A. M.; German, I. M.; Hayes, W. Conformational Control of Bis-Urea Self-Assembled Supramolecular PH Switchable Low-Molecular-Weight Hydrogelators. *Arkivoc* **2021**, *2021* (6), 222–241. https://doi.org/10.24820/ark.5550190.p011.581.

(31) Brown, H. C.; Stocky, T. P. Selective Reductions. 24. Acyloxyboranes in the Controlled Reaction of Carboxylic Acids with Borane-Tetrahydrofuran. Acyloxyboranes as Intermediates in the Fast Reduction of Carboxylic Acids by Borane-Tetrahydrofuran. *J. Am. Chem. Soc.* **1977**, *99* (25), 8218–8226. https://doi.org/10.1021/ja00467a016.

(32) Chen, M.; Inglefield, D. L.; Zhang, K.; Hudson, A. G.; Talley, S. J.; Moore, R. B.; Long, T. E. Synthesis of Urea-Containing ABA Triblock Copolymers: Influence of Pendant Hydrogen Bonding on Morphology and Thermomechanical Properties. *J. Polym. Sci. Part A Polym. Chem.* **2018**, *56* (16), 1844–1852. https://doi.org/10.1002/pola.29066.

(33) Hyder, M.; O'Donnell, A. D.; Chippindale, A. M.; German, I. M.; Harries, J. L.; Shebanova, O.; Hamley, I. W.; Hayes, W. Tailoring Viscoelastic Properties of Dynamic

Supramolecular Poly(Butadiene)-Based Elastomers. *Mater. Today Chem.* **2022**, *26*, 101008. https://doi.org/10.1016/j.mtchem.2022.101008.

(34) Raftopoulos, K. N.; Janowski, B.; Apekis, L.; Pielichowski, K.; Pissis, P. Molecular Mobility and Crystallinity in Polytetramethylene Ether Glycol in the Bulk and as Soft Component in Polyurethanes. *Eur. Polym. J.* **2011**, *47* (11), 2120–2133. https://doi.org/10.1016/j.eurpolymj.2011.07.020.

(35) Chen, Y.; Kushner, A. M.; Williams, G. A.; Guan, Z. Multiphase Design of Autonomic Self-Healing Thermoplastic Elastomers. *Nat. Chem.* **2012**, *4* (6), 467–472. https://doi.org/10.1038/nchem.1314.

(36) Lai, Y.; Kuang, X.; Zhu, P.; Huang, M.; Dong, X.; Wang, D. Colorless, Transparent, Robust, and Fast Scratch-Self-Healing Elastomers via a Phase-Locked Dynamic Bonds Design. *Adv. Mater.* **2018**, *30* (38), 1–8. https://doi.org/10.1002/adma.201802556.

(37) Merino, D. H.; Feula, A.; Melia, K.; Slark, A. T.; Giannakopoulos, I.; Siviour, C. R.; Buckley, C. P.; Greenland, B. W.; Liu, D.; Gan, Y.; Harris, P. J.; Chippindale, A. M.; Hamley, I. W.; Hayes, W. A Systematic Study of the Effect of the Hard End-Group Composition on the Microphase Separation, Thermal and Mechanical Properties of Supramolecular Polyurethanes. *Polymer (Guildf).* **2016**, *107*, 368–378. https://doi.org/10.1016/j.polymer.2016.07.029.

(38) Burattini, S.; Greenland, B. W.; Merino, D. H.; Weng, W.; Seppala, J.; Colquhoun, H. M.; Hayes, W.; MacKay, M. E.; Hamley, I. W.; Rowan, S. J. A Healable Supramolecular Polymer Blend Based on Aromatic π-π Stacking and Hydrogen-Bonding Interactions. *J. Am. Chem. Soc.* **2010**, *132* (34), 12051–12058. https://doi.org/10.1021/ja104446r.

(39) Hermida-Merino, D.; Hart, L. R.; Harris, P. J.; Slark, A. T.; Hamley, I. W.; Hayes, W. The Effect of Chiral End Groups on the Assembly of Supramolecular Polyurethanes. *Polym. Chem.* **2021**, *12* (31), 4488–4500. https://doi.org/10.1039/d1py00714a.

(40) Sivakova, S.; Bohnsack, D. A.; Mackay, M. E.; Suwanmala, P.; Rowan, S. J. Utilization of a Combination of Weak Hydrogen-Bonding Interactions and Phase Segregation to Yield Highly Thermosensitive Supramolecular Polymers. *J. Am. Chem. Soc.* **2005**, *127* (51), 18202–18211. https://doi.org/10.1021/ja055245w.

(41) Bose, R. K.; Hohlbein, N.; Garcia, S. J.; Schmidt, A. M.; Van Der Zwaag, S. Connecting Supramolecular Bond Lifetime and Network Mobility for Scratch Healing in Poly(Butyl Acrylate) Ionomers Containing Sodium, Zinc and Cobalt. *Phys. Chem. Chem. Phys.* **2015**, *17* (3), 1697–1704. https://doi.org/10.1039/c4cp04015e.

(42) Bose, R. K.; Hohlbein, N.; Garcia, S. J.; Schmidt, A. M.; Van Der Zwaag, S. Relationship between the Network Dynamics, Supramolecular Relaxation Time and Healing Kinetics of Cobalt Poly(Butyl Acrylate) Ionomers. *Polymer (Guildf).* **2015**, *69*, 228–232. https://doi.org/10.1016/j.polymer.2015.03.049.

(43) Stukalin, E. B.; Cai, L. H.; Kumar, N. A.; Leibler, L.; Rubinstein, M. Self-Healing of Unentangled Polymer Networks with Reversible Bonds. *Macromolecules* **2013**, *46* (18),

7525–7541. https://doi.org/10.1021/ma401111n.

(44) Aida, T.; Meijer, E. W.; Stupp, S. I. Functional Supramolecular Polymers. *Science (80-.).* **2012**, *335* (6070), 813–817. https://doi.org/10.1126/science.1205962.

(45) Campanella, A.; Döhler, D.; Binder, W. H. Self-Healing in Supramolecular Polymers. *Macromol. Rapid Commun.* **2018**, *39* (17), 1–19. https://doi.org/10.1002/marc.201700739.

(46) Döhler, D.; Peterlik, H.; Binder, W. H. A Dual Crosslinked Self-Healing System: Supramolecular and Covalent Network Formation of Four-Arm Star Polymers. *Polymer (Guildf).* **2015**, *69*, 264–273. https://doi.org/10.1016/j.polymer.2015.01.073.

(47) Chen, S.; Döhler, D.; Binder, W. H. Rheology of Hydrogen-Bonded Dendritic Supramolecular Polymer Networks in the Melt State. *Polymer (Guildf).* **2016**, *107*, 466–473. https://doi.org/10.1016/j.polymer.2016.08.046.

(48) Bode, S.; Enke, M.; Bose, R. K.; Schacher, F. H.; Garcia, S. J.; van der Zwaag, S.; Hager, M. D.; Schubert, U. S. Correlation between Scratch Healing and Rheological Behavior for Terpyridine Complex Based Metallopolymers. *J. Mater. Chem. A* **2015**, *3* (44), 22145–22153. https://doi.org/10.1039/c5ta05545h.

(49) Yanagisawa, Y.; Nan, Y.; Okuro, K.; Aida, T. Mechanically Robust, Readily Repairable Polymers via Tailored Noncovalent Cross-Linking. *Science (80-.).* **2018**, *359* (6371), 72–76. https://doi.org/10.1126/science.aam7588.

(50) Wu, S.; Beckerbauer, R. Chain Entanglement in Homopolymers, Copolymers and Terpolymers of Methyl Methacrylate, Styrene and N-Phenylmaleimide. *Polymer (Guildf).* **1992**, *33* (3), 509–515. https://doi.org/10.1016/0032-3861(92)90727-E.

(51) Wood, D. M.; Greenland, B. W.; Acton, A. L.; Rodríguez-Llansola, F.; Murray, C. A.; Cardin, C. J.; Miravet, J. F.; Escuder, B.; Hamley, I. W.; Hayes, W. PH-Tunable Hydrogelators for Water Purification: Structural Optimisation and Evaluation. *Chem. - A Eur. J.* **2012**, *18* (9), 2692–2699. https://doi.org/10.1002/chem.201102137.

(52) Li, C.-H.; Wang, C.; Keplinger, C.; Zuo, J.-L.; Jin, L.; Sun, Y.; Zheng, P.; Cao, Y.; Lissel, F.; Linder, C.; You, X.-Z.; Bao, Z. A Highly Stretchable Autonomous Self-Healing Elastomer. *Nat. Chem.* **2016**, *8* (6), 618–624. https://doi.org/10.1038/nchem.2492.

(53) Xu, D.; Hawk, J. L.; Loveless, D. M.; Jeon, S. L.; Craig, S. L. Mechanism of Shear Thickening in Reversibly Cross-Linked Supramolecular Polymer Networks. *Macromolecules* **2010**, *43* (7), 3556–3565. https://doi.org/10.1021/ma100093b.

(54) Yan, X.; Liu, Z.; Zhang, Q.; Lopez, J.; Wang, H.; Wu, H.-C. C.; Niu, S.; Yan, H.; Wang, S.; Lei, T.; Li, J.; Qi, D.; Huang, P.; Huang, J.; Zhang, Y.; Wang, Y.; Li, G.; Tok, J. B. H.; Chen, X.; Bao, Z. Quadruple H-Bonding Cross-Linked Supramolecular Polymeric Materials as Substrates for Stretchable, Antitearing, and Self-Healable Thin Film Electrodes. *J. Am. Chem. Soc.* **2018**, *140* (15), 5280–5289. https://doi.org/10.1021/jacs.8b01682.

(55) Yang, L.; Lin, Y.; Wang, L.; Zhang, A. The Synthesis and Characterization of

Supramolecular Elastomers Based on Linear Carboxyl-Terminated Polydimethylsiloxane Oligomers. *Polym. Chem.* **2014**, *5* (1), 153–160. https://doi.org/10.1039/C3PY01005H.

(56) Chen, S.; Bi, X.; Sun, L.; Gao, J.; Huang, P.; Fan, X.; You, Z.; Wang, Y. Poly(Sebacoyl Diglyceride) Cross-Linked by Dynamic Hydrogen Bonds: A Self-Healing and Functionalizable Thermoplastic Bioelastomer. *ACS Appl. Mater. Interfaces* **2016**, *8* (32), 20591–20599. https://doi.org/10.1021/acsami.6b05873.

(57) Song, Y.; Liu, Y.; Qi, T.; Li, G. L. Towards Dynamic but Supertough Healable Polymers through Biomimetic Hierarchical Hydrogen-Bonding Interactions. *Angew. Chemie - Int. Ed.* **2018**, *57* (42), 13838–13842. https://doi.org/10.1002/anie.201807622.

(58) Lamers, B. A. G.; Ślęczkowski, M. L.; Wouters, F.; Engels, T. A. P.; Meijer, E. W.; Palmans, A. R. A. Tuning Polymer Properties of Non-Covalent Crosslinked PDMS by Varying Supramolecular Interaction Strength. *Polym. Chem.* **2020**, *11* (16), 2847–2854. https://doi.org/10.1039/d0py00139b.

(59) Feula, A.; Tang, X.; Giannakopoulos, I.; Chippindale, A. M.; Hamley, I. W.; Greco, F.; Paul Buckley, C.; Siviour, C. R.; Hayes, W. An Adhesive Elastomeric Supramolecular Polyurethane Healable at Body Temperature. *Chem. Sci.* **2016**, *7* (7), 4291–4300. https://doi.org/10.1039/c5sc04864h.

Chapter 5 – Conclusions and Future Work

5.1 Conclusions

Hydrogen-bonding motifs are desirable for a wide range of applications – when incorporated into polymeric materials, they can produce stronger, more elastic, thermoreversible materials that can undergo reversible adhesion and self-heal. In this thesis, the design of hydrogen bonding motifs has been undertaken, which resulted in a library of hydrogelator compounds whereby the strength of the intermolecular interaction was tuned through the installation of *ortho*-methyl substituents. The objective of this study was to better understand the structure to property relationship of low molecular weight gelators. The gelator assembly kinetics were extensively investigated through rheological and NMR experiments, and the strength of the association and robustness of the hydrogelator network was assessed. Furthermore, destructive oscillatory shear experiments were used to assess the kinetics of reassembly after undergoing a damage event. The gelators were further characterised by their ability to uptake a planar organic dye, namely methylene blue, as its planar structure has been shown to intercalate similar gelator networks and be efficiently abstracted from water. It was found that gelators which exhibited 1-dimensional networks, as determined by Avrami plots, allowed for increased dye intercalation compared to the more three-dimensional gelator networks. Gelators that featured ortho-methyl substituents were less effective at sequestering methylene blue because of increased urea-urea interaction favouring three-dimensionality. Furthermore, the gelators which underwent gel-crystal transitions were not suitable as hydrogelators as they were not sufficiently robust as a consequence of their crystallinity. The crystallinity expressed by the more strongly associated hydrogelators could be exploited in future polyurethane designs as an apolar polymer backbone would effectively attenuate the crystallinity.

A series of novel SPUs featuring polar end-groups were synthesised, and structure to property relationships were developed. Most significant was the realisation that in the absence of a nitro substituent, the polymeric materials were found to be exceptionally brittle and unsuitable as elastomers; as such, no tensile testing could be performed. It was discovered that the nitro substituent competes with the urea and urethane carbonyls as a hydrogen bonding acceptor and can disrupt the urea-urea and urethane-urethane hydrogen bonding interactions. With this observation in mind, a library of thirteen polyurethanes were synthesised and extensively characterised by rheological and tensile testing. Furthermore, the ability of the elastomeric materials to act as reversible adhesives to four different substrates was investigated. SAXS and WAXS analysis revealed a microphase-separated morphology critical for the enhanced mechanical properties of SPUs. DSC analysis showed that the SPUs with unhindered nitro substituents exhibited melt transitions around 36 °C. Additionally, the rheological analysis of the SPUs provided further information regarding the reversibility of the supramolecular networks. In the absence of a nitro substituent, a crossover between storage and loss moduli

was not observed, as the material behaved as a covalently crosslinked rubber. Interestingly, when the nitro substituent was twisted out of plane relative to the aryl ring, the same observation was made, and it could not act as a competitive hydrogen bonding acceptor; thus, the urea-urea and urethane-urethane interactions dominated.

A series of chain-extended supramolecular elastomers were designed and synthesised and exhibited exceptional mechanical properties. Detailed rheological analysis revealed that the average supramolecular bond lifetime could be tuned over three orders of magnitude by increasing the concentration of the supramolecular motif from 2.5 mol% to 15 mol%. The ability for polymer chain slippage was evaluated, and the required energy, as determined by Arrhenius plots, increased with the increasing concentration of pendant assembly moieties. The mechanical properties of the SPEs were easily attenuated by increasing the percentage of the pendant supramolecular motif relative to a non-functionalised chain extender. Furthermore, where typically in the design of polyurethane materials, there is a trade-off between UTS and elongation at break, the SPEs synthesised were found to have a similar elongation at break values irrespective of the percentage loading of pendant assembly unit. *Meta* and -*para* regioisomers were compared to one another, and it was discovered that the materials produced with -*meta* nitro substitution exhibited the highest UTS, and by comparison, the para nitro series displayed the highest elongation at break. Finally, the ability for the SPEs to undergo self-healing was assessed, and remarkable recovery of mechanical properties was observed for both the *meta* and -*para* nitro substituted SPEs.

5.2 Future work

This thesis details the structure-to-properties relationships of incorporating bis-urea motifs into multiple supramolecular materials. This has been a successful venture, and an enhanced understanding of the assembly of this subsection of materials will allow for further material development.

As previously discussed, some of the hydrogelators in Chapter 2 that featured -*ortho*-methyl substituents were found to undergo gel-crystal transitions because of the increased urea-urea hydrogen bonding interaction strength. Therefore, the gelator structures were unsuitable as hydrogelators as their gel lifetime was limited, or they did not form robust hydrogels. However, the increased crystallinity of the assembly may be beneficial when designing supramolecular polymers. Selective reduction of the most crystalline gelator molecules, for example, gelator **2.8** (see Scheme 1**A**) to deliver the respective diol (**5.2**) and then chain extension with a PTMG prepolymer (as in Chapter 4) (see Scheme 1**B**) would result in supramolecular networks with exceptional mechanical properties.

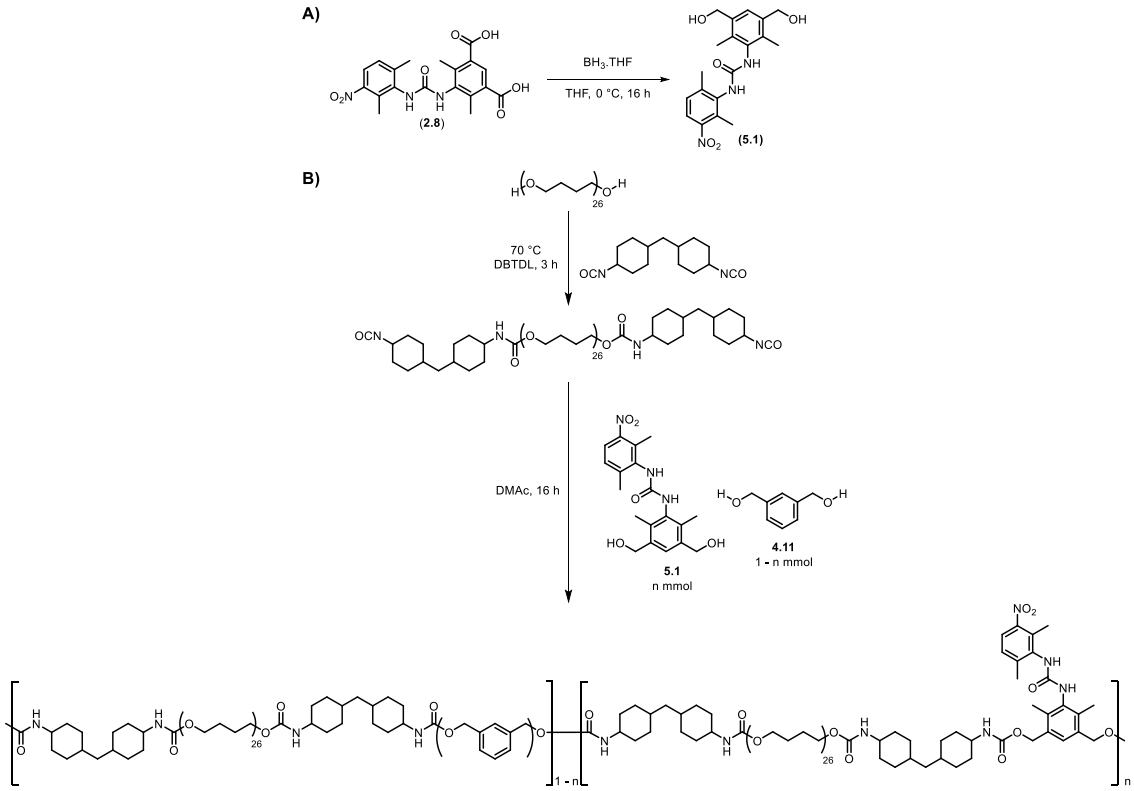

Scheme 21. A) Proposed selective reduction of **5.1** to deliver the diol **5.2. B)** Proposed synthetic route to supramolecular polymers utilising diol **5.2**.

Further material development could include the design of comb polymers similar to that of reported by Long and coworkers.[1–4] A free-radical polymerisation of lauryl methacrylate (**5.3**) and a bis-urea methacrylate (**5.4**), whereby the ratio of monomers would allow for the generation of a library of materials (**5.5**) with tunable mechanical properties (see Scheme 2). Alternatively, the mechanical properties of the resultant materials could be controlled through controlled polymerisations such as RAFT, as demonstrated by Long and coworkers in the synthesis of ABA triblock copolymers.[3,4] In its first iteration, synthesis of copolymers through an uncontrolled manner would quickly provide material that can be assessed for its mechanical properties before committing to more technically challenging controlled polymerisations.

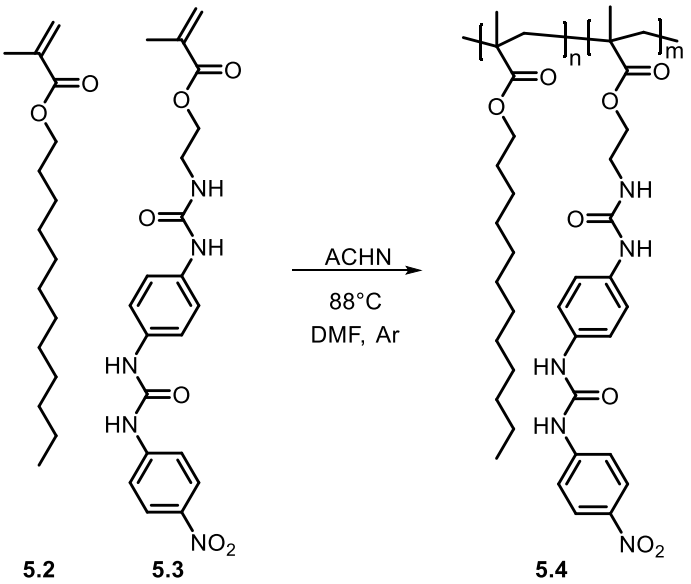

Scheme 2. A free-radical polymerisation between lauryl methacrylate (**5.2**) and a bis-urea methacrylate (**5.3**) to deliver supramolecular methacrylate copolymers (**5.4**)

Another angle that should be investigated further is the introduction of longer poly(butadiene) chains; as Chapter 3 demonstrates, in the assembly of the hard domains where there is no nitro substituent present, the resultant materials were found to be too crystalline, and phase-separated and thus not suitable for mechanical property assessment. A more extended amorphous polymer backbone may alleviate the assembly's strength and thus provide elastomeric supramolecular materials that do not require nitro substituents to disrupt the assembly of the hard domains (see Scheme 3).

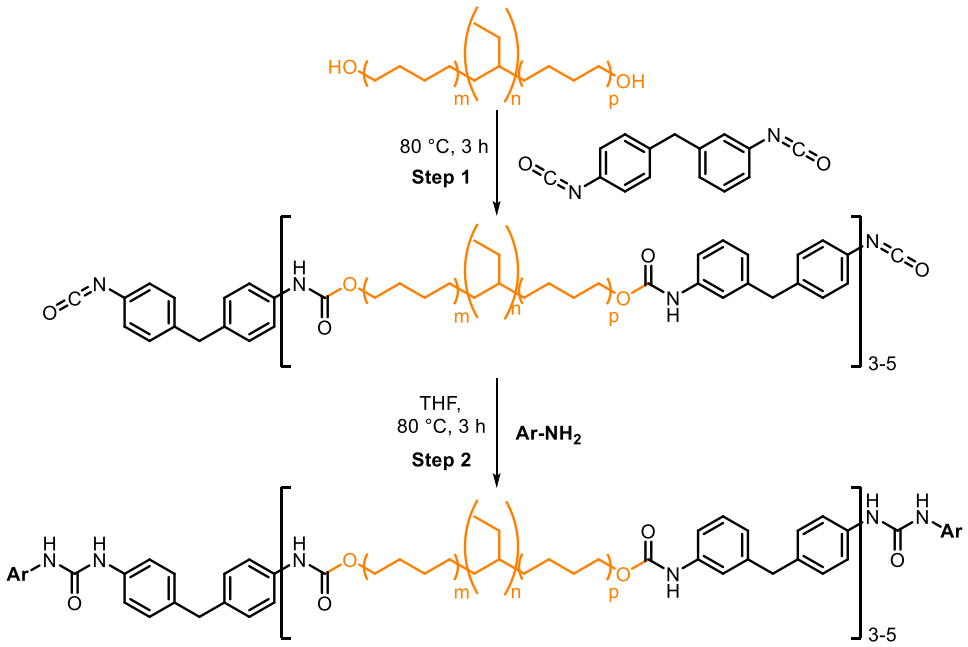

Scheme 3. Synthetic strategy used in Chapter 3 to deliver thermoreversible SPUs whereby the poly(butadiene) block has a molecular weight exceeding 2000 gmol^{-1}.

Finally, it would be prudent to end-cap low molecular weight PTMG chains (M_n = 2000) with aniline derivatives like that reported in Chapter 3, as this would produce interesting thermo-reversible materials (see Scheme 4). HMDI has been chosen as it has been shown in this thesis and in other bodies of work to impart exceptional mechanical properties to the resultant material and simultaneously allow for chain mobility and, thus, thermoreversibility.

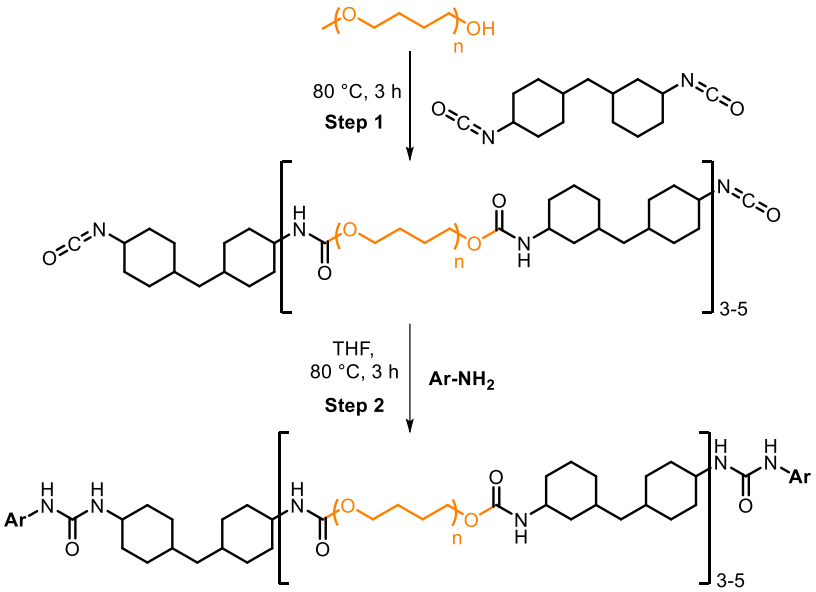

Scheme 4. Proposed synthetic route to end-capped PTMG polyurethanes with interesting thermos-reversible properties.

5.3 References

(1) Yamauchi, K.; Lizotte, J. R.; Long, T. E. Thermoreversible Poly(Alkyl Acrylates) Consisting of Self-Complementary Multiple Hydrogen Bonding. *Macromolecules* **2003**, *36* (4), 1083–1088. https://doi.org/10.1021/ma0212801.

(2) Tao, Y.; Satoh, K.; Kamigaito, M. Nucleobase-Mediated Stereospecific Radical Polymerization and Combination with Raft Polymerization for Simultaneous Control of Molecular Weight and Tacticity. *Macromol. Rapid Commun.* **2011**, *32* (2), 226–232. https://doi.org/10.1002/marc.201000614.

(3) Chen, M.; Inglefield, D. L.; Zhang, K.; Hudson, A. G.; Talley, S. J.; Moore, R. B.; Long, T. E. Synthesis of Urea-Containing ABA Triblock Copolymers: Influence of Pendant Hydrogen Bonding on Morphology and Thermomechanical Properties. *J. Polym. Sci. Part A Polym. Chem.* **2018**, *56* (16), 1844–1852. https://doi.org/10.1002/pola.29066.

(4) Zhang, K.; Aiba, M.; Fahs, G. B.; Hudson, A. G.; Chiang, W. D.; Moore, R. B.; Ueda, M.; Long, T. E. Nucleobase-Functionalized Acrylic ABA Triblock Copolymers and Supramolecular Blends. *Polym. Chem.* **2015**, *6* (13), 2434–2444. https://doi.org/10.1039/c4py01798f.

Appendix 1

Contents

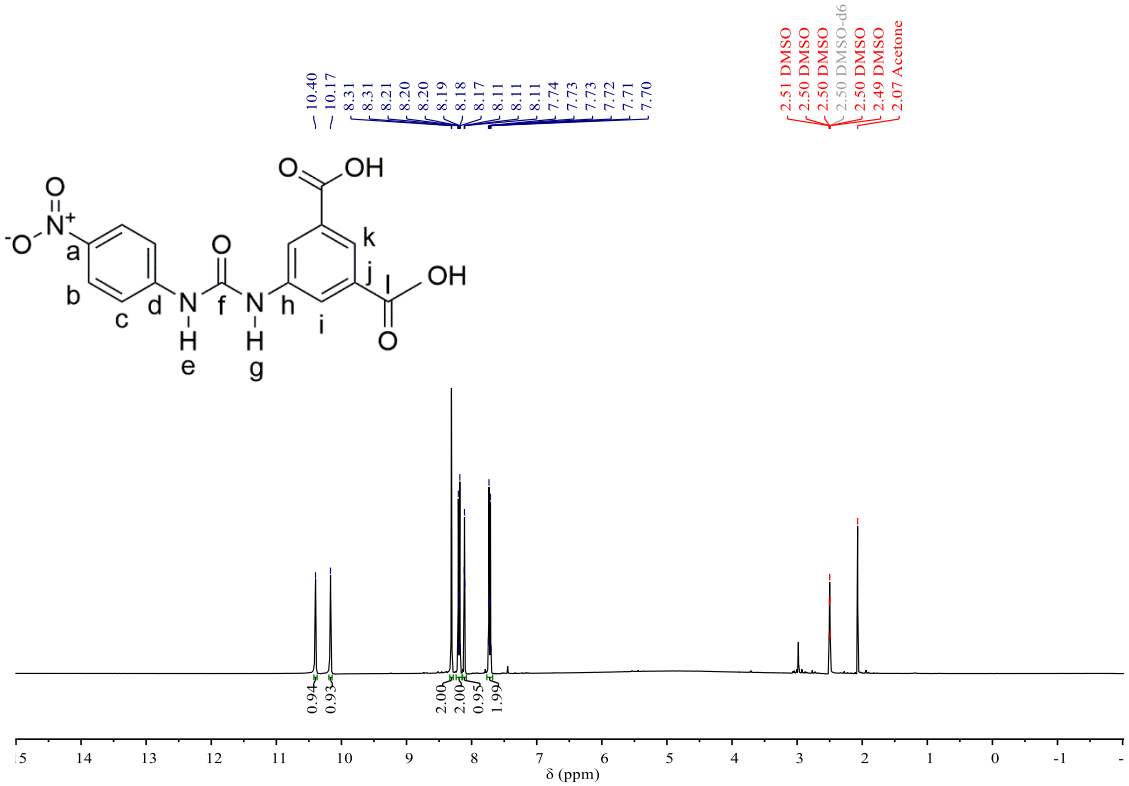

Figure 1. ^{1}H NMR (400 MHz, DMSO-d_6, 298 K of compound 2.1).

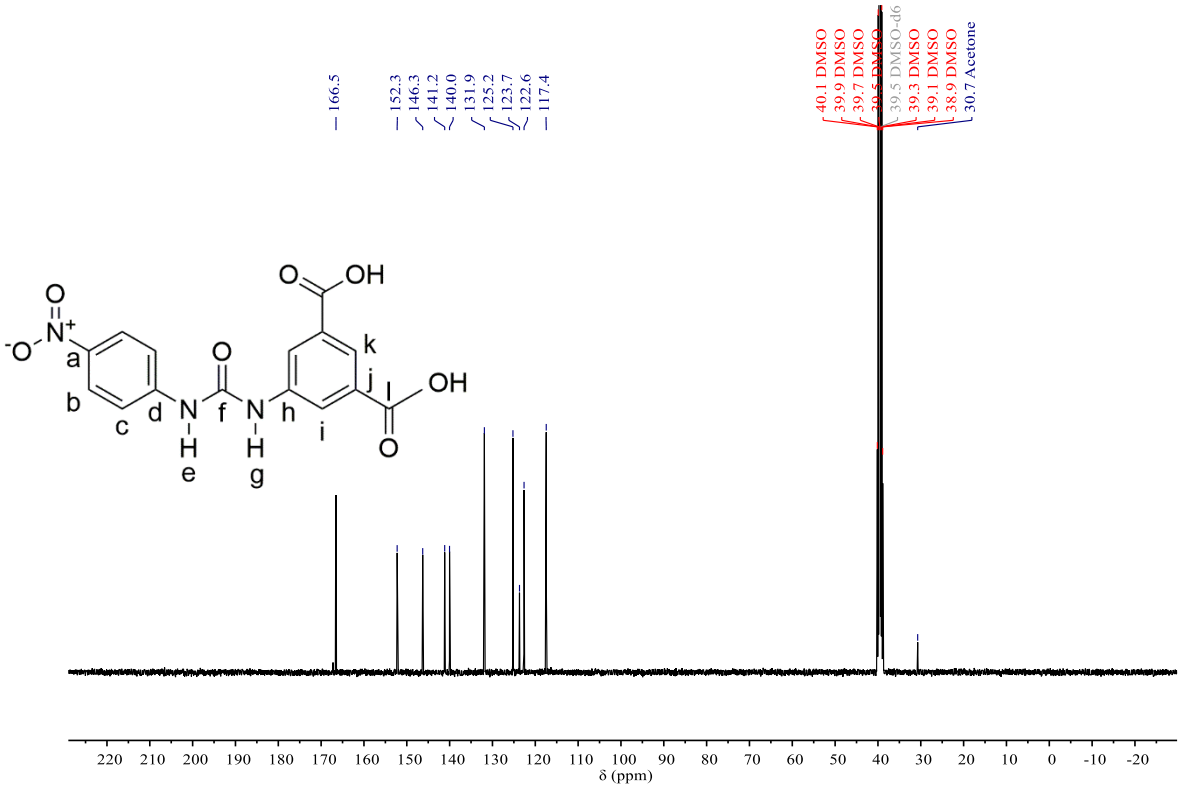

Figure 2. ^{13}C{H} (100 MHz, DMSO-d6, 298 K of compound 2.1).

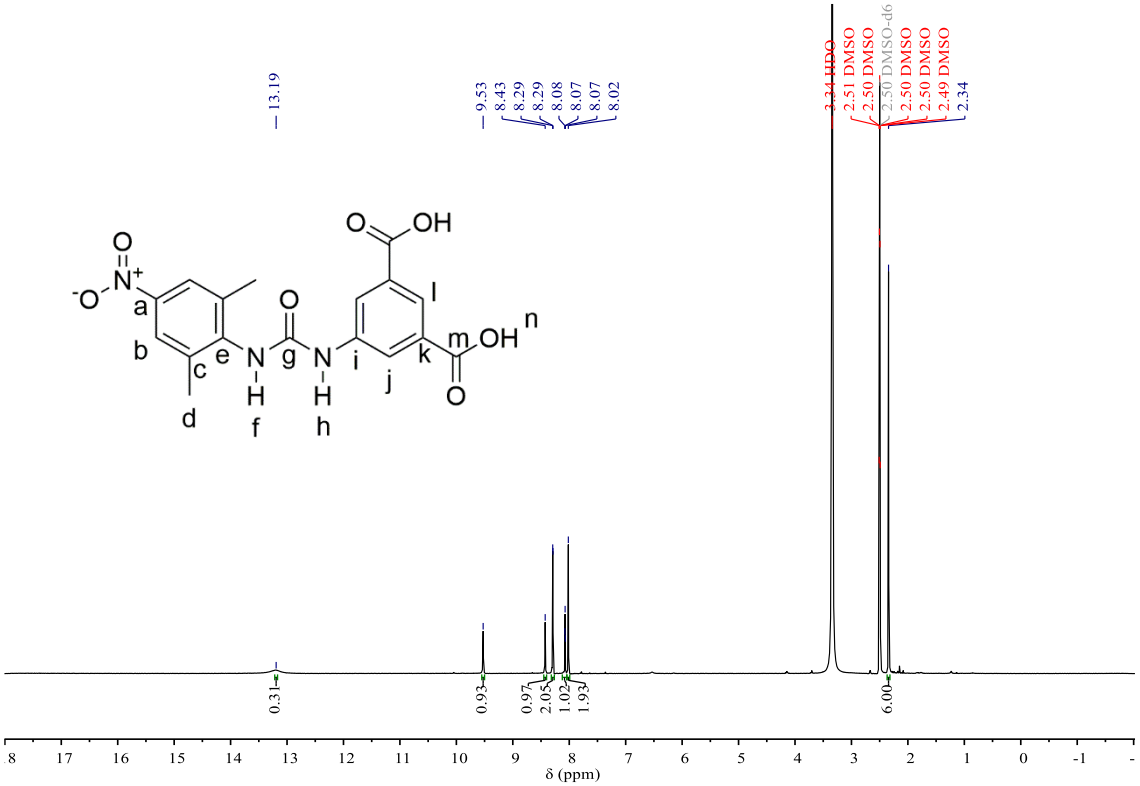

Figure 3. ^{1}H NMR (400 MHz, DMSO-d_6, 298 K of compound **2.2**).

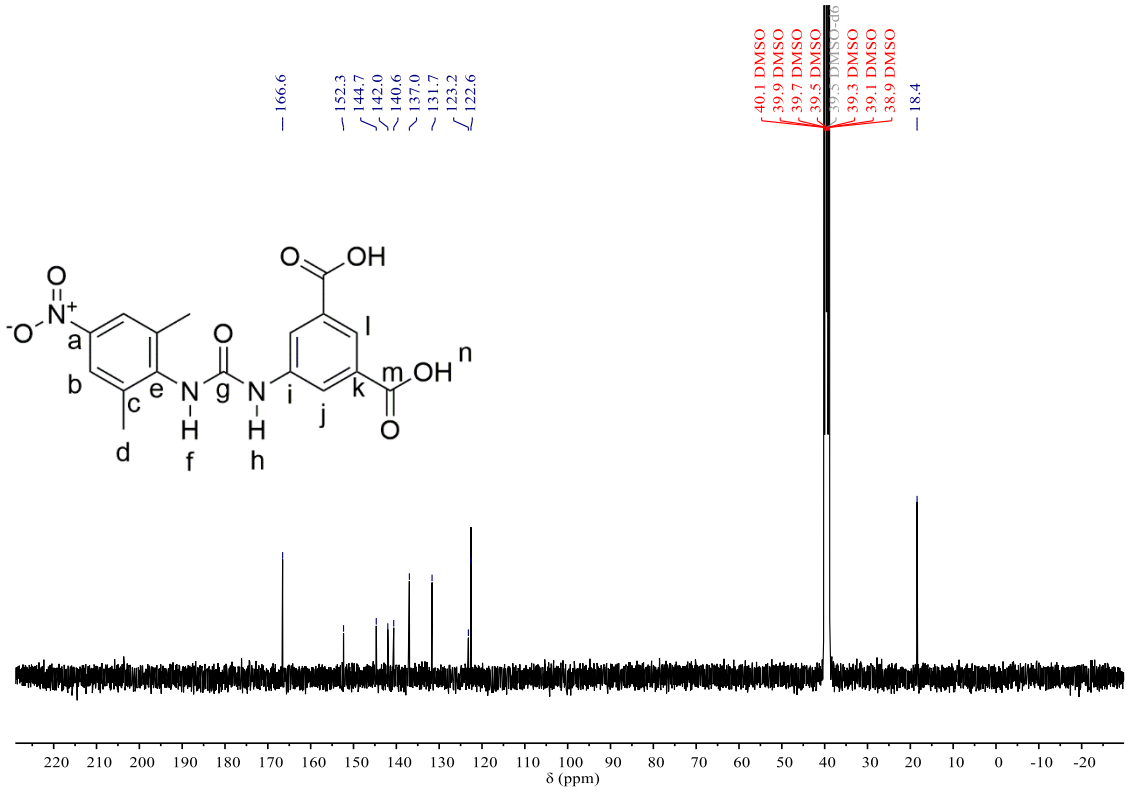

Figure 4. ^{13}C{H} (100 MHz, DMSO-d_6, 298 K of compound **2.2**).

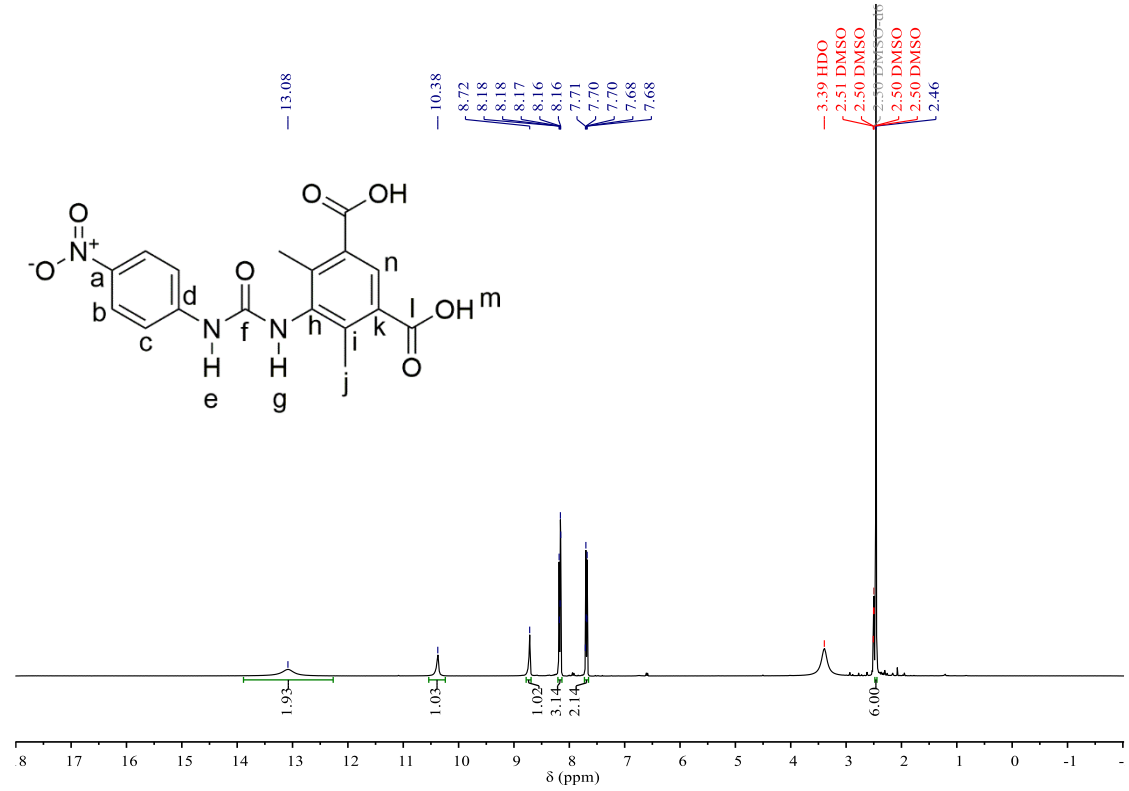

Figure 5. ^{1}H NMR (400 MHz, DMSO-d_6, 298 K of compound **2.3**).

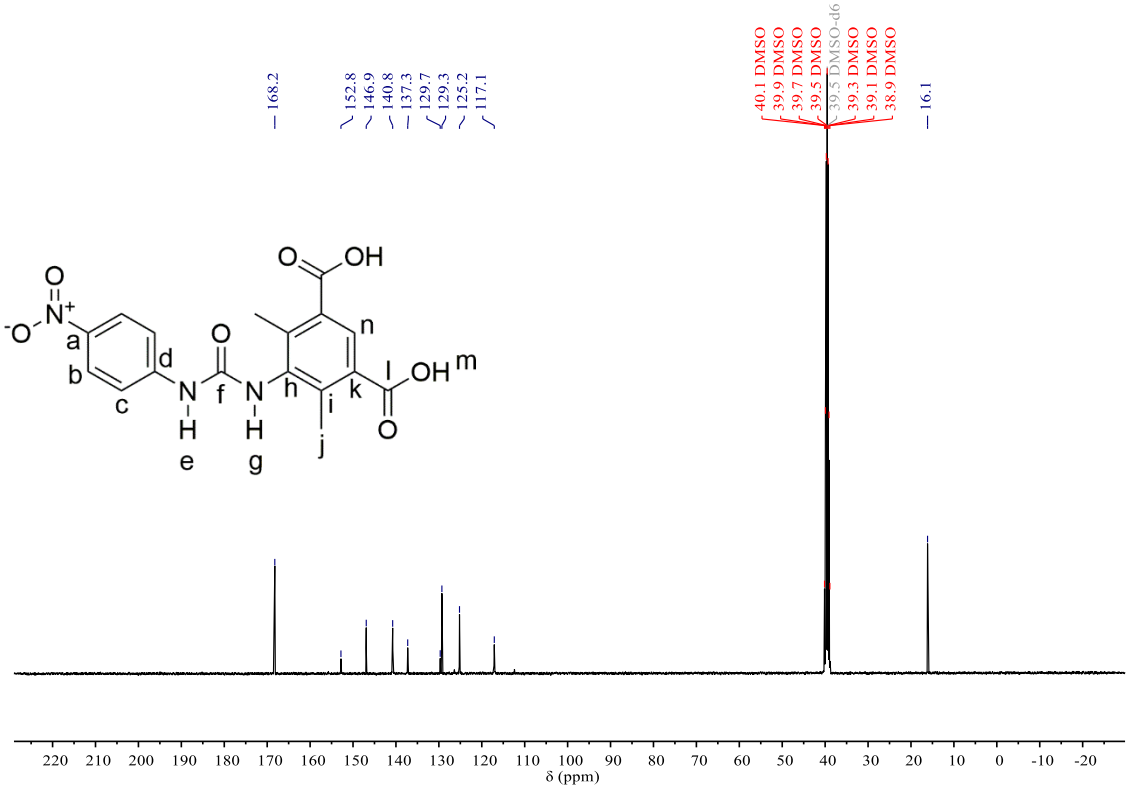

Figure 6. ^{13}C{H} (100 MHz, DMSO-d_6, 298 K of compound **2.3**).

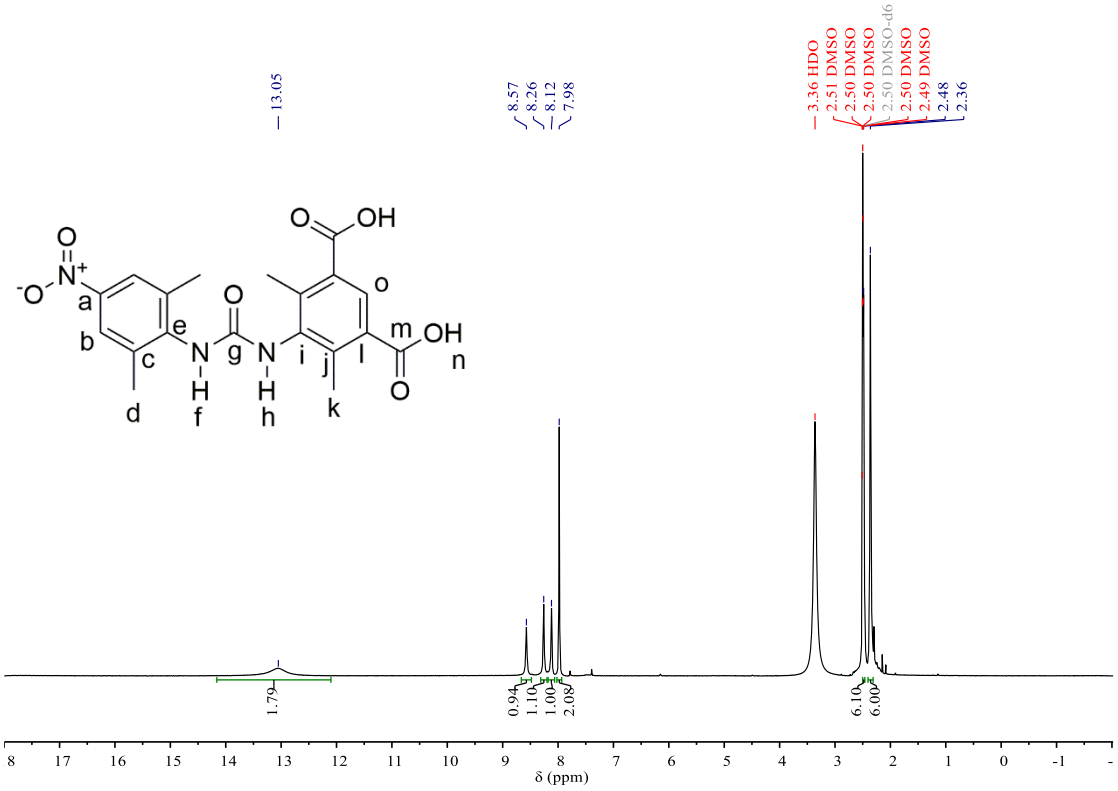

Figure 7. ^{1}H NMR (400 MHz, DMSO-d$_6$, 298 K of compound **2.4**).

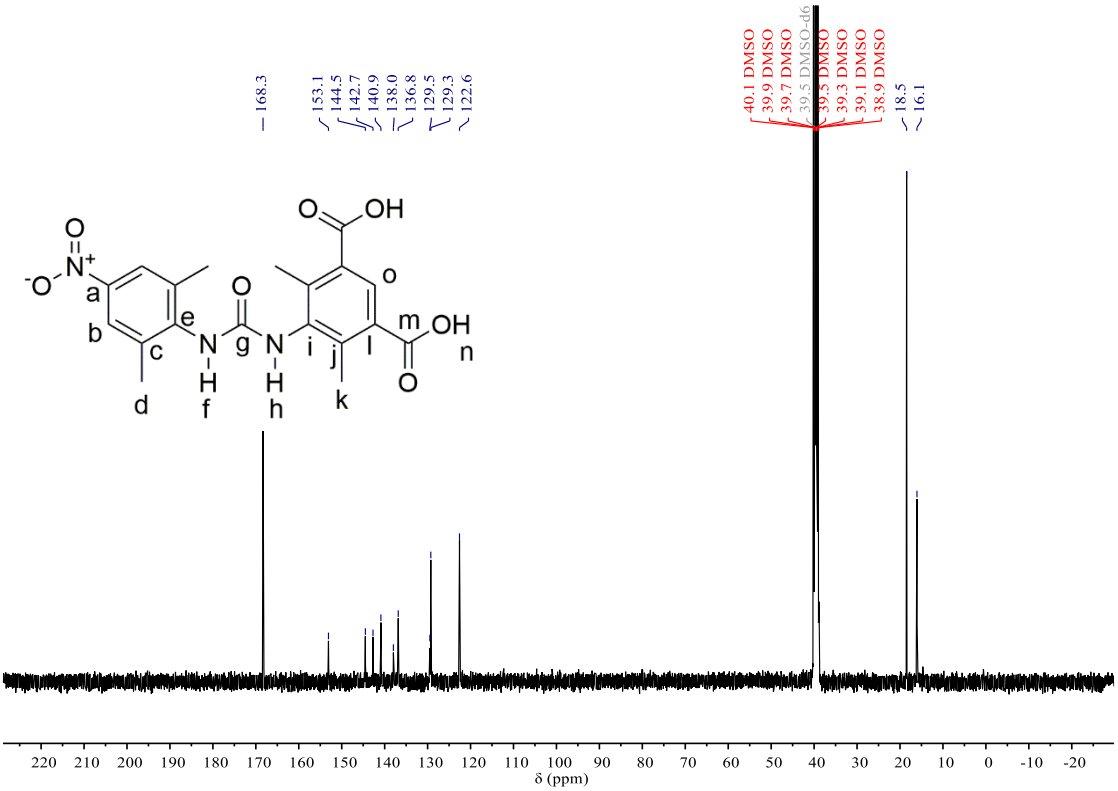

Figure 8. ^{13}C{H} (100 MHz, DMSO-d$_6$, 298 K of compound **2.4**).

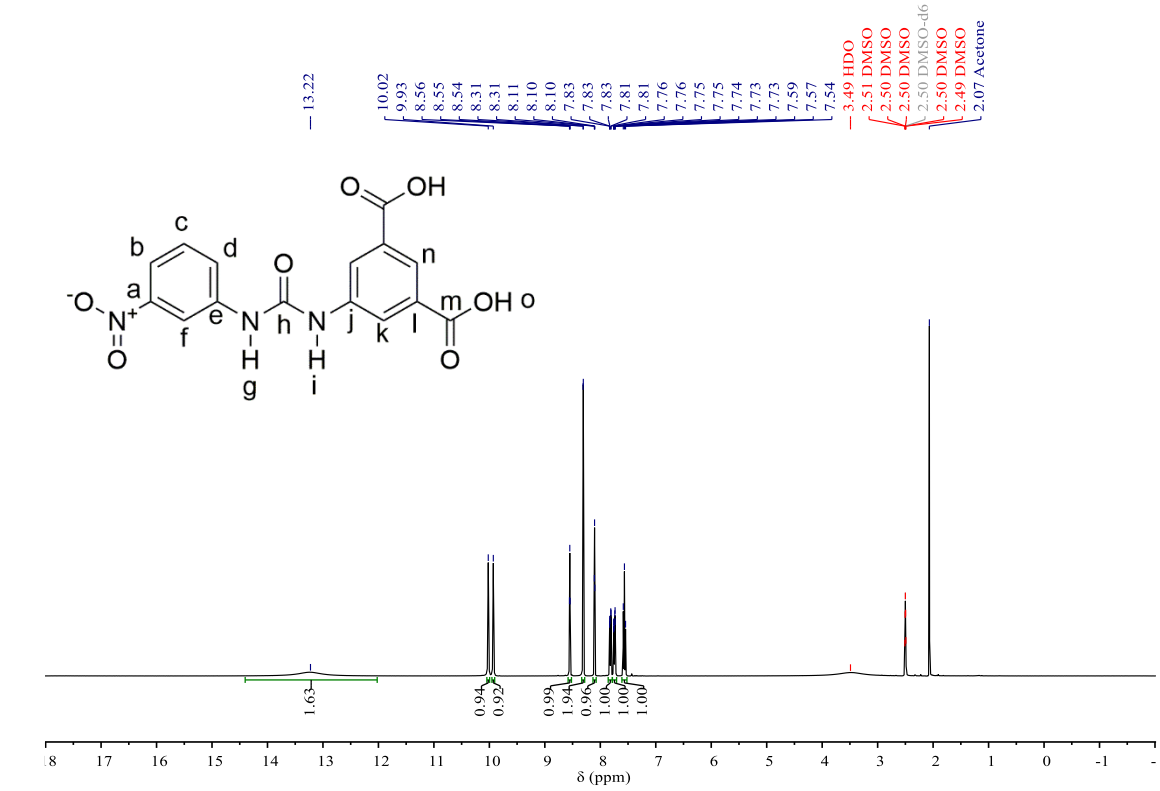

Figure 9. ^{1}H NMR (400 MHz, DMSO-d_6, 298 K of compound **2.5**).

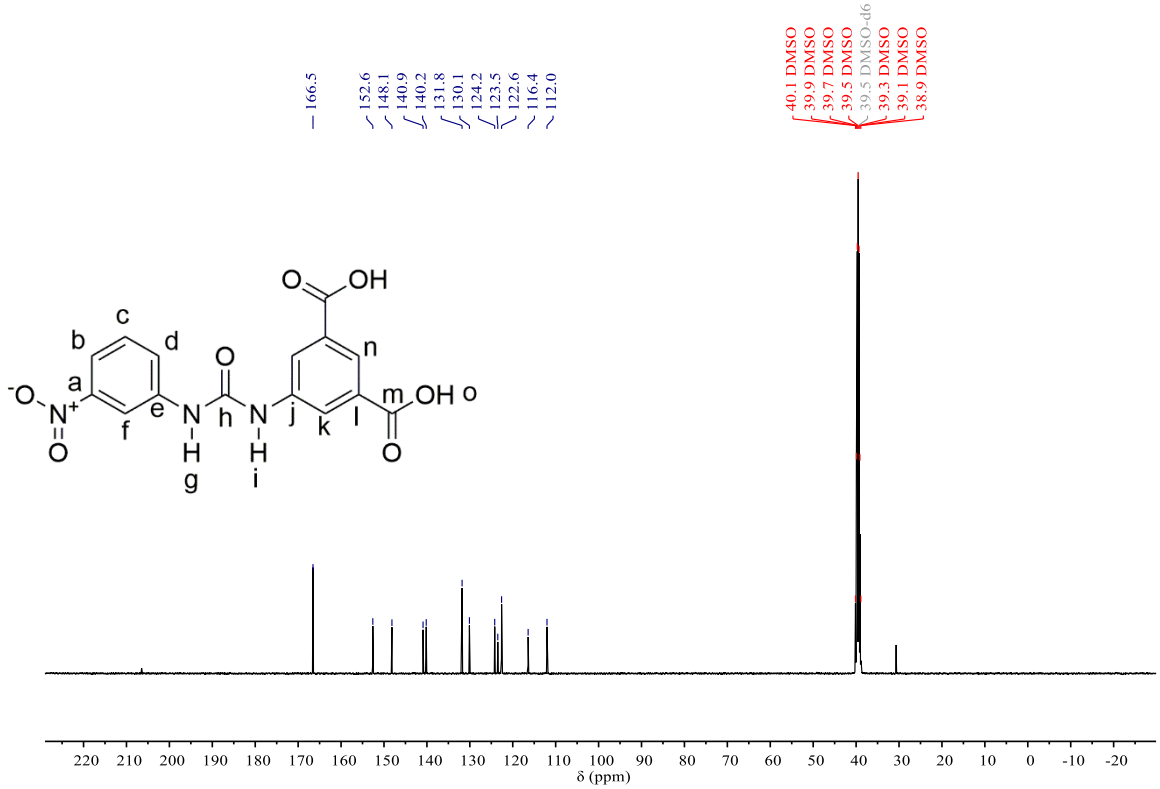

Figure 10. ^{13}C{H} (100 MHz, DMSO-d_6, 298 K of compound **2.5**).

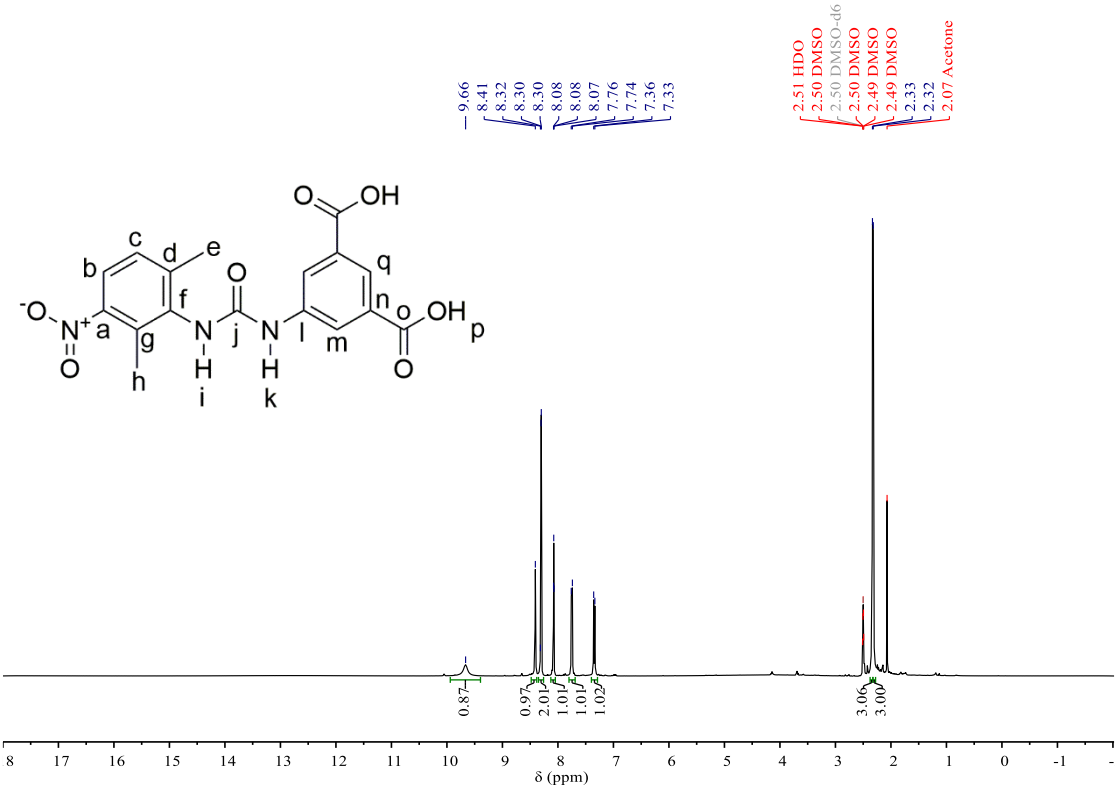

Figure 11. ^{1}H NMR (400 MHz, DMSO-d_6, 298 K of compound **2.6**).

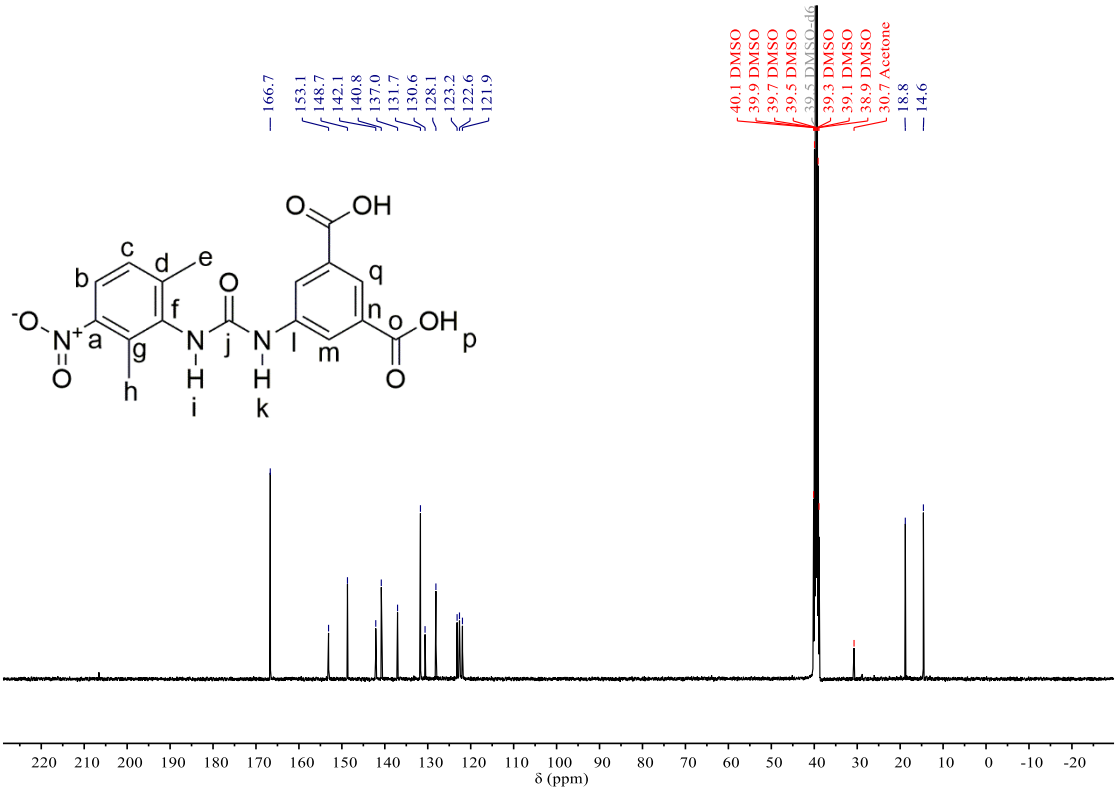

Figure 12. ^{13}C{H} (100 MHz, DMSO-d_6, 298 K of compound **2.6**).

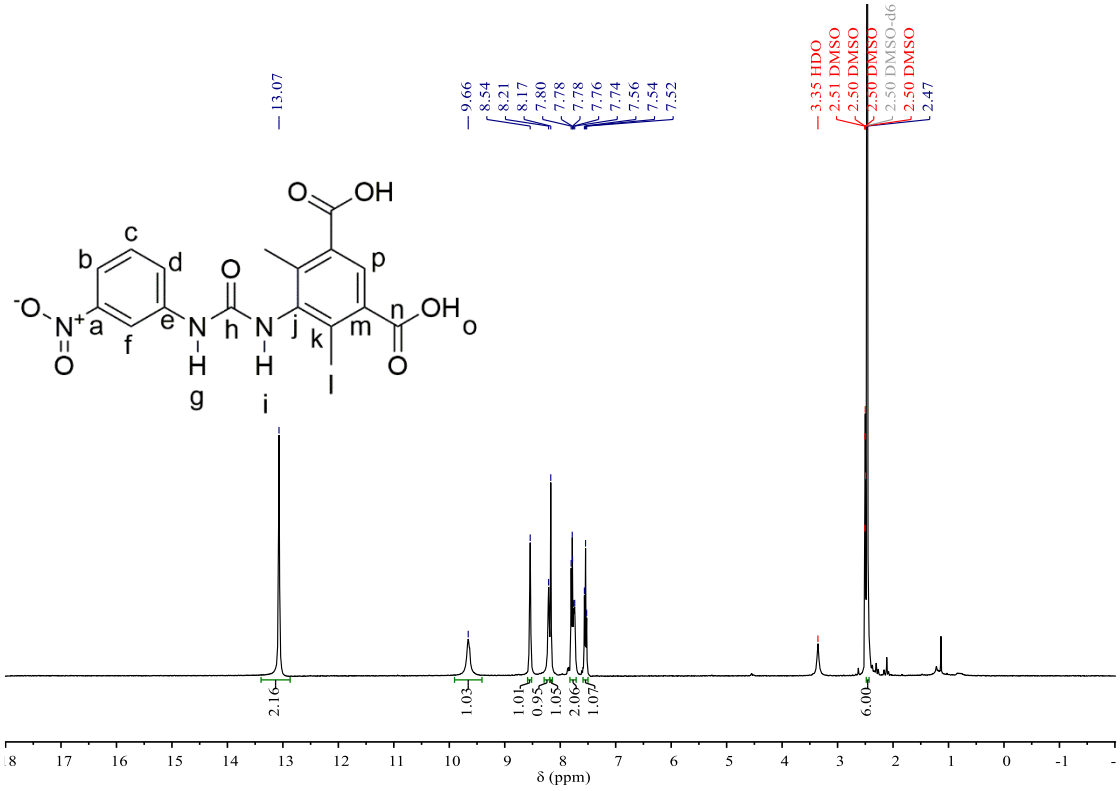

Figure 13. ^{1}H NMR (400 MHz, DMSO-d$_6$, 298 K of compound **2.7**).

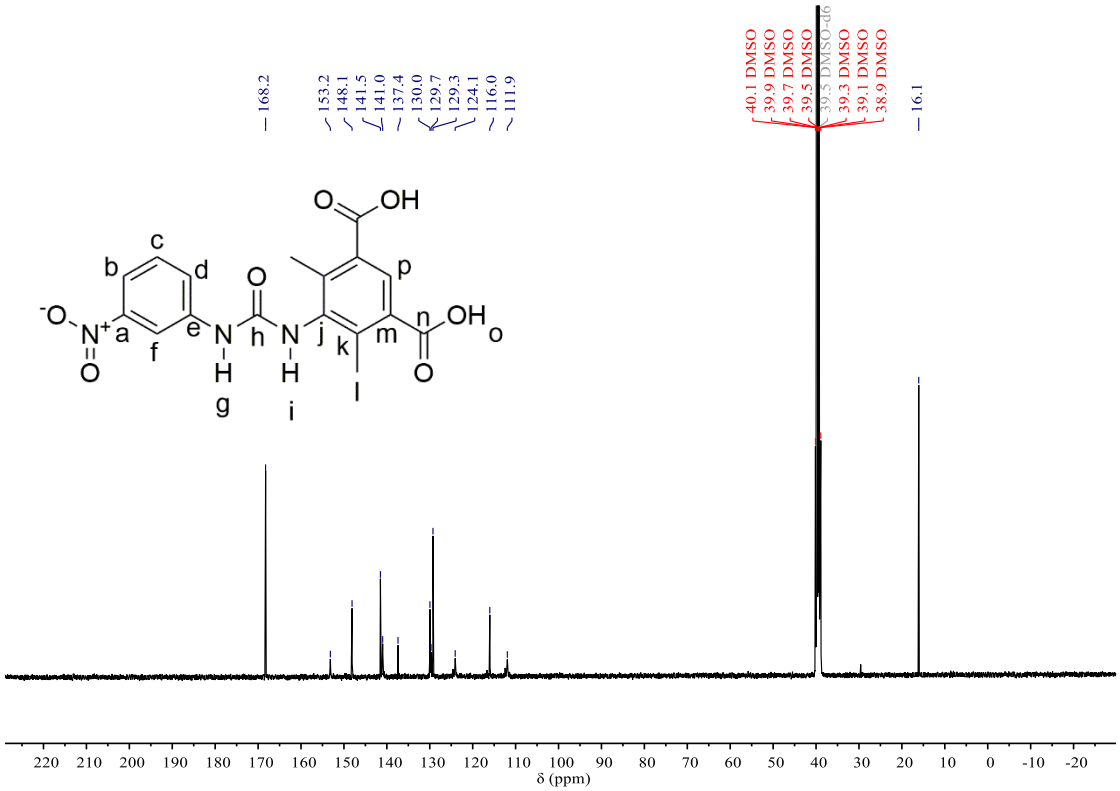

Figure 14. ^{13}C{H} (100 MHz, DMSO-d$_6$, 298 K of compound **2.7**).

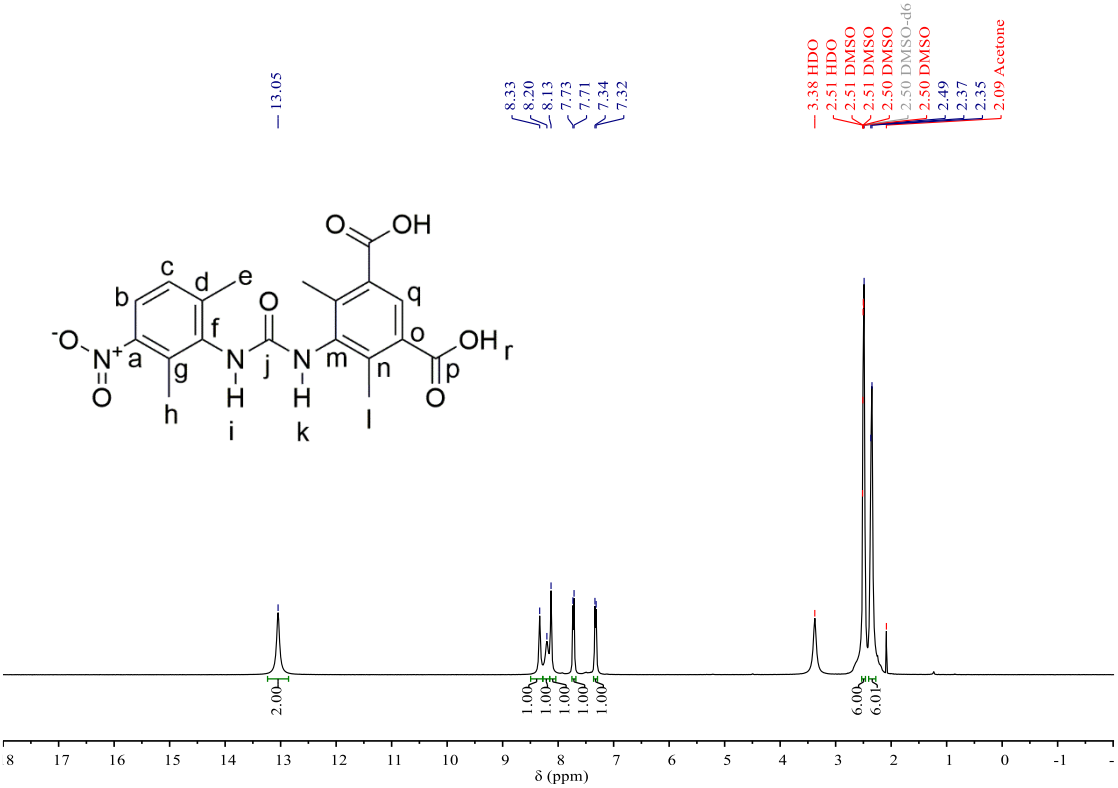

Figure 15. ^{1}H NMR (400 MHz, DMSO-d$_6$**,** 298 K of compound **2.8**).

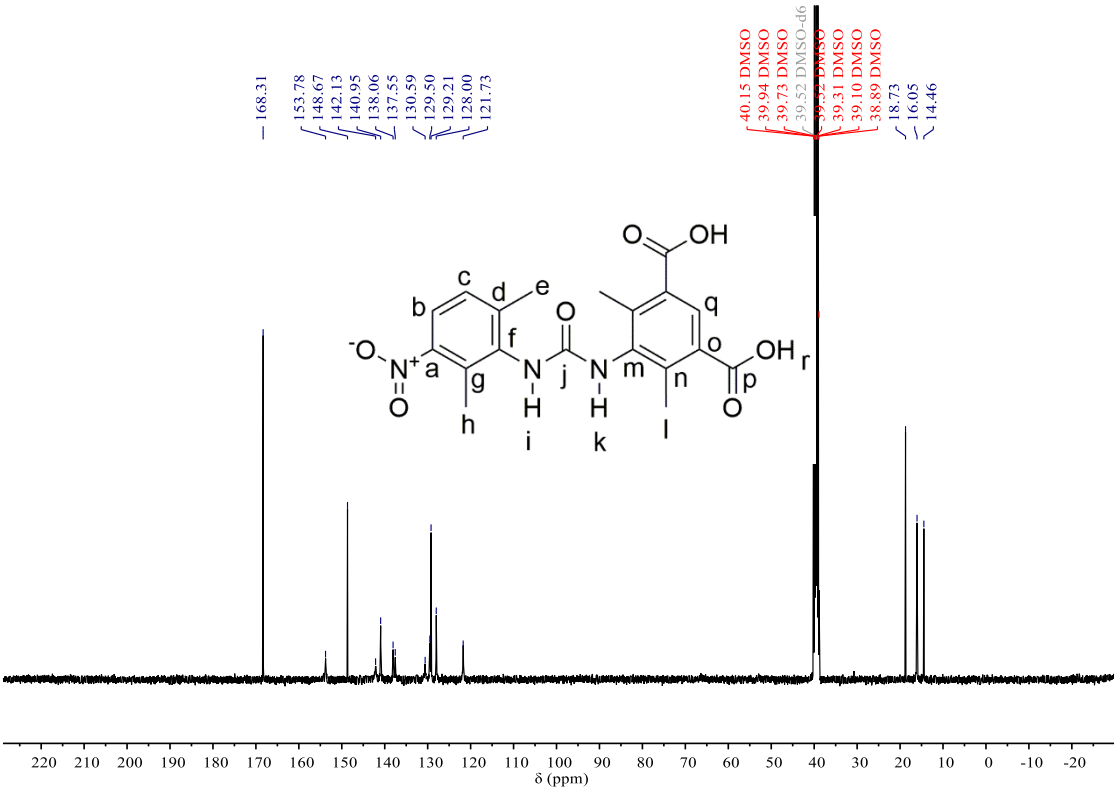

Figure 16. ^{13}C{H} (100 MHz, DMSO-d6, 298 K of compound **2.8**).

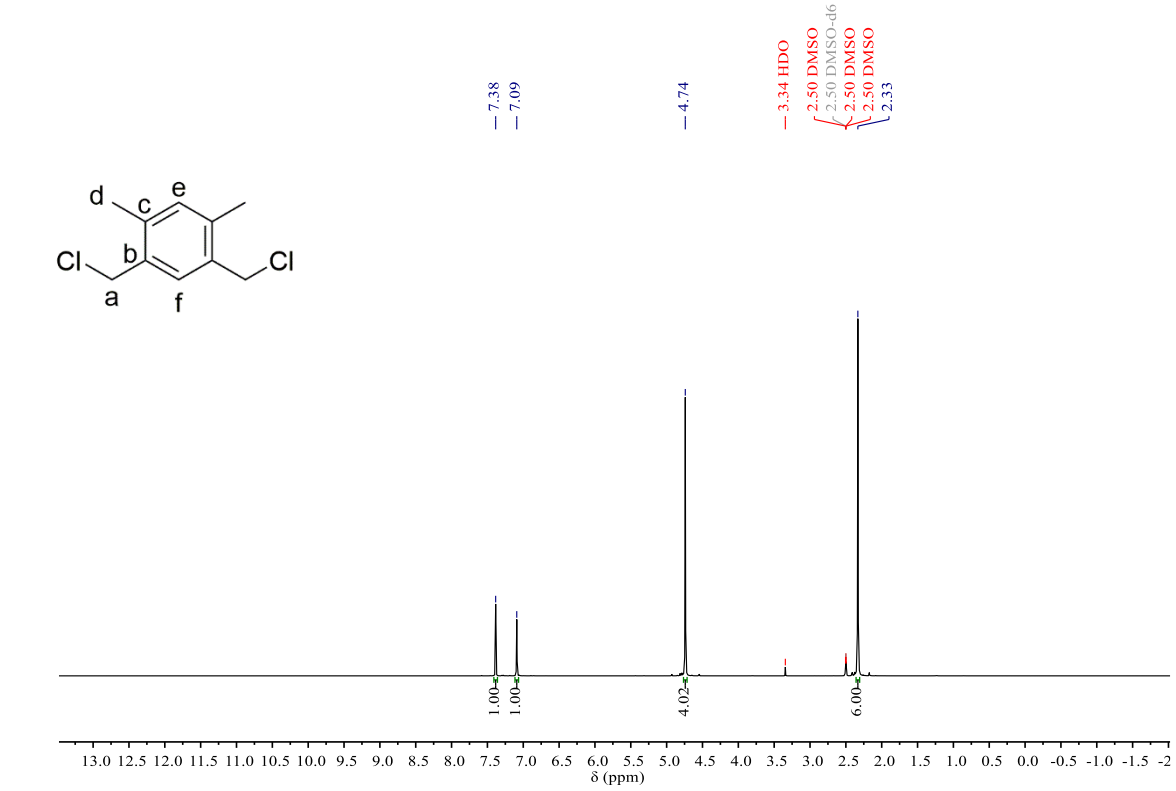

Figure 17. ^{1}H NMR (400 MHz, DMSO-d_6, 298 K of compound **2.9**).

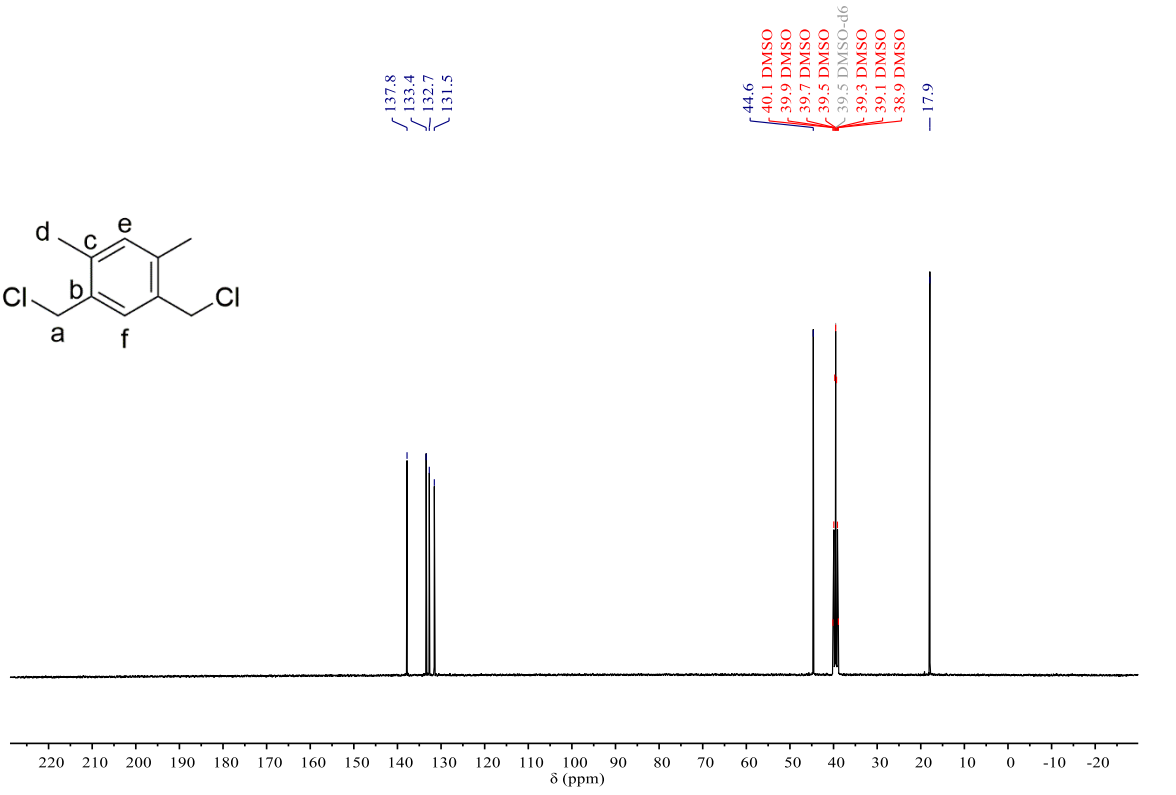

Figure 18. ^{13}C{H} (100 MHz, DMSO-d_6, 298 K of compound **2.9**).

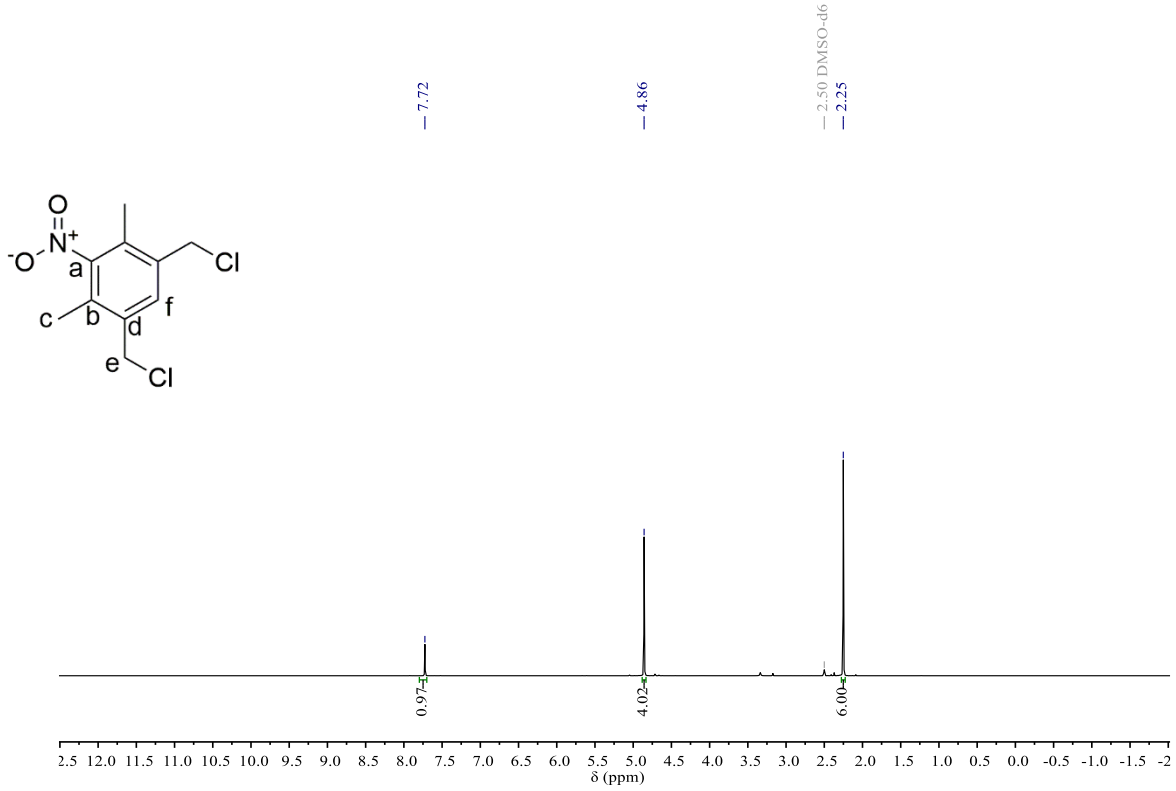

Figure 19. ^{1}H NMR (400 MHz, DMSO-d_6, 298 K of compound **2.10**).

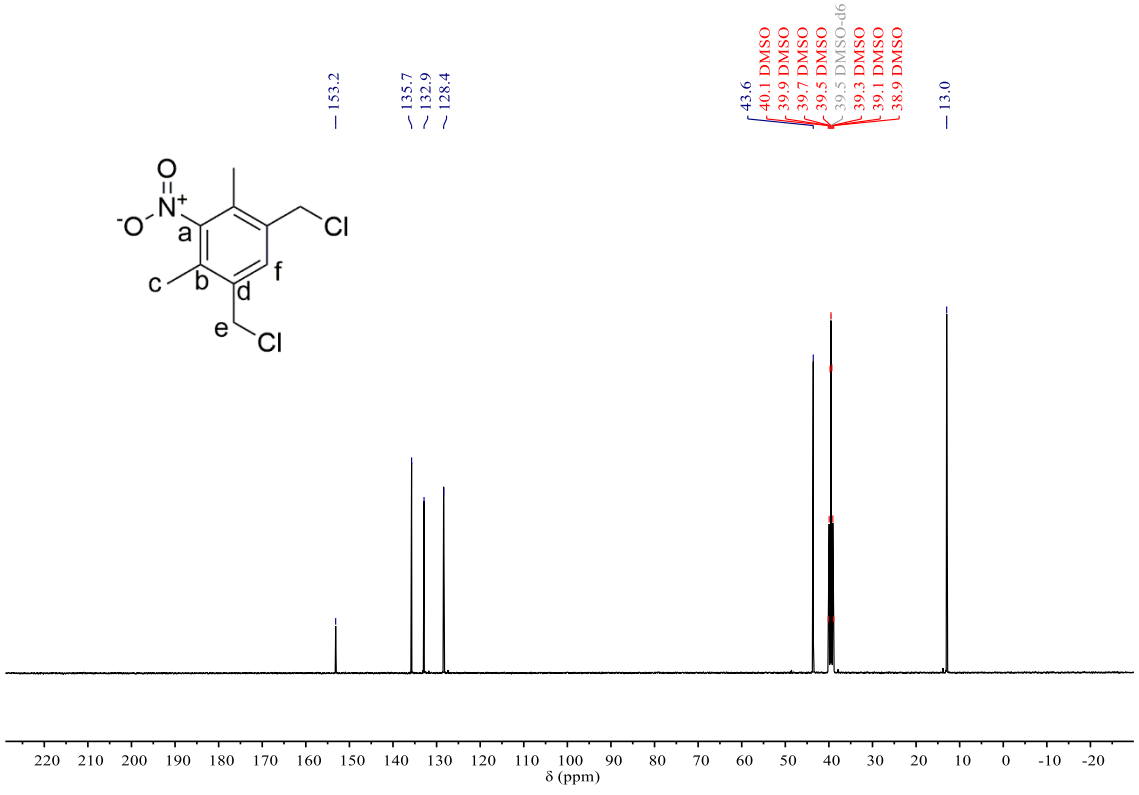

Figure 20. ^{13}C{H}(100 MHz, DMSO-d_6, 298 K of compound **2.10**).

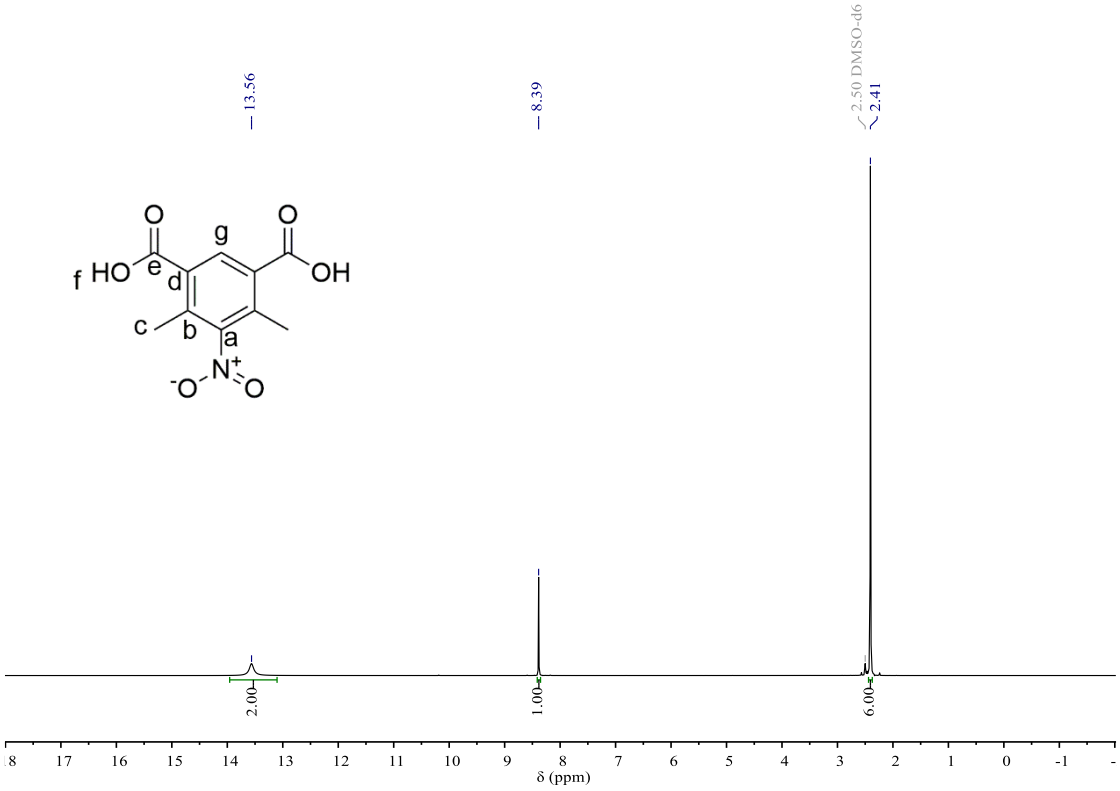

Figure 21. ^{1}H NMR (400 MHz, DMSO-d$_6$, 298 K of compound **2.11**).

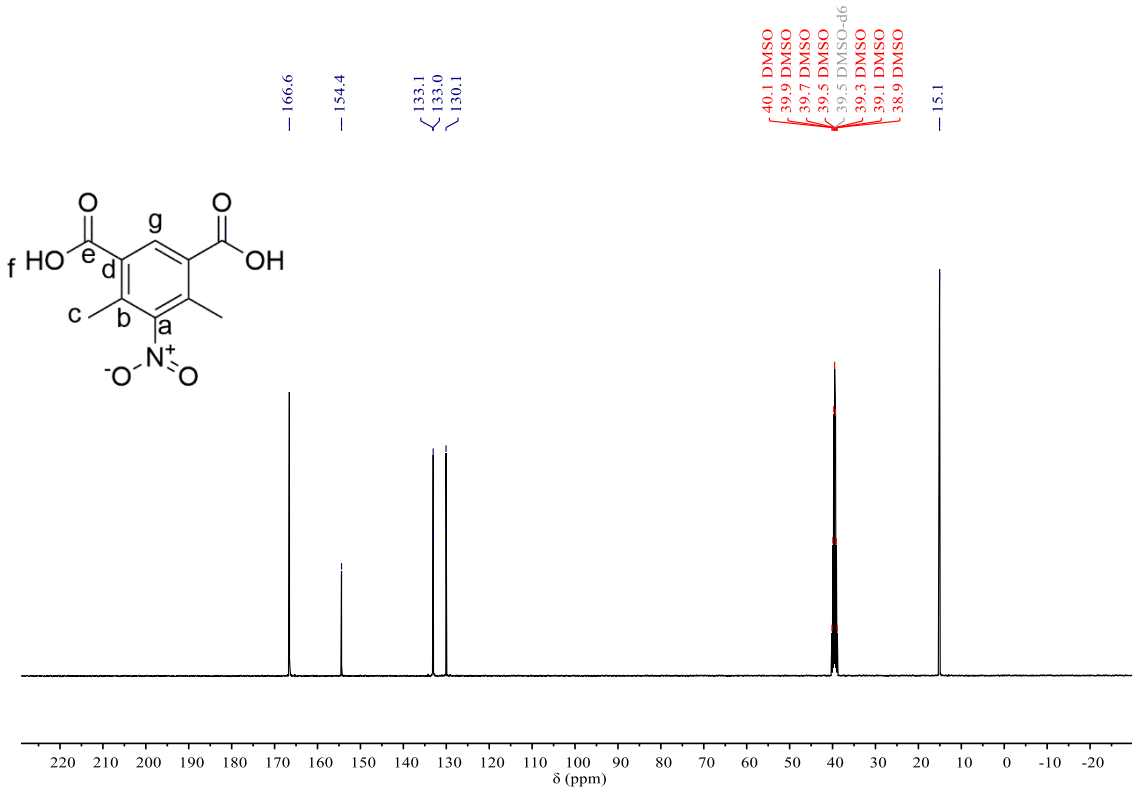

Figure 22. ^{13}C{H} (100 MHz, DMSO-d$_6$, 298 K of compound **2.11**).

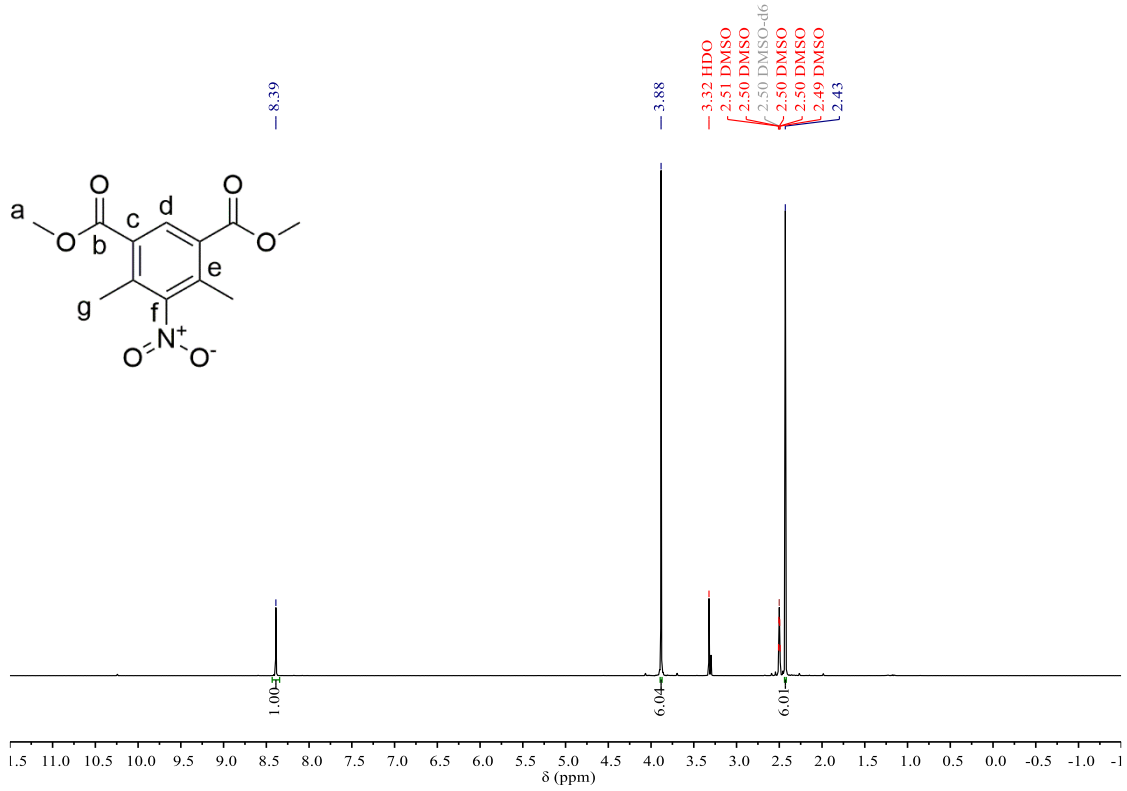

Figure 23. ^{1}H NMR (400 MHz, DMSO-d_6, 298 K of compound **2.12**).

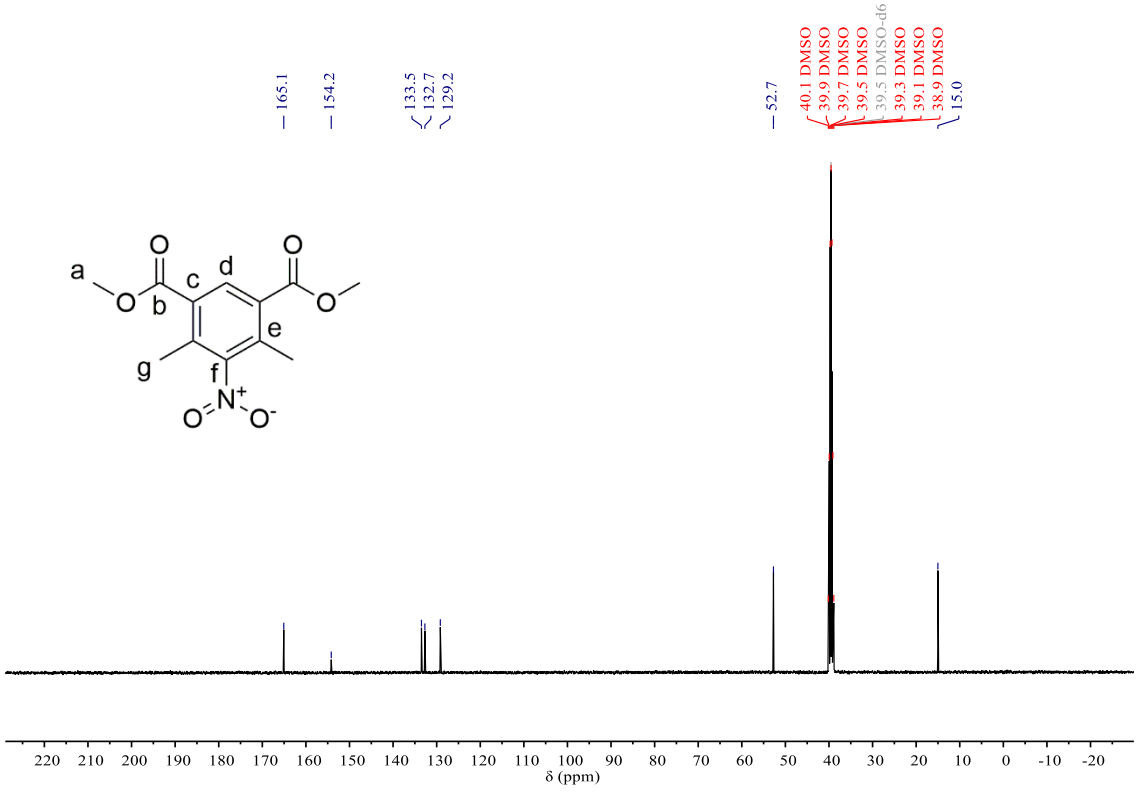

Figure 24. ^{13}C{H} (100 MHz, DMSO-d_6, 298 K of compound **2.12**).

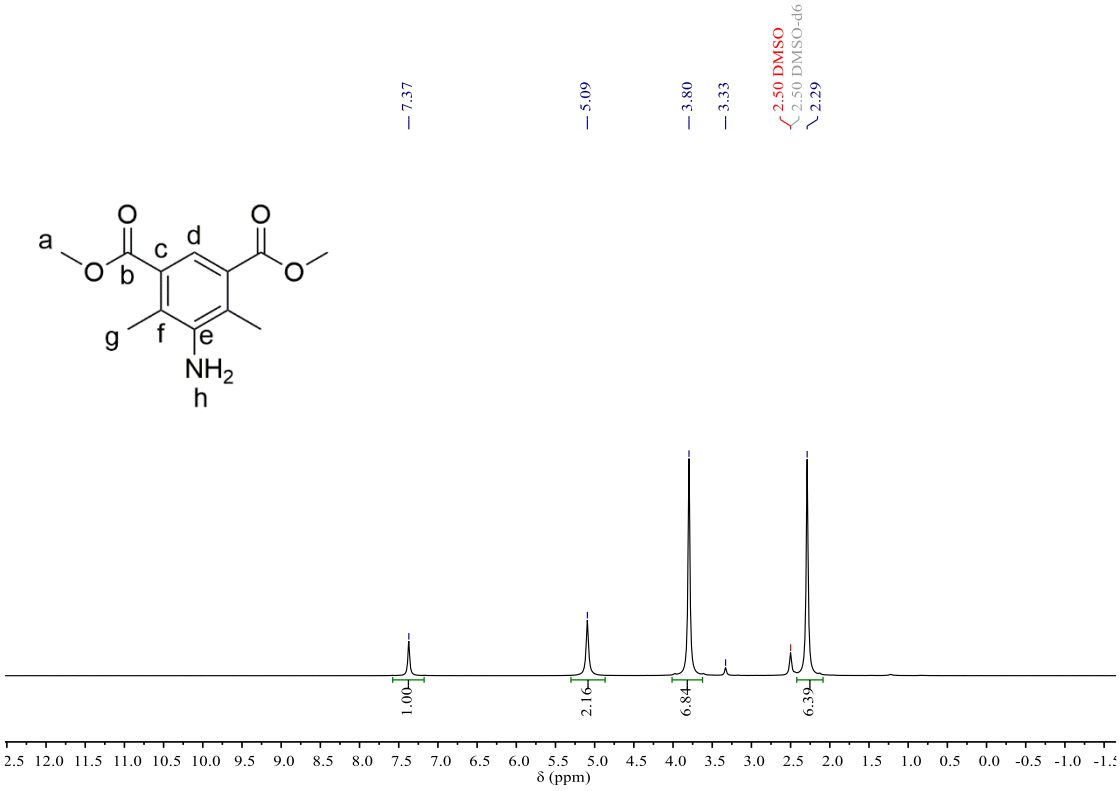

Figure 25. ^{1}H NMR (400 MHz, DMSO-d_6, 298 K of compound **2.13**).

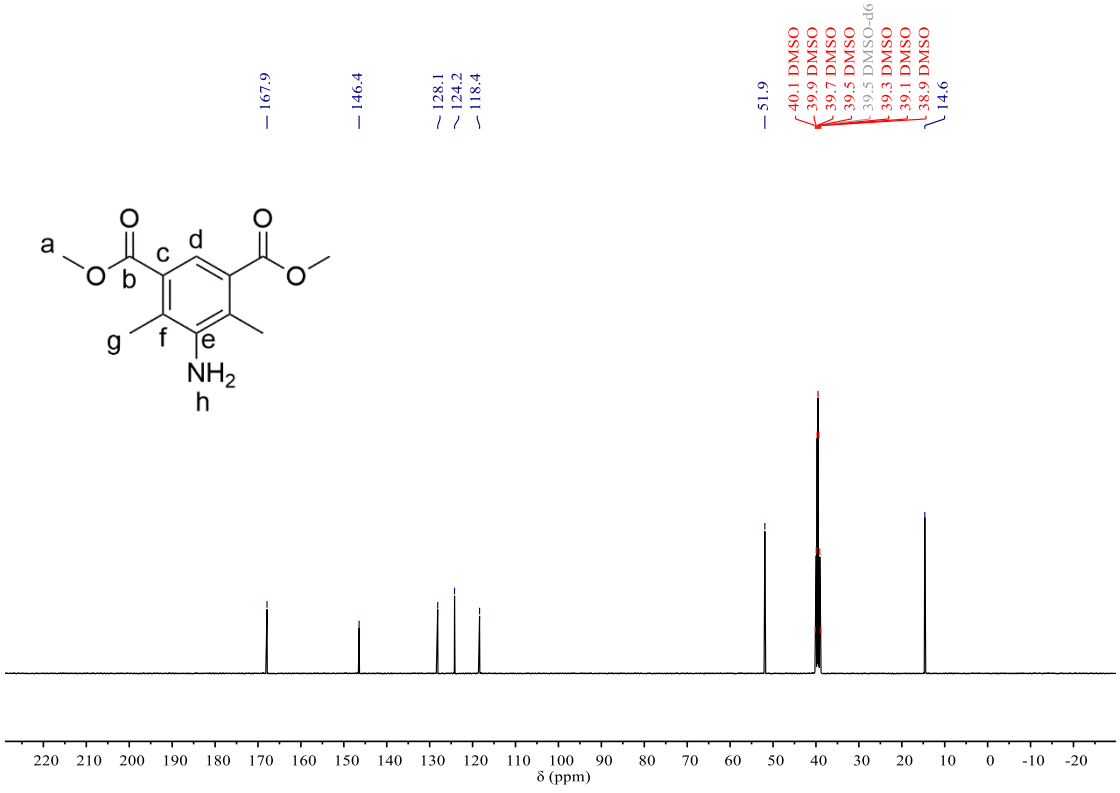

Figure 26. ^{13}C{H} (100 MHz, DMSO-d6, 298 K of compound **2.13**).

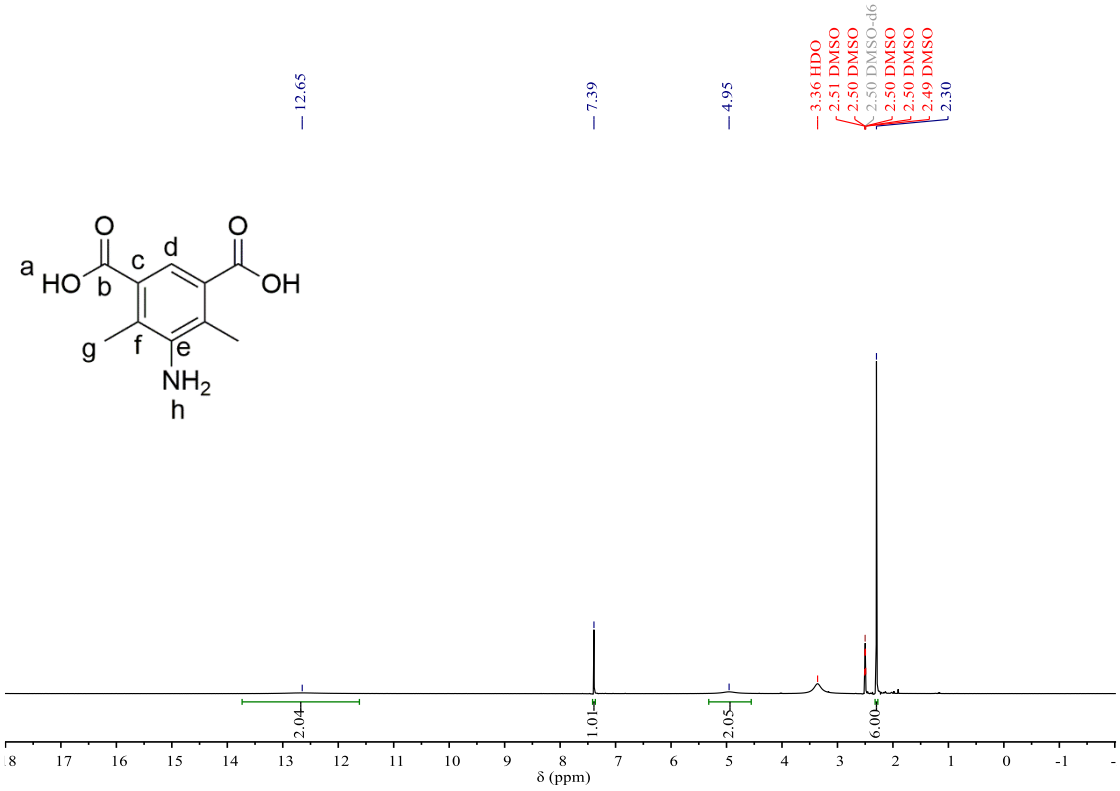

Figure 27. ^{1}H NMR (400 MHz, DMSO-d$_6$, 298 K of compound **2.14**).

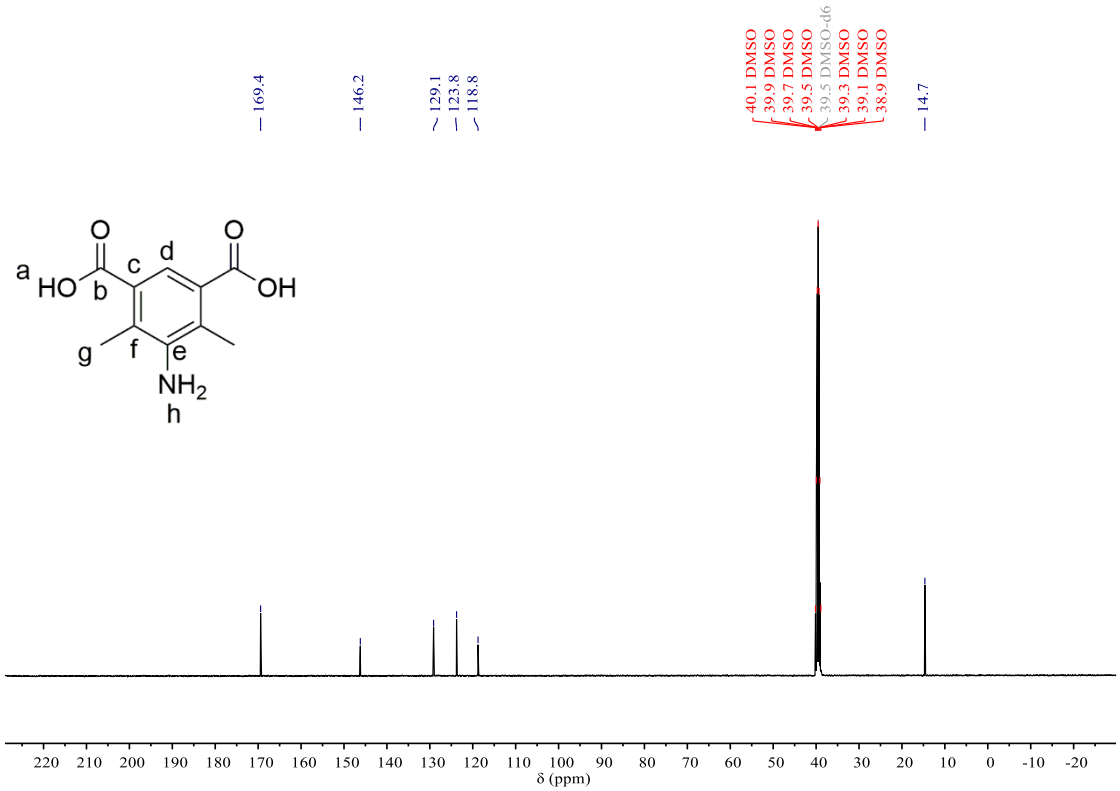

Figure 28. ^{13}C{H} (100 MHz, DMSO-d$_6$, 298 K of compound **2.14**).

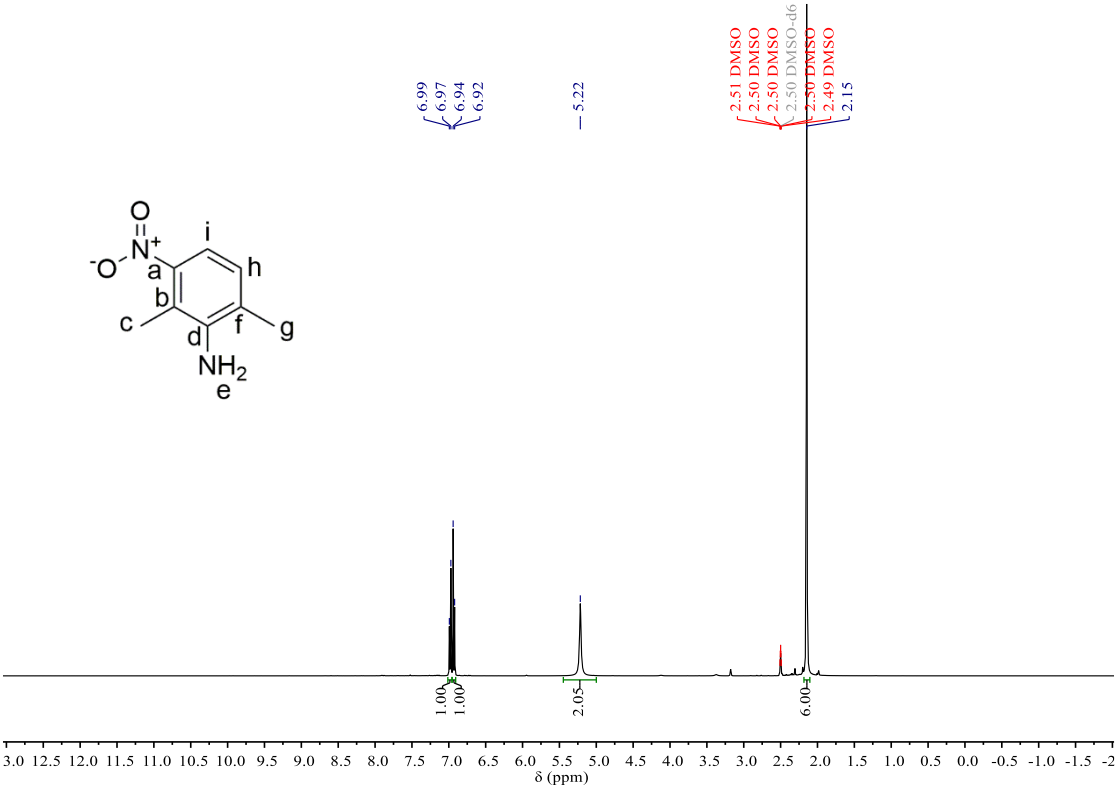

Figure 29. ^{1}H NMR (400 MHz, DMSO-d$_6$, 298 K of compound **2.15**).

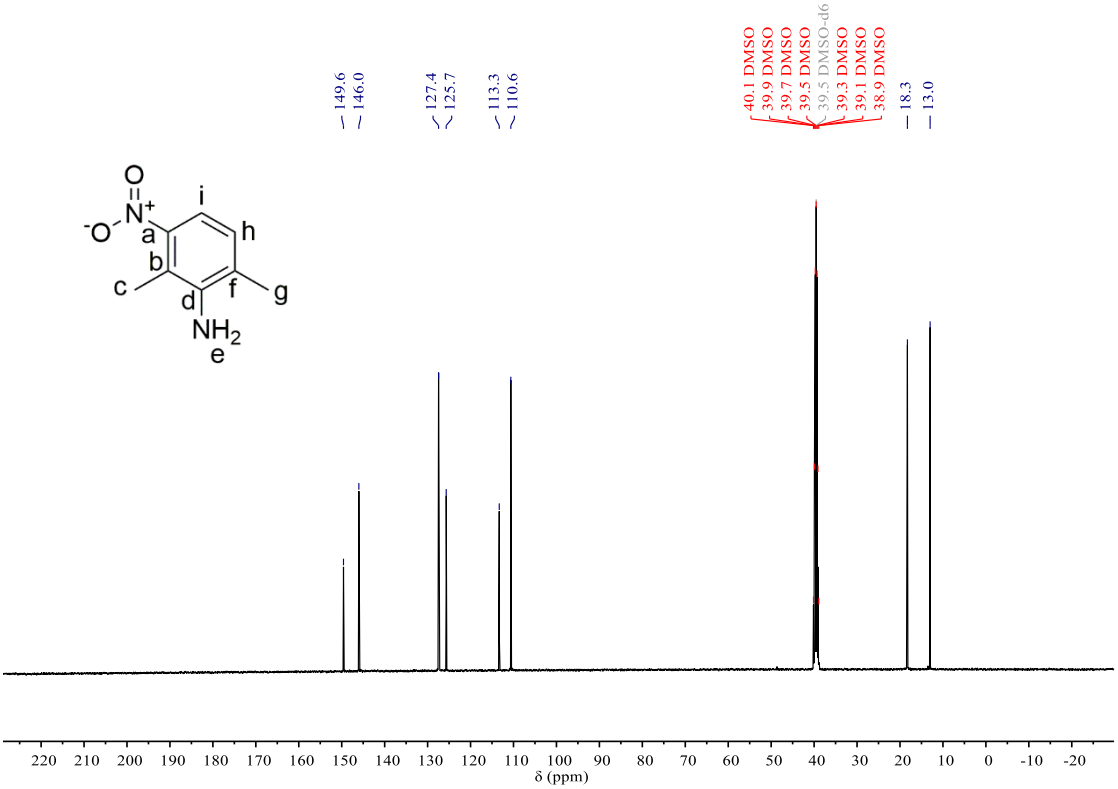

Figure 30. ^{13}C{H} (100 MHz, DMSO-d$_6$, 298 K of compound **2.15**).

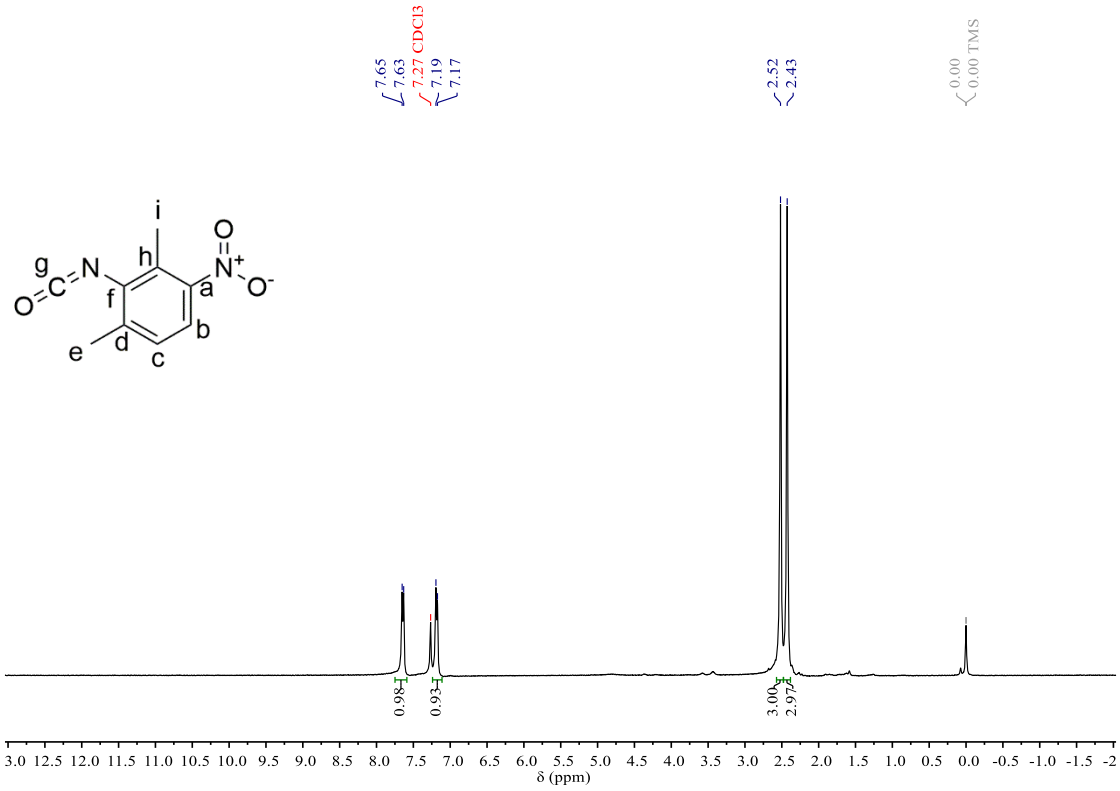

Figure 31. ^{1}H NMR (400 MHz, DMSO-d$_6$, 298 K of compound **2.16**).

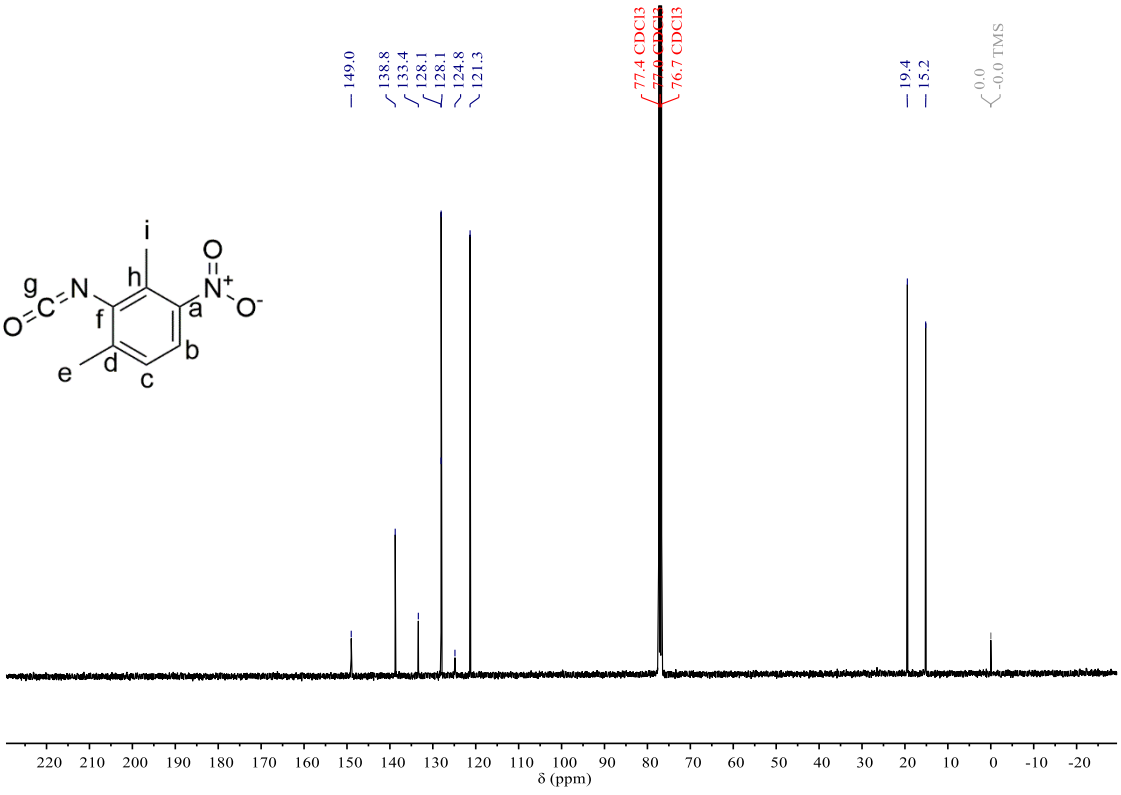

Figure 32. ^{13}C{H} (100 MHz, DMSO-d$_6$, 298 K of compound **2.16**).

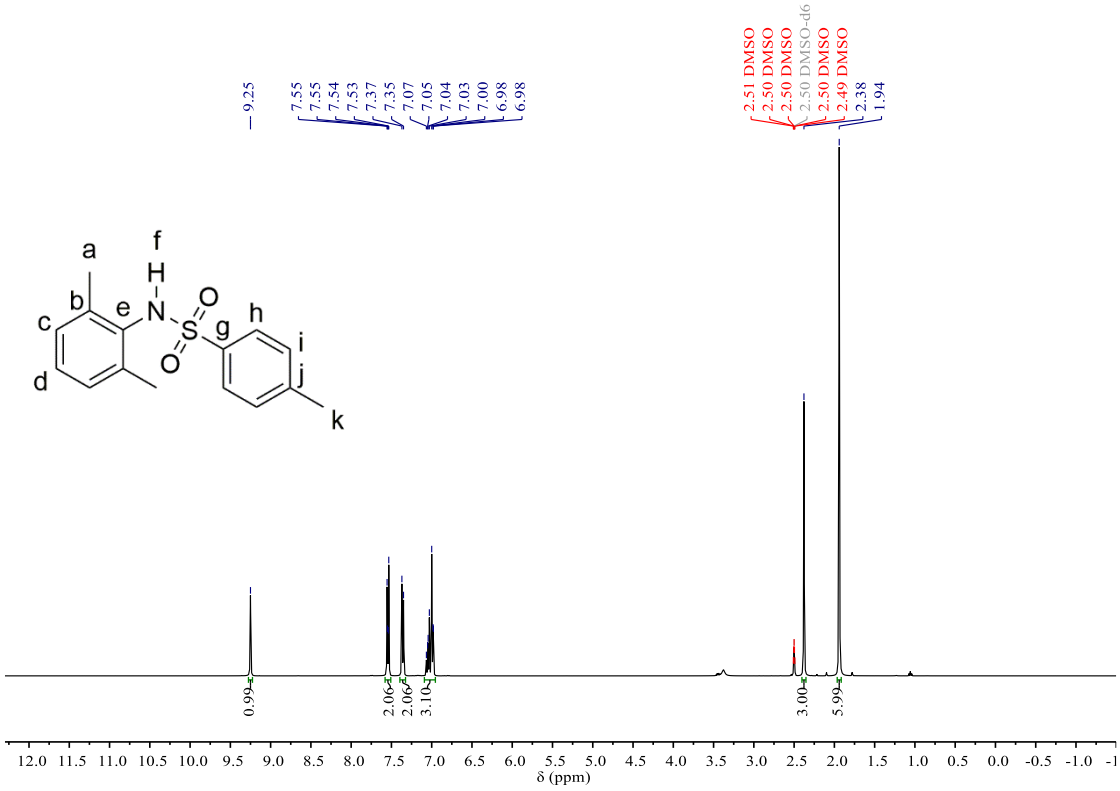

Figure 33. ^{1}H NMR (400 MHz, DMSO-d_6, 298 K of compound **2.17**).

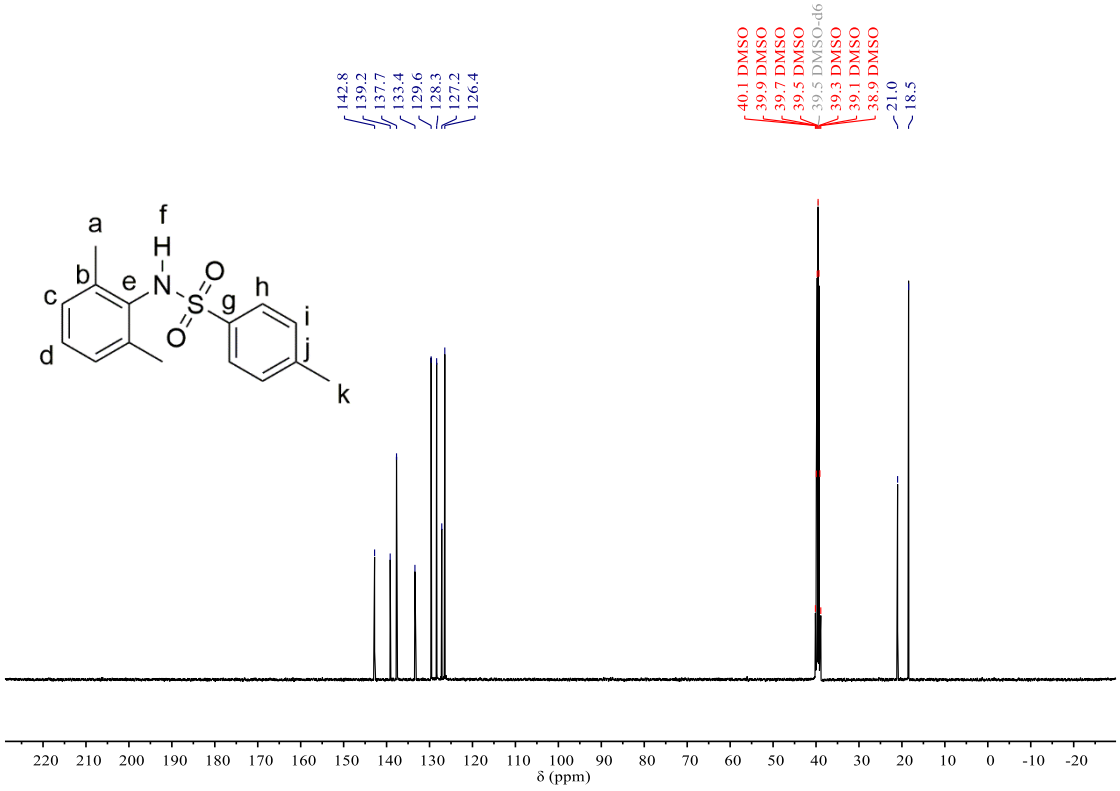

Figure 34. ^{13}C{H**}** (100 MHz, DMSO-d6, 298 K of compound **2.17**).

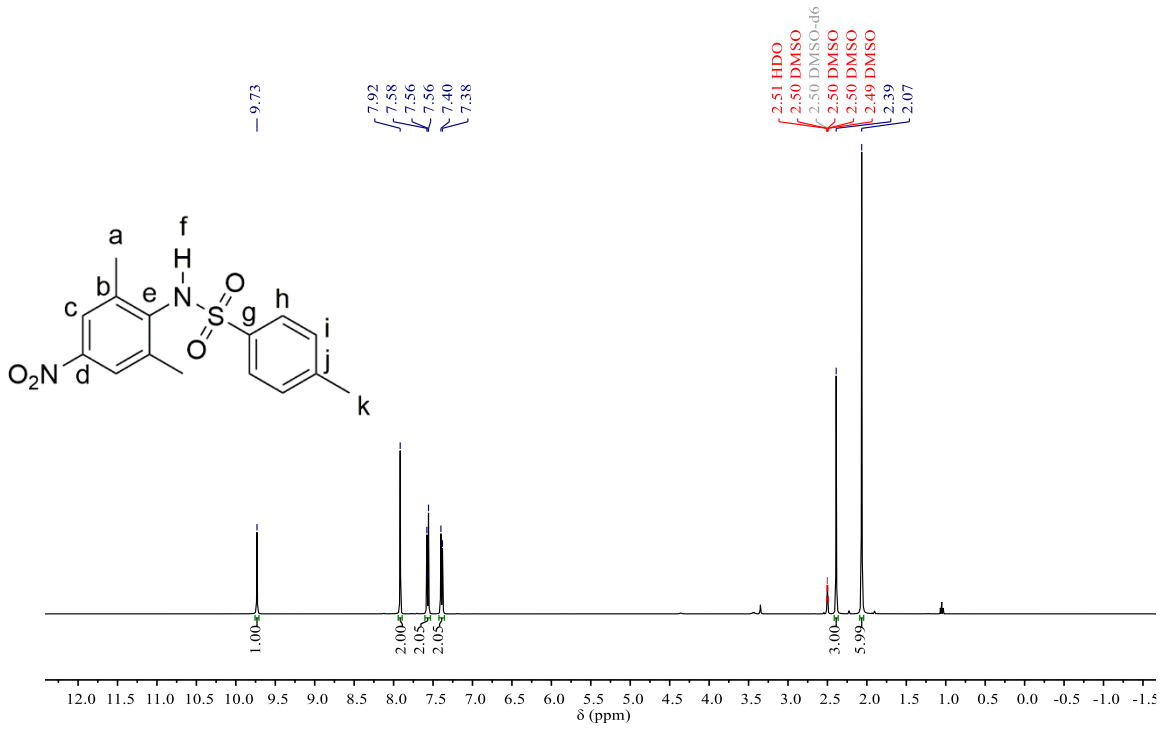

Figure 35. ^{1}H NMR (400 MHz, DMSO-d_6, 298 K of compound **2.18**).

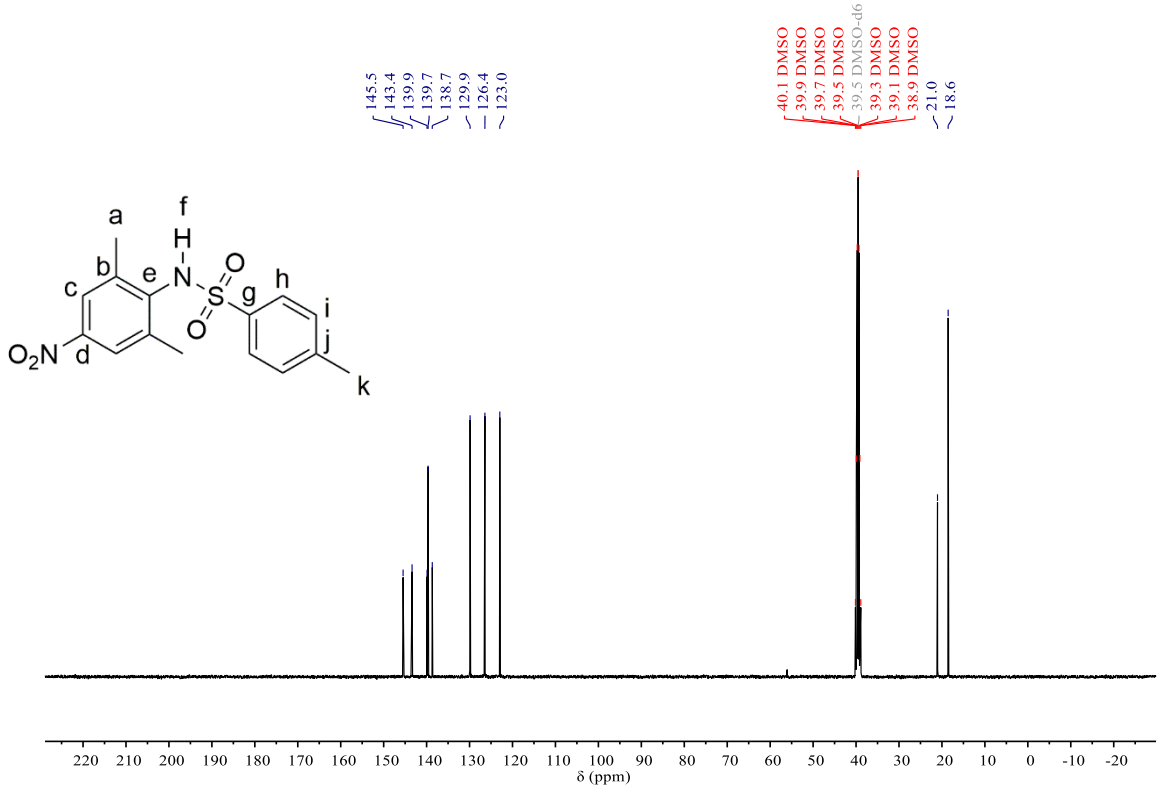

Figure 36. ^{13}C{H} (100 MHz, DMSO-d_6, 298 K of compound **2.18**).

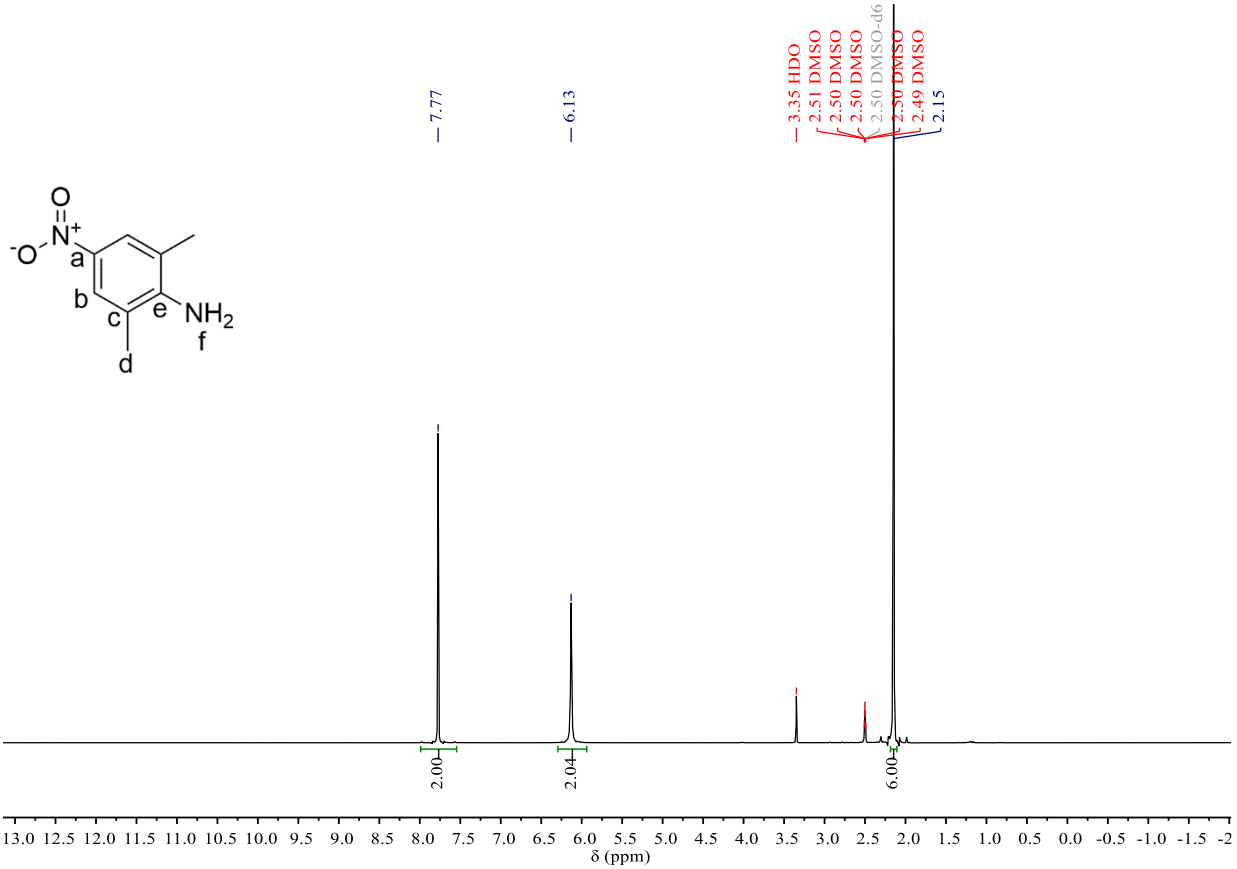

Figure 37. ^{1}H NMR (400 MHz, DMSO-d_6, 298 K of compound **2.19**).

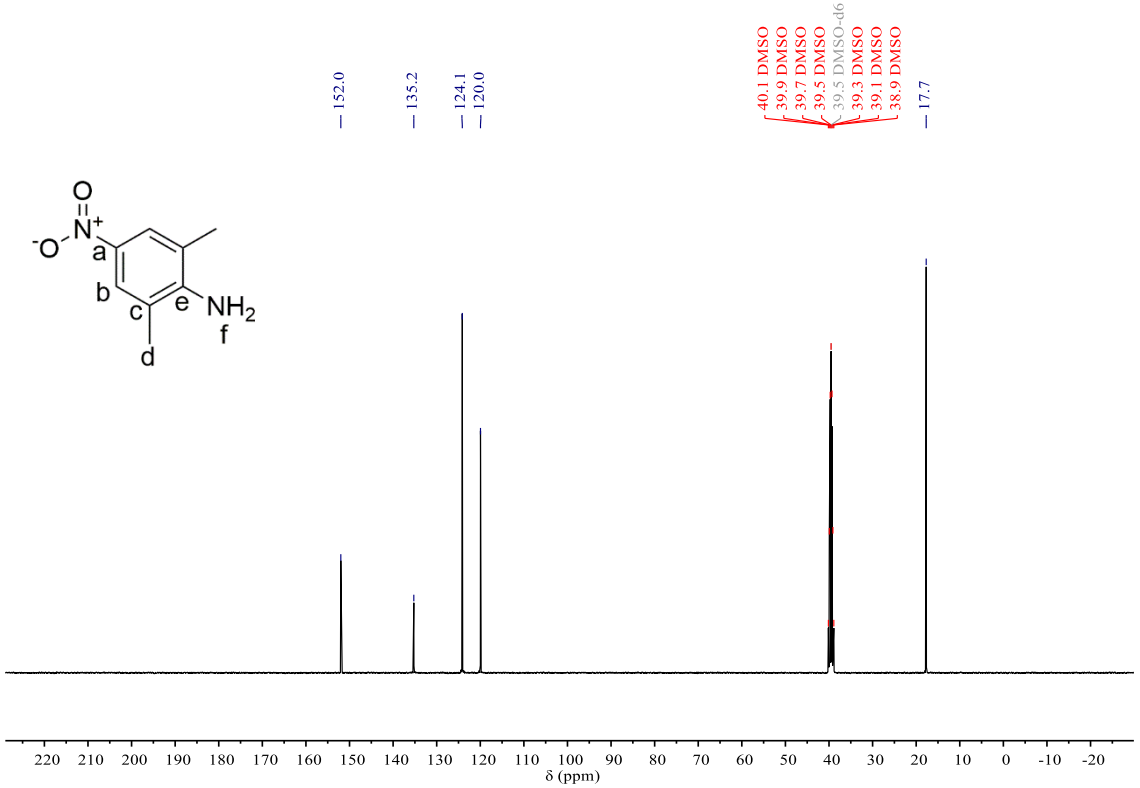

Figure 38. ^{13}C{H} (100 MHz, DMSO-d_6, 298 K of compound **2.19**).

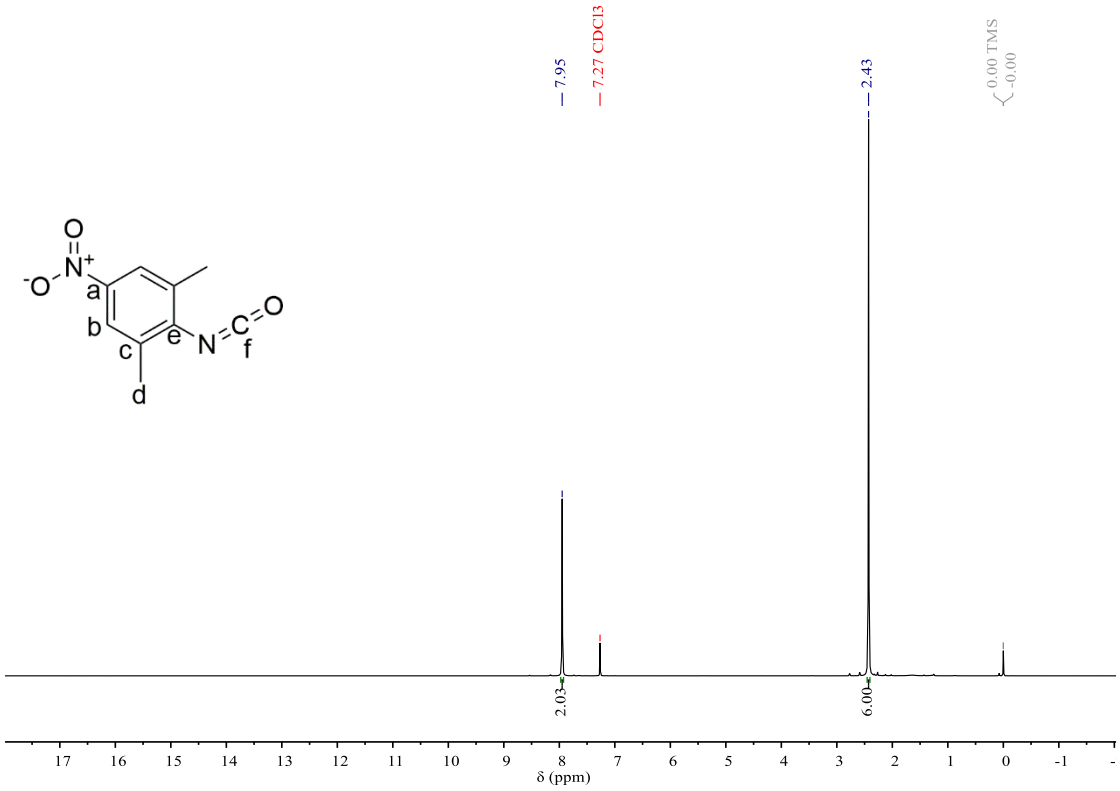

Figure 39. ^{1}H NMR (400 MHz, DMSO-d$_6$, 298 K of compound **2.20**).

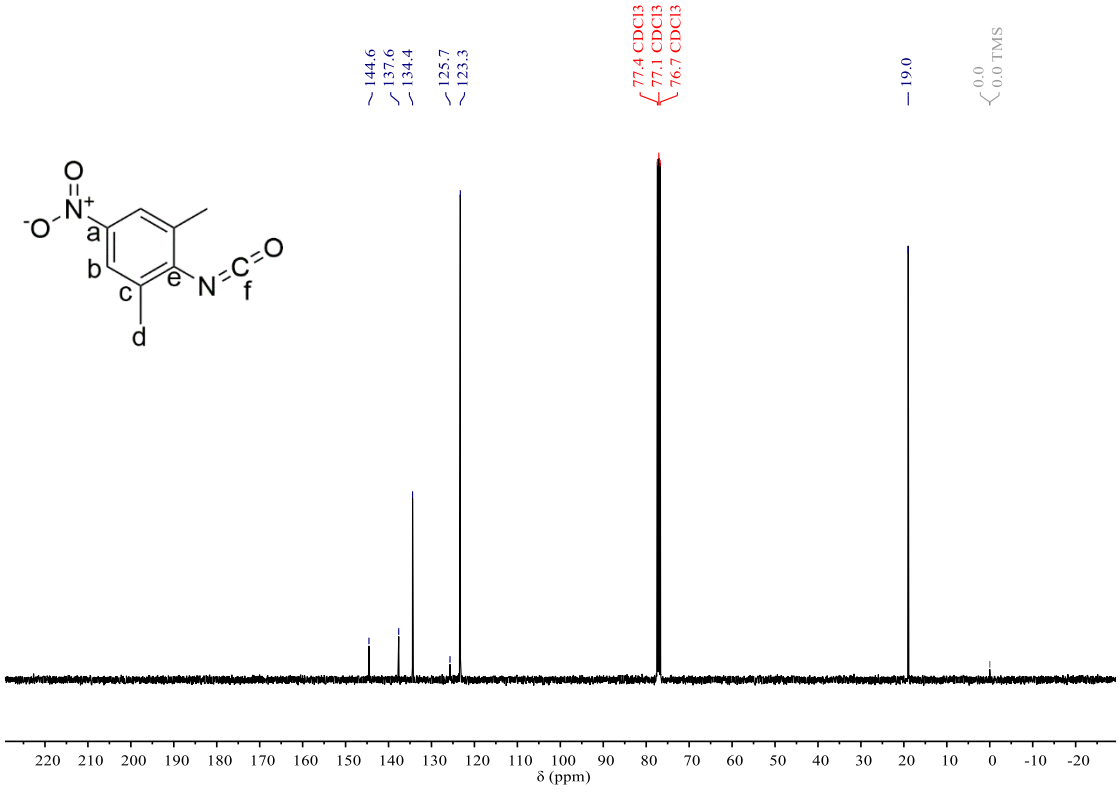

Figure 40. ^{13}C{H} (100 MHz, DMSO-d$_6$, 298 K of compound **2.20**).

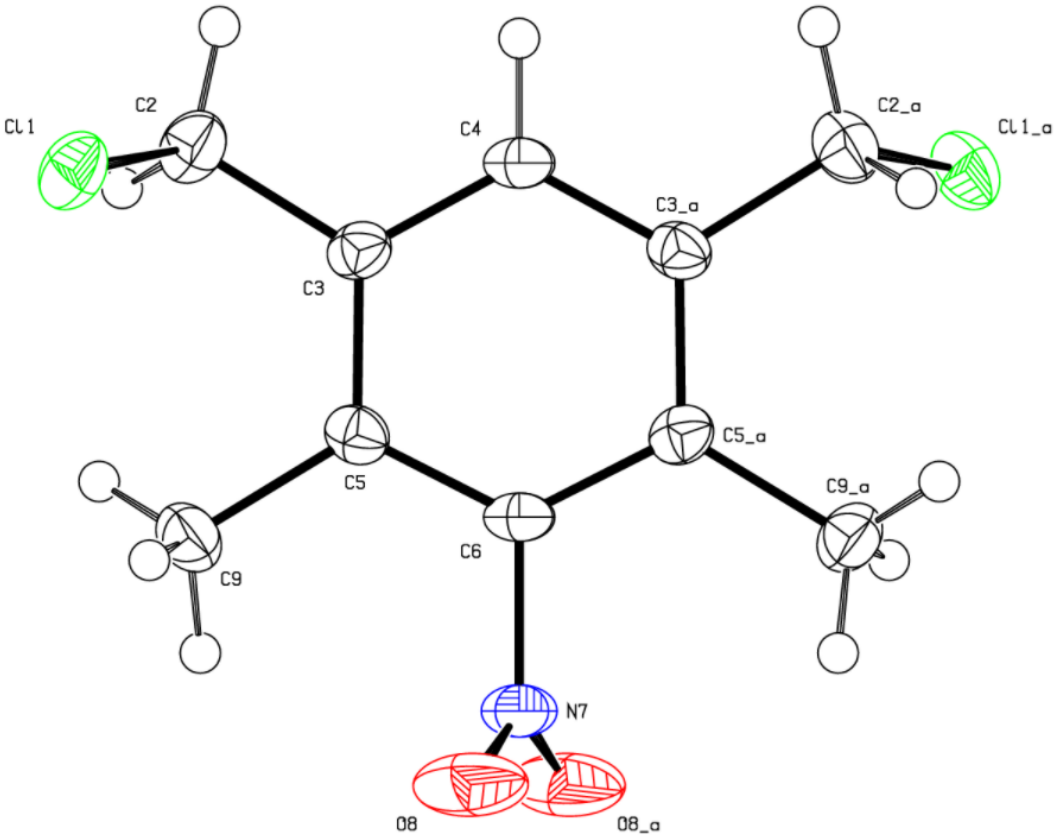

Figure 41. Crystal structure of compound 2.10, ellipsoids drawn at 50% probability.

Symmetry code: (a) 1 – *x*, *y*, 1.5 – *z*.

Table 1. Crystallographic details for compound 2.10.

Formula	$C_{10}\,H_{11}\,Cl_2\,N\,O_2$
M_r	248.11
Crystal system	monoclinic
Space group	C 2/c
Z	4
a /Å	15.72720(2)
b/Å	8.273769(15)
c /Å	8.583140(18)
β / °	95.913(3)
V / Å^3	1110.923(7)
ρ_{calc} / g cm^{-3}	1.483
Crystal habit	Colourless block
Crystal dimensions /mm	0.017 × 0.031 × 0.136
Radiation	Cu K_α (1.54180 Å)
T /K	100
μ /mm^{-1}	5.101
R(*F*), *Rw*(*F*) /%	4.50, 6.89
CCDC cif deposition number	CCDC 2085509

Table 2. Selected bond lengths (Å) and angles (°) for compound 10.

O(8) – N(7)	1.213(2)	O(8) – N(7) – O(8)[a]	124.7(3)
N(7) – C(6)	1.477(3)	O(8) – N(7) – C(6)	117.65(14)
C(2) – C(3)	1.497(3)	Cl(1) – C(2) – C(3)	110.70(16)
C(3) – C(4)	1.393(2)	C(2) – C(3) – C(4)	119.42(19)
C(3) – C(5)	1.404(3)	C(2) – C(3) – C(5)	121.17(18)
C(5) – C(6)	1.390(2)	C(4) – C(3) – C(5)	119.41(18)
C(5) – C(9)	1.507(3)	C(3) – C(4) – C(3)[a]	122.6(3)
		C(3) – C(5) – C(6)	116.12(18)
		C(3) – C(5) – C(9)	122.03(18)
		C(6) – C(5) – C(9)	121.85(19)
		N(7) – C(6) – C(5)	116.86(13)
		C(5) – C(6) – C(5)[a]	126.3(3)

Symmetry code: (a) 1 – *x*, *y*, 1.5 – *z*.

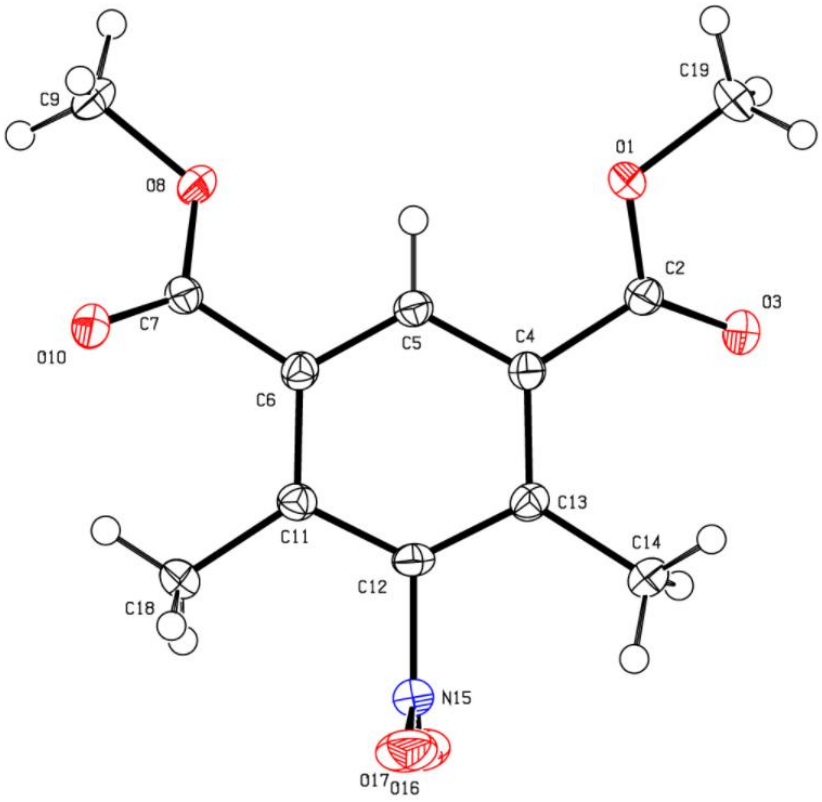

Figure 42. Crystal structure of compound **2.13**, ellipsoids drawn at 50% probability.

Table 3. Crystallographic details for compound **2.13**.

Formula	$C_{12}\,H_{13}\,N\,O_6$
M_r	267.24
Crystal system	monoclinic
Space group	P 2_1/n
Z	4
a /Å	7.94120(1)
b/Å	17.09118(2)
c /Å	9.16055(1)
β / °	102.051(2)
V / Å^3	1215.910(11)
ρ_{calc} / g cm^{-3}	1.460
Crystal habit	Colourless block
Crystal dimensions /mm	0.030 × 0.066 × 0.098
Radiation	Cu K_α (1.54180 Å)
T /K	100
μ /mm^{-1}	1.015
R(*F*), *Rw*(*F*) /%	3.86, 5.32
CCDC cif deposition number	CCDC 2089501

Table 4. Selected bond lengths (Å) and angles (°) for compound **2.13**.

O(1) – C(2)	1.3375(18)	C(2) – O(1) – C(19)	114.98(11)
O(1) – C(19)	1.4461(17)	O(1) – C(2) – O(3)	123.55(13)
C(2) – O(3)	1.2121(18)	O(1) – C(2) – C(4)	111.14(12)
C(2) – C(4)	1.4912(19)	O(3) – C(2) – C(4)	125.28(13)
C(4) – C(5)	1.392(2)	C(2) – C(4) – C(5)	118.75(12)
C(4) – C(13)	1.4070(19)	C(2) – C(4) – C(13)	121.47(13)
C(5) – C(6)	1.390(2)	C(5) – C(4) – C(13)	119.77(13)
C(6) – C(7)	1.4959(19)	C(4) – C(5) – C(6)	122.56(13)
C(6) – C(11)	1.4058(19)	C(5) – C(6) – C(7)	118.11(12)
C(7) – O(8)	1.3400(18)	C(5) – C(6) – C(11)	120.03(13)
C(7) – O(10)	1.2075(18)	C(7) – C(6) – C(11)	121.83(13)
C(8) – C(9)	1.4504(18)	C(6) – C(7) – O(8)	110.58(12)
C(11) – C(12)	1.397(2)	C(6) – C(7) – O(10)	125.55(13)
C(11) – C(18)	1.5043(19)	O(8) – C(7) – O(10)	123.86(13)
C(12) – C(13)	1.393(2)	C(7) – O(8) – C(9)	116.11(12)
C(12) – N(15)	1.4783(18)	C(6) – C(11) – C(12)	115.18(13)
C(13) – C(14)	1.5109(19)	C(6) – C(11) – C(18)	124.66(13)
N(15) – O(16)	1.2215(19)	C(12) – C(11) – C(18)	120.09(13)
N(15) – O(17)	1.2214(19)	C(11) – C(12) – C(13)	127.03(13)
		C(11) – C(12) – N(15)	116.40(12)
		C(13) – C(12) – N(15)	116.57(12)
		C(4) – C(13) – C(12)	115.42(12)
		C(4) – C(13) – C(14)	123.62(13)
		C(12) – C(13) – C(14)	120.96(12)
		C(12) – N15) – O(16)	117.58(13)
		C(12) – N(15) – O(17)	117.75(13)
		O(16) – N(15) – O(17)	124.67(13)

Figure 43. CGC determination vial inversion of gelators **2.2** and **2.3** (20 mM).

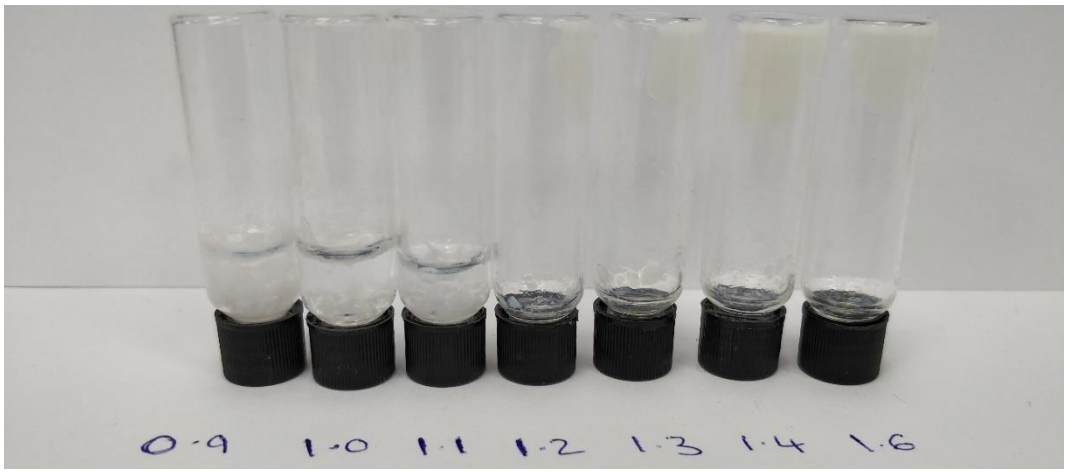

Figure 44. CGC determination vial inversion of gelator **2.4**. Mass of gelator in mg written below each vial.

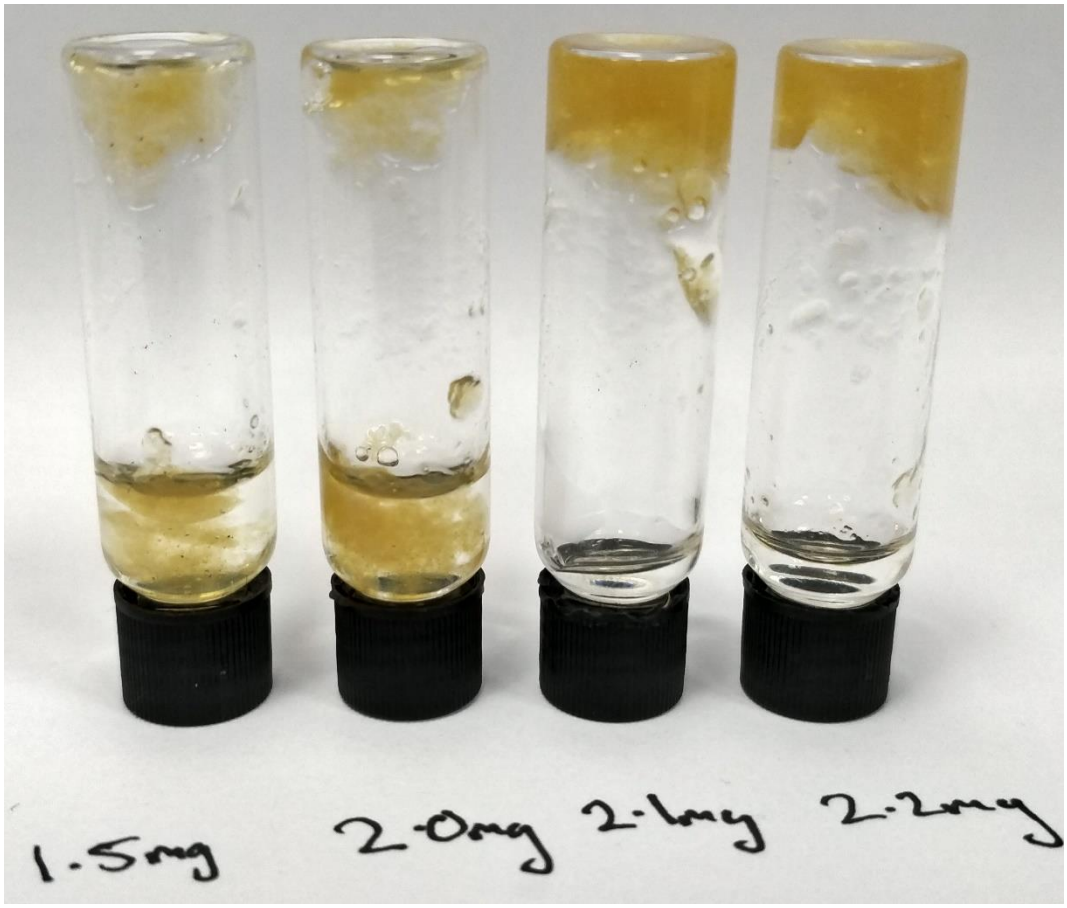

Figure 45. CGC determination vial inversion of gelator **2.6**. Mass of gelator in mg written below each vial.

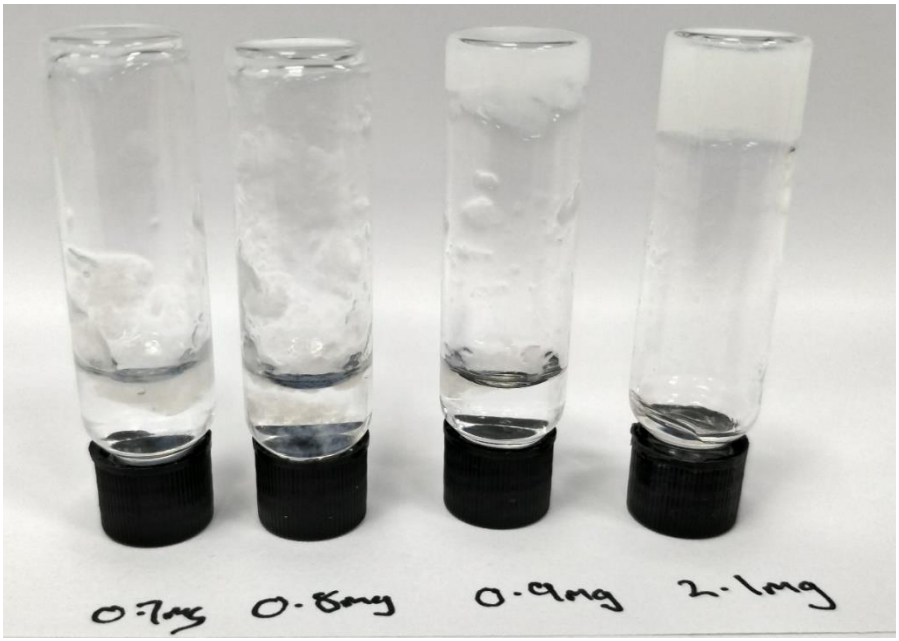

Figure 46. CGC determination vial inversion of gelator **2.7**. Mass of gelator in mg written below each vial.

Appendix 2

Contents

General synthetic protocol for SPU's (**SPU1**- **SPU13**)

Hydrogenated poly(butadiene) (Krasol HLBH-P 2000), molecular weight as supplied = 2100 g mol^{-1}, was dried under vacuum in oven at 80 °C for 2 hours. In the bulk, Krasol HLBH-P 2000 (1.0 equiv.) was mixed with 4,4'-methylenebis(phenyl isocyanate) (4,4'-MDI) (2.05 equiv.) at 80 °C under argon for 3 hours with gentle stirring. The colourless pre-polymer obtained was dissolved in dry THF (40 mL) and the aniline derivative (2.05 equiv.) was then added to the solution which was then brought to and maintained under reflux for 3 hours under argon. The supramolecular polymer solution was precipitated into ice cold methanol (3 x 1000 mL), the solid material filtered off and then dried *in vacuo*.

Protocol for casting of SPUs (**SPU1**-**SPU13**)

The precipitated polymer was dissolved in a minimum volume of THF (approximately 3 mL per 1 g of polymer) at 40 °C whilst stirring. Once fully dissolved, the polymer solution was poured into a 15 cm × 15 cm mould with a PTFE base. The solvent was allowed to slowly evaporate over 24 hours at room temperature and pressure. The mould was placed into a vacuum oven at 60 °C for 24 hours, then under partial vacuum (approximately 800 mbar) at 60 °C for 24 hours, the polymer film was then allowed to reach room temperature before being removed from the mould.

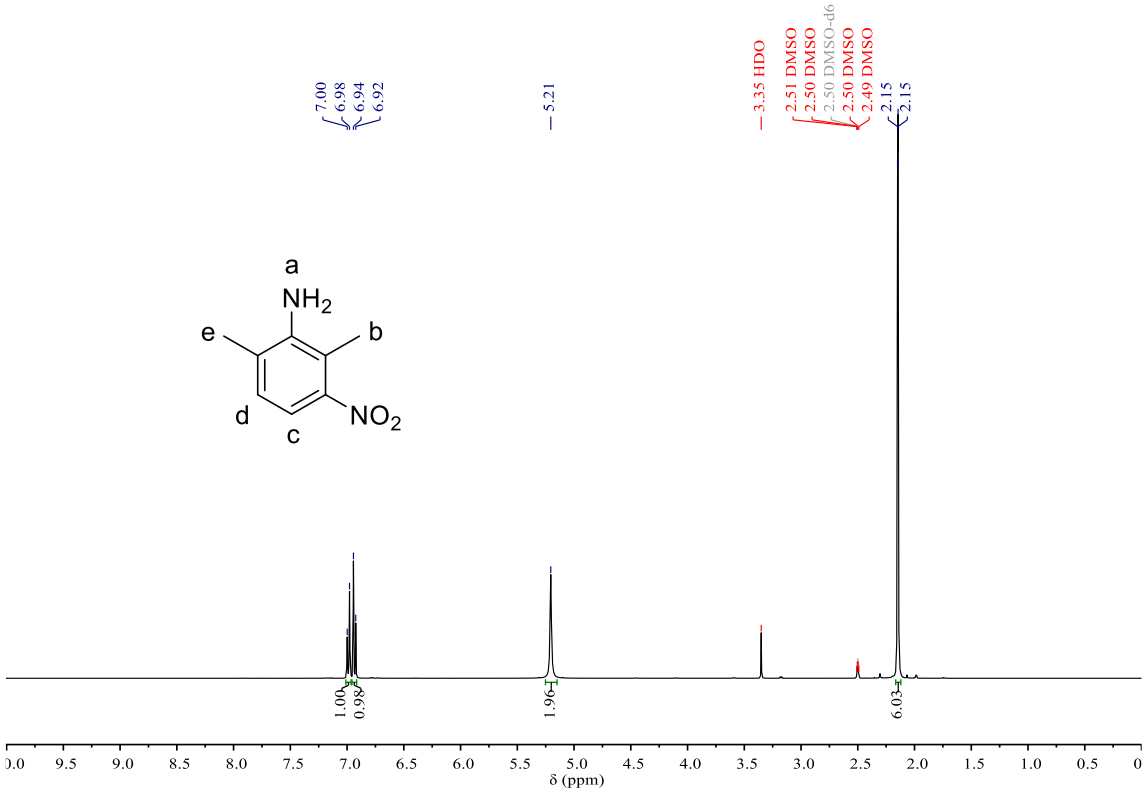

Figure 1. ^{1}H NMR spectrum of **3.1** (400 MHz, DMSO-d_6, 298 K).

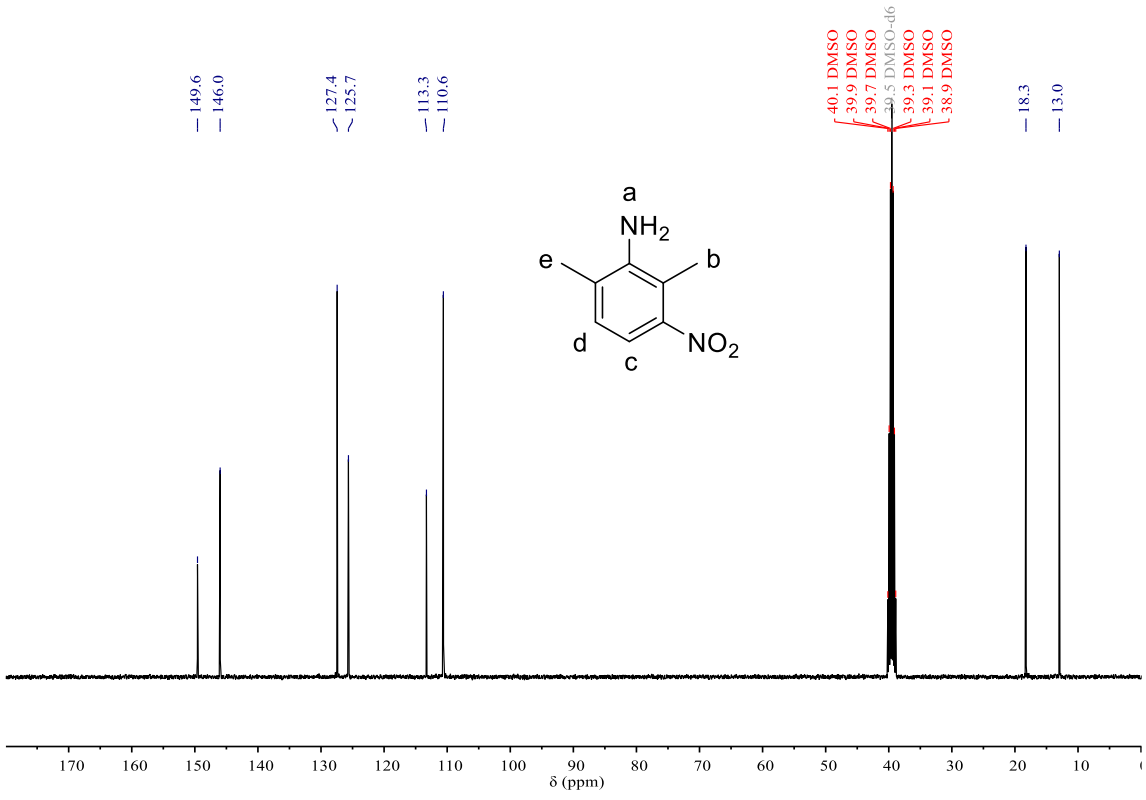

Figure 2. ^{13}C {H} NMR spectrum of **3.1** (100 MHz, DMSO-d_6, 298 K).

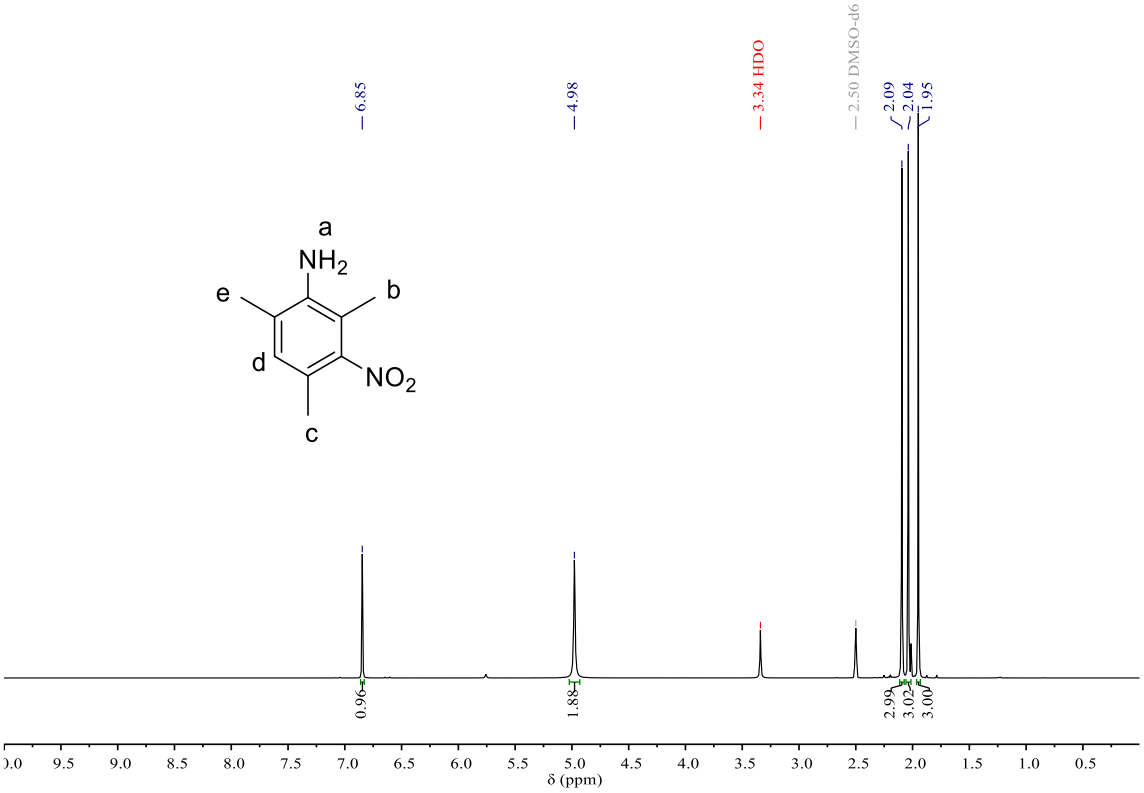

Figure 3. ^{1}H NMR spectrum of **3.2** (400 MHz, DMSO-d_6, 298 K).

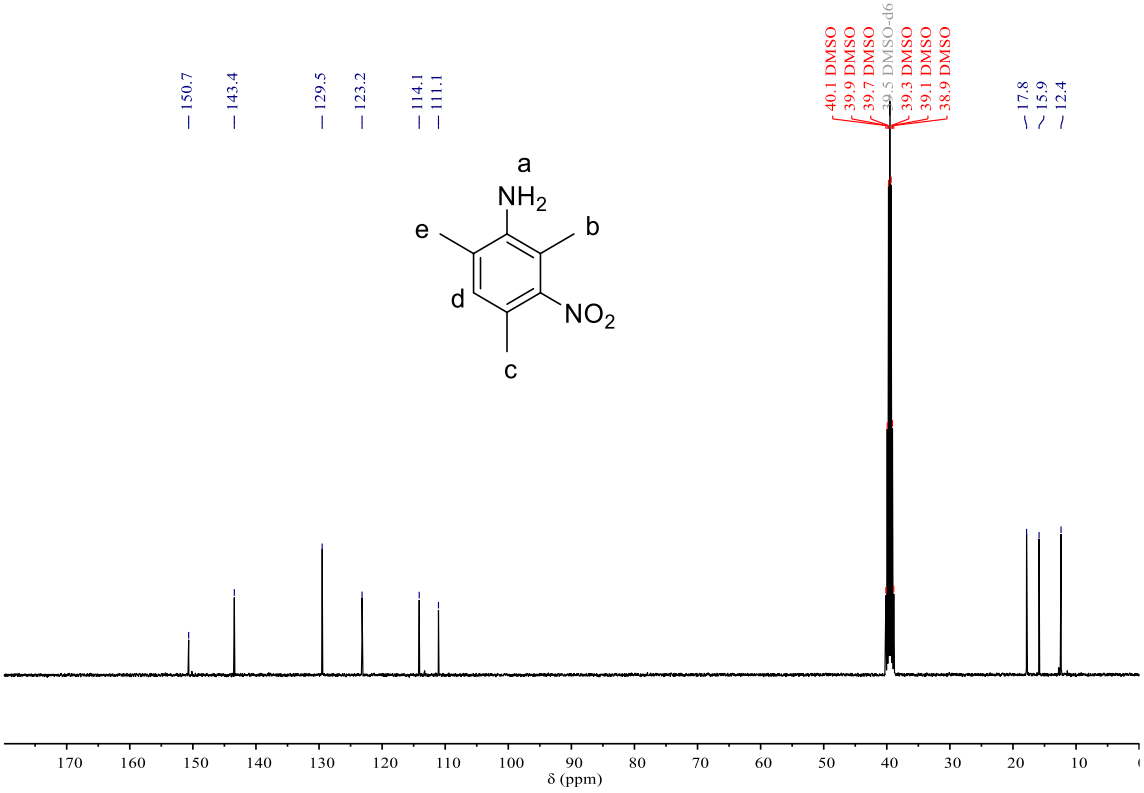

Figure 4. ^{13}C {H} NMR spectrum of **3.2** (100 MHz, DMSO-d_6, 298 K).

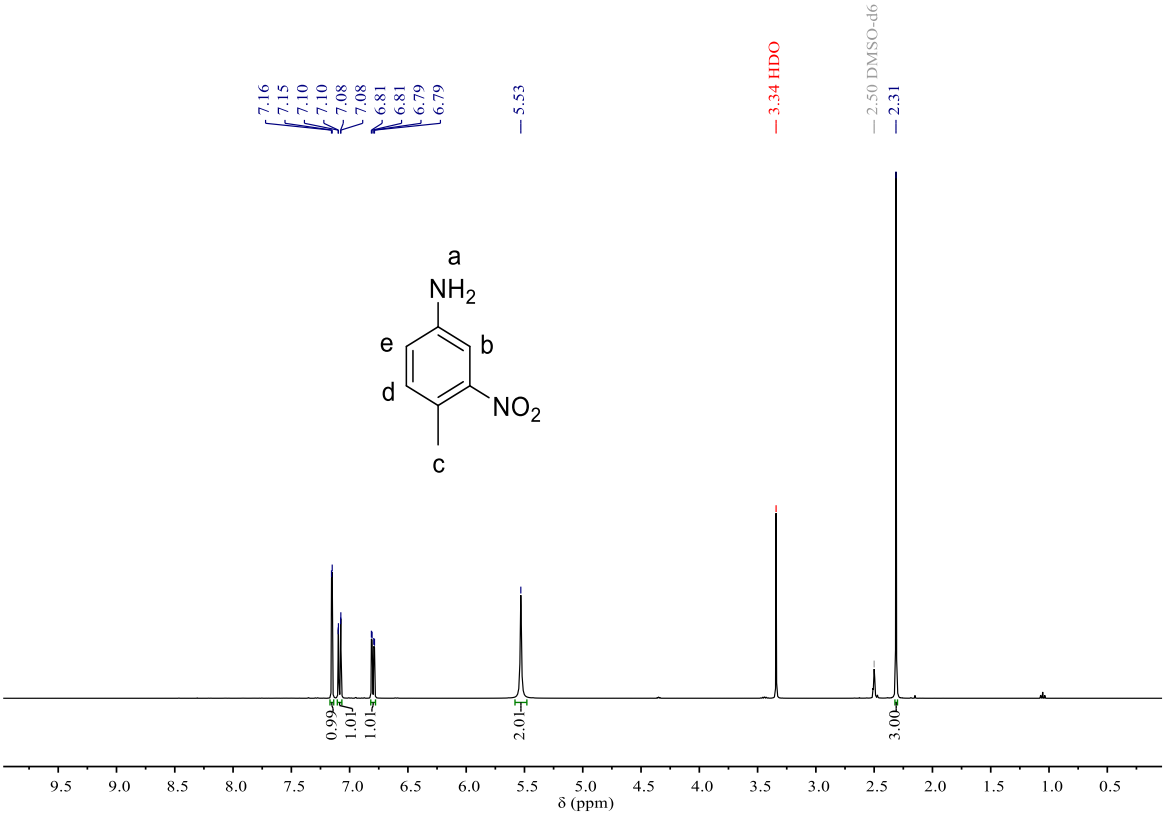

Figure 5. ^{1}H NMR spectrum of **3.3** (400 MHz, DMSO-d_6, 298 K).

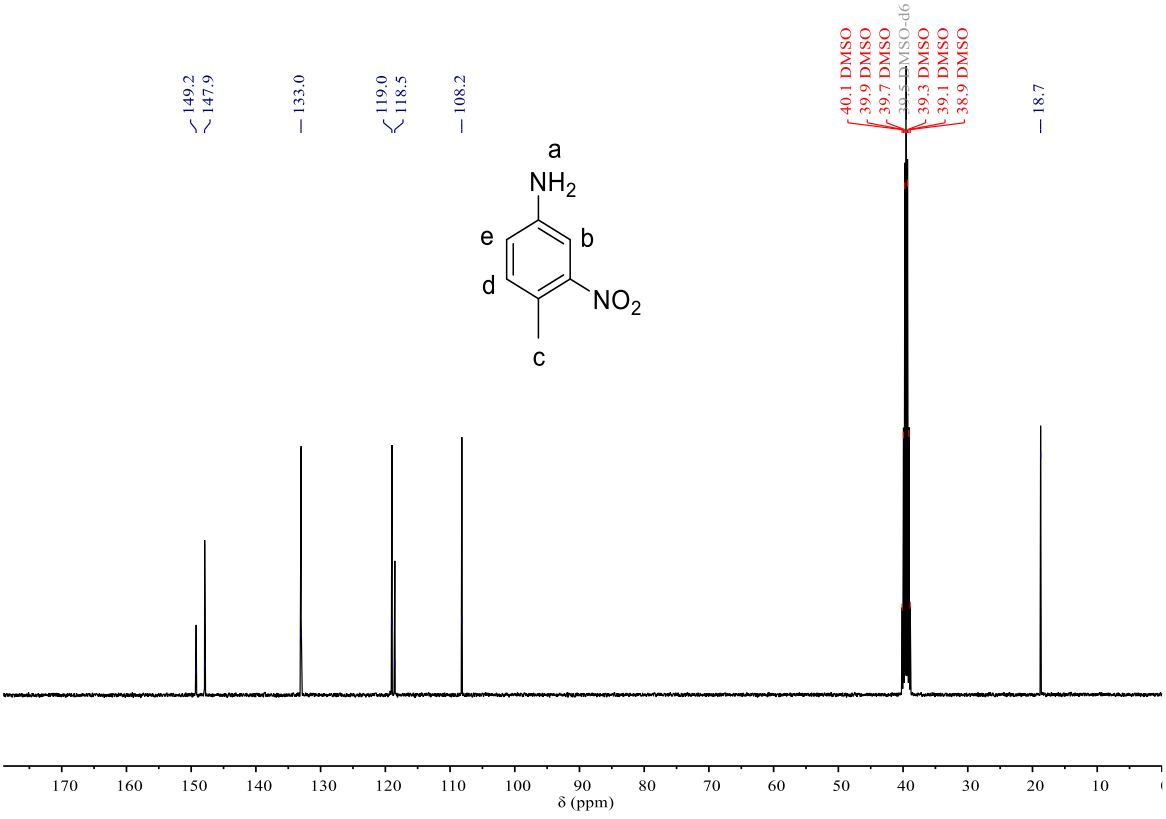

Figure 6. 13C {H} NMR spectrum of 3.3 (100 MHz, DMSO-d6, 298 K).

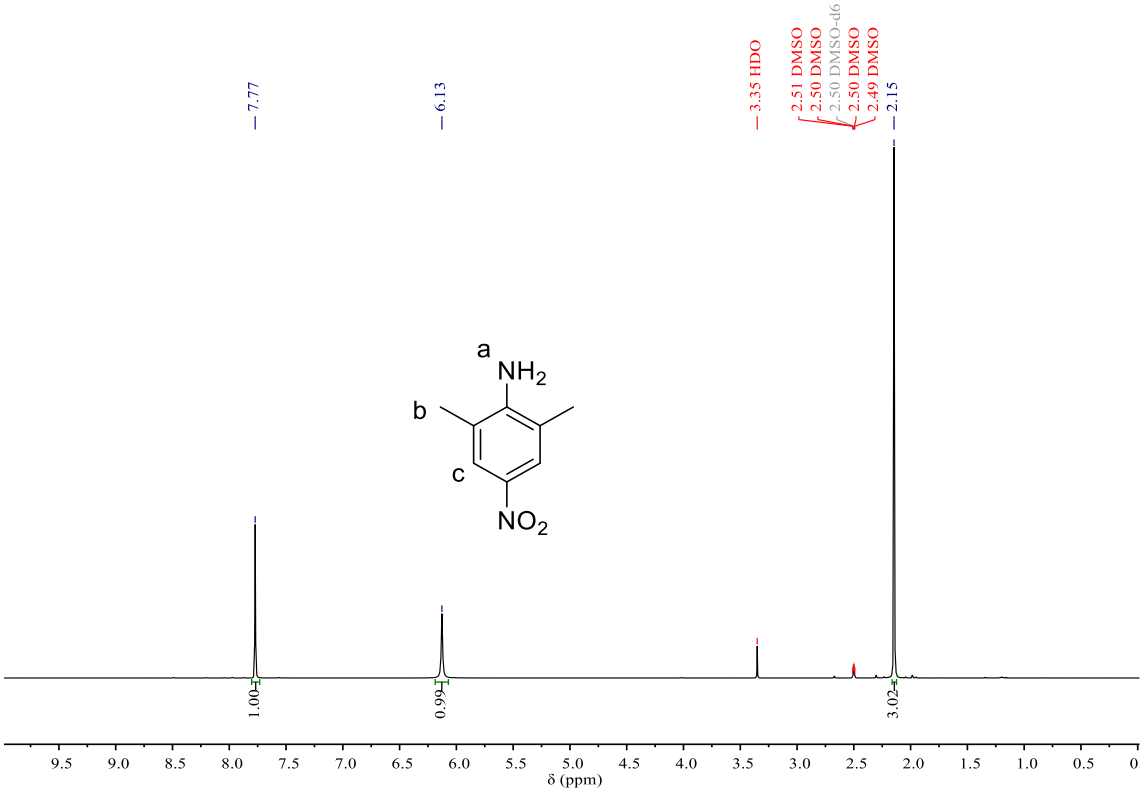

Figure 7. ^{1}H NMR spectrum of **3.4** (400 MHz, DMSO-d_6, 298 K).

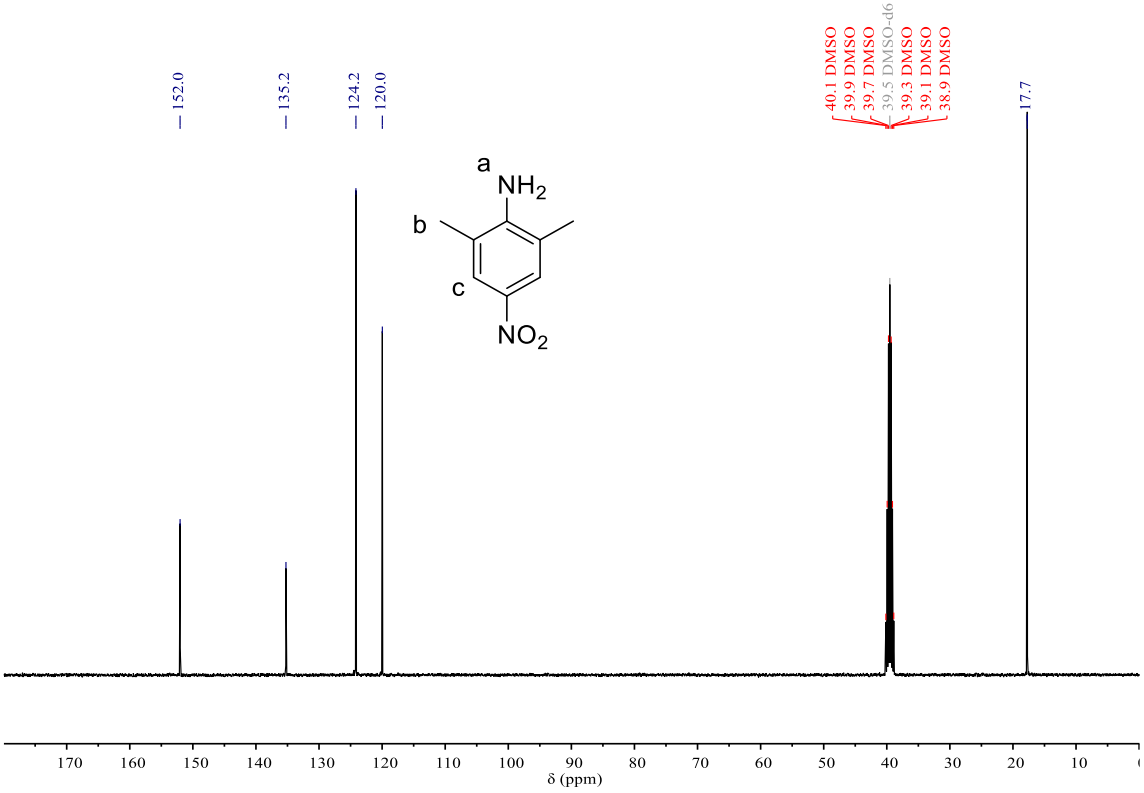

Figure 8. ^{13}C {H} NMR spectrum of **3.4** (100 MHz, DMSO-d_6, 298 K).

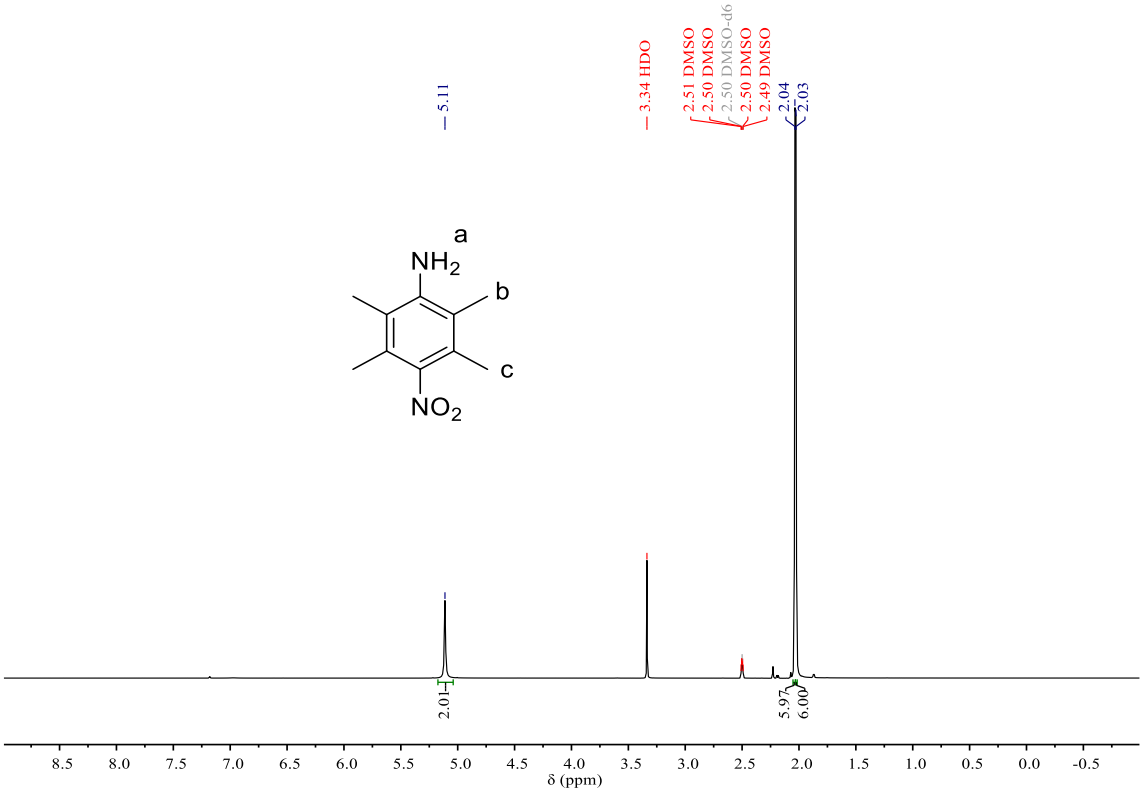

Figure 9. ^{1}H NMR spectrum of **3.5** (400 MHz, DMSO-d_6, 298 K).

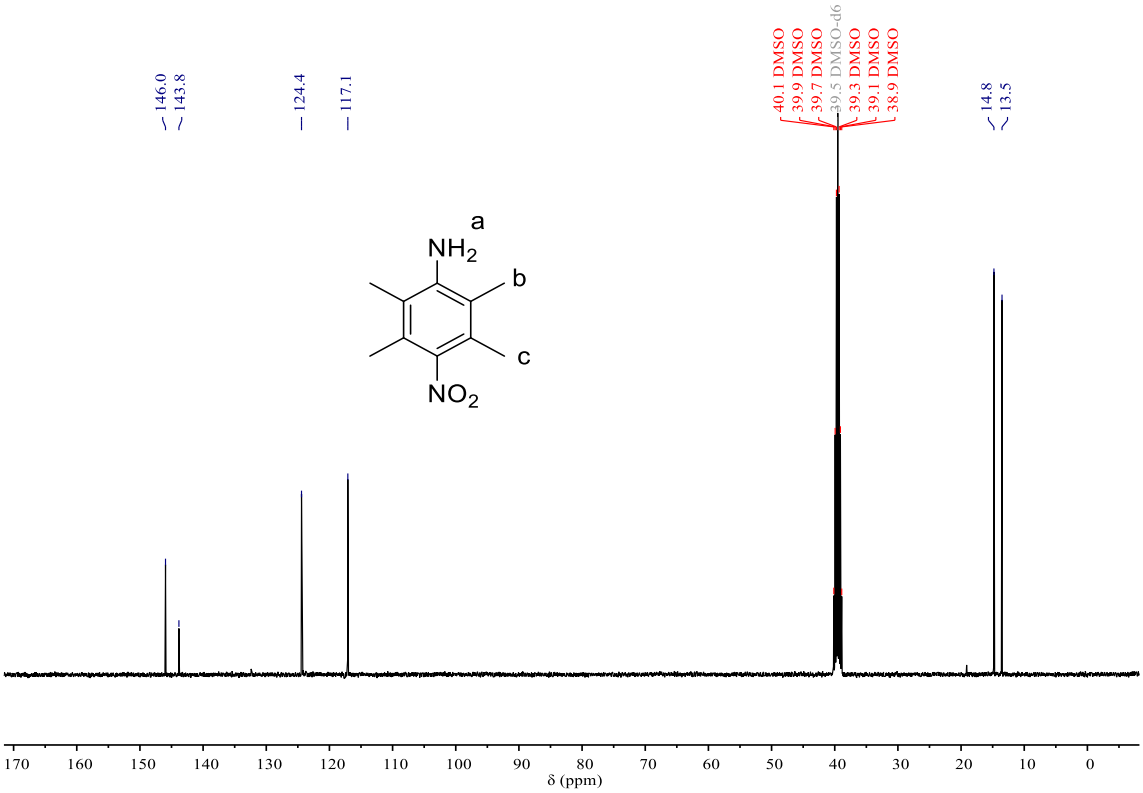

Figure 10. ^{13}C {H} NMR spectrum of **3.5** (100 MHz, DMSO-d_6, 298 K).

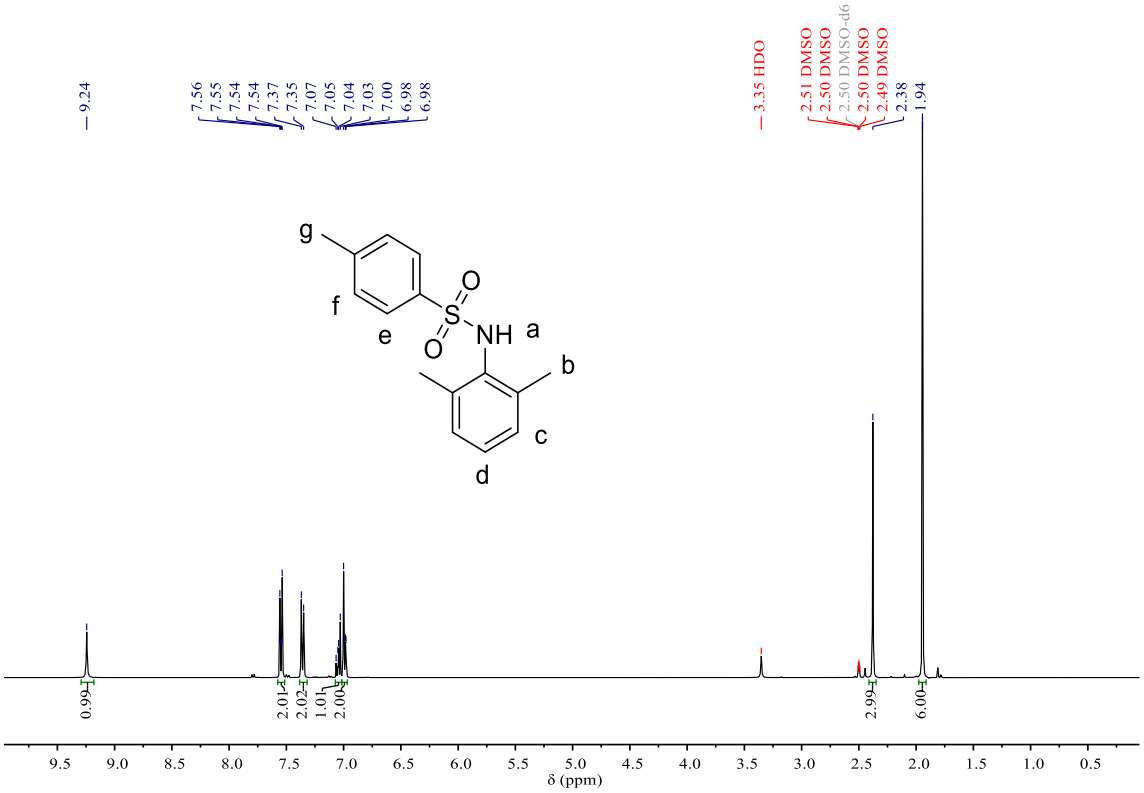

Figure 11. ^{1}H NMR spectrum of **3.6** (400 MHz, DMSO-d_6, 298 K).

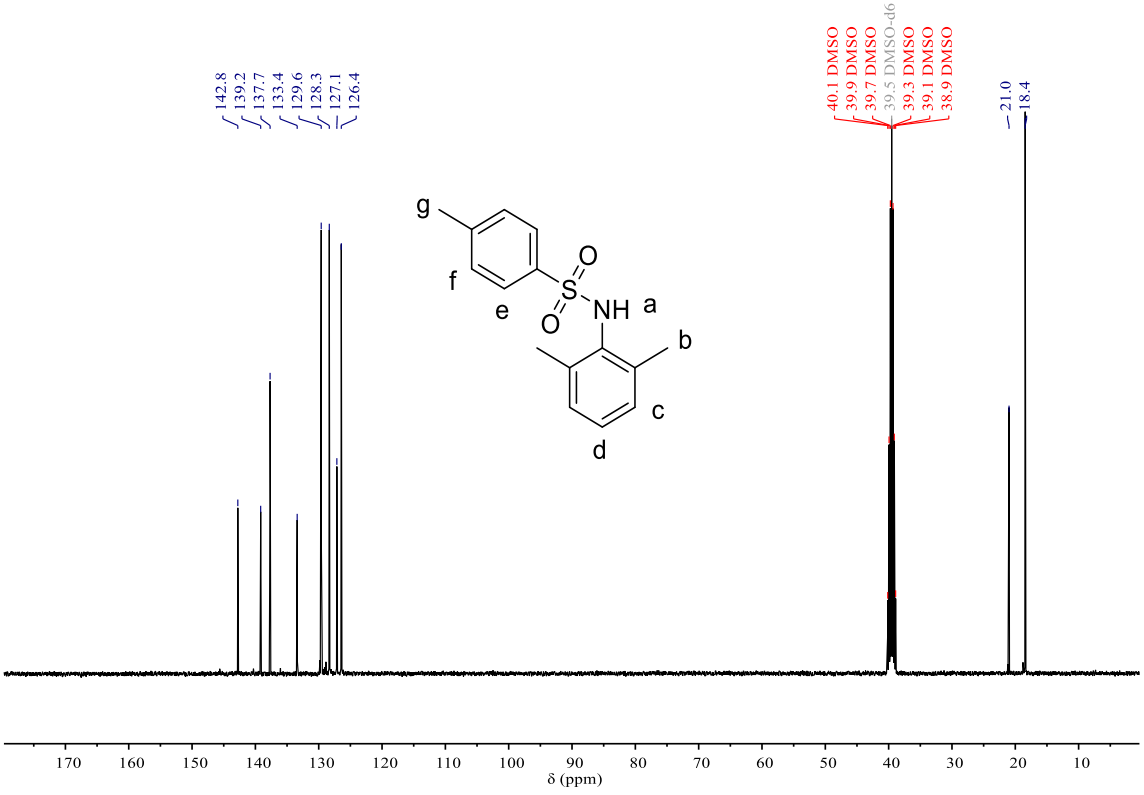

Figure 12. ^{13}C {H} NMR spectrum of **3.6** (100 MHz, DMSO-d_6, 298 K).

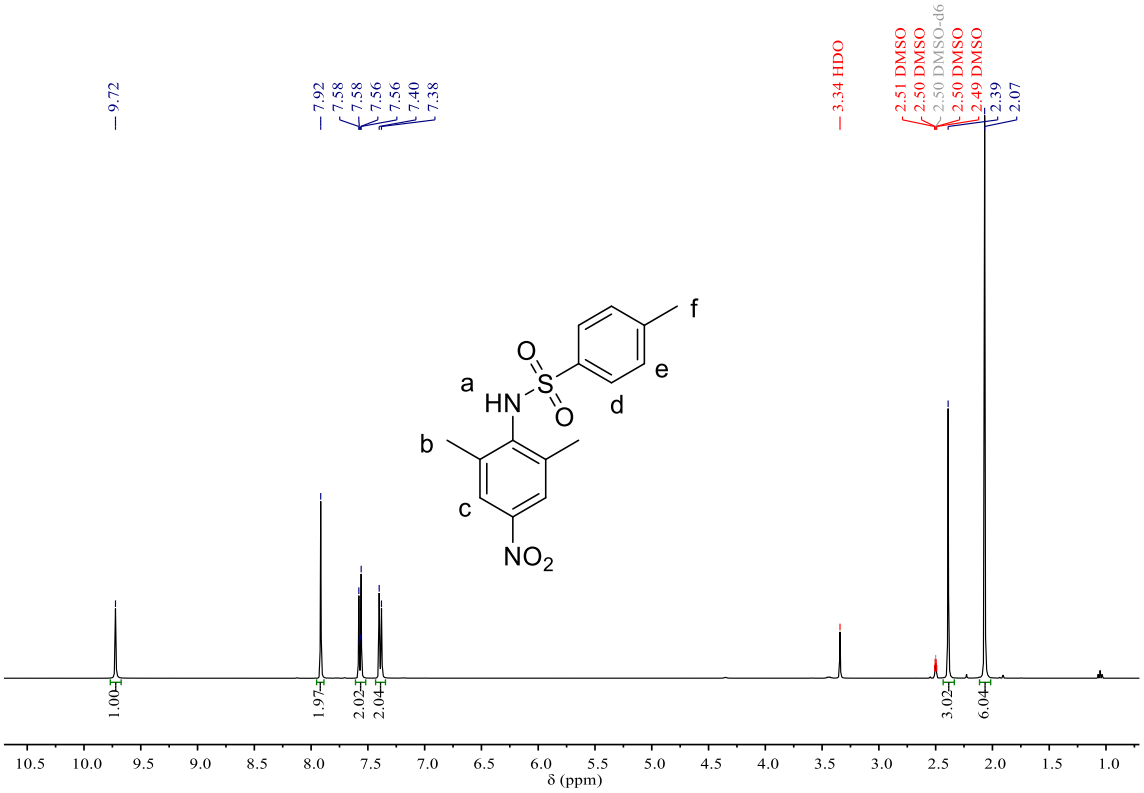

Figure 13. ^{1}H NMR spectrum of **3.7** (400 MHz, DMSO-d_6, 298 K).

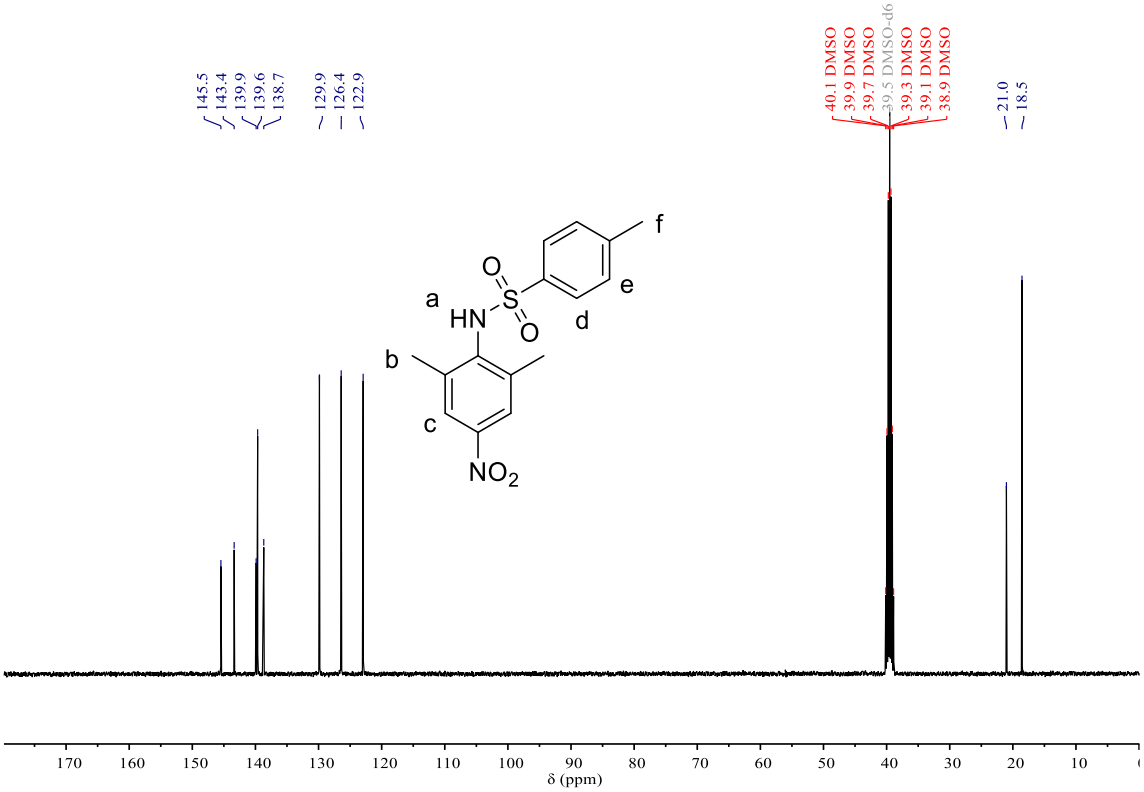

Figure 14. ^{13}C {H} NMR spectrum of **3.7** (100 MHz, DMSO-d_6, 298 K).

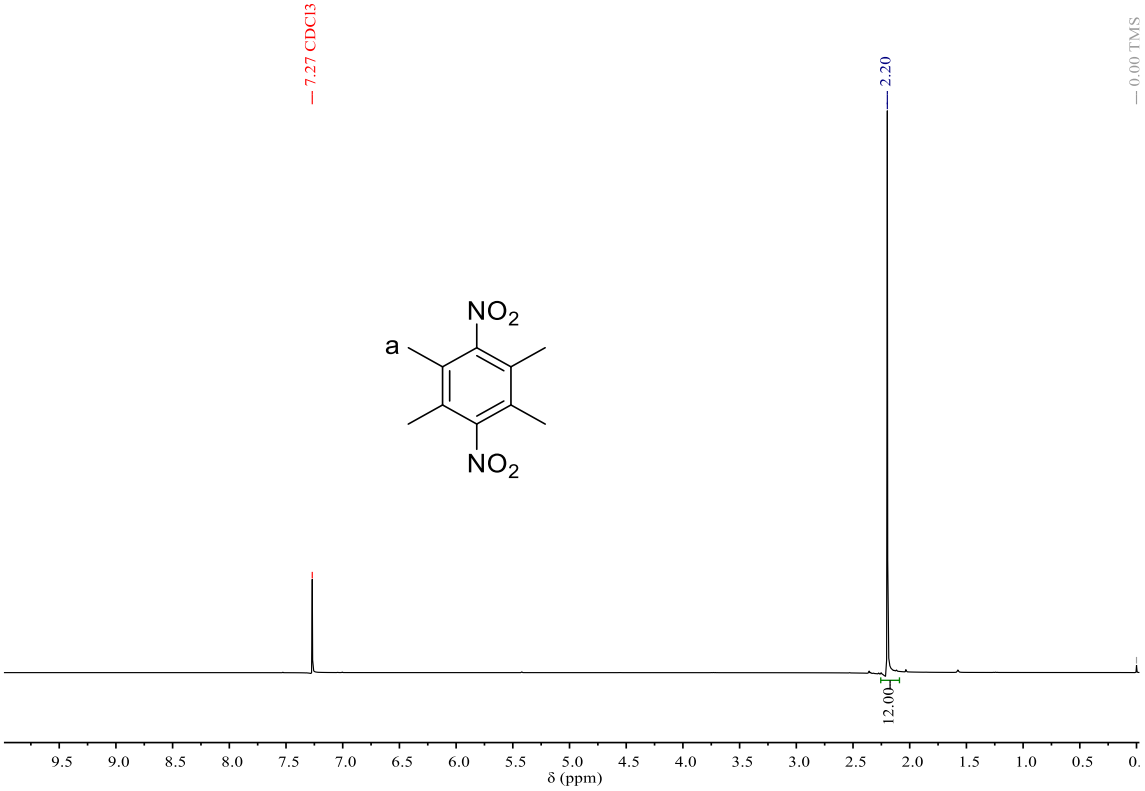

Figure 15. [1]H NMR spectrum of **3.8** (400 MHz, DMSO-d_6, 298 K).

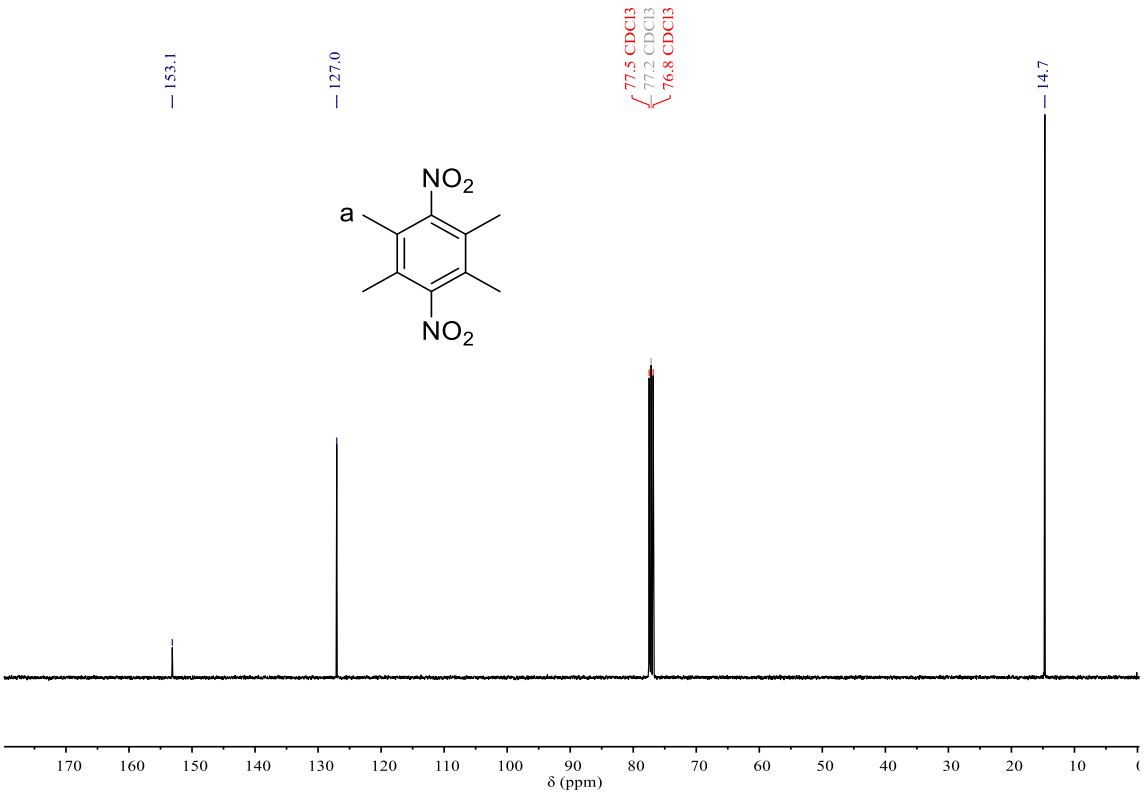

Figure 16. [13]C {H} NMR spectrum of **3.8** (100 MHz, DMSO-d_6, 298 K).

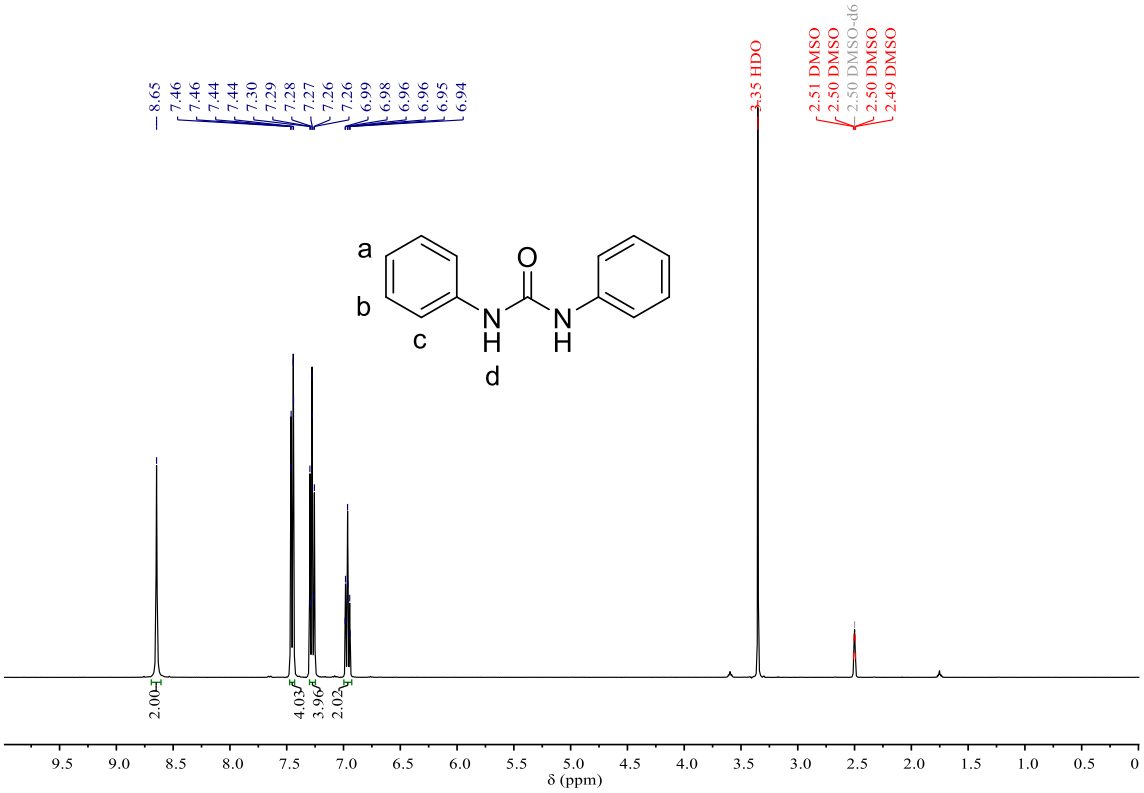

Figure 17. [1]H NMR spectrum of **3.9** (400 MHz, DMSO-d_6, 298 K).

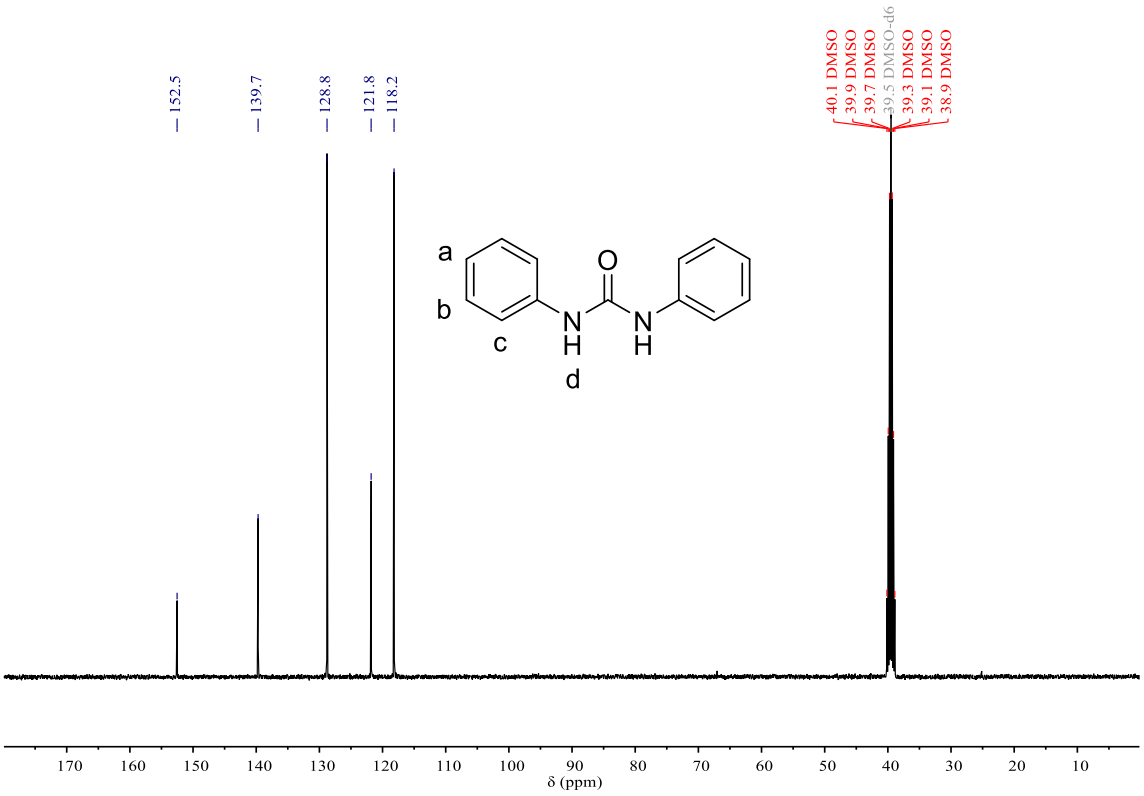

Figure 18. [13]C {H} NMR spectrum of **3.9** (100 MHz, DMSO-d_6, 298 K).

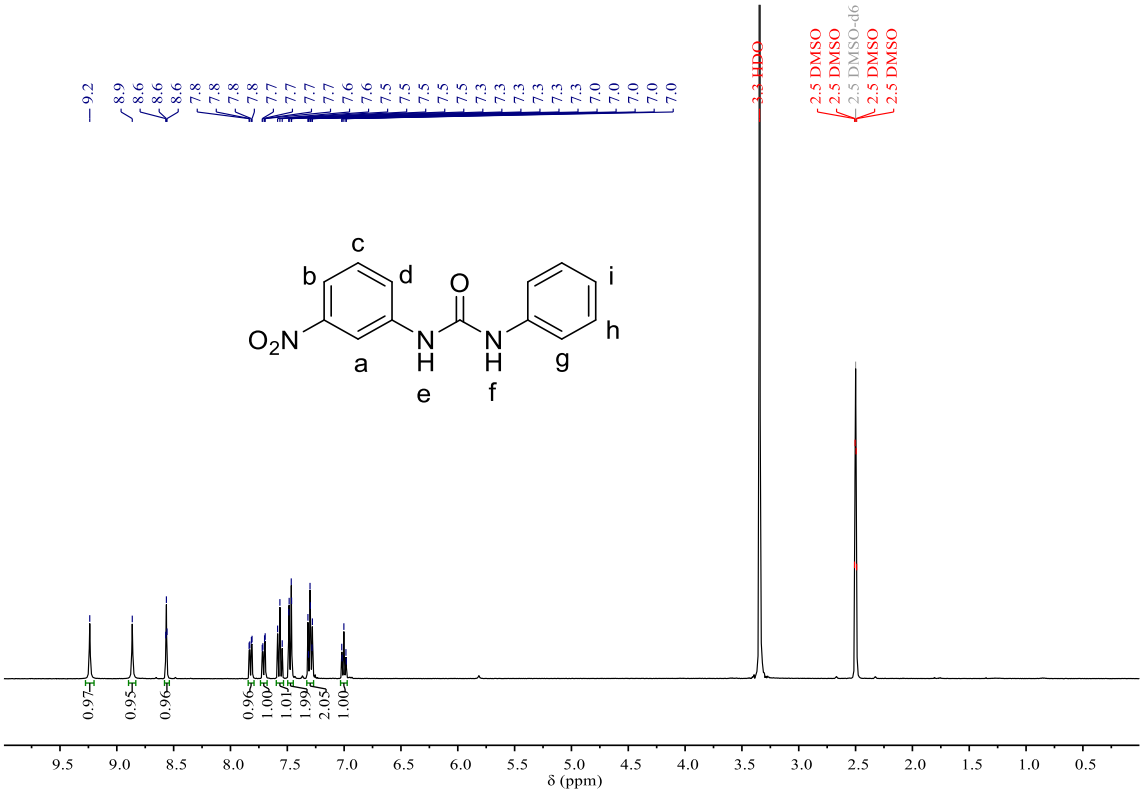

Figure 19. ^{1}H NMR spectrum of **3.10** (400 MHz, DMSO-d_6, 298 K).

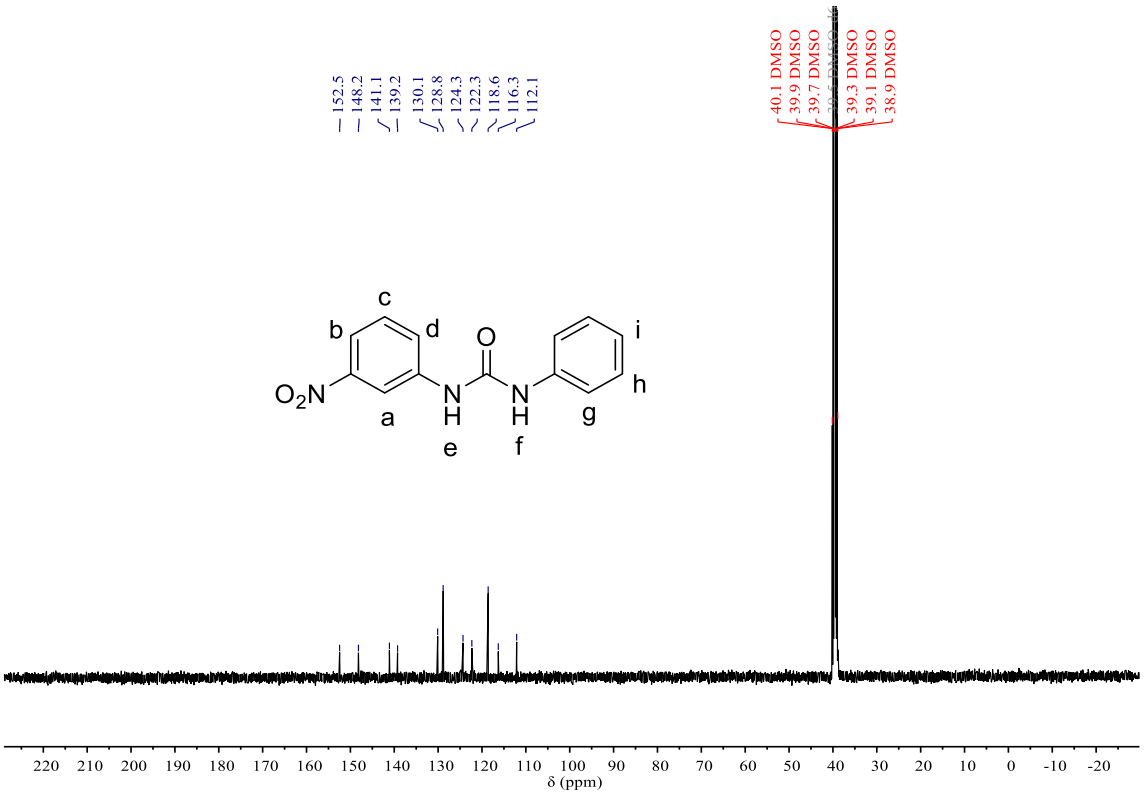

Figure 20. ^{13}C {H} NMR spectrum of **3.10** (100 MHz, DMSO-d_6, 298 K).

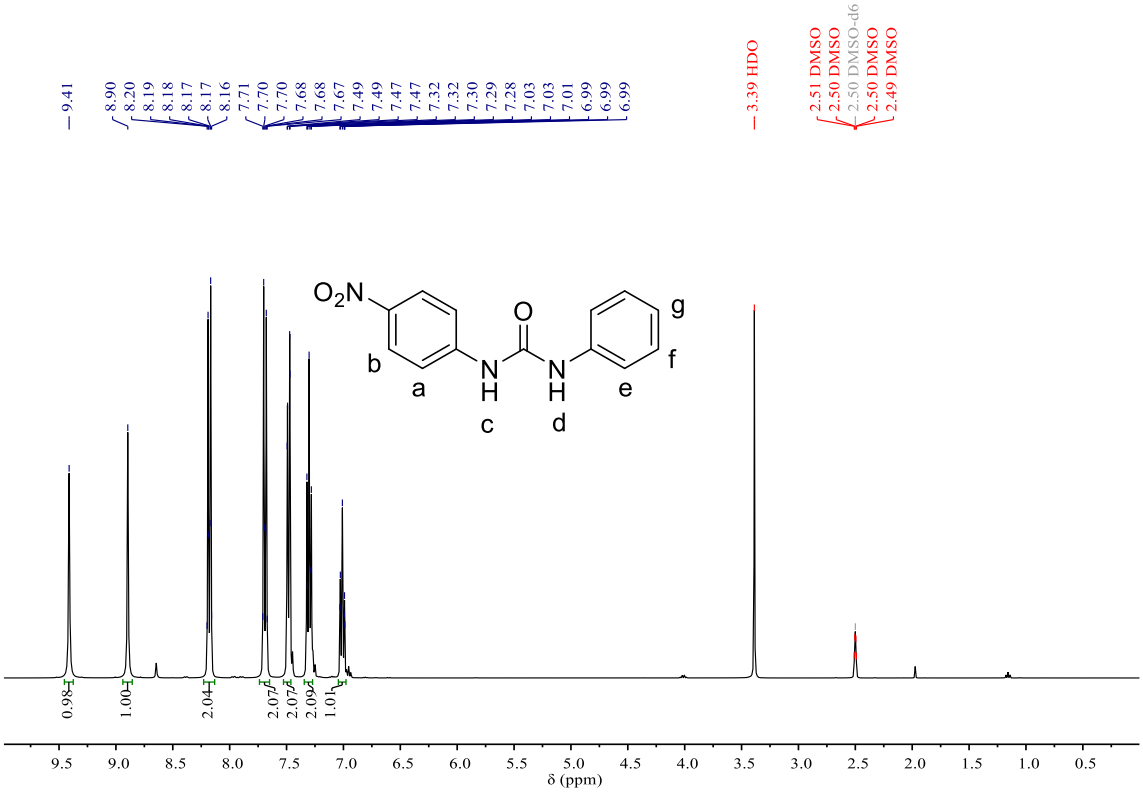

Figure 21. ^{1}H NMR spectrum of **3.11** (400 MHz, DMSO-d_6, 298 K).

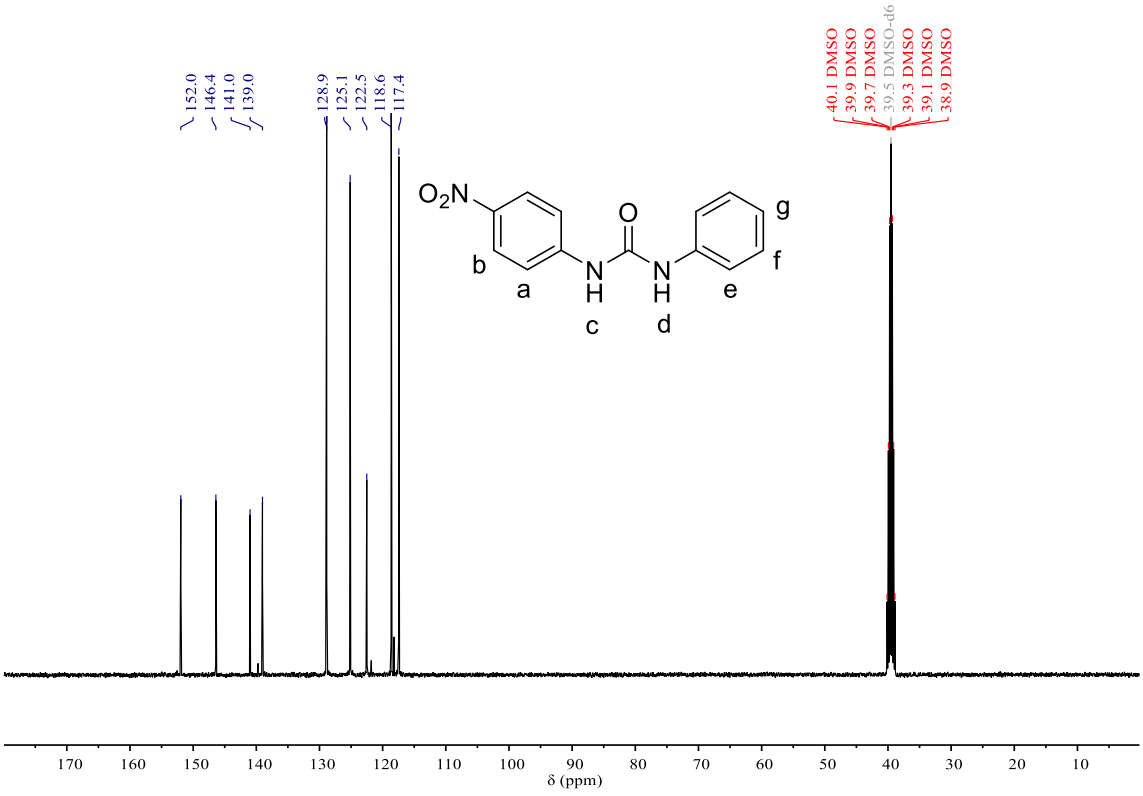

Figure 22. ^{13}C {H} NMR spectrum of **3.11** (100 MHz, DMSO-d_6, 298 K).

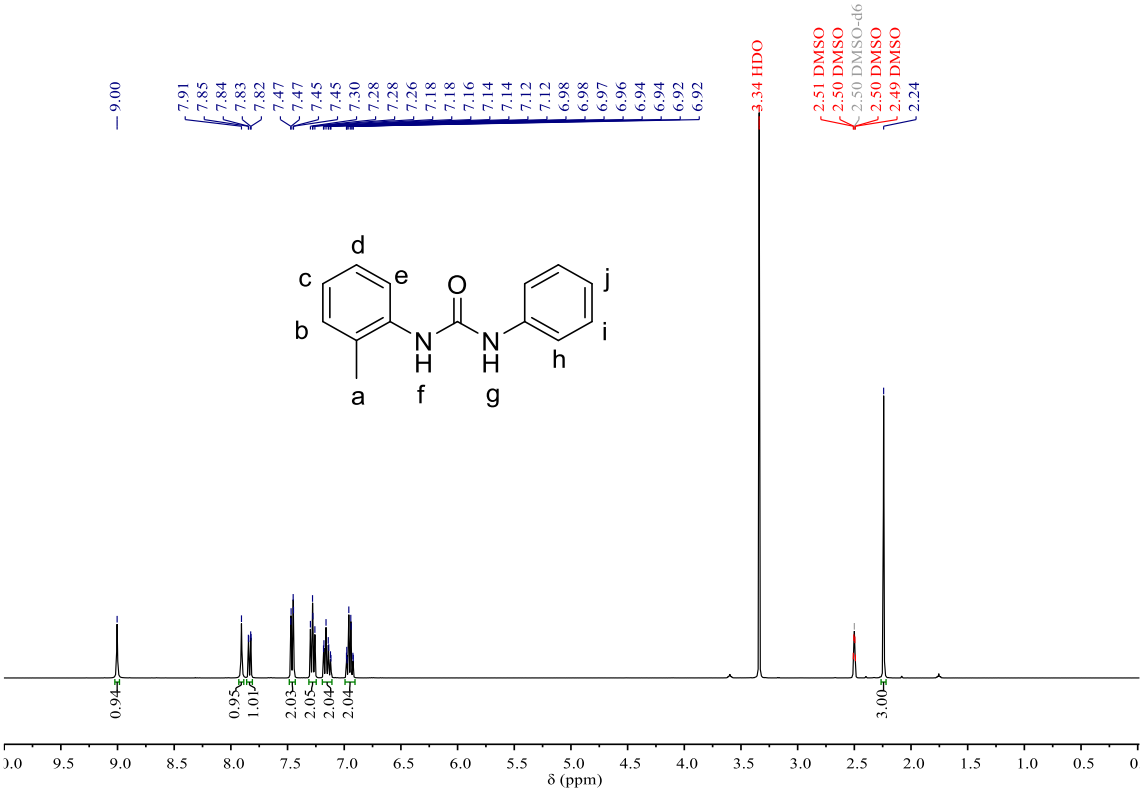

Figure 23. ^{1}H NMR spectrum of **3.12** (400 MHz, DMSO-d_6, 298 K).

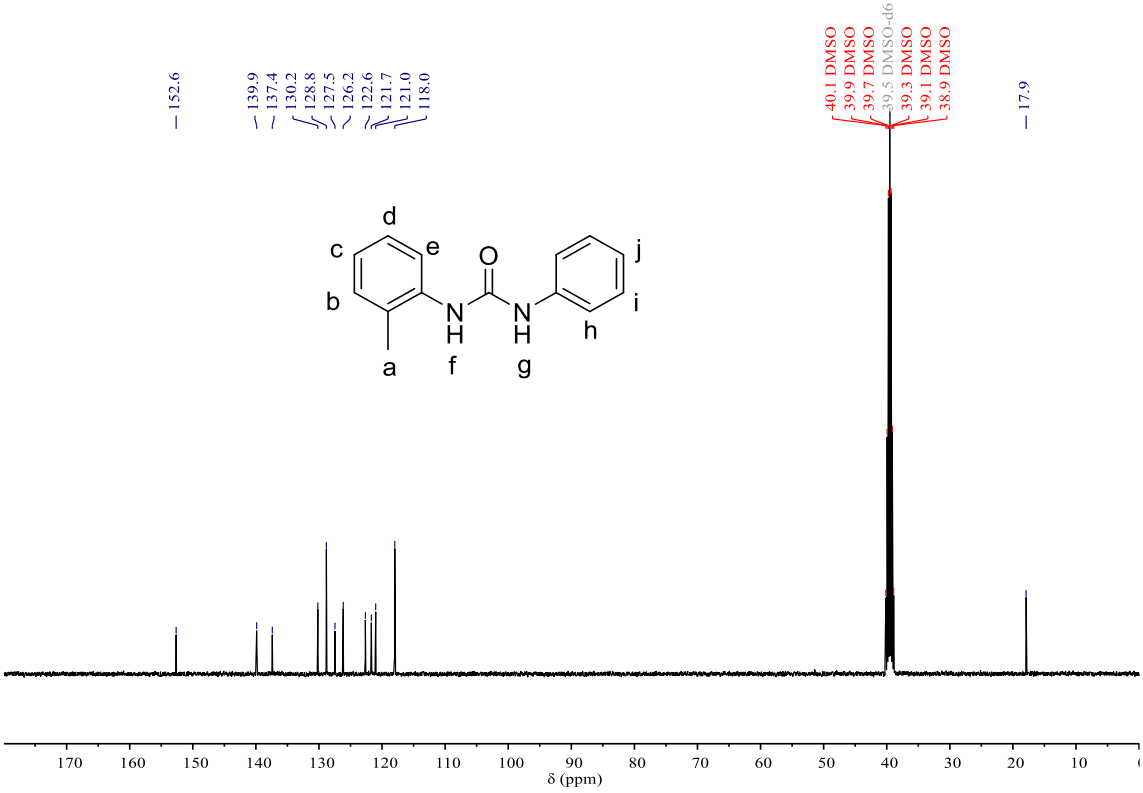

Figure 24. ^{13}C {H} NMR spectrum of **3.12** (100 MHz, DMSO-d_6, 298 K).

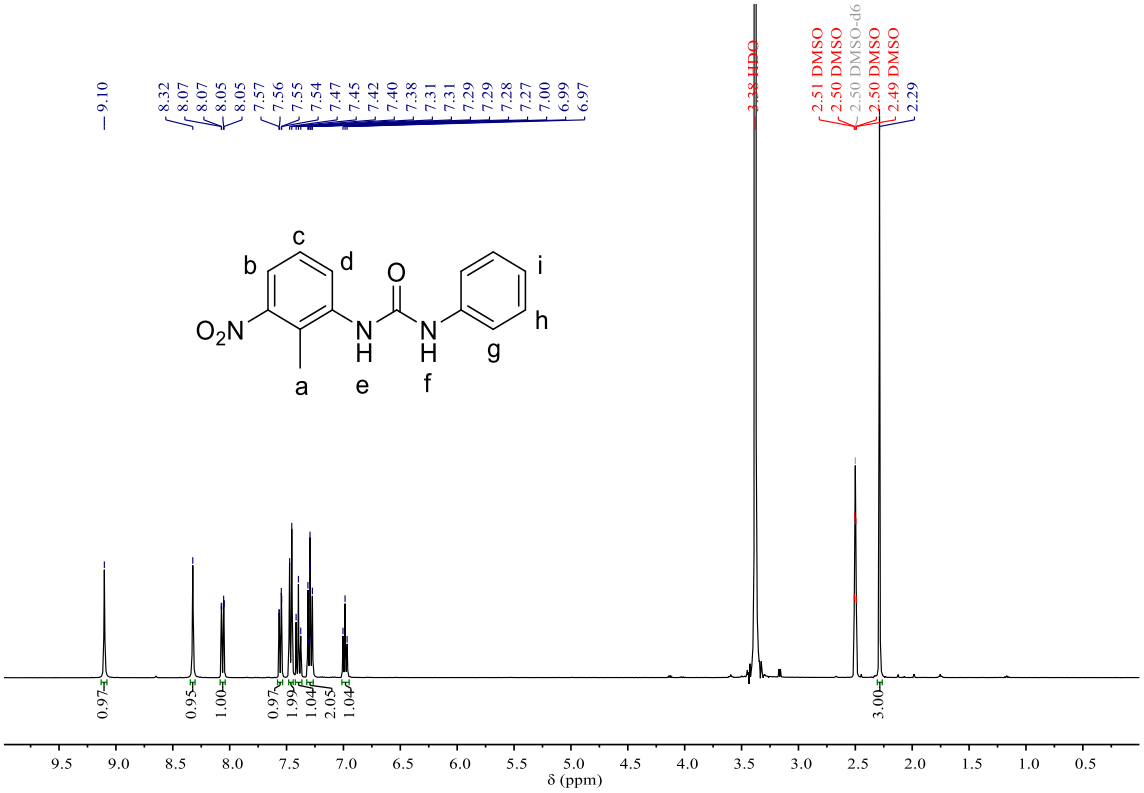

Figure 25. ^{1}H NMR spectrum of **3.13** (400 MHz, DMSO-d_6, 298 K).

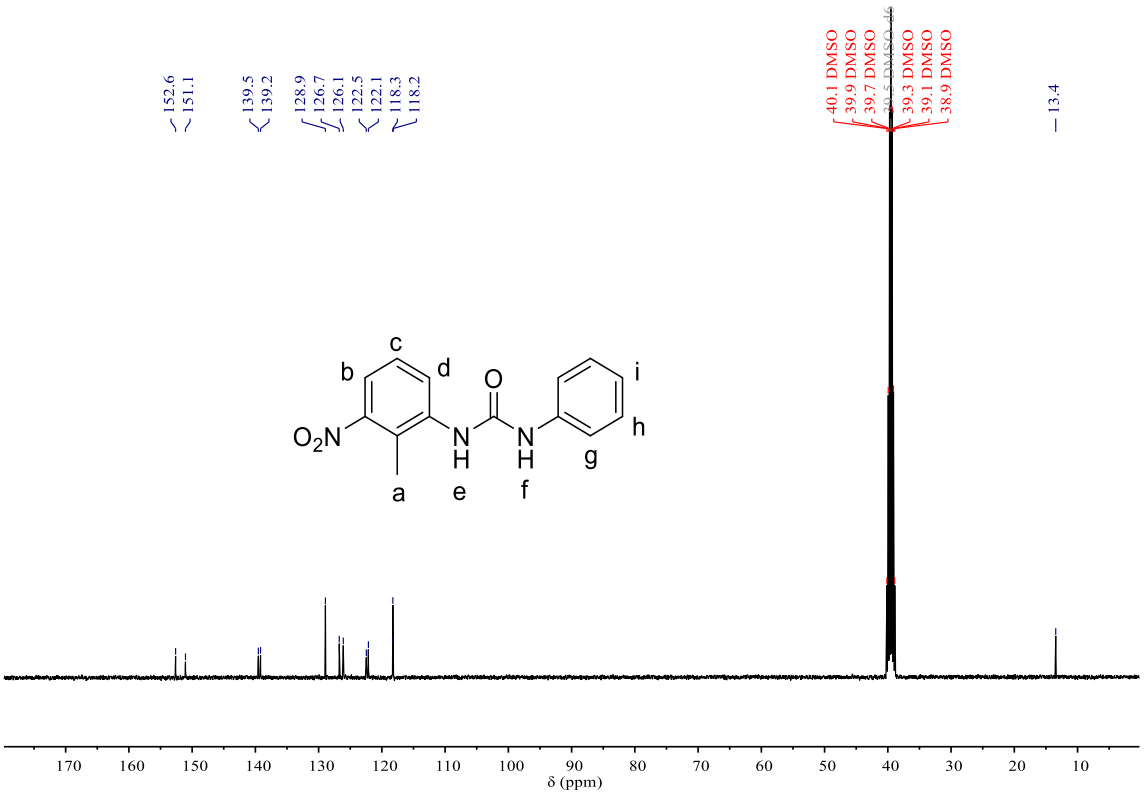

Figure 26. ^{13}C {H} NMR spectrum of **3.13** (100 MHz, DMSO-d_6, 298 K).

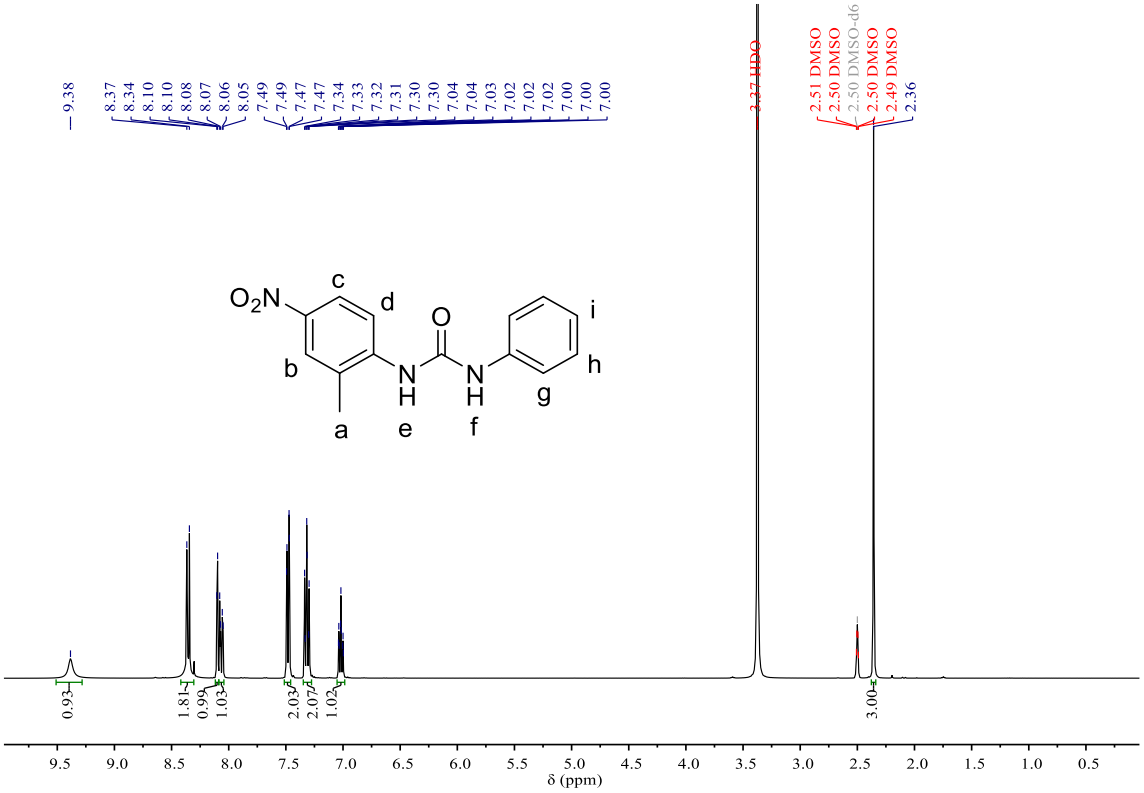

Figure 27. ^{1}H NMR spectrum of **3.14** (400 MHz, DMSO-d_6, 298 K).

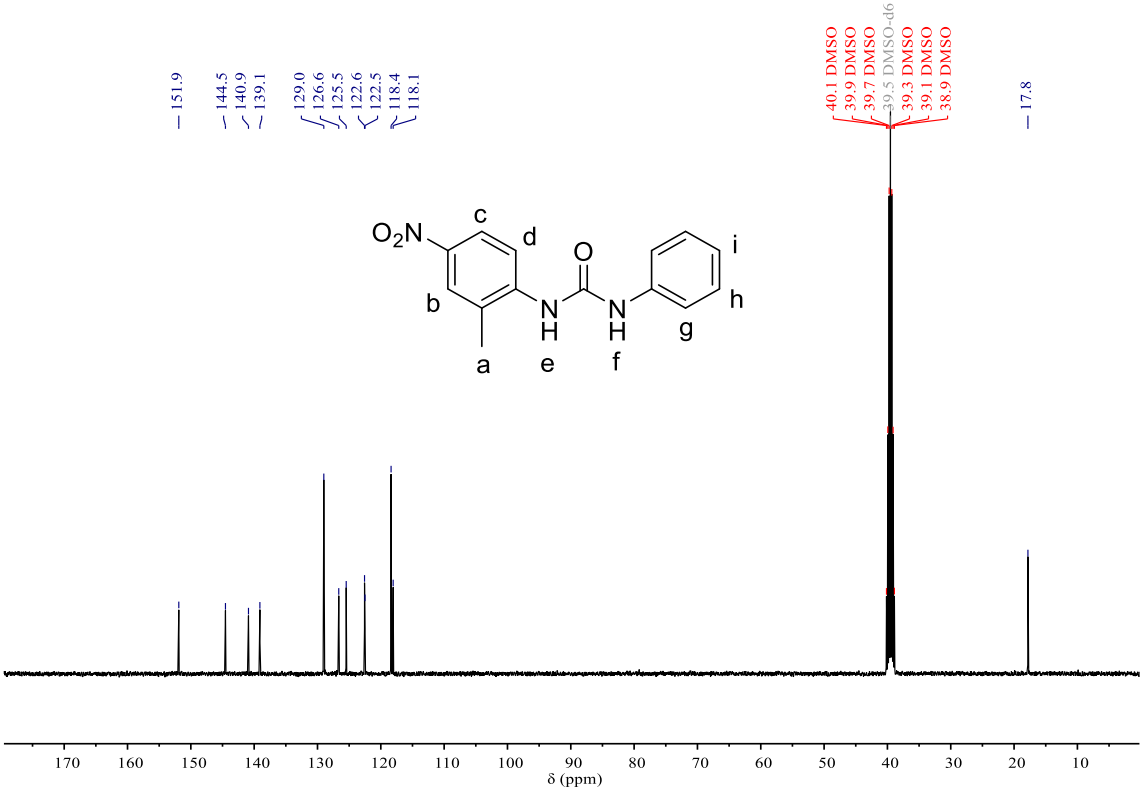

Figure 28. ^{13}C {H} NMR spectrum of **3.14** (100 MHz, DMSO-d_6, 298 K).

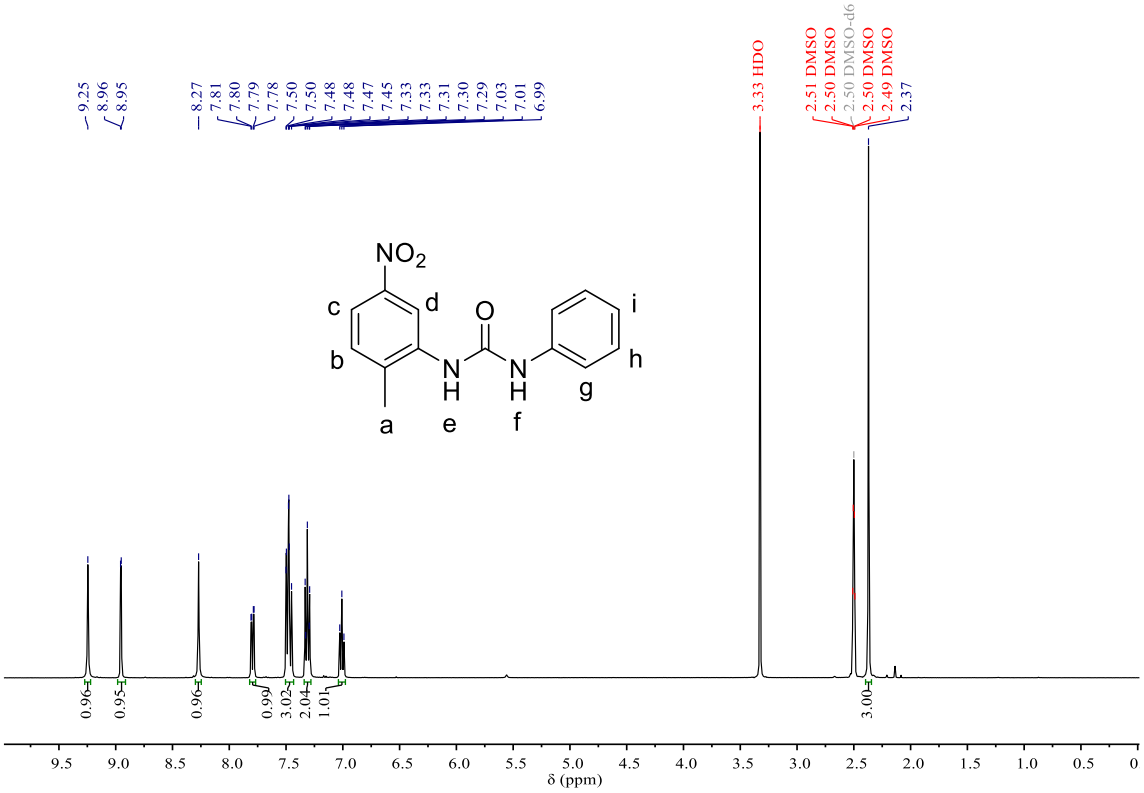

Figure 29. ^{1}H NMR spectrum of **3.15** (400 MHz, DMSO-d_6, 298 K).

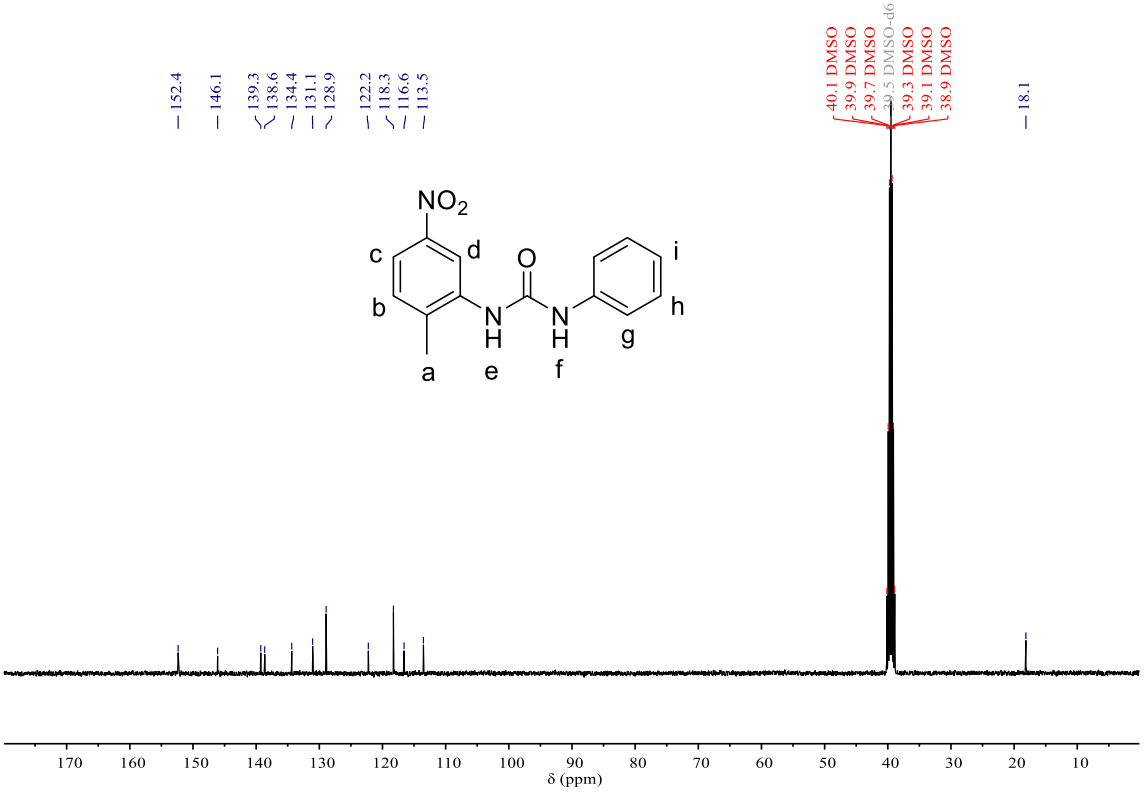

Figure 30. ^{13}C {H} NMR spectrum of **3.15** (100 MHz, DMSO-d_6, 298 K).

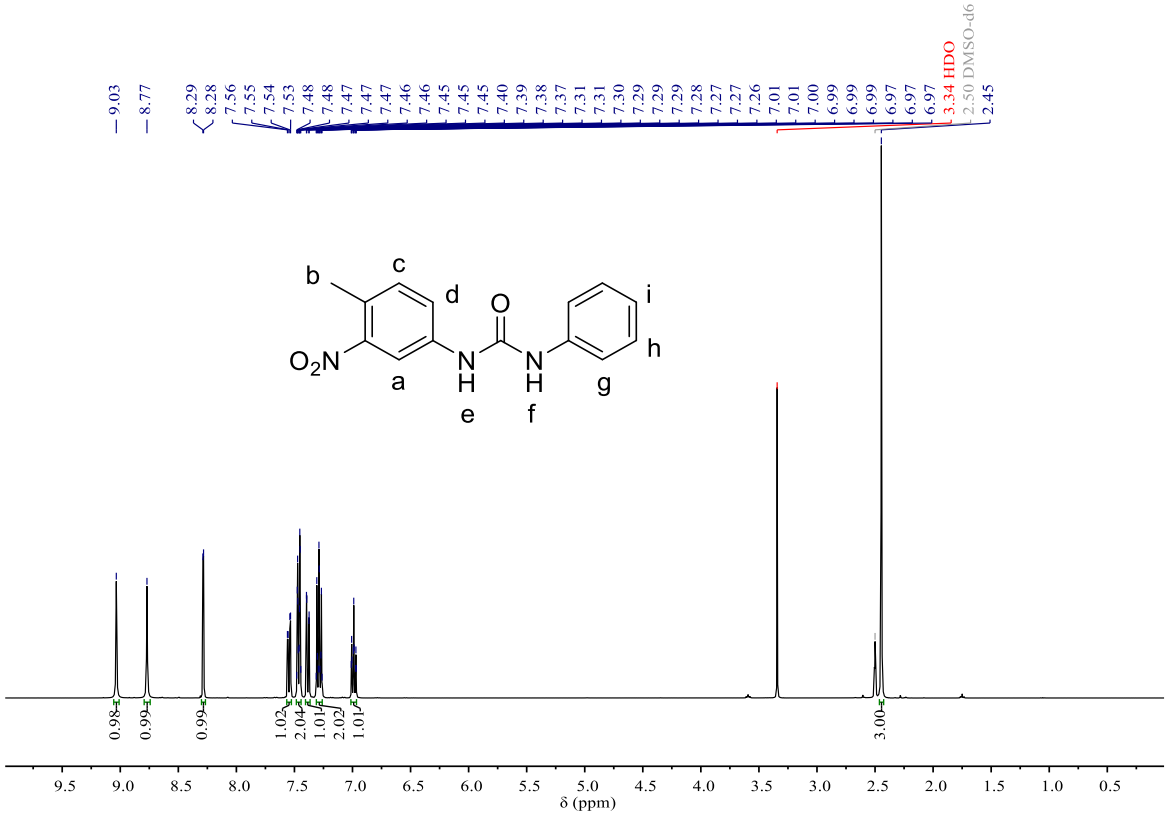

Figure 31. ^{1}H NMR spectrum of **3.16** (400 MHz, DMSO-d_6, 298 K).

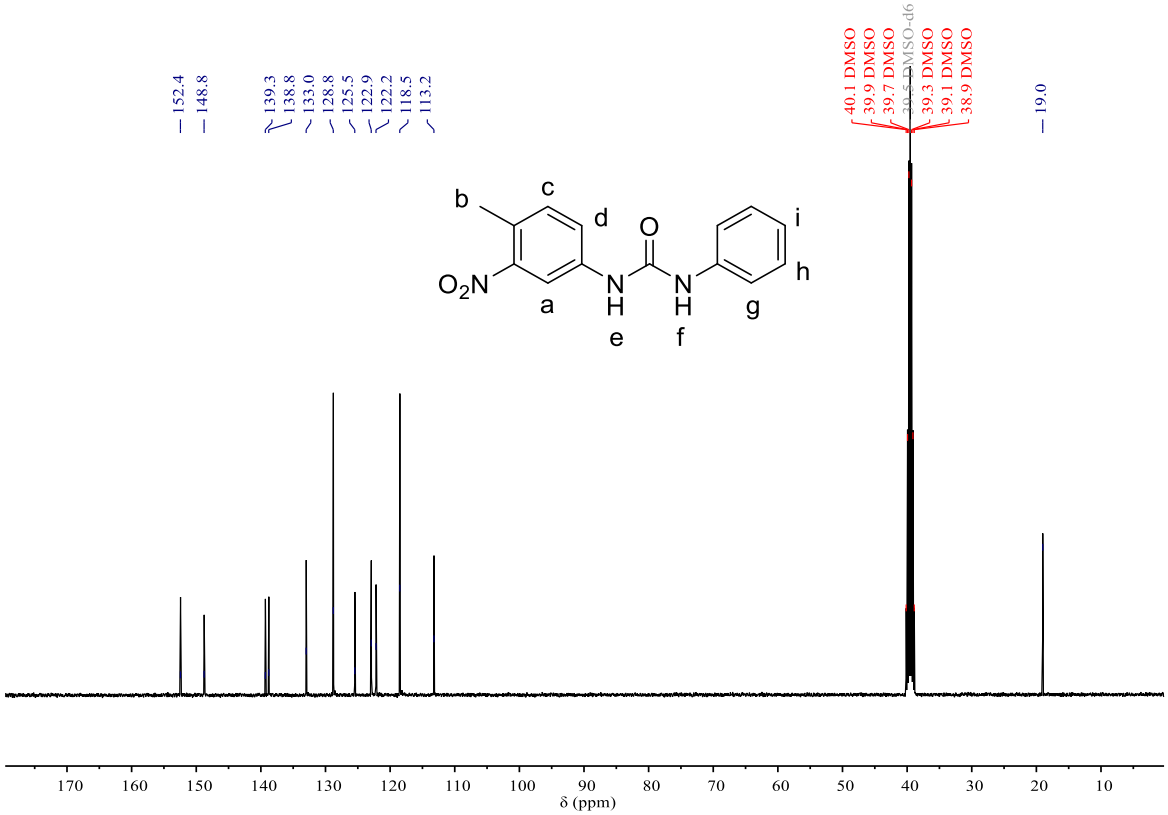

Figure 32. ^{13}C {H} NMR spectrum of **3.16** (100 MHz, DMSO-d_6, 298 K).

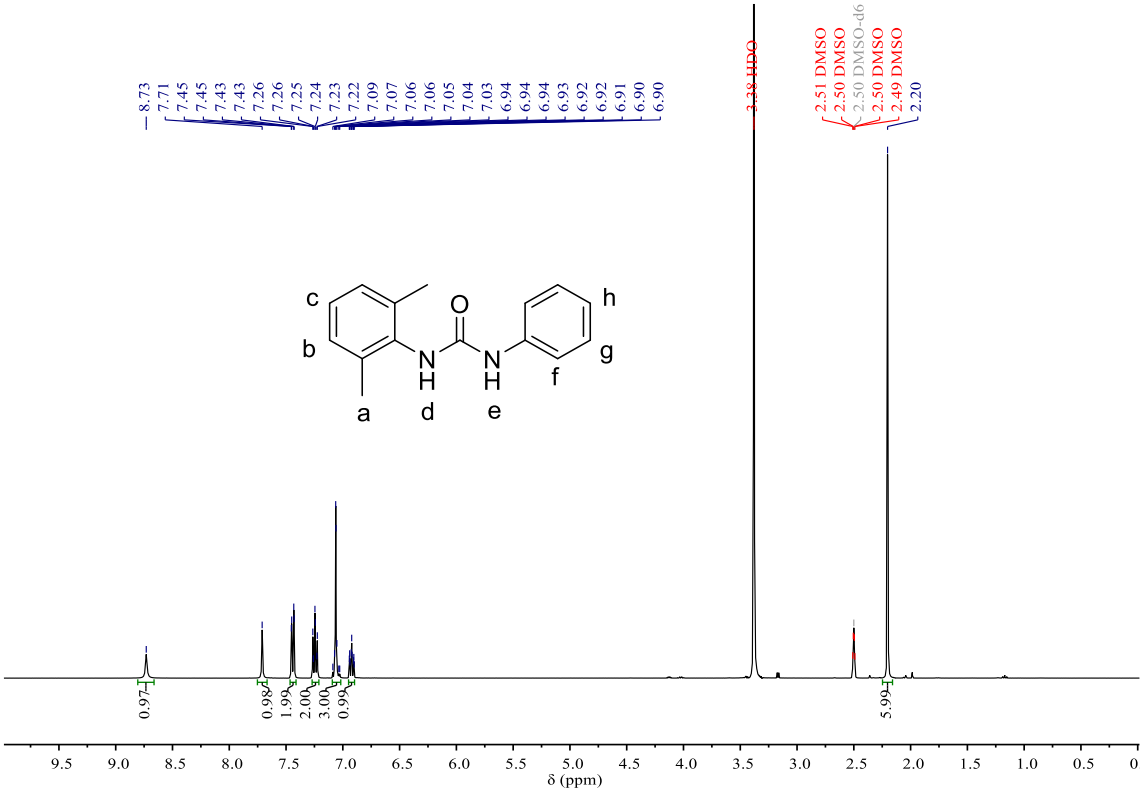

Figure 33. ^{1}H NMR spectrum of **3.17** (400 MHz, DMSO-d_6, 298 K).

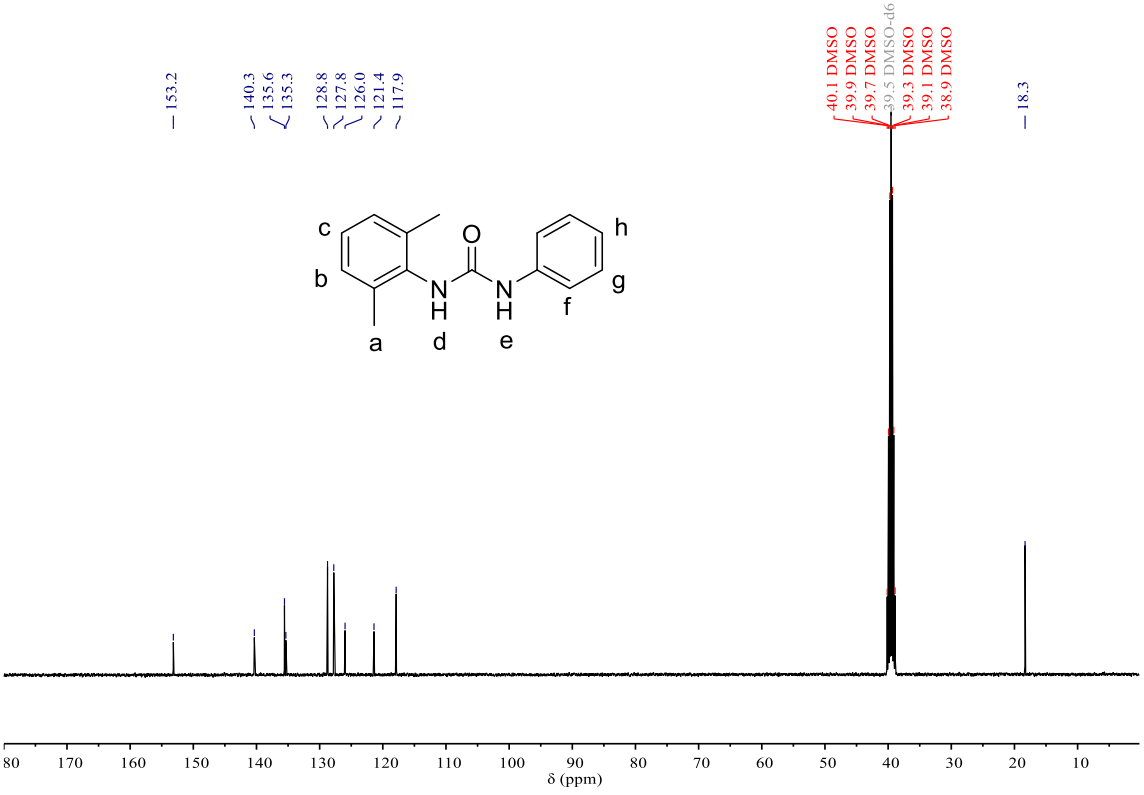

Figure 34. ^{13}C {H} NMR spectrum of **3.17** (100 MHz, DMSO-d_6, 298 K).

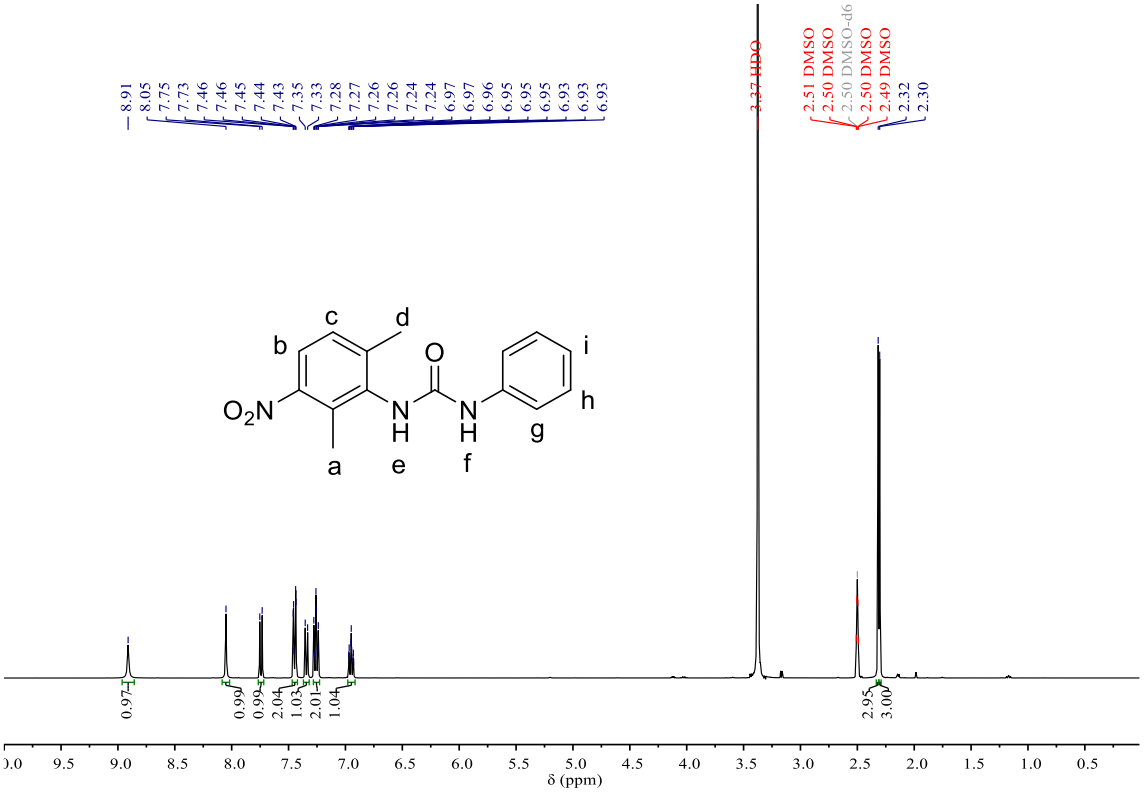

Figure 35. ^{1}H NMR spectrum of **3.18** (400 MHz, DMSO-d_6, 298 K).

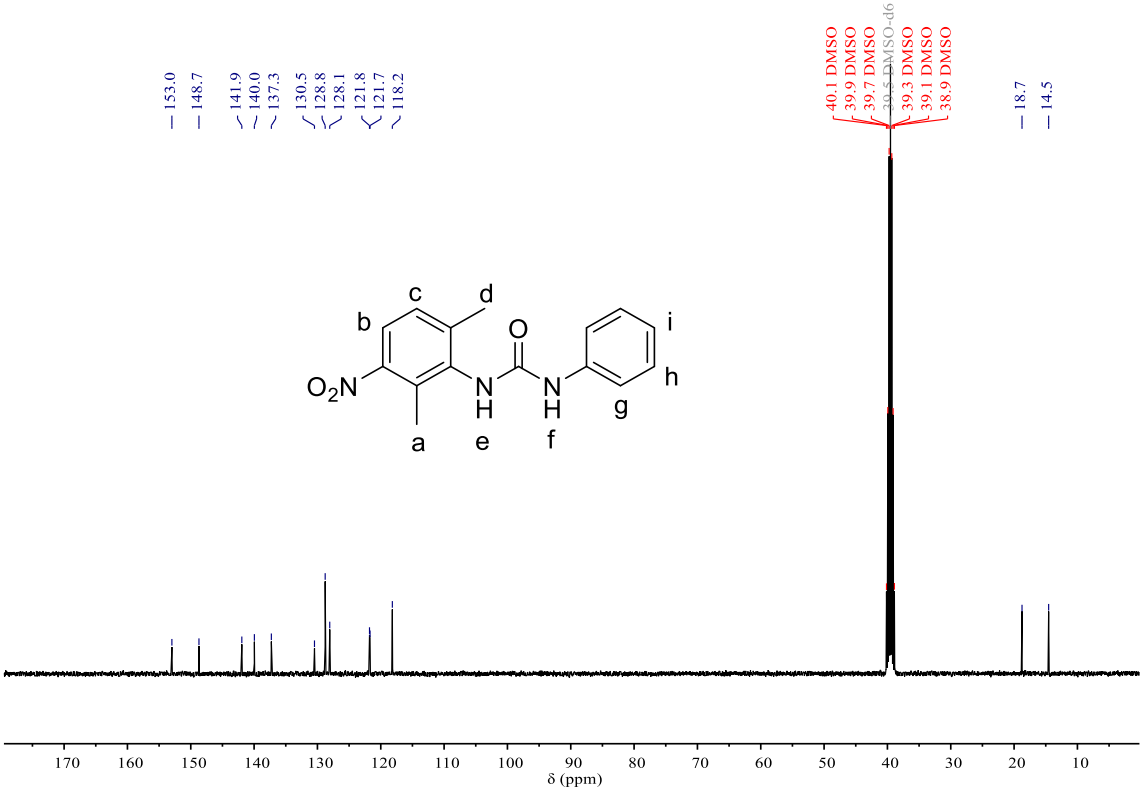

Figure 36. ^{13}C {H} NMR spectrum of **3.18** (100 MHz, DMSO-d_6, 298 K).

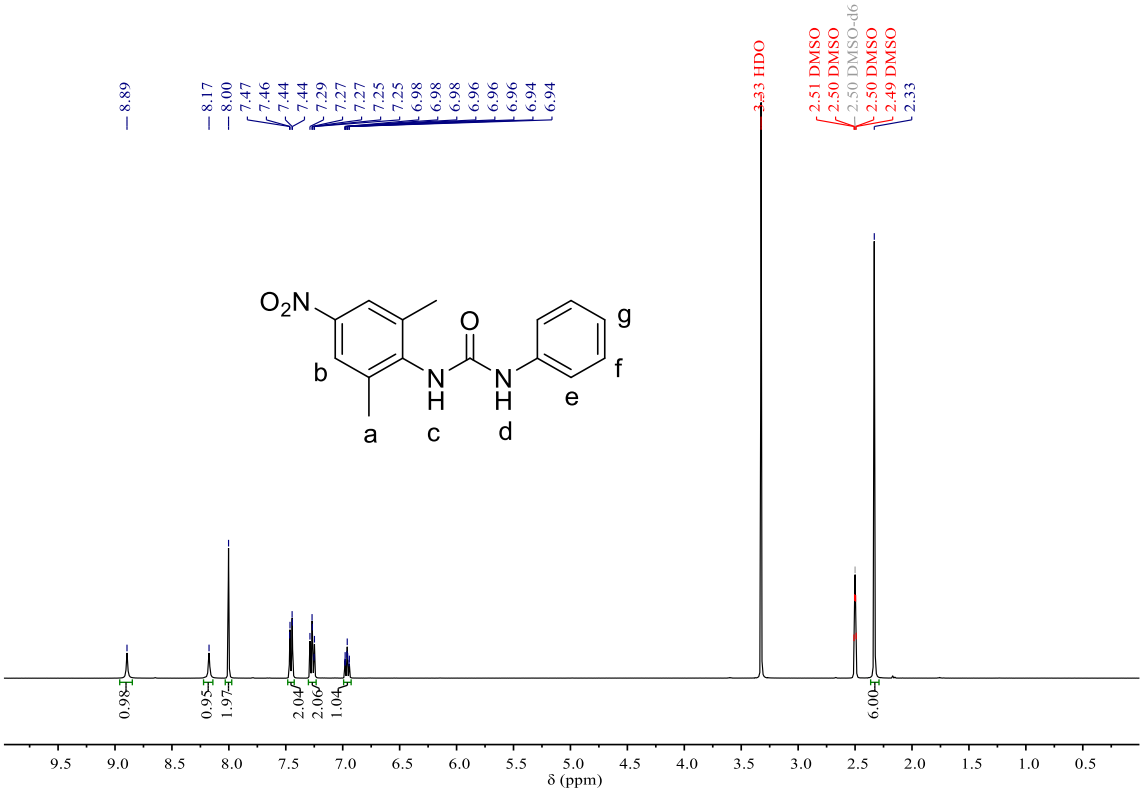

Figure 37. ^{1}H NMR spectrum of **3.19** (400 MHz, DMSO-d_6, 298 K).

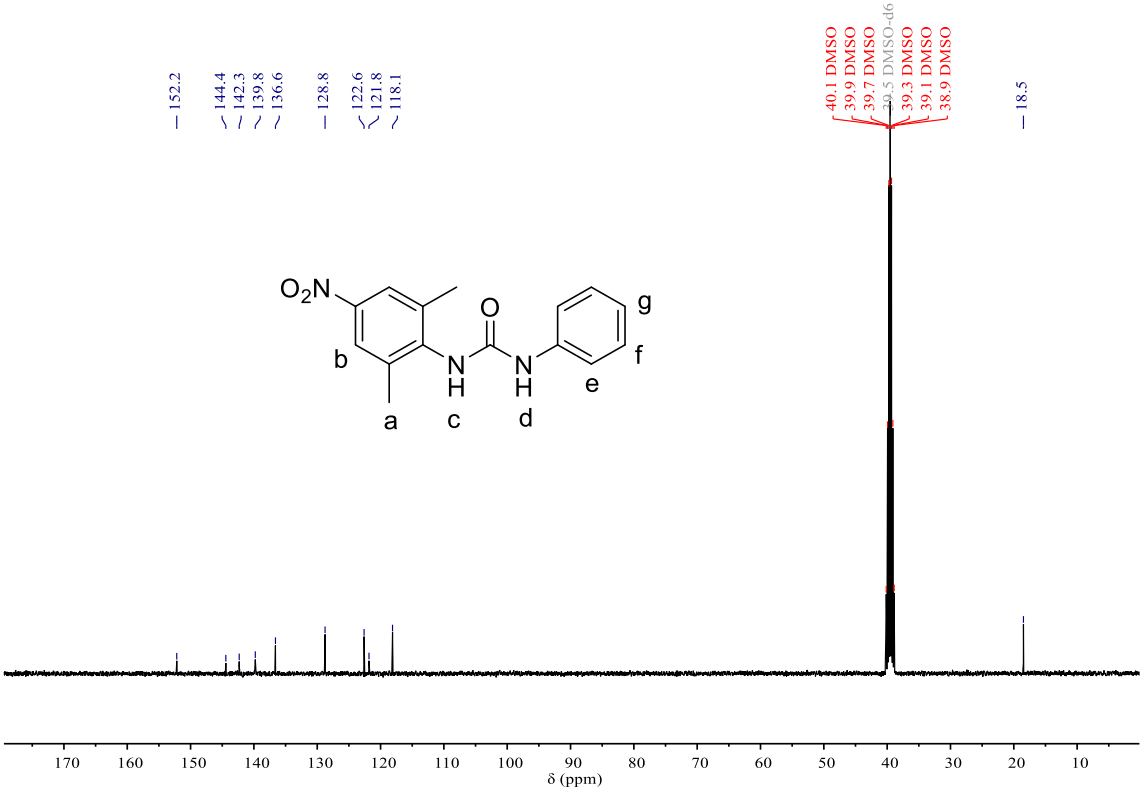

Figure 38. ^{13}C {H} NMR spectrum of **3.19** (100 MHz, DMSO-d_6, 298 K).

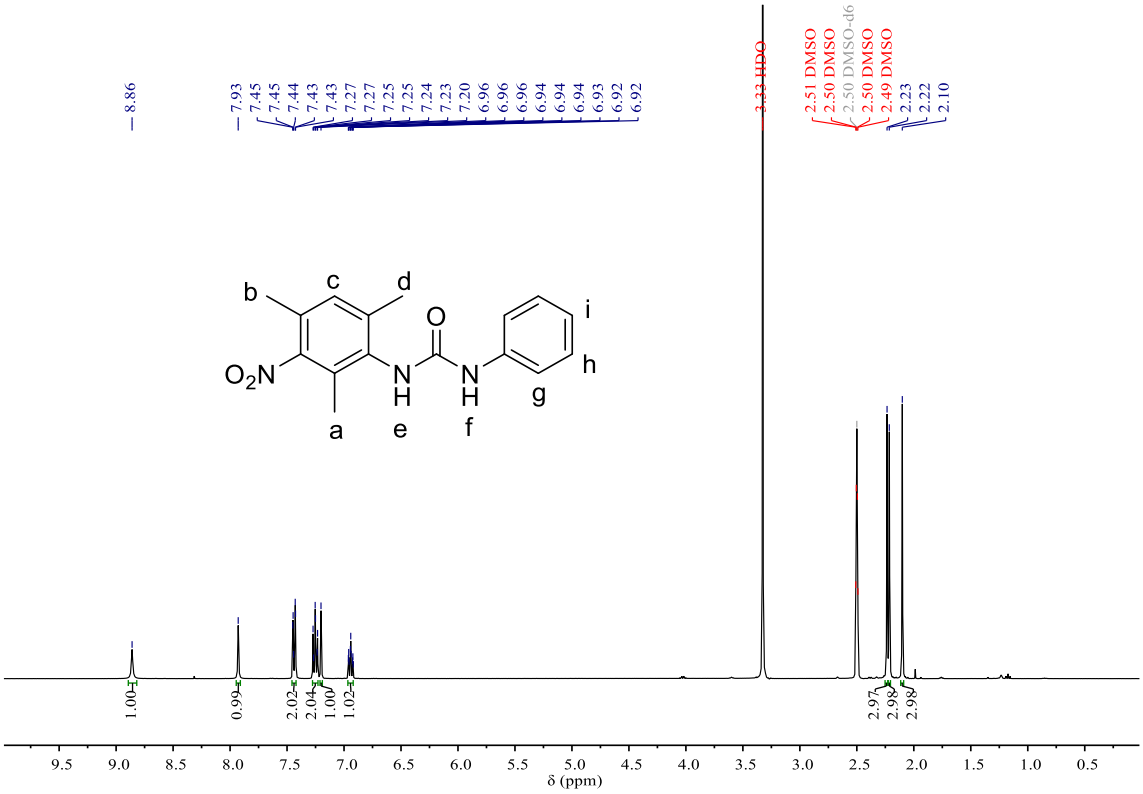

Figure 39. ^{1}H NMR spectrum of **3.20** (400 MHz, DMSO-d_6, 298 K).

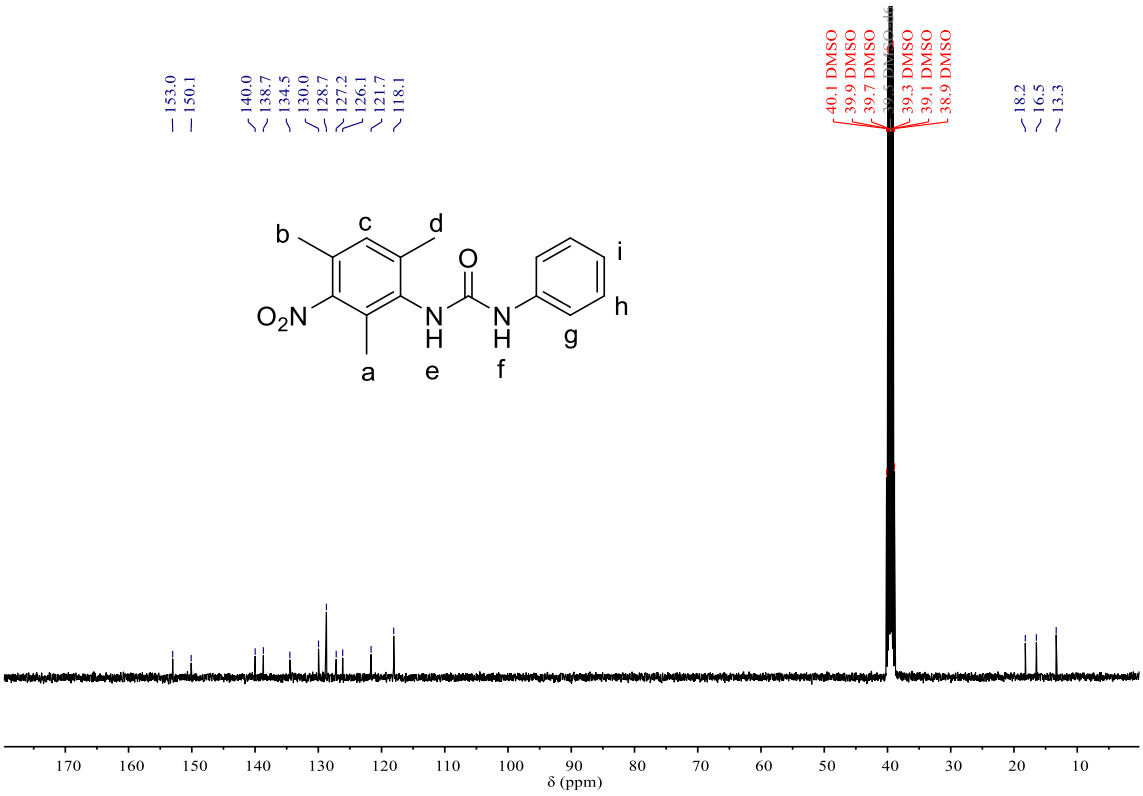

Figure 40. ^{13}C {H} NMR spectrum of **3.20** (100 MHz, DMSO-d_6, 298 K).

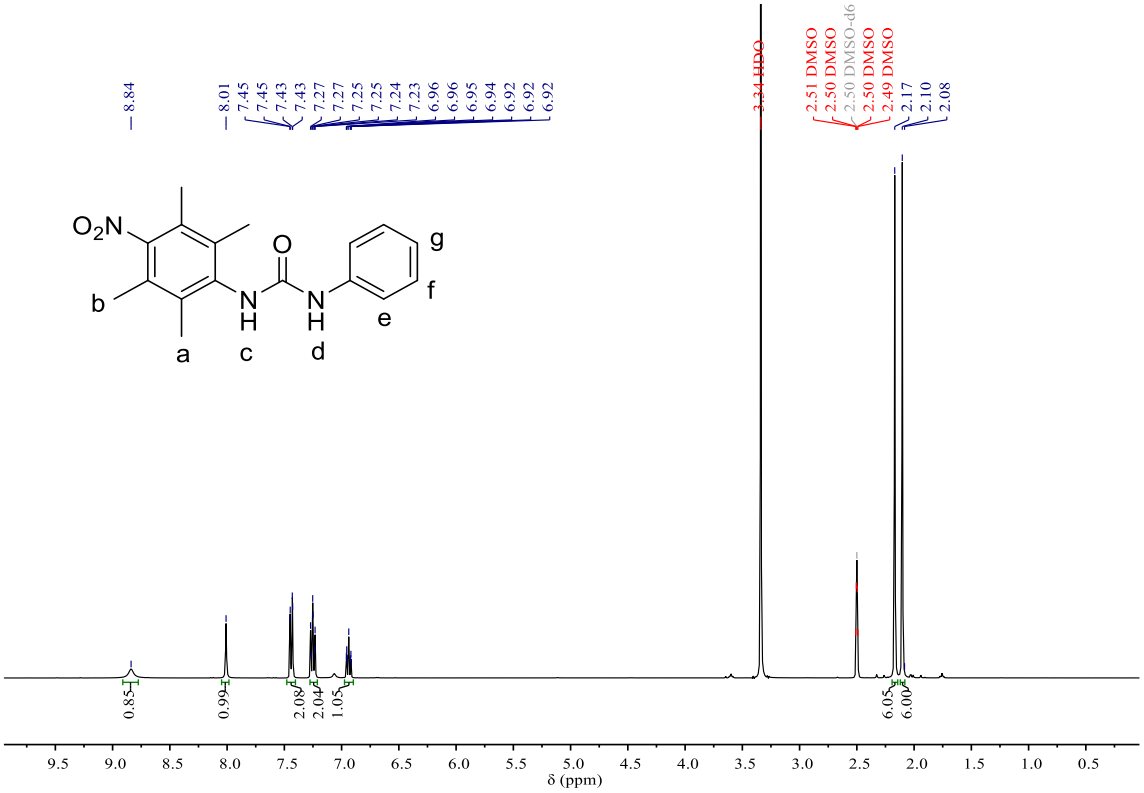

Figure 41 ^{1}H NMR spectrum of **3.21** (400 MHz, DMSO-d_6, 298 K).

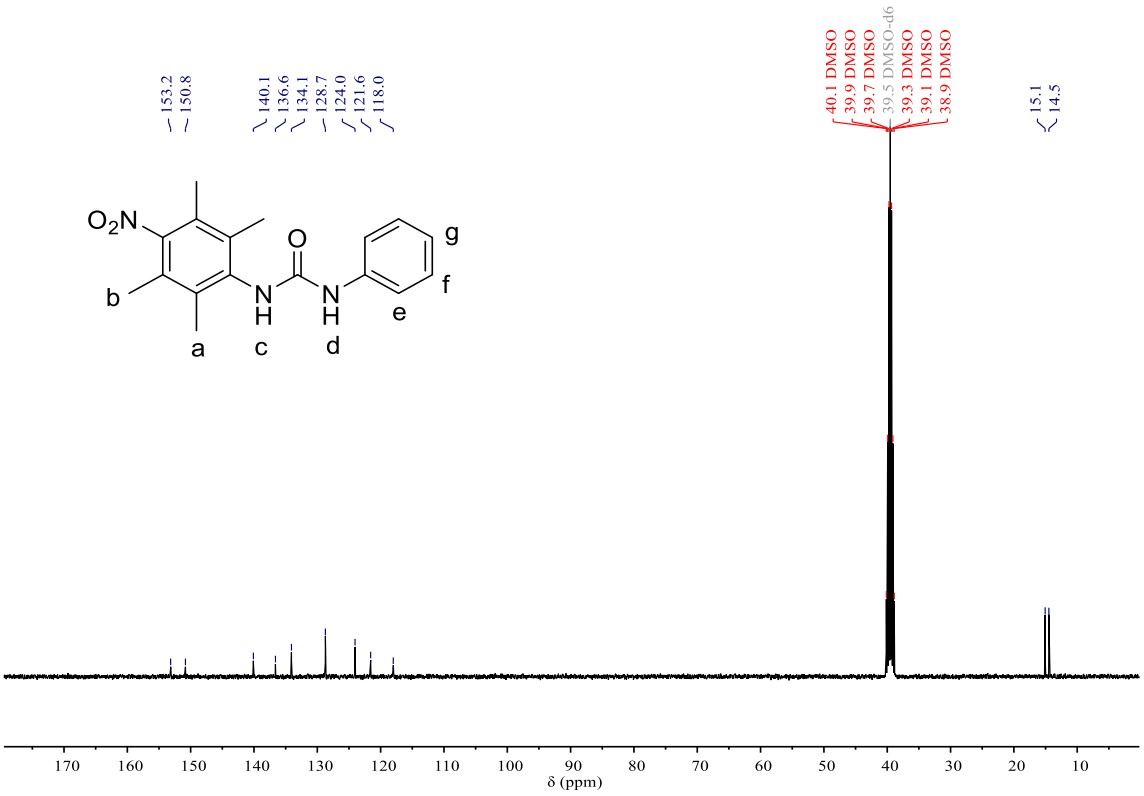

Figure 42. ^{13}C {H} NMR spectrum of **3.21** (100 MHz, DMSO-d_6, 298 K).

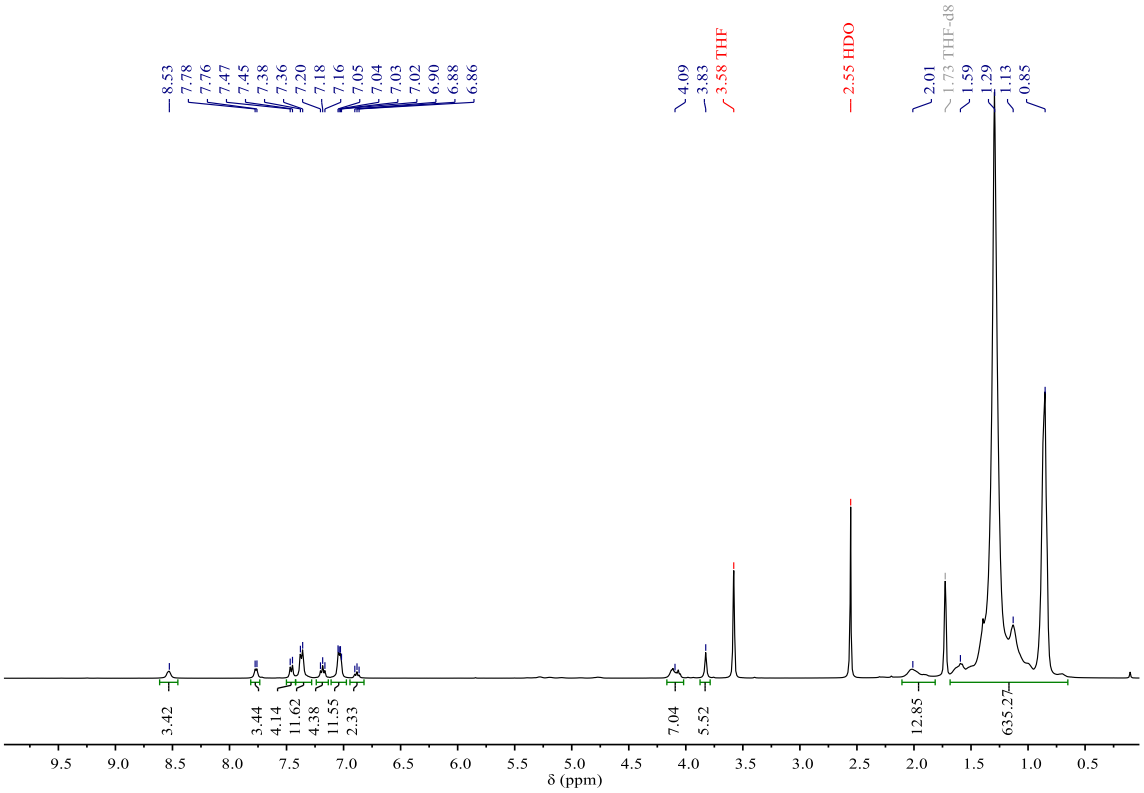

Figure 43. ^{1}H NMR spectrum of **SPU1** (400 MHz, THF-d_8, 298 K).

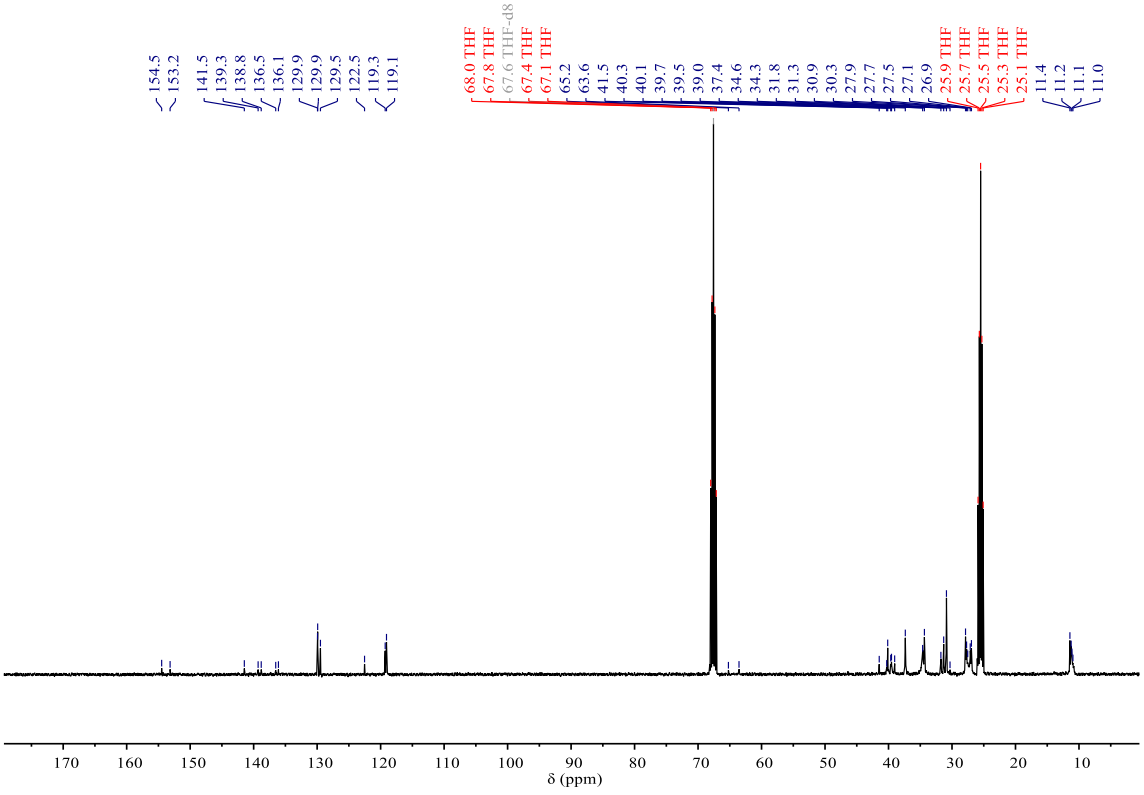

Figure 44. ^{13}C {H} NMR spectrum of **SPU1** (100 MHz, THF-d_8, 298 K).

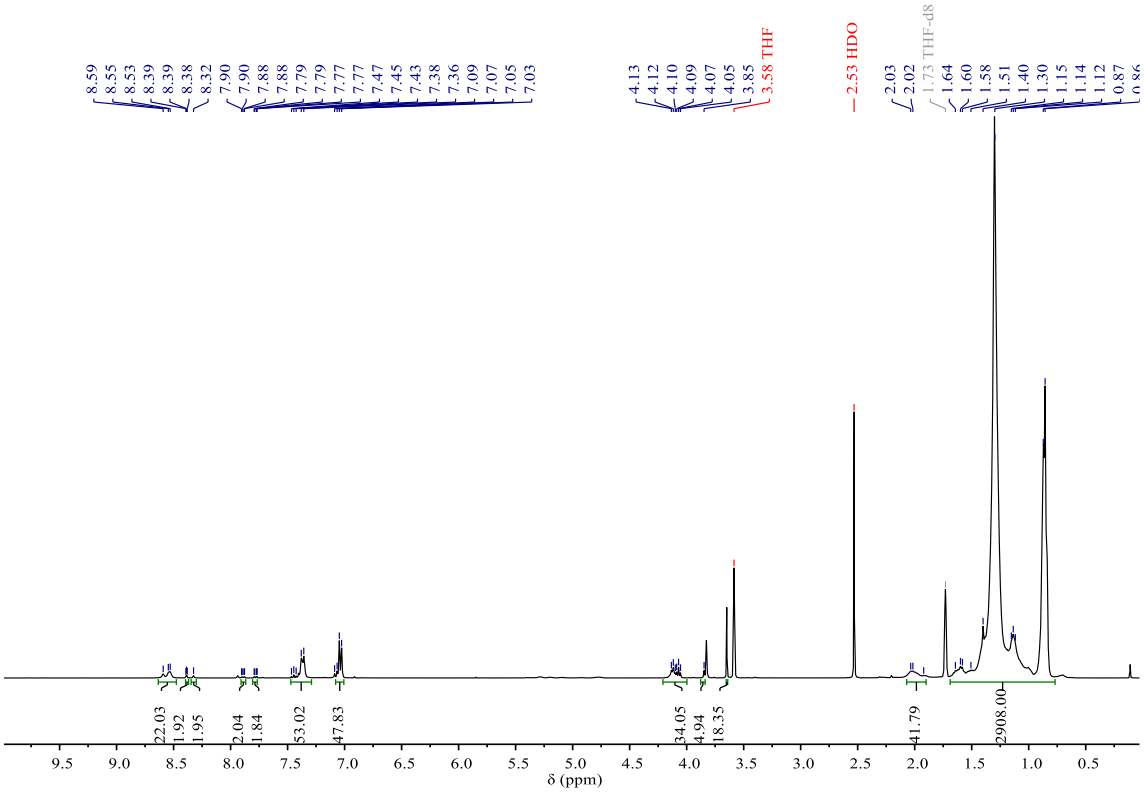

Figure 45. ^{1}H NMR spectrum of **SPU2** (400 MHz, THF-d_8, 298 K).

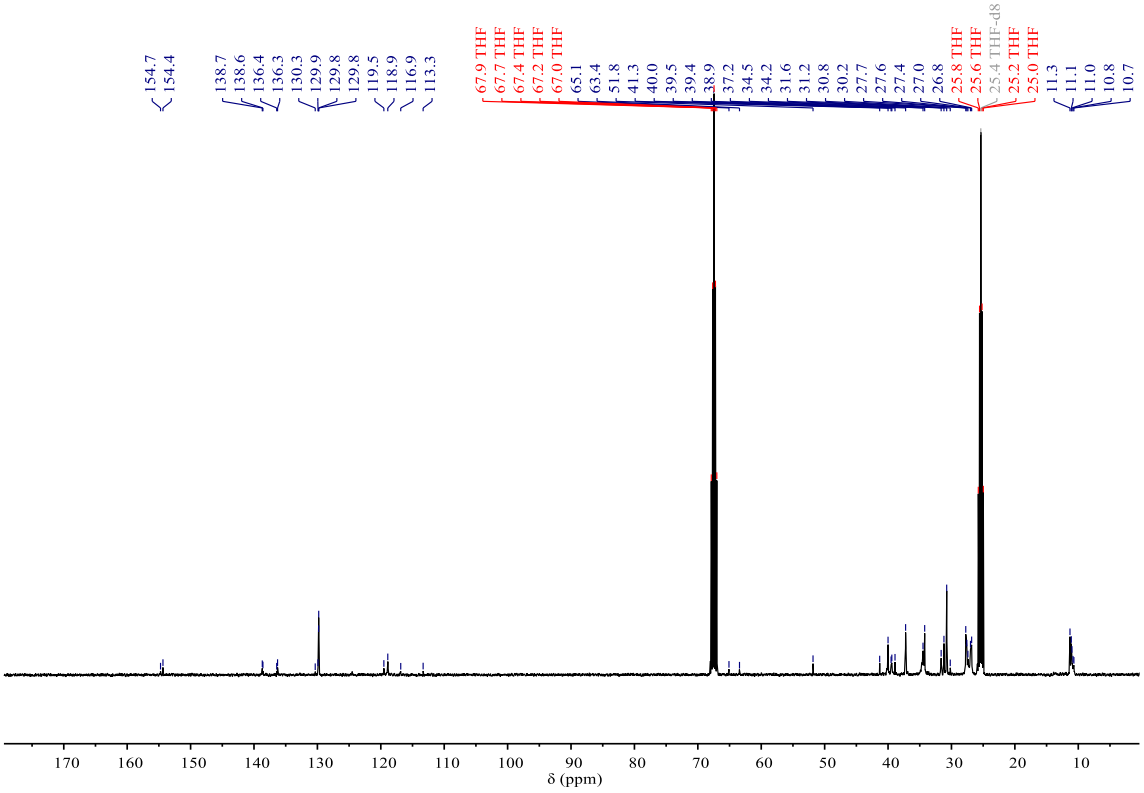

Figure 46. ^{13}C {H} NMR spectrum of **SPU2** (100 MHz, THF-d_8, 298 K).

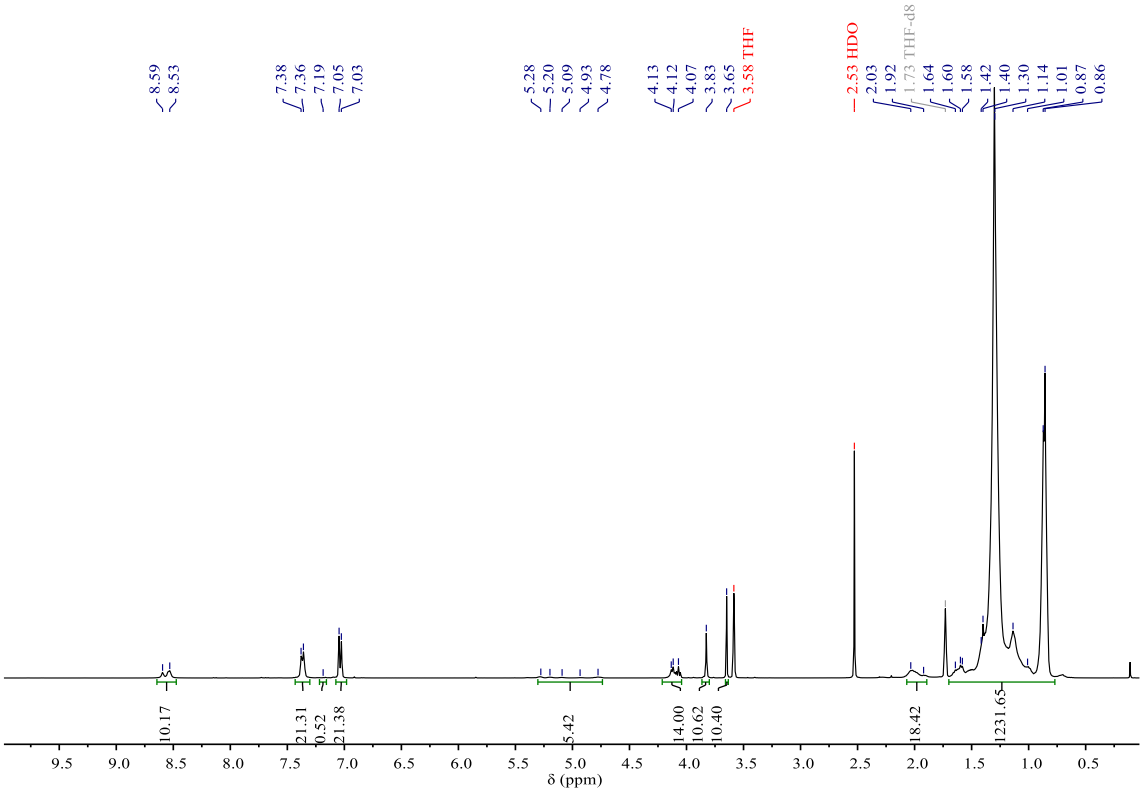

Figure 47. ^{1}H NMR spectrum of **SPU3** (400 MHz, THF-d_8, 298 K).

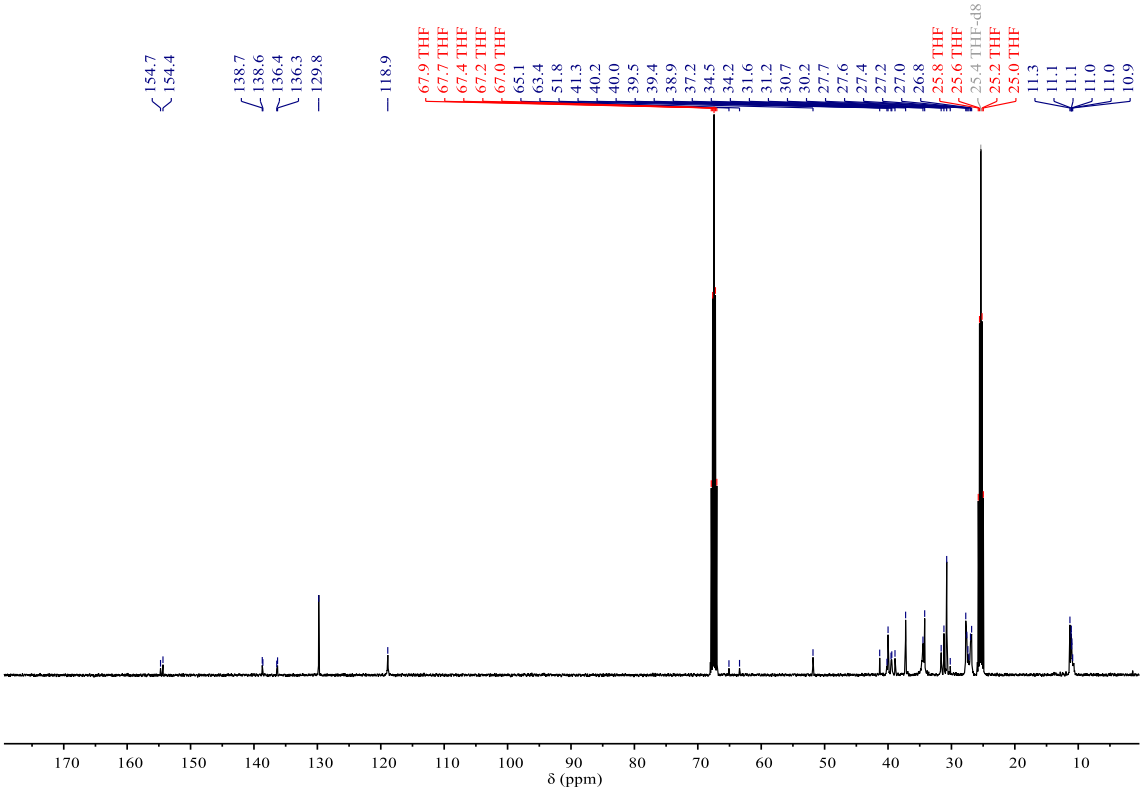

Figure 48. ^{13}C {H} NMR spectrum of **SPU3** (100 MHz, THF-d_8, 298 K).

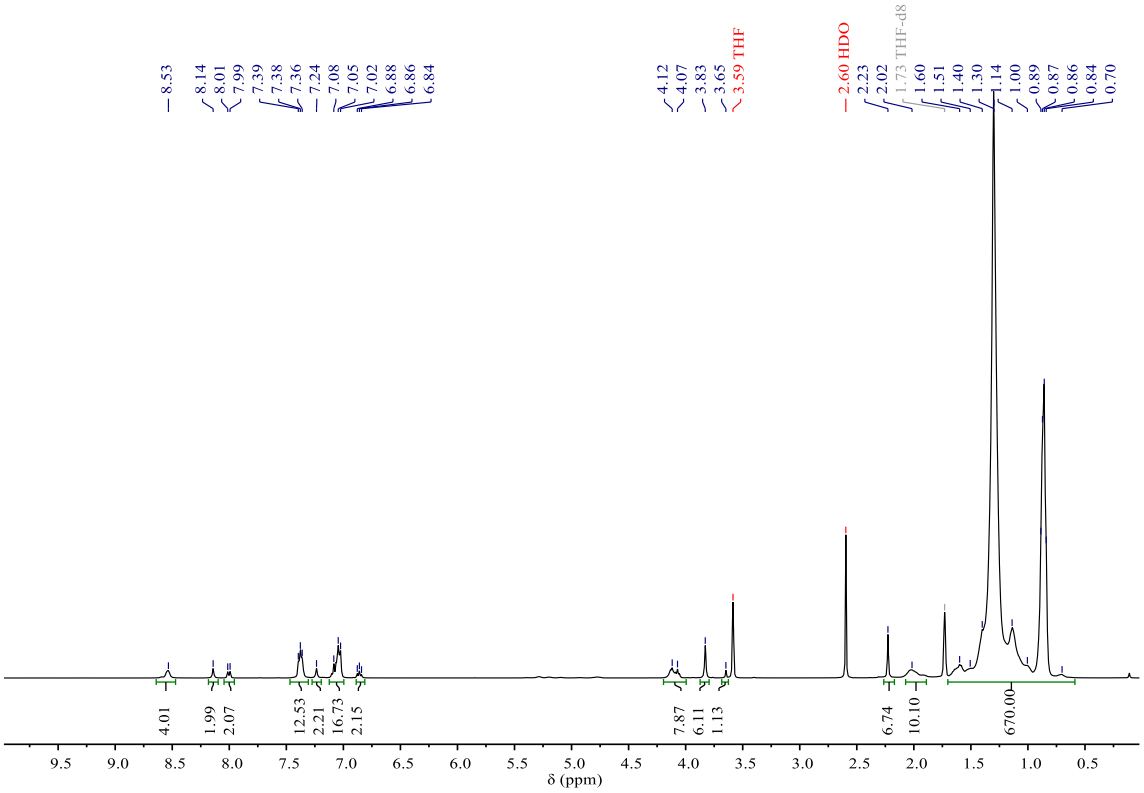

Figure 49. ^{1}H NMR spectrum of **SPU4** (400 MHz, THF-d_8, 298 K).

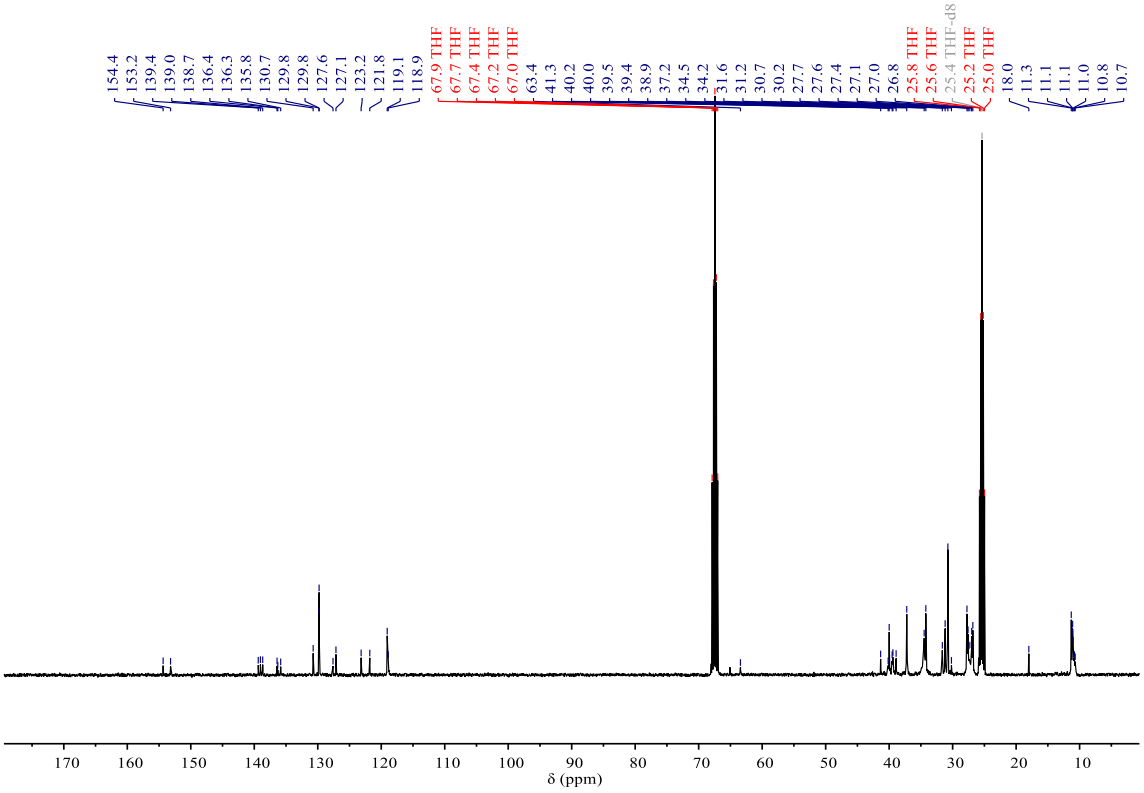

Figure 50. ^{13}C {H} NMR spectrum of **SPU4** (100 MHz, THF-d_8, 298 K).

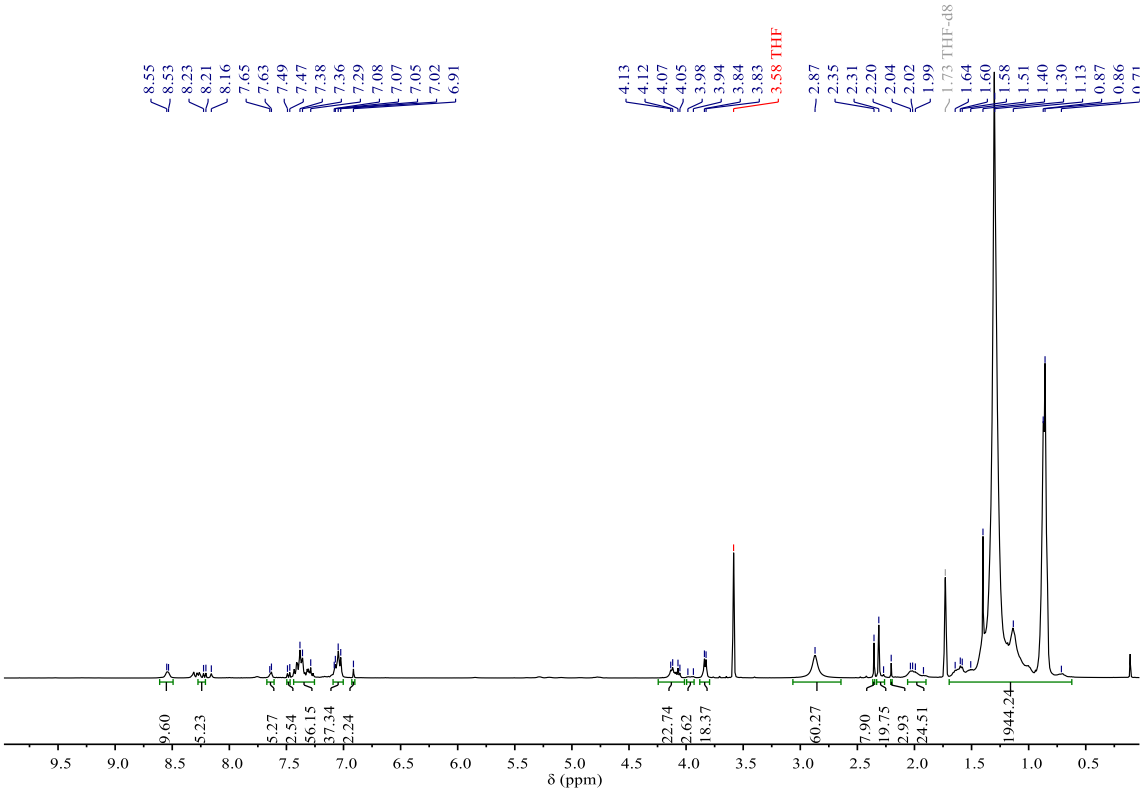

Figure 51. ^{1}H NMR spectrum of **SPU5** (400 MHz, THF-d_8, 298 K).

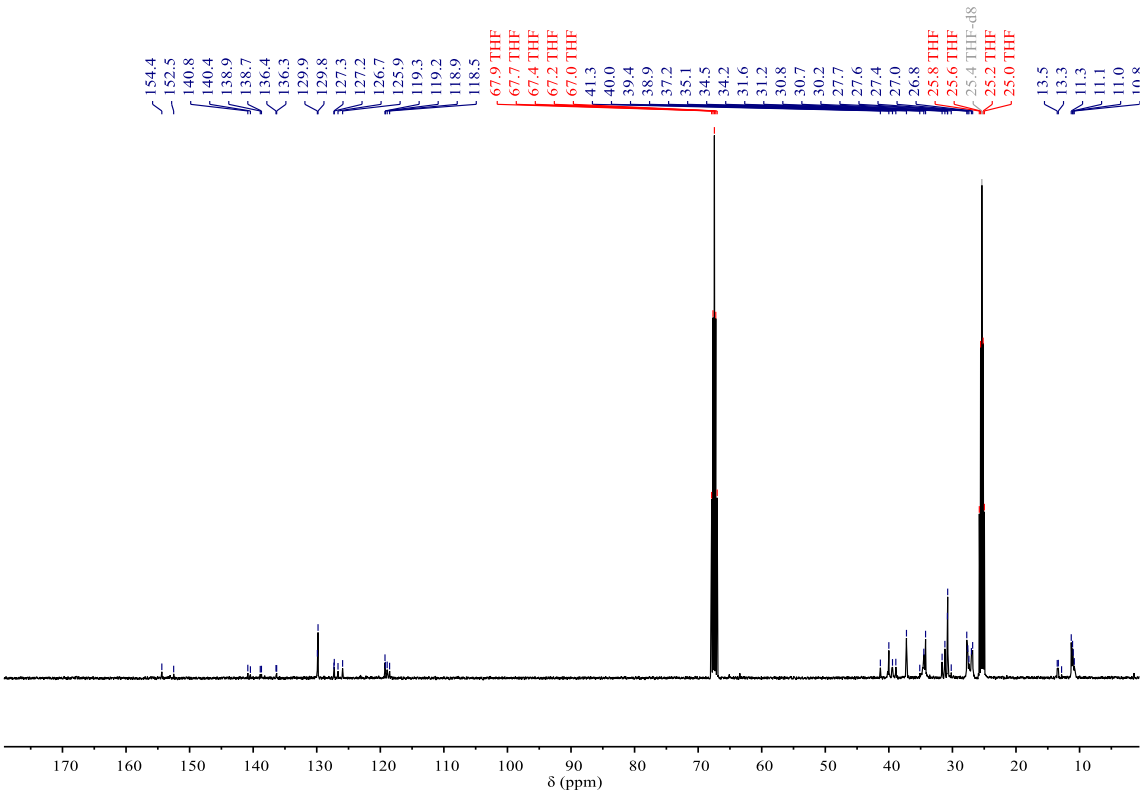

Figure 52. ^{13}C {H} NMR spectrum of **SPU5** (100 MHz, THF-d_8, 298 K).

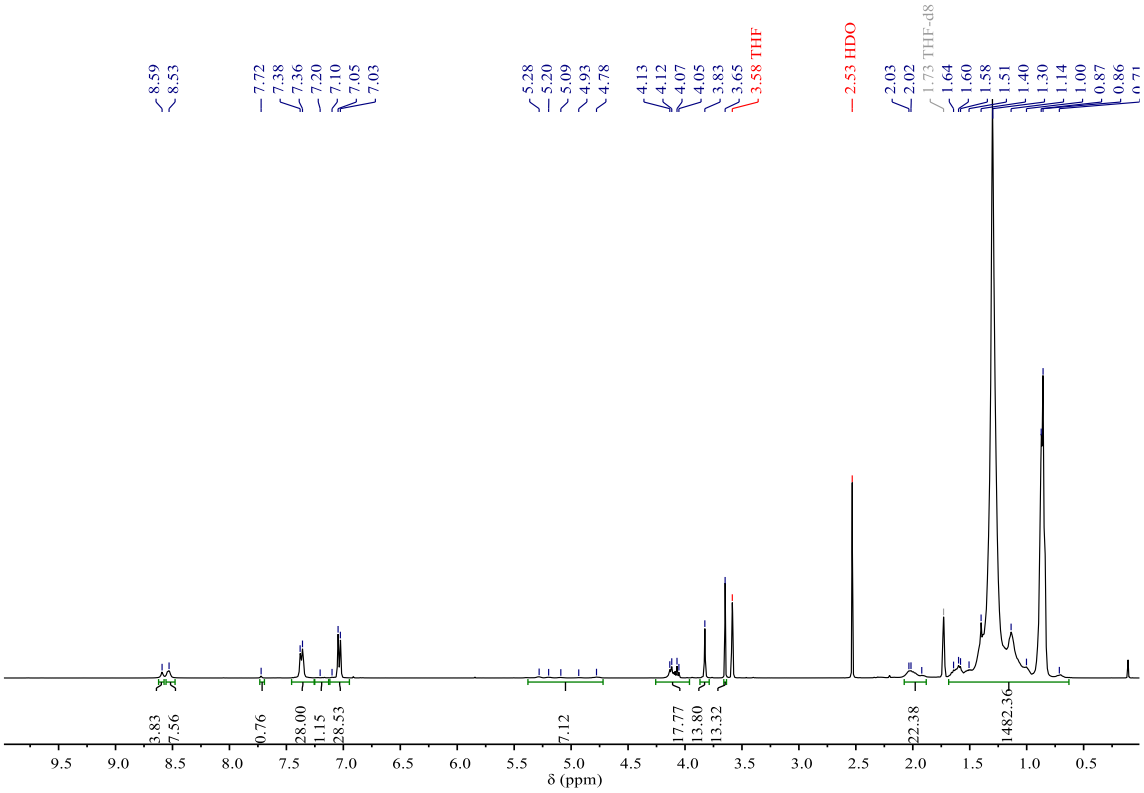

Figure 53. ^{1}H NMR spectrum of **SPU6** (400 MHz, THF-d_8, 298 K).

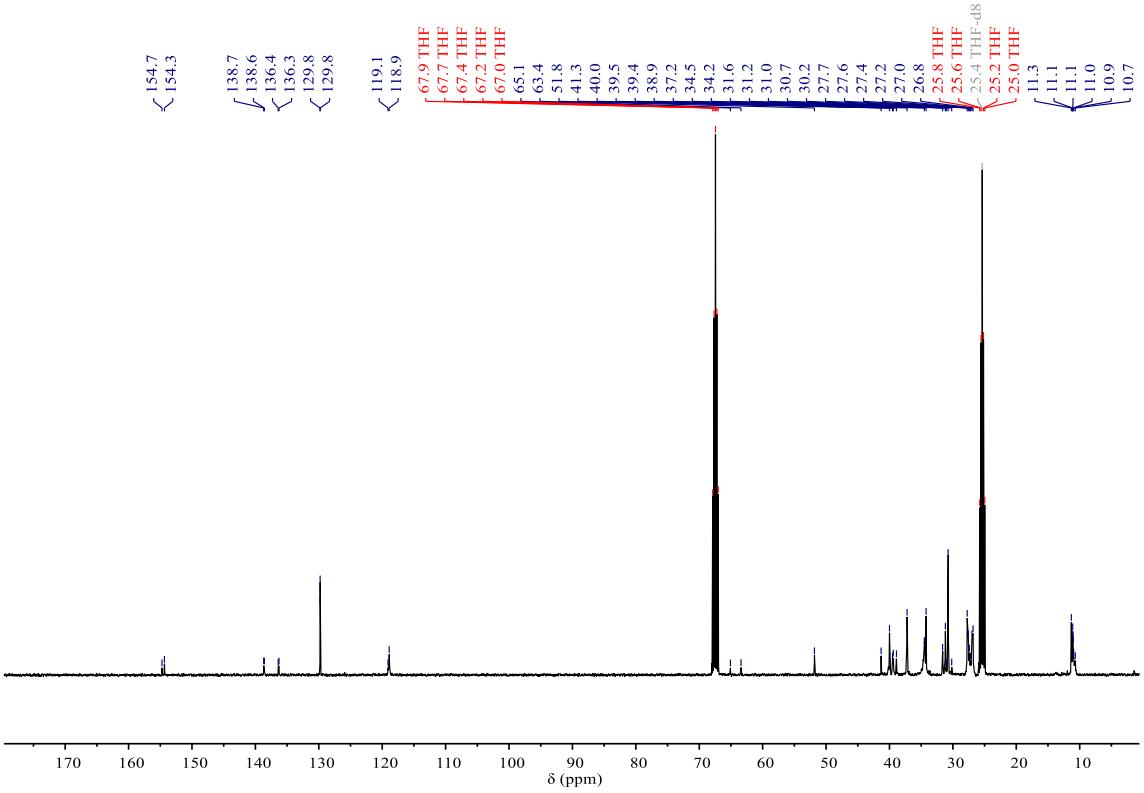

Figure 54. ^{13}C {H} NMR spectrum of **SPU6** (100 MHz, THF-d_8, 298 K).

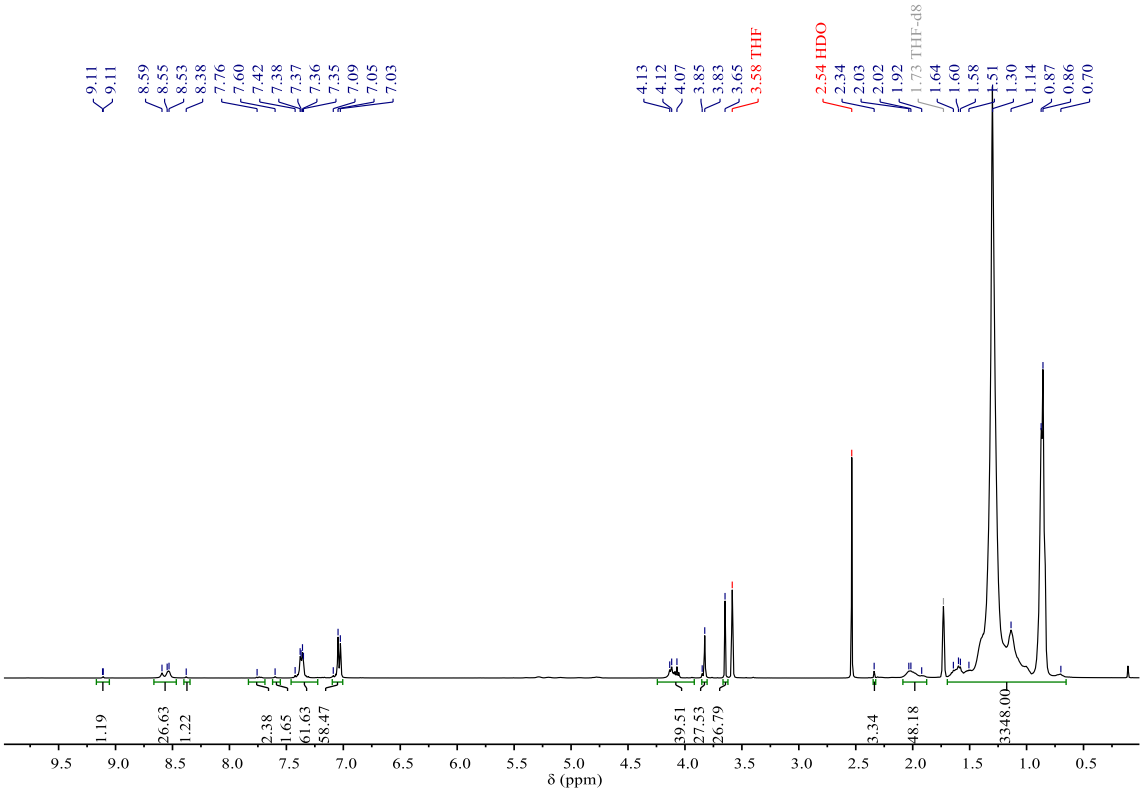

Figure 55. ^{1}H NMR spectrum of **SPU7** (400 MHz, THF-d_8, 298 K).

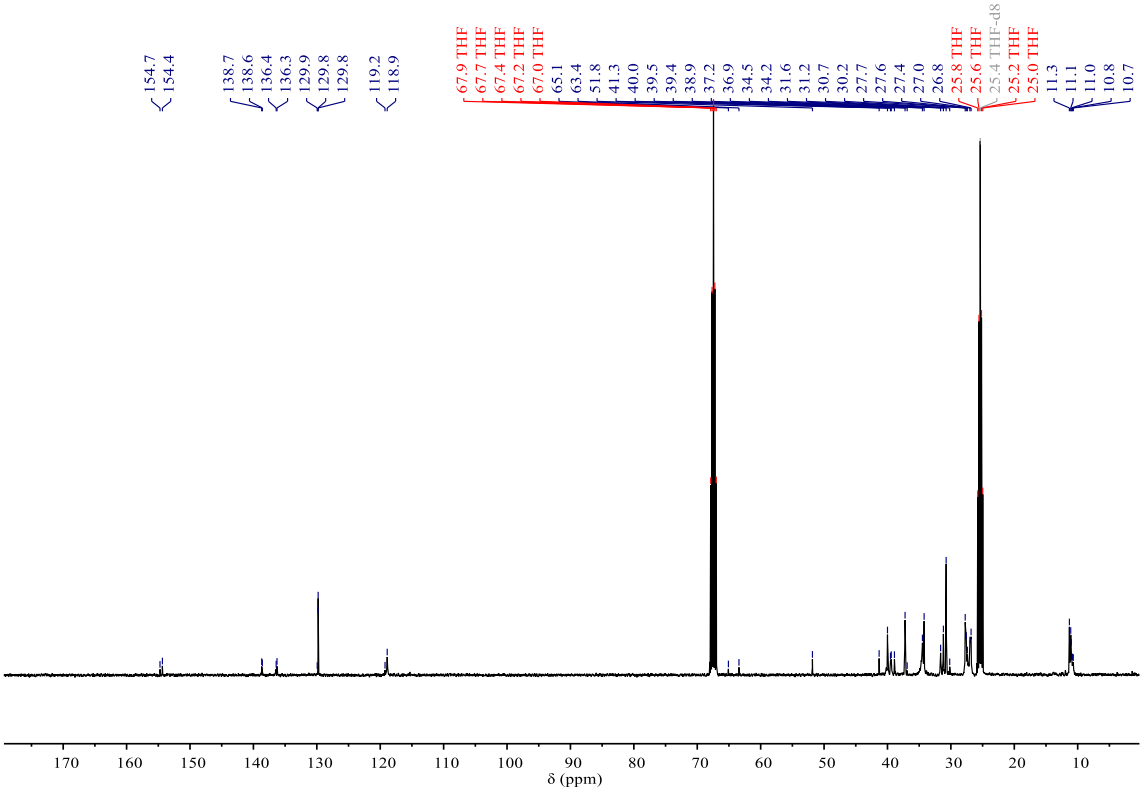

Figure 56. ^{13}C {H} NMR spectrum of **SPU7** (100 MHz, THF-d_8, 298 K).

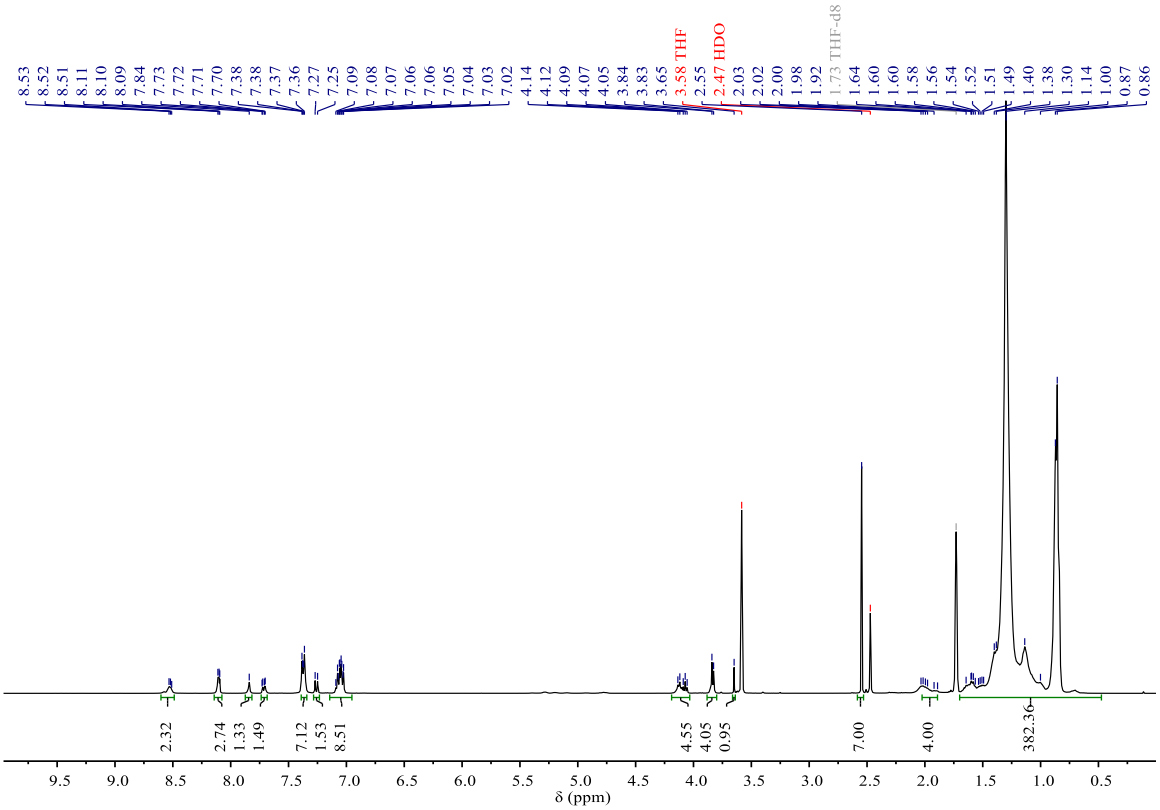

Figure 57. ^{1}H NMR spectrum of **SPU8** (400 MHz, THF-d_8, 298 K).

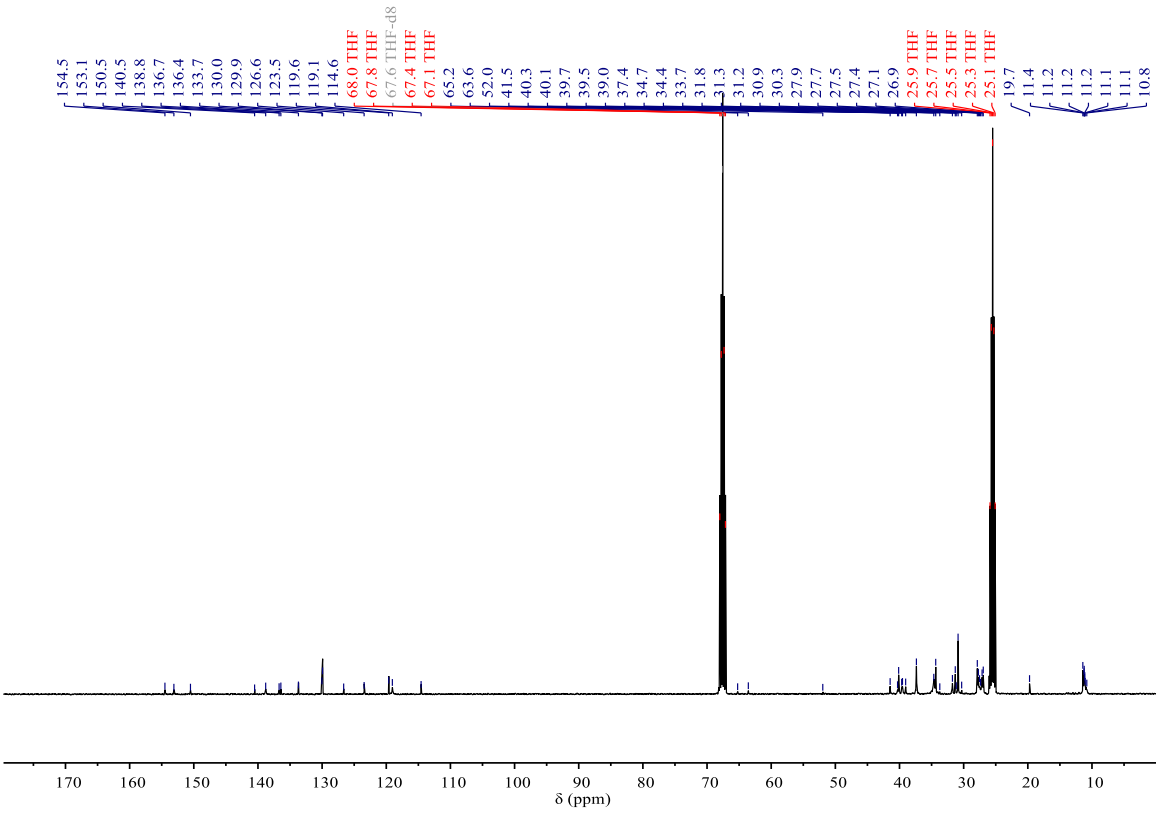

Figure 58. ^{13}C {H} NMR spectrum of **SPU8** (100 MHz, THF-d_8, 298 K).

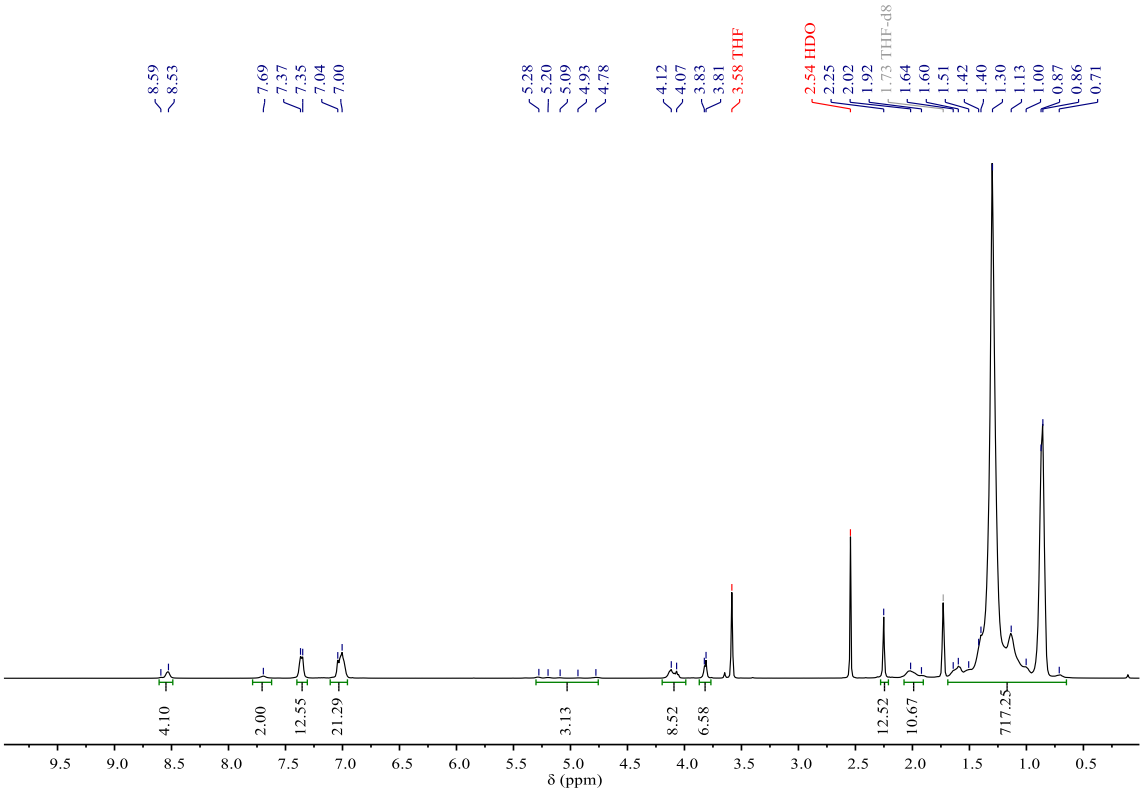

Figure 59. ^{1}H NMR spectrum of **SPU9** (400 MHz, THF-d_8, 298 K).

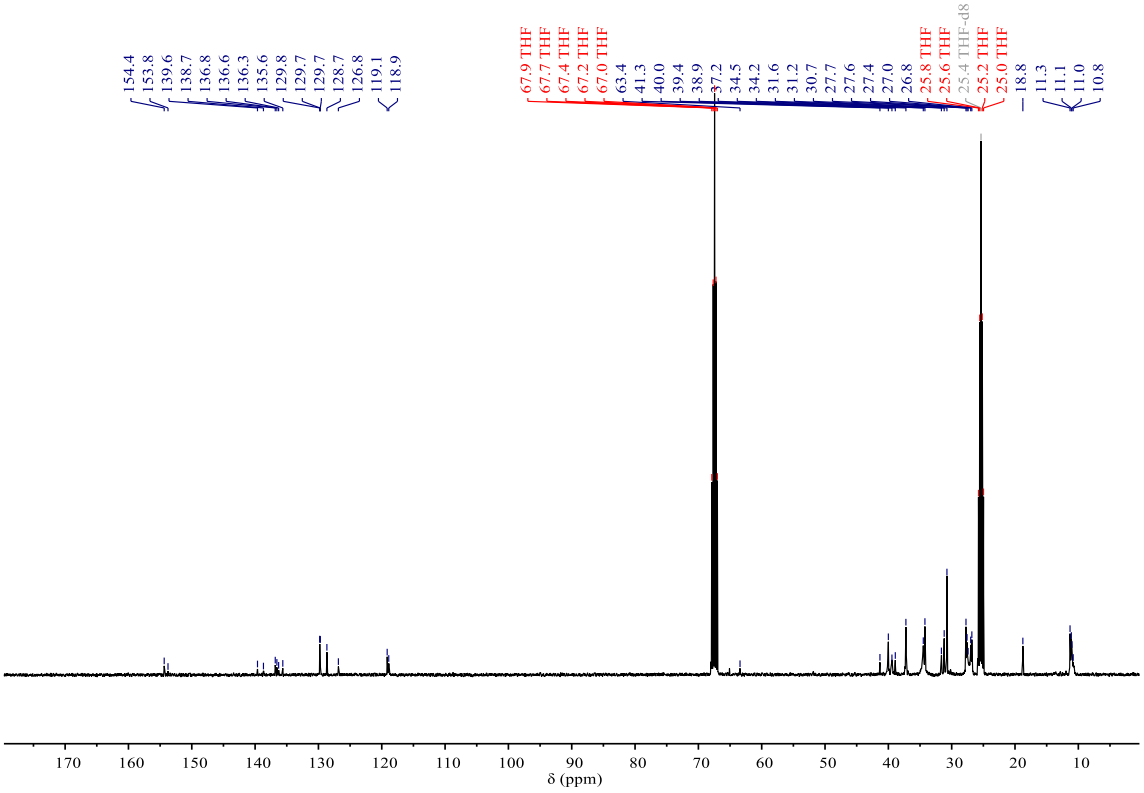

Figure 60. ^{13}C {H} NMR spectrum of **SPU9** (100 MHz, THF-d_8, 298 K).

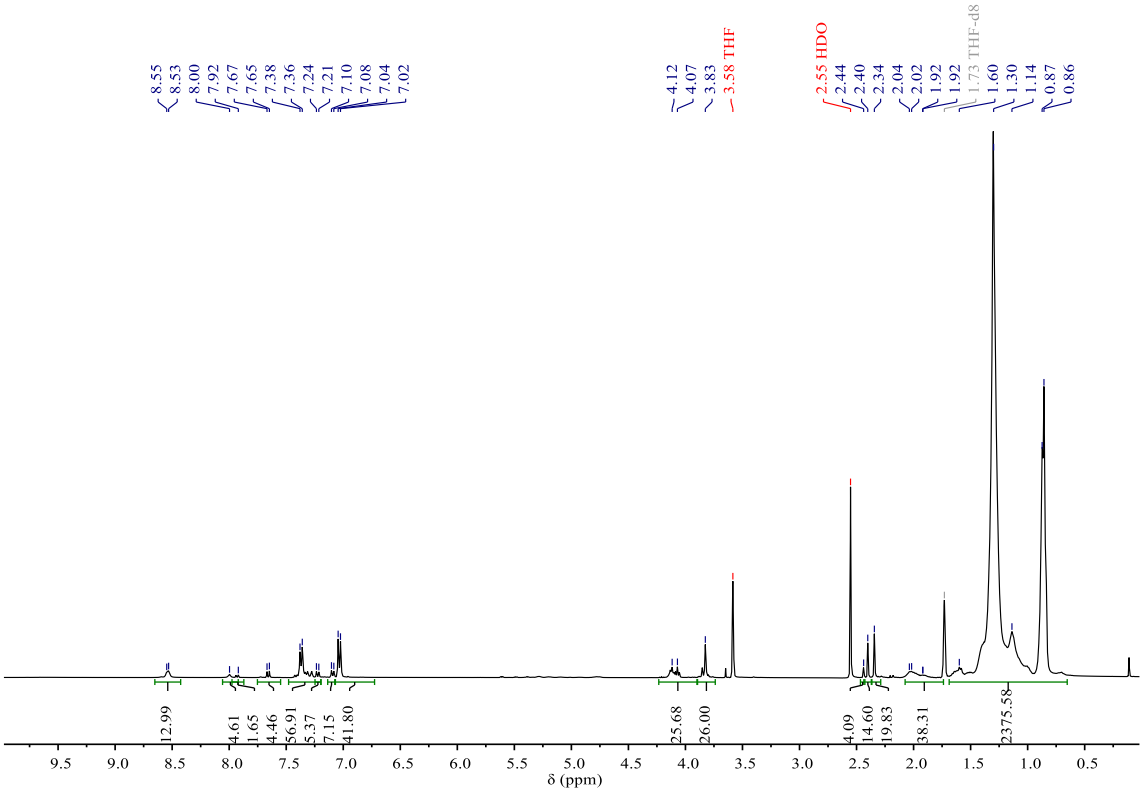

Figure 61. ^{1}H NMR spectrum of **SPU10** (400 MHz, THF-d_8, 298 K).

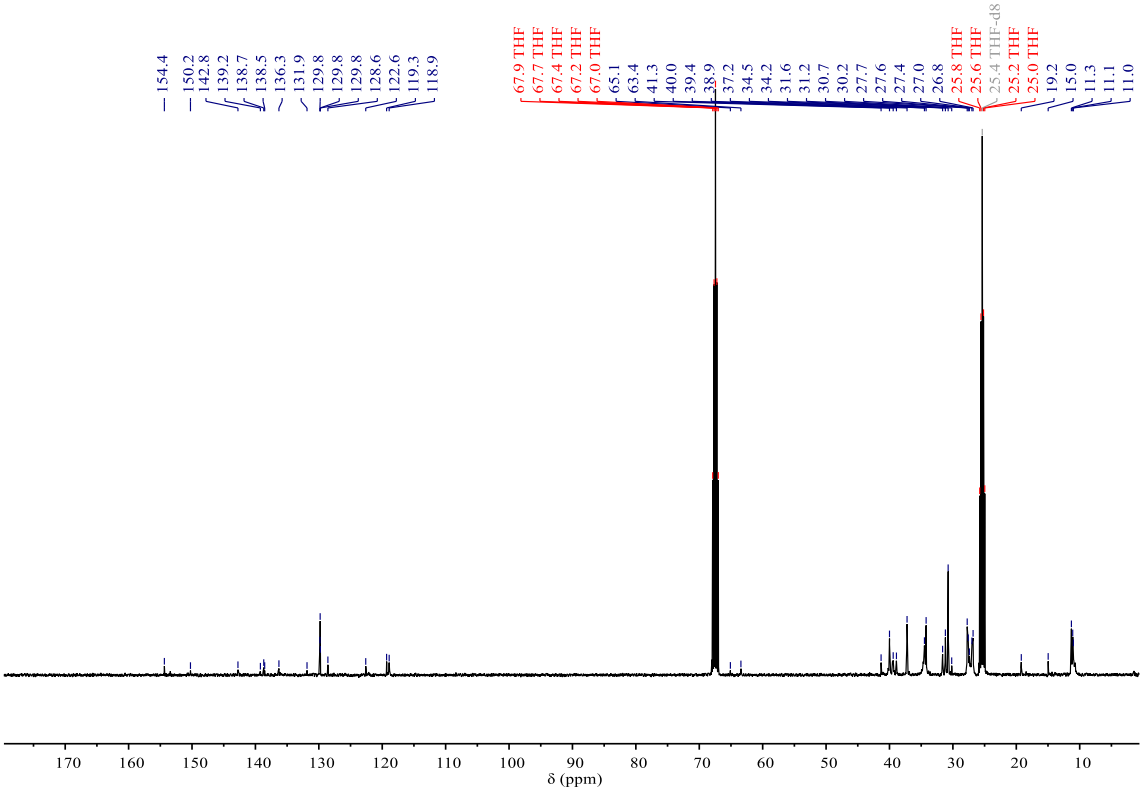

Figure 62. ^{13}C {H} NMR spectrum of **SPU10** (100 MHz, THF-d_8, 298 K).

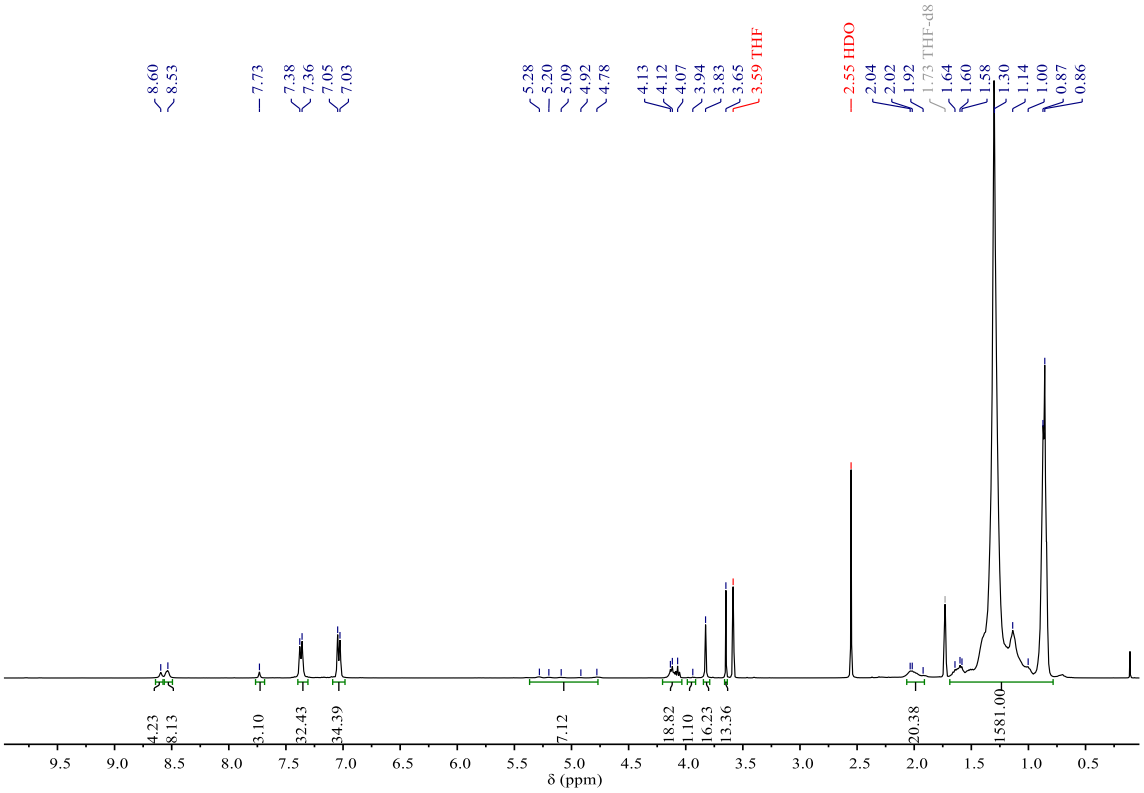

Figure 63. ^{1}H NMR spectrum of **SPU11** (400 MHz, THF-d_8, 298 K).

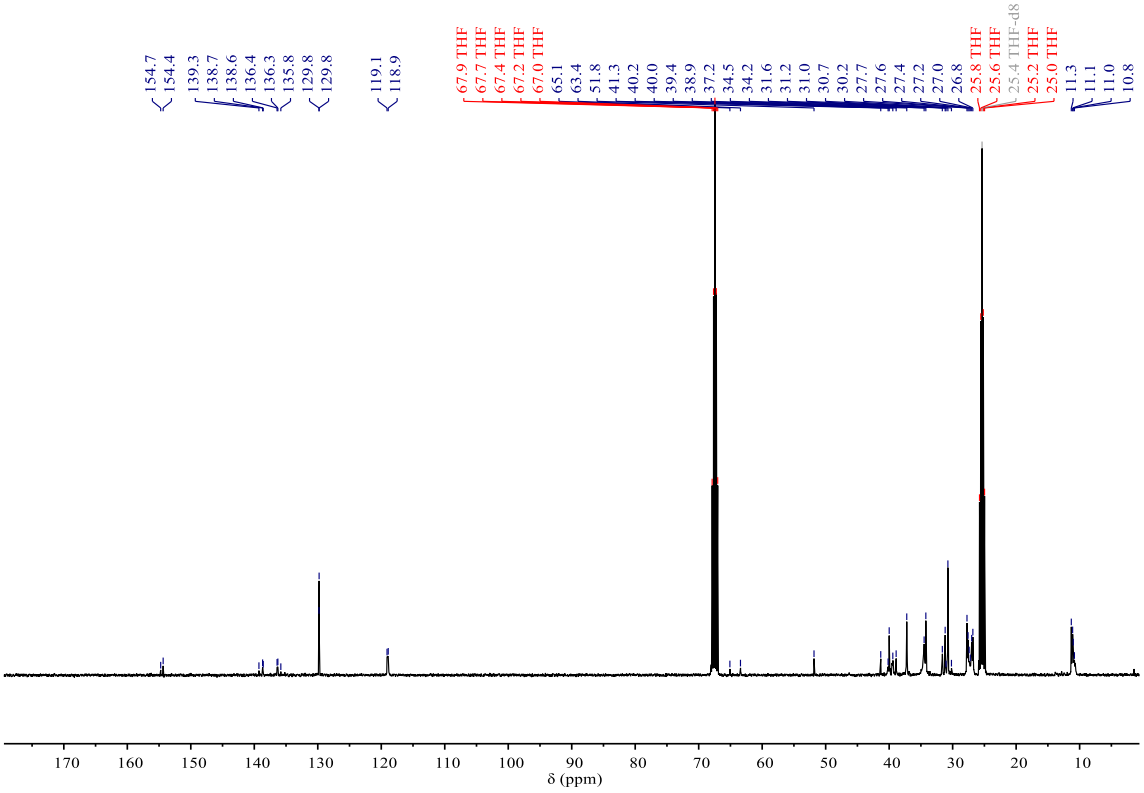

Figure 64. ^{13}C {H} NMR spectrum of **SPU11** (100 MHz, THF-d_8, 298 K).

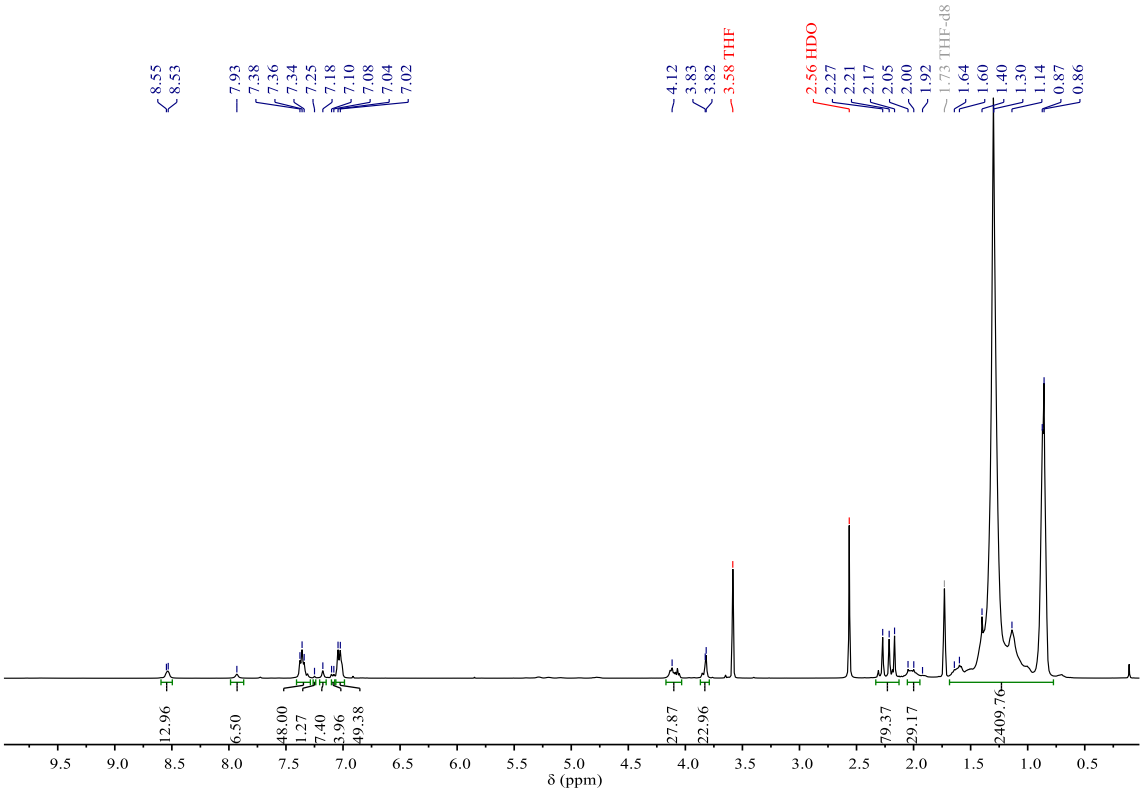

Figure 65. ^{1}H NMR spectrum of **SPU12** (400 MHz, THF-d_8, 298 K).

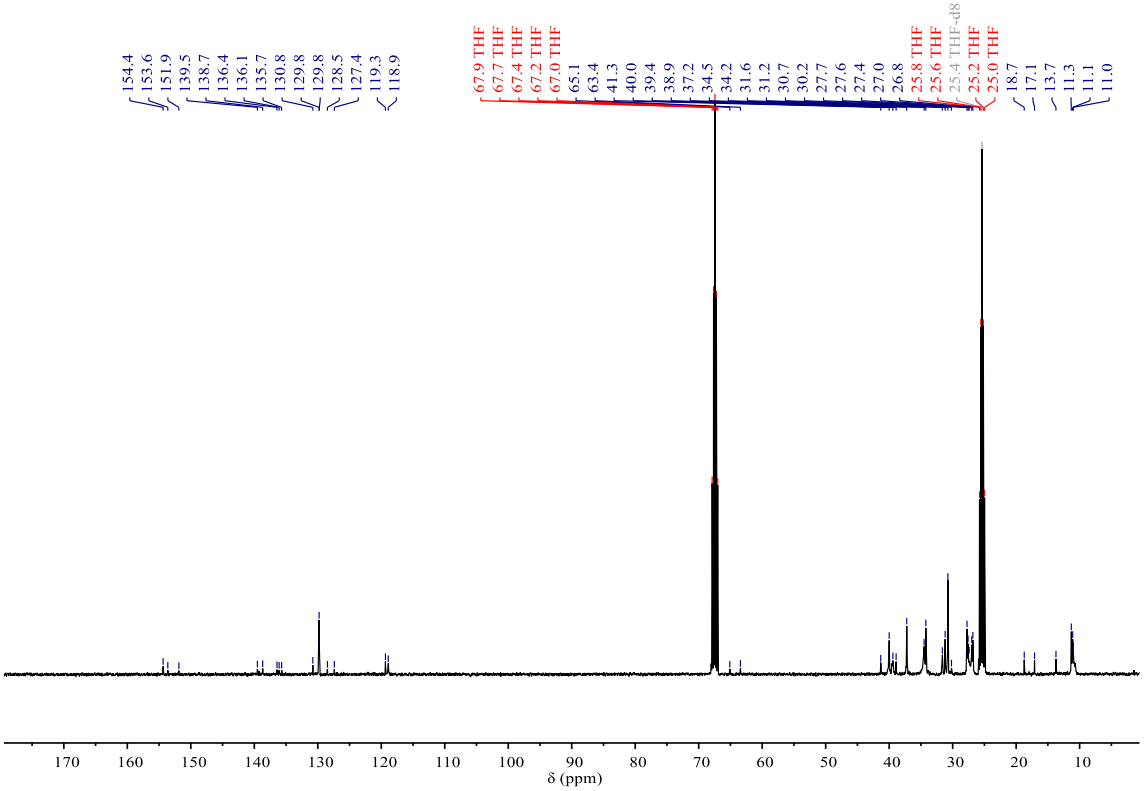

Figure 66. ^{13}C {H} NMR spectrum of **SPU12** (100 MHz, THF-d_8, 298 K).

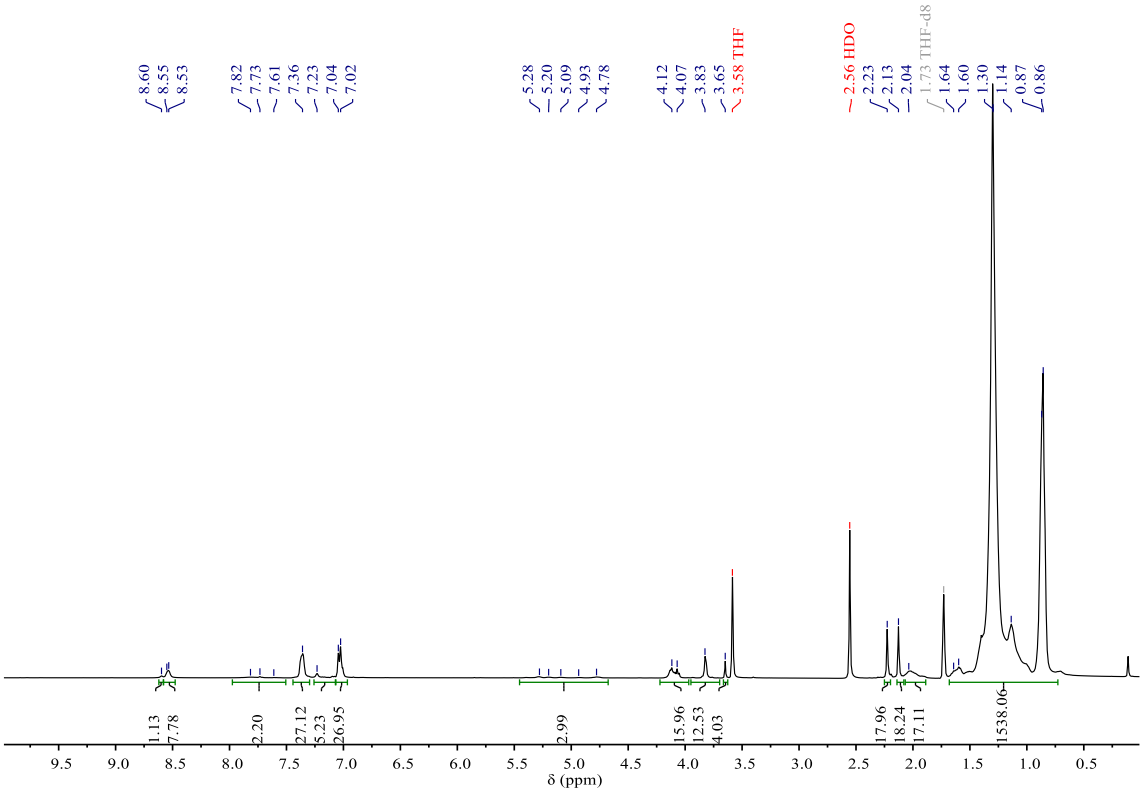

Figure 67. ^{1}H NMR spectrum of **SPU13** (400 MHz, THF-d_8, 298 K).

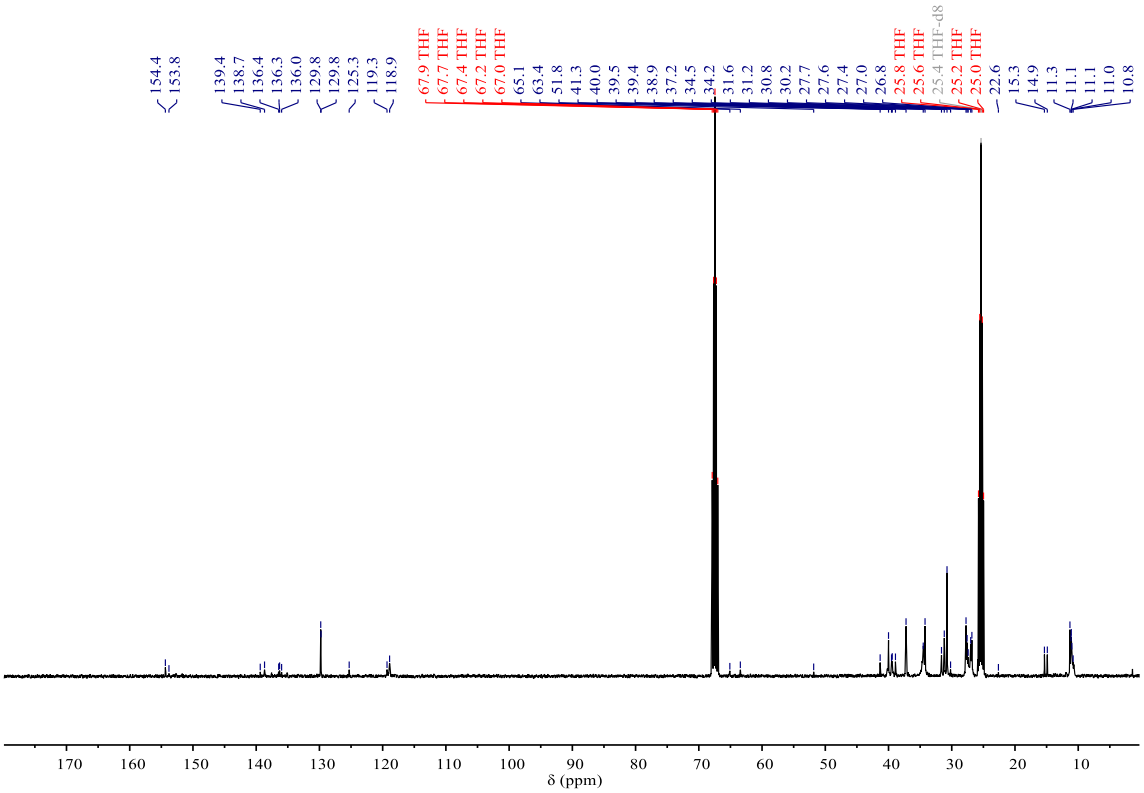

Figure 68. ^{13}C {H} NMR spectrum of **SPU13** (100 MHz, THF-d_8, 298 K).

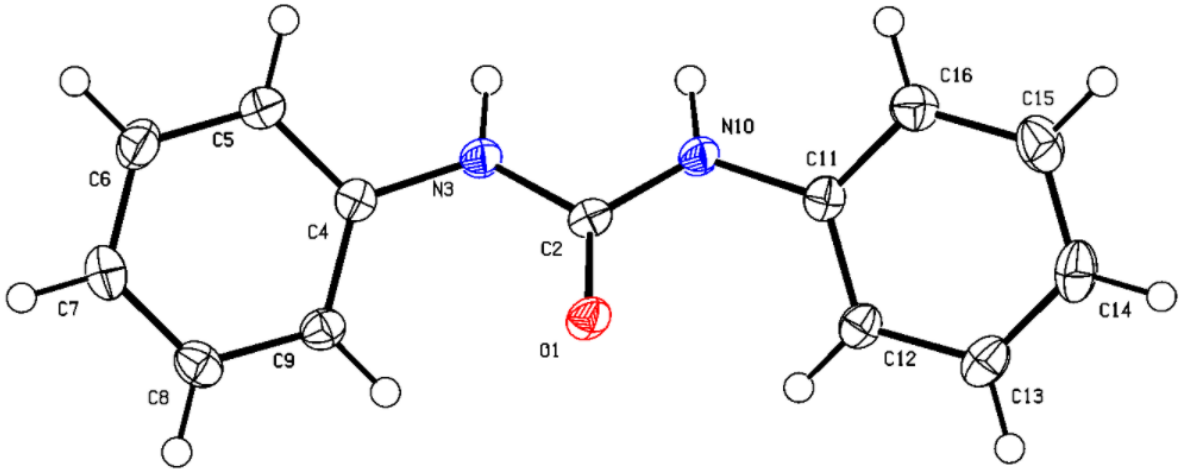

Figure 69. Molecular Structure of 1,3-diphenylurea, **3.9**, ellipsoids drawn at 50% probability.

Table 1. Crystallographic details for compound **3.9**.

Formula	$C_{13}\,H_{12}\,N_2\,O$
M_r	212.25
Crystal system	orthorhombic
Space group	P $na2_1$
Z	4
a /Å	9.05398(1)
b/Å	10.33258(1)
c /Å	11.72508(1)
V / Å^3	1096.839 (2)
ρ_{calc} / g cm^{-3}	1.285
Crystal habit	Colourless block
Crystal dimensions /mm	0.068 × 0.133 × 0.180
Radiation	Cu K_α (1.54184 Å)
T /K	100
μ /mm^{-1}	0.666
R(*F*), *Rw*(*F*) /%	2.61, 3.29
CCDC cif deposition number	CCDC 2131759

Table 2. Selected bond lengths (Å) and angles (°) for compound **3.9**.

O(1) – C(2)	1.2365(14)	O(1) – C(2) – N(3)	122.43(13)
C(2) – N(3)	1.3664(18)	O(1) – C(2) – N(10)	123.45(13)
C(2) – N(10)	1.3568(18)	N(3) – C(2) – N(10)	114.10(10)
C(4) – N(3)	1.416(2)	C(2) – N(3) – C(4)	124.56(11)
C(4) – C(5)	1.394(2)	N(3) – C(4) – C(5)	118.02(11)
C(4) – C(9)	1.3956(18)	N(3) – C(4) – C(9)	122.31(13)
C(5) – C(6)	1.386(2)	C(5) – C(4) – C(9)	119.64(13)
C(6) – C(7)	1.390(2)	C(4) – C(5) – C(6)	120.10(12)
C(7) – C(8)	1.386(2)	C(5) – C(6) – C(7)	120.40(14)
C(8) – C(9)	1.388(2)	C(6) – C(7) – C(8)	119.37(13)
C(11) – N(10)	1.4168(19)	C(7) – C(8) – C(9)	120.86(12)
C(11) – C(12)	1.392(2)	C(4) – C(9) – C(8)	119.60(13)
C(11) – C(16)	1.3929(19)	C(2) – N(10) – C(11)	125.17(11)
C(12) – C(13)	1.387(2)	N(10) – C(11) – C(12)	121.88(12)
C(13) – C(14)	1.388(2)	N(10) – C(11) – C(16)	118.11(12)
C(14) – C(15)	1.389(2)	C(12) – C(11) – C(16)	119.94(14)
C(15) – C(16)	1.387(2)	C(11) – C(12) – C(13)	119.49(13)
		C(12) – C(13) – C(14)	120.88(15)
		C(13) – C(14) – C(15)	119.32(15)
		C(14) – C(15) – C(16)	120.39(14)
		C(11) – C(16) – C(15)	119.94(14)

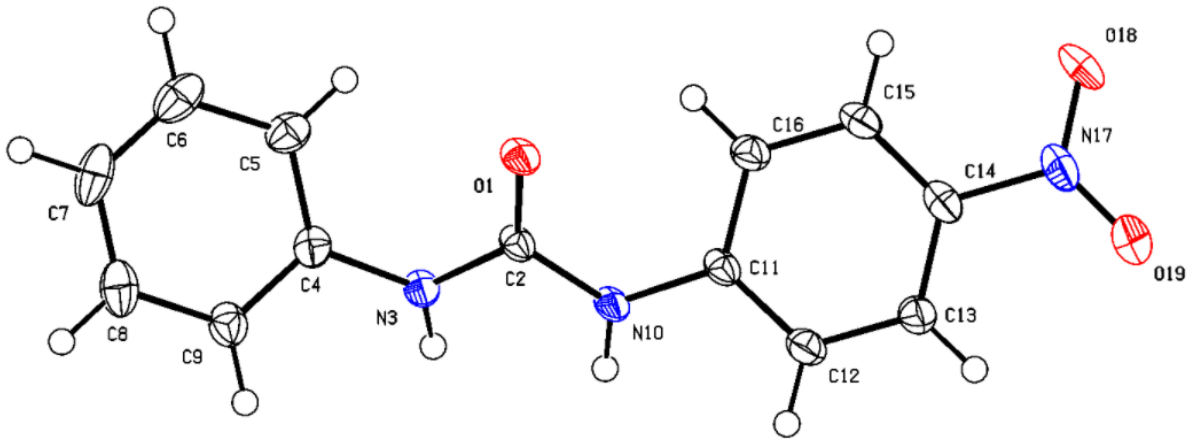

Figure 70. Molecular Structure of 1-(4-nitrophenyl)-3-phenylurea, **3.11**, ellipsoids drawn at 50% probability.

Table 3. Crystallographic details for compound **3.11**.

Formula	$C_{13}\,H_{11}\,N_3\,O_3$
M_r	257.25
Crystal system	monoclinic
Space group	P c
Z	2
a /Å	6.39508(1)
b/Å	4.67150(1)
c /Å	19.65687(2)
β / °	96.795(2)
V / Å^3	583.117(3)
ρ_{calc} / g cm^{-3}	1.465
Crystal habit	Colourless plate
Crystal dimensions /mm	0.044 × 0.125 × 0.207
Radiation	Cu K_α (1.54184 Å)
T /K	100
μ /mm^{-1}	0.894
R(*F*), *Rw*(*F*) /%	4.24, 5.61
CCDC cif deposition number	CCDC 2131884

Table 4. Selected bond lengths (Å) and angles (°) for compound **3.11**.

O(1) – C(2)	1.240(2)	O(1) – C(2) – N(3)	123.90(17)
C(2) – N(3)	1.360(2)	O(1) – C(2) – N(10)	122.19(16)
C(2) – N(10)	1.373(2)	N(3) – C(2) – N(10)	113.90(15)
C(4) – N(3)	1.416(2)	C(2) – N(3) – C(4)	124.71(16)
C(4) – C(5)	1.393(3)	N(3) – C(4) – C(5)	121.89(18)
C(4) – C(9)	1.394(3)	N(3) – C(4) – C(9)	117.96(17)
C(5) – C(6)	1.392(3)	C(5) – C(4) – C(9)	120.10(18)
C(6) – C(7)	1.387(4)	C(4) – C(5) – C(6)	118.83(19)
C(7) – C(8)	1.384(4)	C(5) – C(6) – C(7)	121.2(2)
C(8) – C(9)	1.387(3)	C(6) – C(7) – C(8)	119.60(19)
C(11) – N(10)	1.401(2)	C(7) – C(8) – C(9)	120.1(2)
C(11) – C(12)	1.391(3)	C(4) – C(9) – C(8)	120.23(19)
C(11) – C(16)	1.406(3)	C(2) – N(10) – C(11)	125.76(15)
C(12) – C(13)	1.382(3)	N(10) – C(11) – C(12)	118.78(16)
C(13) – C(14)	1.386(3)	N(10) – C(11) – C(16)	121.55(17)
C(14) – C(15)	1.387(3)	C(12) – C(11) – C(16)	119.59(17)
C(15) – C(16)	1.377(3)	C(11) – C(12) – C(13)	120.80(16)
C(14) – N(17)	1.458(2)	C(12) – C(13) – C(14)	118.50(17)
O(18) – N(17)	1.234(2)	C(13) – C(14) – C(15)	121.91(18)
O(19) – N(17)	1.220(2)	C(14) – C(15) – C(16)	119.31(17)
		N(17) – C(14) – C(13)	118.74(18)
		N(17) – C(14) – C(15)	119.34(17)
		C(11) – C(16) – C(15)	119.85(17)
		O(18) – N(17) – O(19)	123.05(17)
		O(18) – N(17) – C(14)	117.98(17)
		O(19) – N(17) – C(14)	118.97(17)

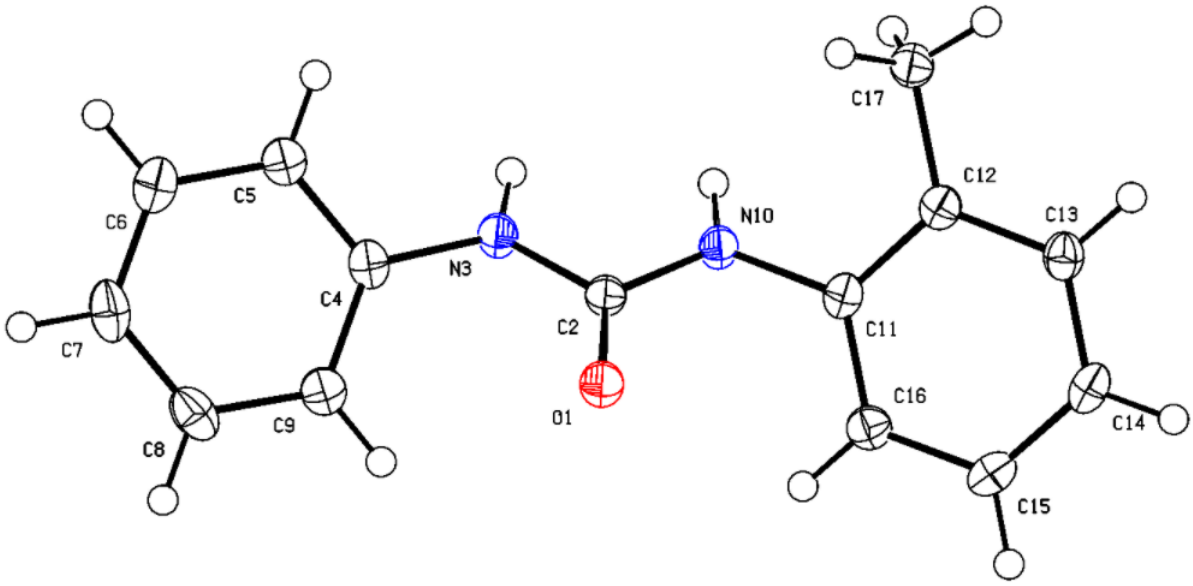

Figure 71. Molecular Structure of 1-phenyl-3-(*o*-tolyl)urea, **3.12**, ellipsoids drawn at 50% probability.

Table 5. Crystallographic details for compound **3.12**.

Formula	$C_{14}\,H_{14}\,N_2\,O_1$
M_r	226.28
Crystal system	monoclinic
Space group	*P* $2_1/c$
Z	4
a /Å	5.91524(1)
b/Å	4.62600(1)
c /Å	41.73024(2)
β / °	90.764(2)
V / Å^3	1141.801(3)
ρ_{calc} / g cm^{-3}	1.316
Crystal habit	Colourless rod
Crystal dimensions /mm	0.016 × 0.036 × 0.327
Radiation	Cu K_α (1.54184 Å)
T /K	100
μ /mm^{-1}	0.672
R(*F*), *Rw*(*F*) /%	3.98, 3.73
CCDC cif deposition number	CCDC 2157688

Table 6. Selected bond lengths (Å) and angles (°) for compound **3.12**.

O(1) – C(2)	1.2373(13)	O(1) – C(2) – N(3)	123.30(10)
C(2) – N(3)	1.3634(15)	O(1) – C(2) – N(10)	123.07(10)
C(2) – N(10)	1.3613(14)	N(3) – C(2) – N(10)	113.62(10)
C(4) – N(3)	1.4140(14)	C(2) – N(3) – C(4)	125.23 (10)
C(4) – C(5)	1.3930(16)	N(3) – C(4) – C(5)	118.14(11)
C(4) – C(9)	1.3964(17)	N(3) – C(4) – C(9)	122.09(10)
C(5) – C(6)	1.3847(17)	C(5) – C(4) – C(9)	119.69(10)
C(6) – C(7)	1.3868(19)	C(4) – C(5) C(6)	120.14(11)
C(7) – C(8)	1.3894(19)	C(5) – C(6) – C(7)	120.41(11)
C(8) – C(9)	1.3881(17)	C(6) – C(7) – C(8)	119.50(11)
C(11) – N(10)	1.4216(14)	C(7) – C(8) – C(9)	120.65(12)
C(11) – C(12)	1.4027(16)	C(4) – C(9) – C(8)	119.60 (11)
C(11) – C(16)	1.3911 (16)	N(10) – C(11) – C(12)	118.66(10)
C(12) – C(13)	1.3967(15)	N(10) – C(11) – C(16)	120.54(10)
C(12) – C(17)	1.4987(16)	C(12) – C(11) – C(16)	120.76(10)
C(13) – C(14)	1.3899(17)	C(11) – C(12) – C(13)	117.85(10)
C(14) – C(15)	1.3846(17)	C(11) – C(12) – C(17)	120.94(10)
C(15) – C(16)	1.3885(16)	C(13) – C(12) – C(17)	121.20(10)
		C(12) – C(13) – C(14)	121.51(11)
		C(13) – C(14) – C(15)	119.72(11)
		C(14) – C(15) – C(16)	119.96(11)
		C(11) – C(16) – C(15)	120.17(11)

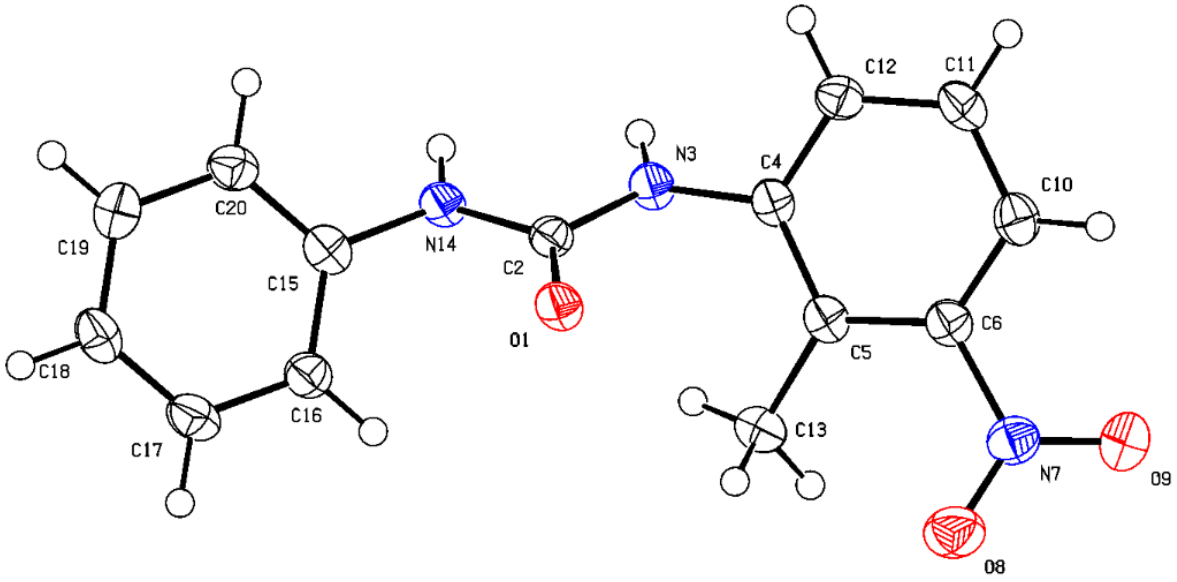

Figure 72. Molecular Structure of 1-(2-methyl-3-nitrophenyl)-3-phenylurea, **3.13**, ellipsoids drawn at 50% probability.

Table 7. Crystallographic details for compound **3.13**.

Formula	$C_{14}\,H_{13}\,N_3\,O_3$
M_r	271.28
Crystal system	triclinic
Space group	*P* -1
Z	2
a /Å	4.56762(2)
b/Å	11.26186(3)
c /Å	12.56552(2)
α /°	77.333(4)
β / °	87.787(4)
γ / °	89.120(5)
V / Å^3	630.150(11)
ρ_{calc} / g cm^{-3}	1.430
Crystal habit	Colourless plate
Crystal dimensions /mm	0.012 × 0.037 × 0.155
Radiation	Cu K_α (1.54184 Å)
T /K	100
μ /mm^{-1}	0.856
R(*F*), *Rw*(*F*) /%	5.86, 7.08
CCDC cif deposition number	CCDC 2173628

Table 8. Selected bond lengths (Å) and angles (°) for compound **3.13**.

O(1) – C(2)	1.238(4)	O(1) – C(2) – N(3)	122.2(3)
C(2) – N(3)	1.365(4)	O(1) – C(2) – N(14)	123.2(3)
C(2) – N(14)	1.358(4)	N(3) – C(2) – N(17)	113.5(3)
C(4) – N(3)	1.414(4)	N(3) – C(2) – N(14)	114.6(3)
C(4) – C(5)	1.399(5)	C(2) – N(3) – C(4)	123.9(3)
C(4) – C(12)	1.395(4)	N(3) – C(4) – C(5)	120.8(3)
C(5) – C(6)	1.409(5)	N(3) – C(4) – C(12)	117.8(3)
C(5) – C(13)	1.498(4)	C(5) – C(4) – C(12)	121.3 (3)
C(6) – N(7)	1.463(4)	C(4) – C(5) – C(6)	115.5(3)
C(6) – C(10)	1.390(5)	C(4) – C(5) – C(13)	121.4(3)
N(7) – O(8)	1.222(4)	C(6) – C(5) – C(13)	122.8(3)
N(7) – O(9)	1.231(4)	C(5) – C(6) – N(7)	120.1(3)
C(10) – C(11)	1.372(5)	C(5) – C(6) – C(10)	123.6(3)
C(11) – C(12)	1.394(5)	N(7) – C(6) – C(10)	116.2(3)
N(14) – N(15)	1.422(4)	C(6) – N(7) – O(8)	118.7(3)
C(15) – C(16)	1.392(5)	C(6) – N(7) – O(9)	118.2(3)
C(15) – C(20)	1.383 (5)	O(8) – N(7) – O(9)	123.1(3)
C(16) – C(17)	1.387(5)	C(6) – C(10) – C(11)	119.2(3)
C(17) – C(18)	1.385(5)	C(10) – C(11) – C(12)	119.3(3)
C(18) – C(19)	1.384(5)	C(4) – C(12) – C(11)	121.0(3)
C(19) – C(20)	1.395(5)	C(2) – N(14) – C(15)	123.5(3)
		N(14) – C(15) – C(16)	120.5(3)
		N(14) – C(15) – C(20)	119.2(3)
		C(16) – C(15) – C(20)	120.1(3)
		C(15) – C(16) – C(17)	119.5(3)
		C(16) – C(17) – C(18)	120.6(3)
		C(17) – C(18) – C(19)	119.9(3)
		C(18) – C(19) – C(20)	119.3(3)
		C(15) – C(20) – C(19)	120.0(3)

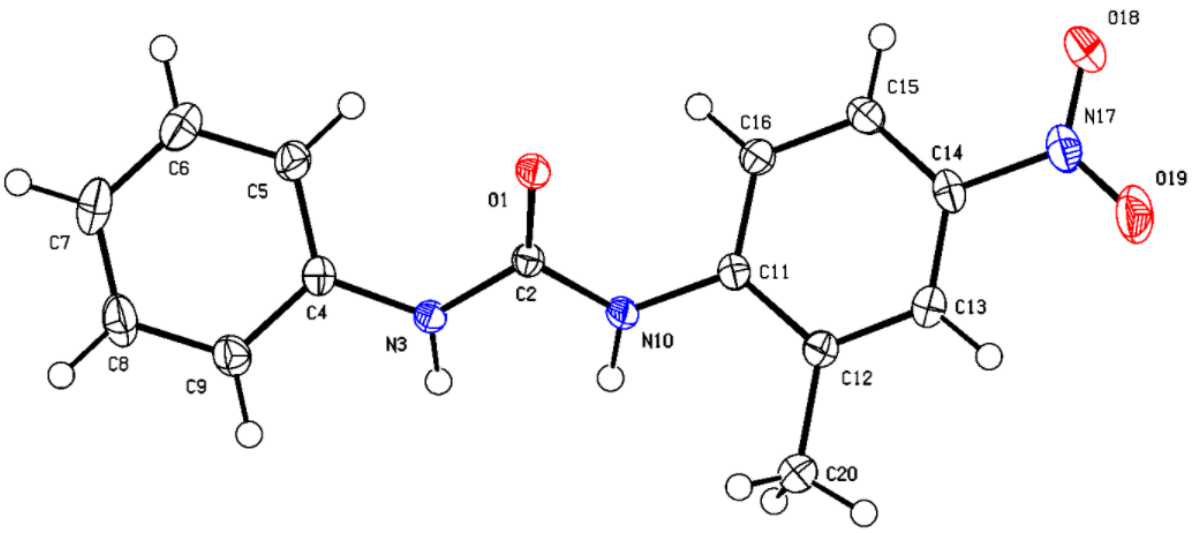

Figure 73. Molecular Structure of 1-(2-methyl-4-nitrophenyl)-3-phenylurea, **3.14**, ellipsoids drawn at 50% probability.

Table 9. Crystallographic details for compound **3.14**.

Formula	$C_{14}\,H_{13}\,N_3\,O_3$
M_r	271.27
Crystal system	orthorhombic
Space group	P bca
Z	8
a /Å	11.89416(1)
b/Å	8.92325(1)
c /Å	24.54875(2)
V / Å^3	2605.472(4)
ρ_{calc} / g cm^{-3}	1.383
Crystal habit	Colourless plate
Crystal dimensions /mm	0.051 × 0.074 × 0.129
Radiation	Cu K_α (1.54184 Å)
T /K	100
μ /mm^{-1}	0.828
R(*F*), *Rw*(*F*) /%	3.42, 4.38
CCDC cif deposition number	CCDC 2131885

Table 10. Selected bond lengths (Å) and angles (°) for compound **3.14**.

O(1) – C(2)	1.2366(15)	O(1) – C(2) – N(3)	123.65(11)
C(2) – N(3)	1.3581(15)	O(1) – C(2) – N(10)	122.91(11)
C(2) – N(10)	1.3708(16)	N(3) – C(2) – N(10)	113.41(11)
C(4) – N(3)	1.4114(16)	C(2) – N(3) – C(4)	126.80(11)
C(4) – C(5)	1.3942(18)	N(3) – C(4) – C(5)	122.84(11)
C(4) – C(9)	1.3919(18)	N(3) – C(4) – C(9)	117.49(11)
C(5) – C(6)	1.3878(19)	C(5) – C(4) – C(9)	119.59(12)
C(6) – C(7)	1.385(2)	C(4) – C(5) – C(6)	119.67(13)
C(7) – C(8)	1.382(2)	C(5) – C(6) – C(7)	120.74(13)
C(8) – C(9)	1.3896(19)	C(6) – C(7) – C(8)	119.54(13)
C(11) – N(10)	1.4137(15)	C(7) – C(8) – C(9)	120.41(13)
C(11) – C(12)	1.4044(17)	C(4) – C(9) – C(8)	120.03(13)
C(11) – C(16)	1.3962(17)	C(2) – N(10) – C(11)	123.74(10)
C(12) – C(13)	1.3865(17)	N(10) – C(11) – C(12)	119.02(11)
C(12) – C(20)	1.4969(18)	N(10) – C(11) – C(16)	120.03(11)
C(13) – C(14)	1.3854(18)	C(12) – C(11) – C(16)	120.94(11)
C(14) – C(15)	1.3799(19)	C(11) – C(12) – C(13)	118.16(11)
C(15) – C(16)	1.3836(17)	C(11) – C(12) – C(20)	121.10(11)
C(14) – N(17)	1.4633(16)	C(13) – C(12) – C(20)	120.73(11)
O(18) – N(17)	1.2312(16)	C(12) – C(13) – C(14)	119.85(12)
O(19) – N(17)	1.2262(16)	C(13) – C(14) – C(15)	122.47(12)
		N(17) – C(14) – C(13)	118.74(12)
		N(17) – C(14) – C(15)	118.78(11)
		C(14) – C(15) – C(16)	118.18(12)
		C(11) – C(16) – C(15)	120.27(12)
		O(18) – N(17) – O(19)	123.30(12)
		O(18) – N(17) – C(15)	118.43(11)
		O(19) – N(17) – C(15)	118.26(11)

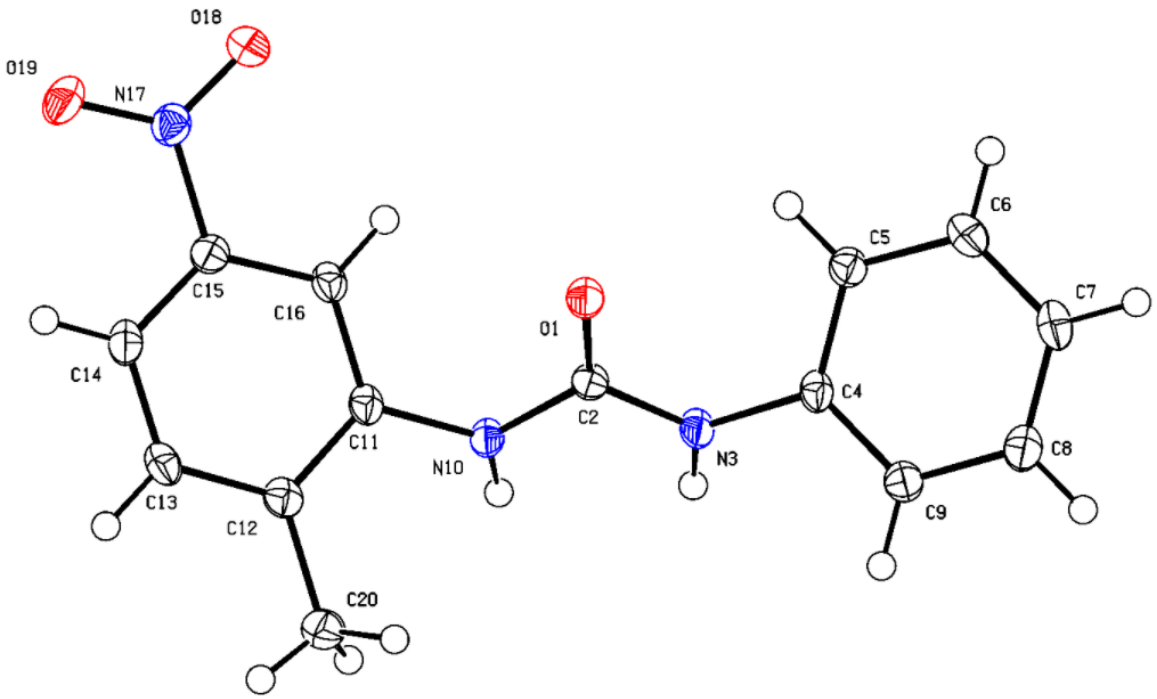

Figure 74. Molecular Structure of 1-(2-methyl-5-nitrophenyl)-3-phenylurea, **3.15**, ellipsoids drawn at 50% probability.

Table 11. Crystallographic details for compound **3.15**.

Formula	$C_{14}\,H_{13}\,N_3\,O_3$
M_r	271.27
Crystal system	triclinic
Space group	*P* -1
Z	2
a /Å	4.61564(1)
b/Å	11.61380(2)
c /Å	11.74758(2)
α /°	94.595(3)
β / °	92.736(3)
γ / °	95.401(3)
V / Å^3	623.950(5)
ρ_{calc} / g cm^{-3}	1.444
Crystal habit	Colourless rod
Crystal dimensions /mm	0.012 × 0.023 × 0.121
Radiation	Cu K_α (1.54184 Å)
T /K	100
μ /mm^{-1}	0.865
R(*F*), *Rw*(*F*) /%	3.82, 4.42
CCDC cif deposition number	CCDC 2131760

Table 12. Selected bond lengths (Å) and angles (°) for compound **3.15**.

O(1) – C(2)	1.2375(15)	O(1) – C(2) – N(3)	123.56(11)
C(2) – N(3)	1.3547(17)	O(1) – C(2) – N(10)	122.51(12)
C(2) – N(10)	1.3687(17)	N(3) – C(2) – N(10)	113.92(11)
C(4) – N(3)	1.4248(17)	C(2) – N(3) – C(4)	124.87(11)
C(4) – C(5)	1.3967(19)	N(3) – C(4) – C(5)	121.05(12)
C(4) – C(9)	1.3897(19)	N(3) – C(4) – C(9)	118.53(12)
C(5) – C(6)	1.3942(19)	C(5) – C(4) – C(9)	120.33(12)
C(6) – C(7)	1.386(2)	C(4) – C(5) – C(6)	119.09(13)
C(7) – C(8)	1.386(2)	C(5) – C(6) – C(7)	120.70(13)
C(8) – C(9)	1.3931(19)	C(6) – C(7) – C(8)	119.88(13)
C(11) – N(10)	1.4153(17)	C(7) – C(8) – C(9)	120.15(13)
C(11) – C(12)	1.4086(19)	C(4) – C(9) – C(8)	119.84(13)
C(11) – C(16)	1.3896(19)	C(2) – N(10) – C(11)	123.43(11)
C(12) – C(13)	1.3978(19)	N(10) – C(11) – C(12)	118.91(12)
C(12) – C(20)	1.4984(19)	N(10) – C(11) – C(16)	120.44(12)
C(13) – C(14)	1.383(2)	C(12) – C(11) – C(16)	120.64(12)
C(14) – C(15)	1.3856(19)	C(11) – C(12) – C(13)	118.32(12)
C(15) – C(16)	1.3826(18)	C(11) – C(12) – C(20)	120.94(12)
C(15) – N(17)	1.4698(18)	C(13) – C(12) – C(20)	120.72(12)
O(18) – N(17)	1.2272(16)	C(12) – C(13) – C(14)	121.81(12)
O(19) – N(17)	1.2304(15)	C(13) – C(14) – C(15)	117.96(12)
		C(14) – C(15) – C(16)	122.64(13)
		N(17) – C(15) – C(14)	118.70(12)
		N(17) – C(15) – C(16)	118.66(12)
		C(11) – C(16) – C(15)	118.60(12)
		O(18) – N(17) – O(19)	123.50(12)
		O(18) – N(17) – C(15)	118.08(11)
		O(19) – N(17) – C(15)	118.42(11)

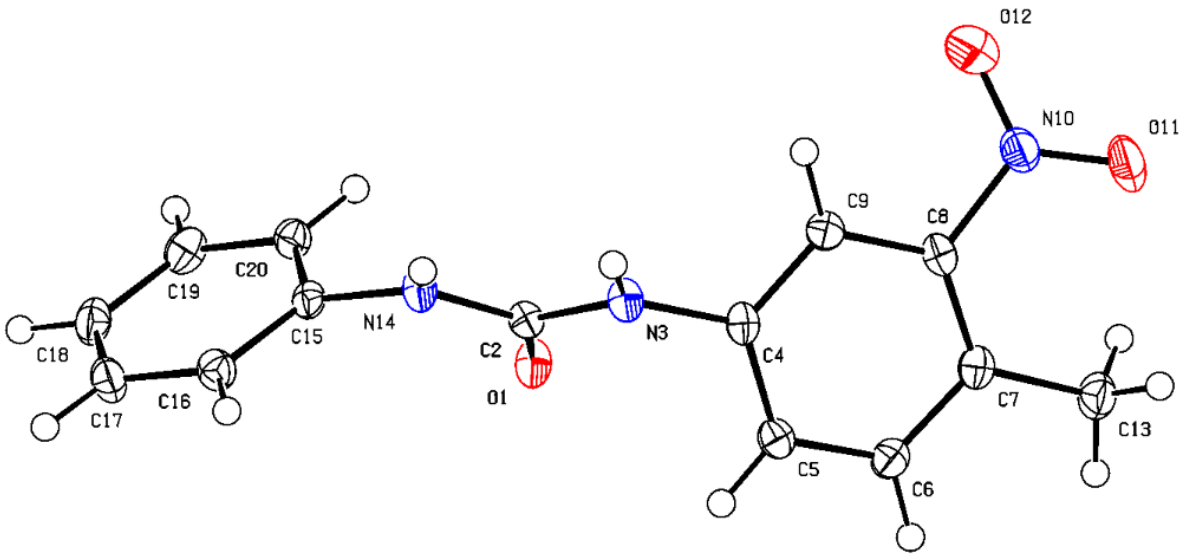

Figure 75. Molecular Structure of 1-(4-methyl-3-nitrophenyl)-3-phenylurea, **3.16**, ellipsoids drawn at 50% probability.

Table 13. Crystallographic details for compound **3.16**.

Formula	$C_{14}\,H_{13}\,N_3\,O_3$
M_r	271.28
Crystal system	monoclinic
Space group	*P* $2_1/c$
Z	4
a /Å	14.20923(1)
b/Å	9.10438(1)
c /Å	10.19123(1)
β / °	107.602(2)
V / Å^3	1256.677(14)
ρ_{calc} / g cm^{-3}	1.434
Crystal habit	Colourless plate
Crystal dimensions /mm	0.023 × 0.041 × 0.105
Radiation	Cu K_α (1.54184 Å)
T /K	100
μ /mm^{-1}	0.859
R(*F*), *Rw*(*F*) /%	5.36, 6.64
CCDC cif deposition number	CCDC 2173818

Table 14. Selected bond lengths (Å) and angles (°) for compound **3.16**.

O(1) – C(2)	1.241(3)	O(1) – C(2) – N(3)	122.2(3)
C(2) – N(3)	1.364(2)	O(1) – C(2) – N(3)	121.84(15)
C(2) – N(14)	1.356(2)	O(1) – C(2) – N(14)	122.63(15)
C(4) – N(3)	1.421(2)	N(3) – C(2) – N(14)	115.53(15)
C(4) – C(5)	1.393(2)	C(2) – N(3) – C(4)	121.07(14)
C(4) – C(9)	1.384(2)	N(3) – C(4) – C(5)	121.18(15)
C(5) – C(6)	1.386(2)	N(3) – C(4) – C(9)	119.74(16)
C(6) – C(7)	1.399(2)	C(5) – C(4) – C(9)	119.08(16)
C(7) – C(8)	1.394(3)	C(4) – C(5) – C(6)	120.12(16)
C(7) – C(13)	1.504(2)	C(5) – C(6) – C(7)	122.85(17)
C(8) – C(9)	1.394(2)	C(6) – C(7) – C(8)	114.98(16)
C(8) – N(10)	1.469(2)	C(7) – C(8) – C(13)	119.47(16)
N(10) – O(11)	1.201(2)	C(8) – C(7) – C(13)	125.54(16)
N(10) – O(12)	1.241(2)	C(7) – C(8) – C(9)	123.76(16))
N(14) – C(15)	1.430 (2)	C(7) – C(8) – N(10)	120.76(16)
C(15) – C(16)	1.388(2)	C(9) – C(8) – N(10)	115.41(16)
C(15) – C(20)	1.387(3)	C(4) – C(9) – C(8)	119.19(16)
C(16) – C(17)	1.395(3)	C(8) – N(10) – C(11)	120.32(16)
C(17) – C(18)	1.384(3)	C(8) – N(10) – O(12)	117.24(15)
C(18) – C(19)	1.388(3)	O(11) – N(10) – O(12)	122.26(17)
C(19) – C(20)	1.390(3)	C(2) – N(14) – C(15)	121.78(14)
		N(14) – C(15) – C(16)	120.03(16)
		N(14) – C(15) – C(20)	119.80(15)
		C(15) – C(16) – C(17)	119.46(17)
		C(16) – C(17) – C(18)	120.64(17)
		C(17) – C(18) – C(19)	119.45(17)
		C(18) – C(19) – C(20)	120.37(17)

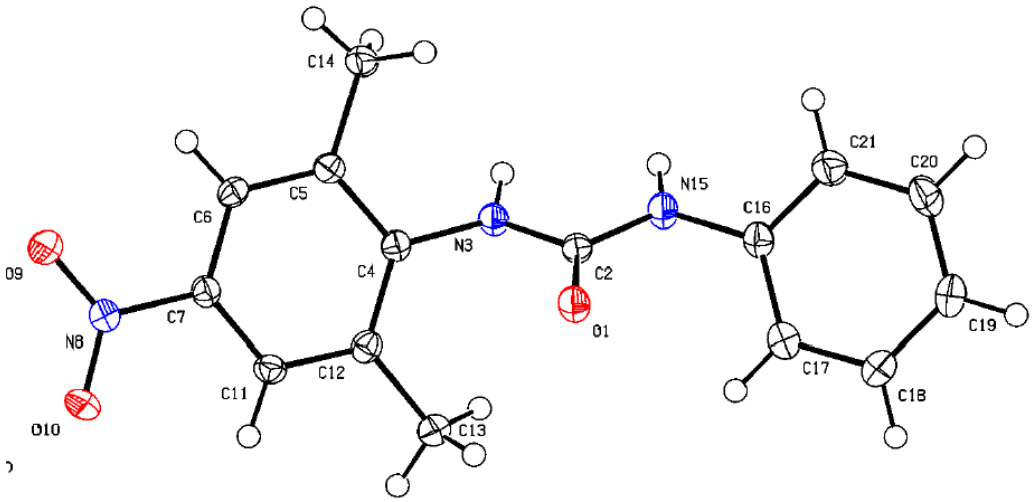

Figure 76. Molecular Structure of 1-(2,6-dimethyl-4-nitrophenyl)-3-phenylurea, **3.19**, ellipsoids drawn at 50% probability.

Table 15. Crystallographic details for compound **3.19**.

Formula	$C_{15}\,H_{15}\,N_3\,O_3$
M_r	285.30
Crystal system	triclinic
Space group	*P* -1
Z	2
a /Å	4.58331(1)
b/Å	9.41844(1)
c /Å	15.68112(2)
α /°	85.985(2)
β / °	86.174(2)
γ / °	85.883(2)
V / Å^3	672.216(3)
ρ_{calc} / g cm^{-3}	1.409
Crystal habit	Colourless rod
Crystal dimensions /mm	0.022 × 0.031 × 0.096
Radiation	Cu K_α (1.54184 Å)
T /K	100
μ /mm^{-1}	0.830
R(*F*), *Rw*(*F*) /%	4.07, 4.81
CCDC cif deposition number	CCDC 2172066

Table 16. Selected bond lengths (Å) and angles (°) for compound **3.19**.

O(1) – C(2)	1.2390(16)	O(1) – C(2) – N(3)	122.48(12)
C(2) – N(3)	1.3657(17)	O(1) – C(2) – N(15)	123.12(12)
C(2) – N(15)	1.3566(18)	N(3) – C(2) – N(15)	114.40(11)
C(4) – N(3)	1.4166(17)	C(2) – N(3) – C(4)	123.71(11)
C(4) – C(5)	1.4086(19)	N(3) – C(4) – C(5)	117.80(12)
C(4) – C(12)	1.4081(19)	N(3) – C(4) – C(12)	120.48(12)
C(5) – C(6)	1.3861(19)	C(5) – C(4) – C(12)	121.66(12)
C(5) – C(14)	1.5061(18)	C(4) – C(5) – C(6)	118.73(12)
C(6) – C(7)	1.3853(19)	C(4) – C(5) – C(14)	120.65(12)
C(7) – N(8)	1.4697(17)	C(6) – C(5) – C(14)	120.62(12)
C(7) – C(11)	1.383(2)	C(5) – C(6) – C(7)	119.21(12)
N(8) – O(9)	1.2280(16)	C(6) – C(7) – N(8)	118.51(12)
N(8) – O(10)	1.2274(15)	C(6) – C(7) – C(11)	122.54(13)
C(11) – C(12)	1.391(2)	N(8) – C(7) – C(11)	118.94(12)
C(12) – C(13)	1.5049(19)	C(7) – N(8) – O(9)	118.35(11)
N(15) – C(16)	1.4212(18)	C(7) – N(8) – O(10)	118.59(11)
C(16) – C(17)	1.391(2)	O(9) – N(8) – O(10)	123.06(12)
C(16) – C(21)	1.390(2)	C(7) – C(11) – C(12)	119.55(13)
C(17) – C(18)	1.383(2)	C(4) – C(12) – C(11)	118.21(12)
C(18) – C(19)	1.386(2)	C(4) – C(12) – C(13)	122.28(12)
C(19) – C(20)	1.382(2)	C(11) – C(12) – C(13)	119.48(12)
C(20) – C(21)	1.387(2)	C(2) – N(15) – C(16)	123.40(11)
		N(15) – C(16) – C(17)	120.60(13)
		N(15) – C(16) – C(21)	119.86(13)
		C(17) – C(16) – C(21)	119.42(13)
		C(16) – C(17) – C(18)	119.94(14)
		C(17) – C(18) – C(19)	120.65(14)
		C(18) – C(19) – C(20)	119.43(14)
		C(19) – C(20) – C(21)	120.37(14)
		C(16) – C(21) – C(20)	120.17(14)

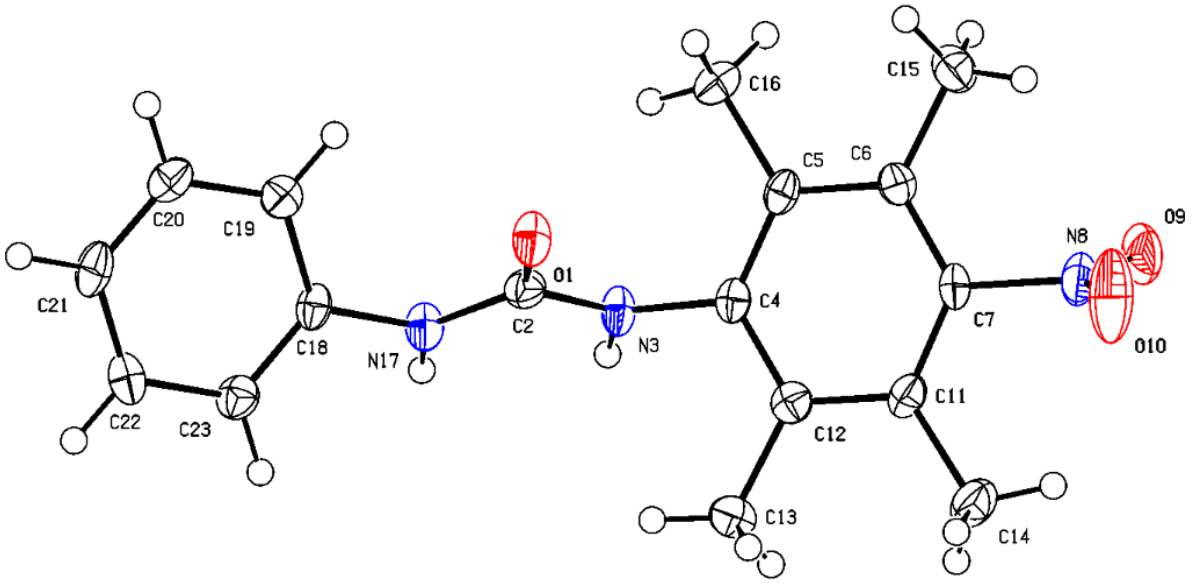

Figure 77. Molecular Structure of 1-phenyl-3-(2,3,5,6-tetramethyl-4-nitrophenyl)urea, **3.21**, ellipsoids drawn at 50% probability.

Table 17. Crystallographic details for compound **3.21**.

Formula	$C_{17}H_{19}N_3O_3$
M_r	313.36
Crystal system	orthorhombic
Space group	$P\,2_12_12_1$
Z	4
a /Å	4.54001 (1)
b/Å	12.86167 (2)
c /Å	26.93044 (3)
V / Å^3	1572.525 (5)
ρ_{calc} / g cm^{-3}	1.323
Crystal habit	Colourless rod
Crystal dimensions /mm	0.015 × 0.023 × 0.140
Radiation	Cu K_α (1.54184 Å)
T /K	100
μ /mm^{-1}	0.756
R(*F*), *Rw*(*F*) /%	4.27, 4.51
CCDC cif deposition number	CCDC 2172071

Table 18. Selected bond lengths (Å) and angles (°) for compound **3.21**.

O(1) – C(2)	1.228(4)	O(1) – C(2) – N(3)	123.0(3)
C(2) – N(3)	1.368(4)	O(1) – C(2) – N(17)	123.5(3)
C(2) – N(17)	1.364(4)	N(3) – C(2) – N(17)	113.5(3)
C(4) – N(3)	1.442(4)	C(2) – N(3) – C(4)	121.2(3)
C(4) – C(5)	1.392(5)	N(3) – C(4) – C(5)	119.4(3)
C(4) – C(12)	1.398(5)	N(3) – C(4) – C(12)	117.1(3)
C(5) – C(6)	1.410(4)	C(5) – C(4) – C(12)	123.4(3)
C(5) – C(16)	1.510(4)	C(4) – C(5) – C(6)	118.5(3)
C(6) – C(7)	1.386(4)	C(4) – C(5) – C(16)	122.4(3)
C(6) – C(15)	1.508(4)	C(6) – C(5) – C(16)	119.1(3)
C(7) – N(8)	1.480(4)	C(5) – C(6) – C(7)	116.8(3)
C(7) – C(11)	1.389(5)	C(5) – C(6) – C(15)	121.1(3)
N(8) – O(9)	1.211(4)	C(7) – C(6) – C(15)	122.0(3)
N(8) – O(10)	1.218(4)	C(6) – C(7) – N(8)	117.1(3)
C(11) – C(12)	1.406(5)	C(6) – C(7) – C(11)	125.8(3)
C(11) – C(14)	1.509(5)	N(8) – C(7) – C(11)	117.1(3)
C(12) – C(13)	1.500(4)	C(7) – N(8) – O(9)	117.7(3)
N(17) – C(18)	1.431(4)	C(7) – N(8) – O(10)	118.1(3)
C(18) – C(19)	1.397(4)	O(9) – N(8) – O(10)	124.1(3)
C(18) – C(23)	1.380(4)	C(7) – C(11) – C(12)	116.7(3)
C(19) – C(20)	1.390(5)	C(7) – C(11) – C(14)	122.6(3)
C(20) – C(21)	1.368(5)	C(12) – C(11) – C(14)	120.6(3)
C(21) – C(22)	1.391(5)	C(4) – C(12) – C(11)	118.6(3)
C(22) – C(23)	1.391(5)	C(4) – C(12) – C(13)	121.1(3)
		C(11) – C(12) – C(13)	120.3(3)
		C(2) – N(17) – C(18)	124.7(3)
		N(17) – C(18) – C(19)	120.9(3)
		N(17) – C(18) – C(23)	118.4(3)
		C(19) – C(18) – C(23)	120.6(3)
		C(18) – C(19) – C(20)	118.8(3)
		C(19) – C(20) – C(21)	120.8(3)
		C(20) – C(21) – C(22)	120.2(3)
		C(21) – C(22) – C(23)	119.8(3)
		C(18) – C(23) – C(22)	119.7(3)

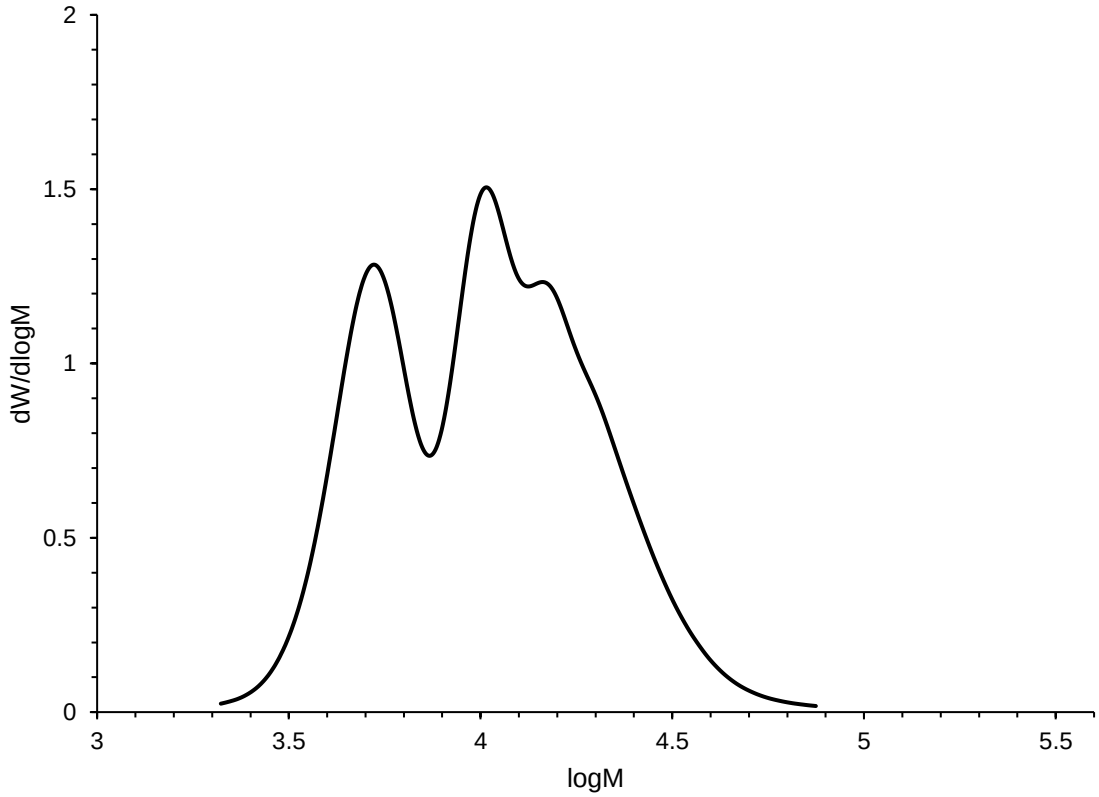

Figure 78. GPC eluogram of **SPU1** in THF.

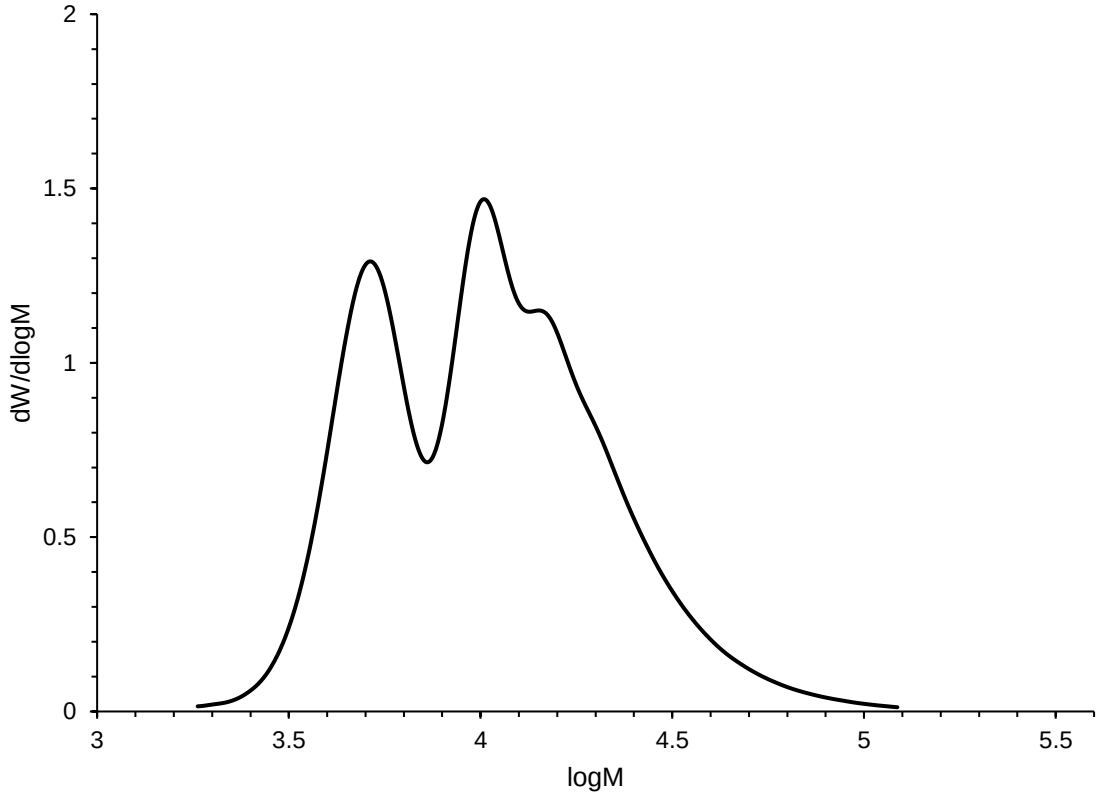

Figure 79. GPC eluogram of **SPU2** in THF.

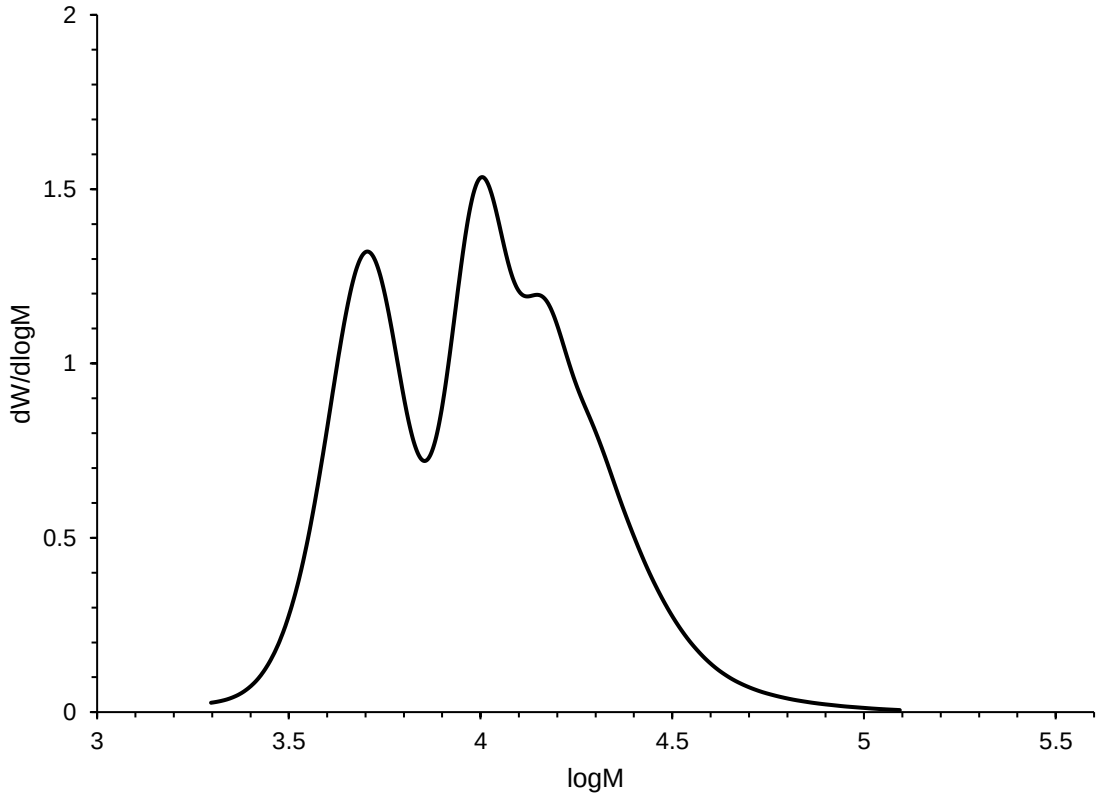

Figure 80. GPC eluogram of **SPU3** in THF.

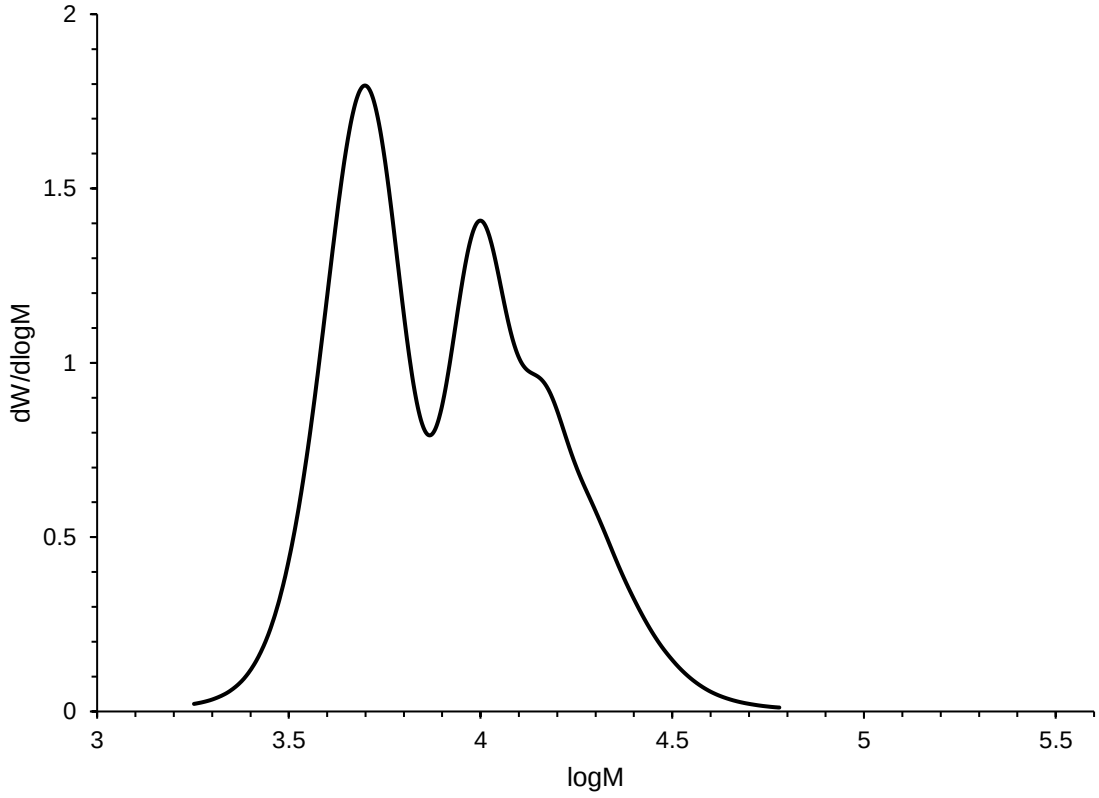

Figure 81. GPC eluogram of **SPU4** in THF.

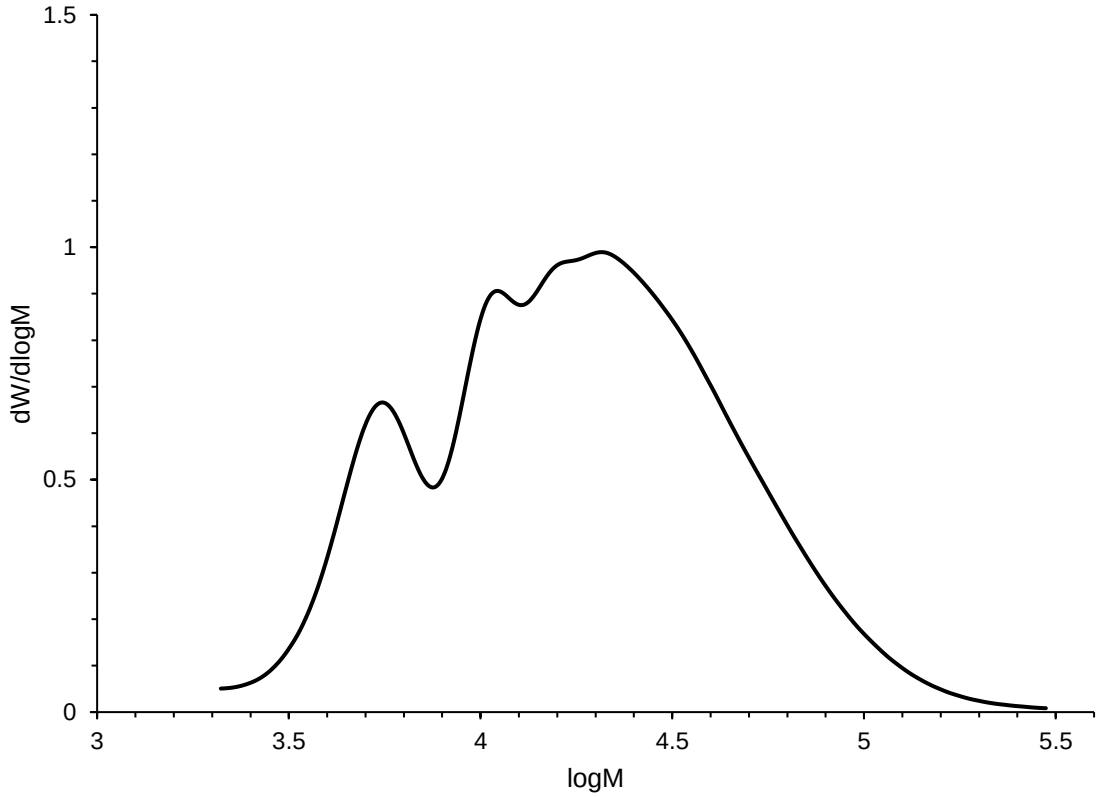

Figure 82. GPC eluogram of **SPU5** in THF.

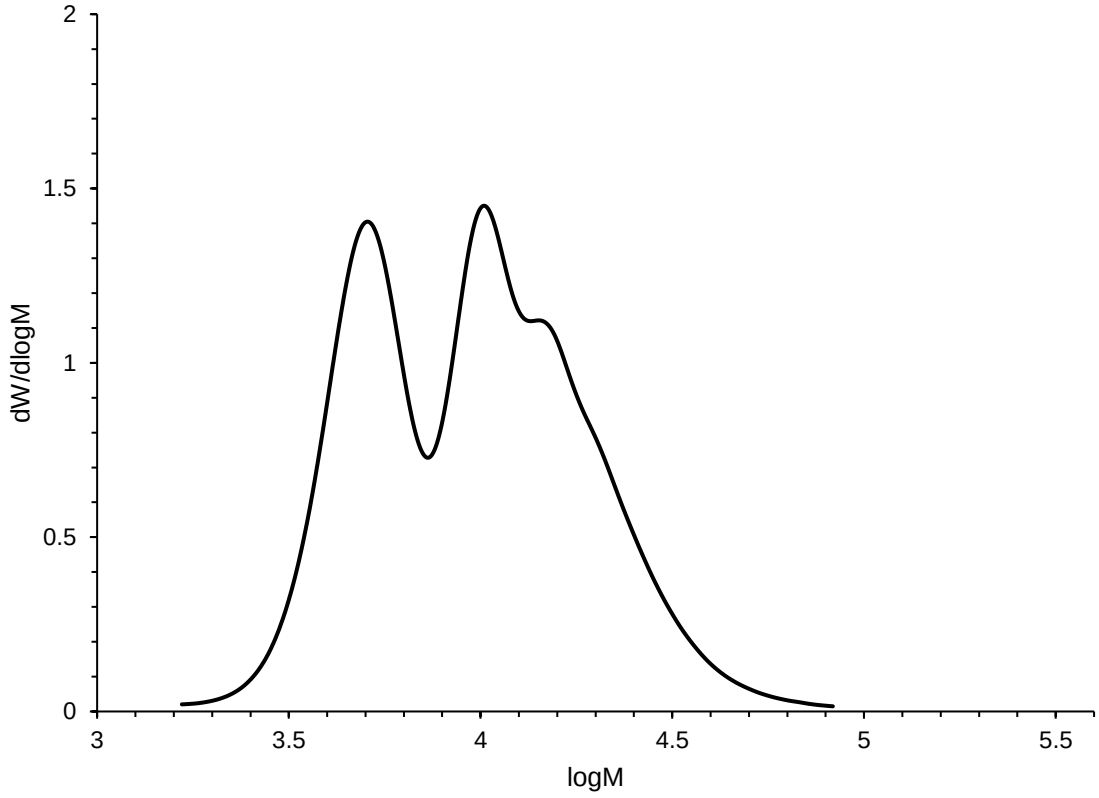

Figure 83. GPC eluogram of **SPU6** in THF.

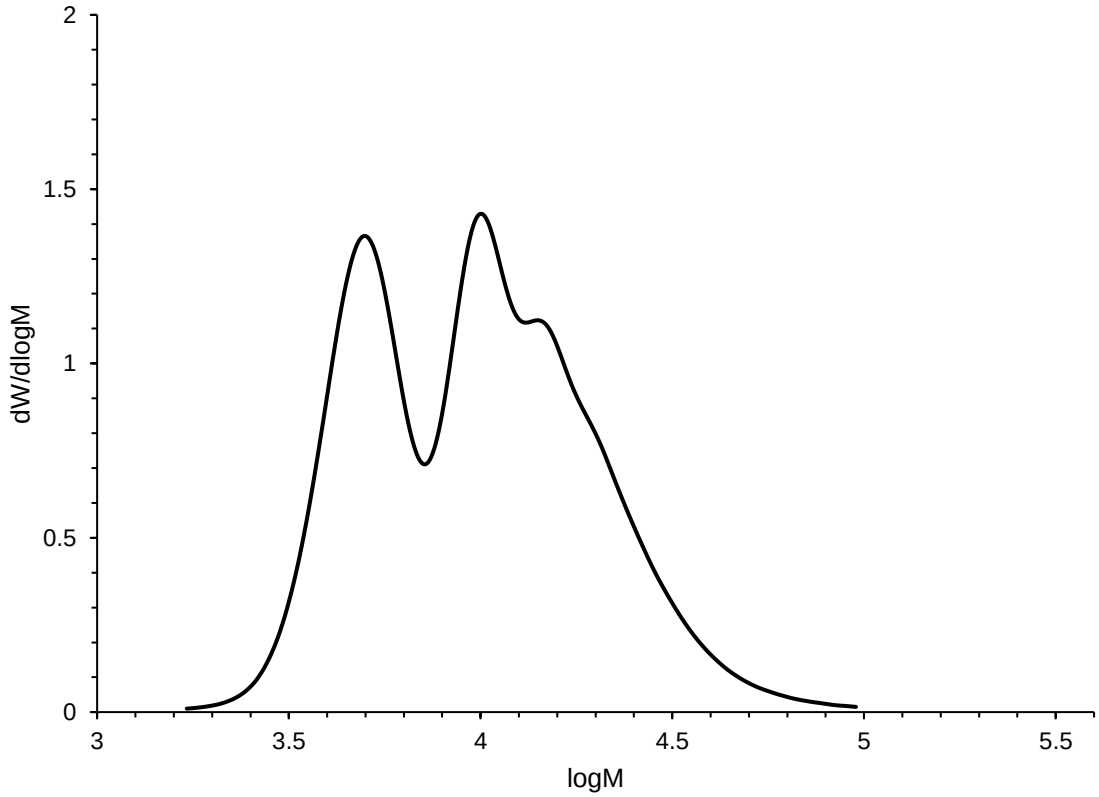

Figure 84. GPC eluogram of **SPU7** in THF.

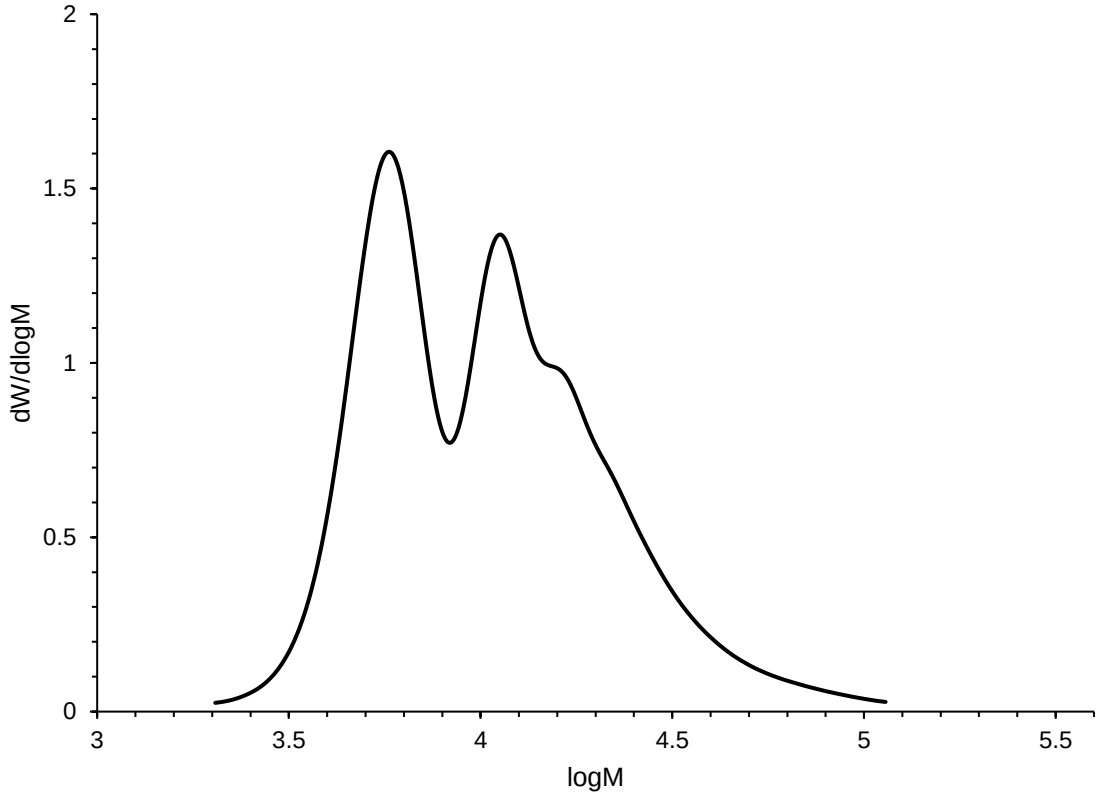

Figure 85. GPC eluogram of **SPU8** in THF.

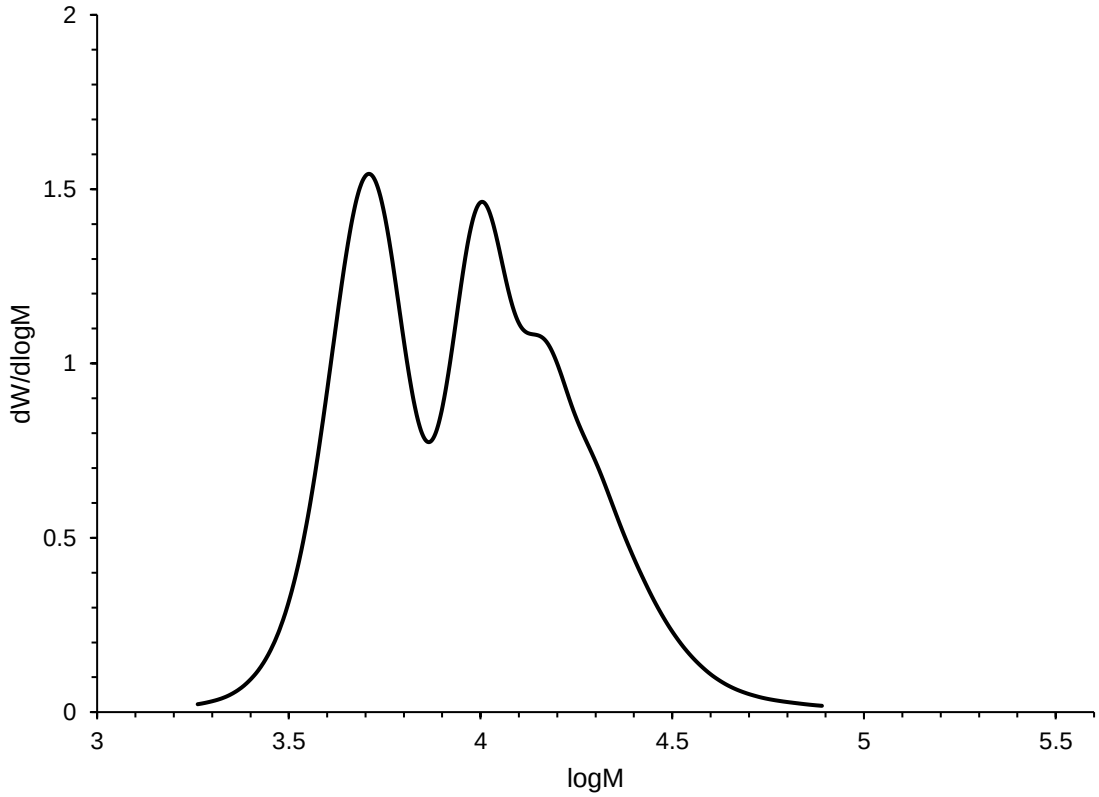

Figure 86. GPC eluogram of **SPU9** in THF.

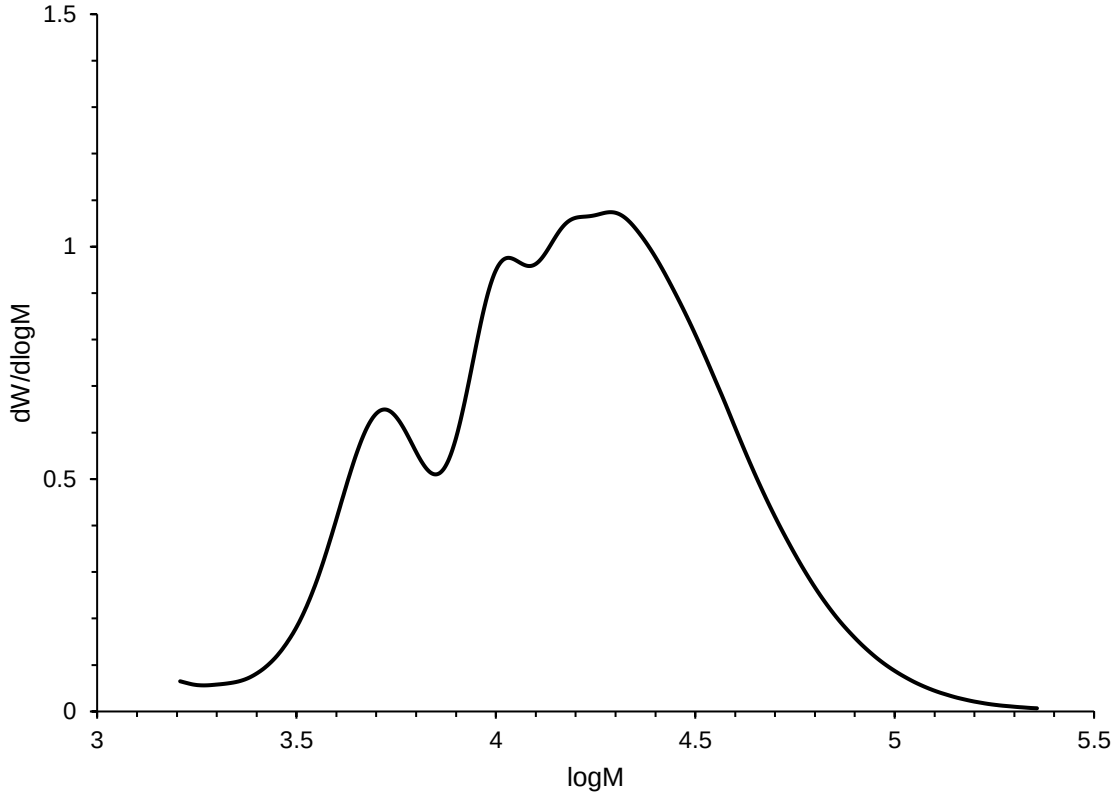

Figure 87. GPC eluogram of **SPU10** in THF.

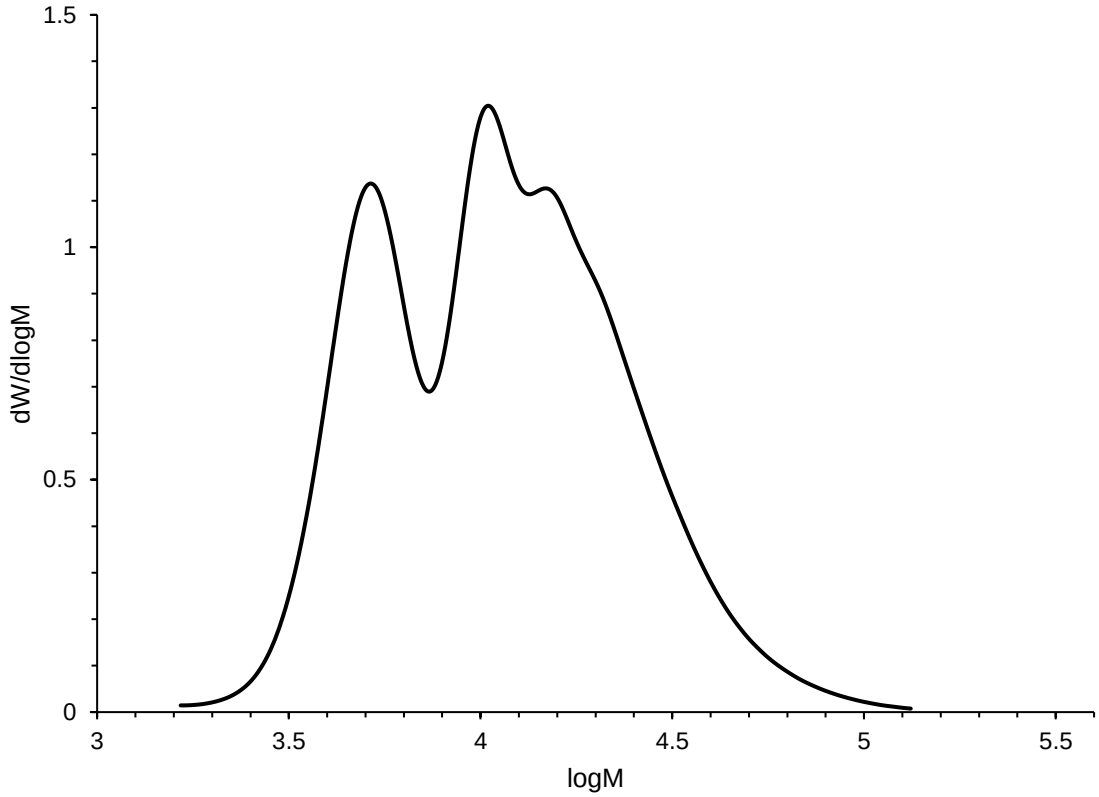

Figure 88. GPC eluogram of **SPU11** in THF.

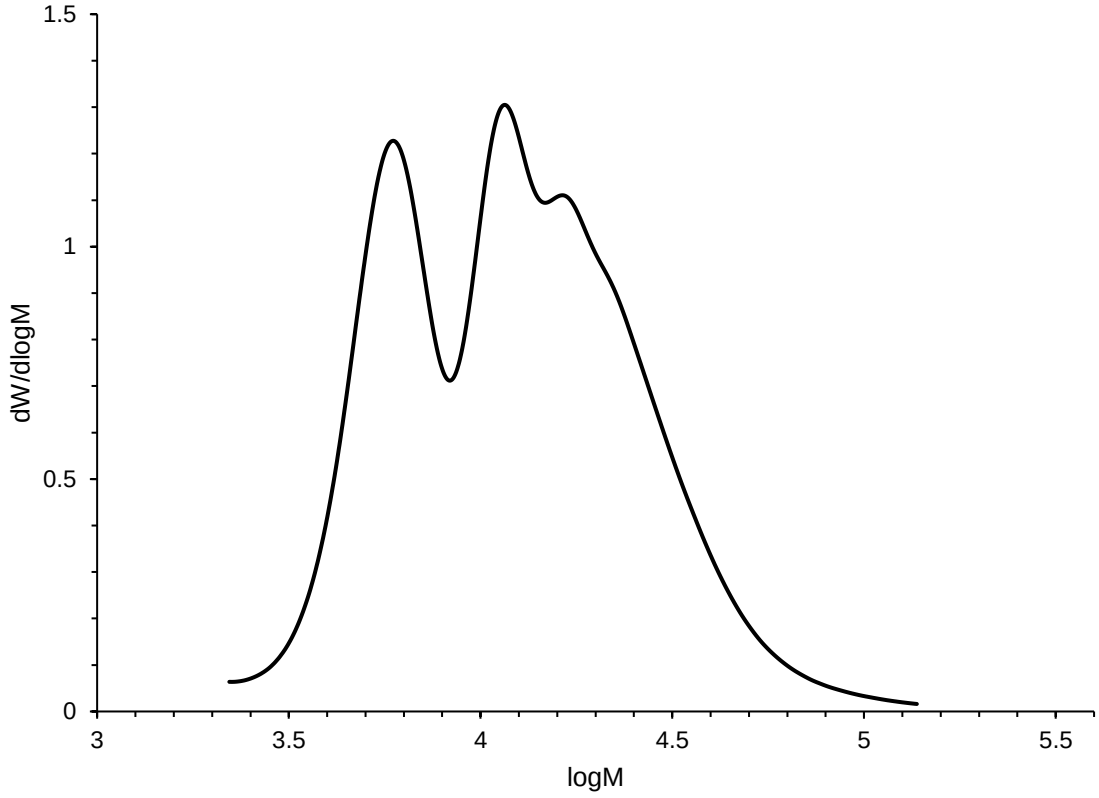

Figure 89. GPC eluogram of **SPU12** in THF.

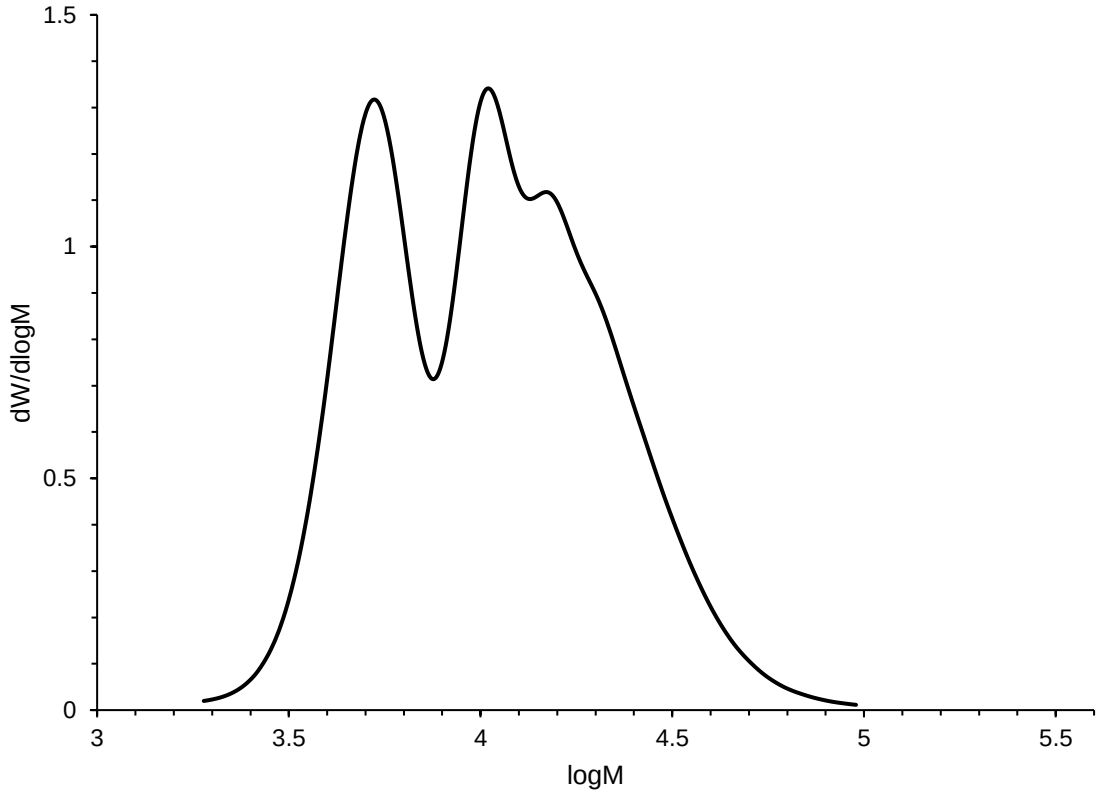

Figure 90. GPC eluogram of SPU13 in THF.

Table 19. Molecular weight and polydispersity data of the supramolecular polymers **SPU1**-**SPU13**.

	M_n (g/mol)	$Đ_M$
SPU1	8463	1.49
SPU2	8374	1.61
SPU3	8060	1.54
SPU4	6785	1.44
SPU5	12344	2.15
SPU6	7735	1.54
SPU7	7898	1.57
SPU8	8434	1.63
SPU9	7507	1.50
SPU10	10906	2.00
SPU11	8762	1.68
SPU12	9562	1.67
SPU13	8429	1.59

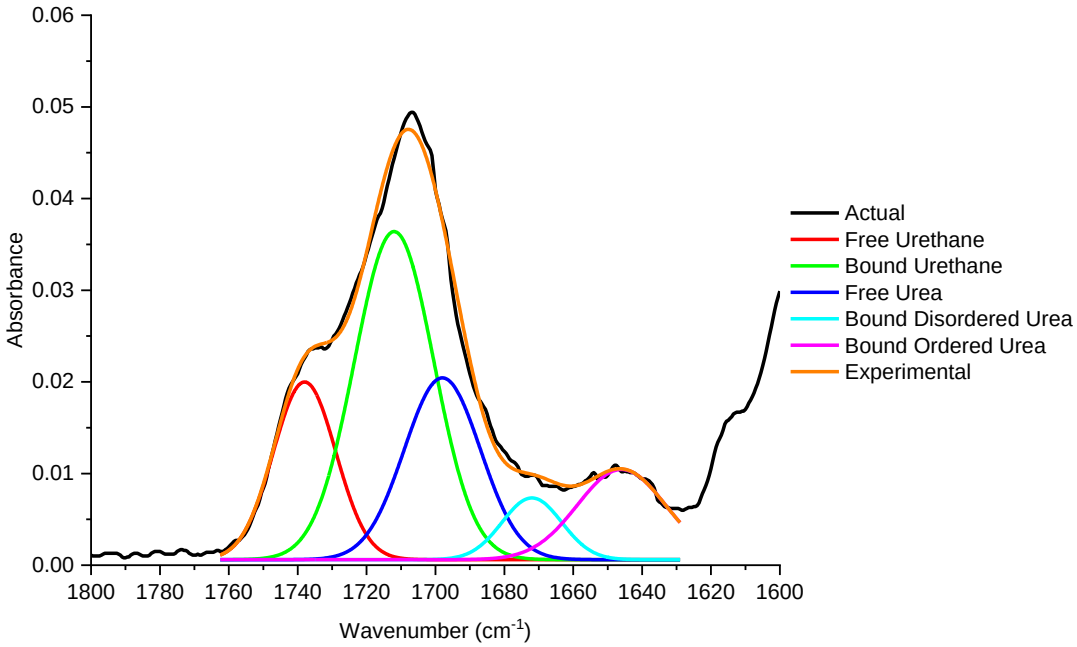

Figure 91. Example of the deconvolution of IR spectroscopic data; shown for **SPU11** at 25 °C in the carbonyl region 1800-1600 cm^{-1}.

Table 20. Reduced Chi-squared and R-squared values for fitting of deconvoluted polymer film samples (**SPU1-SPU13**) using Gaussian fitting under the OriginLab software "spectral fit" module.

Polymer	End-cap	Reduced Chi-Sqr	R-Squared
SPU1	aniline	4.77117×10^{-6}	0.92670
SPU2	3-nitroaniline	1.07966×10^{-6}	0.99396
SPU3	4-nitroaniline	1.40813×10^{-6}	0.99419
SPU4	2-methylaniline	3.92098×10^{-6}	0.97966
SPU5	2-methyl-3-nitroaniline	1.79320×10^{-6}	0.98020
SPU6	2-methyl-4-nitroaniline	1.77302×10^{-6}	0.99358
SPU7	2-methyl-5-nitroaniline	1.25060×10^{-6}	0.99450
SPU8	4-methyl-3-nitroaniline	1.09522×10^{-6}	0.99282
SPU9	2,6-dimethylaniline	2.61100×10^{-6}	0.97655
SPU10	2,6-dimethyl-3-nitroaniline	2.76753×10^{-6}	0.96509
SPU11	2,6-dimethyl-4-nitroaniline	0.86636×10^{-6}	0.99540
SPU12	2,4,6-trimethyl-3-nitroaniline	1.24946×10^{-6}	0.98561
SPU13	2,3,5,6-tetramethyl-4-nitroaniline	0.51924×10^{-6}	0.99277

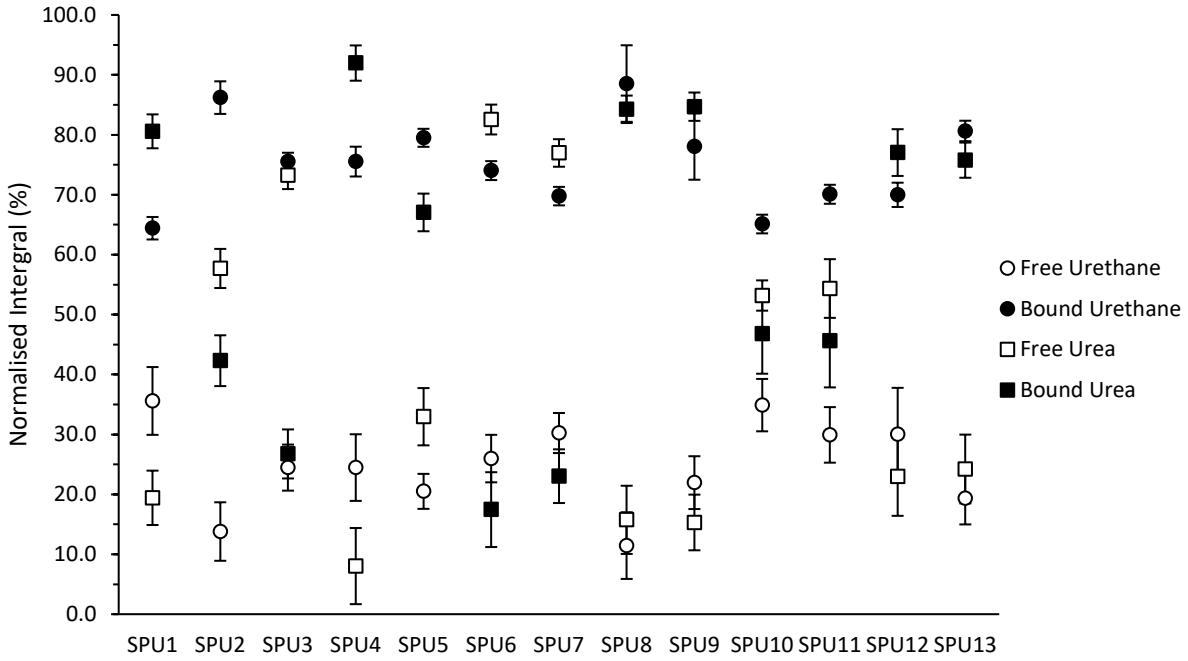

Figure 92. Normalised integrals (after deconvolution into a sum of single Gaussian signals) of polymer films **SPU1**-**SPU13**, recorded at 20 °C after deconvolution of absorbances assigned to free and bound urethane and urea carbonyls, error bars shown as a percentage from the Gaussian fit after deconvolution.

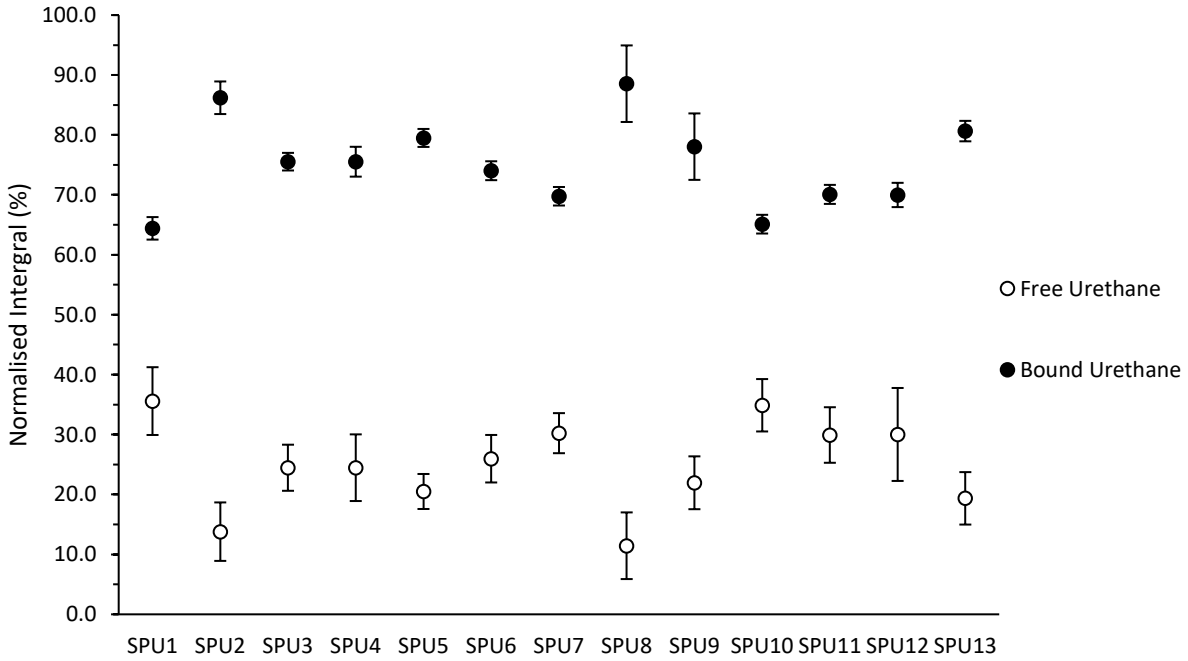

Figure 93. Normalised integrals (after deconvolution into a sum of single Gaussian signals) of polymer films **SPU1**-**SPU13**, recorded at 20 °C after deconvolution of absorbances assigned to free and bound urethane carbonyls, error bars shown as a percentage from the Gaussian fit after deconvolution.

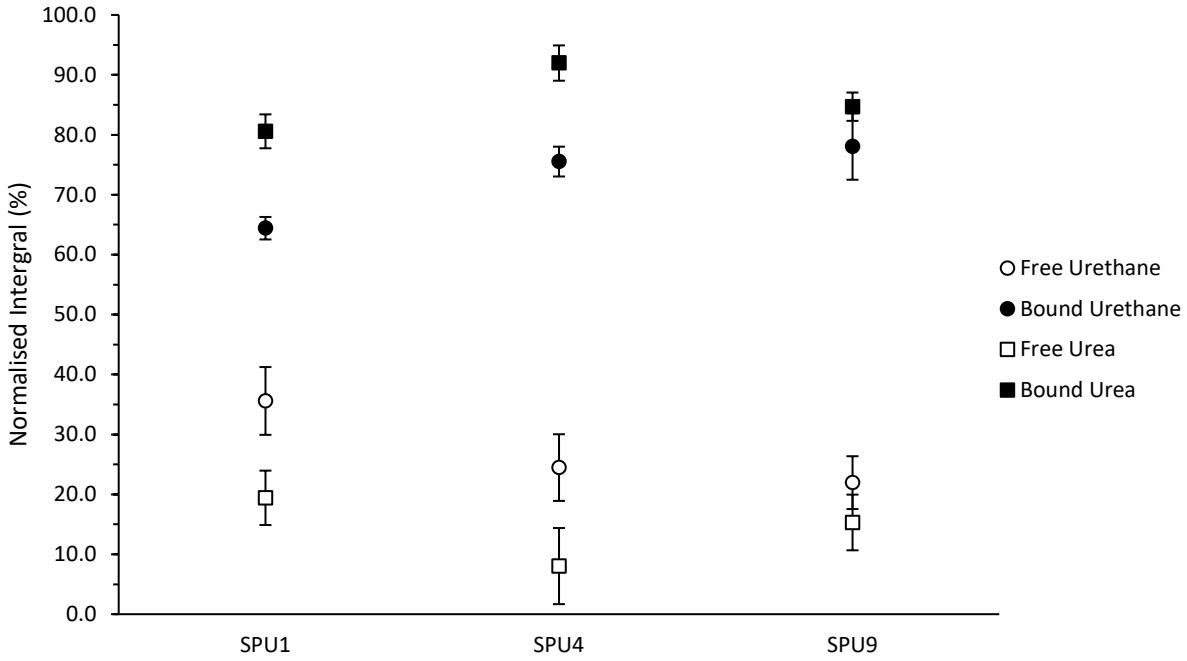

Figure 94. Normalised integrals (after deconvolution into a sum of single Gaussian signals) of polymer films **SPU1**, **SPU4**, and **SPU9**, recorded at 20 °C after deconvolution of absorbances assigned to free and bound urethane and urea carbonyls, error bars shown as a percentage from the Gaussian fit after deconvolution.

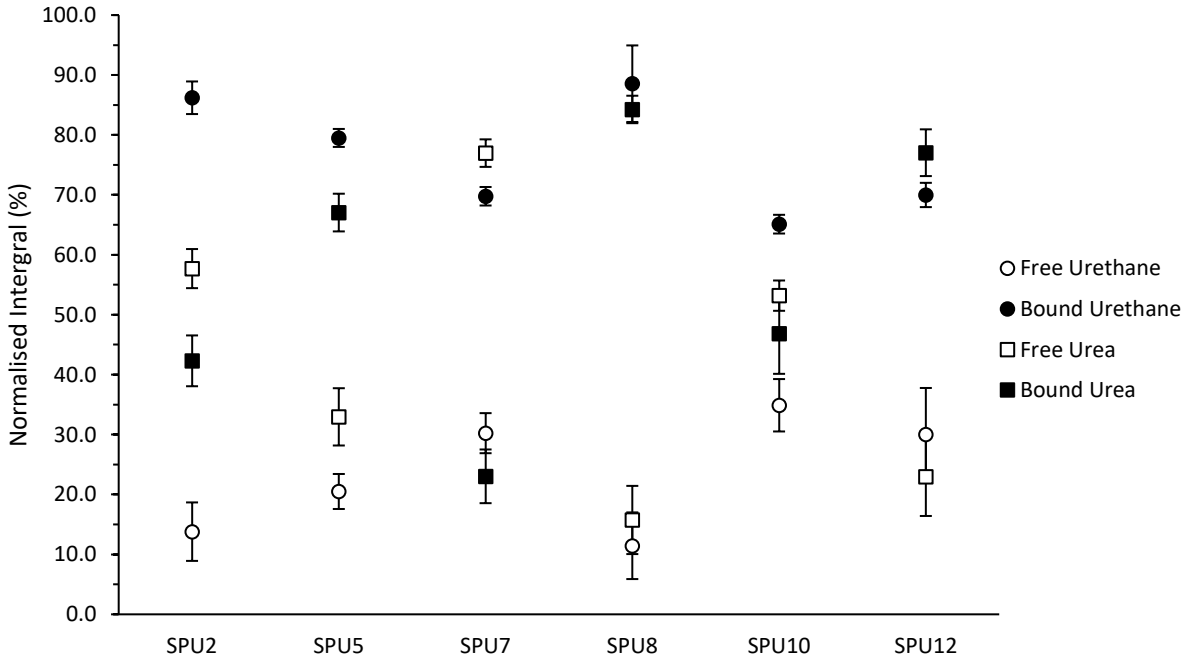

Figure 95. Normalised integrals (after deconvolution into a sum of single Gaussian signals) of *meta*-nitro finctionalsed polymer films **SPU2**, **SPU5**, **SPU7**, **SPU8**, **SPU10**, and **SPU12**, recorded at 20 °C after deconvolution of absorbances assigned to free and bound urethane and urea carbonyls, error bars shown as a percentage from the Gaussian fit after deconvolution.

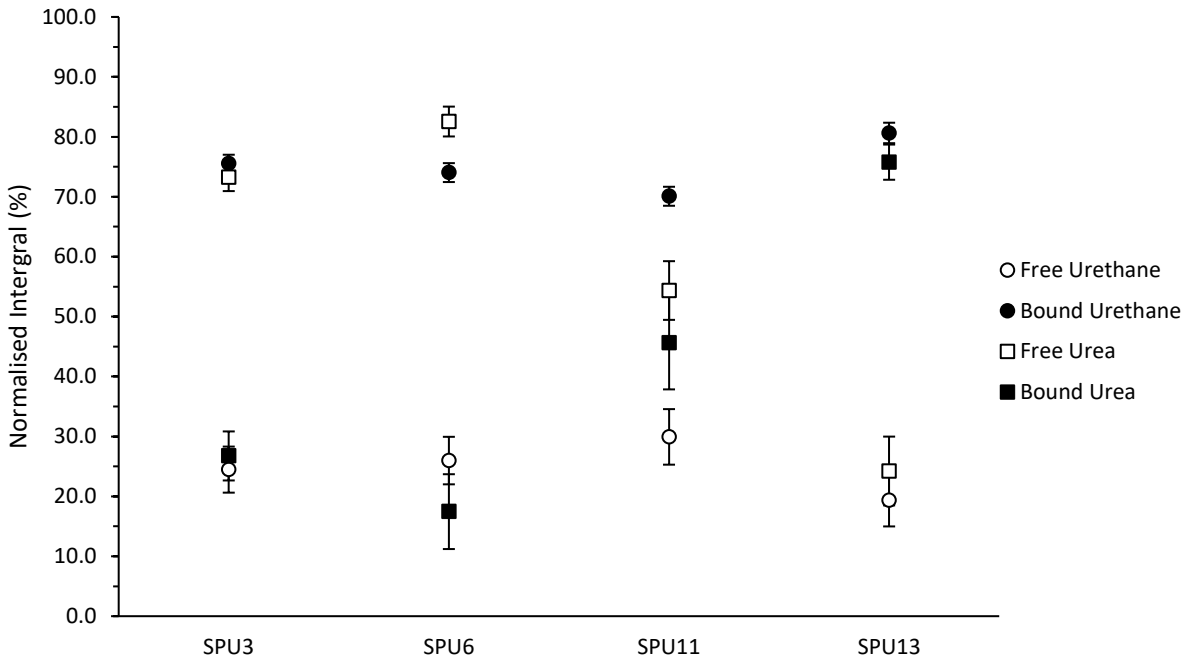

Figure 96. Normalised integrals (after deconvolution into a sum of single Gaussian signals) of *para*- nitro functionalsed polymer films **SPU3**, **SPU6**, **SPU11**, and **SPU13**, recorded at 20 °C after deconvolution of absorbances assigned to free and bound urethane and urea carbonyls, error bars shown as a percentage from the Gaussian fit after deconvolution.

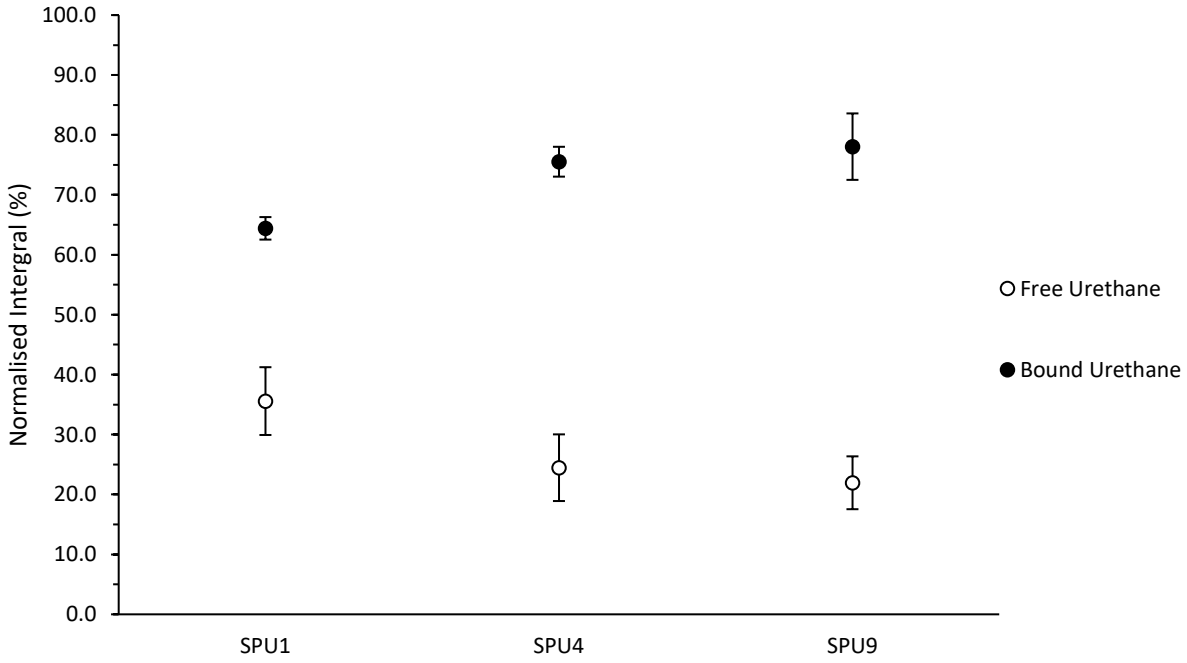

Figure 97. Normalised integrals (after deconvolution into a sum of single Gaussian signals) of polymer films **SPU1**, **SPU4**, and **SPU9**, recorded at 20 °C after deconvolution of absorbances assigned to free and bound urethane carbonyls, error bars shown as a percentage from the Gaussian fit after deconvolution.

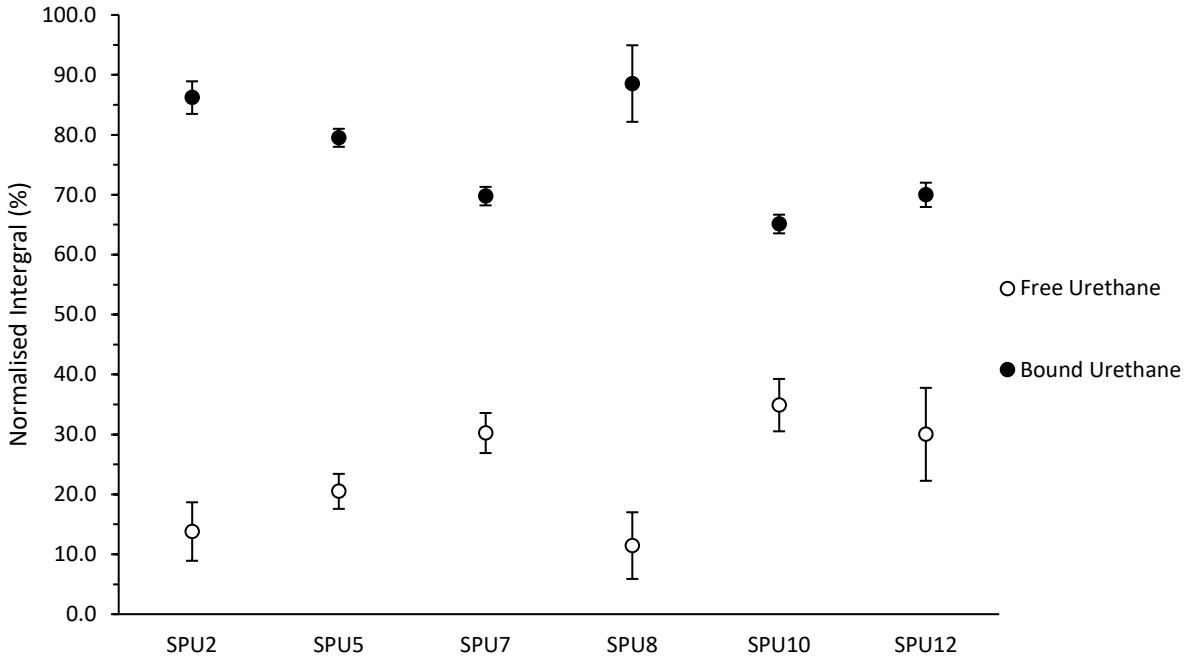

Figure 98. Normalised integrals (after deconvolution into a sum of single Gaussian signals) of *meta*-nitro functionalsed polymer films **SPU2**, **SPU5**, **SPU7**, **SPU8**, **SPU10**, and **SPU12**, recorded at 20 °C after deconvolution of absorbances assigned to free and bound urethane carbonyls, error bars shown as a percentage from the Gaussian fit after deconvolution.

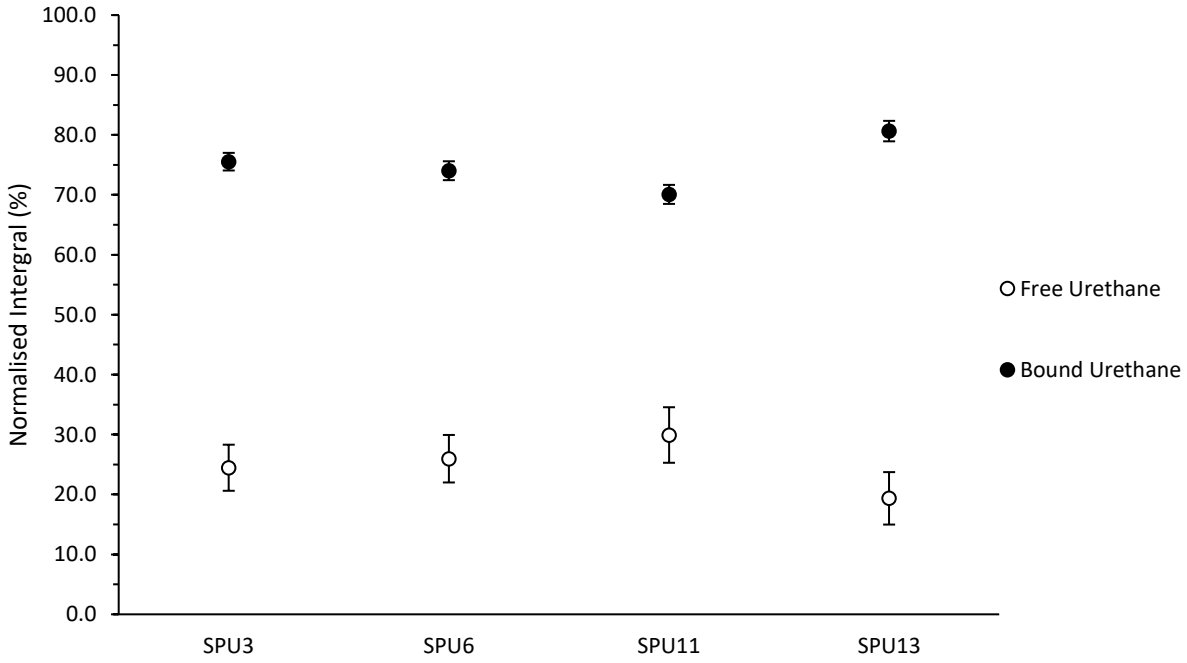

Figure 99. Normalised integrals (after deconvolution into a sum of single Gaussian signals) of *para*-nitro functionalsed polymer films **SPU3**, **SPU6**, **SPU11**, and **SPU13**, recorded at 20 °C after deconvolution of absorbances assigned to free and bound urethane carbonyls, error bars shown as a percentage from the Gaussian fit after deconvolution.

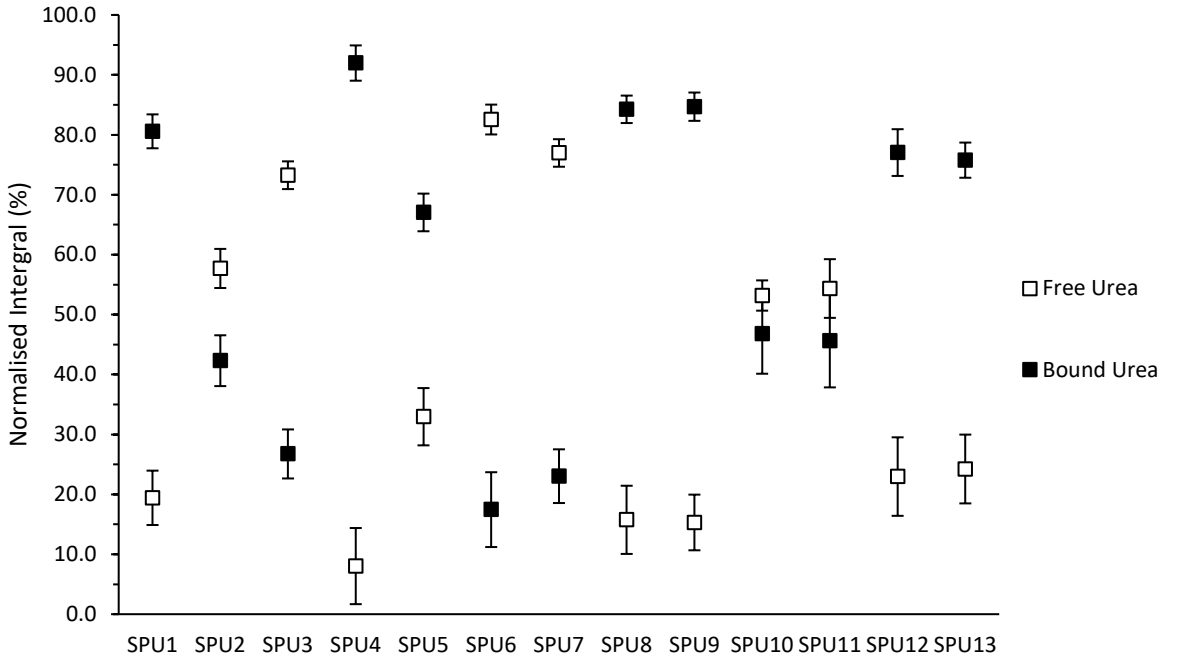

Figure 100. Normalised integrals (after deconvolution into a sum of single Gaussian signals) of polymer films **SPU1**-**SPU13**, recorded at 20 °C after deconvolution of absorbances assigned to free and bound urea carbonyls, error bars shown as a percentage from the Gaussian fit after deconvolution.

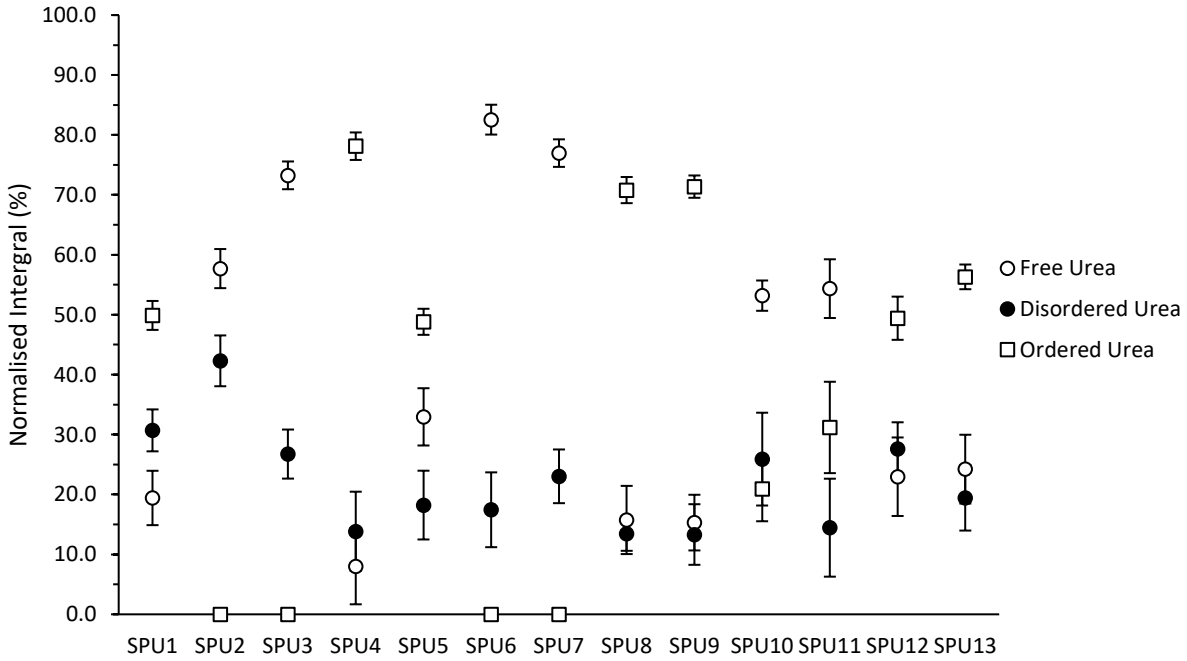

Figure 101. Normalised integrals (after deconvolution into a sum of single Gaussian signals) of polymer films **SPU1**-**SPU13**, recorded at 20 °C after deconvolution of absorbances assigned to free, disordered and ordered urea carbonyls, error bars shown as a percentage from the Gaussian fit after deconvolution.

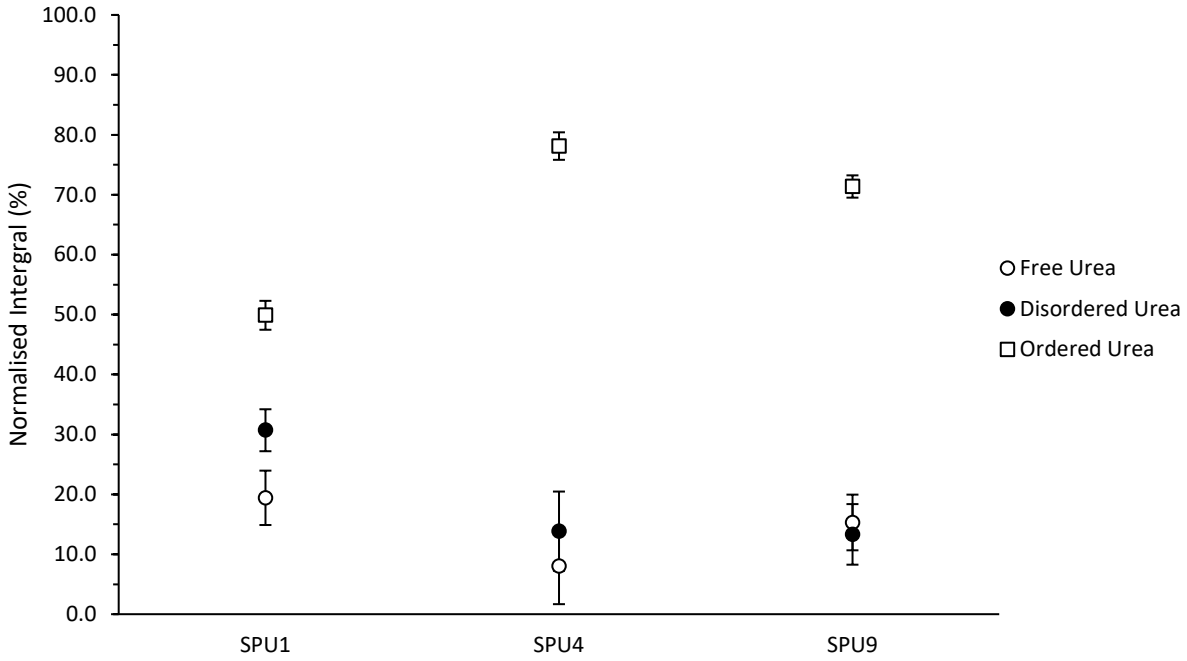

Figure 102. Normalised integrals (after deconvolution into a sum of single Gaussian signals) of polymer films **SPU1**, **SPU4**, and **SPU9**, recorded at 20 °C after deconvolution of absorbances assigned to free, disordered and ordered urea carbonyls, error bars shown as a percentage from the Gaussian fit after deconvolution.

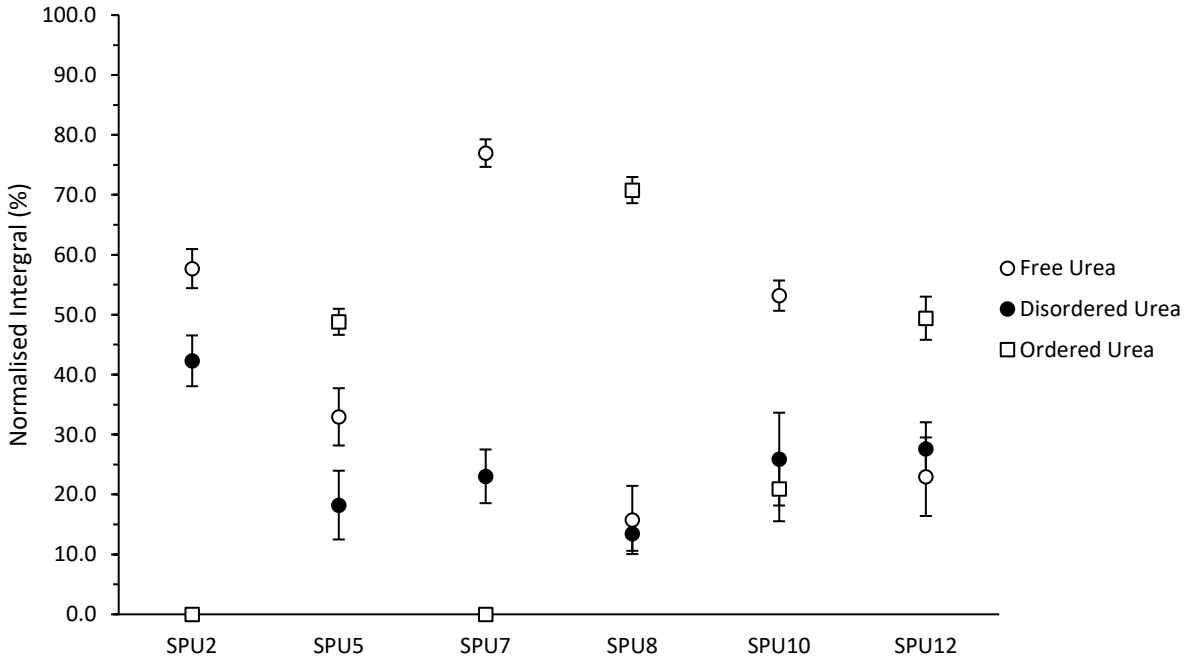

Figure 103. Normalised integrals (after deconvolution into a sum of single Gaussian signals) of *meta*-nitro functionalsed polymer films **SPU2**, **SPU5**, **SPU7**, **SPU8**, **SPU10**, and **SPU12**, recorded at 20 °C after deconvolution of absorbances assigned to free, disordered and ordered urea carbonyls, error bars shown as a percentage from the Gaussian fit after deconvolution.

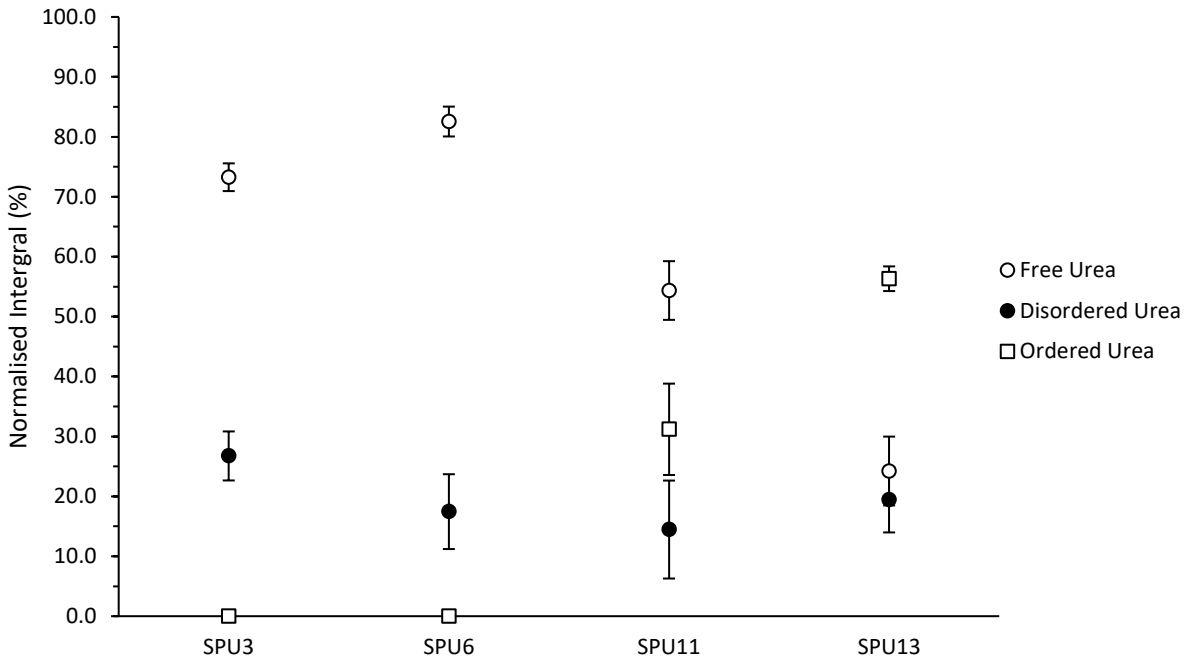

Figure 104. Normalised integrals (after deconvolution into a sum of single Gaussian signals) of *para*-nitro functionalsed polymer films **SPU3**, **SPU6**, **SPU11**, and **SPU13**, recorded at 20 °C after deconvolution of absorbances assigned to free, disordered and ordered urea carbonyls, error bars shown as a percentage from the Gaussian fit after deconvolution.

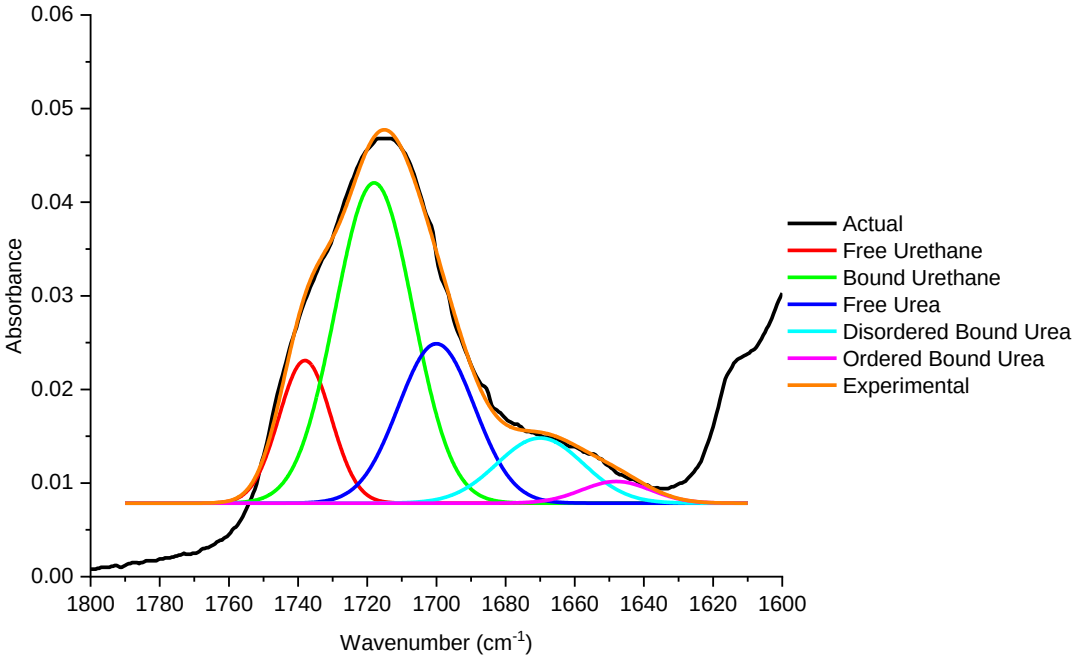

Figure 105. Example of the deconvolution of IR spectroscopic data: **SPU5** (loaded in KBr disc, with KBr:**SPU5** 1:0.1 % wt) at 25 °C in the carbonyl region 1800-1600 cm^{-1}.

Table 21. Reduced Chi-squared and R-squared values for fitting of deconvoluted **SPU5** VT-IR sample using gaussian fitting under the OriginLab software "spectral fit" module from 25-200 °C.

Temperature (°C)	Reduced Chi-Sqr	R-Squared
25	17.7777×10^{-6}	0.90535
40	12.7564×10^{-6}	0.93964
60	1.62574×10^{-6}	0.99283
80	0.50779×10^{-6}	0.99787
100	0.80870×10^{-6}	0.99691
120	1.25025×10^{-6}	0.99542
140	1.68476×10^{-6}	0.99403
160	1.67883×10^{-6}	0.99358
180	0.86600×10^{-6}	0.99562
200	1.72332×10^{-6}	0.99219

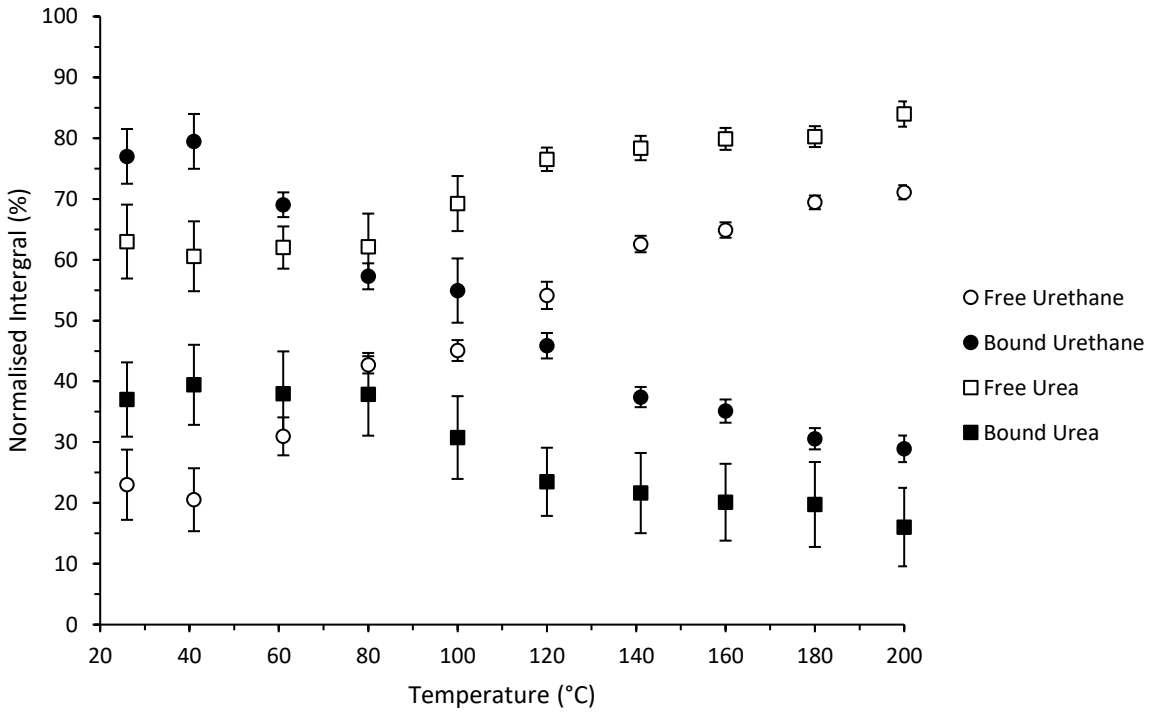

Figure 106. Normalised integrals (after deconvolution into a sum of single Gaussian signals) of **SPU5**, recorded from 25-200 °C after deconvolution of absorbances assigned to free and bound urethane and urea carbonyls, error bars shown as a percentage from the Gaussian fit after deconvolution.

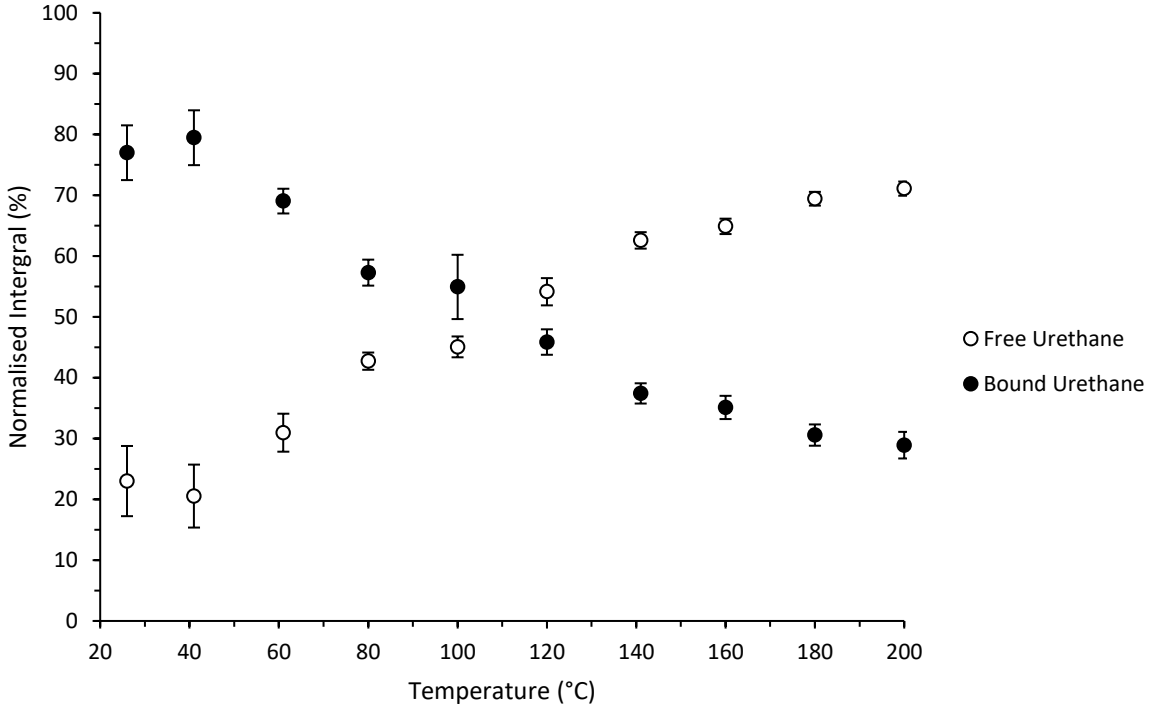

Figure 107. Normalised integrals (after deconvolution into a sum of single Gaussian signals) of **SPU5**, recorded from 25-200 °C after deconvolution of absorbances assigned to free and bound urethane carbonyls, error bars shown as a percentage from the Gaussian fit after deconvolution.

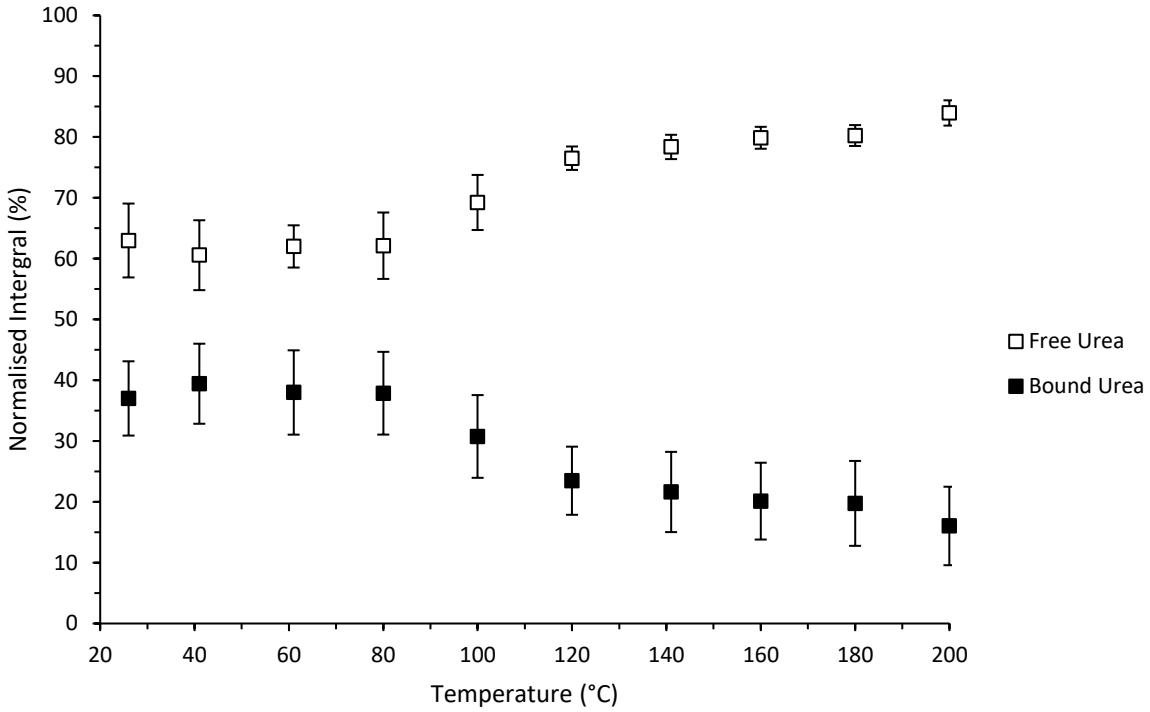

Figure 108. Normalised integrals (after deconvolution into a sum of single Gaussian signals) of **SPU5**, recorded from 25-200 °C after deconvolution of absorbances assigned to free and bound urea carbonyls, error bars shown as a percentage from the Gaussian fit after deconvolution.

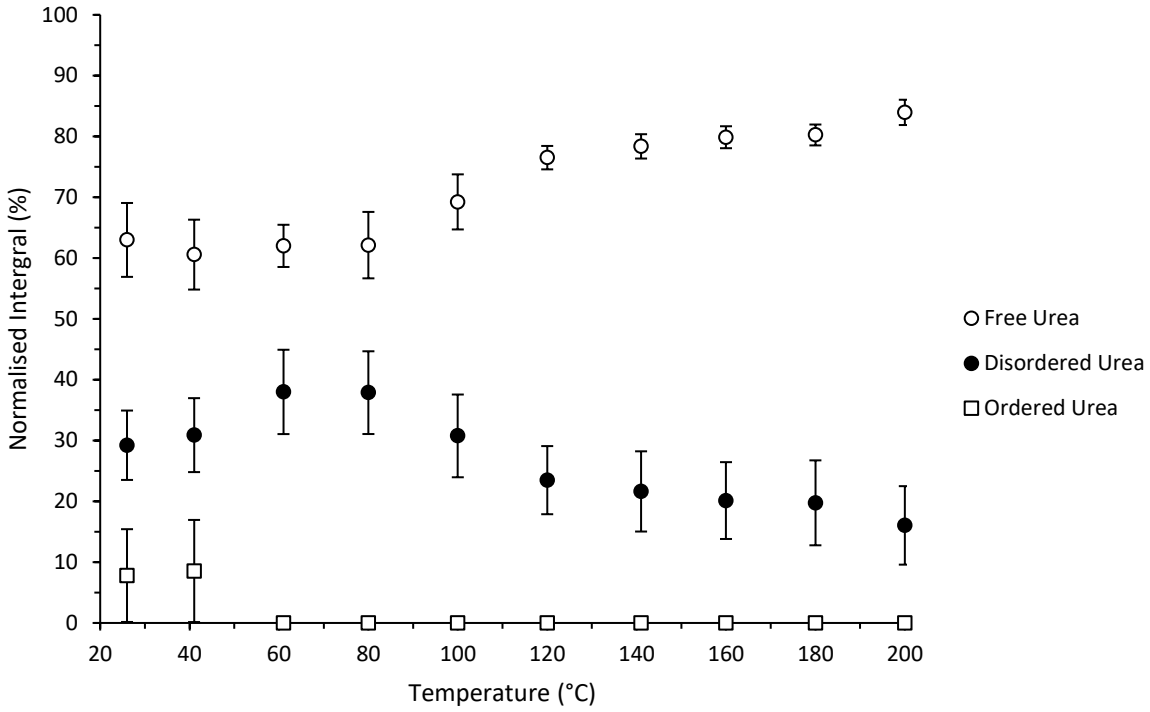

Figure 109. Normalised integrals (after deconvolution into a sum of single Gaussian signals) of **SPU5**, recorded from 25-200 °C after deconvolution of absorbances assigned to free, disordered and ordered urea carbonyls, error bars shown as a percentage from the Gaussian fit after deconvolution.

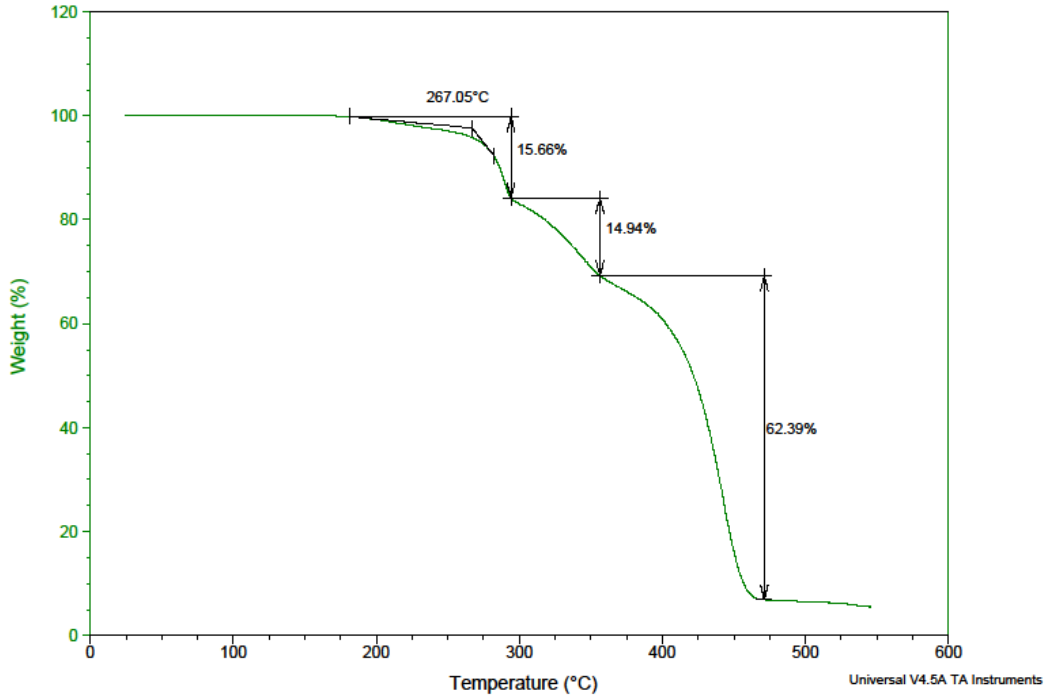

Figure 110. TGA plot of **SPU1** at 10 °C/min under nitrogen.

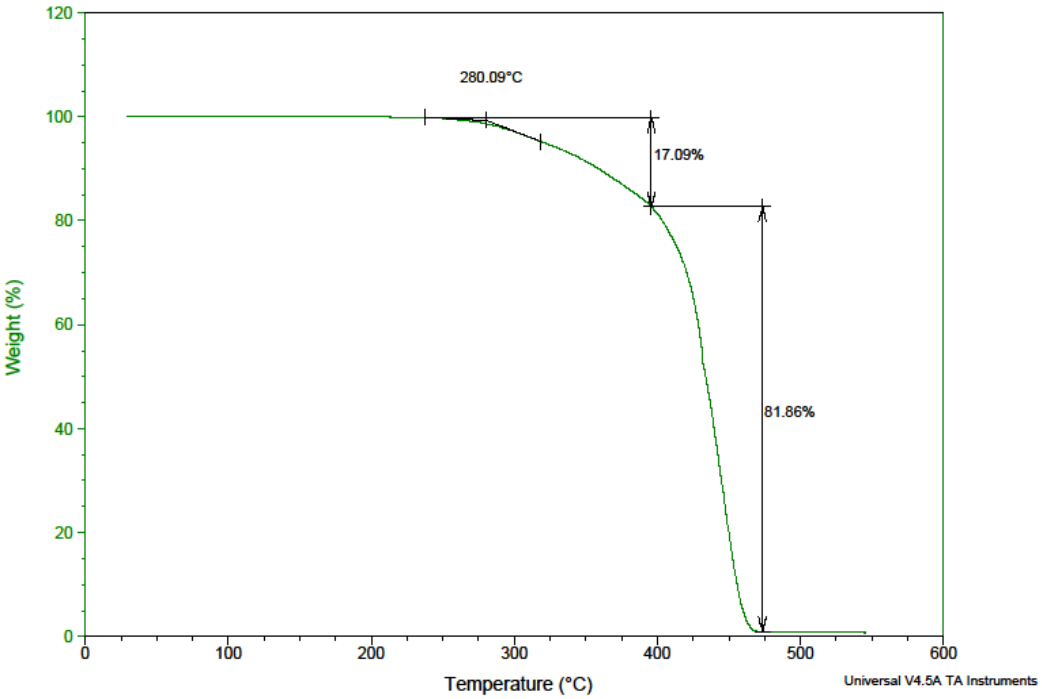

Figure 111. TGA plot of **SPU3** at 10 °C/min under nitrogen.

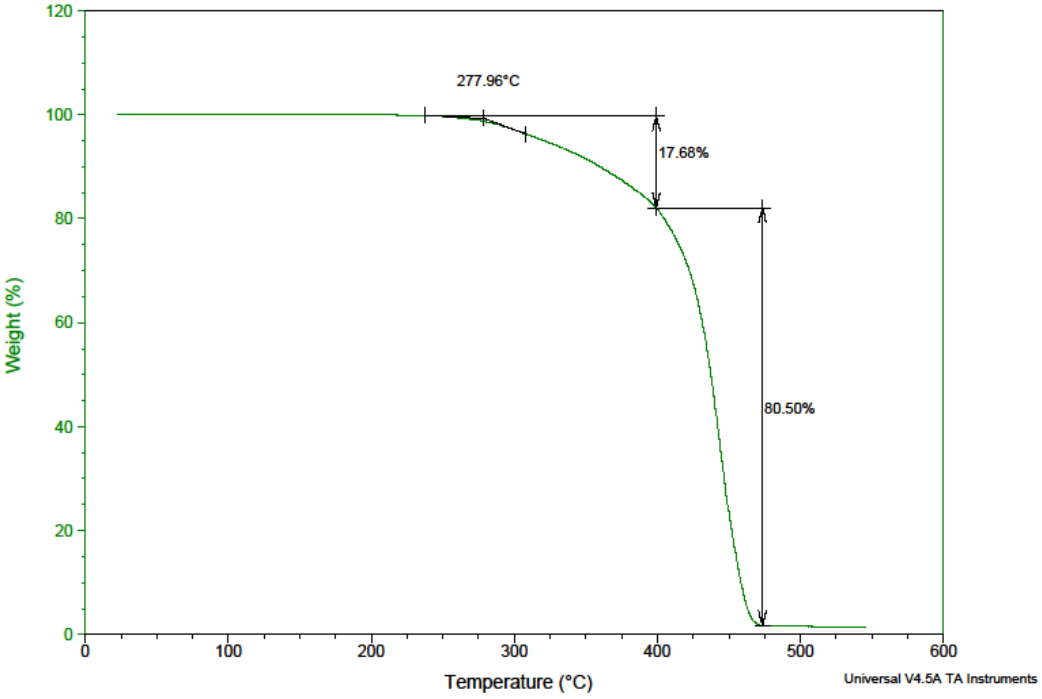

Figure 112. TGA plot of **SPU6** at 10 °C/min under nitrogen.

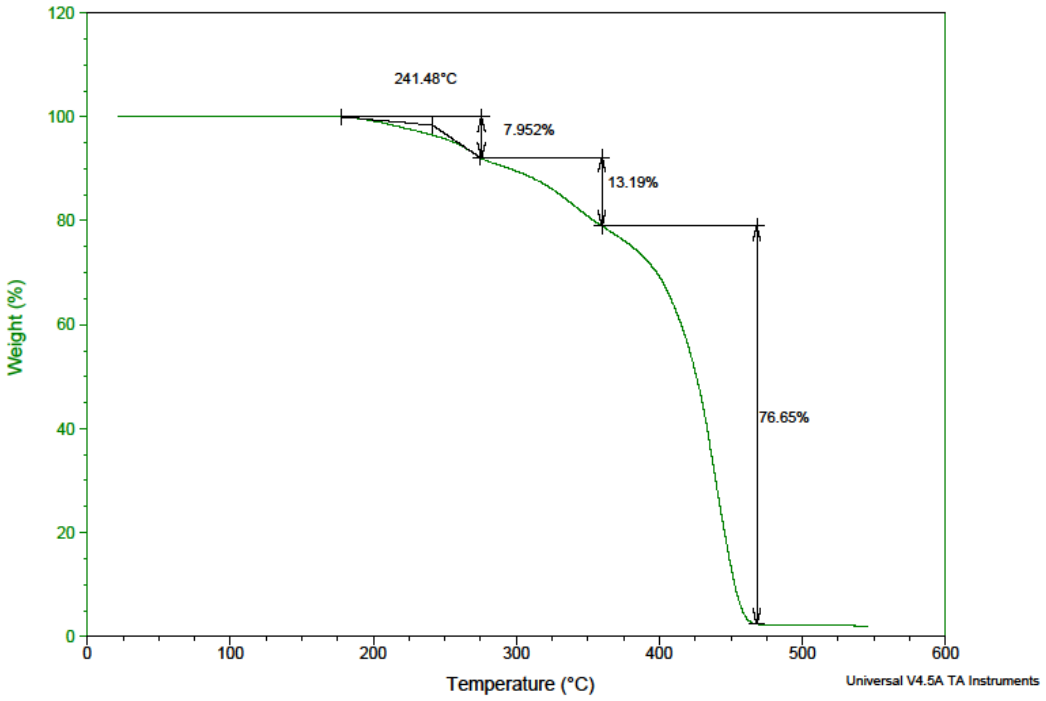

Figure 113. TGA plot of **SPU9** at 10 °C/min under nitrogen.

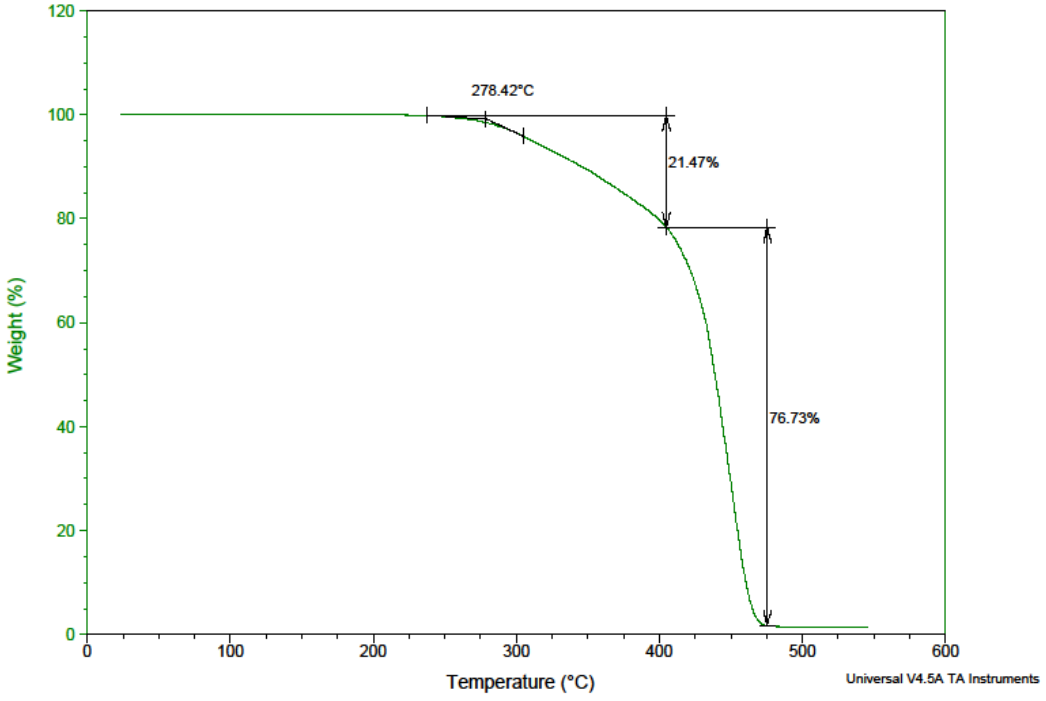

Figure 114. TGA plot of **SPU11** at 10 °C/min under nitrogen.

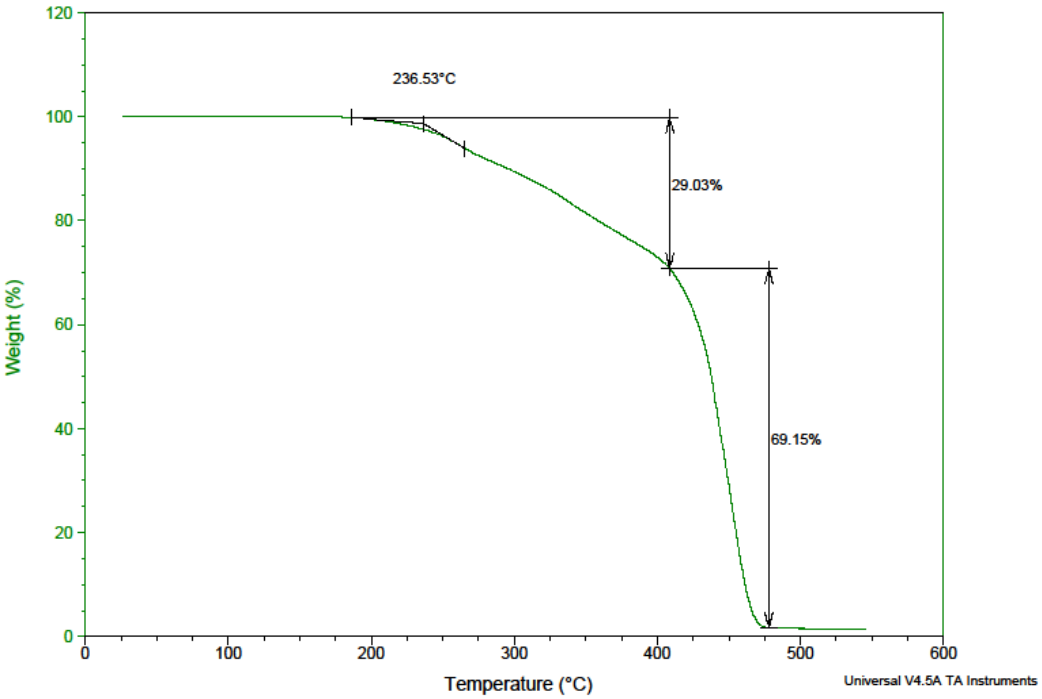

Figure 115. TGA plot of **SPU13** at 10 °C/min under nitrogen.

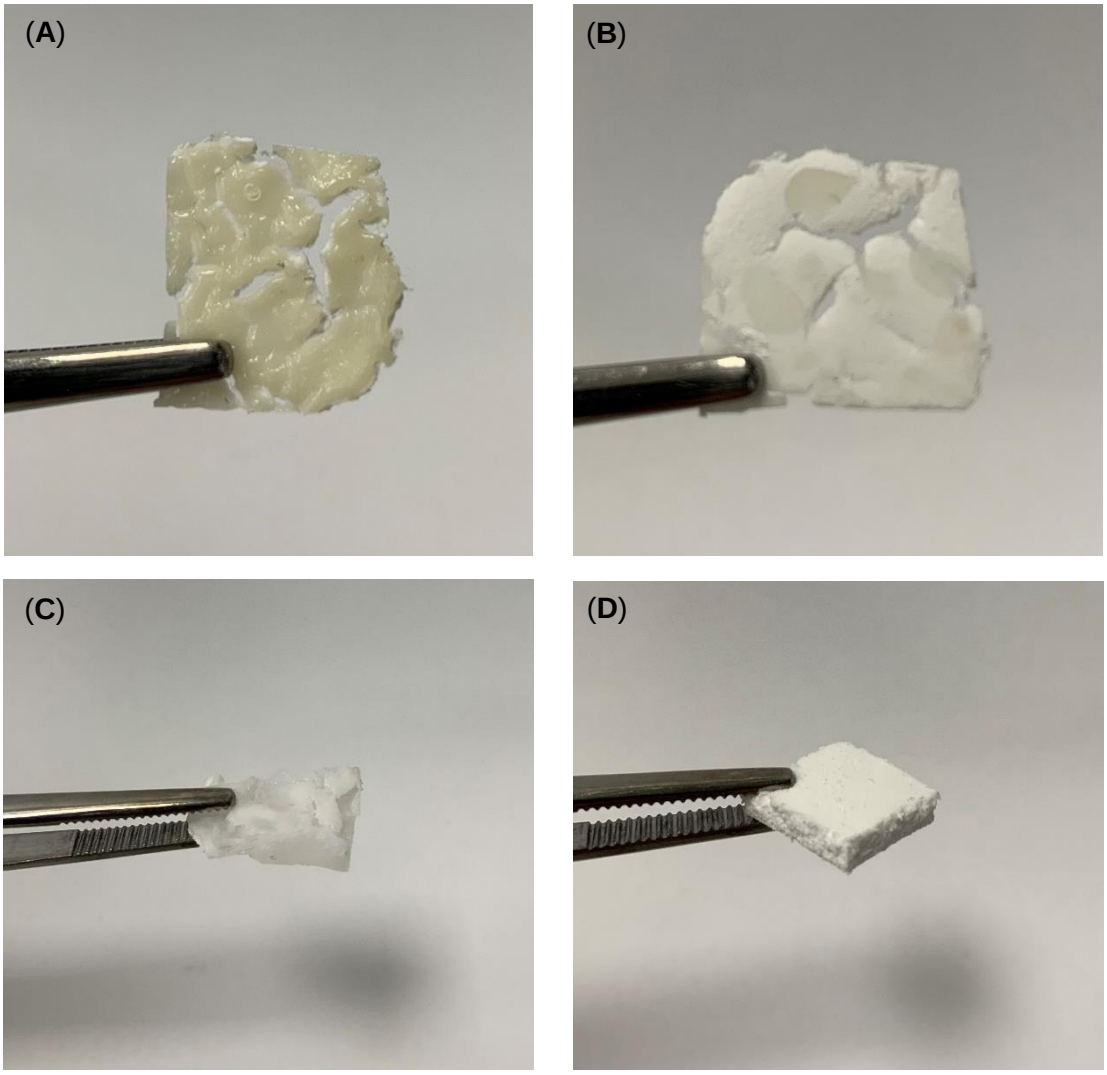

Figure 116. Cast polymer films of (**A**) **SPU1** top face, (**B**) **SPU1** bottom face, (**C**) **SPU4** and (**D**) **SPU9**.

Figure 117. Representative homogeneous cast translucent film of **SPU12** in 10 cm × 10 cm aluminium mould.

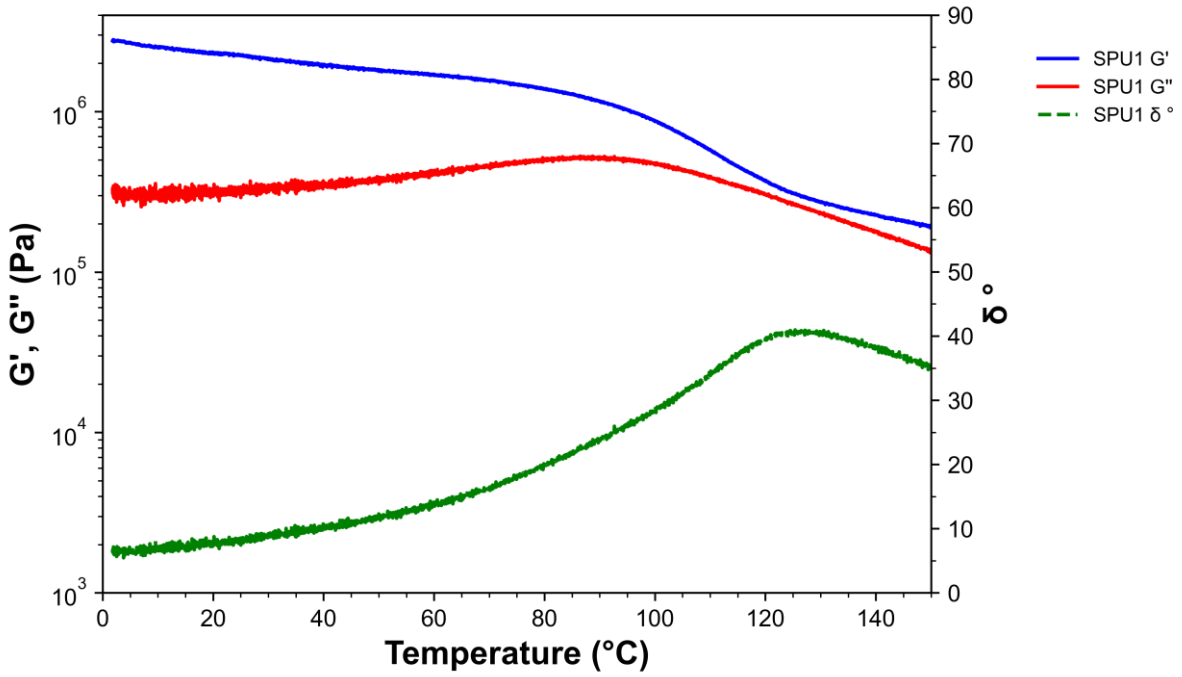

Figure 118. Temperature sweep analysis of **SPU1** over a temperature regime of 0 °C to 150 °C, using a normal force of 1 N and a frequency of 1 Hz. With G' (blue), G'' (red) and phase shift (δ) (green) against temperature.

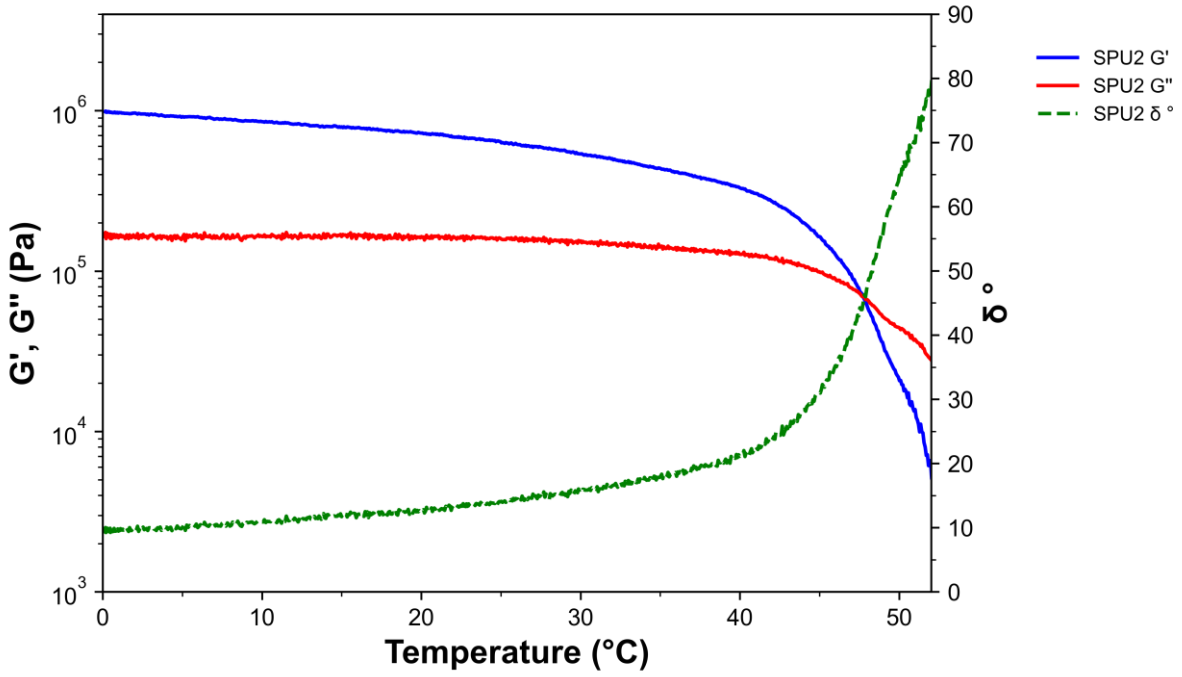

Figure 119. Temperature sweep analysis of **SPU2** over a temperature regime of 0 °C to 150 °C, using a normal force of 1 N and a frequency of 1 Hz. With G' (blue), G'' (red) and phase shift (δ) (green) against temperature.

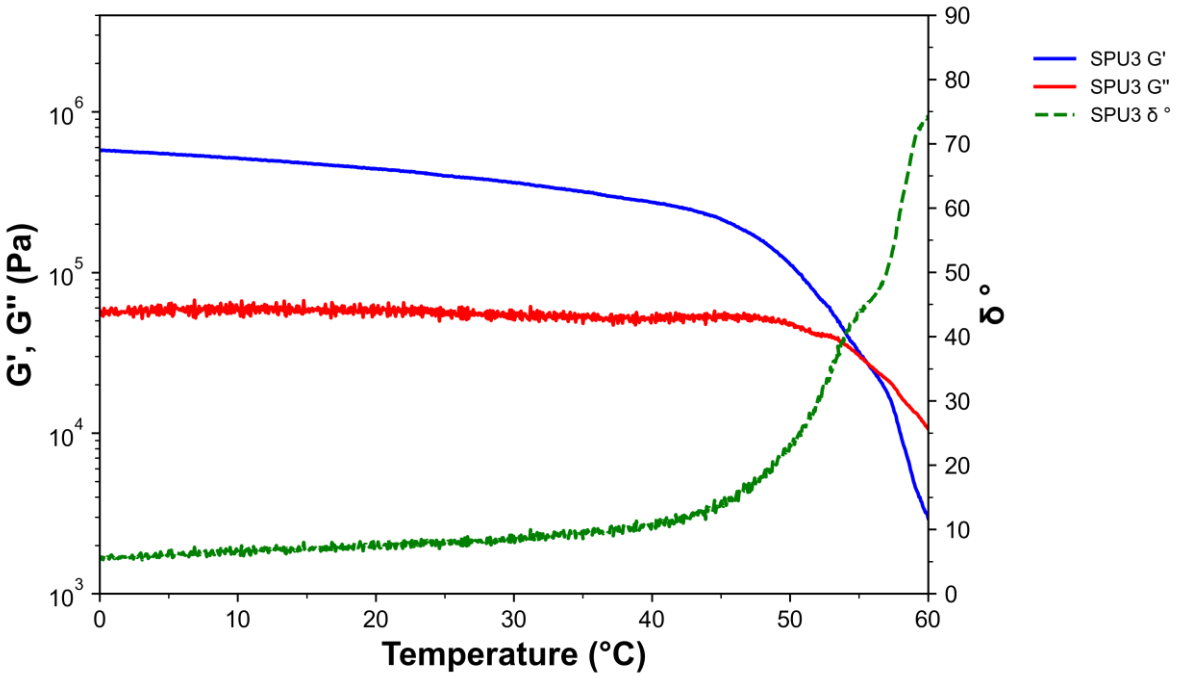

Figure 120. Temperature sweep analysis of **SPU3** over a temperature regime of 0 °C to 150 °C, using a normal force of 1 N and a frequency of 1 Hz. With G' (blue), G'' (red) and phase shift (δ) (green) against temperature.

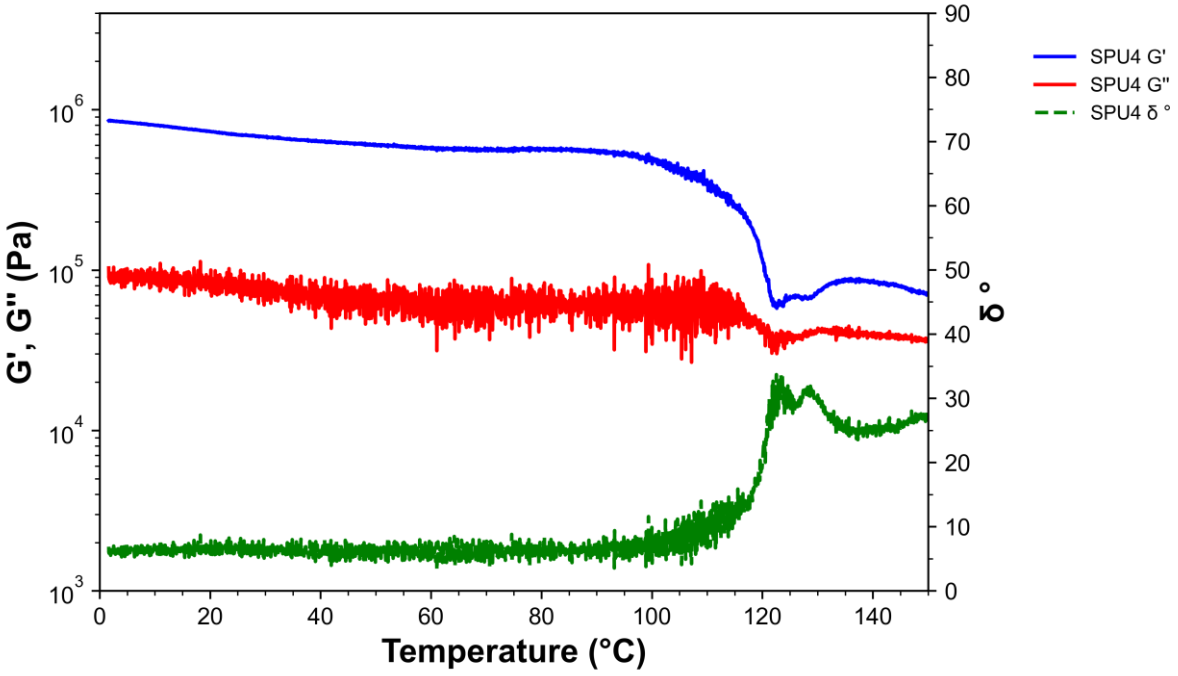

Figure 121. Temperature sweep analysis of **SPU4** over a temperature regime of 0 °C to 150 °C, using a normal force of 1 N and a frequency of 1 Hz. With G' (blue), G'' (red) and phase shift (δ) (green) against temperature.

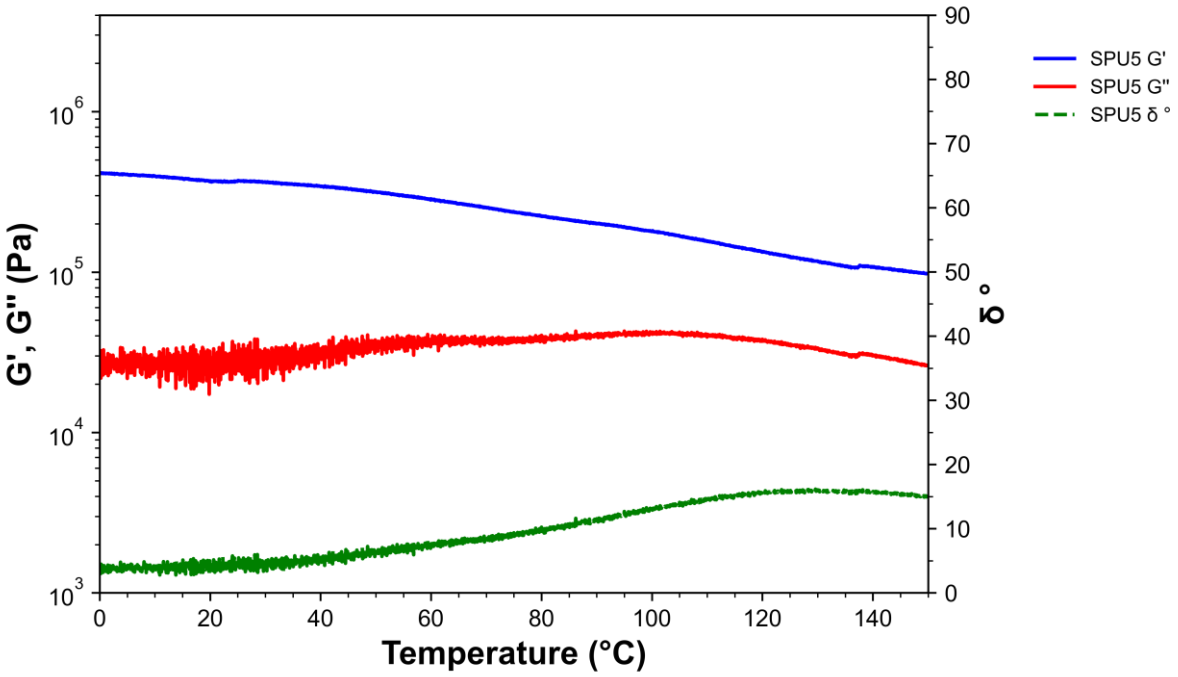

Figure 122. Temperature sweep analysis of **SPU5** over a temperature regime of 0 °C to 150 °C, using a normal force of 1 N and a frequency of 1 Hz. With G' (blue), G'' (red) and phase shift (δ) (green) against temperature.

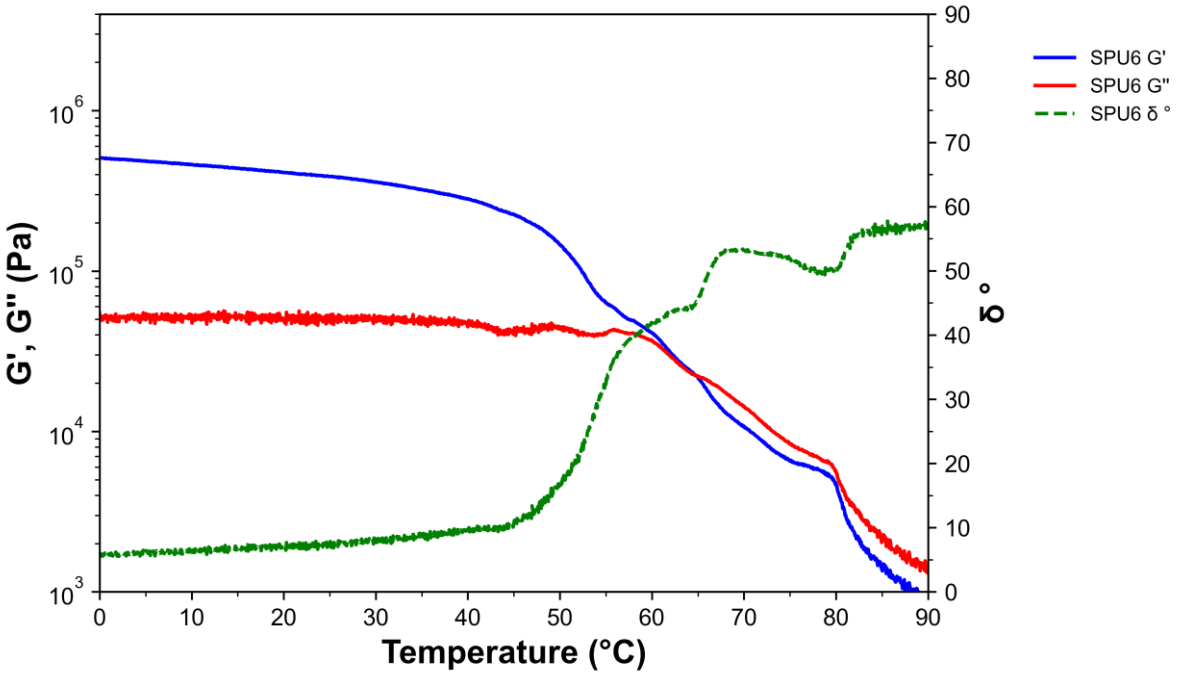

Figure 123. Temperature sweep analysis of **SPU6** over a temperature regime of 0 °C to 150 °C, using a normal force of 1 N and a frequency of 1 Hz. With G' (blue), G'' (red) and phase shift (δ) (green) against temperature.

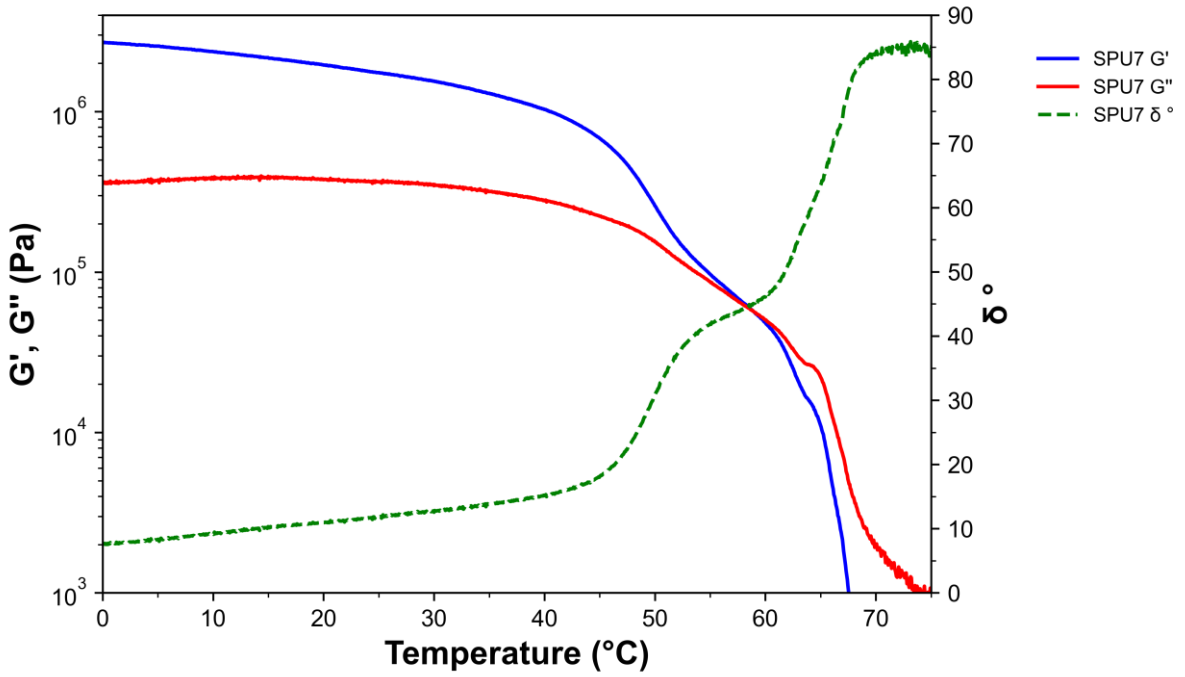

Figure 124. Temperature sweep analysis of **SPU7** over a temperature regime of 0 °C to 150 °C, using a normal force of 1 N and a frequency of 1 Hz. With G' (blue), G'' (red) and phase shift (δ) (green) against temperature.

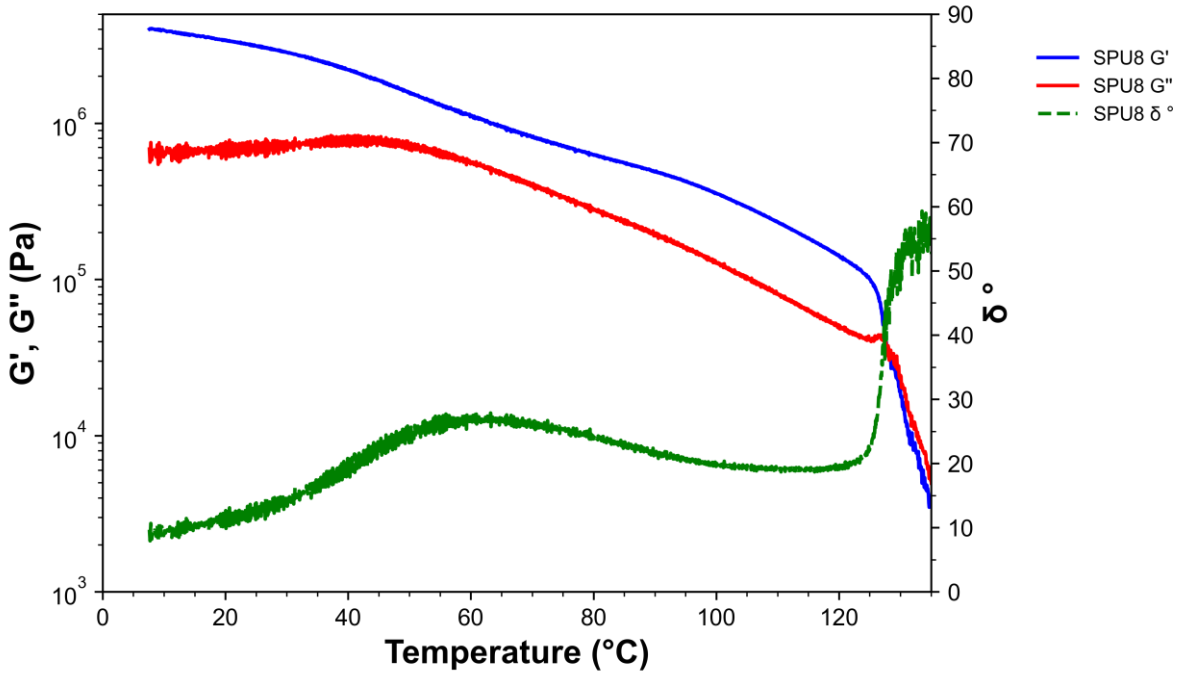

Figure 125. Temperature sweep analysis of **SPU8** over a temperature regime of 0 °C to 150 °C, using a normal force of 1 N and a frequency of 1 Hz. With G' (blue), G'' (red) and phase shift (δ) (green) against temperature.

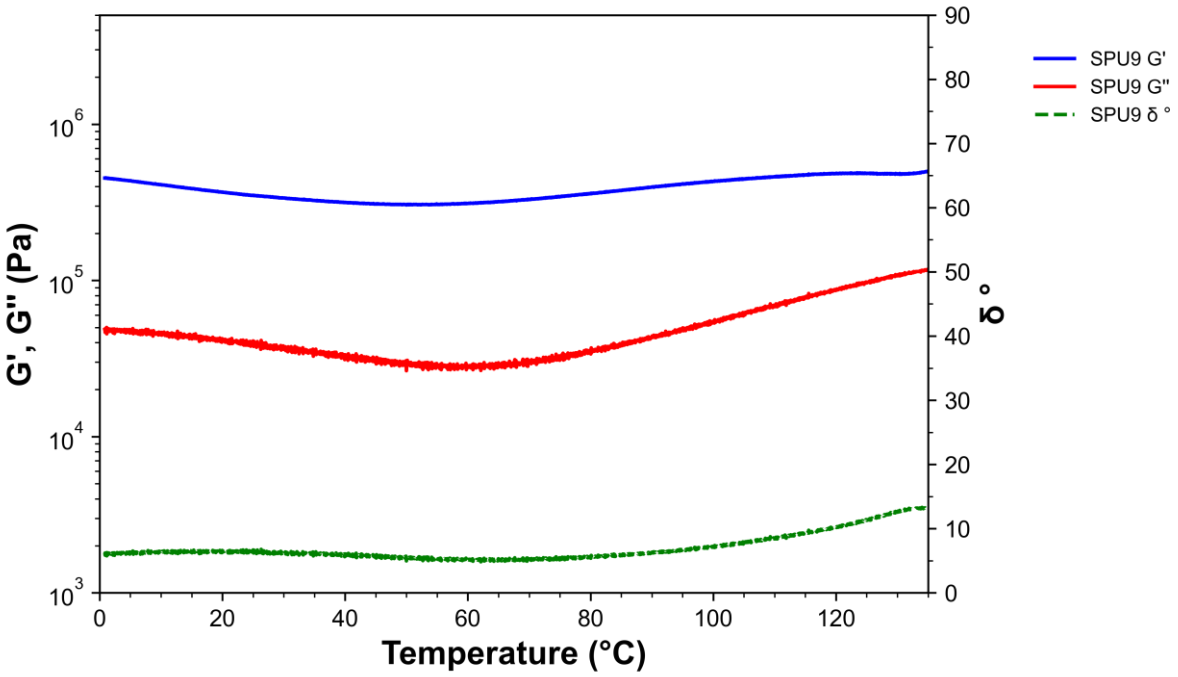

Figure 126. Temperature sweep analysis of **SPU9** over a temperature regime of 0 °C to 150 °C, using a normal force of 1 N and a frequency of 1 Hz. With G' (blue), G'' (red) and phase shift (δ) (green) against temperature.

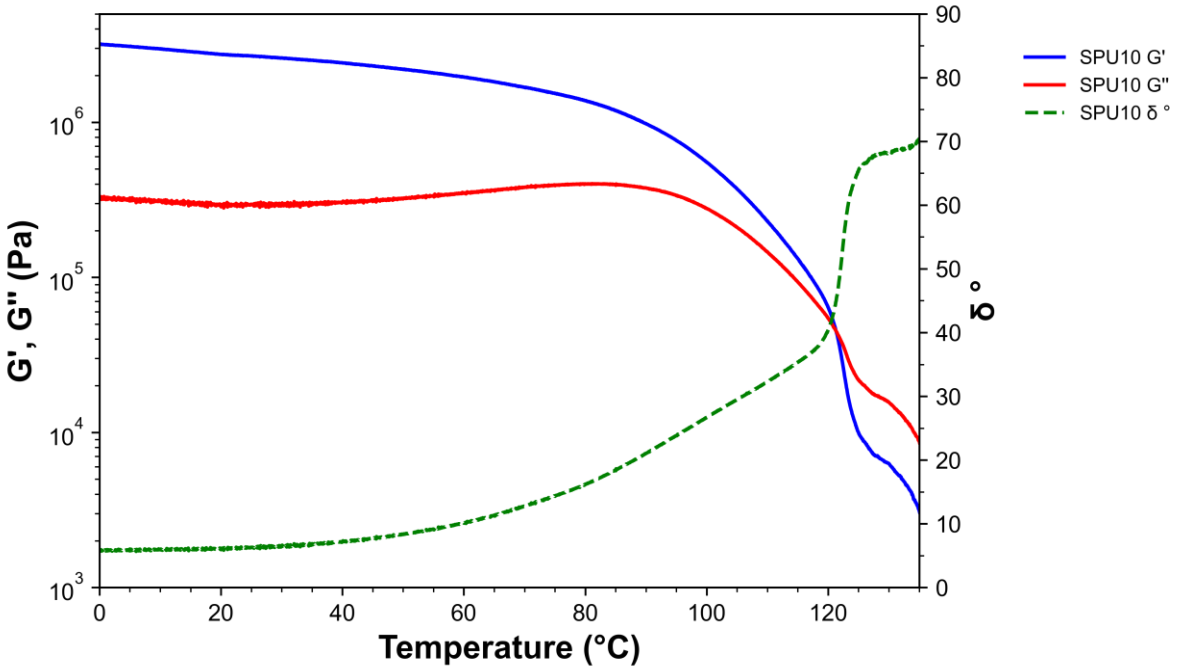

Figure 127. Temperature sweep analysis of **SPU10** over a temperature regime of 0 °C to 150 °C, using a normal force of 1 N and a frequency of 1 Hz. With G' (blue), G'' (red) and phase shift (δ) (green) against temperature.

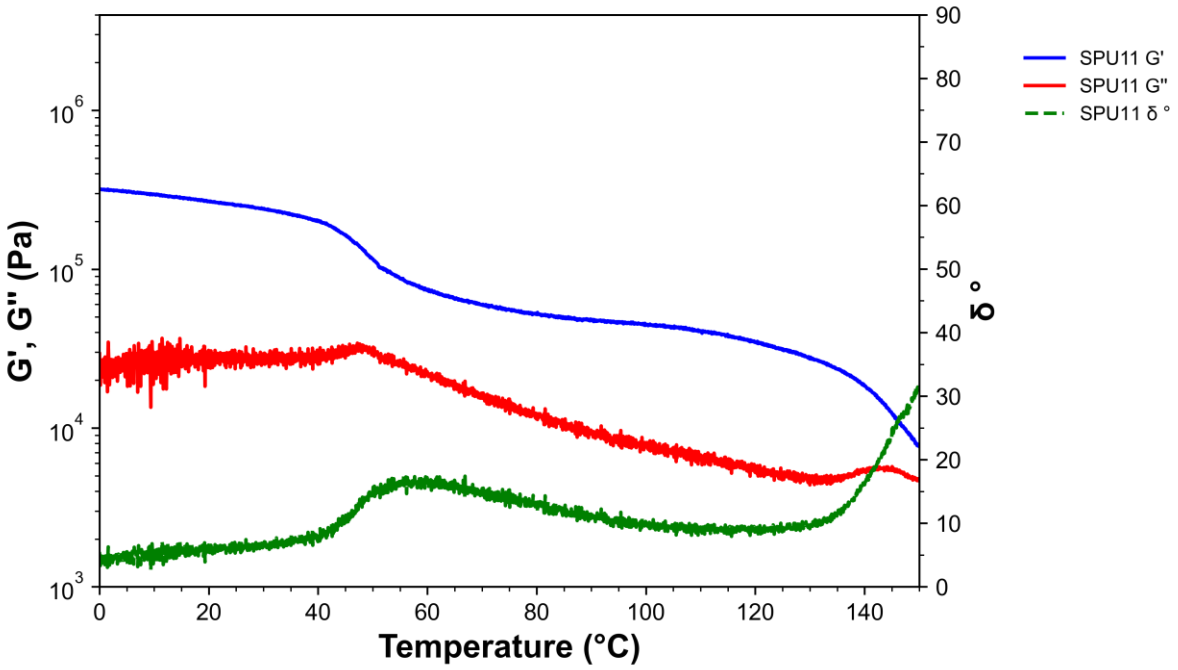

Figure 128. Temperature sweep analysis of **SPU11** over a temperature regime of 0 °C to 150 °C, using a normal force of 1 N and a frequency of 1 Hz. With G' (blue), G'' (red) and phase shift (δ) (green) against temperature.

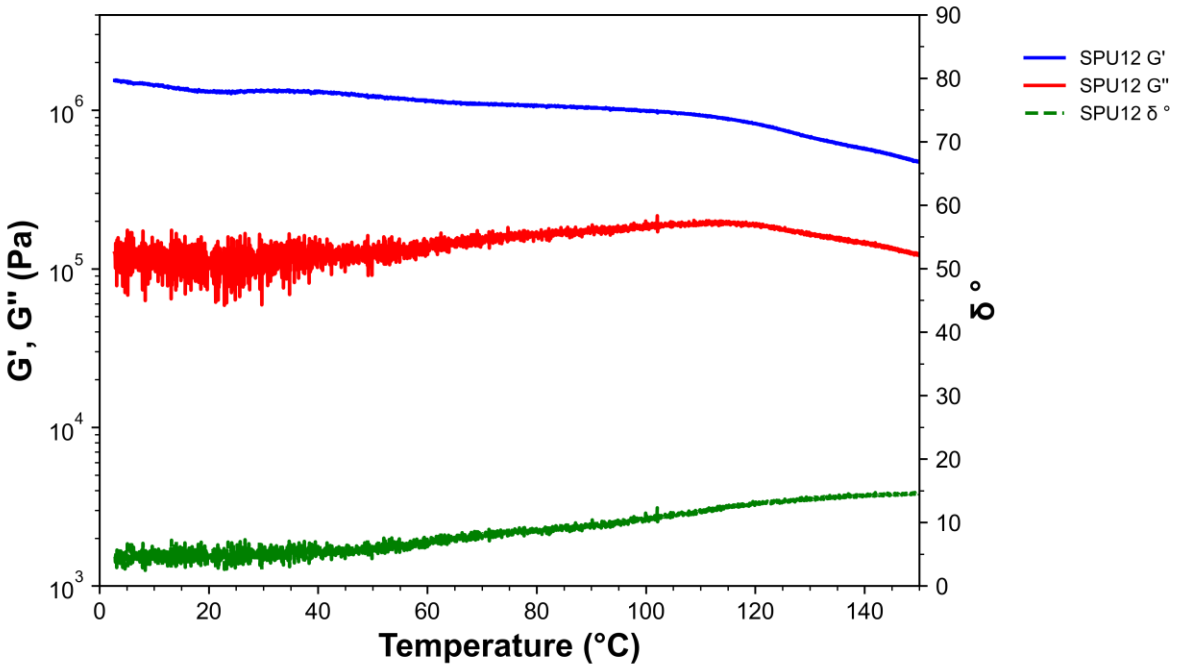

Figure 129. Temperature sweep analysis of **SPU12** over a temperature regime of 0 °C to 150 °C, using a normal force of 1 N and a frequency of 1 Hz. With G' (blue), G'' (red) and phase shift (δ) (green) against temperature.

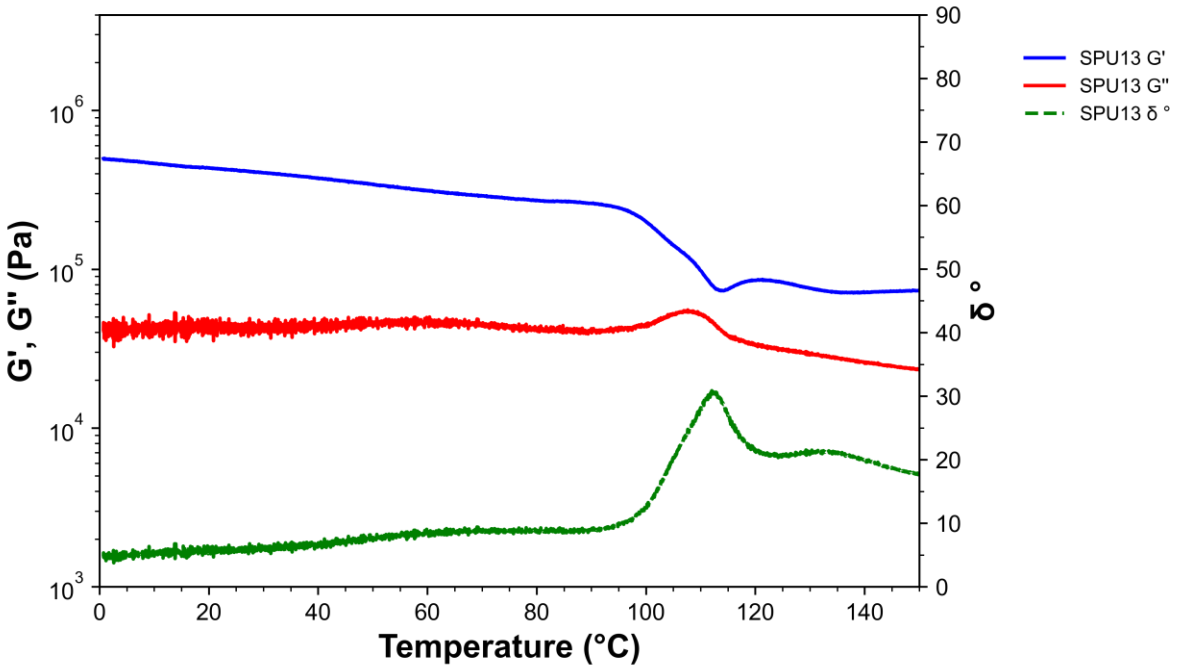

Figure 130. Temperature sweep analysis of **SPU13** over a temperature regime of 0 °C to 150 °C, using a normal force of 1 N and a frequency of 1 Hz. With G', G'' and phase shift (δ) against temperature.

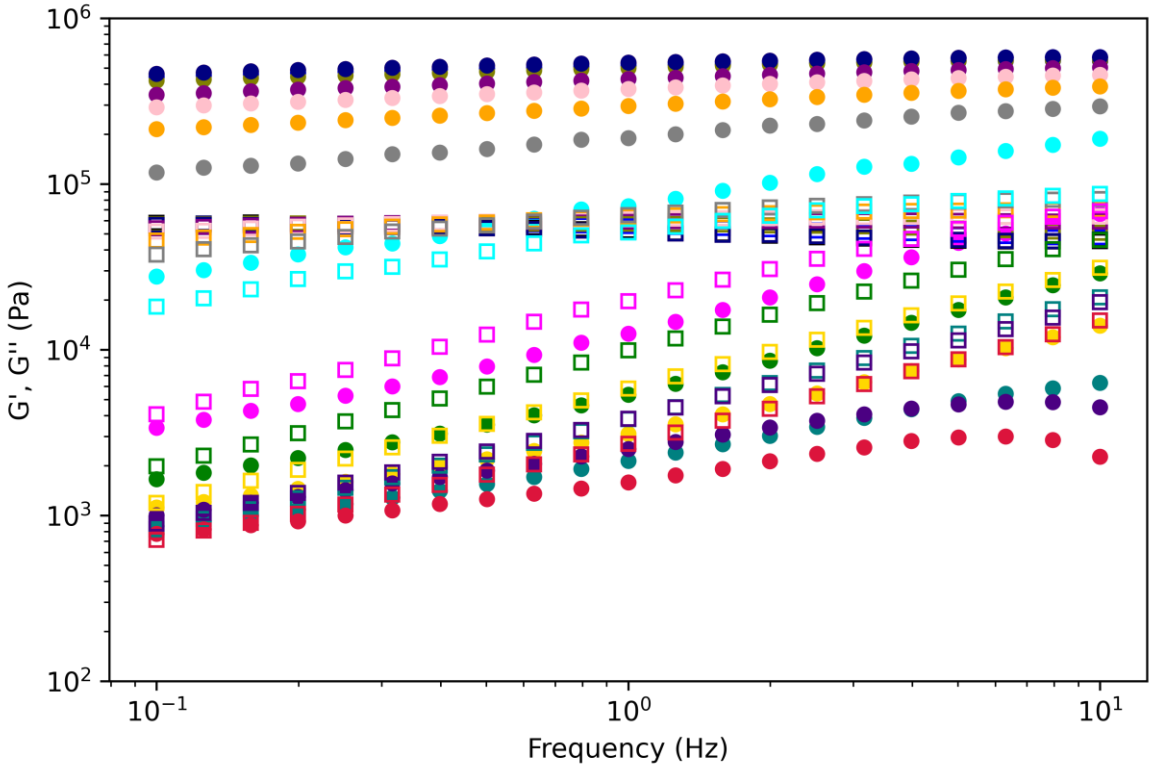

Figure 131. Frequency sweep rheological analysis of **SPU2** at 0 (black), 5 (red), 10 (blue), 15 (olive), 20 (navy), 25 (purple), 30 (pink), 35 (orange), 40 (gray), 45 (cyan), 50 (magenta), 55 (green), 60 (gold), 65 (teal), 70 (crimson), 75 °C (indigo). G' closed symbols and G'' open symbols frequency sweeps were performed between 0.1 to 10 Hz at an applied strain of 0.1%.

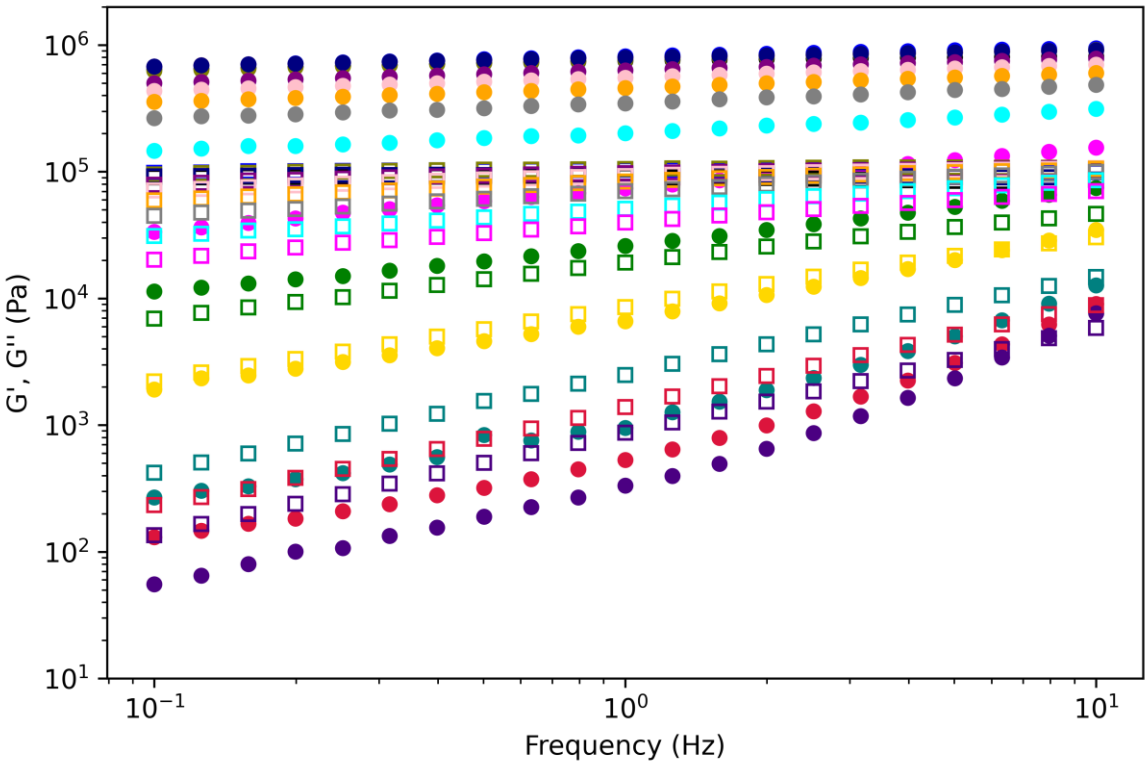

Figure 132. Frequency sweep rheological analysis of **SPU3** at 0 (black), 5 (red), 10 (blue), 15 (olive), 20 (navy), 25 (purple), 30 (pink), 35 (orange), 40 (gray), 45 (cyan), 50 (magenta), 55 (green), 60 (gold), 65 (teal), 70 (crimson), 75 °C (indigo). G' closed symbols and G'' open symbols frequency sweeps were performed between 0.1 to 10 Hz at an applied strain of 0.1%.

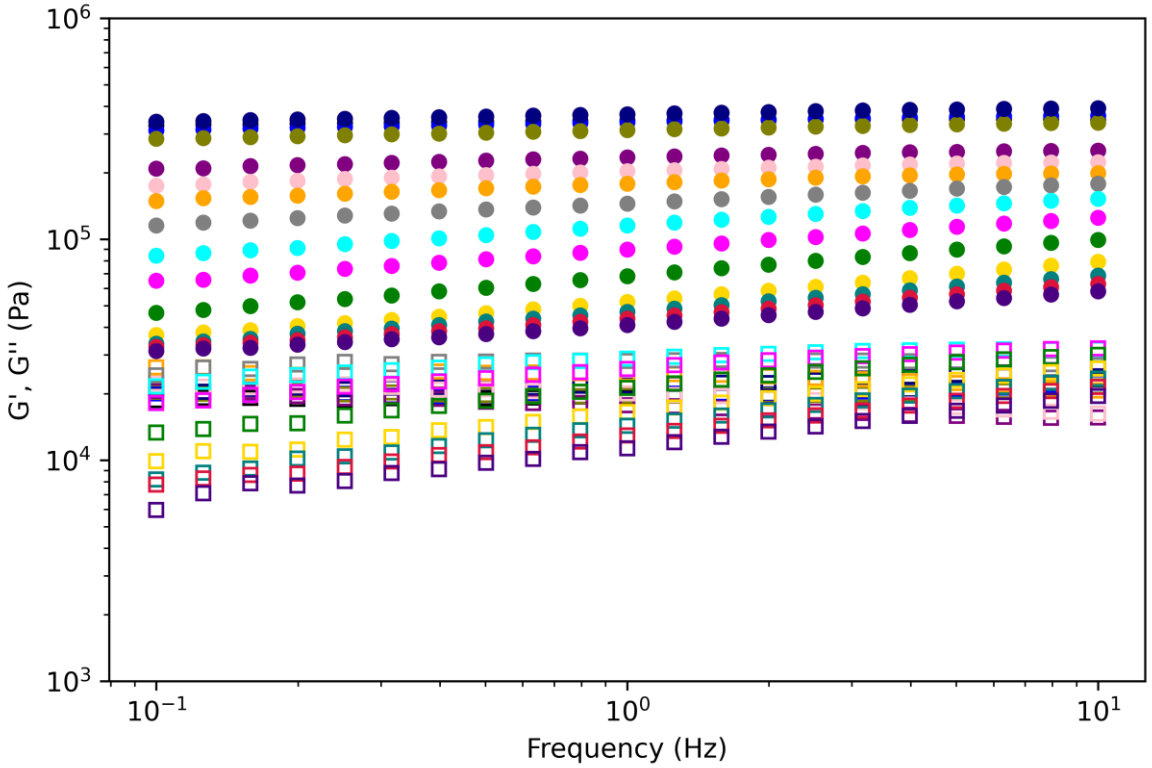

Figure 133. Frequency sweep rheological analysis of **SPU5** at 0 (black), 10 (red), 20 (blue), 30 (olive), 40 (navy), 50 (purple), 60 (pink), 70 (orange), 80 (gray), 90 (cyan), 100 (magenta), 110 (green), 120 (gold), 130 (teal), 140 (crimson), 150 °C (indigo). G' closed symbols and G'' open symbols frequency sweeps were performed between 0.1 to 10 Hz at an applied strain of 0.1%.

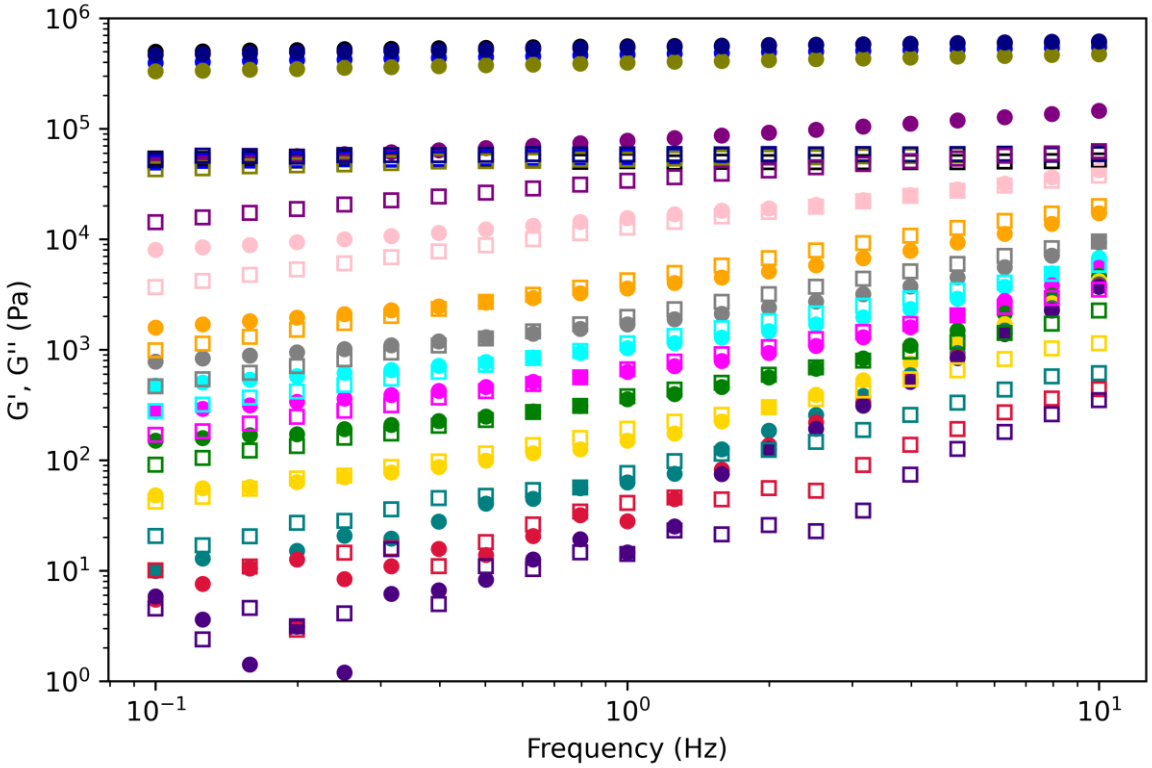

Figure 134. Frequency sweep rheological analysis of **SPU6** at 0 (black), 10 (red), 20 (blue), 30 (olive), 40 (navy), 50 (purple), 60 (pink), 70 (orange), 80 (gray), 90 (cyan), 100 (magenta), 110 (green), 120 (gold), 130 (teal), 140 (crimson), 150 °C (indigo). G' closed symbols and G'' open symbols frequency sweeps were performed between 0.1 to 10 Hz at an applied strain of 0.1%.

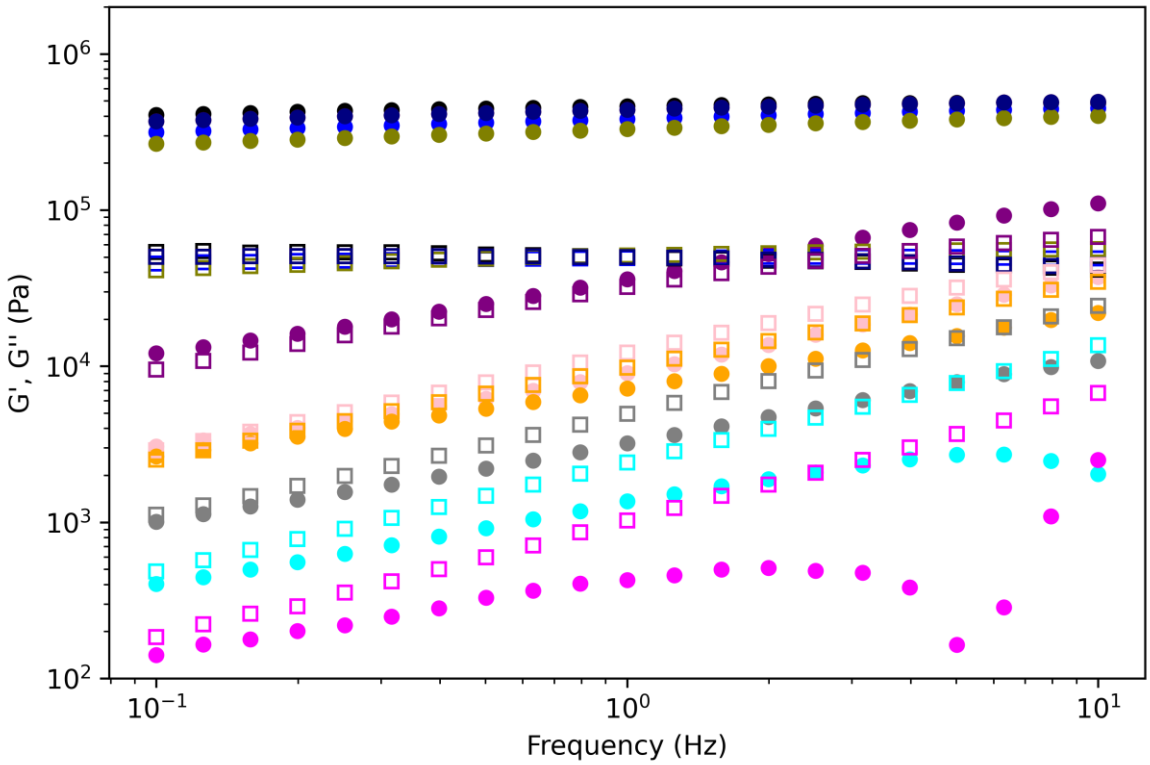

Figure 135. Frequency sweep rheological analysis of **SPU7** at 0 (black), 10 (red), 20 (blue), 30 (olive), 40 (navy), 50 (purple), 60 (pink), 70 (orange), 80 (gray), 90 (cyan), 100 (magenta). G' closed symbols and G'' open symbols frequency sweeps were performed between 0.1 to 10 Hz at an applied strain of 0.1%.

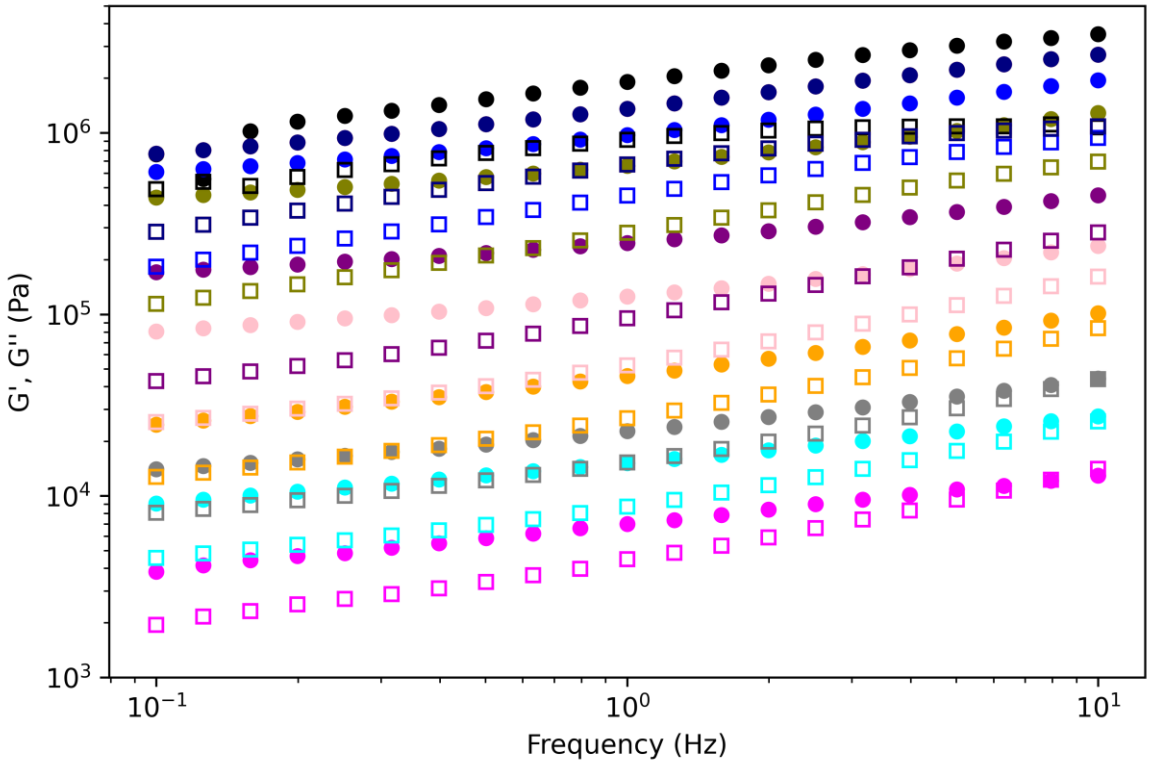

Figure 136. Frequency sweep rheological analysis of **SPU8** at 50 (black), 60 (red), 70 (blue), 80 (olive), 90 (navy), 100 (purple), 110 (pink), 120 (orange), 130 (gray), 140 (cyan), 150 (magenta). G' closed symbols and G'' open symbols frequency sweeps were performed between 0.1 to 10 Hz at an applied strain of 0.1%.

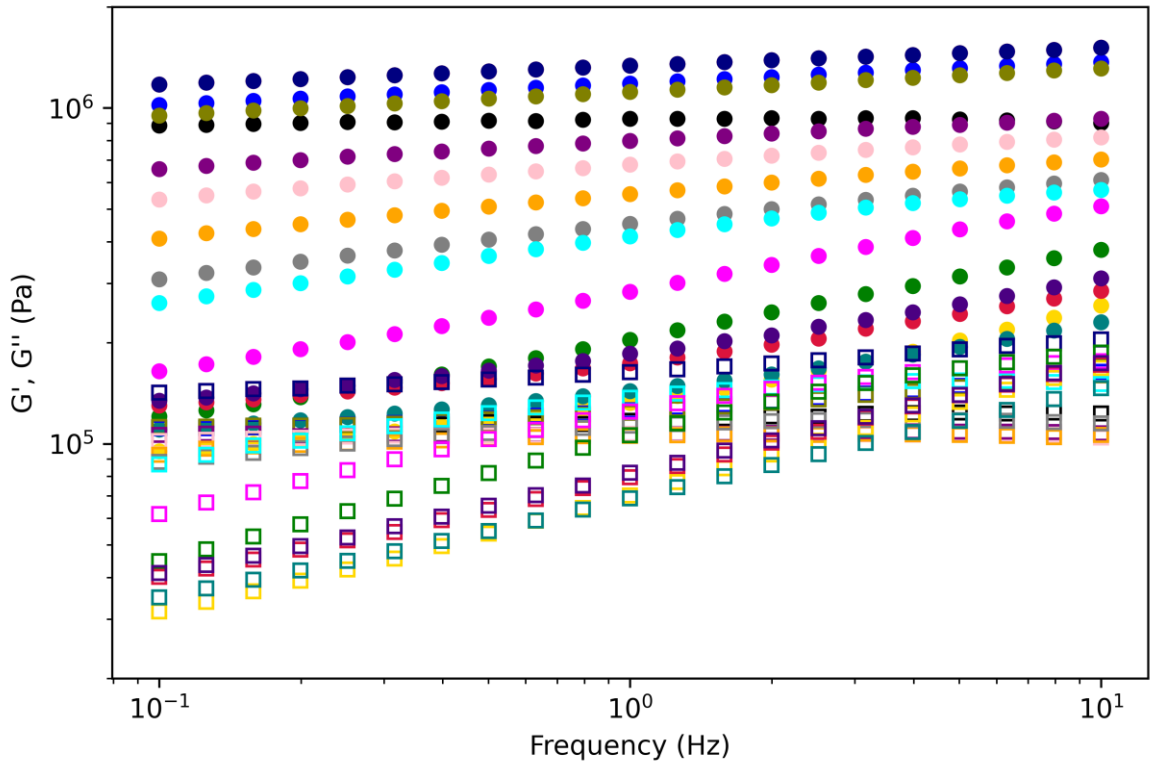

Figure 137. Frequency sweep rheological analysis of **SPU10** at 0 (black), 10 (red), 20 (blue), 30 (olive), 40 (navy), 50 (purple), 60 (pink), 70 (orange), 80 (gray), 90 (cyan), 100 (magenta), 110 (green), 120 (gold), 130 (teal), 140 (crimson), 150 °C (indigo). G' closed symbols and G'' open symbols frequency sweeps were performed between 0.1 to 10 Hz at an applied strain of 0.1%.

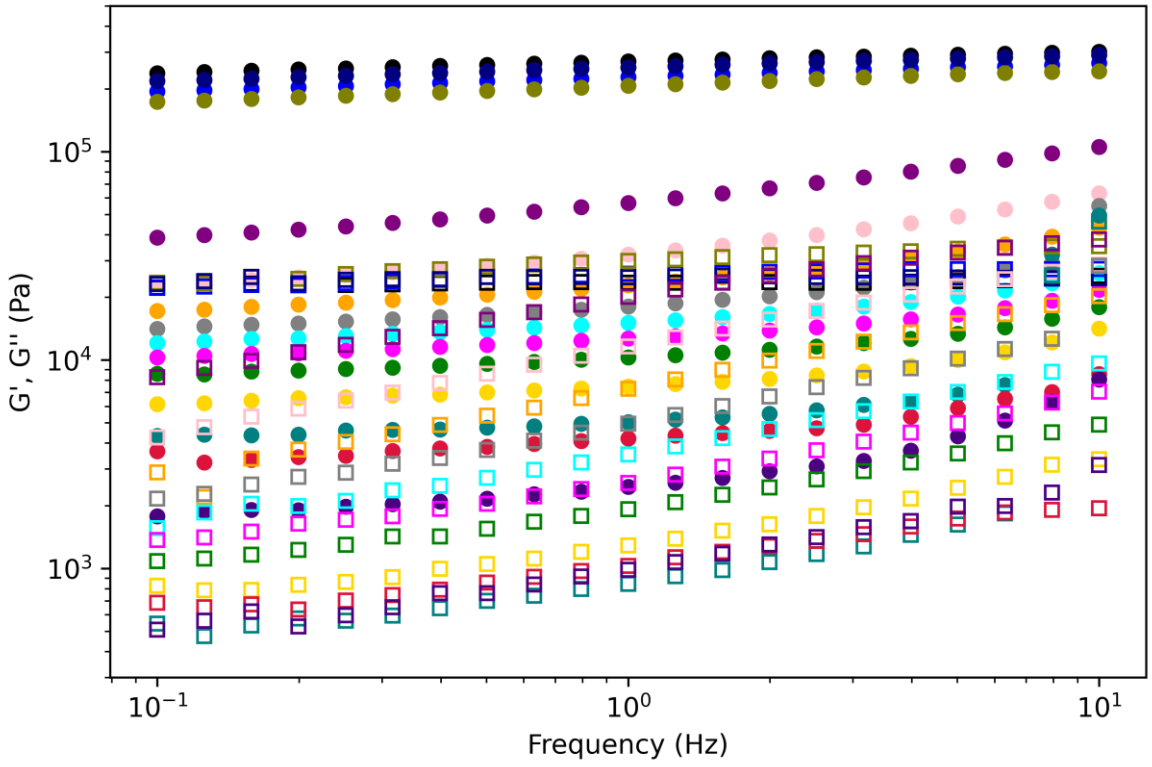

Figure 138. Frequency sweep rheological analysis of **SPU11** at 0 (black), 10 (red), 20 (blue), 30 (olive), 40 (navy), 50 (purple), 60 (pink), 70 (orange), 80 (gray), 90 (cyan), 100 (magenta), 110 (green), 120 (gold), 130 (teal), 140 (crimson), 150 °C (indigo). G' closed symbols and G'' open symbols frequency sweeps were performed between 0.1 to 10 Hz at an applied strain of 0.1%.

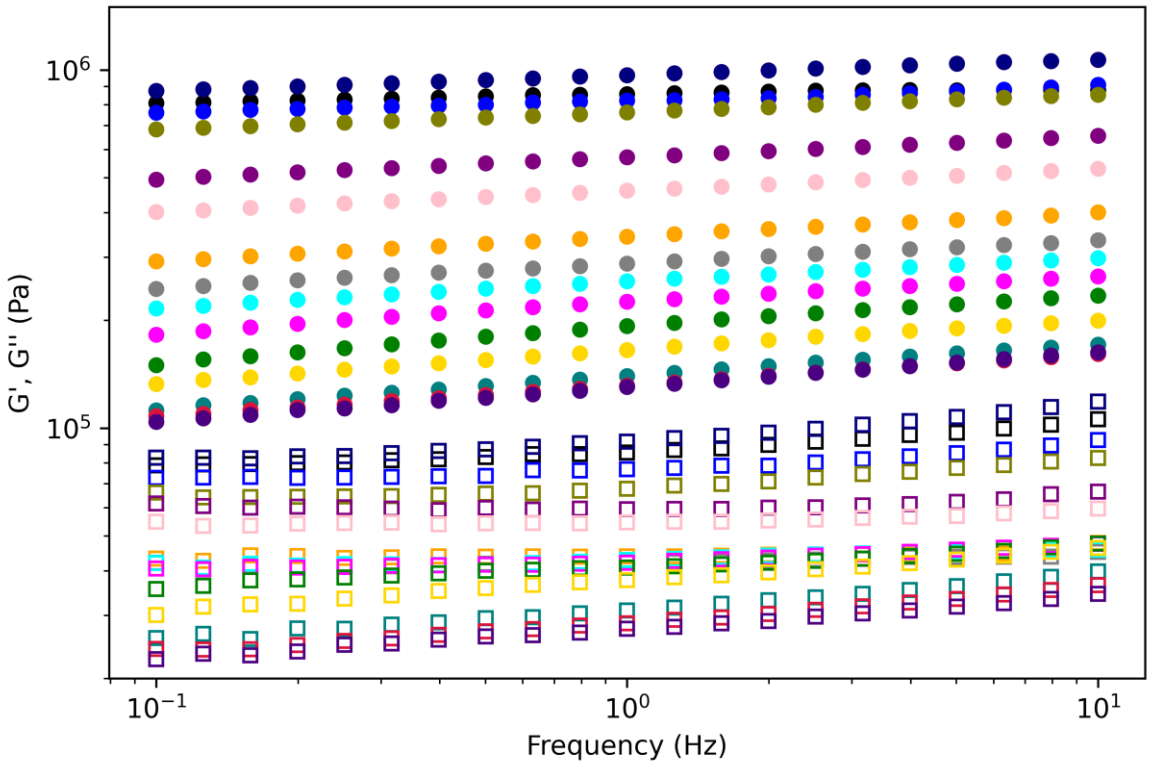

Figure 139. Frequency sweep rheological analysis of **SPU12** at 0 (black), 10 (red), 20 (blue), 30 (olive), 40 (navy), 50 (purple), 60 (pink), 70 (orange), 80 (gray), 90 (cyan), 100 (magenta), 110 (green), 120 (gold), 130 (teal), 140 (crimson), 150 °C (indigo). G' closed symbols and G'' open symbols frequency sweeps were performed between 0.1 to 10 Hz at an applied strain of 0.1%.

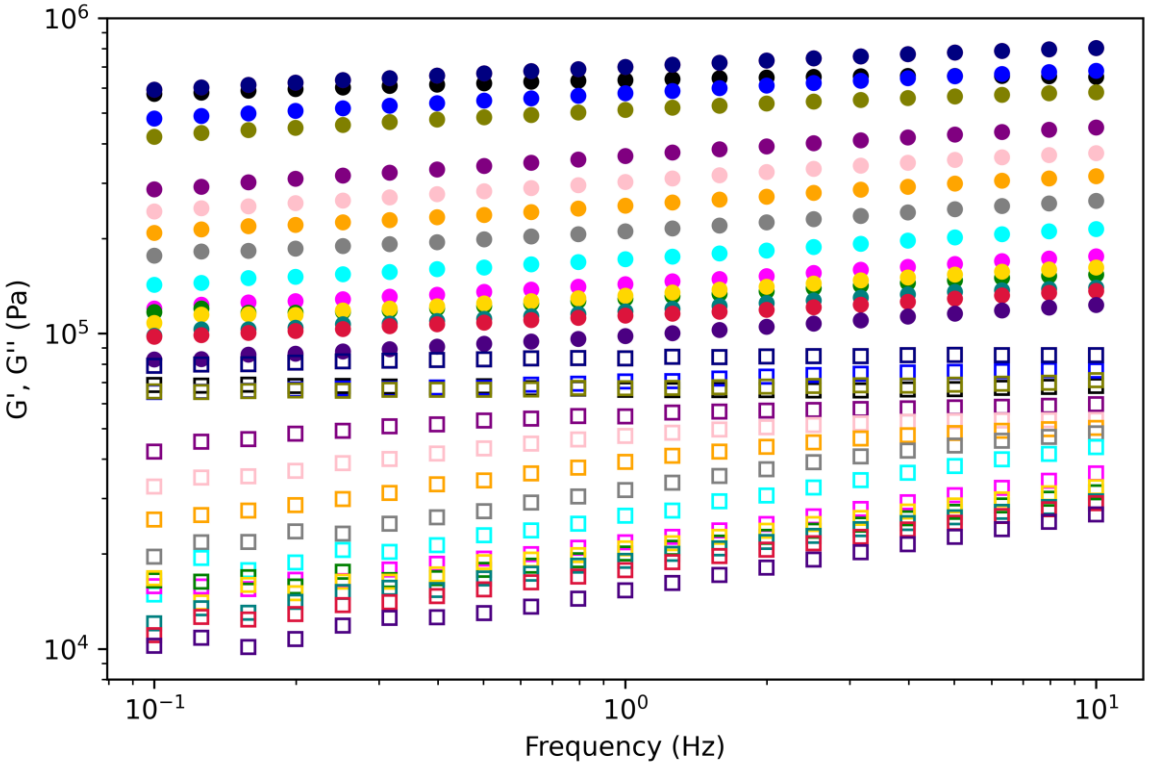

Figure 140. Frequency sweep rheological analysis of **SPU13** at 0 (black), 10 (red), 20 (blue), 30 (olive), 40 (navy), 50 (purple), 60 (pink), 70 (orange), 80 (gray), 90 (cyan), 100 (magenta), 110 (green), 120 (gold), 130 (teal), 140 (crimson), 150 °C (indigo). G' closed symbols and G'' open symbols frequency sweeps were performed between 0.1 to 10 Hz at an applied strain of 0.1%.

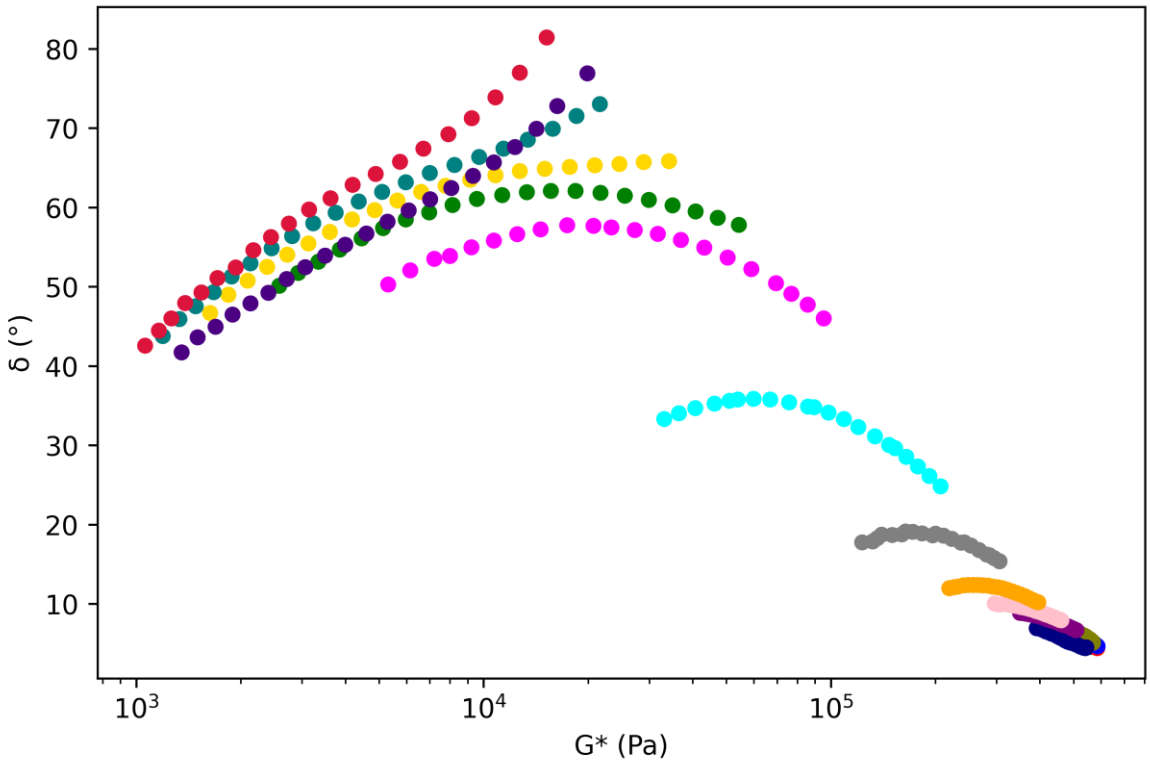

Figure 141. van Gurp-Palmen plot of **SPU2** at 0 (black), 5 (red), 10 (blue), 15 (olive), 20 (navy), 25 (purple), 30 (pink), 35 (orange), 40 (gray), 45 (cyan), 50 (magenta), 55 (green), 60 (gold), 65 (teal), 70 (crimson), 75 °C (indigo). Frequency sweeps were performed between 0.1 to 10 Hz at an applied strain of 0.1%.

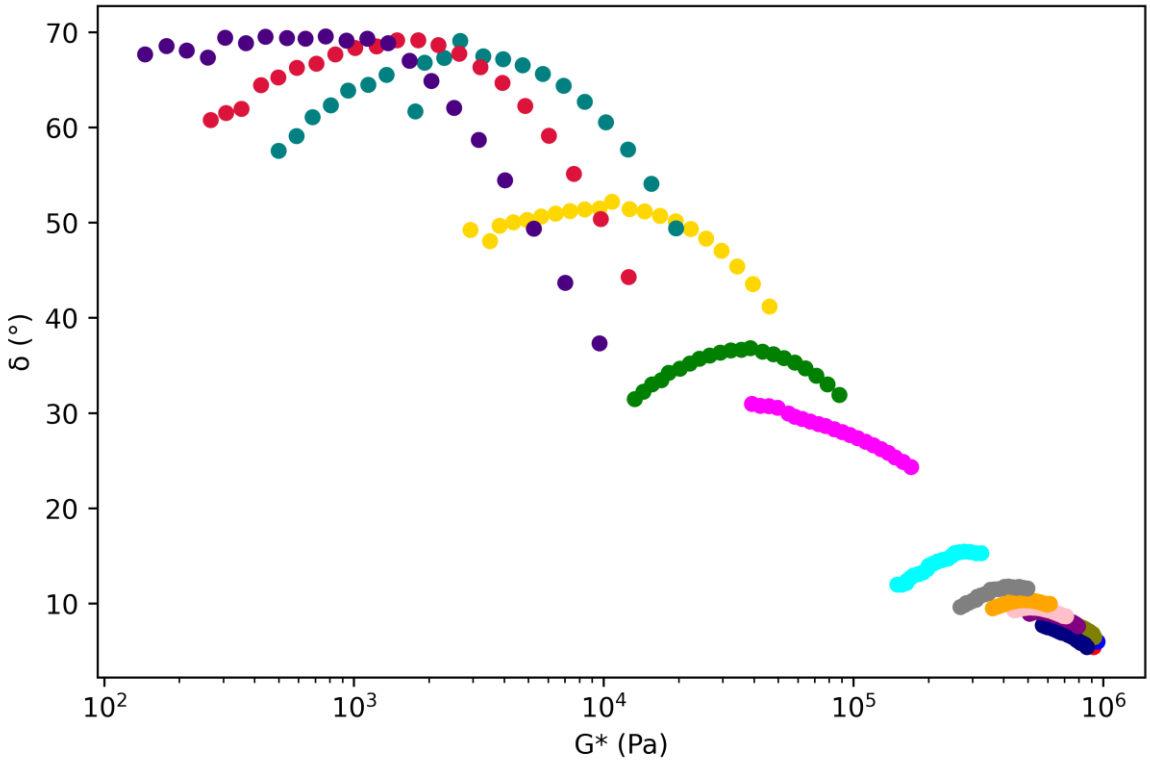

Figure 142. van Gurp-Palmen plot of **SPU3** at 0 (black), 5 (red), 10 (blue), 15 (olive), 20 (navy), 25 (purple), 30 (pink), 35 (orange), 40 (gray), 45 (cyan), 50 (magenta), 55 (green), 60 (gold), 65 (teal), 70 (crimson), 75 °C (indigo). Frequency sweeps were performed between 0.1 to 10 Hz at an applied strain of 0.1%.

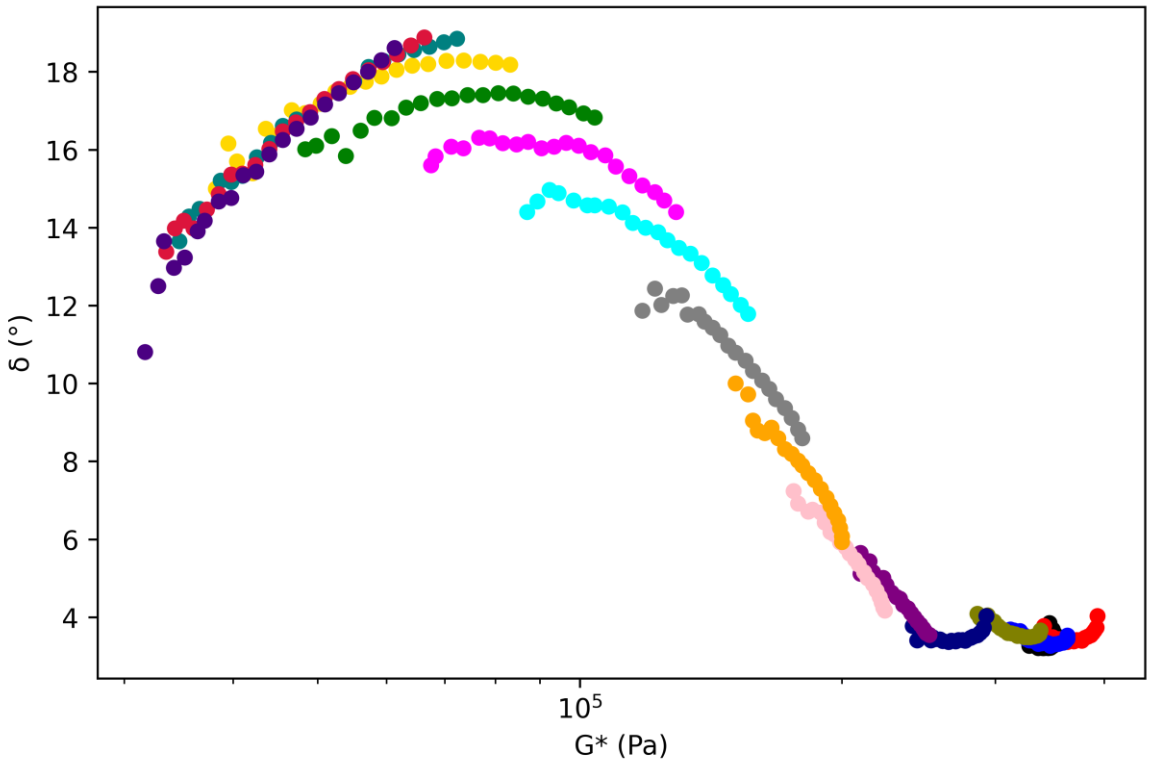

Figure 143. van Gurp-Palmen plot of **SPU5** at 0 (black), 10 (red), 20 (blue), 30 (olive), 40 (navy), 50 (purple), 60 (pink), 70 (orange), 80 (gray), 90 (cyan), 100 (magenta), 110 (green), 120 (gold), 130 (teal), 140 (crimson), 150 °C (indigo). Frequency sweeps were performed between 0.1 to 10 Hz at an applied strain of 0.1%.

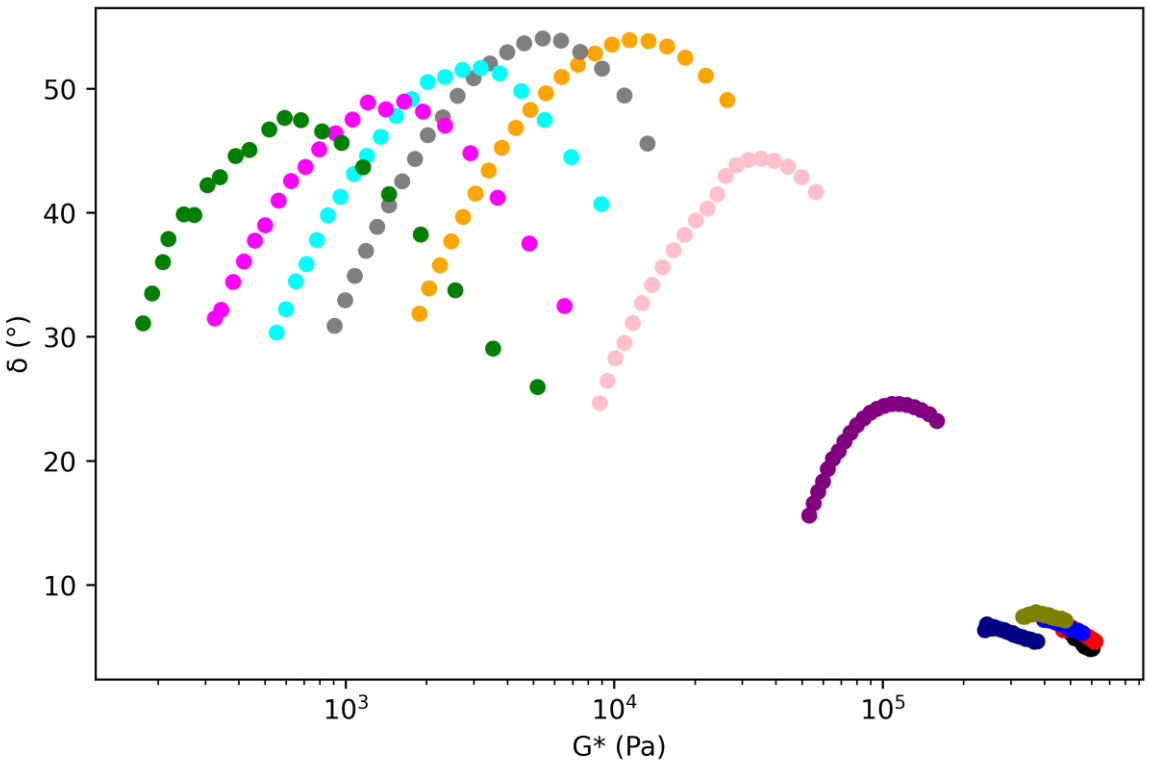

Figure 144. van Gurp-Palmen plot of **SPU6** at 0 (black), 10 (red), 20 (blue), 30 (olive), 40 (navy), 50 (purple), 60 (pink), 70 (orange), 80 (gray), 90 (cyan), 100 (magenta), 110 (green), 120 (gold), 130 (teal), 140 (crimson), 150 °C (indigo). Frequency sweeps were performed between 0.1 to 10 Hz at an applied strain of 0.1%.

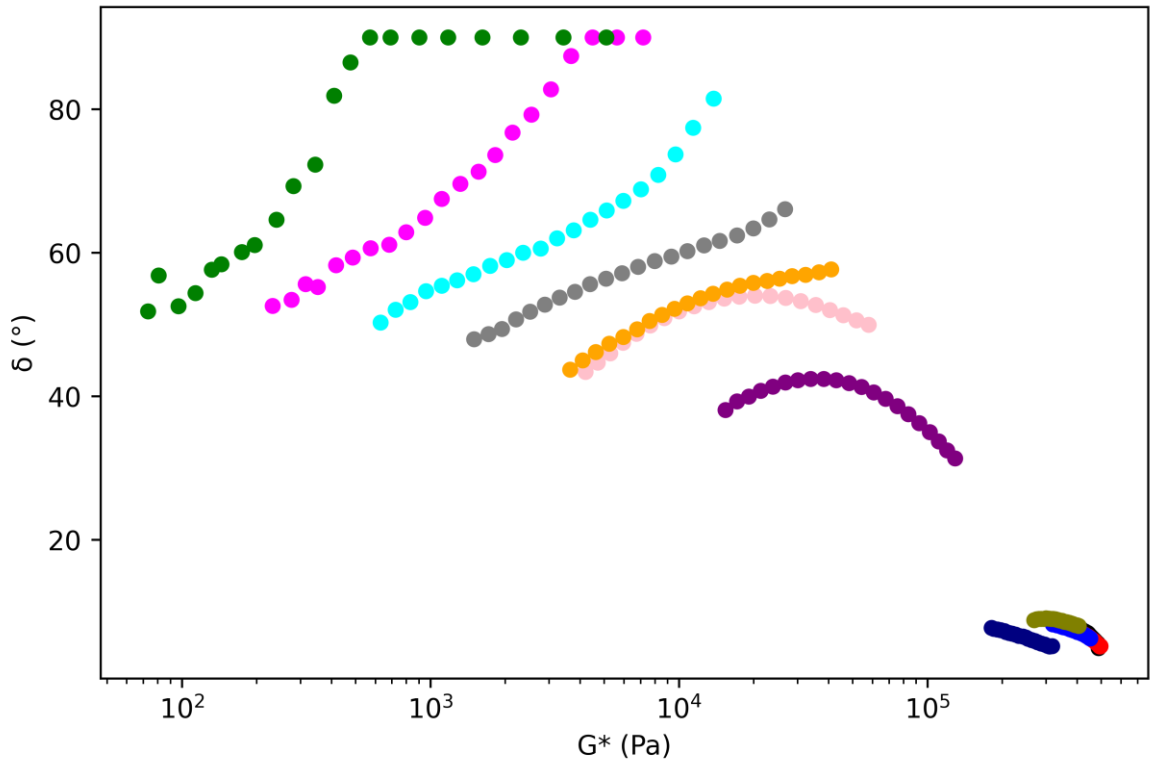

Figure 145. van Gurp-Palmen plot of **SPU7** at 0 (black), 10 (red), 20 (blue), 30 (olive), 40 (navy), 50 (purple), 60 (pink), 70 (orange), 80 (gray), 90 (cyan), 100 (magenta). Frequency sweeps were performed between 0.1 to 10 Hz at an applied strain of 0.1%.

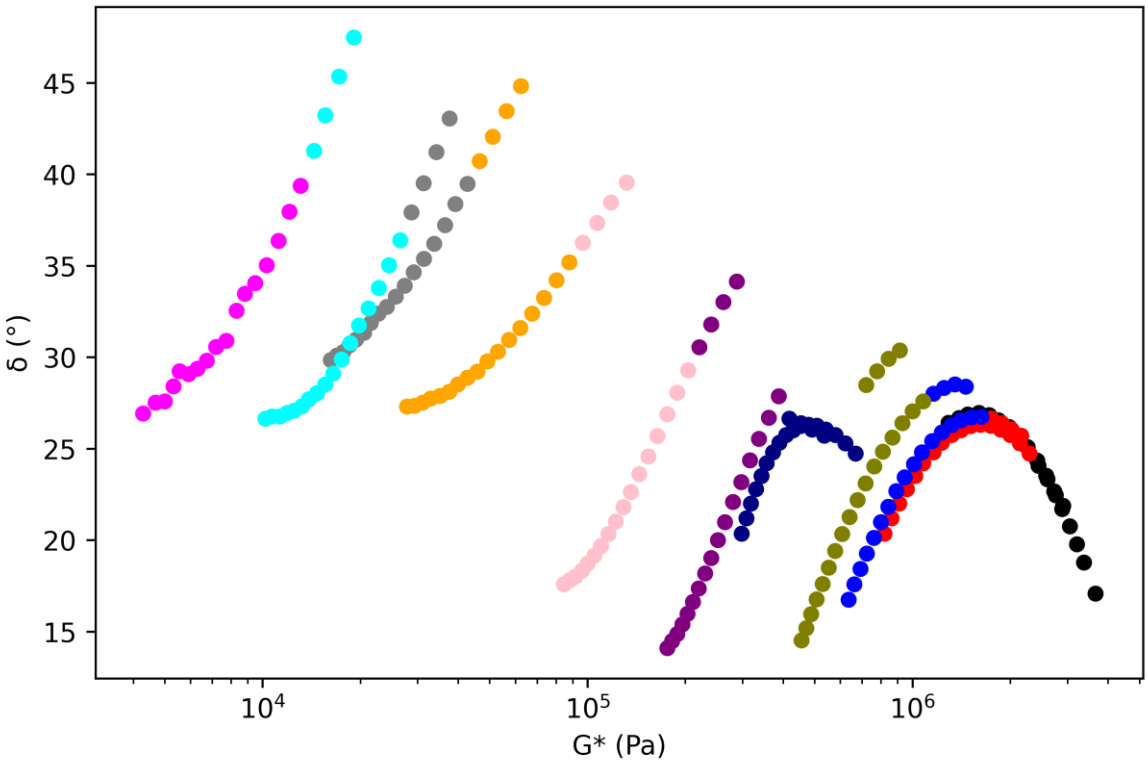

Figure 146. van Gurp-Palmen plot of **SPU8** at 50 (black), 60 (red), 70 (blue), 80 (olive), 90 (navy), 100 (purple), 110 (pink), 120 (orange), 130 (gray), 140 (cyan), 150 (magenta). G' closed symbols and G'' open symbols frequency sweeps were performed between 0.1 to 10 Hz at an applied strain of 0.1%.

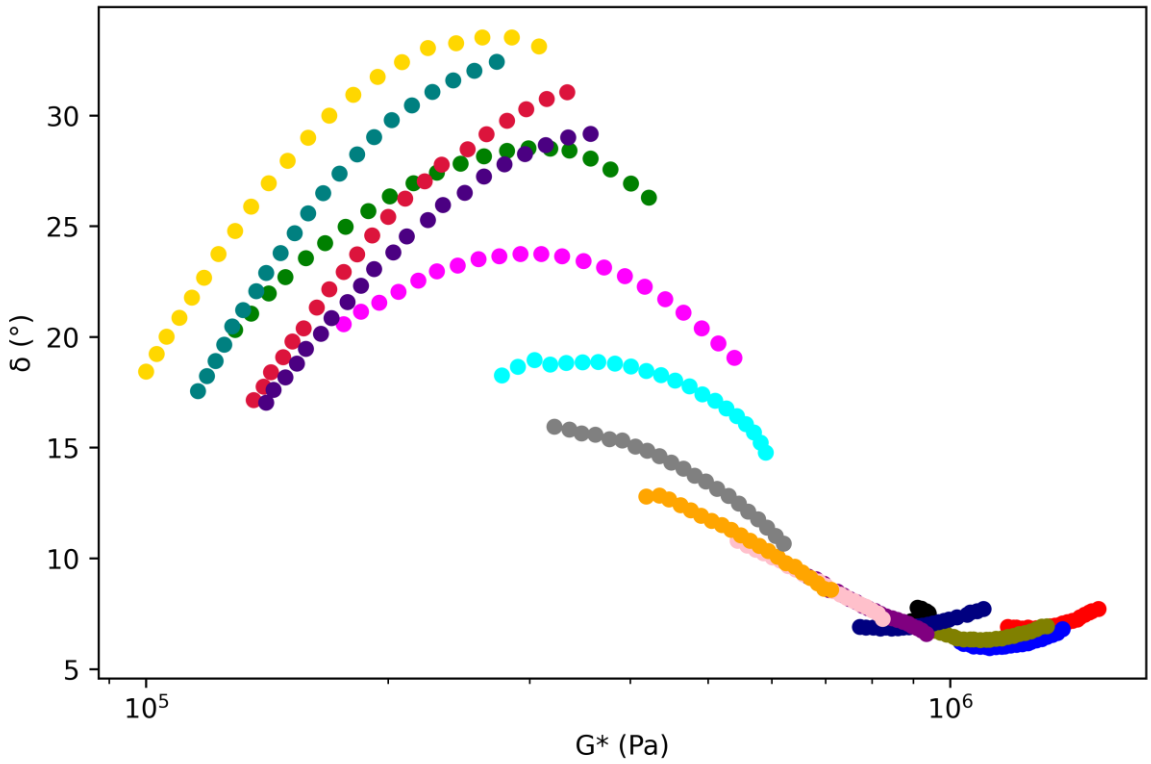

Figure 147. van Gurp-Palmen plot of **SPU10** at 0 (black), 10 (red), 20 (blue), 30 (olive), 40 (navy), 50 (purple), 60 (pink), 70 (orange), 80 (gray), 90 (cyan), 100 (magenta), 110 (green), 120 (gold), 130 (teal), 140 (crimson), 150 °C (indigo). Frequency sweeps were performed between 0.1 to 10 Hz at an applied strain of 0.1%.

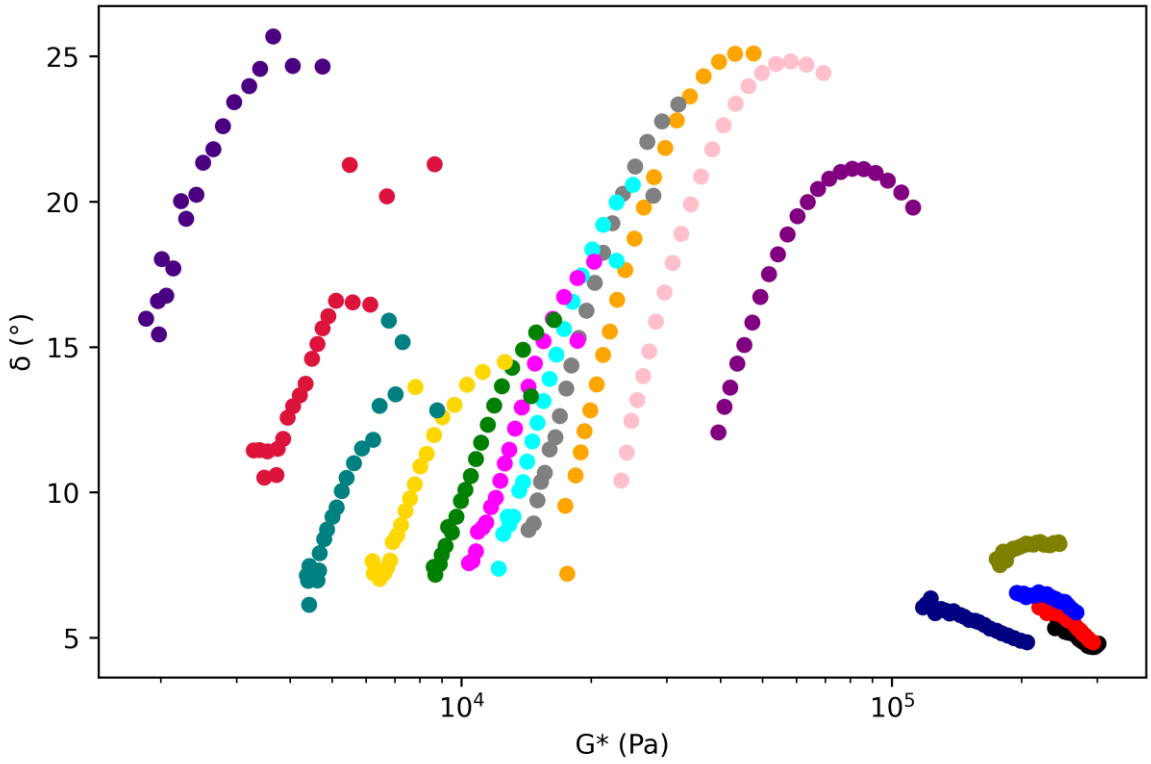

Figure 148. van Gurp-Palmen plot of **SPU11** at 0 (black), 10 (red), 20 (blue), 30 (olive), 40 (navy), 50 (purple), 60 (pink), 70 (orange), 80 (gray), 90 (cyan), 100 (magenta), 110 (green), 120 (gold), 130 (teal), 140 (crimson), 150 °C (indigo). Frequency sweeps were performed between 0.1 to 10 Hz at an applied strain of 0.1%.

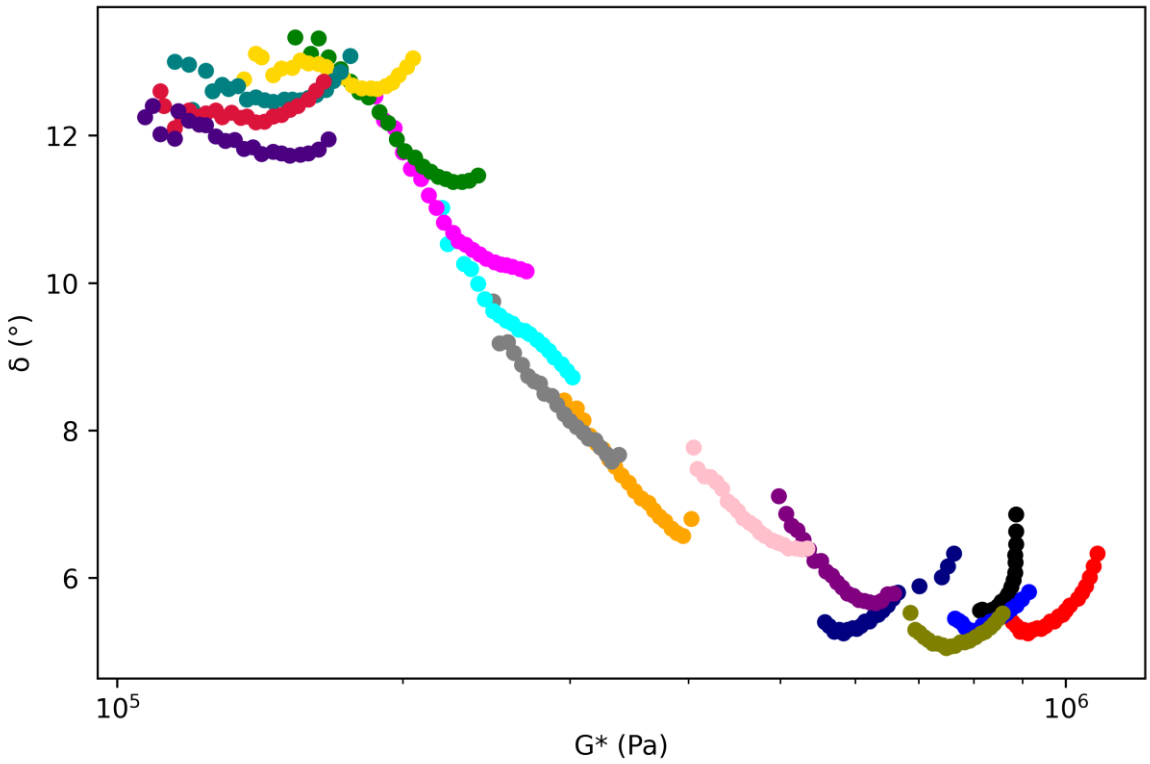

Figure 149. van Gurp-Palmen plot of **SPU12** at 0 (black), 10 (red), 20 (blue), 30 (olive), 40 (navy), 50 (purple), 60 (pink), 70 (orange), 80 (gray), 90 (cyan), 100 (magenta), 110 (green), 120 (gold), 130 (teal), 140 (crimson), 150 °C (indigo). Frequency sweeps were performed between 0.1 to 10 Hz at an applied strain of 0.1%.

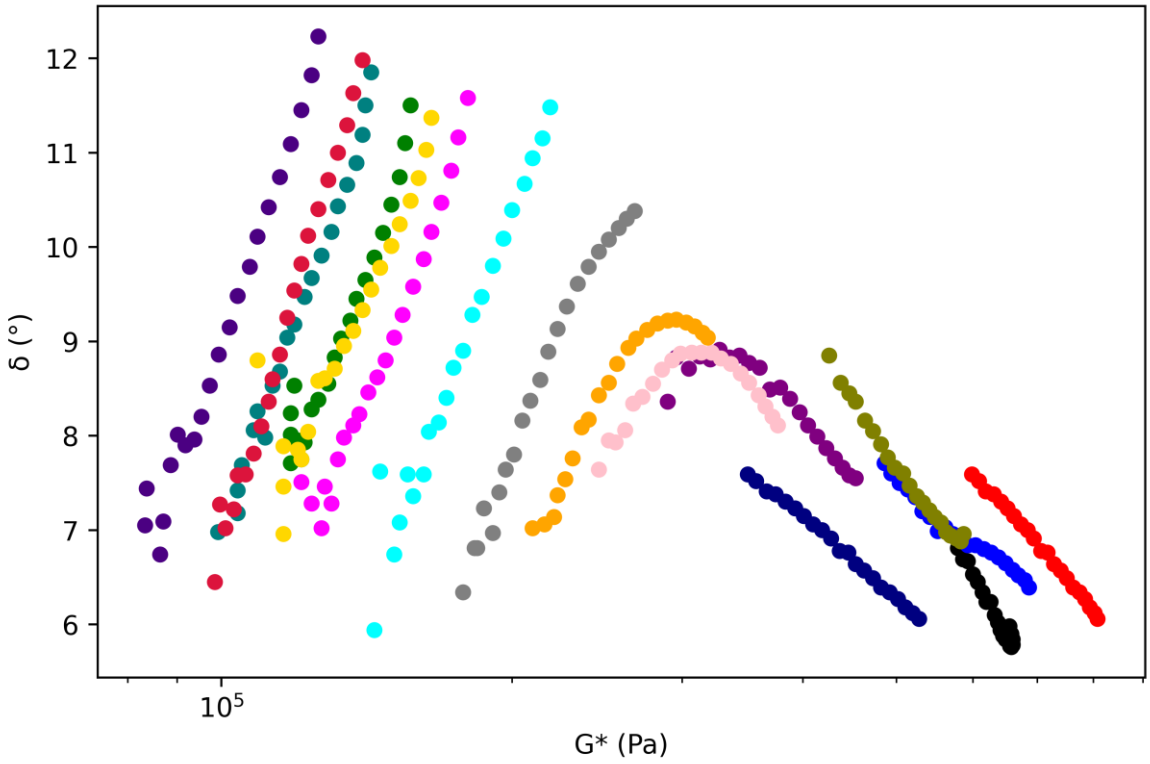

Figure 150. van Gurp-Palmen plot of **SPU13** at 0 (black), 10 (red), 20 (blue), 30 (olive), 40 (navy), 50 (purple), 60 (pink), 70 (orange), 80 (gray), 90 (cyan), 100 (magenta), 110 (green), 120 (gold), 130 (teal), 140 (crimson), 150 °C (indigo). Frequency sweeps were performed between 0.1 to 10 Hz at an applied strain of 0.1%.

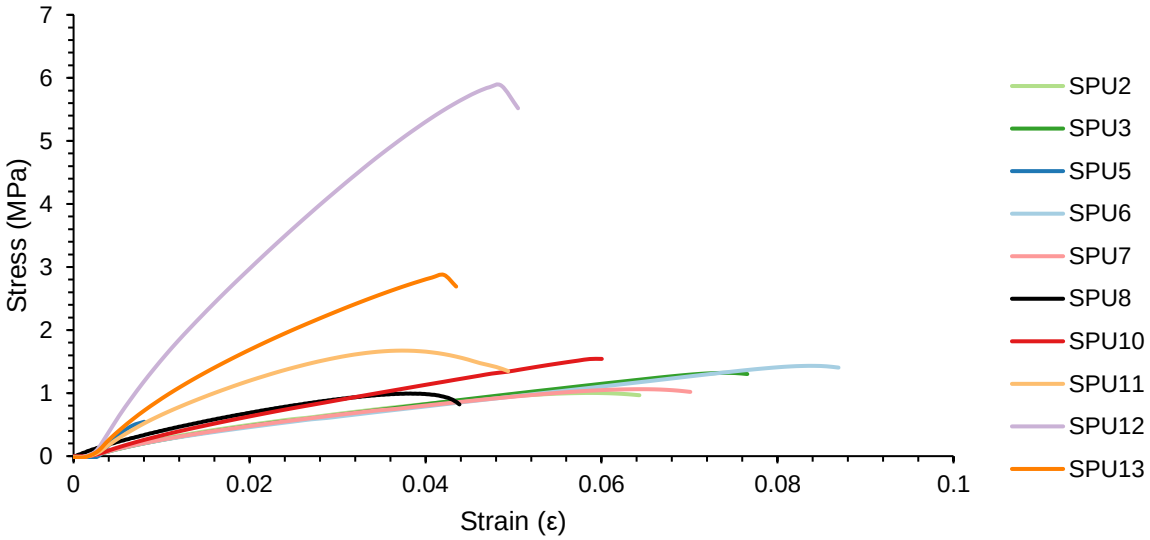

Figure 151. Representative stress-strain curves of the adhered supramolecular elastomers **SPU2**, **SPU3**, **SPU5**-**SPU8**, and **SPU10**-**SPU13** to glass.

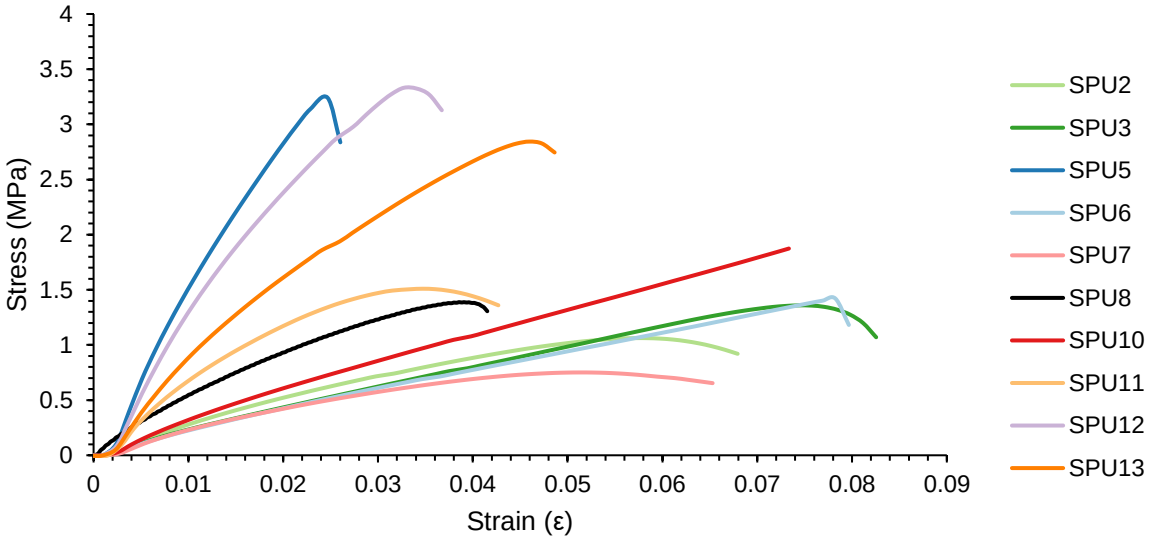

Figure 152. Representative stress-strain curves of the adhered supramolecular elastomers **SPU2**, **SPU3**, **SPU5**-**SPU8**, and **SPU10**-**SPU13** to aluminium.

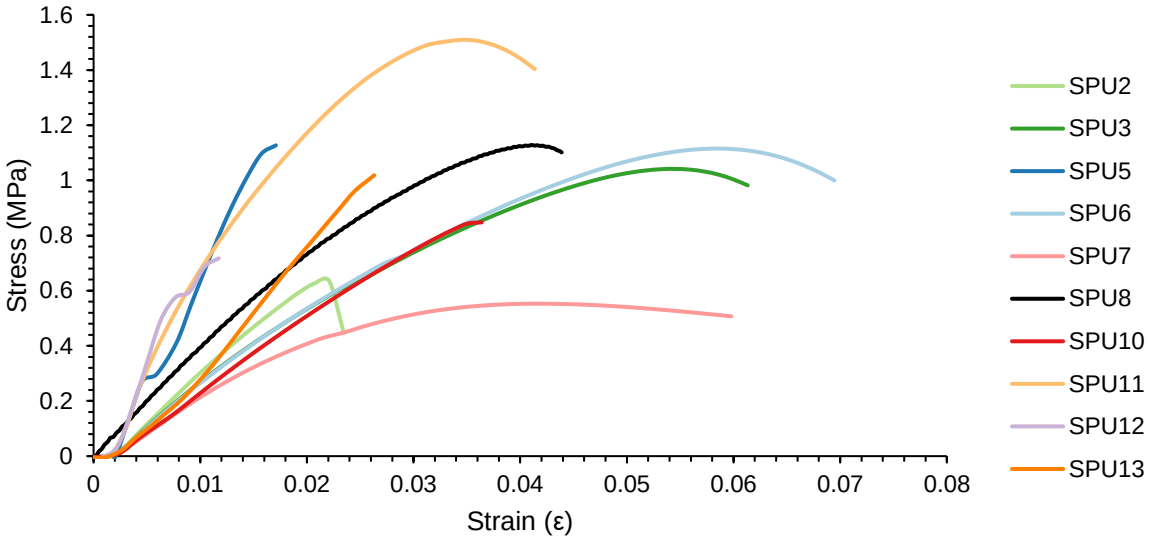

Figure 153. Representative stress-strain curves of the adhered supramolecular elastomers **SPU2**, **SPU3**, **SPU5**-**SPU8**, and **SPU10**-**SPU13** to HDPE.

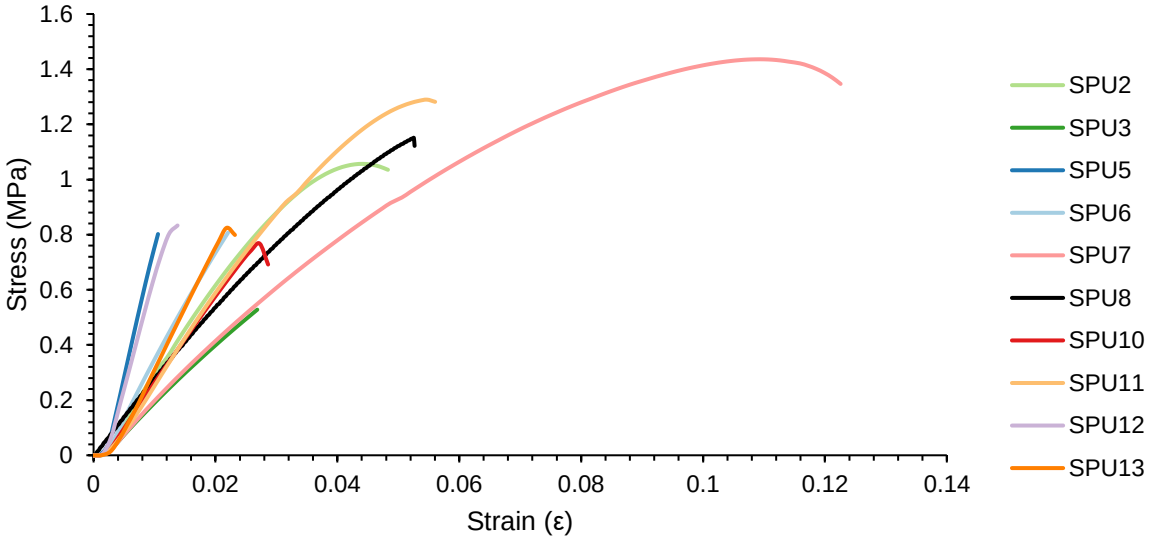

Figure 154. Representative stress-strain curves of the adhered supramolecular elastomers **SPU2**, **SPU3**, **SPU5**-**SPU8**, and **SPU10**-**SPU13** to PP.

Figure 155. An image of a 7 mm diameter sample of **SPU12** adhered between 2 glass slides holding a 2 lb (0.907 Kg) weight.

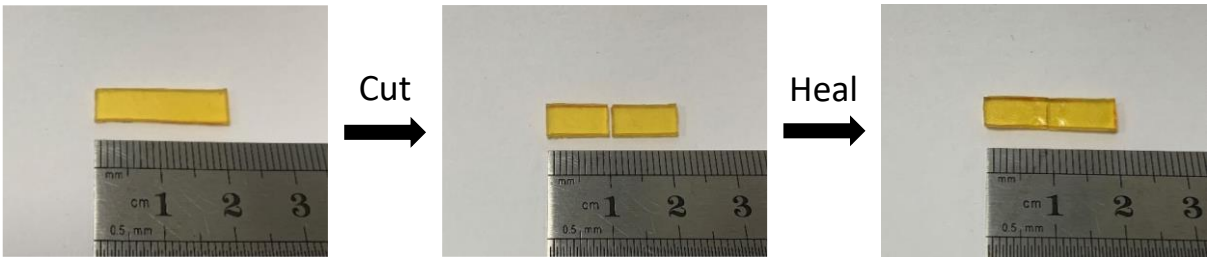

Figure 156. Images of the healing process for SPU SPU11.

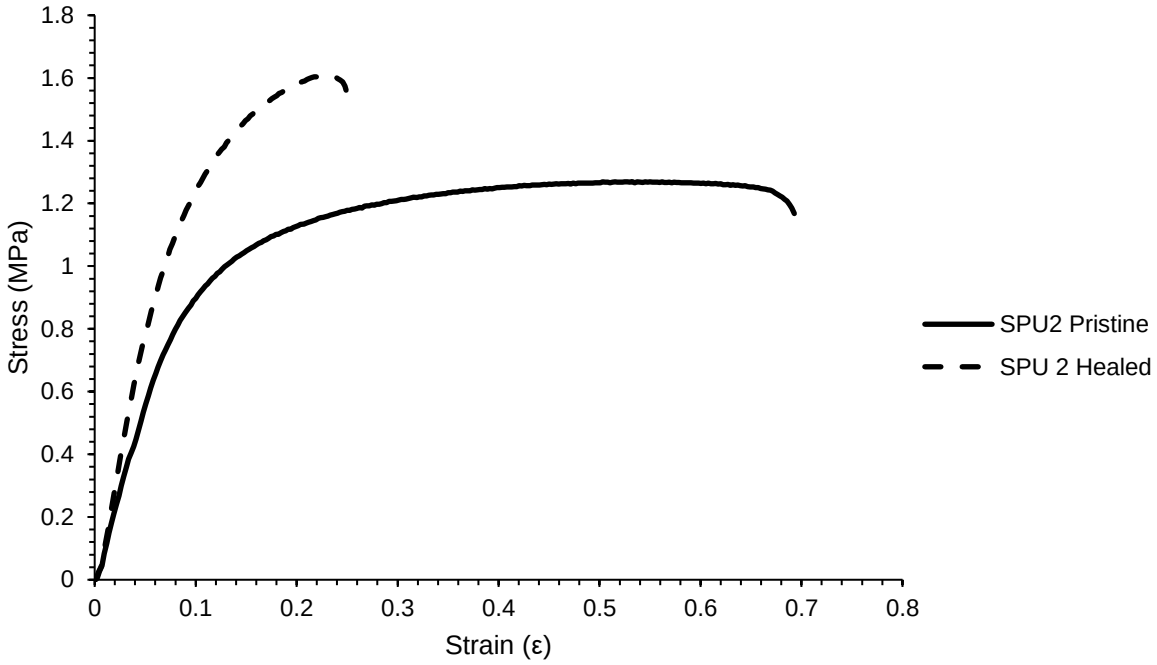

Figure 157. Representative stress-strain curves of the pristine and healed supramolecular elastomer **SPU2**.

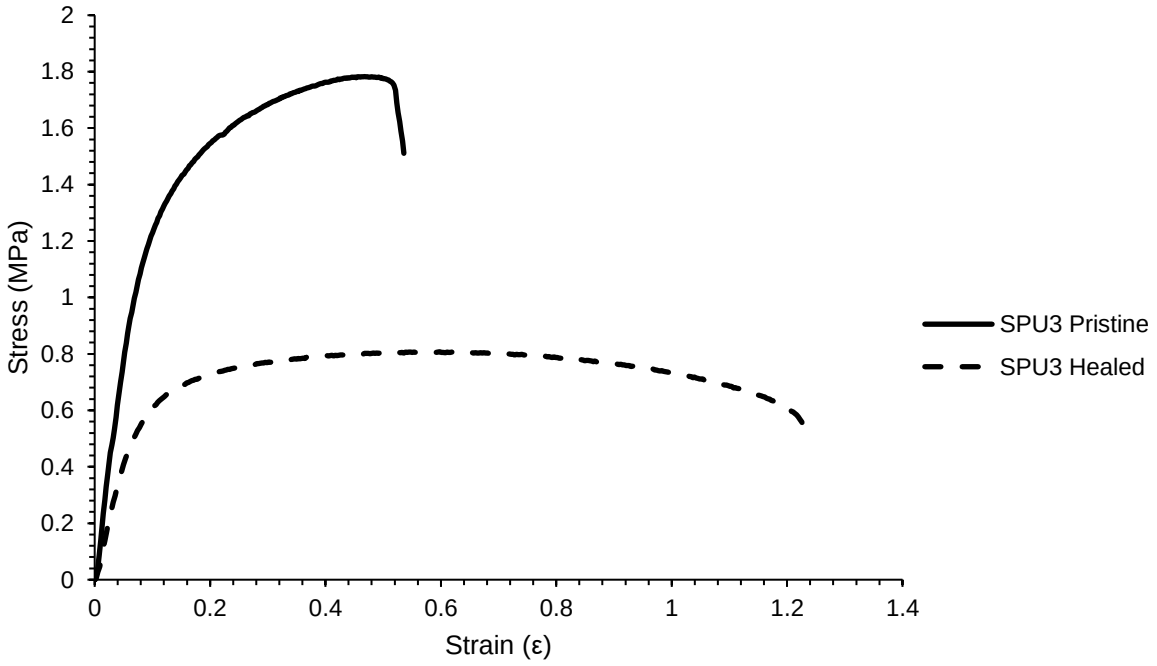

Figure 158. Representative stress-strain curves of the pristine and healed supramolecular elastomer **SPU3**.

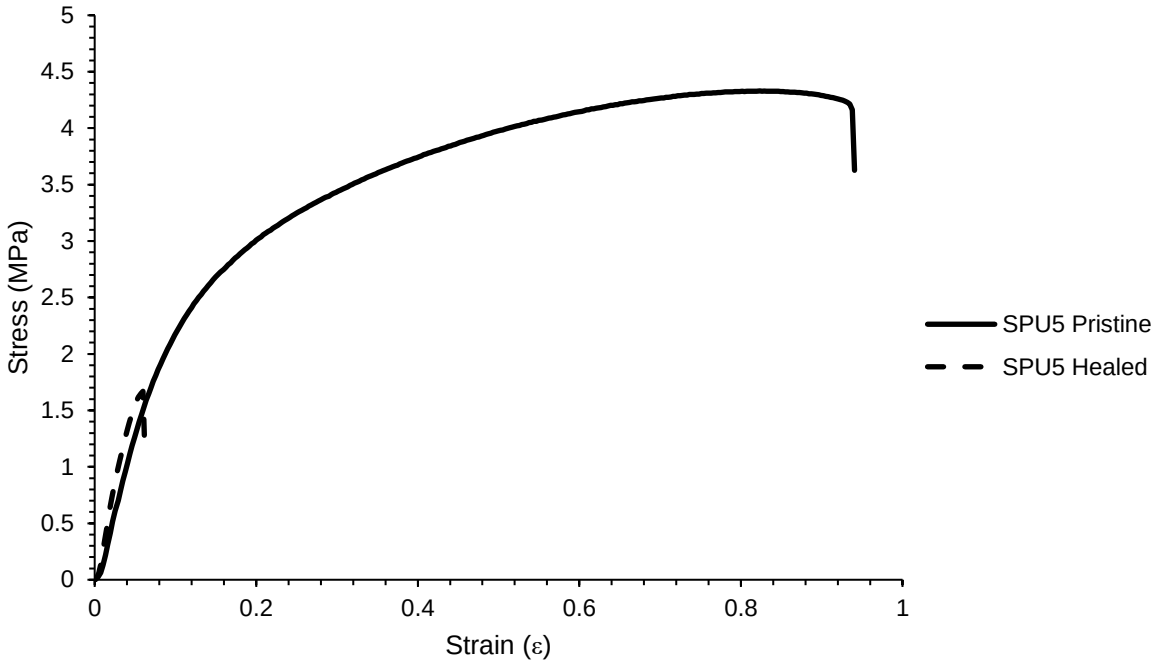

Figure 159. Representative stress-strain curves of the pristine and healed supramolecular elastomer **SPU5**.

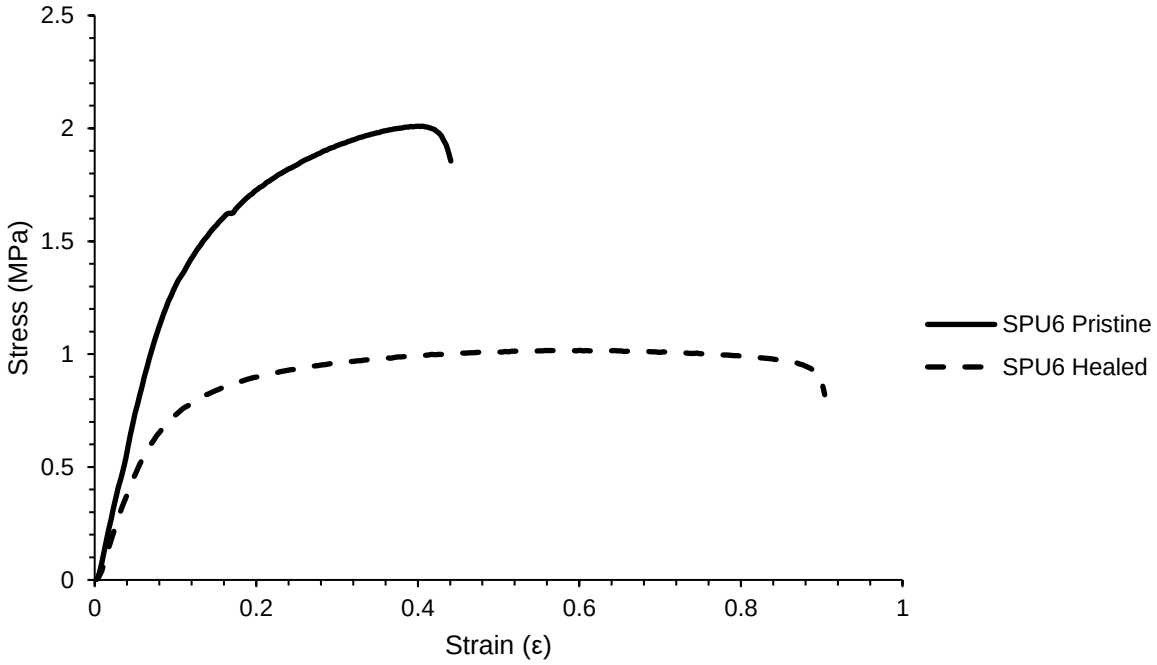

Figure 160. Representative stress-strain curves of the pristine and healed supramolecular elastomer **SPU6**.

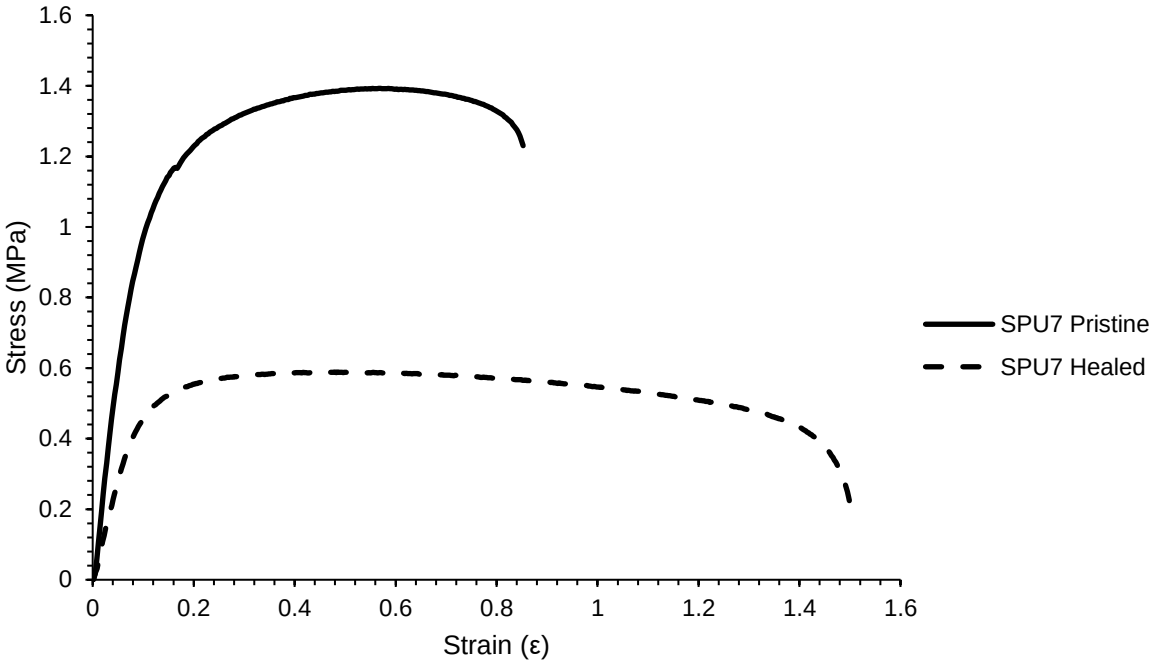

Figure 161. Representative stress-strain curves of the pristine and healed supramolecular elastomer **SPU7**.

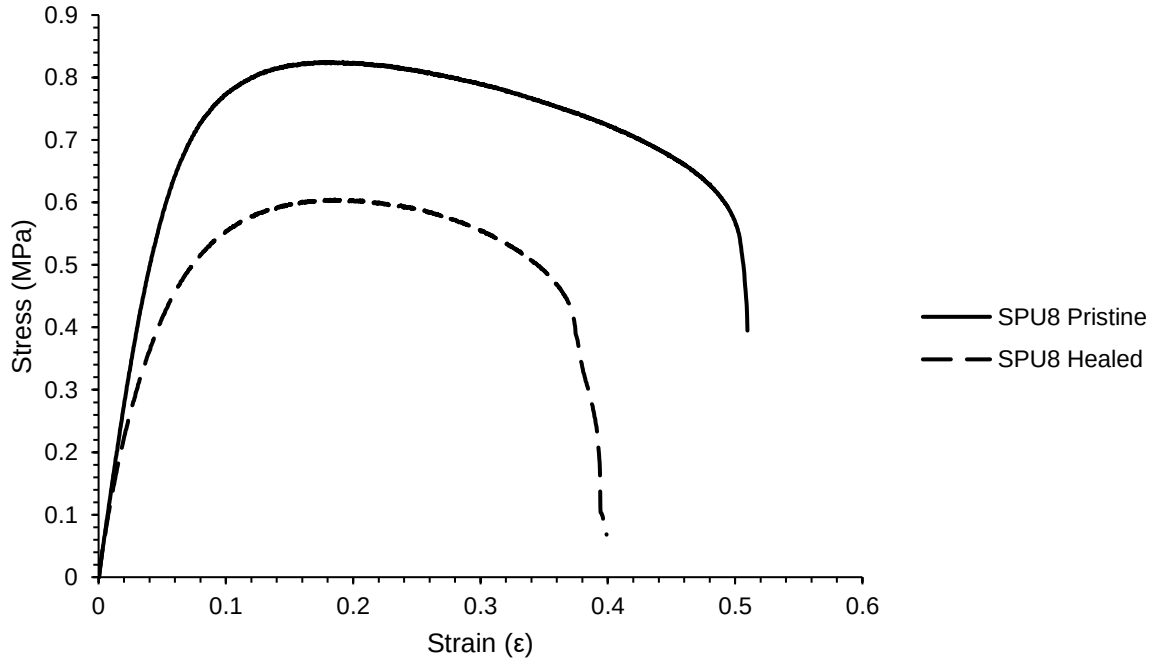

Figure 162. Representative stress-strain curves of the pristine and healed supramolecular elastomer **SPU8**.

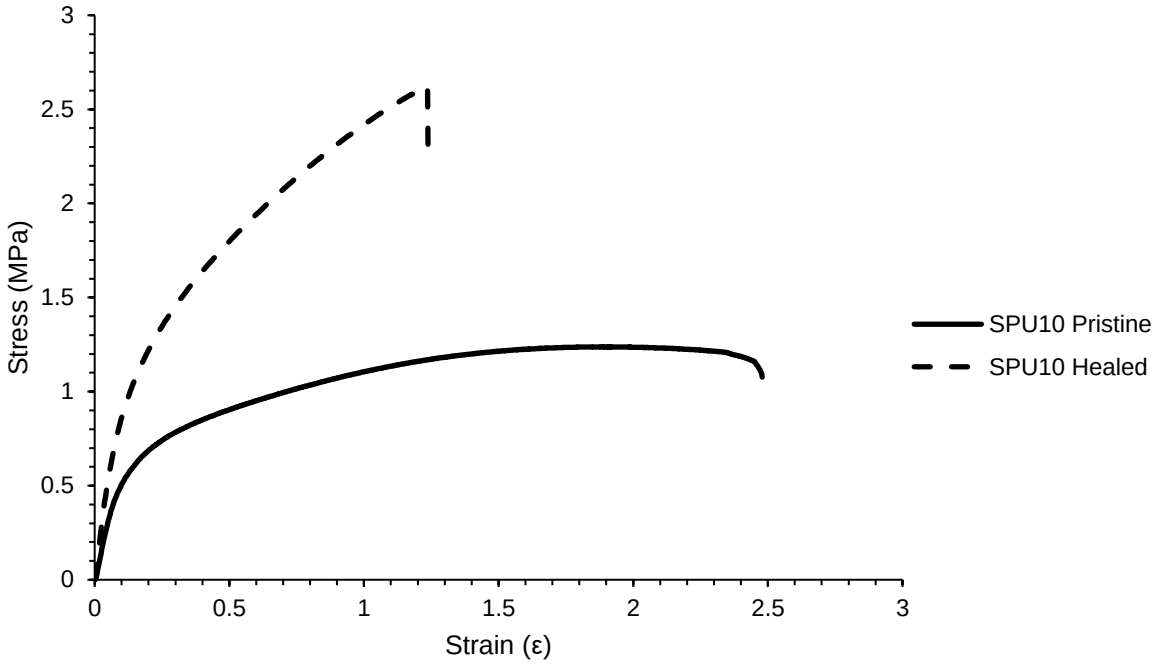

Figure 163. Representative stress-strain curves of the pristine and healed supramolecular elastomer **SPU10**.

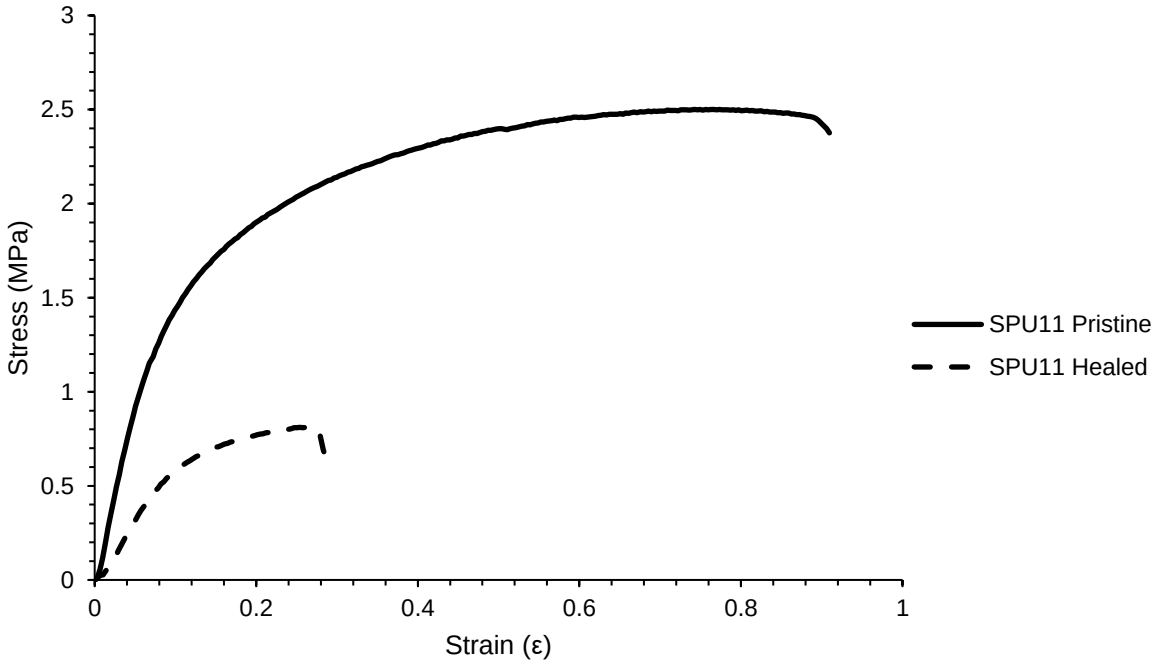

Figure 164. Representative stress-strain curves of the pristine and healed supramolecular elastomer **SPU11**.

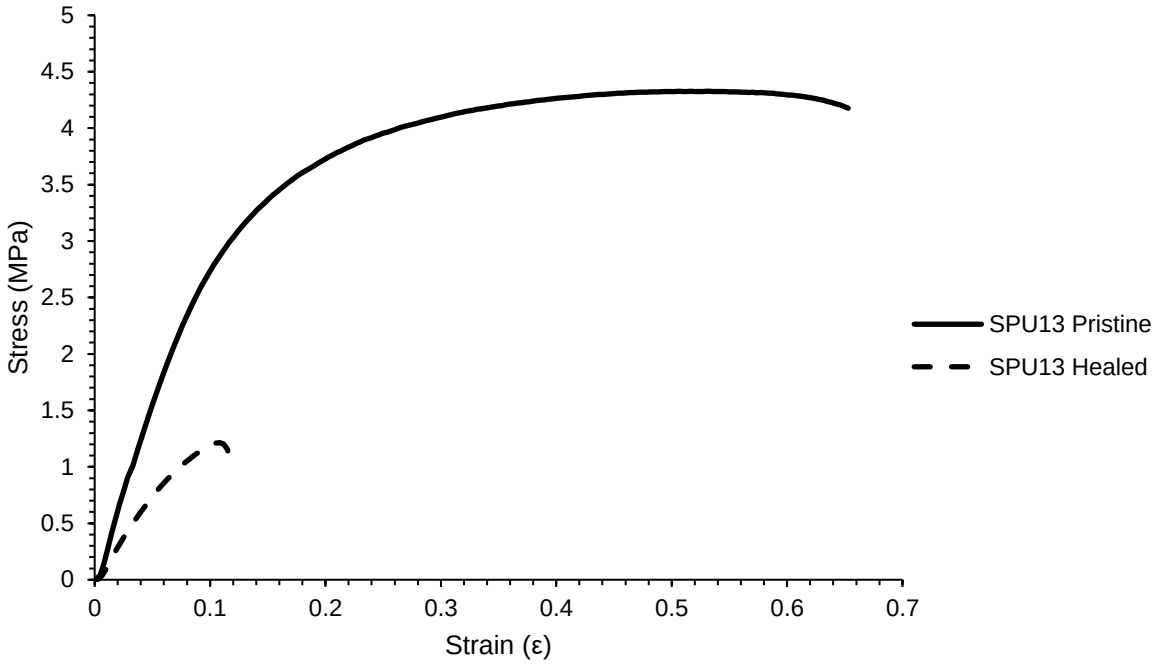

Figure 165. Representative stress-strain curves of the pristine and healed supramolecular elastomer **SPU13**.

References

(1) ODonnell, A. D.; Gavriel, A. G.; Christie, W.; Chippindale, A. M.; German, I. M.; Hayes, W. Conformational Control of Bis-Urea Self-Assembled Supramolecular PH Switchable Low-Molecular-Weight Hydrogelators. *Arkivoc* **2021**, *2021* (6), 222–241. https://doi.org/10.24820/ark.5550190.p011.581.

(2) Harnying, W.; Neudörfl, J. M.; Berkessel, A. Enantiospecific Synthesis of Nepetalactones by One-Step Oxidative NHC Catalysis. *Org. Lett.* **2020**, *22* (2), 386–390. https://doi.org/10.1021/acs.orglett.9b04034.

(3) Sura, T. P.; Ramana, M. M. V.; Kudav, N. A. Urea Nitrate: A Reagent for Regioselective Nitration of Aromatic Amines. *Synth. Commun.* **1988**, *18* (16–17), 2161–2165. https://doi.org/10.1080/00397918808068287.

(4) Ingham, C. E.; Hampson, G. C. 209. An Investigation of Steric Influences on the Phenomenon of Resonance. Part II. *J. Chem. Soc.* **1939**, 981. https://doi.org/10.1039/jr9390000981.

(5) Birtles, R. H.; Hampson, G. C. 3. An Investigation of Steric Influences on the Phenomenon of Mesomerism. *J. Chem. Soc.* **1937**, No. June, 10. https://doi.org/10.1039/jr9370000010.

(6) Evans, D. H.; Hu, K. Inverted Potentials in Two-Electron Processes in Organic Electrochemistry. *J. Chem. Soc. Faraday Trans.* **1996**, *92* (20), 3983. https://doi.org/10.1039/ft9969203983.

(7) Guan, Z. H.; Lei, H.; Chen, M.; Ren, Z. H.; Bai, Y.; Wang, Y. Y. Palladium-Catalyzed Carbonylation of Amines: Switchable Approaches to Carbamates and N,N′-Disubstituted Ureas. *Adv. Synth. Catal.* **2012**, *354* (2–3), 489–496. https://doi.org/10.1002/adsc.201100545.

(8) Kadam, S. A.; Haav, K.; Toom, L.; Haljasorg, T.; Leito, I. NMR Method for Simultaneous Host-Guest Binding Constant Measurement. *J. Org. Chem.* **2014**, *79* (6), 2501–2513. https://doi.org/10.1021/jo4027963.

(9) Zhu, X.; Xu, M.; Sun, J.; Guo, D.; Zhang, Y.; Zhou, S.; Wang, S. Hydroamination and Hydrophosphination of Isocyanates/Isothiocyanates under Catalyst-Free Conditions. *European J. Org. Chem.* **2021**, *2021* (37), 5213–5218. https://doi.org/10.1002/ejoc.202100932.

(10) Simons, D. M.; Arnold, R. G. Relative Reactivity of the Isocyanate Groups in Toluene-2,4-Diisocyanate. *J. Am. Chem. Soc.* **1956**, *78* (8), 1658–1659. https://doi.org/10.1021/ja01589a044.

Appendix 3

Contents

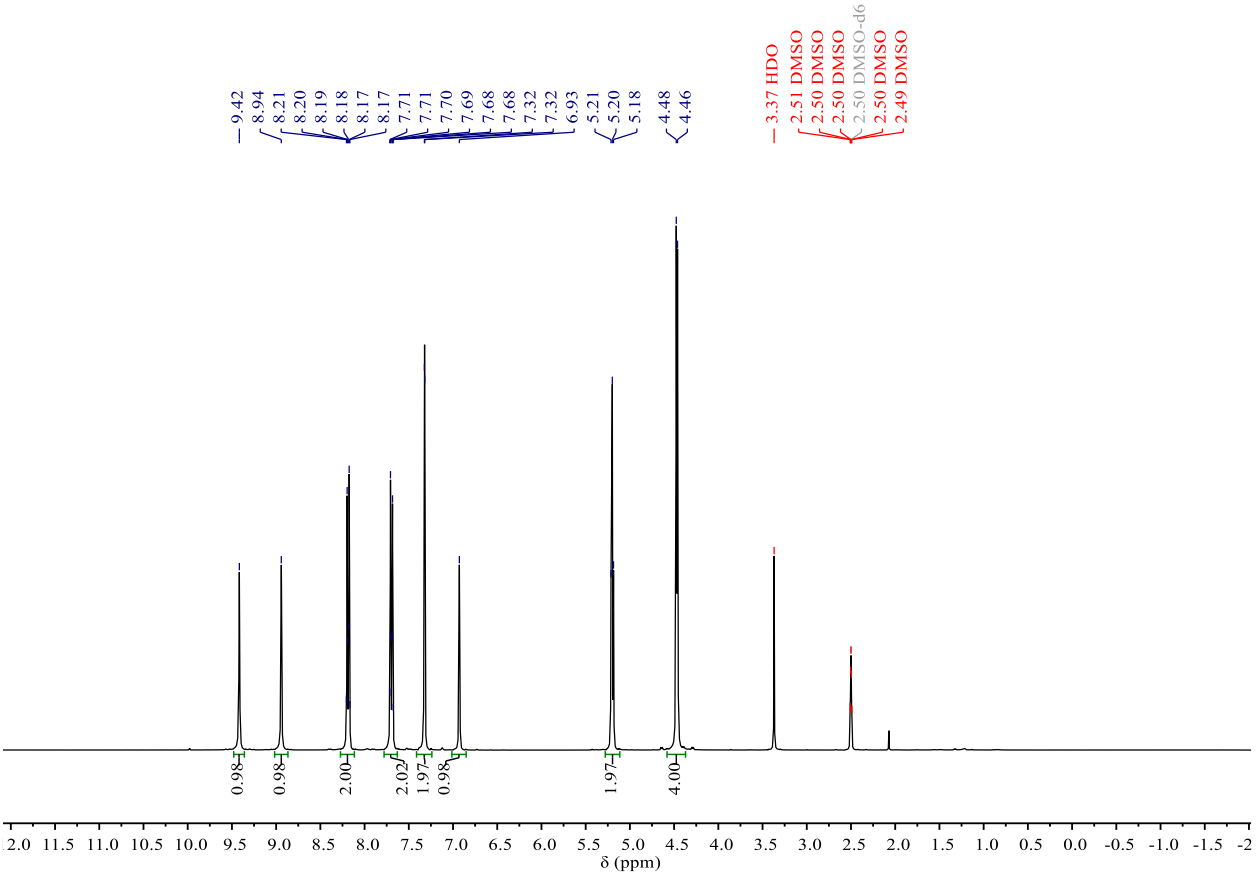

Figure 1. ^{1}H NMR (400 MHz, DMSO-d_6, 298 K of compound **4.12**).

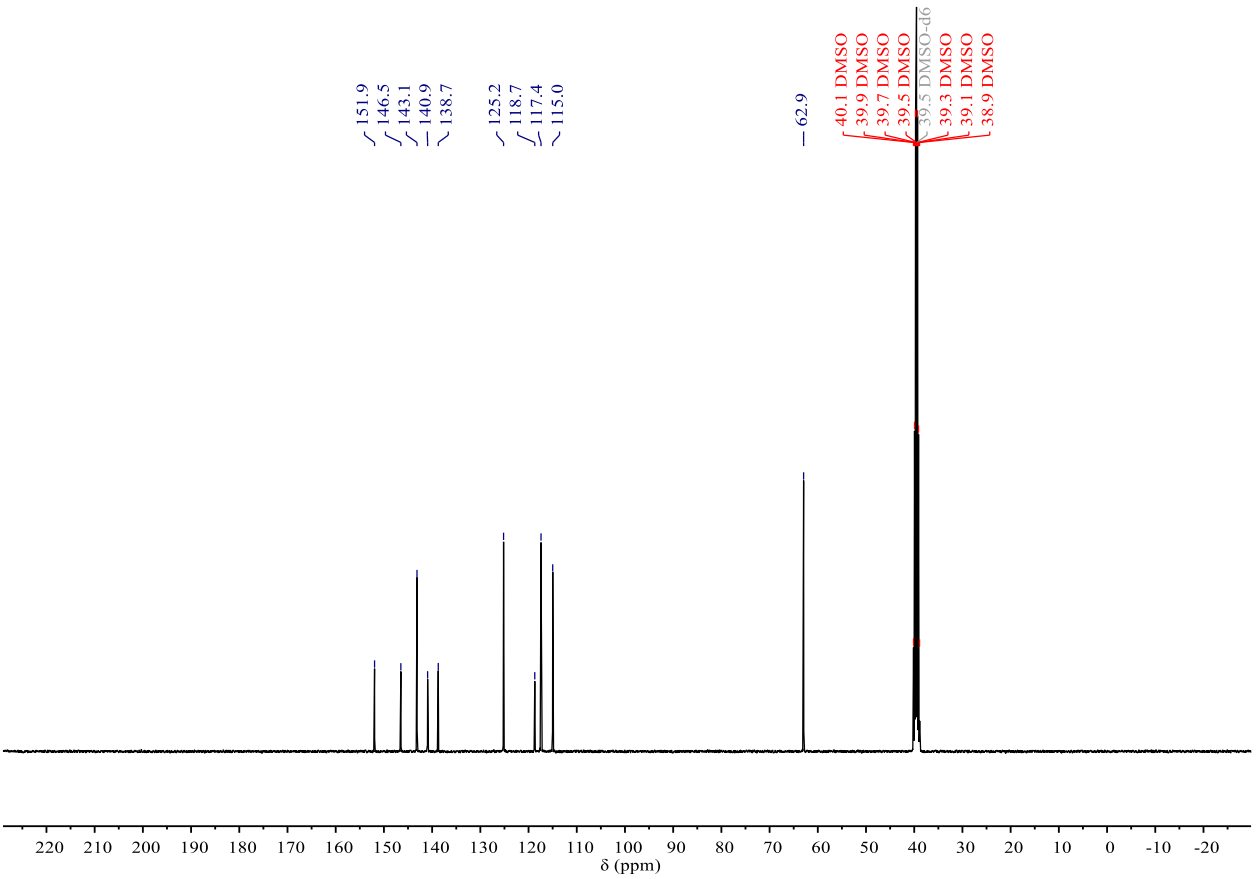

Figure 2. ^{13}C{H} (100 MHz, DMSO-d_6, 298 K of compound **4.12**).

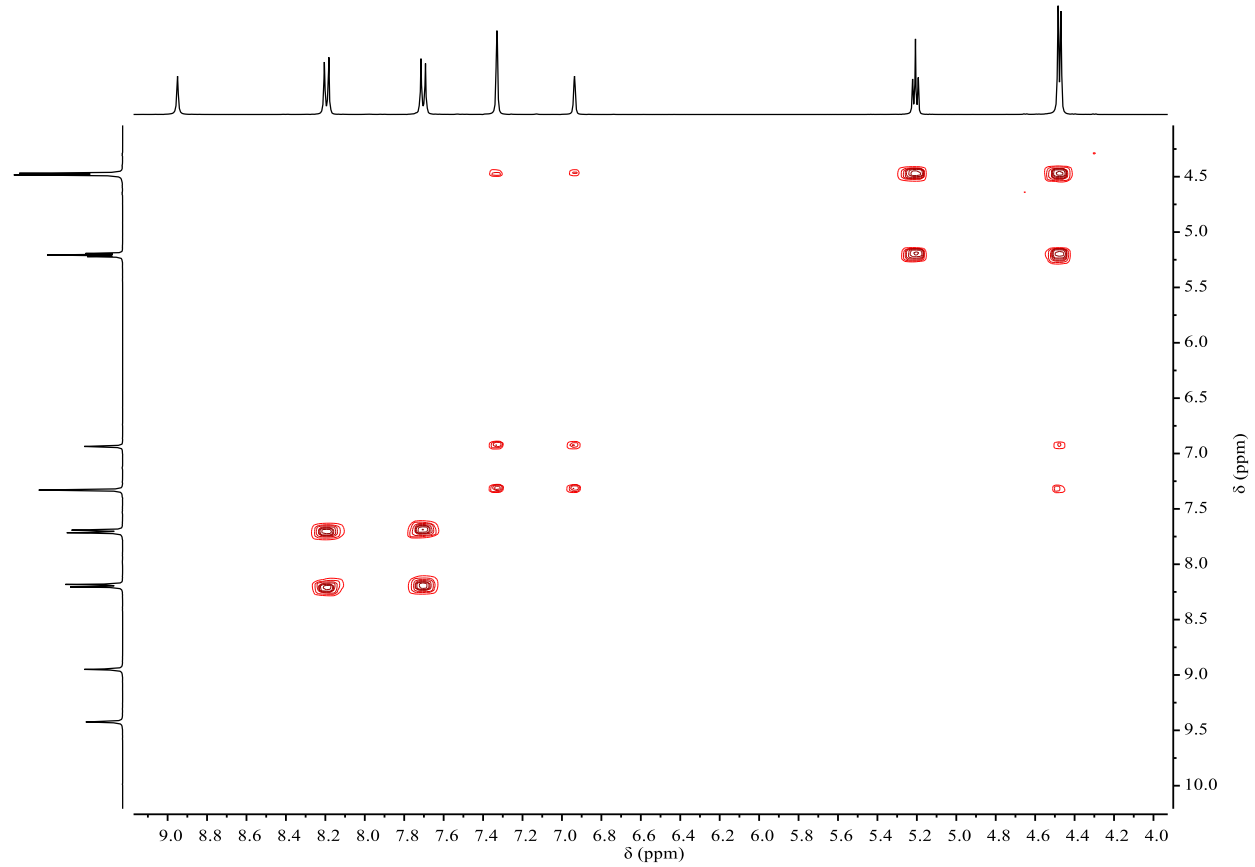

Figure 3. ^{1}H-^{1}H COSY (400 MHz, DMSO-d_6, 298 K of compound **4.12**).

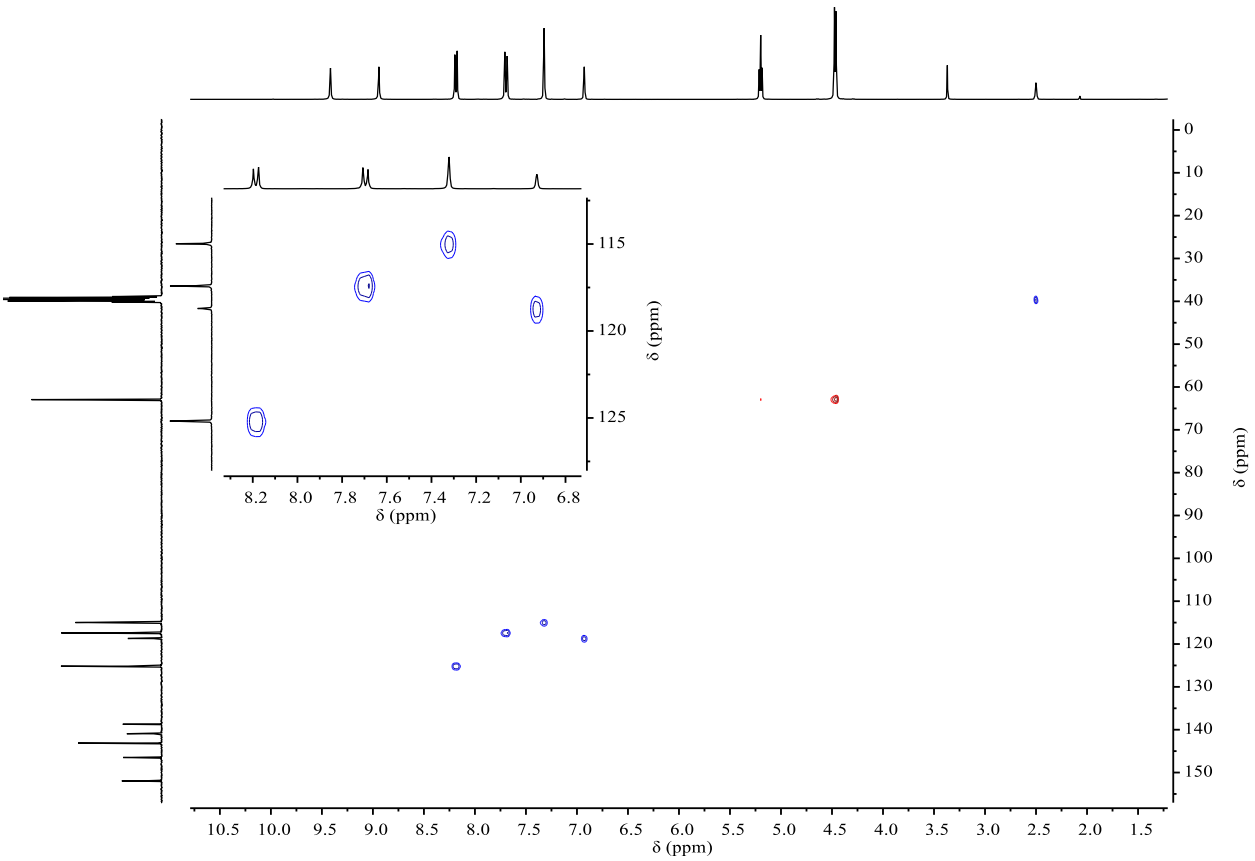

Figure 4. Multiplicity-edited HSQC **(**400, 100 MHz, DMSO-d_6, 298 K of compound **4.12**).

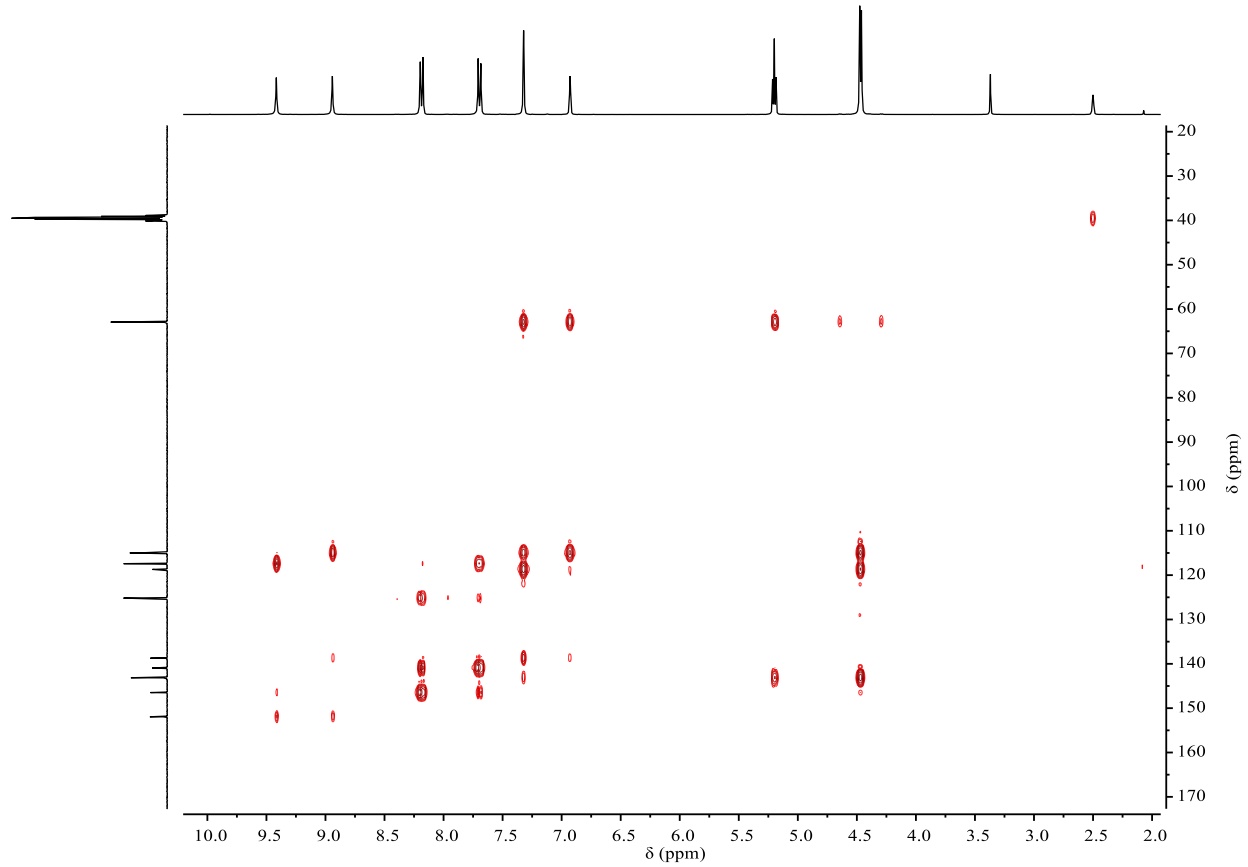

Figure 5. HMBC **(**400, 100 MHz, DMSO-d_6, 298 K of compound **4.12**).

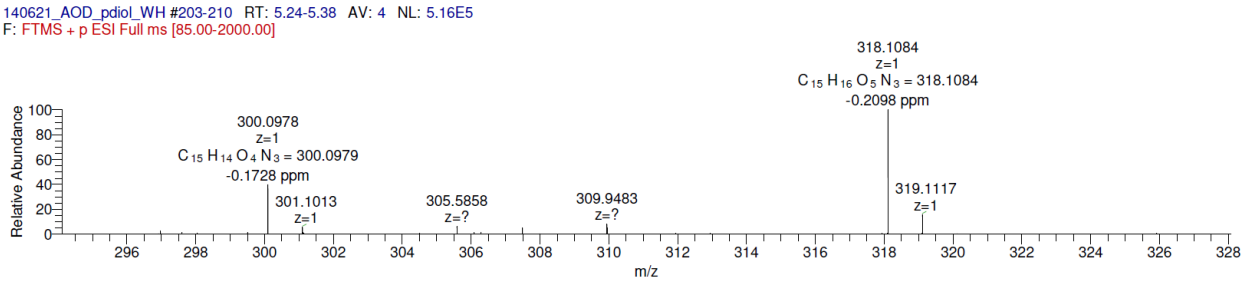

Figure 6. HRMS of compound **4.12**).

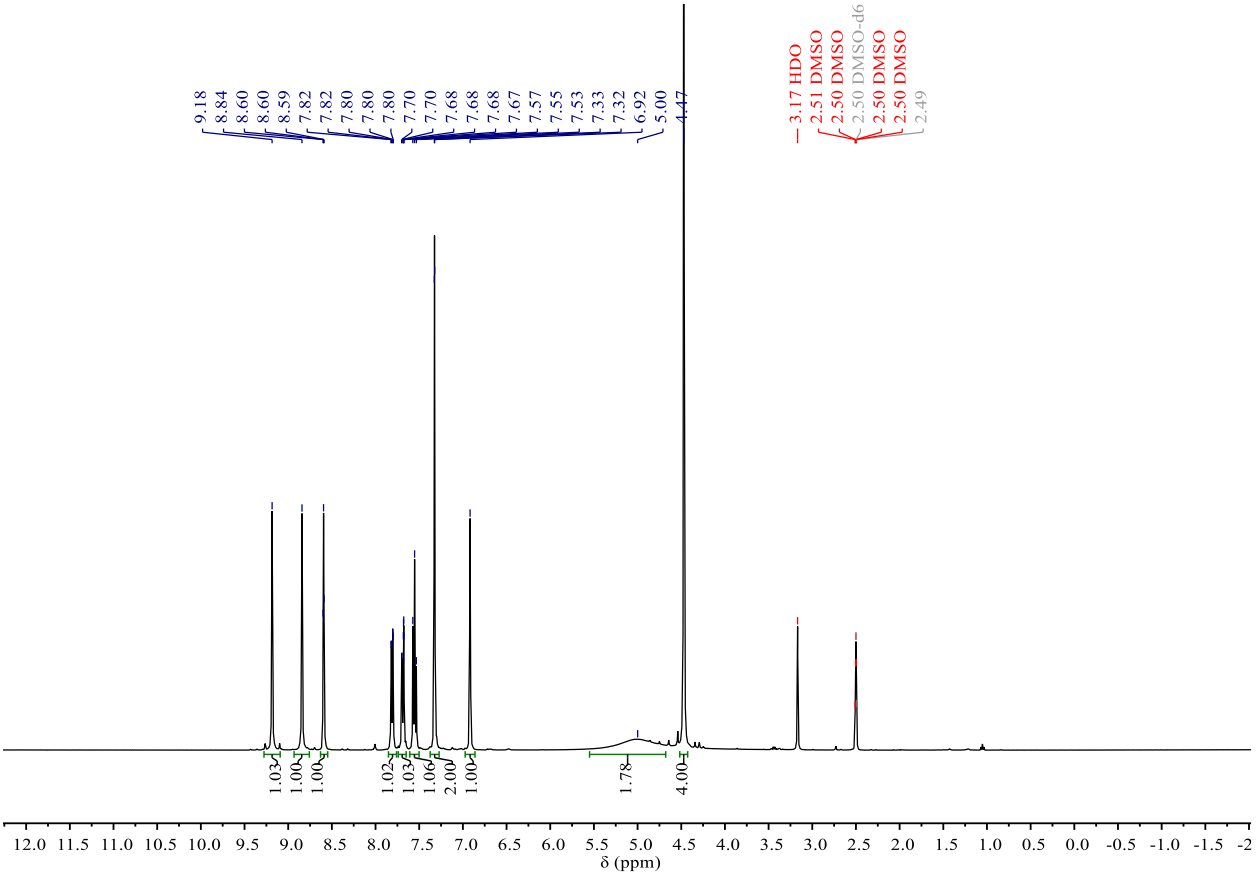

Figure 7. ^{1}H NMR (400 MHz, DMSO-d_6, 298 K of compound **4.13**).

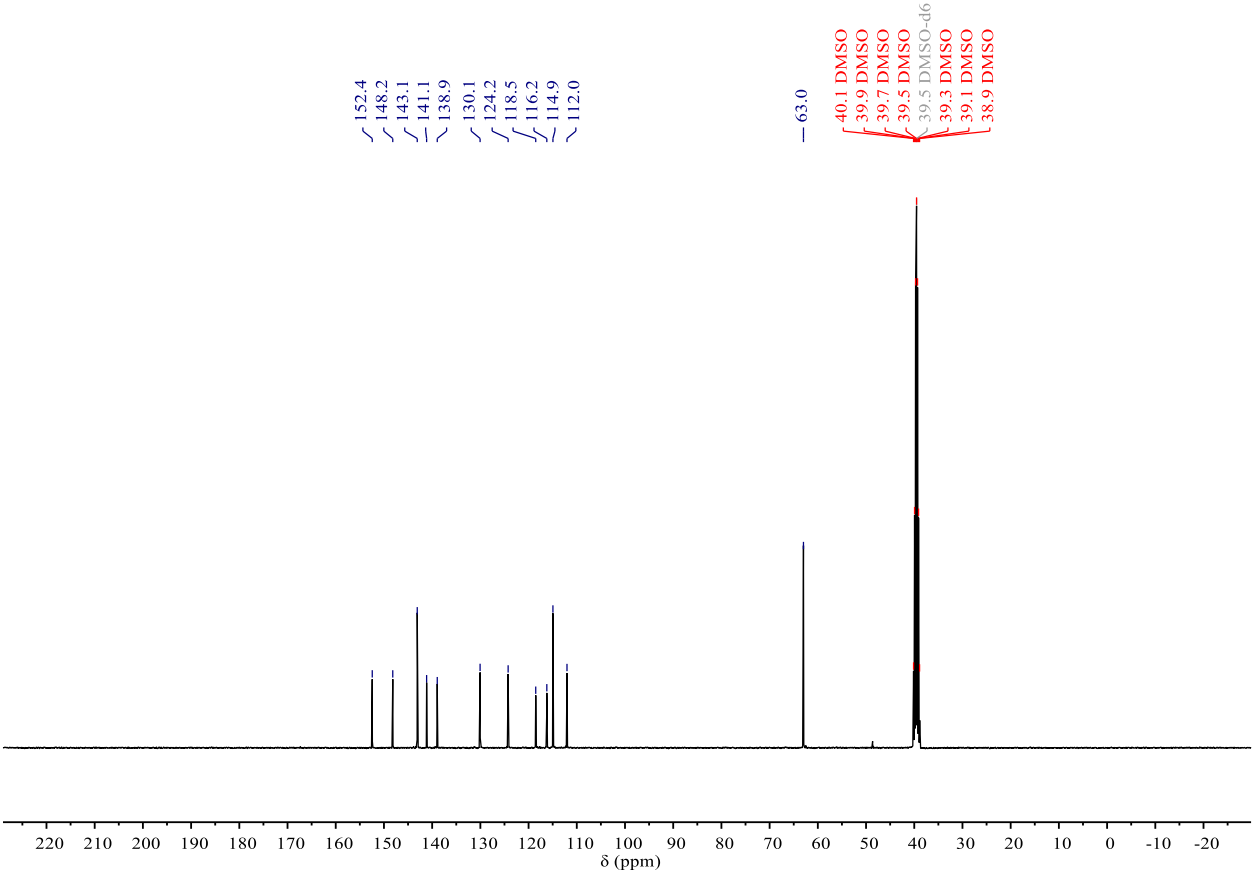

Figure 8. ^{13}C{H} (100 MHz, DMSO-d_6, 298 K of compound **4.13**).

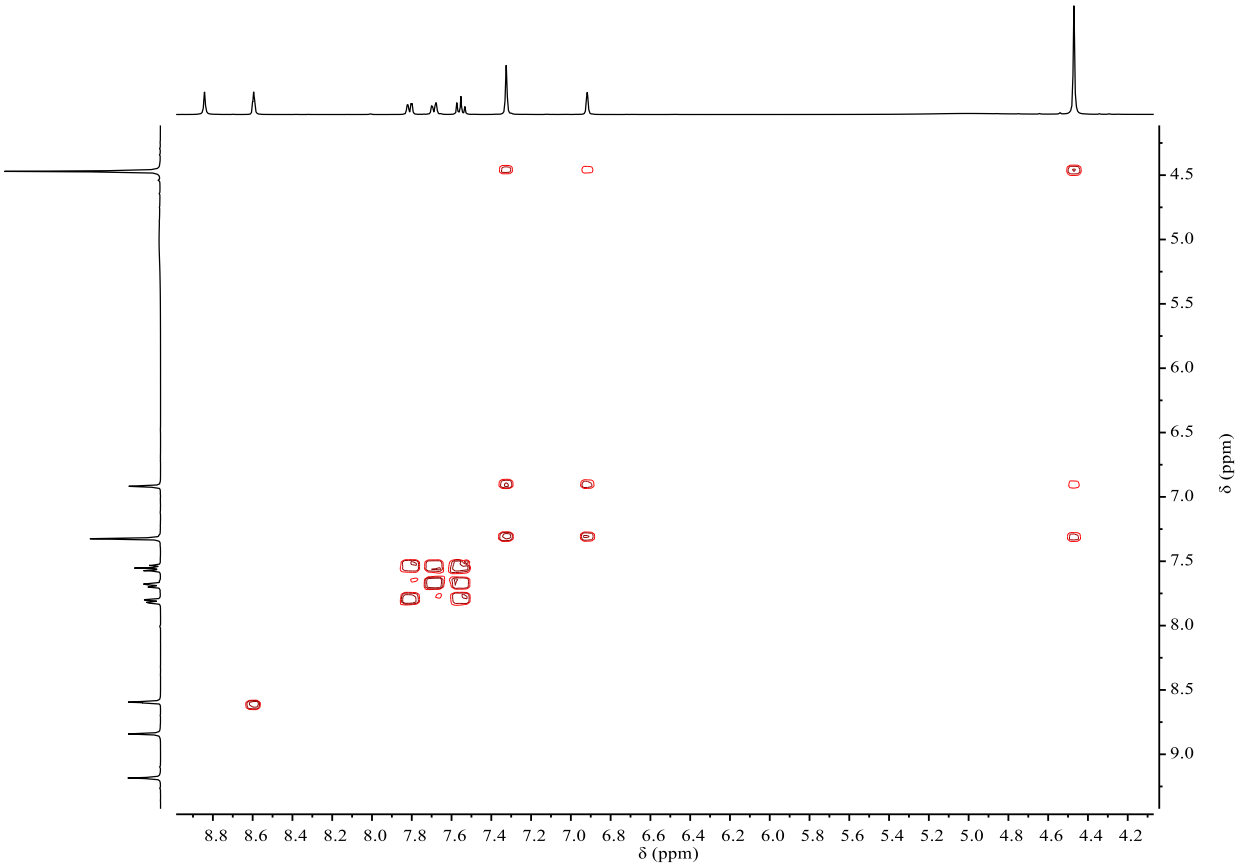

Figure 9. ^{1}H-^{1}H COSY (400 MHz, DMSO-d_6, 298 K of compound **4.13**).

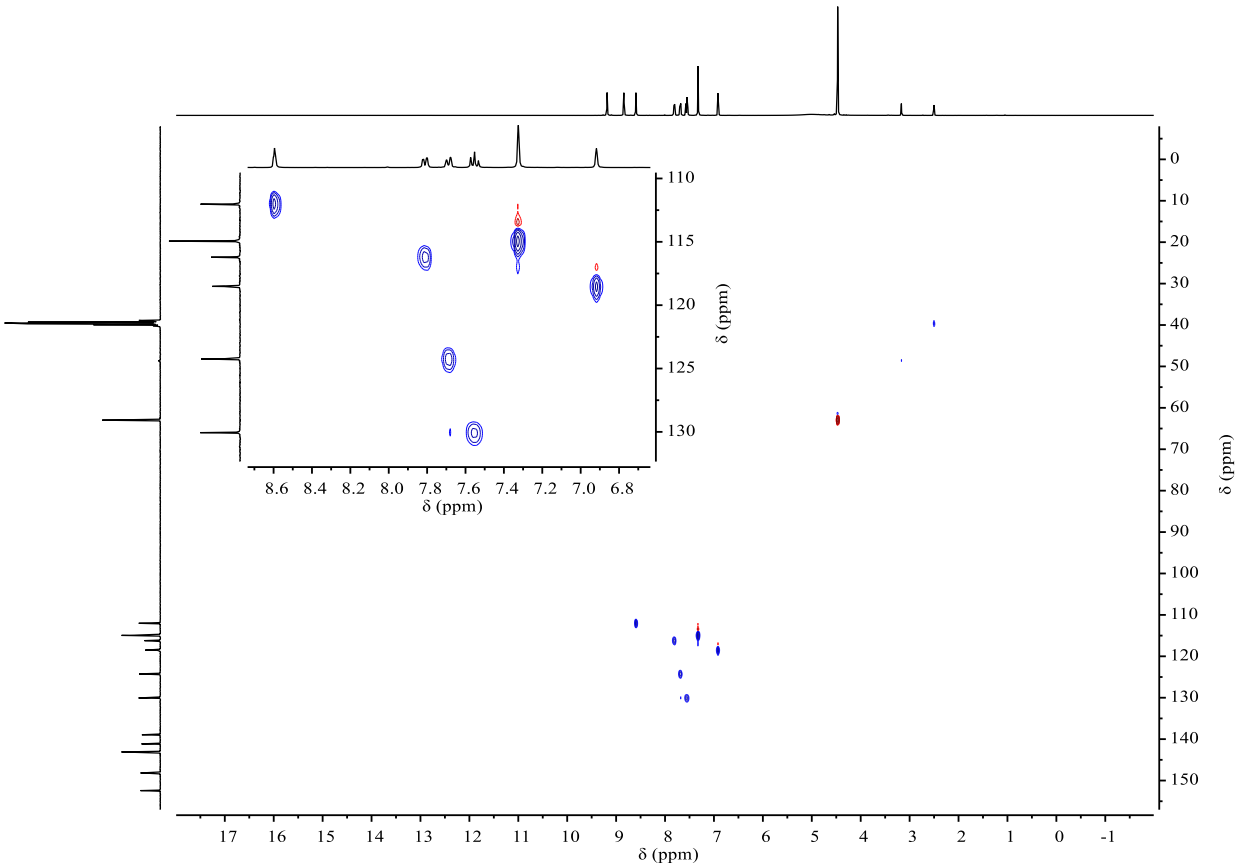

Figure 10. Multiplicity-edited HSQC **(**400, 100 MHz, DMSO-d_6, 298 K of compound **4.13**).

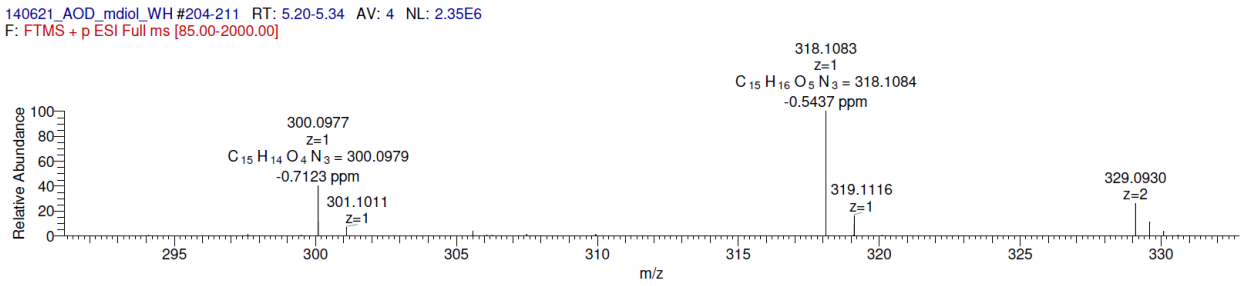

Figure 11. HRMS of compound 4.13

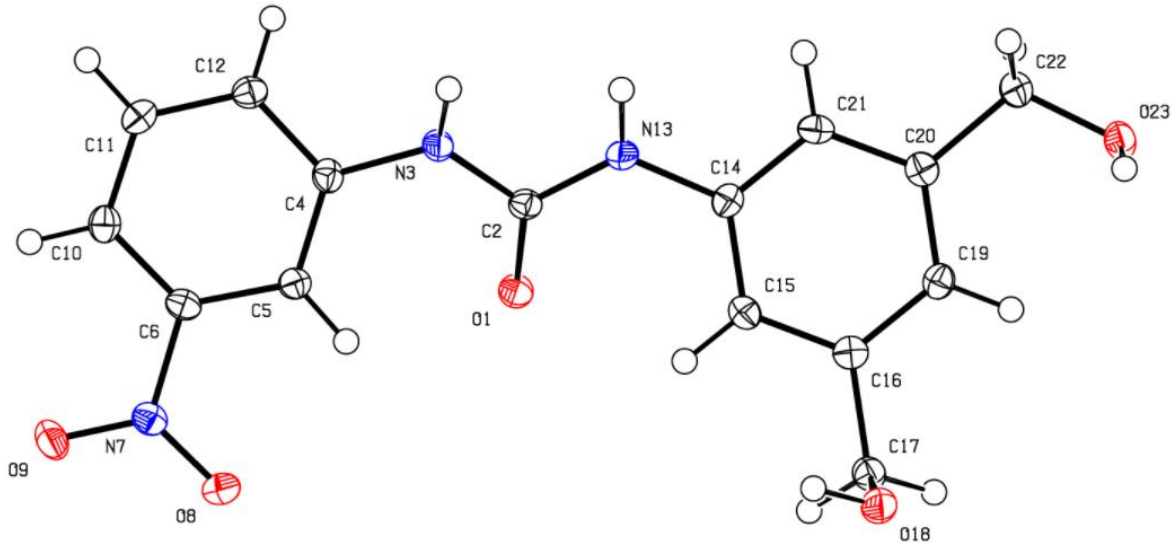

Figure 12. Asymmetric unit of **4.13** with ellipsoids drawn at 50% probability

Table 1. Crystallographic details for compound*C15 H15 N3 O5

Formula	$C_{15}\,H_{15}\,N_3\,O_5$
M_r	317.30
Crystal system	orthorhombic
Space group	$P\,2_1\,2_1\,2_1$
Z	4
a /Å	4.739410(9)
b/Å	7.106140(10)
c /Å	41.69148(3)
V / Å^3	1404.123(3)
D_{calc} / g cm^{-3}	1.501
Crystal habit	Colourless rod
Crystal dimensions /mm	0.025 × 0.026 × 0.071
Radiation	Cu K_α (1.54184 Å)
T /K	100
μ /mm^{-1}	0.968
R(*F*), *Rw*(*F*)	2.92, 3.80
CCDC cif deposition number	CCDC ***

Table 2. Selected bond lengths (Å) and angles (°) for Compound *****

O(1) – C(2)	1.2256(19)	C(2) – N(3) – C(4)	125.37(13)
O(8) – N(7)	1.2310(17)	O(8) – N(7) – O(9)	123.39(13)
O(9) – N(7)	1.2297(17)	O(8) – N(7) – C(6)	118.02(12)
O(18) – C(17)	1.4415(19)	O(9) – N(7) – C(6)	118.58(12)
O(23) – C(22)	1.4233(18)	C(2) – N(13) – C(14)	126.75(14)
N(3) – C(2)	1.373(2)	O(1) – C(2) – N(3)	123.08(13)
N(3) – C(4)	1.4069(19)	O(1) – C(2) – N(13)	124.05(14)
N(7) – C(6)	1.4674(19)	N(3) – C(2) – N(13)	112.86(13)
N(13) – C(2)	1.359(2)	N(3) – C(4) – C(5)	122.74(13)
N(13) – C(14)	1.420(2)	N(3) – C(4) – C(12)	117.53(13)
C(4) – C(5)	1.388(2)	C(5) – C(4) – C(12)	119.70(14)
C(4) – C(12)	1.403(2)	C(4) – C(5) – C(6)	117.98(14)
C(5) – C(6)	1.391(2)	N(7) – C(6) – C(5)	117.38(13)
C(6) – C(10)	1.383(2)	N(7) – C(6) – C(10)	118.97(13)
C(10) – C(11)	1.385(2)	C(5) – C(6) – C(10)	123.65(14)
C(11) – C(12)	1.392(2)	C(6) – C(10) – C(11)	117.53(14)
C(14) – C(15)	1.393(2)	C(10) – C(11) – C(12)	120.72(14)
C(14) – C(21)	1.394(2)	C(4) – C(12) – C(11)	120.41(14)
C(15) – C(16)	1.390(2)	N(13) – C(14) – C(15)	122.13(14)
C(16) – C(17)	1.505(2)	N(13) – C(14) – C(21)	117.56(14)
C(16) – C(19)	1.393(2)	C(15) – C(14) – C(21)	120.16(14)
C(19) – C(20)	1.392(2)	C(14) – C(15) – C(16)	119.49(13)
C(20) – C(21)	1.394(2)	C(15) – C(16) – C(17)	119.08(13)
C(20) – C(22)	1.515(2)	C(15) – C(16) – C(19)	120.34(14)
		C(17) – C(16) – C(19)	120.33(14)
		O(18) – C(17) – C(16)	110.22(13)
		C(16) – C(19) – C(20)	120.31(14)
		C(19) – C(20) – C(21)	119.34(14)
		C(19) – C(20) – C(22)	121.66(13)
		C(21) – C(20) – C(22)	118.99(14)
		C(14) – C(21) – C(20)	120.33(14)
		O(23) – C(22) – C(20)	113.42(13)

Table 3. Hydrogen-bond geometry (Å, °) for 4.13

D – H•••A	*D* – H	H•••*A*	*D* •••*A*	*D* – H•••*A*
N(13) – H(131)•••O(8)^{i}	0.82(2)	2.22(2)	2.992 (2)	158.9(19)
N(3) – H(31)•••O(1)^{i}	0.86(3)	2.07(3)	2.836(2)	148(2)
O(18) – H(181)•••O(23)^{ii}	0.92(2)	1.91(2)	2.813(2)	169.1(19)
O(23) – H(231)•••O(18)^{iii}	0.91(2)	1.82(2)	2.727(2)	172.8(19)

Symmetry Codes: (i) 1+*x*, 1+*y*, *z*; (ii) *x*, *y* – 1, *z*; (iii) 2– *x*, 1/2+*y*, 1/2 – *z*.

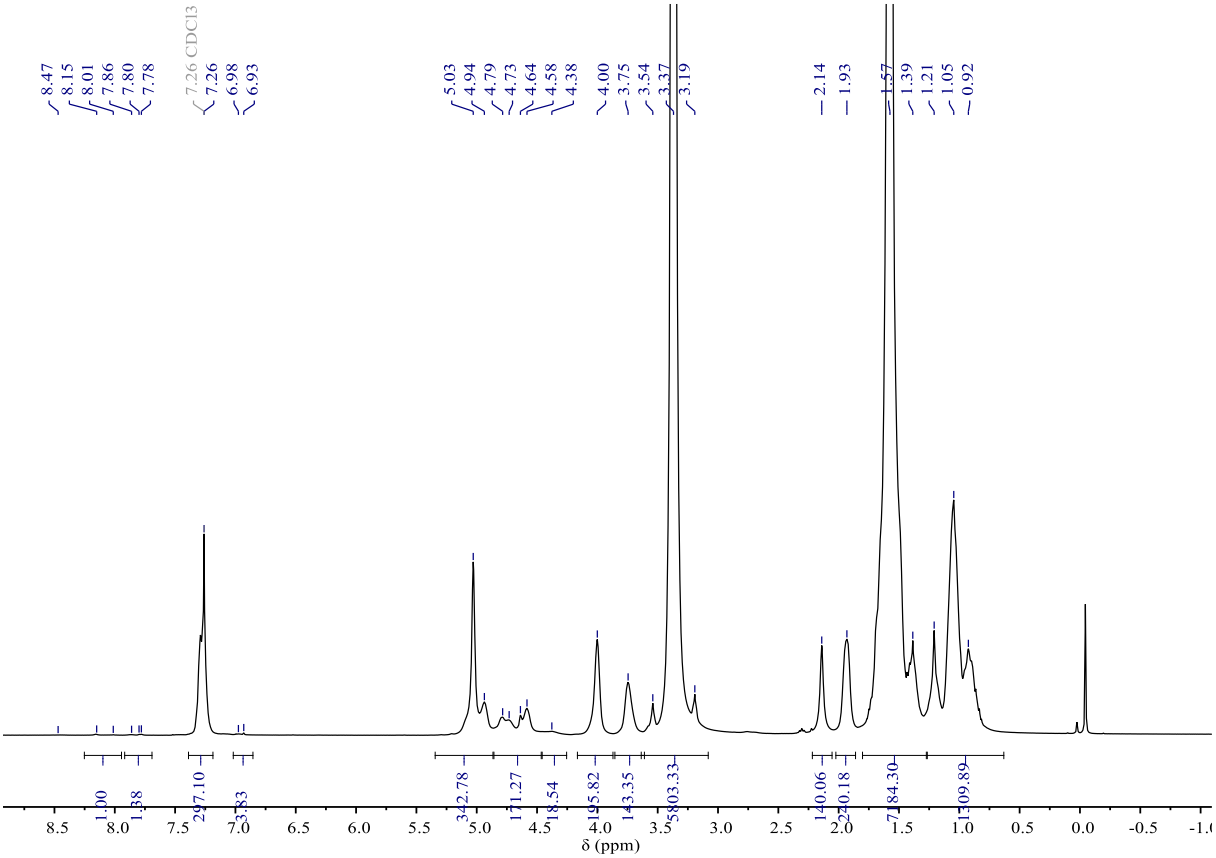

Figure 13. ^{1}H NMR spectrum of **SPE1**(400 MHz, $CDCl_3$, 298 K).

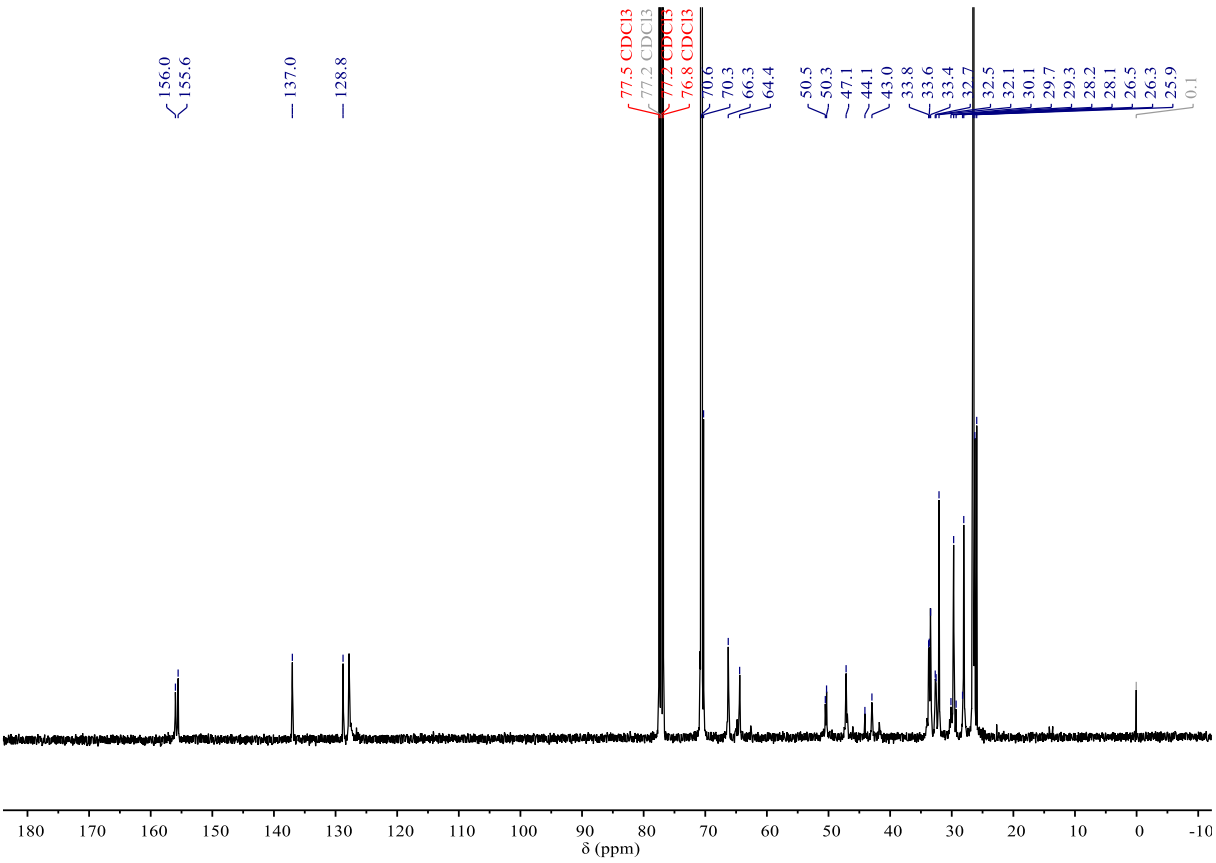

Figure 14. ^{13}C{H} NMR spectrum of **SPE1**(100 MHz, $CDCl_3$, 298 K).

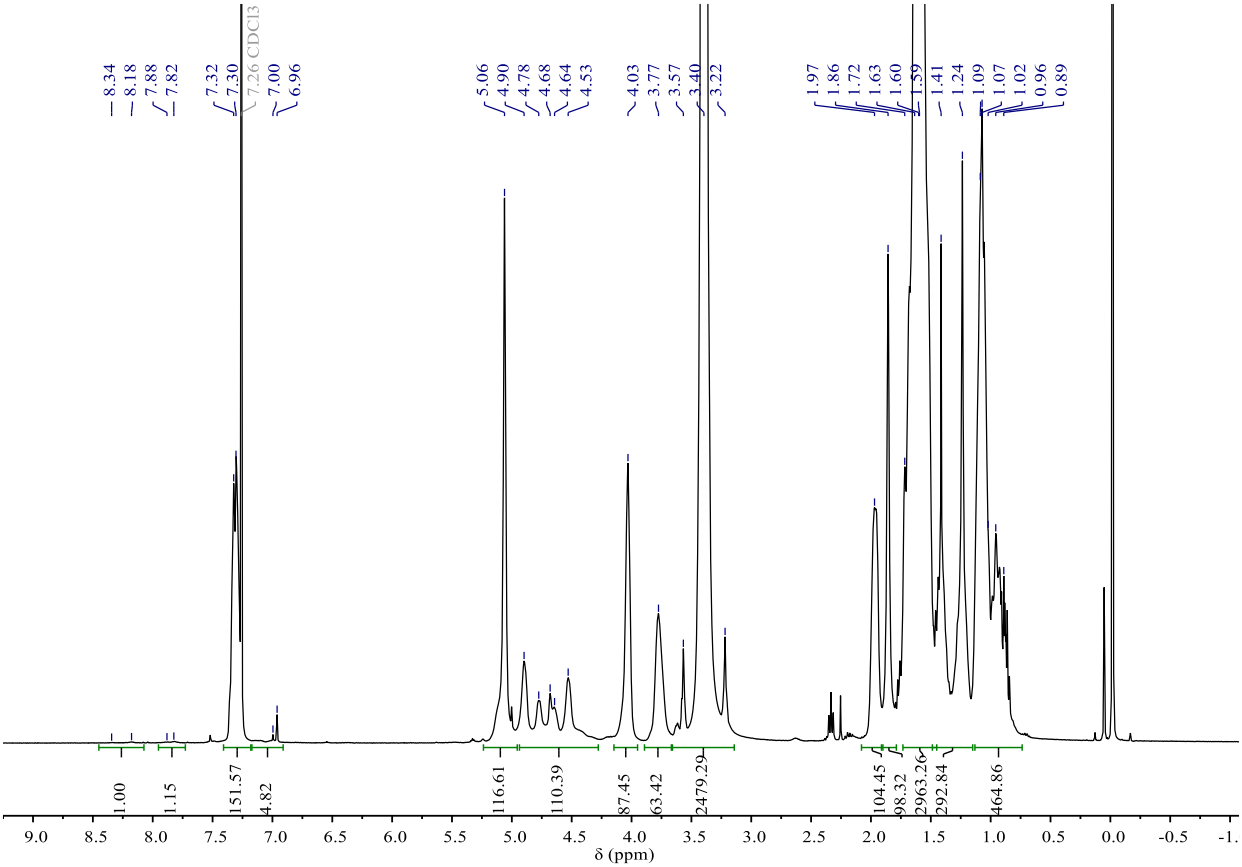

Figure 15. ^{1}H NMR spectrum of **SPE2** 400 MHz, $CDCl_3$, 298 K).

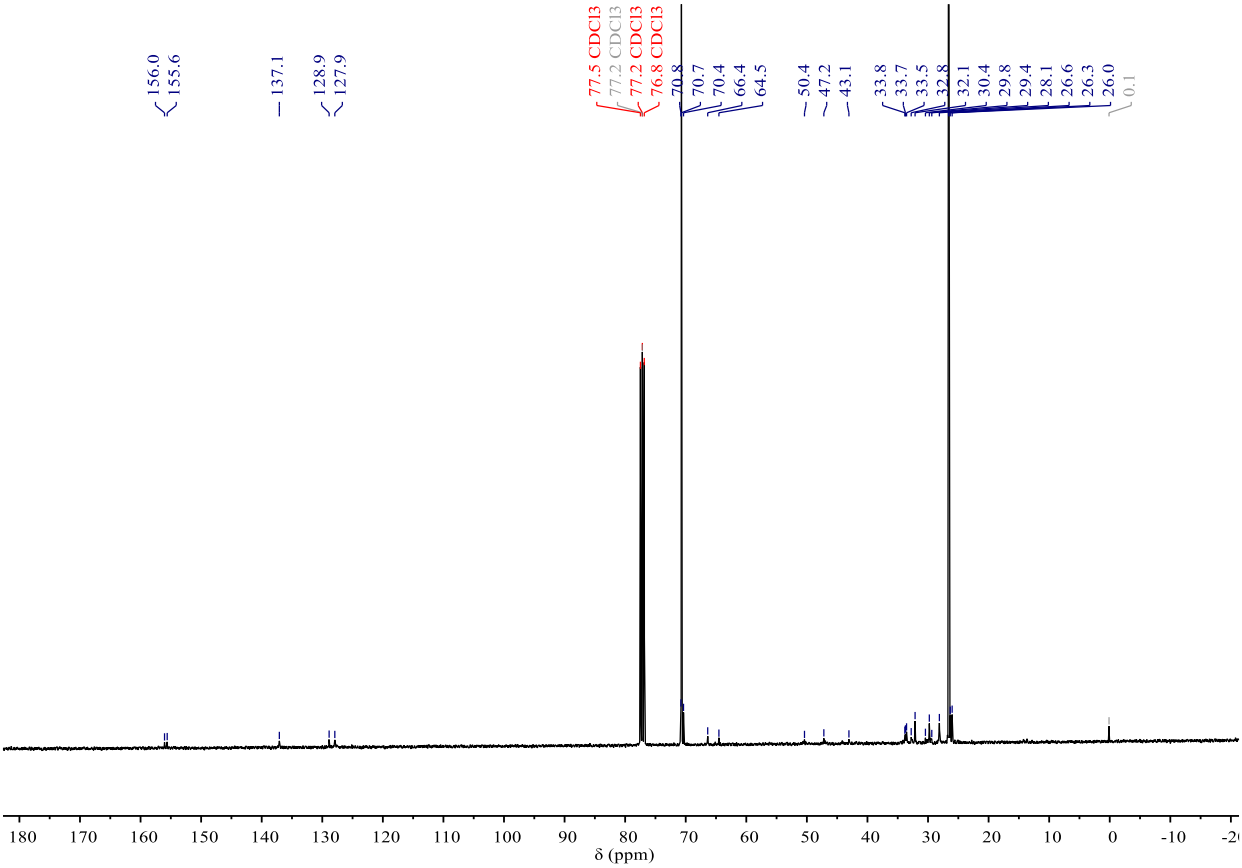

Figure 16. ^{13}C{H} NMR spectrum of **SPE2** (100 MHz, $CDCl_3$, 298 K).

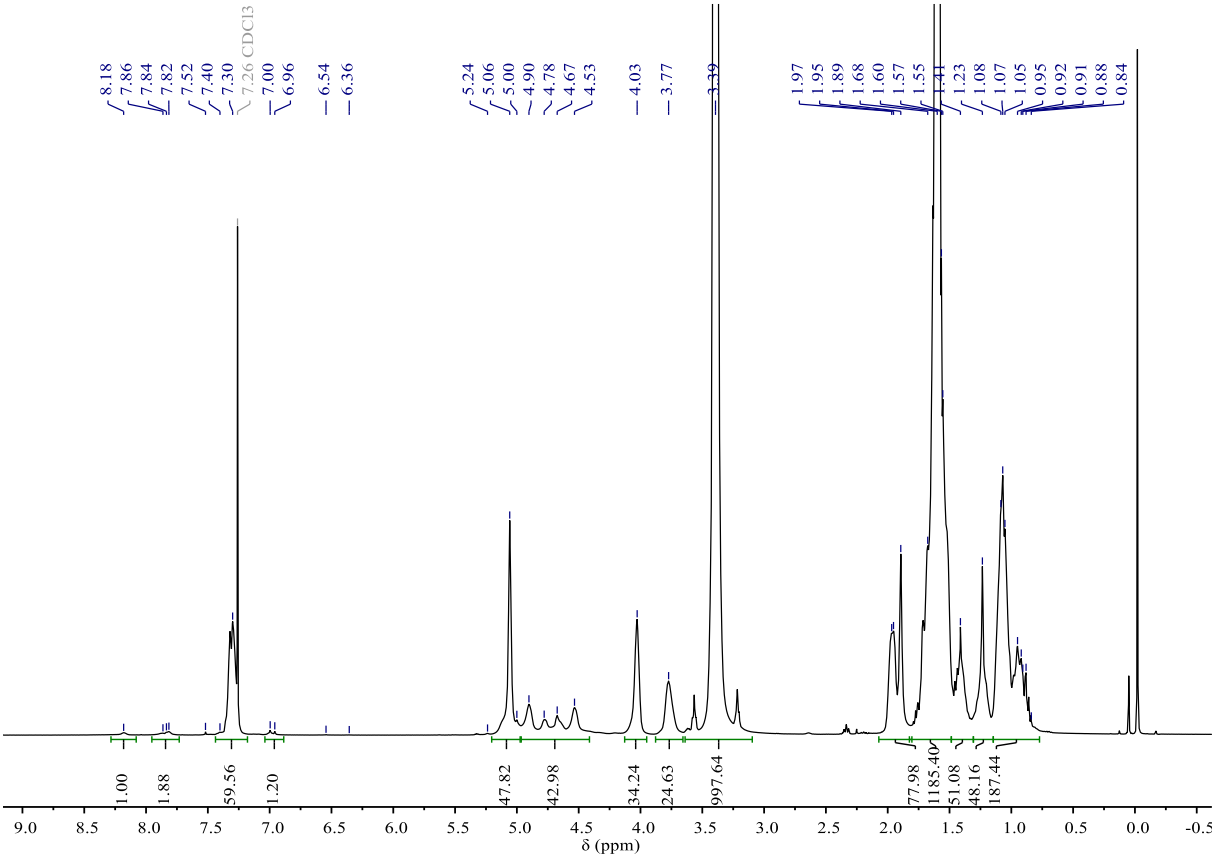

Figure 17. ^{1}H NMR spectrum of **SPE3**(400 MHz, $CDCl_3$, 298 K).

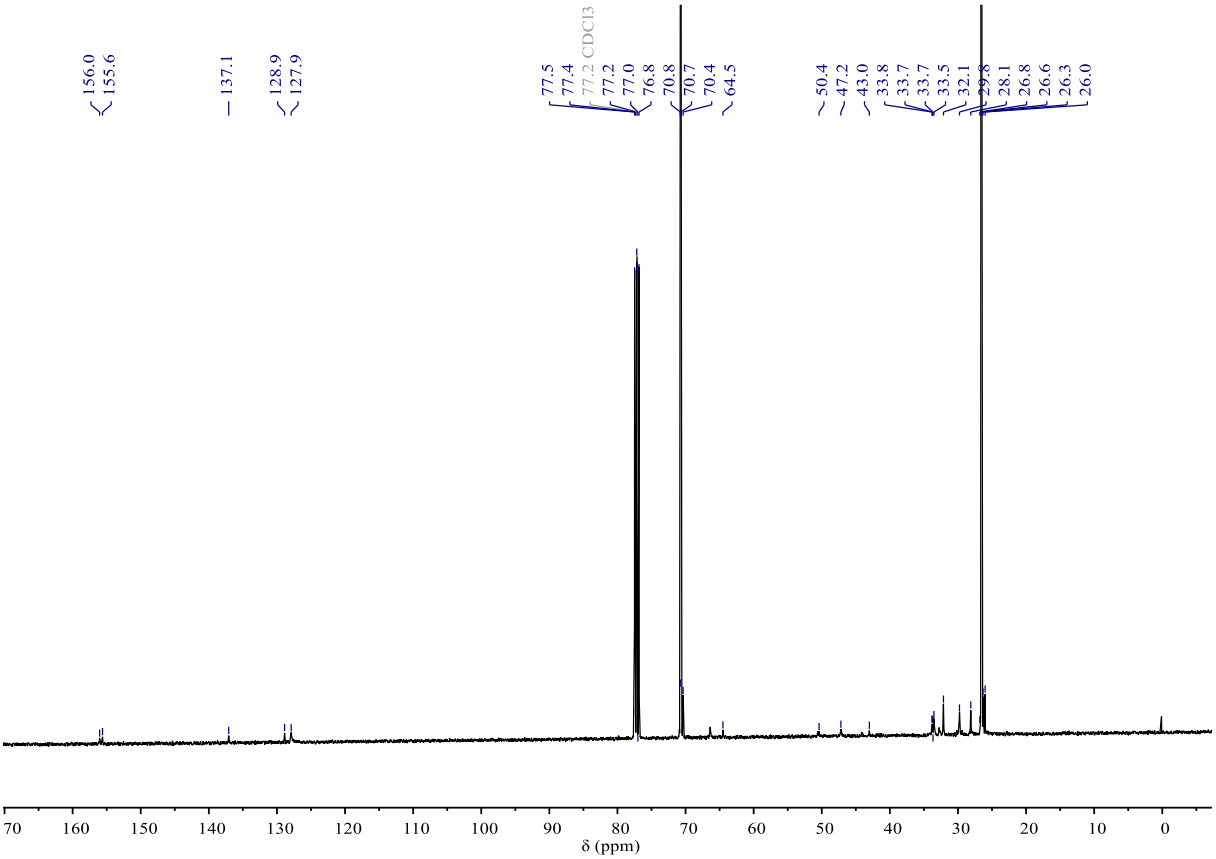

Figure 18. ^{13}C{H} NMR spectrum of **SPE3**(100 MHz, $CDCl_3$, 298 K).

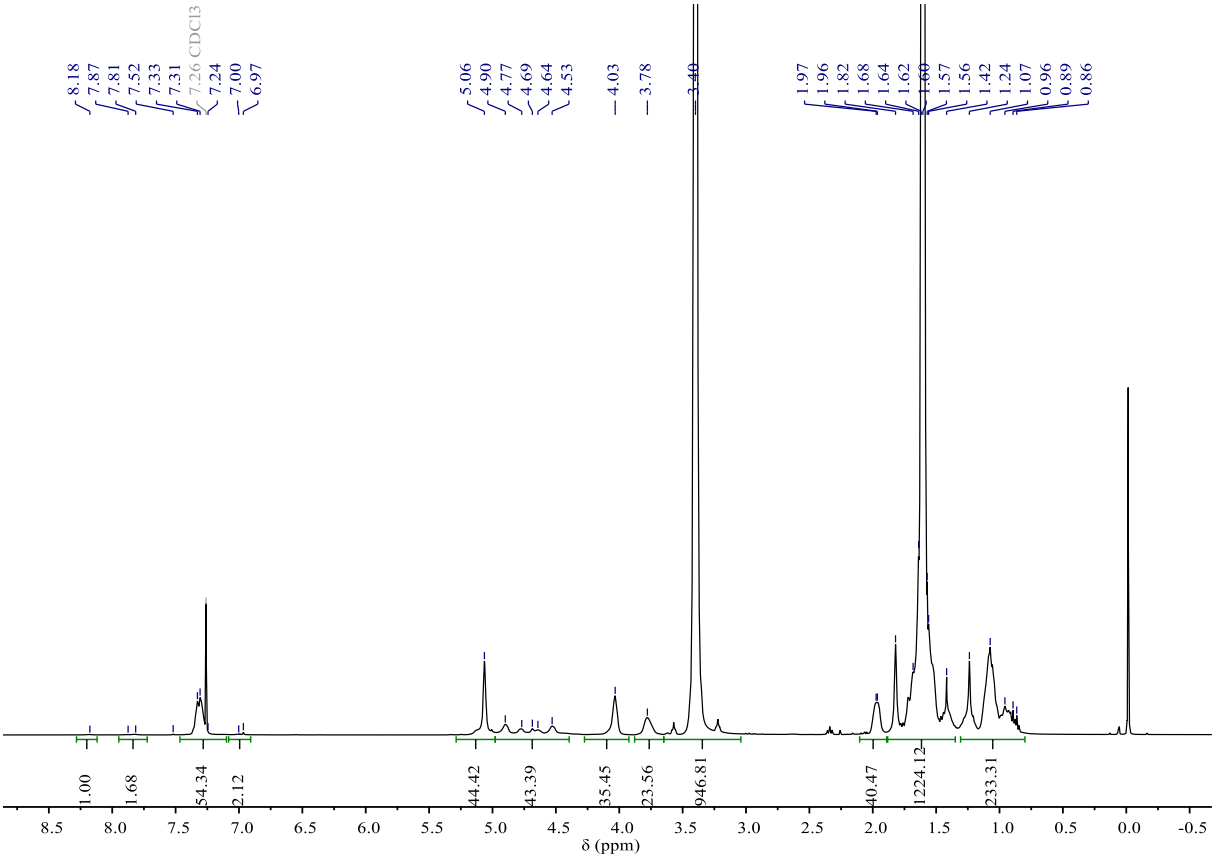

Figure 19. ^{1}H NMR spectrum of **SPE4**(400 MHz, $CDCl_3$, 298 K).

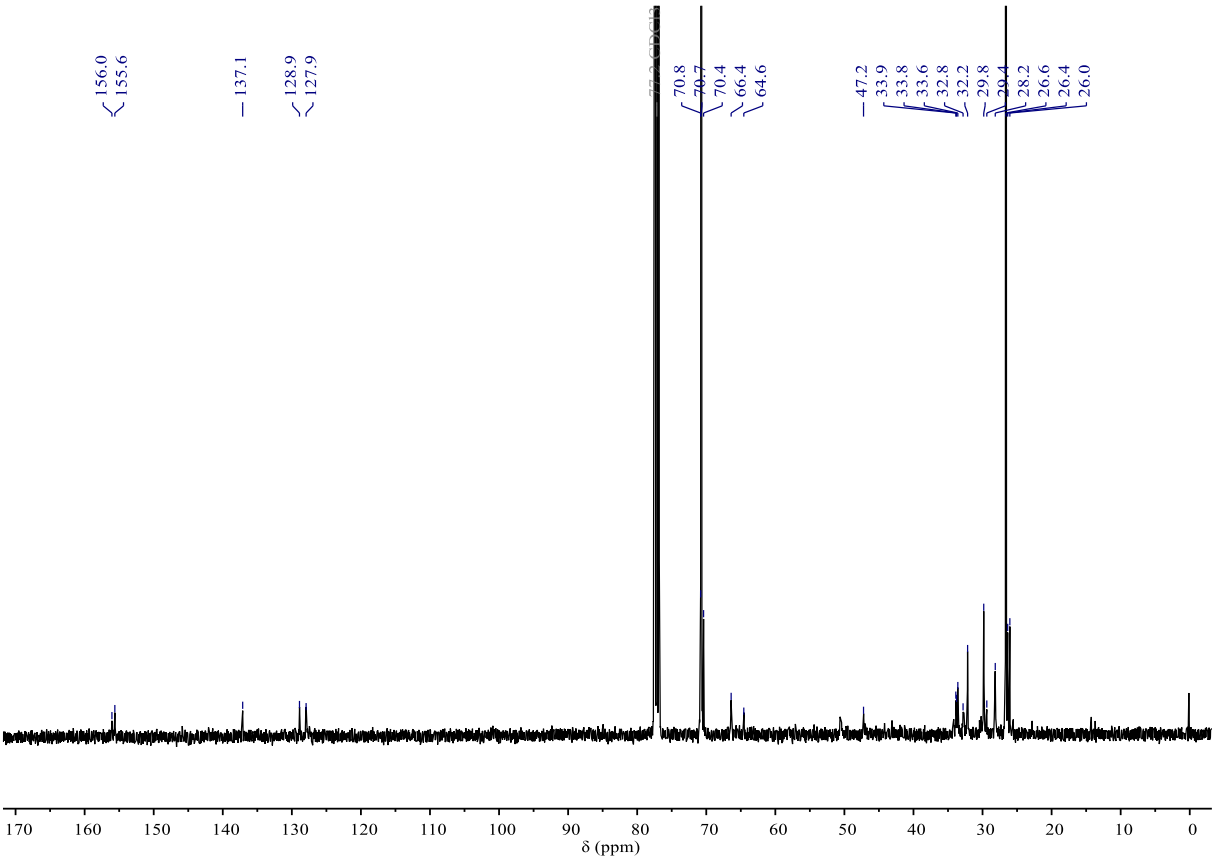

Figure 20. ^{13}C{H} NMR spectrum of **SPE4**(100 MHz, $CDCl_3$, 298 K).

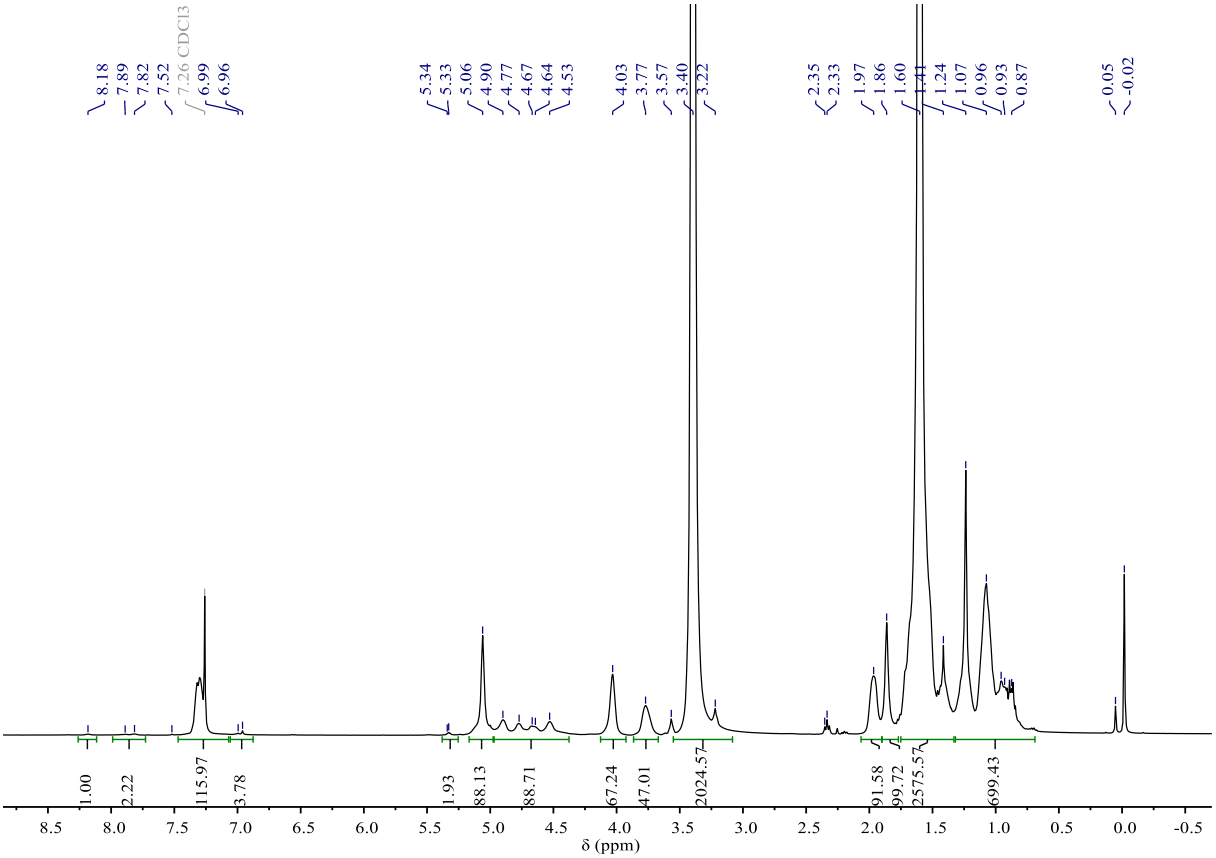

Figure 21. ^{1}H NMR spectrum of **SPE5**(400 MHz, $CDCl_3$, 298 K)

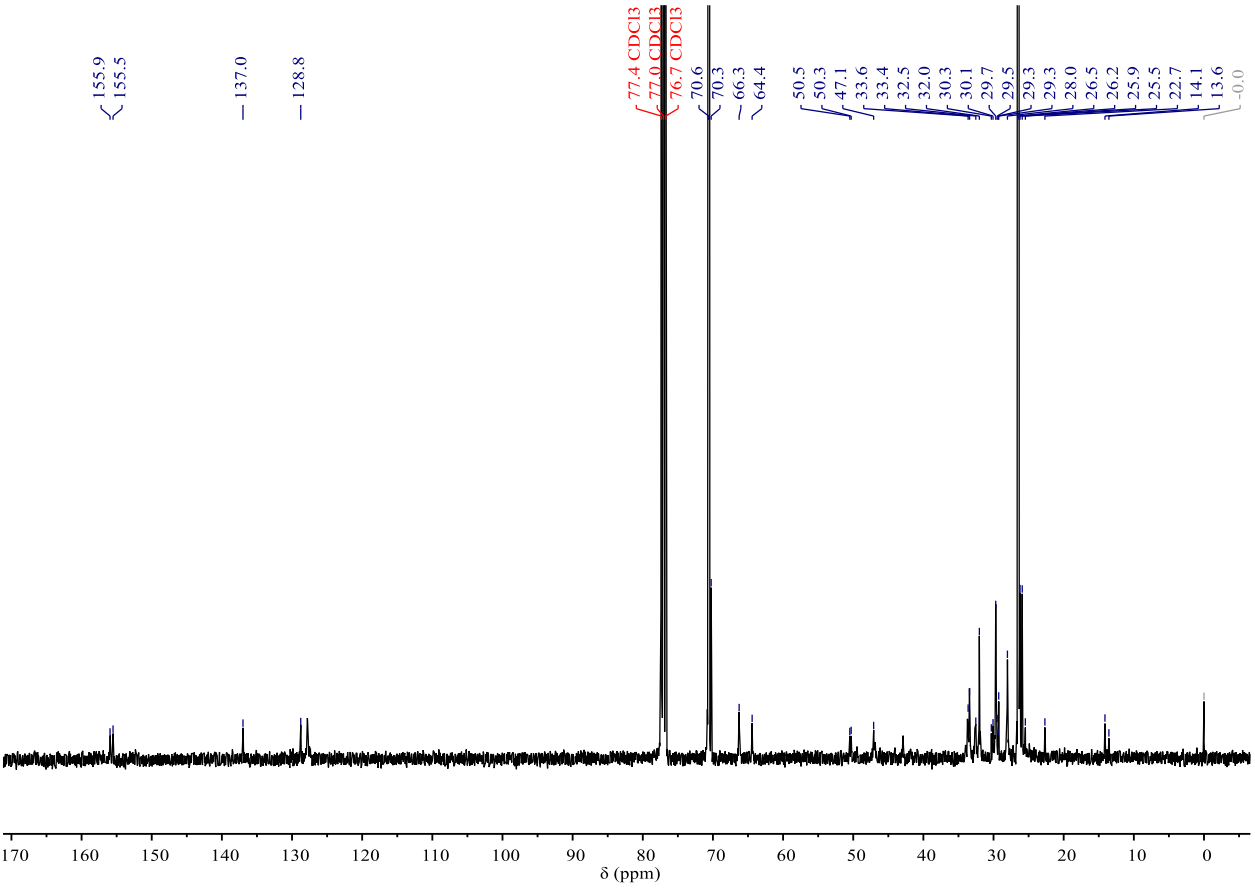

Figure 22. ^{13}C{H} NMR spectrum of **SPE5**(100 MHz, $CDCl_3$, 298 K).

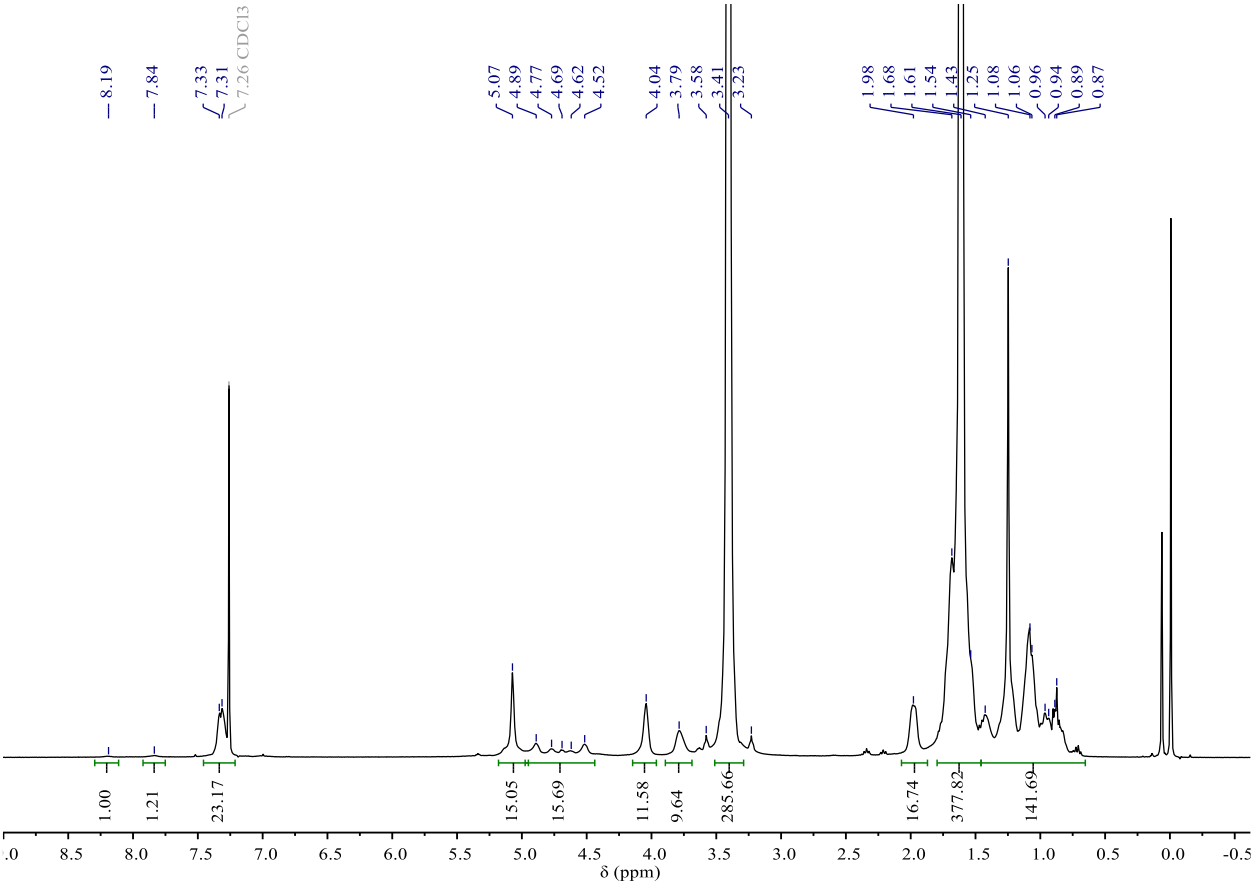

Figure 23. ^{1}H NMR spectrum of **SPE6** (400 MHz, $CDCl_3$, 298 K).

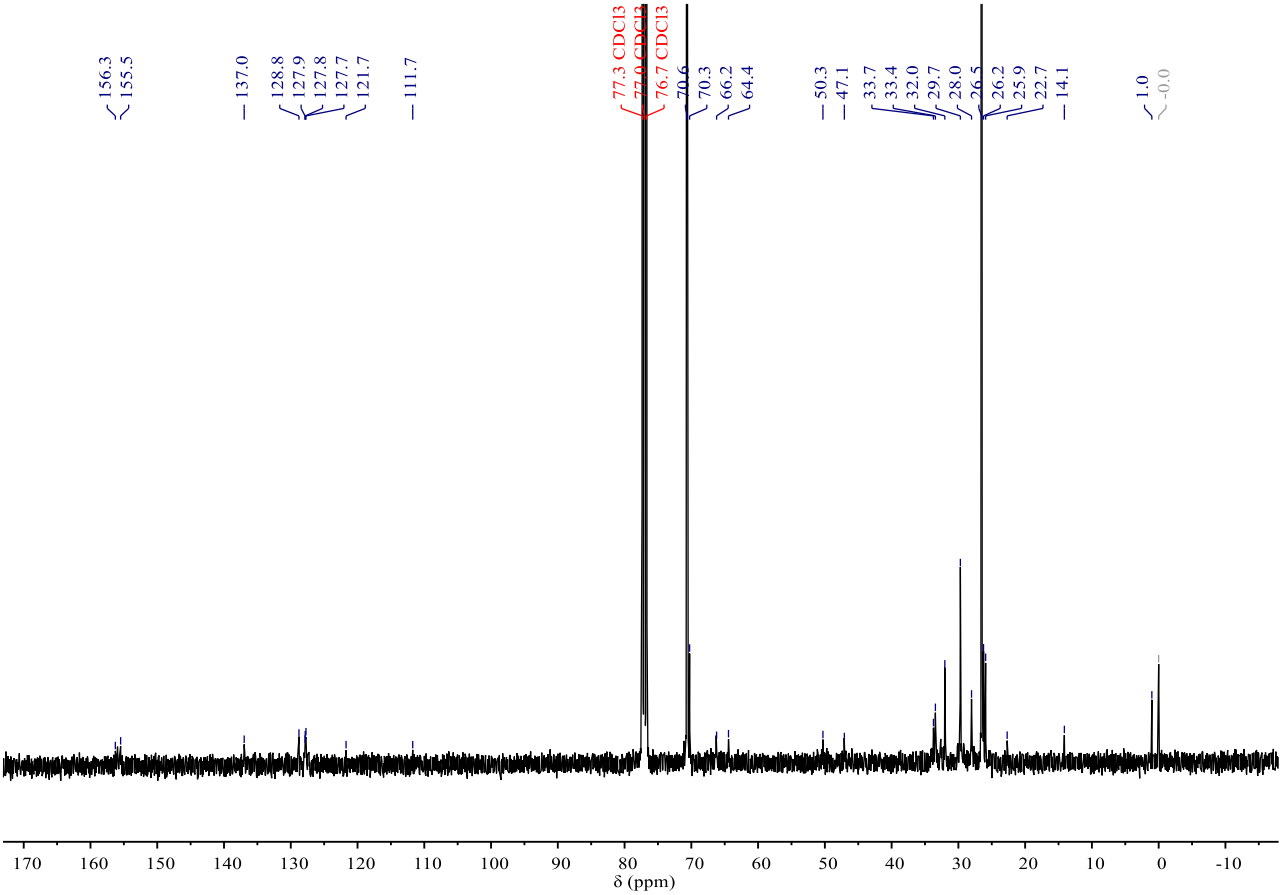

Figure 24. ^{13}C{H} NMR spectrum of **SPE6** (100 MHz, $CDCl_3$, 298 K).

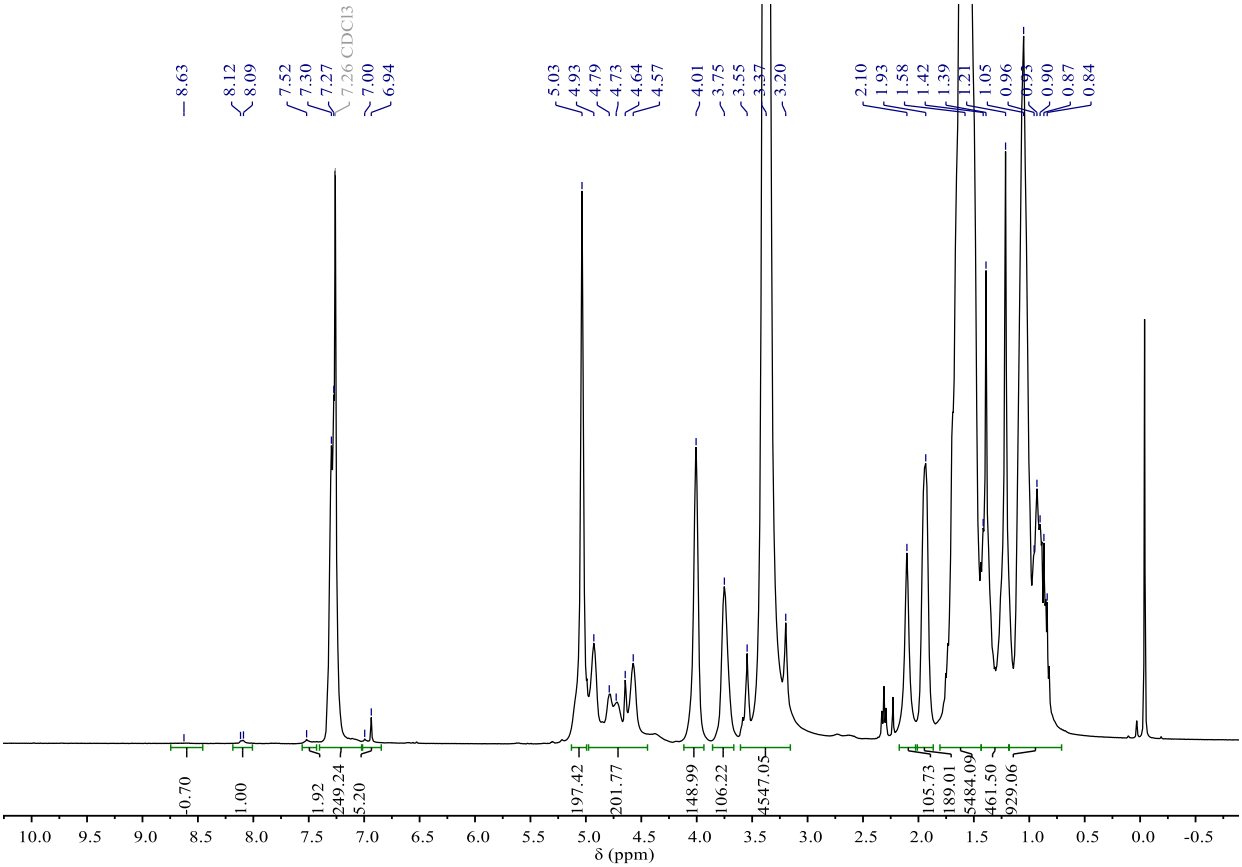

Figure 47. ^{1}H NMR spectrum of **SPE7** (400 MHz, $CDCl_3$, 298 K).

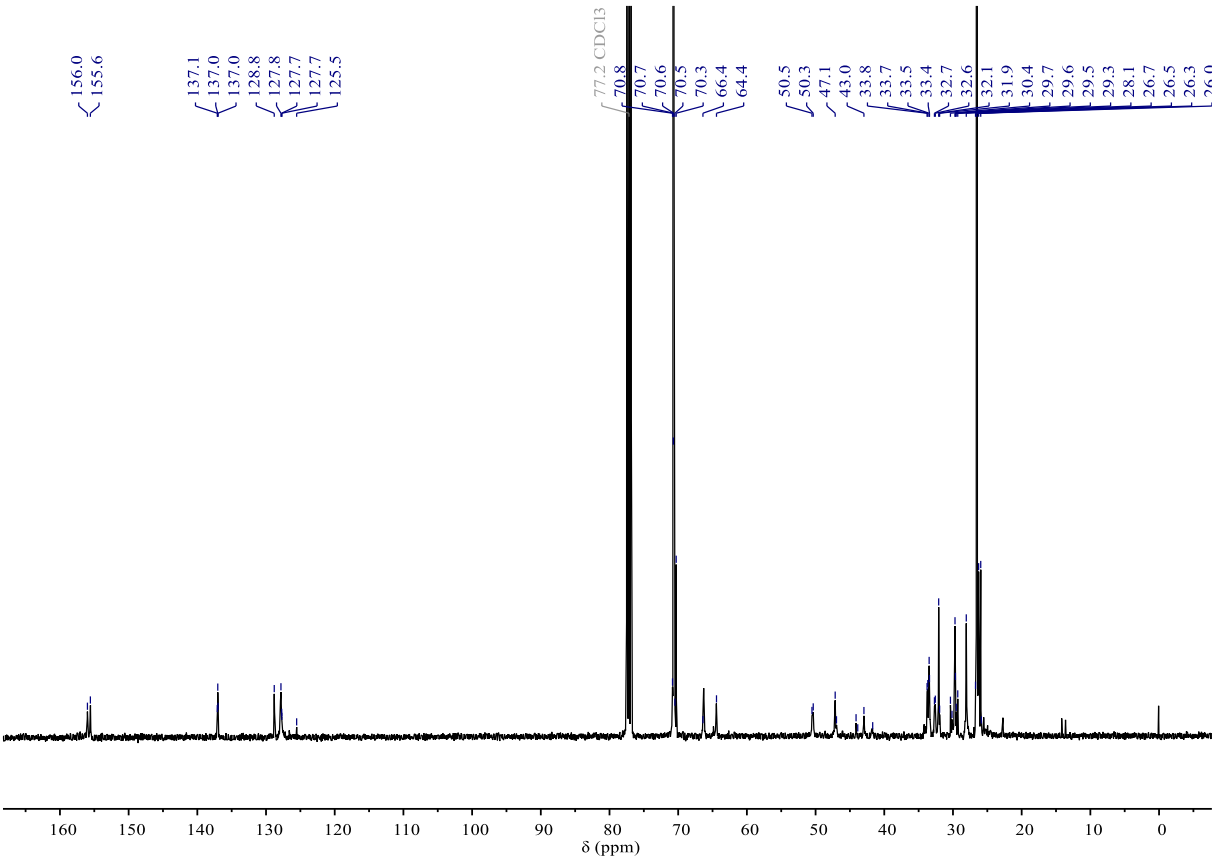

Figure 26. ^{13}C{H} NMR spectrum of **SPE7** (100 MHz, $CDCl_3$, 298 K).

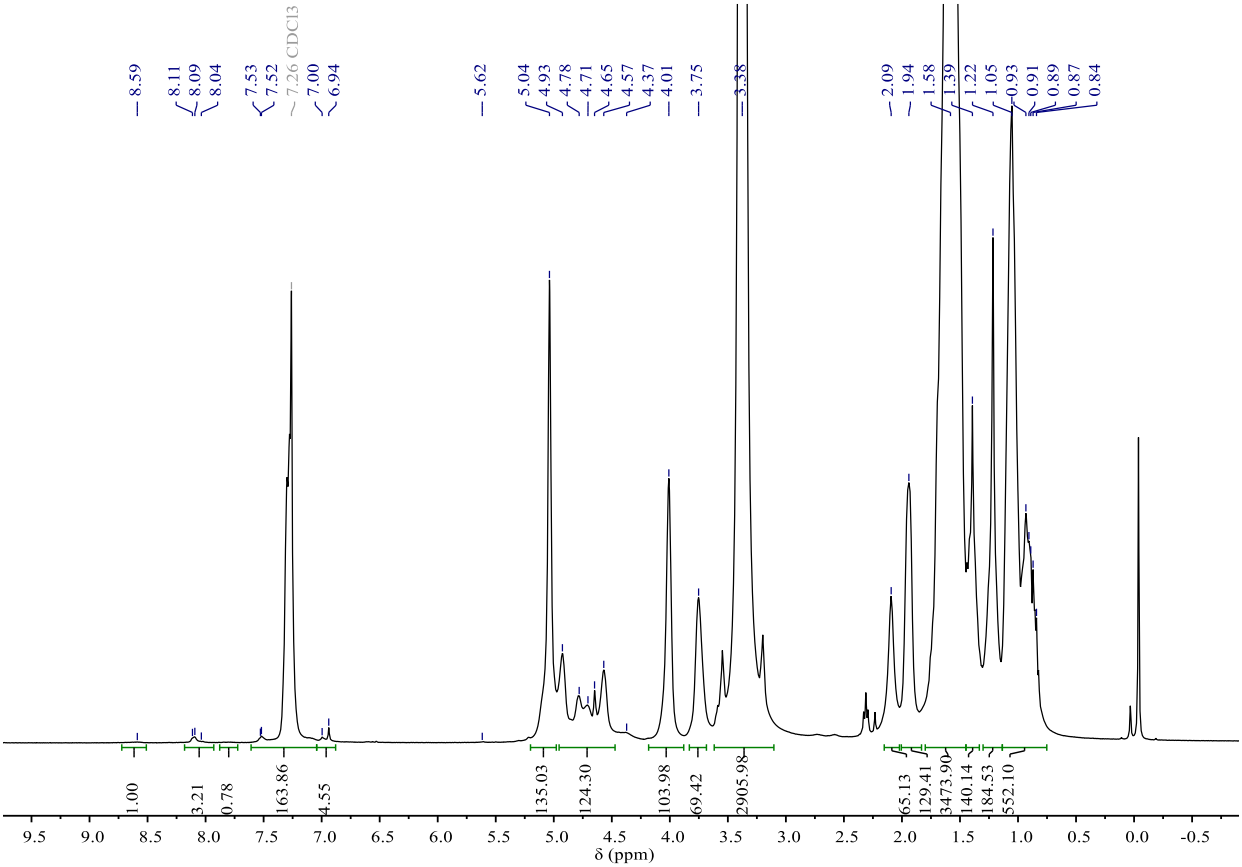

Figure 27. ^{1}H NMR spectrum of **SPE8** (400 MHz, $CDCl_3$, 298 K).

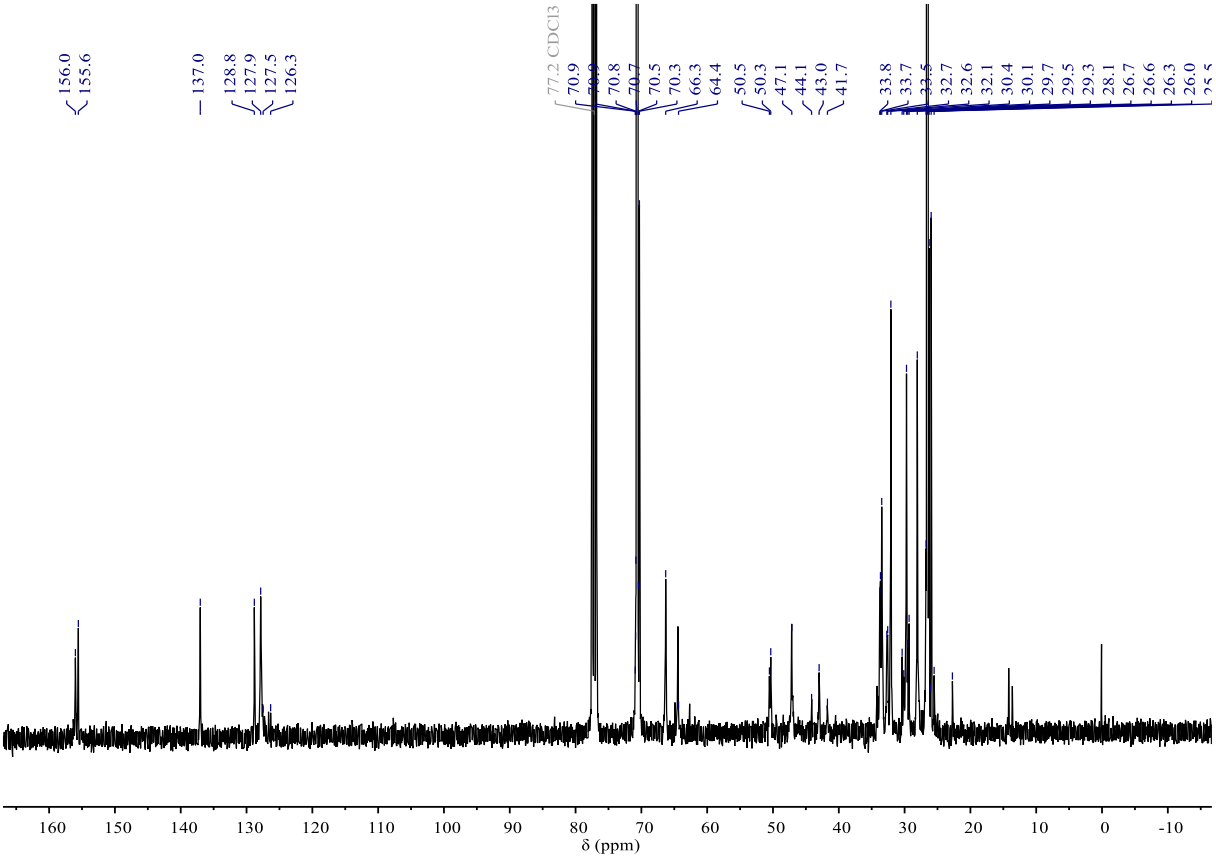

Figure 28. ^{13}C{H} NMR spectrum of **SPE8** (100 MHz, $CDCl_3$, 298 K).

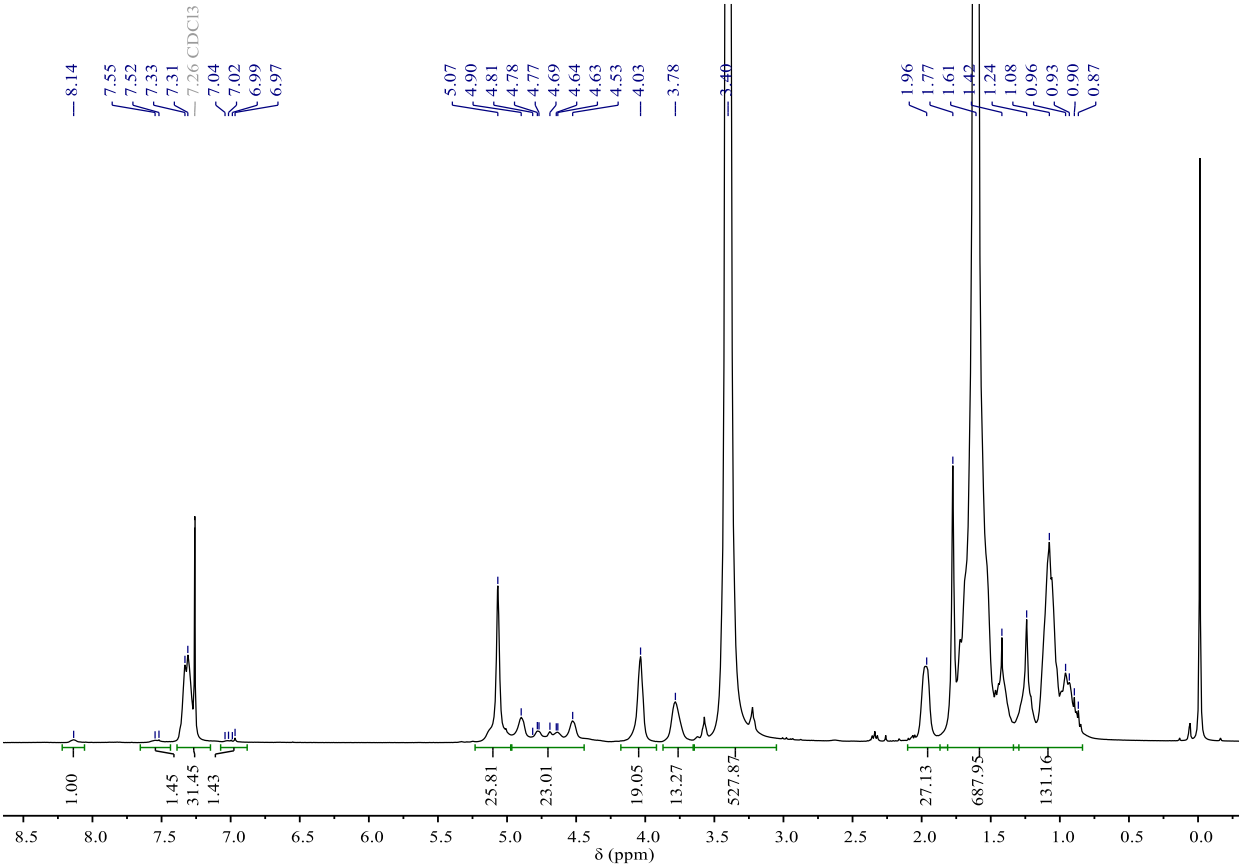

Figure 29. ^{1}H NMR spectrum of **SPE9** (400 MHz, $CDCl_3$, 298 K).

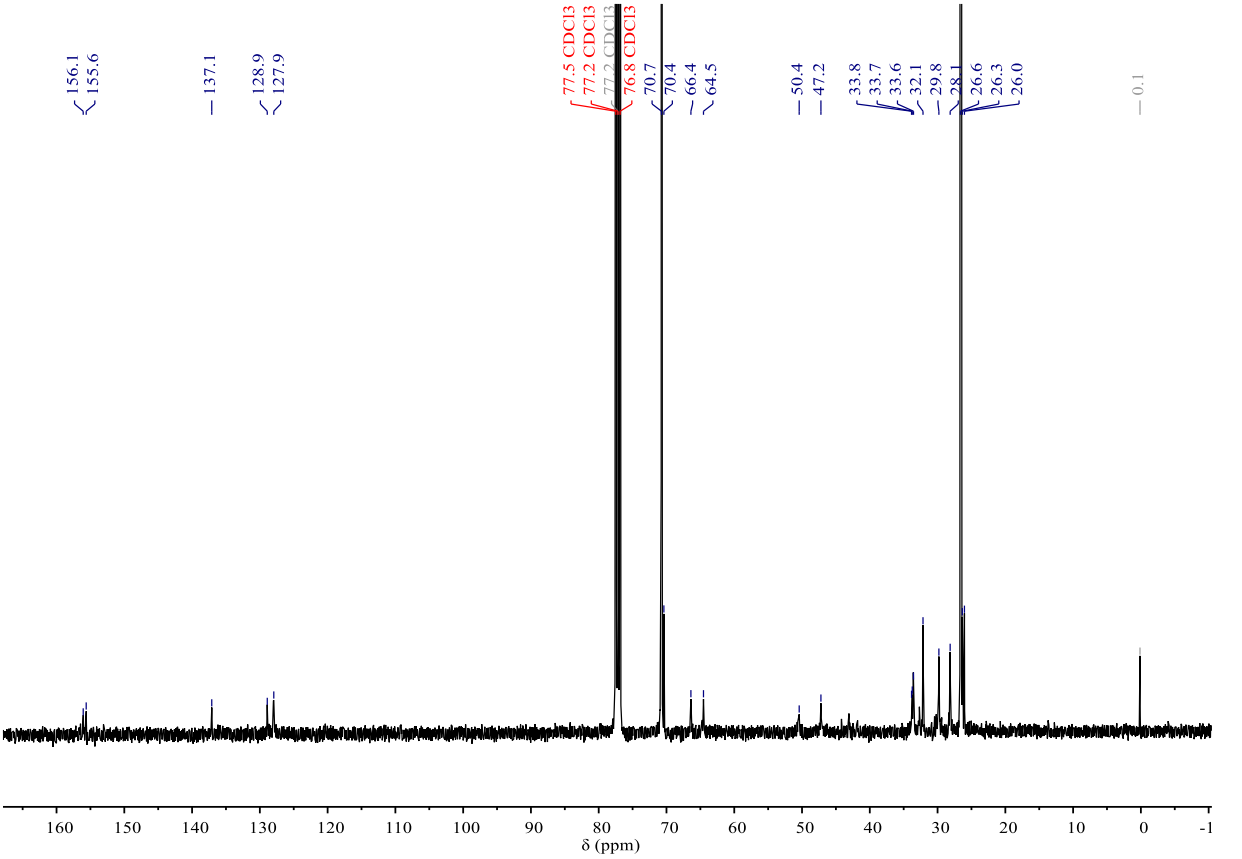

Figure 30. ^{13}C{H} NMR spectrum of **SPE9** (100 MHz, $CDCl_3$, 298 K).

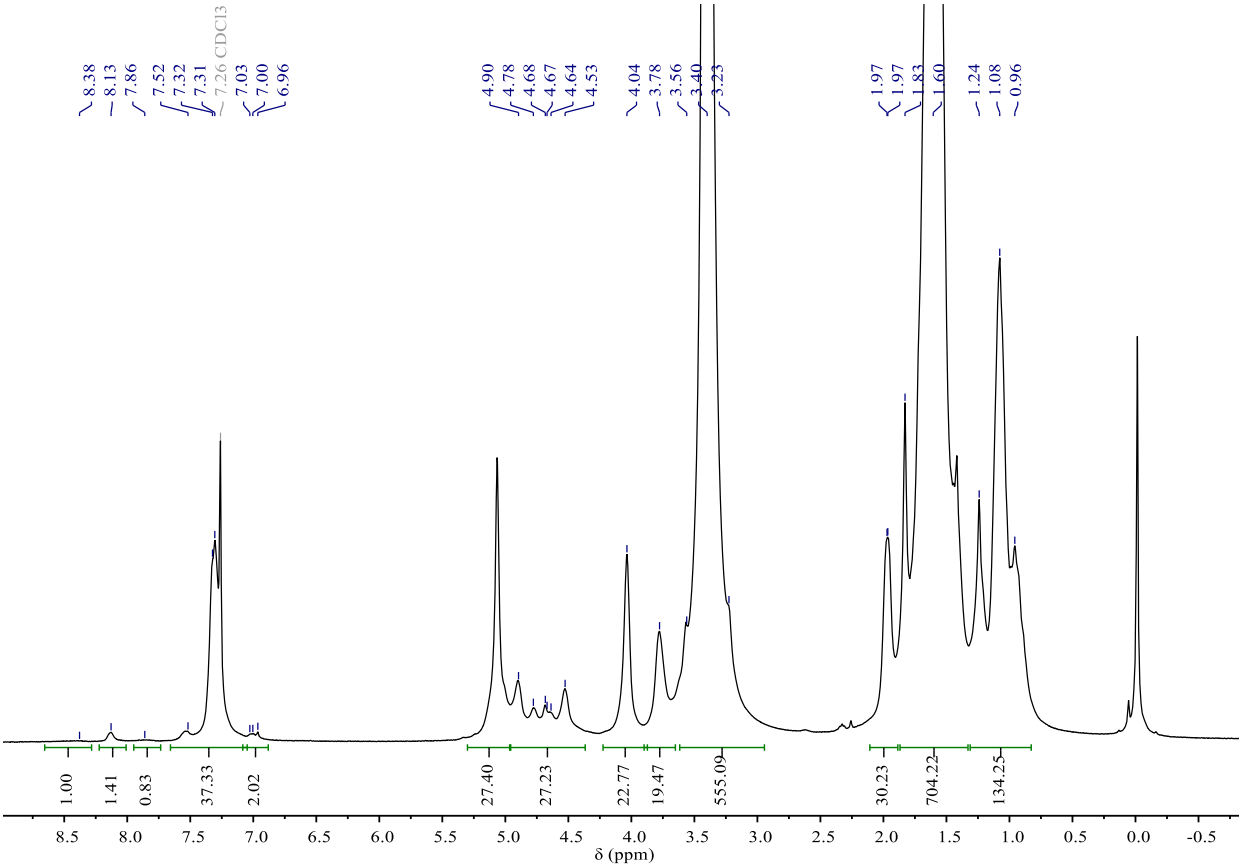

Figure 31. ^{1}H NMR spectrum of **SPE10** (400 MHz, $CDCl_3$, 298 K).

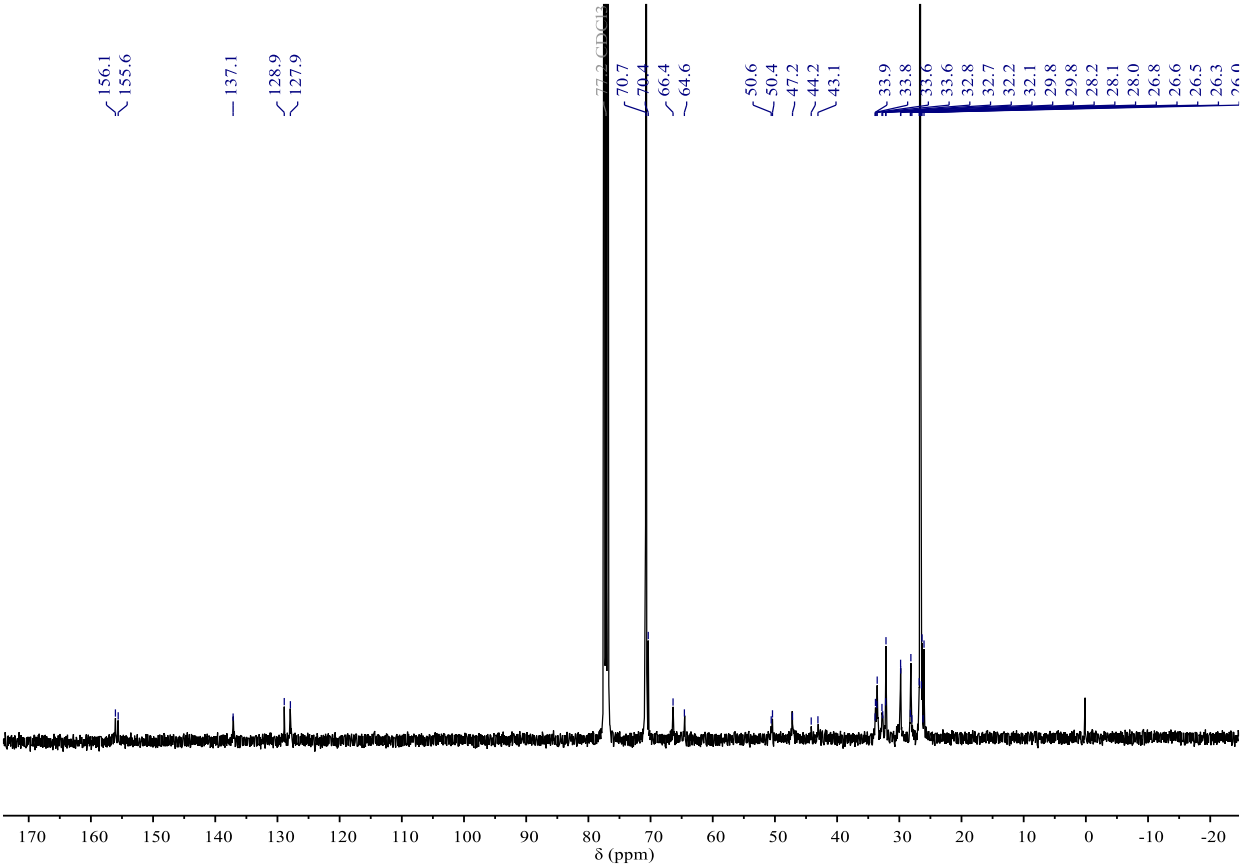

Figure 32. ^{13}C{H} NMR spectrum of **SPE10** (100 MHz, $CDCl_3$, 298 K).

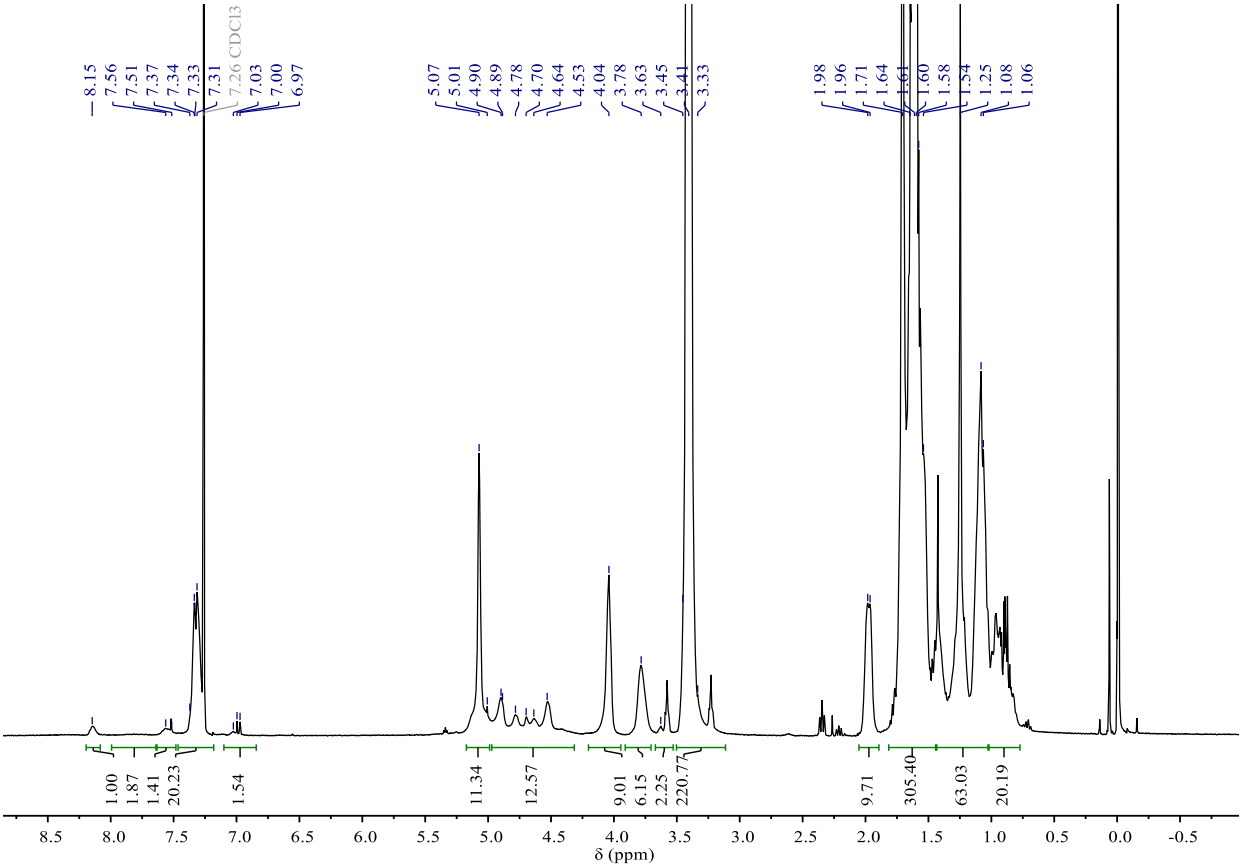

Figure 33. ^{1}H NMR spectrum of **SPE11** (400 MHz, $CDCl_3$, 298 K).

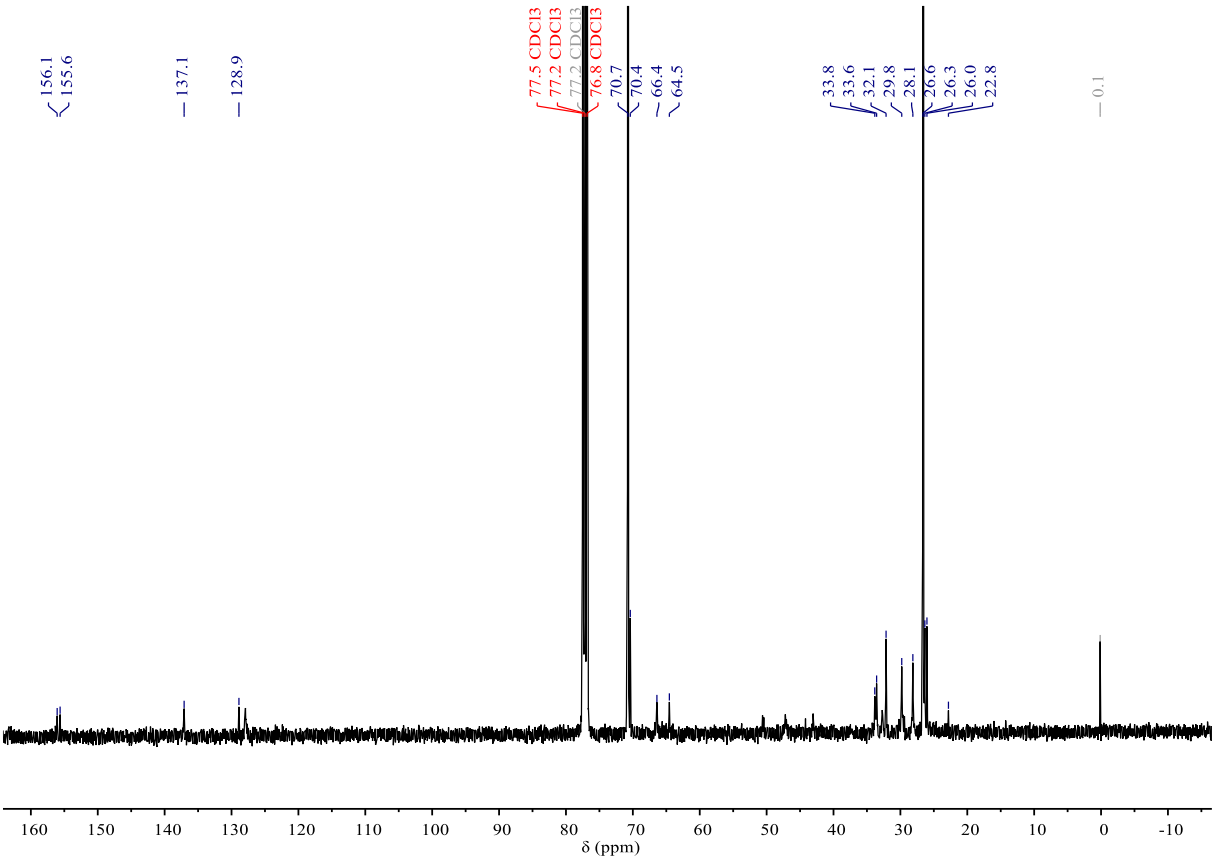

Figure 34. ^{13}C{H} NMR spectrum of **SPE11** (100 MHz, $CDCl_3$, 298 K).

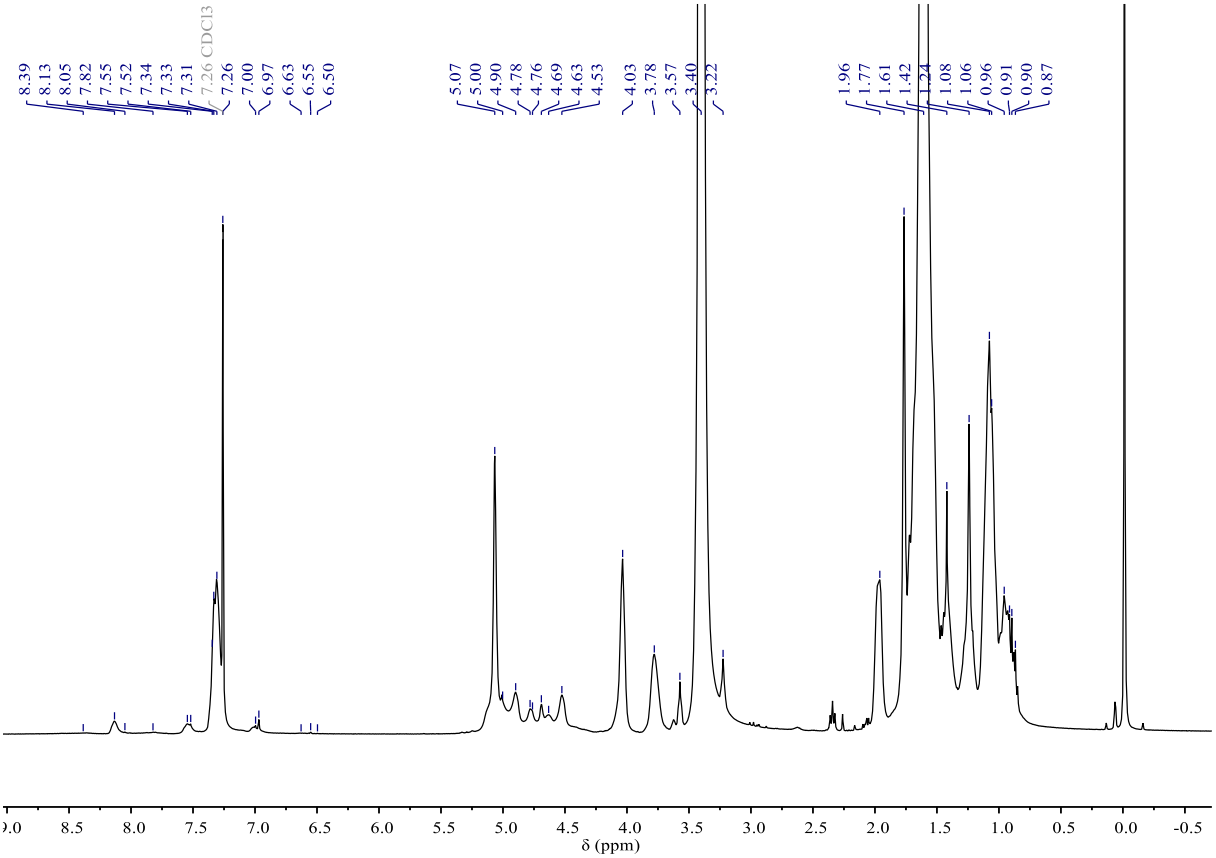

Figure 35. ^{1}H NMR spectrum of **SPE12** (400 MHz, $CDCl_3$, 298 K).

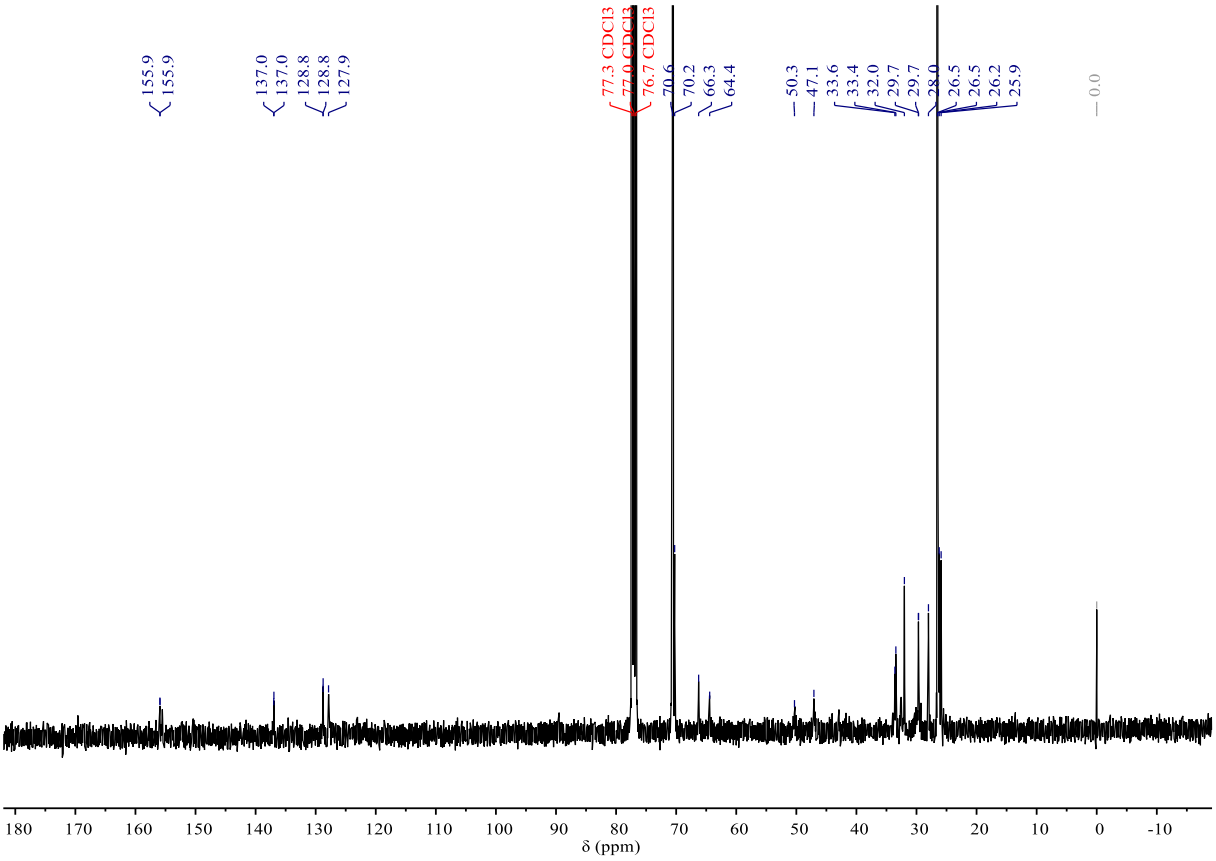

Figure 36. ^{13}C{H} NMR spectrum of **SPE12** (100 MHz, $CDCl_3$, 298 K).

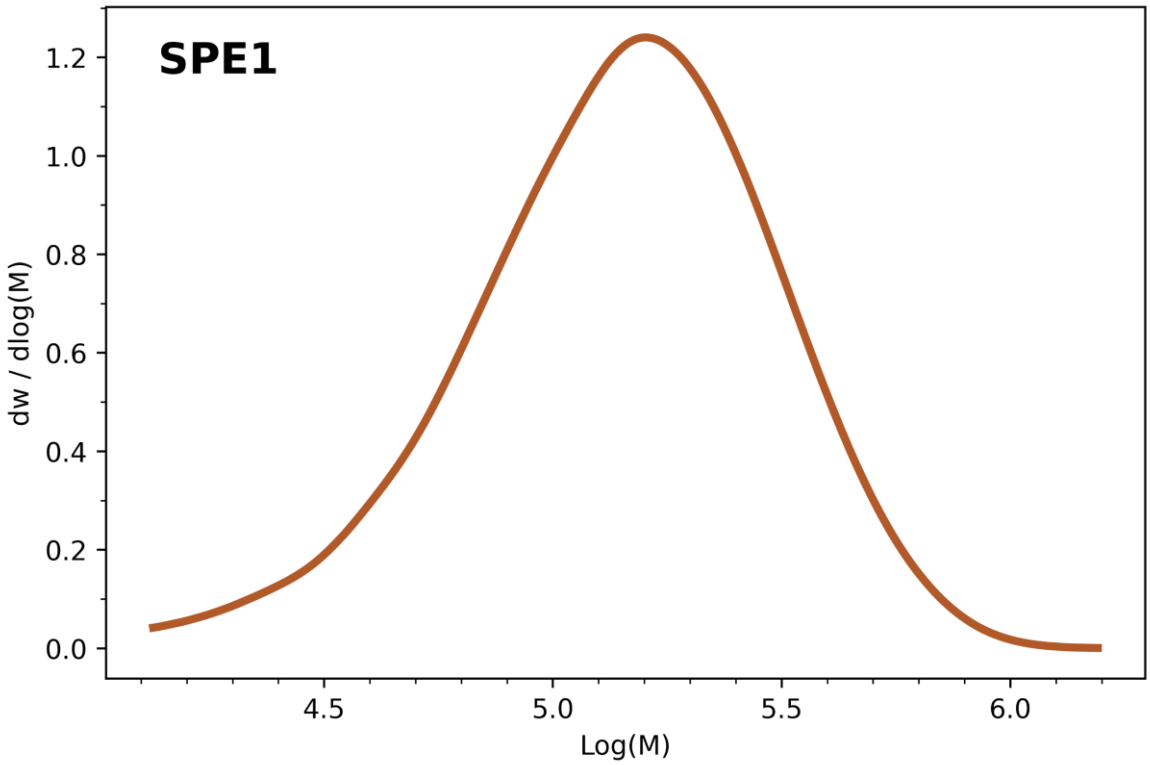

Figure 37. GPC Eluogram of **SPE1** (DMF, room temperature).

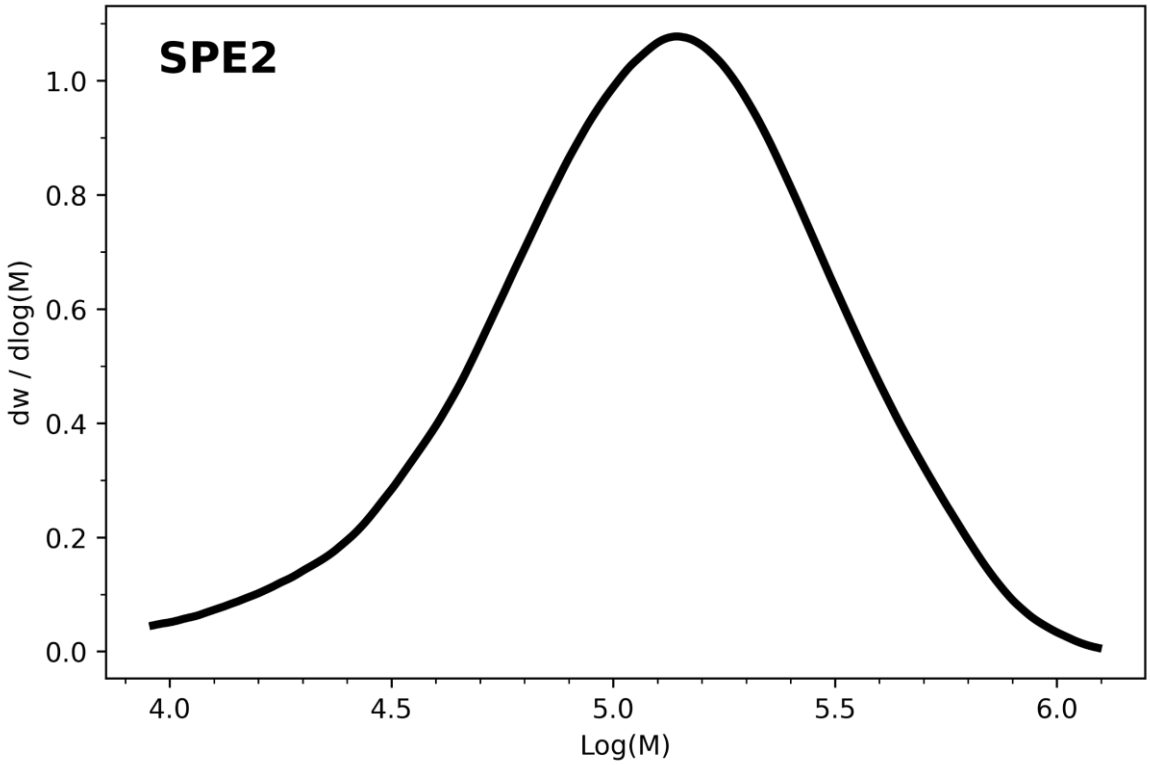

Figure 38. GPC Eluogram of **SPE2** (DMF, room temperature).

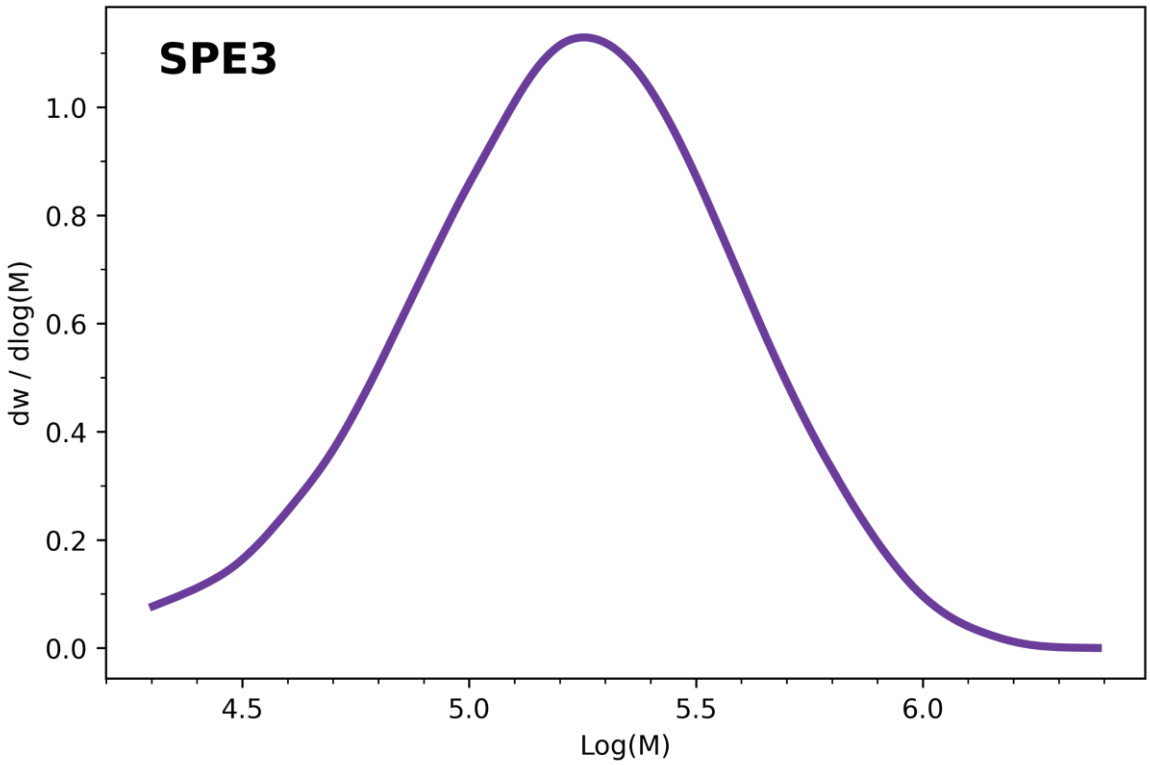

Figure 39. GPC Eluogram of **SPE3** (DMF, room temperature).

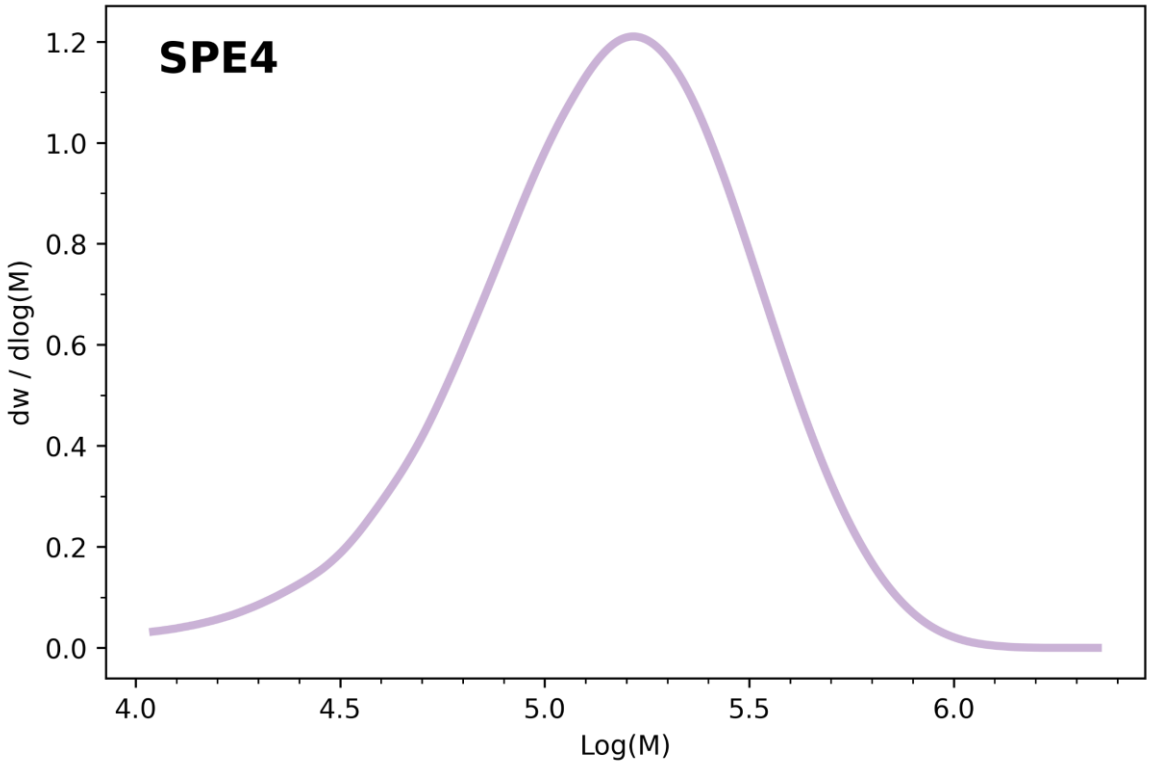

Figure 40. GPC Eluogram of **SPE4** (DMF, room temperature).

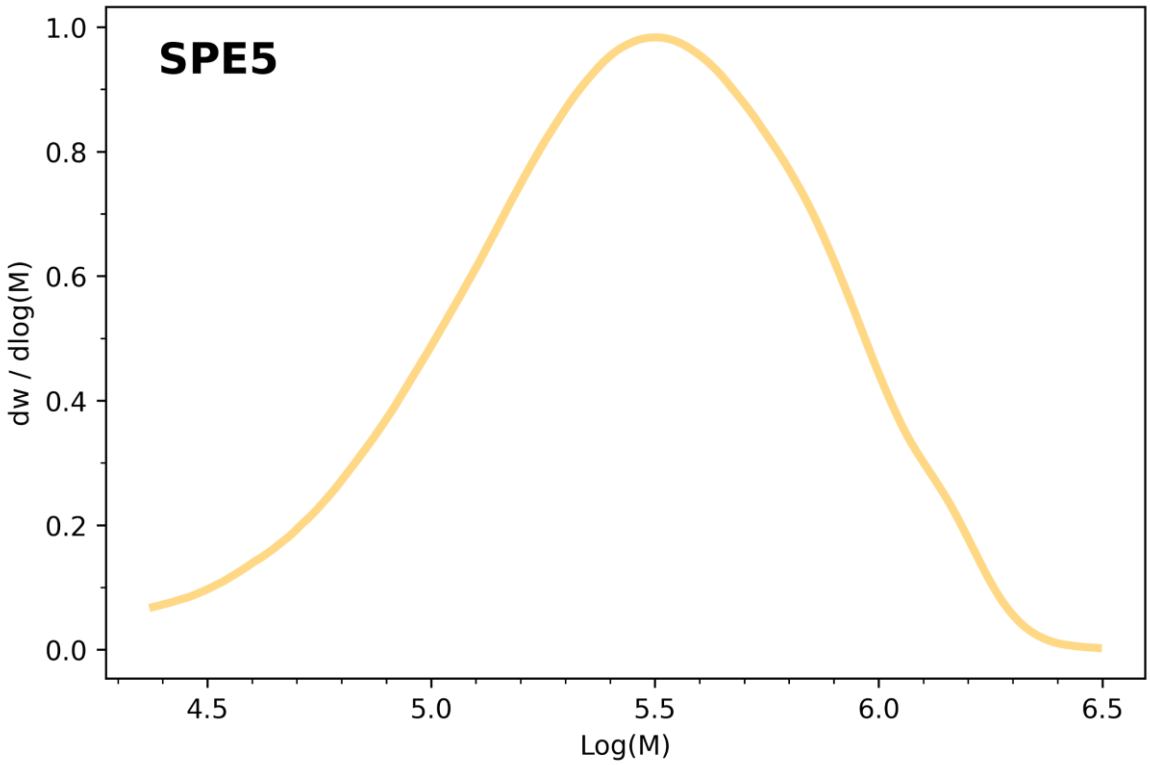

Figure 41. GPC Eluogram of **SPE5** (DMF, room temperature).

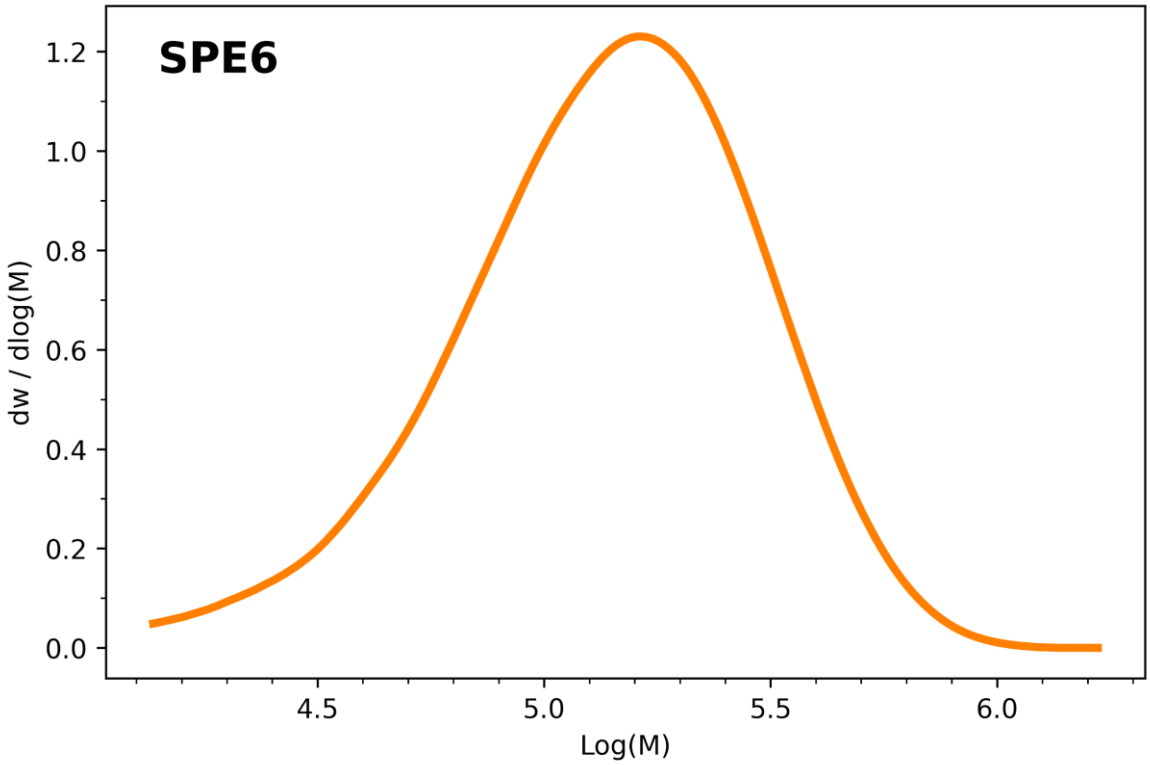

Figure 42. GPC Eluogram of **SPE6** (DMF, room temperature).

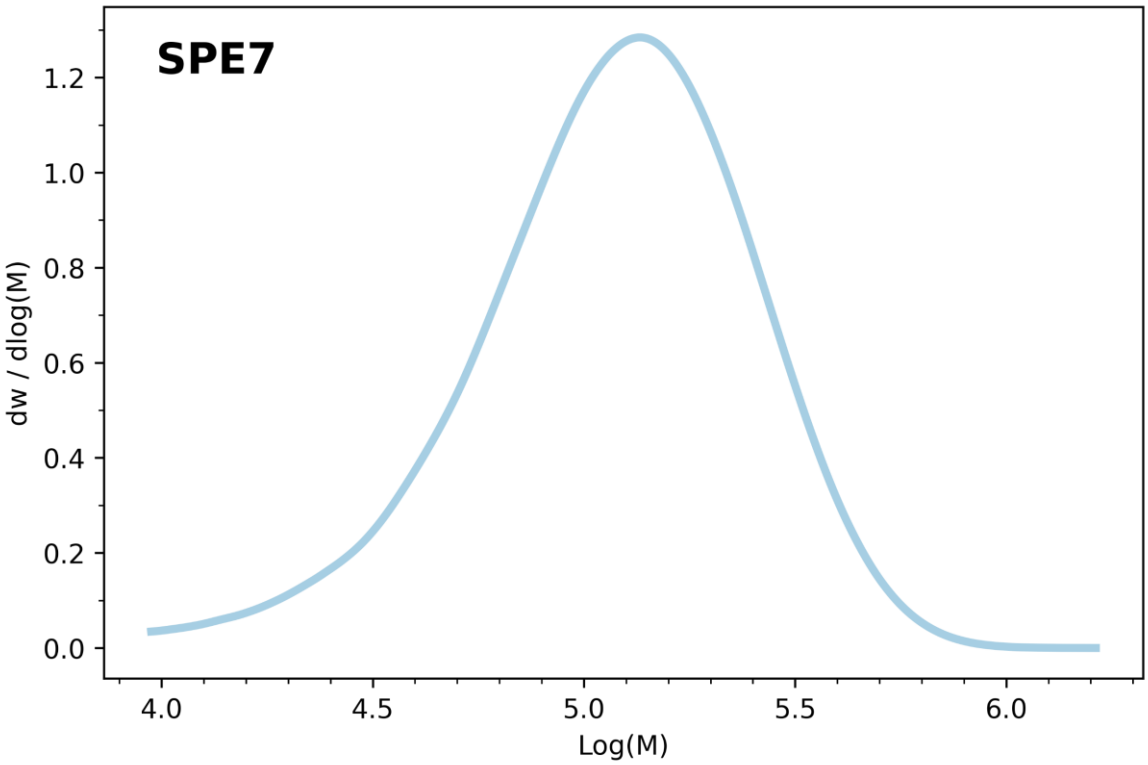

Figure 43. GPC Eluogram of **SPE7** (DMF, room temperature).

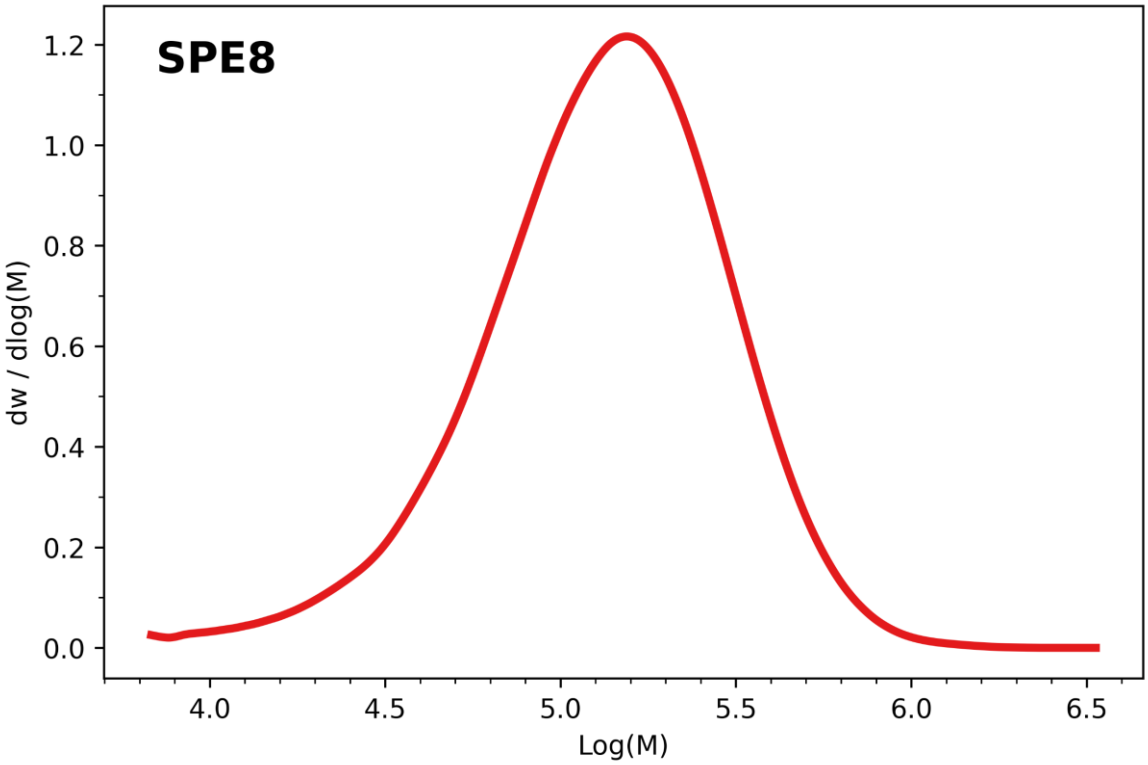

Figure 44. GPC Eluogram of **SPE8** (DMF, room temperature).

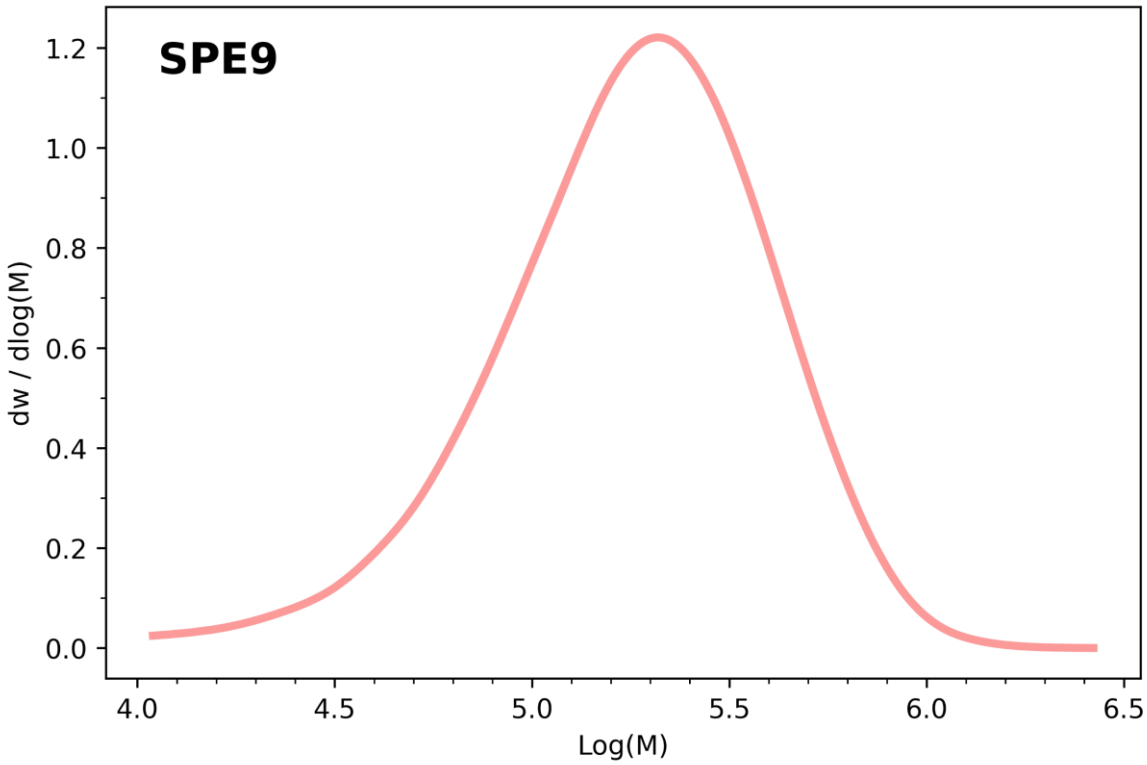

Figure 45. GPC Eluogram of **SPE9** (DMF, room temperature).

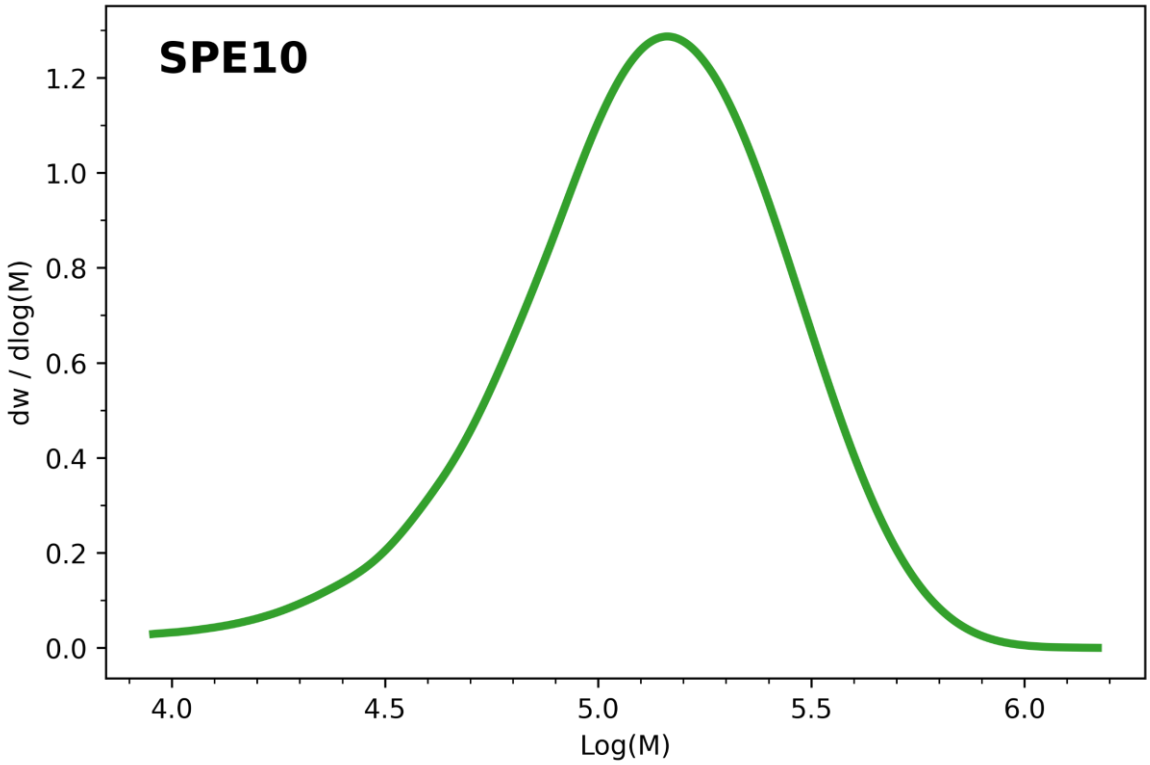

Figure 46. GPC Eluogram of **SPE10** (DMF, room temperature).

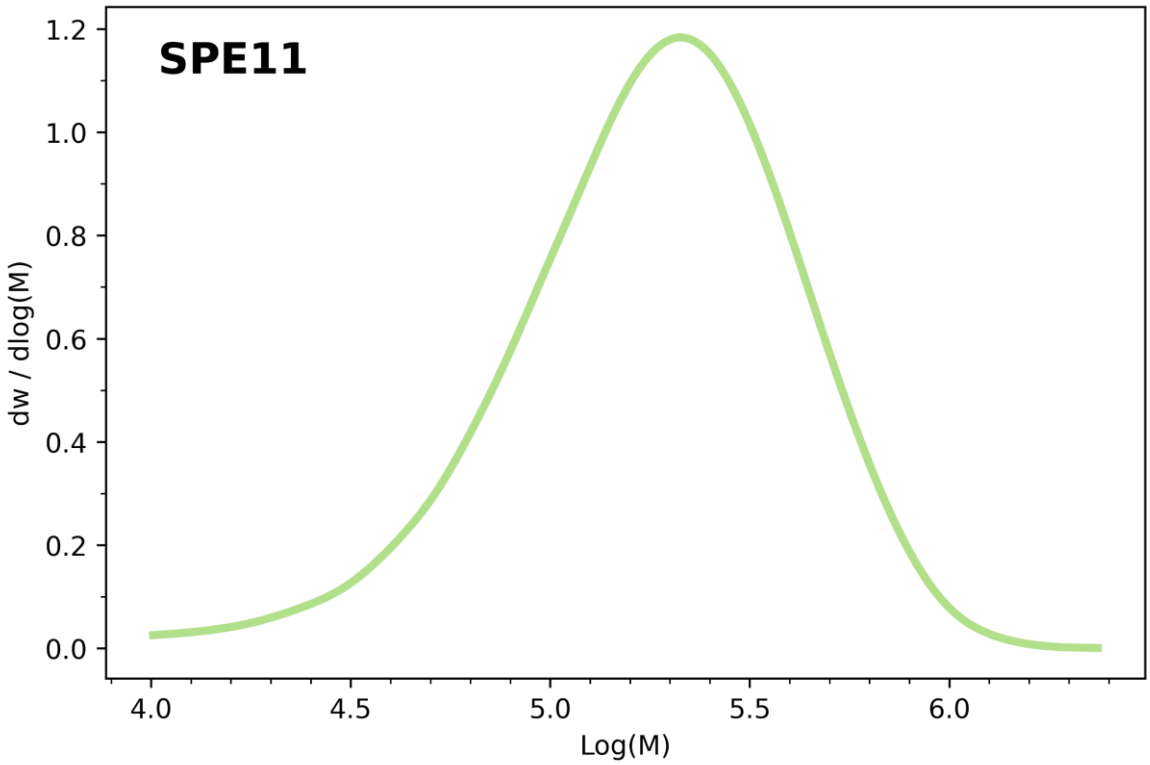

Figure 47. GPC Eluogram of **SPE11** (DMF, room temperature).

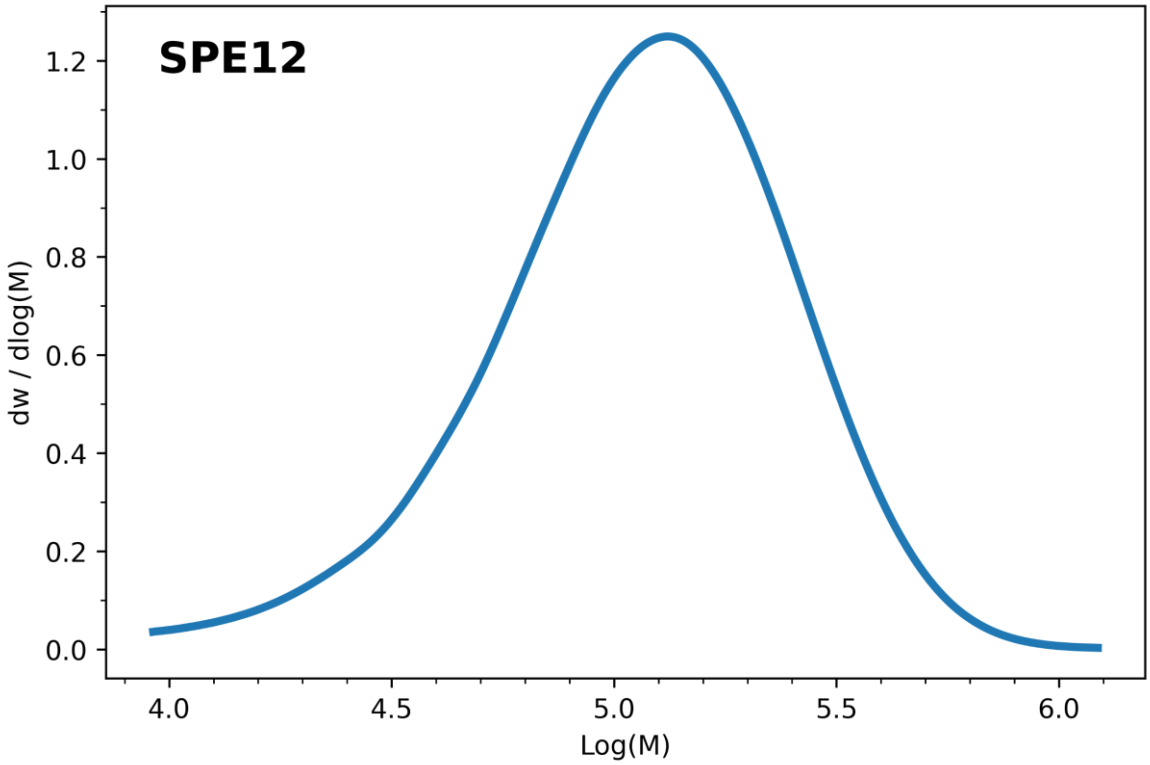

Figure 48. GPC Eluogram of **SPE12** (DMF, room temperature).

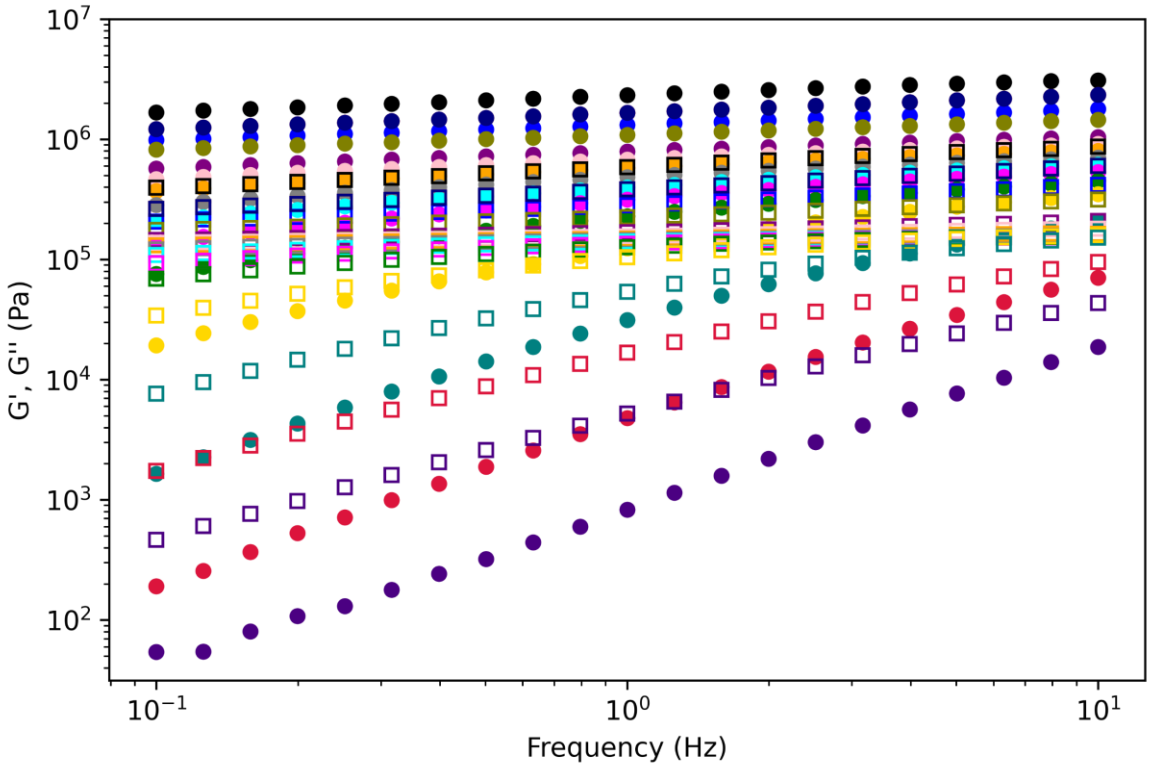

Figure 49. Frequency sweeps of **SPE1** at 0 (black), 10 (red), 20 (blue), 30 (olive), 40 (navy), 50 (purple), 60 (pink), 70 (orange), 80 (gray), 90 (cyan), 100 (magenta), 110 (green), 120 (gold), 130 (teal), 140 (crimson), 150 °C (indigo). G' closed symbols and G'' open symbols frequency sweeps were performed between 0.1 to 10 Hz at an applied strain of 0.1%.

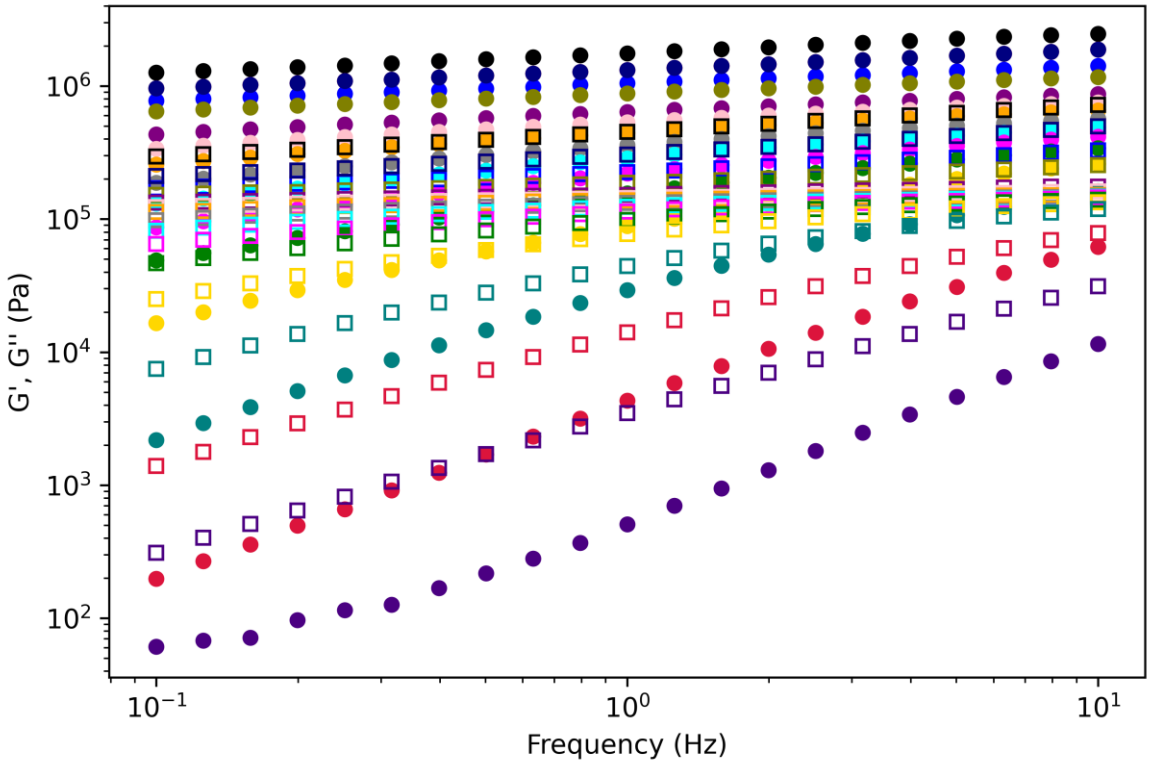

Figure 50. Frequency sweeps of **SPE2** at 0 (black), 10 (red), 20 (blue), 30 (olive), 40 (navy), 50 (purple), 60 (pink), 70 (orange), 80 (gray), 90 (cyan), 100 (magenta), 110 (green), 120 (gold), 130 (teal), 140 (crimson), 150 °C (indigo). G' closed symbols and G'' open symbols frequency sweeps were performed between 0.1 to 10 Hz at an applied strain of 0.1%.

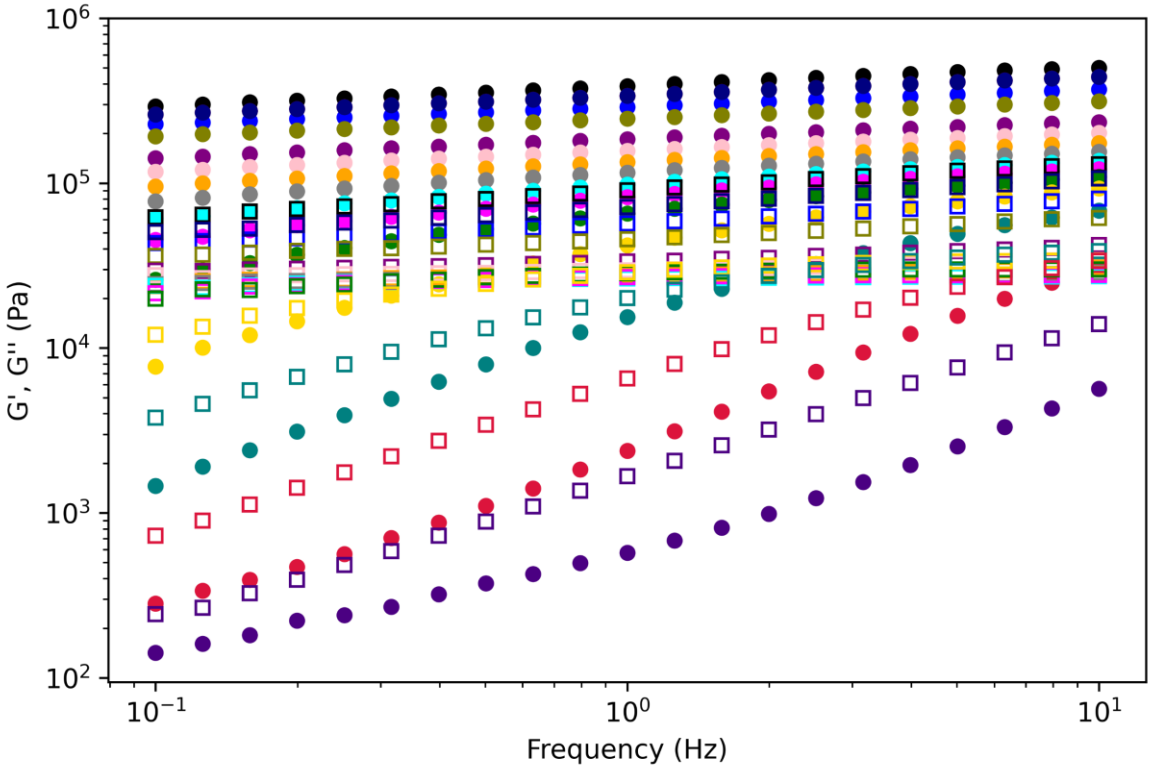

Figure 51. Frequency sweeps of **SPE3** at 0 (black), 10 (red), 20 (blue), 30 (olive), 40 (navy), 50 (purple), 60 (pink), 70 (orange), 80 (gray), 90 (cyan), 100 (magenta), 110 (green), 120 (gold), 130 (teal), 140 (crimson), 150 °C (indigo). G' closed symbols and G'' open symbols frequency sweeps were performed between 0.1 to 10 Hz at an applied strain of 0.1%.

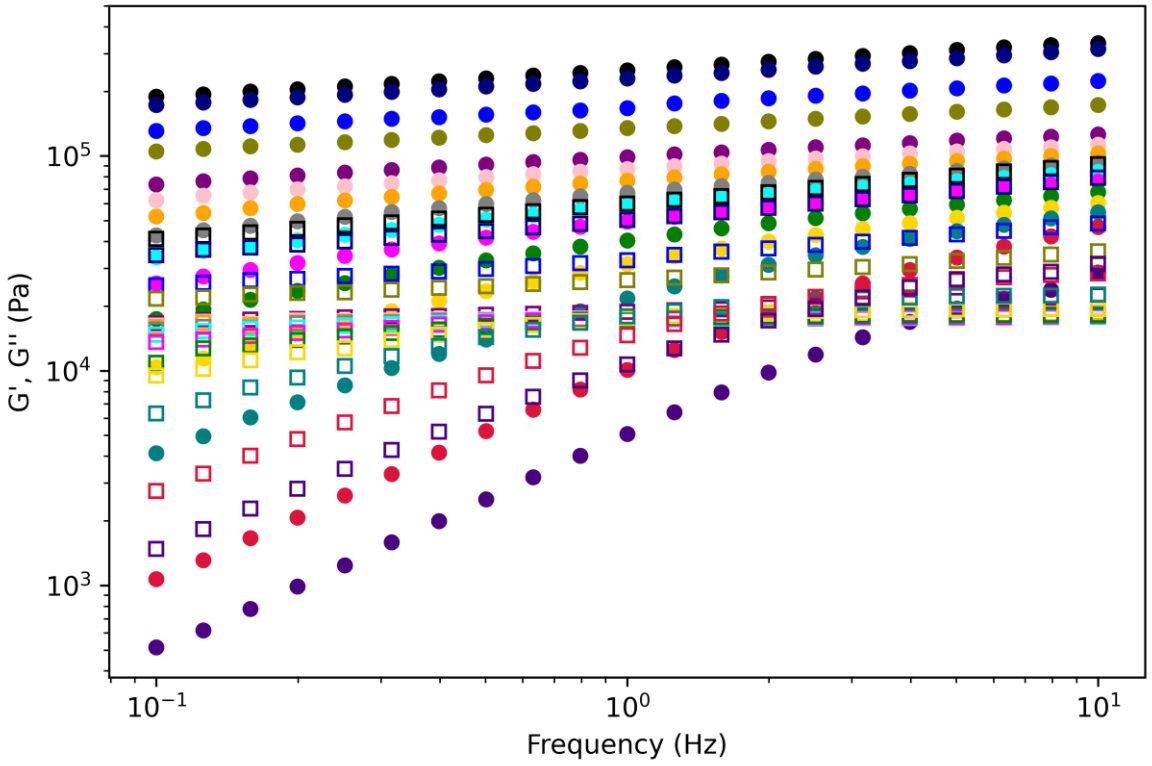

Figure 52. Frequency sweeps of **SPE4** at 0 (black), 10 (red), 20 (blue), 30 (olive), 40 (navy), 50 (purple), 60 (pink), 70 (orange), 80 (gray), 90 (cyan), 100 (magenta), 110 (green), 120 (gold), 130 (teal), 140 (crimson), 150 °C (indigo). G' closed symbols and G'' open symbols frequency sweeps were performed between 0.1 to 10 Hz at an applied strain of 0.1%.

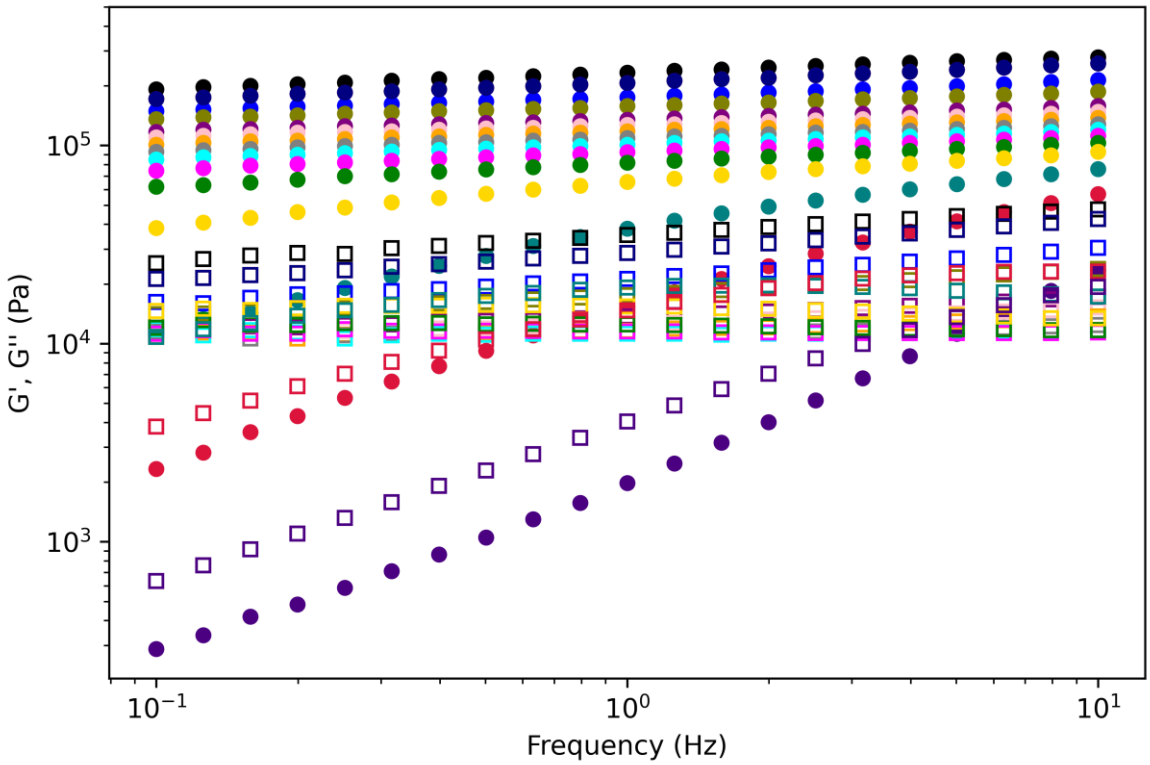

Figure 53. Frequency sweeps of **SPE5** at 0 (black), 10 (red), 20 (blue), 30 (olive), 40 (navy), 50 (purple), 60 (pink), 70 (orange), 80 (gray), 90 (cyan), 100 (magenta), 110 (green), 120 (gold), 130 (teal), 140 (crimson), 150 °C (indigo). G' closed symbols and G'' open symbols frequency sweeps were performed between 0.1 to 10 Hz at an applied strain of 0.1%.

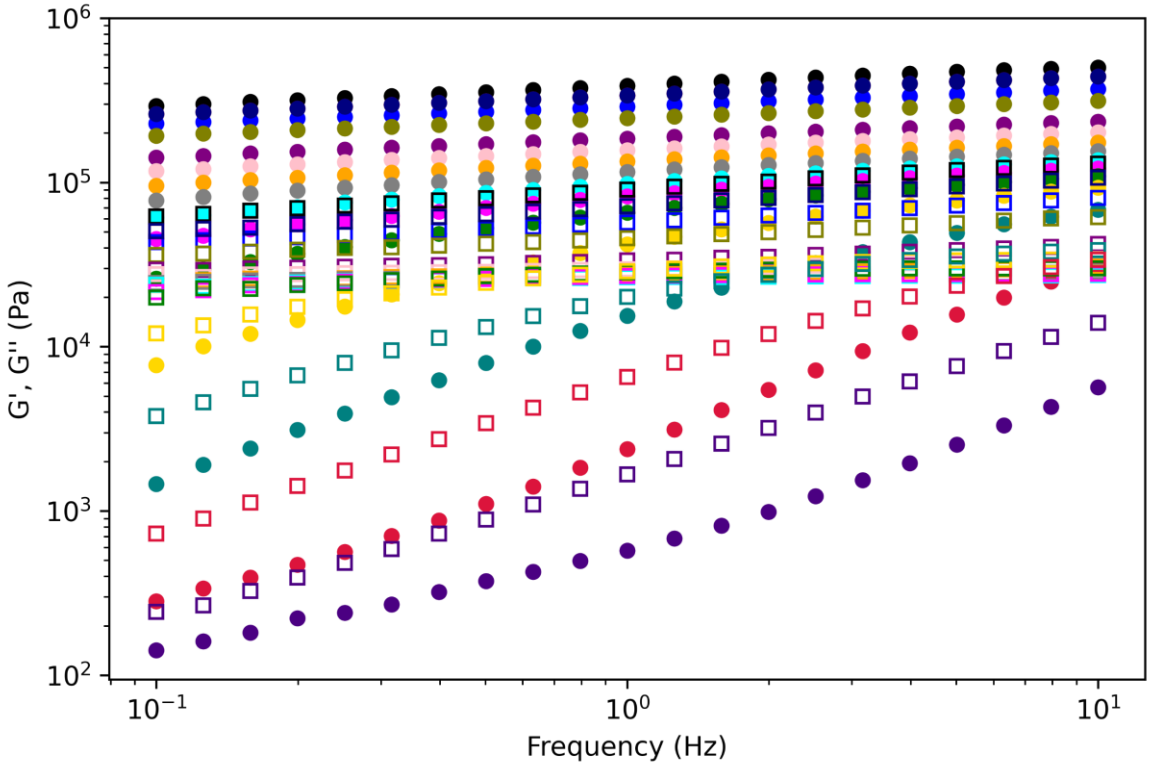

Figure 54. Frequency sweeps of **SPE6** at 0 (black), 10 (red), 20 (blue), 30 (olive), 40 (navy), 50 (purple), 60 (pink), 70 (orange), 80 (gray), 90 (cyan), 100 (magenta), 110 (green), 120 (gold), 130 (teal), 140 (crimson), 150 °C (indigo). G' closed symbols and G'' open symbols frequency sweeps were performed between 0.1 to 10 Hz at an applied strain of 0.1%.

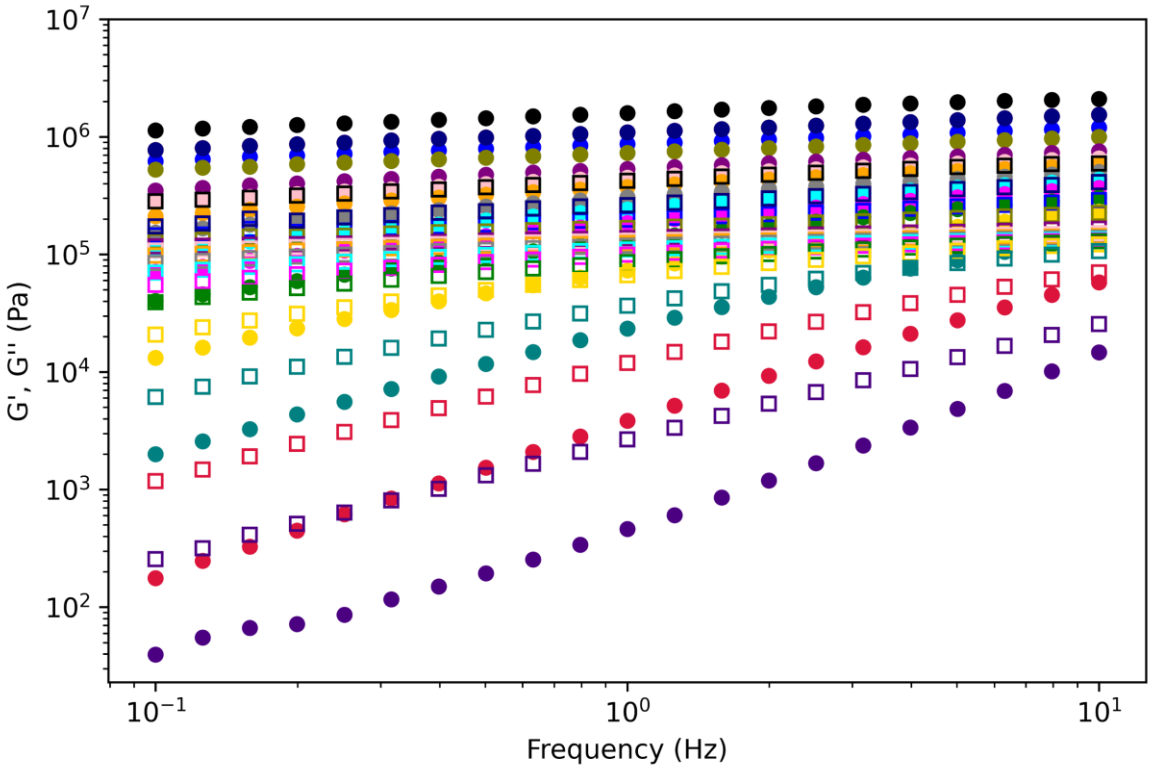

Figure 55. Frequency sweeps of **SPE7** at 0 (black), 10 (red), 20 (blue), 30 (olive), 40 (navy), 50 (purple), 60 (pink), 70 (orange), 80 (gray), 90 (cyan), 100 (magenta), 110 (green), 120 (gold), 130 (teal), 140 (crimson), 150 °C (indigo). G' closed symbols and G'' open symbols frequency sweeps were performed between 0.1 to 10 Hz at an applied strain of 0.1%.

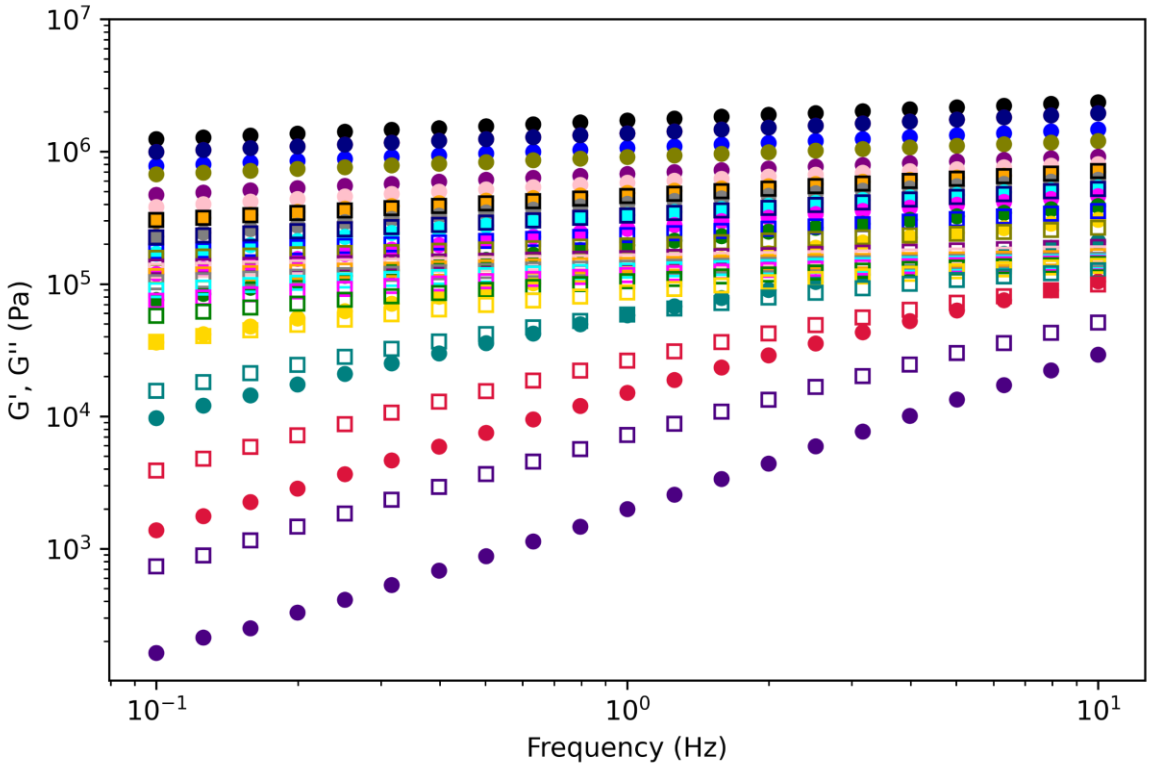

Figure 56. Frequency sweeps of **SPE8** at 0 (black), 10 (red), 20 (blue), 30 (olive), 40 (navy), 50 (purple), 60 (pink), 70 (orange), 80 (gray), 90 (cyan), 100 (magenta), 110 (green), 120 (gold), 130 (teal), 140 (crimson), 150 °C (indigo). G' closed symbols and G'' open symbols frequency sweeps were performed between 0.1 to 10 Hz at an applied strain of 0.1%.

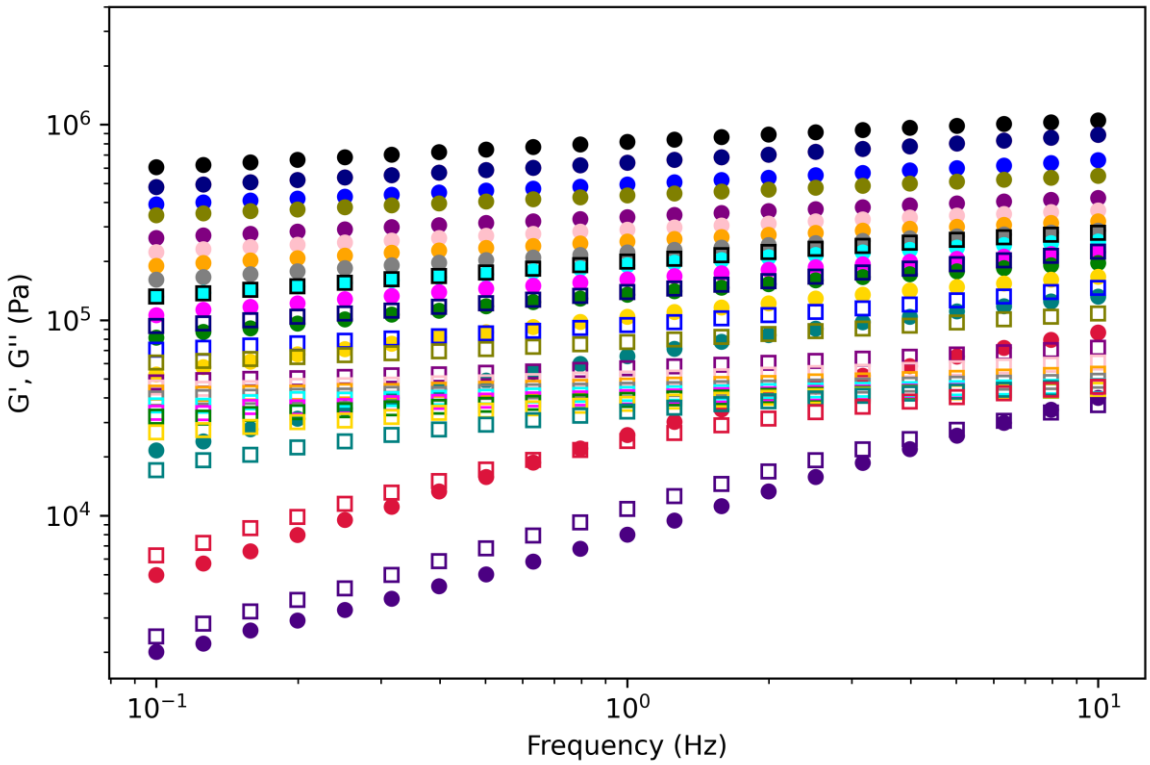

Figure 57. Frequency sweeps of **SPE9** at 0 (black), 10 (red), 20 (blue), 30 (olive), 40 (navy), 50 (purple), 60 (pink), 70 (orange), 80 (gray), 90 (cyan), 100 (magenta), 110 (green), 120 (gold), 130 (teal), 140 (crimson), 150 °C (indigo). G' closed symbols and G'' open symbols frequency sweeps were performed between 0.1 to 10 Hz at an applied strain of 0.1%.

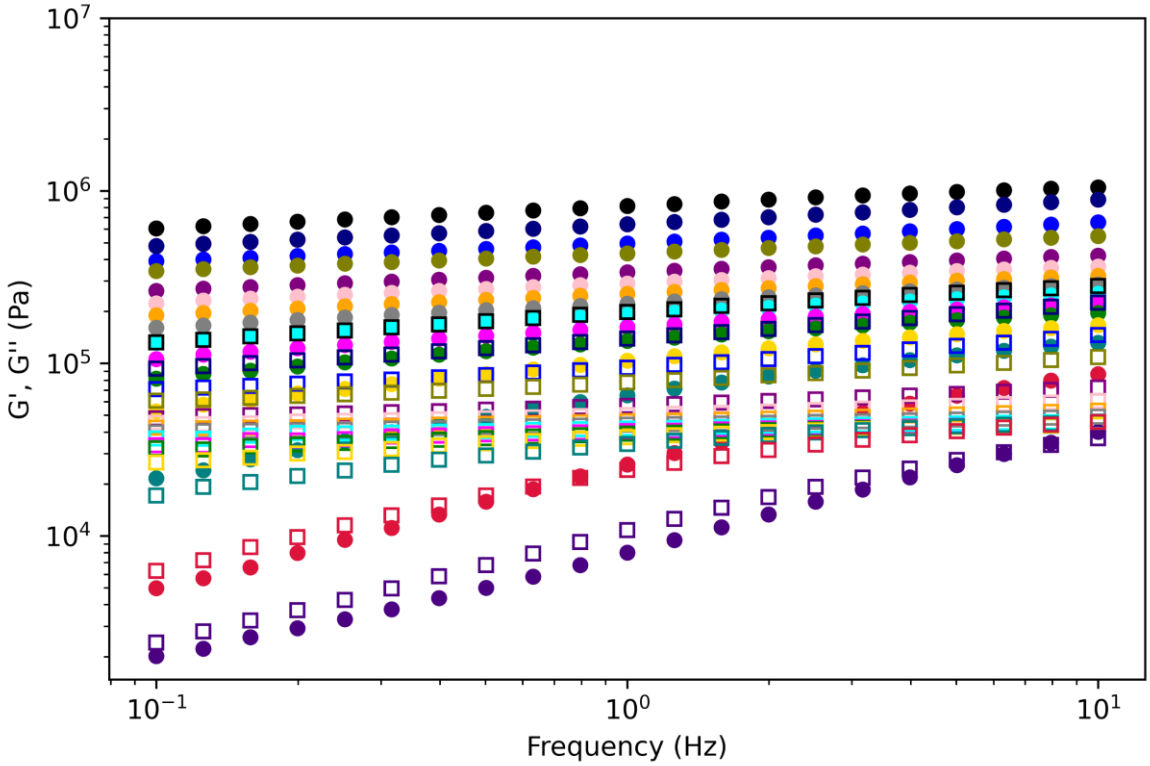

Figure 58. Frequency sweeps of **SPE10** at 0 (black), 10 (red), 20 (blue), 30 (olive), 40 (navy), 50 (purple), 60 (pink), 70 (orange), 80 (gray), 90 (cyan), 100 (magenta), 110 (green), 120 (gold), 130 (teal), 140 (crimson), 150 °C (indigo). G' closed symbols and G'' open symbols frequency sweeps were performed between 0.1 to 10 Hz at an applied strain of 0.1%.

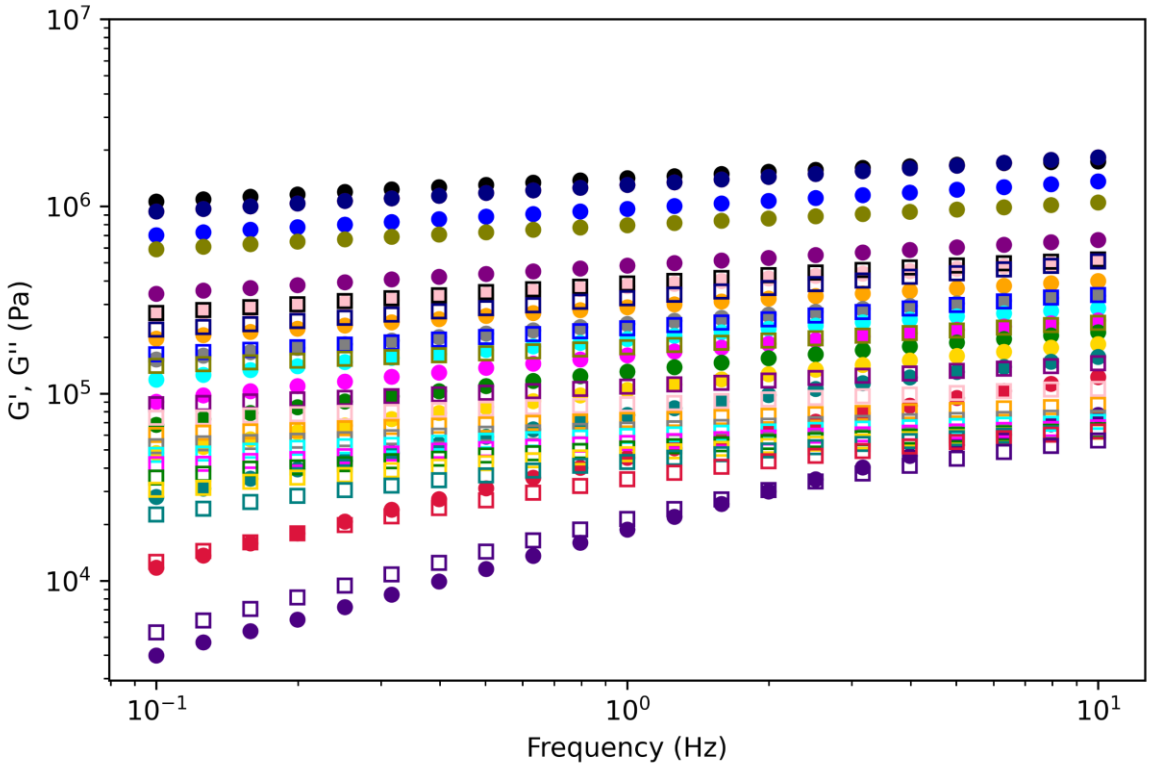

Figure 59. Frequency sweeps of **SPE11** at 0 (black), 10 (red), 20 (blue), 30 (olive), 40 (navy), 50 (purple), 60 (pink), 70 (orange), 80 (gray), 90 (cyan), 100 (magenta), 110 (green), 120 (gold), 130 (teal), 140 (crimson), 150 °C (indigo). G' closed symbols and G'' open symbols frequency sweeps were performed between 0.1 to 10 Hz at an applied strain of 0.1%.

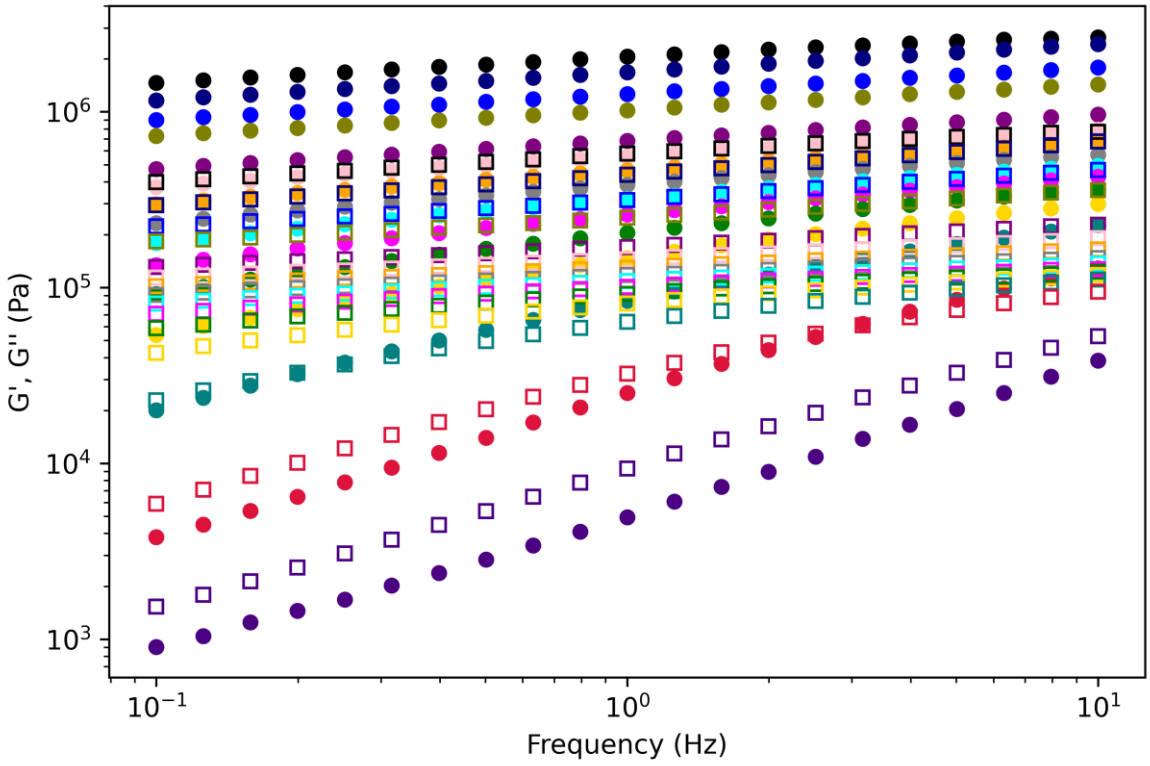

Figure 60. Frequency sweeps of **SPE12** at 0 (black), 10 (red), 20 (blue), 30 (olive), 40 (navy), 50 (purple), 60 (pink), 70 (orange), 80 (gray), 90 (cyan), 100 (magenta), 110 (green), 120 (gold), 130 (teal), 140 (crimson), 150 °C (indigo). G' closed symbols and G'' open symbols frequency sweeps were performed between 0.1 to 10 Hz at an applied strain of 0.1%.

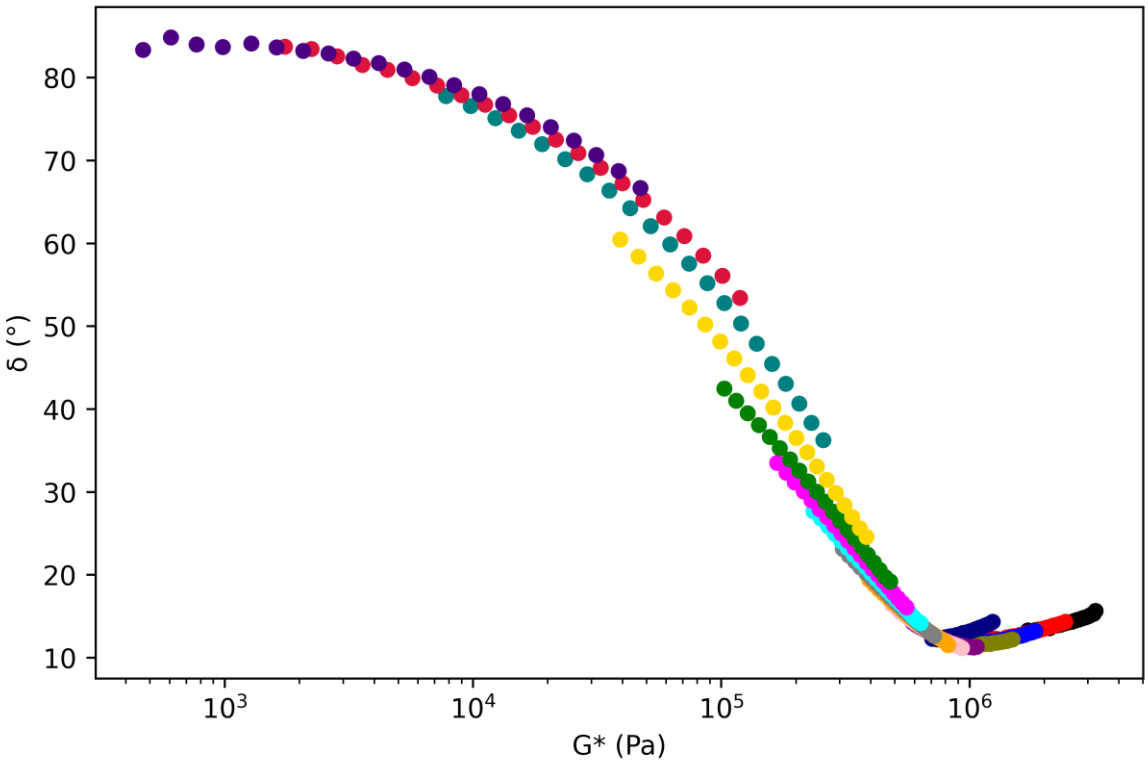

Figure 61. van Gurp-Palmen plot of **SPE1** at 0 (black), 10 (red), 20 (blue), 30 (olive), 40 (navy), 50 (purple), 60 (pink), 70 (orange), 80 (gray), 90 (cyan), 100 (magenta), 110 (green), 120 (gold), 130 (teal), 140 (crimson), 150 °C (indigo). Frequency sweeps were performed between 0.1 to 10 Hz at an applied strain of 0.1%.

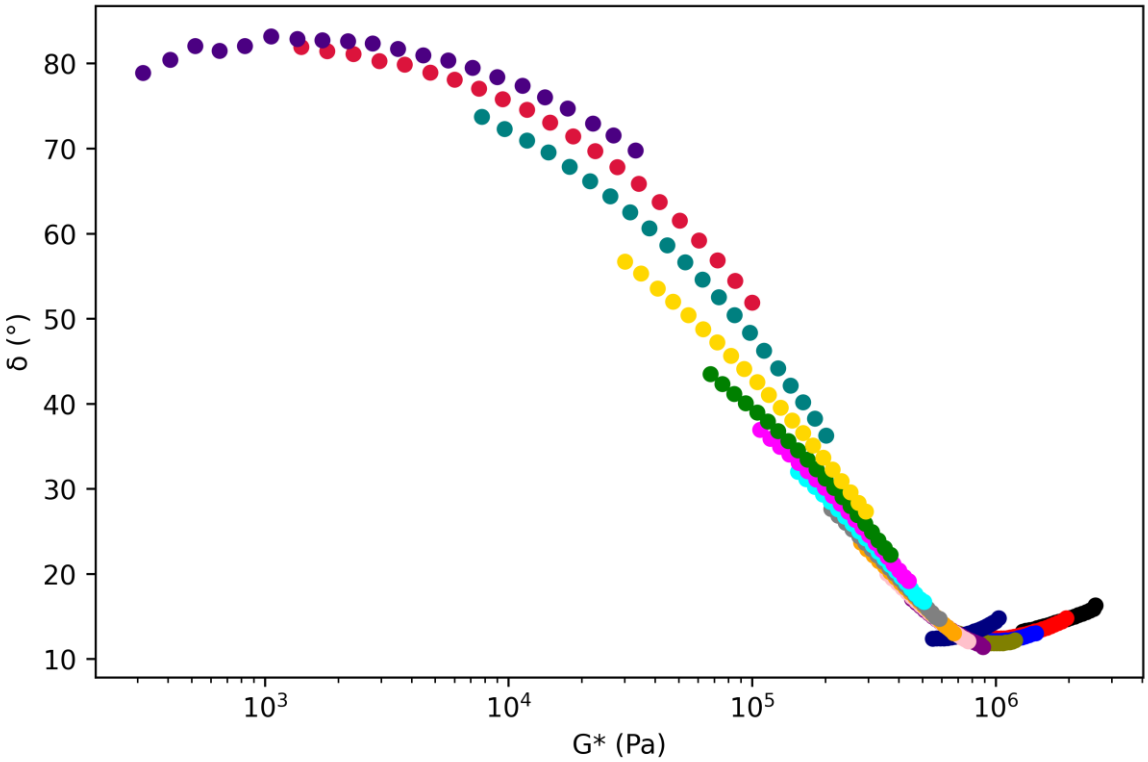

Figure 62. van Gurp-Palmen plot of **SPE2** at 0 (black), 10 (red), 20 (blue), 30 (olive), 40 (navy), 50 (purple), 60 (pink), 70 (orange), 80 (gray), 90 (cyan), 100 (magenta), 110 (green), 120 (gold), 130 (teal), 140 (crimson), 150 °C (indigo). Frequency sweeps were performed between 0.1 to 10 Hz at an applied strain of 0.1%.

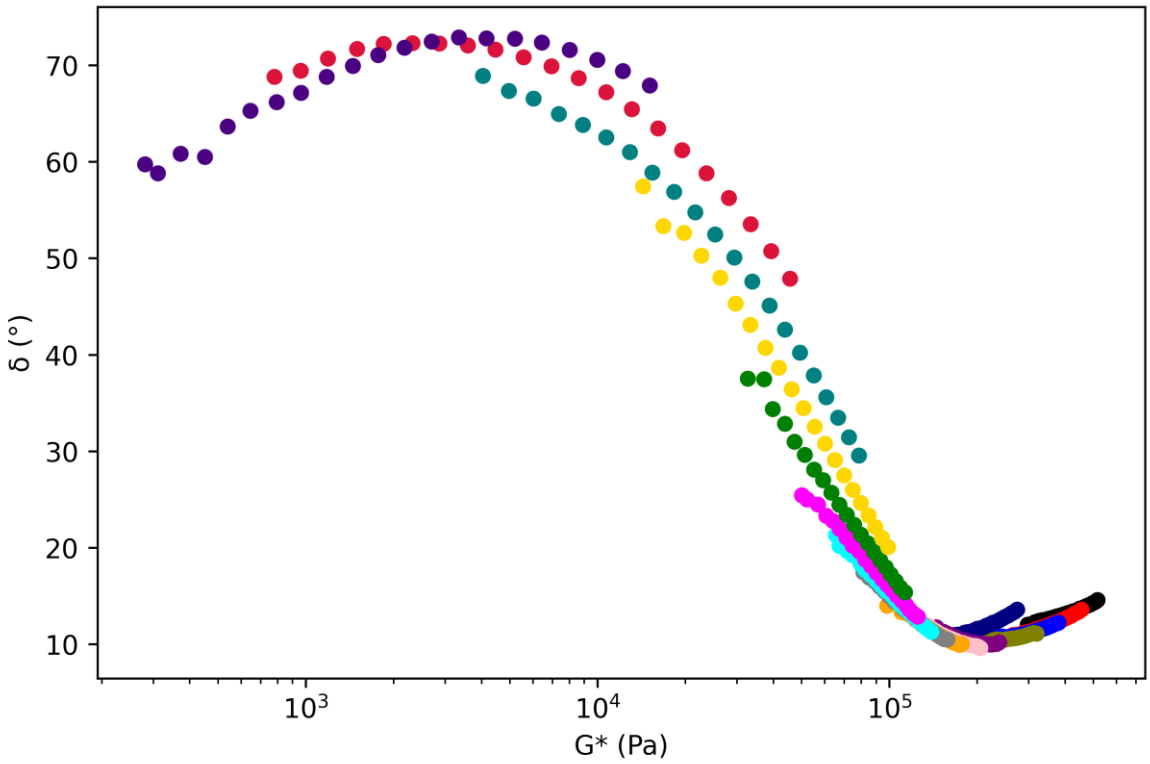

Figure 63. van Gurp-Palmen plot of **SPE3** at 0 (black), 10 (red), 20 (blue), 30 (olive), 40 (navy), 50 (purple), 60 (pink), 70 (orange), 80 (gray), 90 (cyan), 100 (magenta), 110 (green), 120 (gold), 130 (teal), 140 (crimson), 150 °C (indigo). Frequency sweeps were performed between 0.1 to 10 Hz at an applied strain of 0.1%.

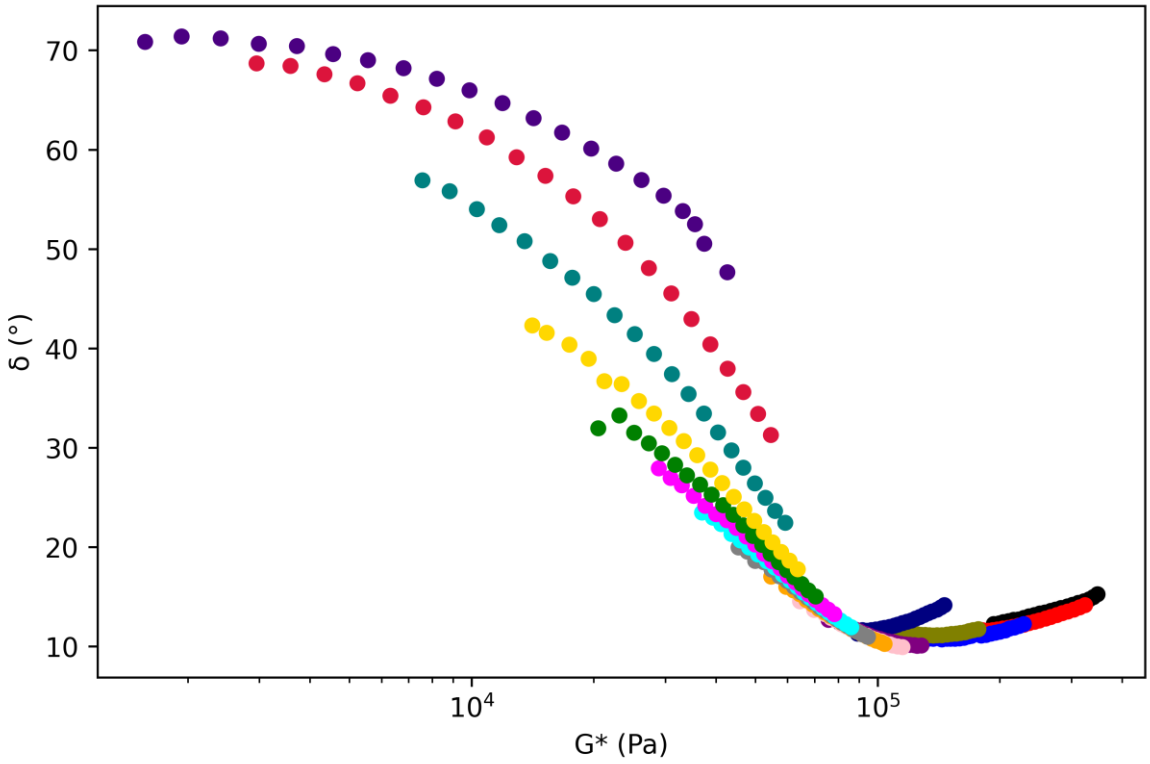

Figure 64. van Gurp-Palmen plot of **SPE4** at 0 (black), 10 (red), 20 (blue), 30 (olive), 40 (navy), 50 (purple), 60 (pink), 70 (orange), 80 (gray), 90 (cyan), 100 (magenta), 110 (green), 120 (gold), 130 (teal), 140 (crimson), 150 °C (indigo). Frequency sweeps were performed between 0.1 to 10 Hz at an applied strain of 0.1%.

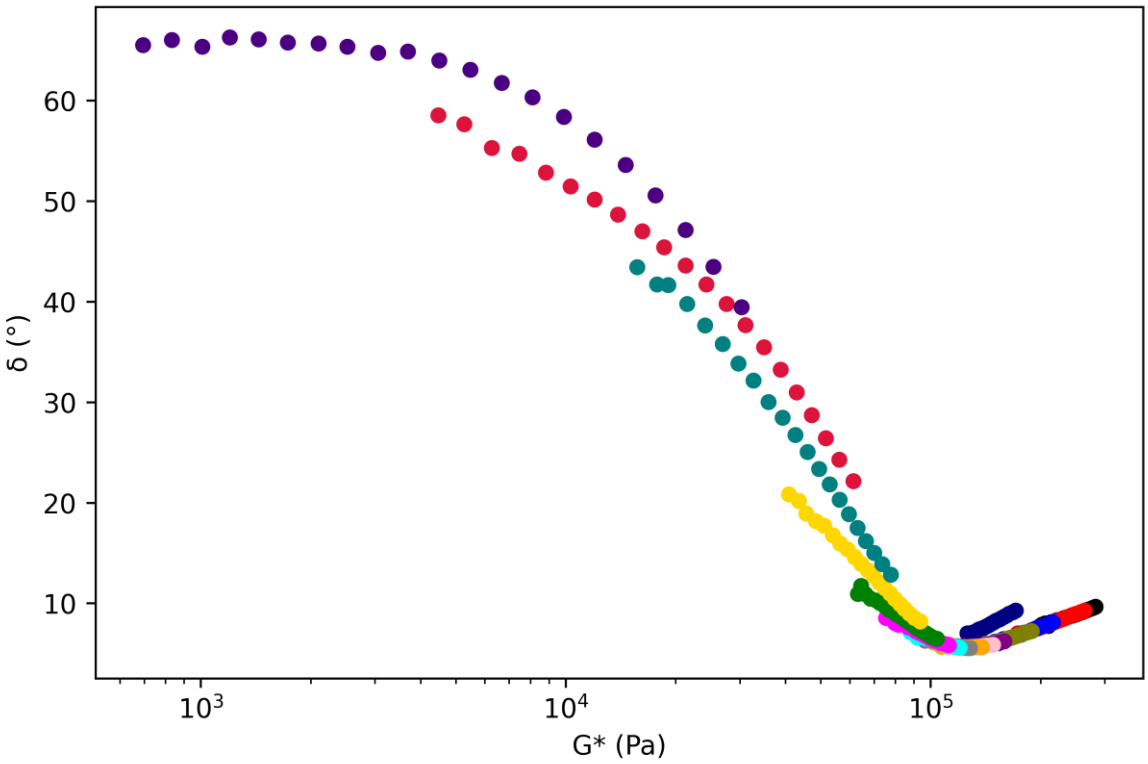

Figure 65. van Gurp-Palmen plot of **SPE5** at 0 (black), 10 (red), 20 (blue), 30 (olive), 40 (navy), 50 (purple), 60 (pink), 70 (orange), 80 (gray), 90 (cyan), 100 (magenta), 110 (green), 120 (gold), 130 (teal), 140 (crimson), 150 °C (indigo). Frequency sweeps were performed between 0.1 to 10 Hz at an applied strain of 0.1%.

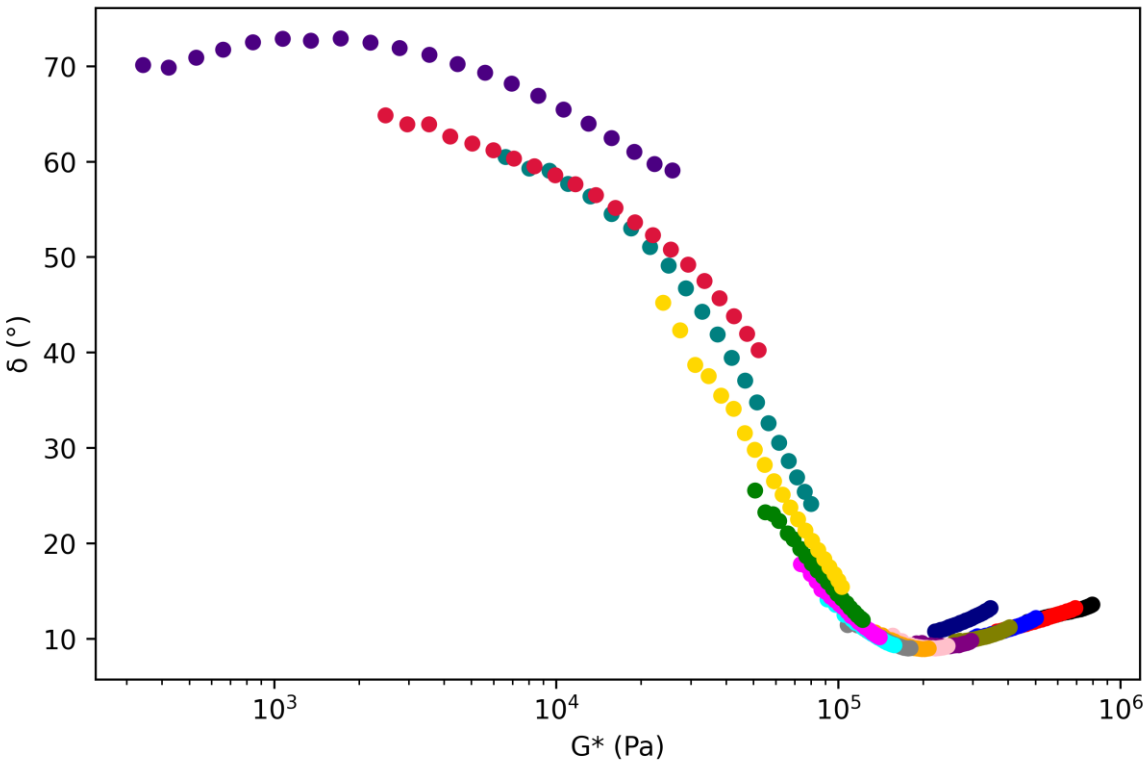

Figure 66. van Gurp-Palmen plot of **SPE6** at 0 (black), 10 (red), 20 (blue), 30 (olive), 40 (navy), 50 (purple), 60 (pink), 70 (orange), 80 (gray), 90 (cyan), 100 (magenta), 110 (green), 120 (gold), 130 (teal), 140 (crimson), 150 °C (indigo). Frequency sweeps were performed between 0.1 to 10 Hz at an applied strain of 0.1%.

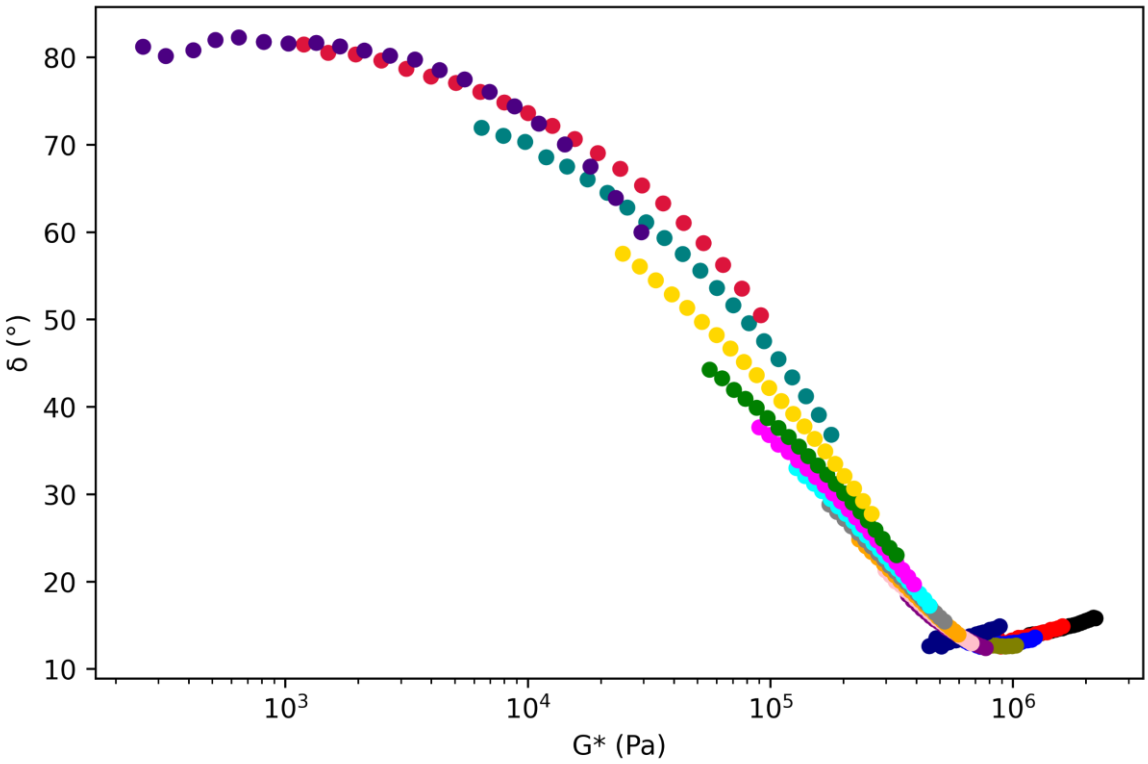

Figure 67. van Gurp-Palmen plot of **SPE7** at 0 (black), 10 (red), 20 (blue), 30 (olive), 40 (navy), 50 (purple), 60 (pink), 70 (orange), 80 (gray), 90 (cyan), 100 (magenta), 110 (green), 120 (gold), 130 (teal), 140 (crimson), 150 °C (indigo). Frequency sweeps were performed between 0.1 to 10 Hz at an applied strain of 0.1%.

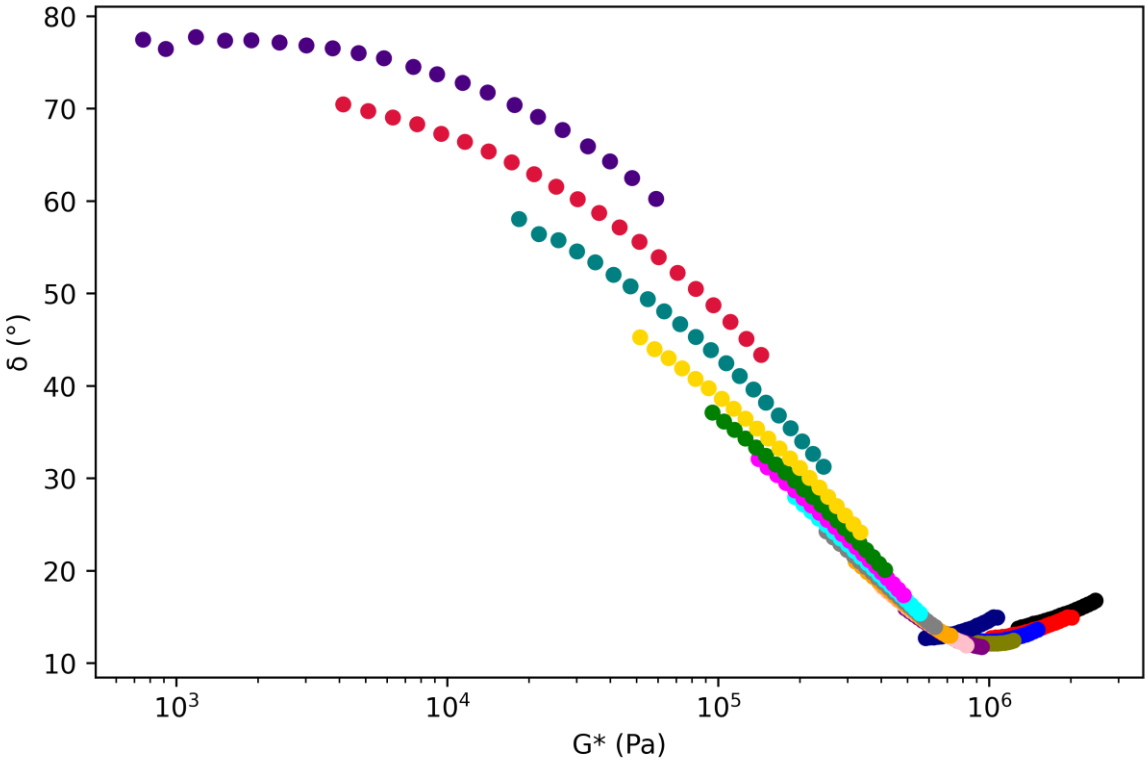

Figure 68. van Gurp-Palmen plot of **SPE8** at 0 (black), 10 (red), 20 (blue), 30 (olive), 40 (navy), 50 (purple), 60 (pink), 70 (orange), 80 (gray), 90 (cyan), 100 (magenta), 110 (green), 120 (gold), 130 (teal), 140 (crimson), 150 °C (indigo). Frequency sweeps were performed between 0.1 to 10 Hz at an applied strain of 0.1%.

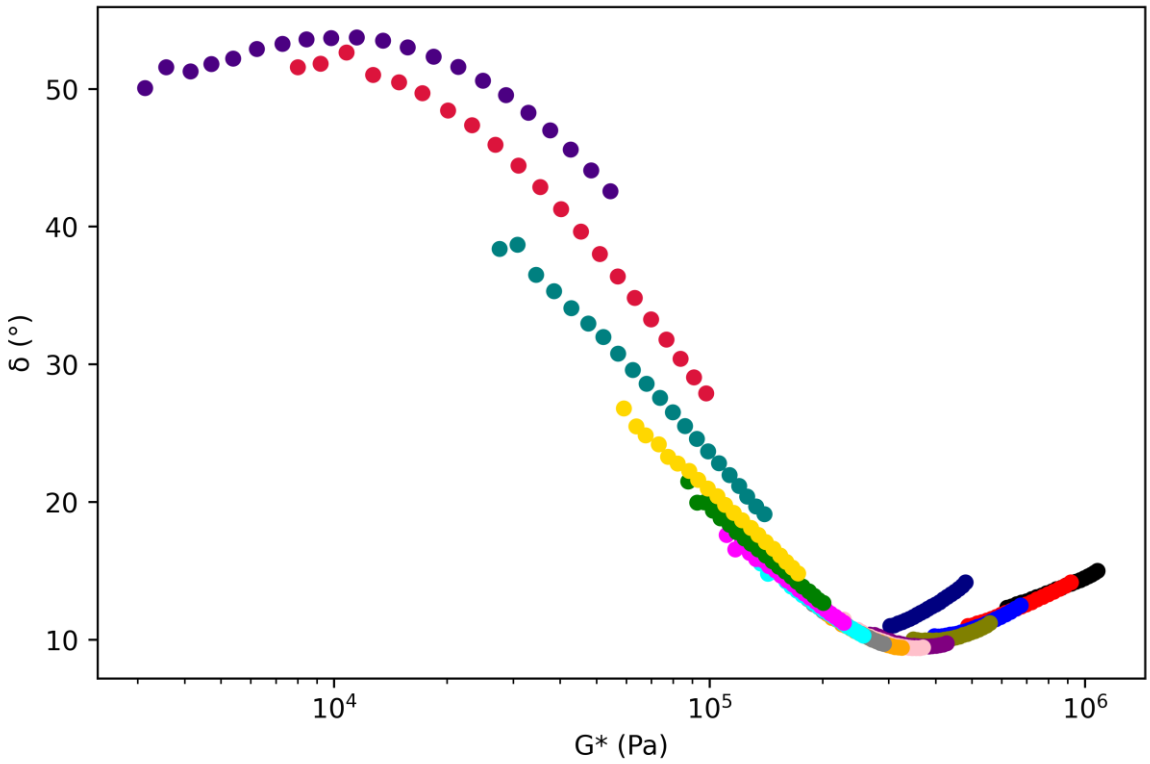

Figure 69. Frequency sweeps of **SPE9** at 0 (black), 10 (red), 20 (blue), 30 (olive), 40 (navy), 50 (purple), 60 (pink), 70 (orange), 80 (gray), 90 (cyan), 100 (magenta), 110 (green), 120 (gold), 130 (teal), 140 (crimson), 150 °C (indigo). G' closed symbols and G'' open symbols frequency sweeps were performed between 0.1 to 10 Hz at an applied strain of 0.1%

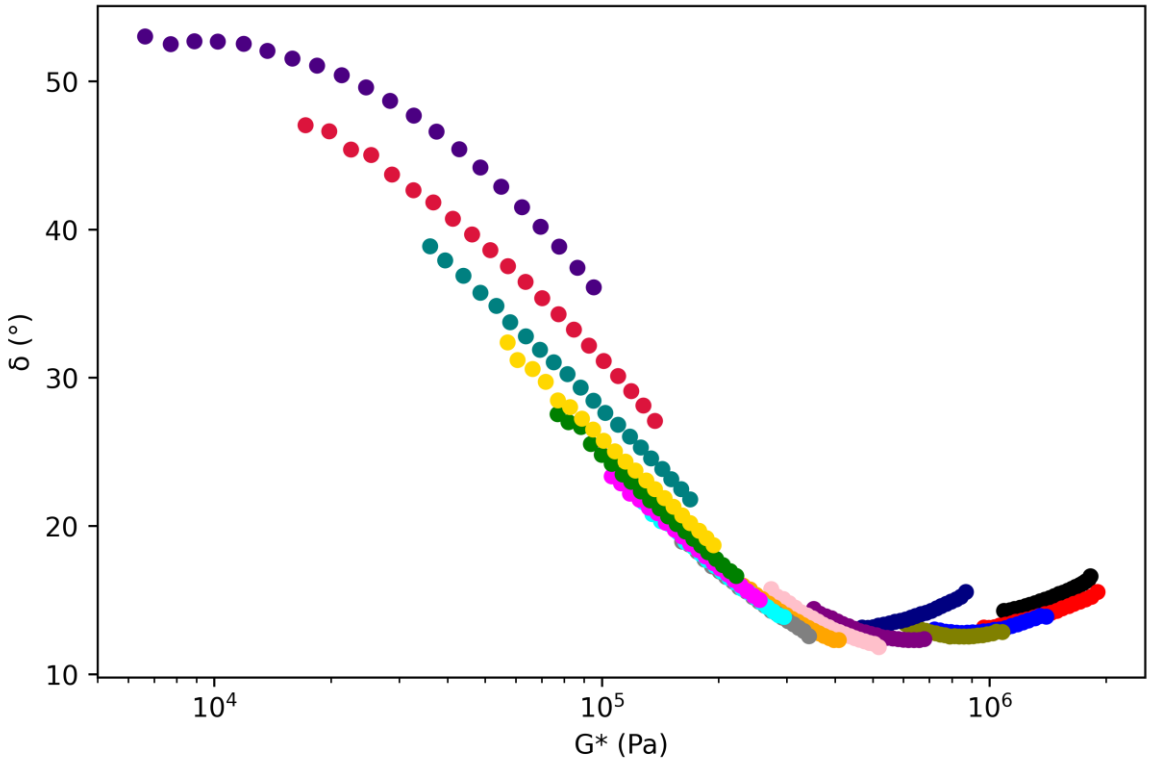

Figure 70. Frequency sweeps of **SPE10** at 0 (black), 10 (red), 20 (blue), 30 (olive), 40 (navy), 50 (purple), 60 (pink), 70 (orange), 80 (gray), 90 (cyan), 100 (magenta), 110 (green), 120 (gold), 130 (teal), 140 (crimson), 150 °C (indigo). G' closed symbols and G'' open symbols frequency sweeps were performed between 0.1 to 10 Hz at an applied strain of 0.1%.

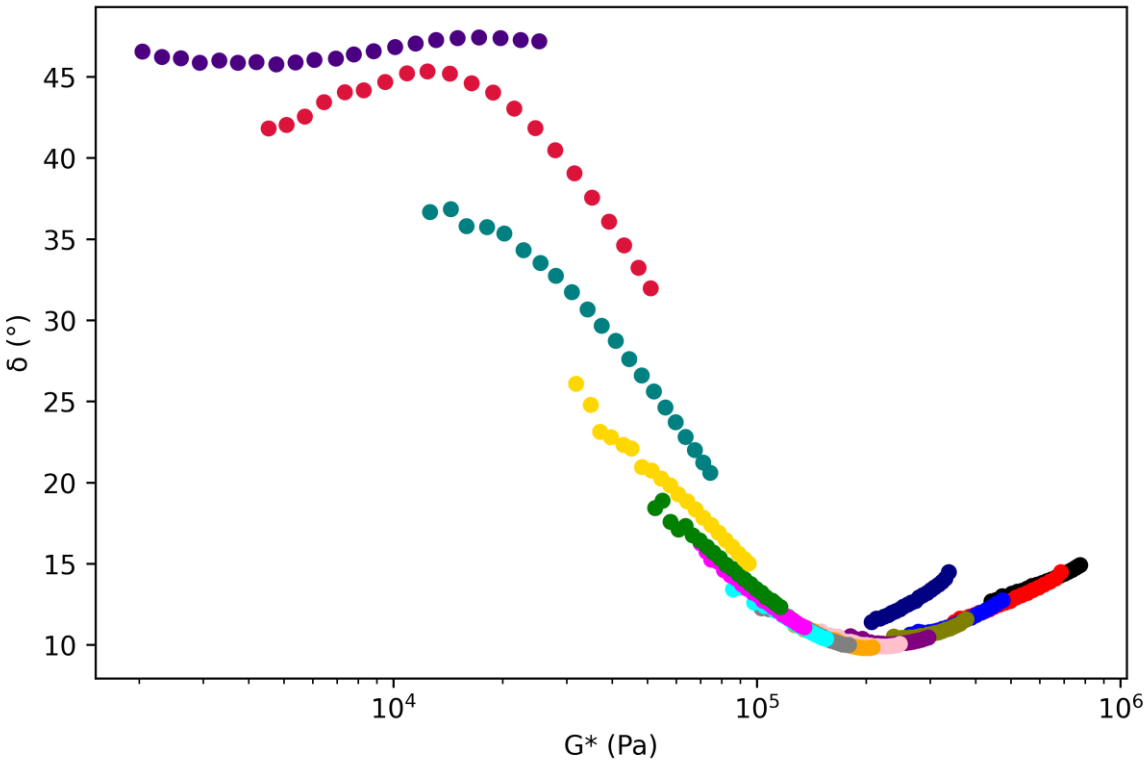

Figure 71. Frequency sweeps of **SPE11** at 0 (black), 10 (red), 20 (blue), 30 (olive), 40 (navy), 50 (purple), 60 (pink), 70 (orange), 80 (gray), 90 (cyan), 100 (magenta), 110 (green), 120 (gold), 130 (teal), 140 (crimson), 150 °C (indigo). G' closed symbols and G'' open symbols frequency sweeps were performed between 0.1 to 10 Hz at an applied strain of 0.1%.

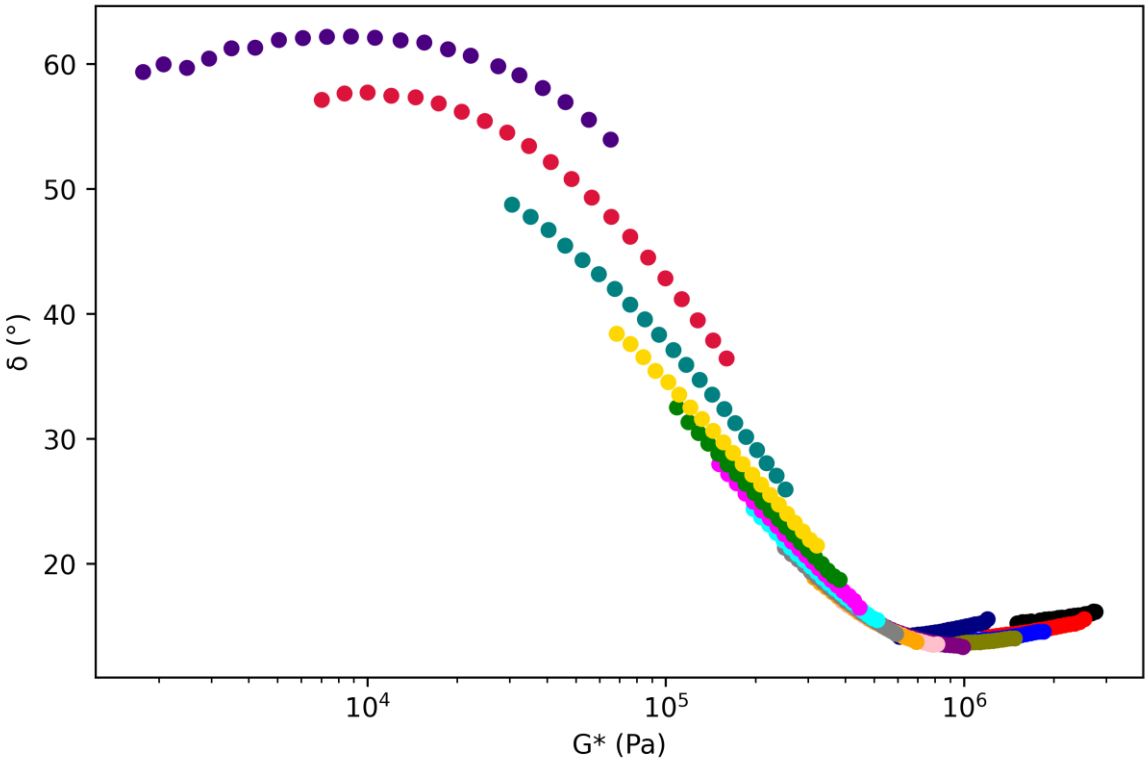

Figure 72. Frequency sweeps of **SPE12** at 0 (black), 10 (red), 20 (blue), 30 (olive), 40 (navy), 50 (purple), 60 (pink), 70 (orange), 80 (gray), 90 (cyan), 100 (magenta), 110 (green), 120 (gold), 130 (teal), 140 (crimson), 150 °C (indigo). G' closed symbols and G'' open

symbols frequency sweeps were performed between 0.1 to 10 Hz at an applied strain of 0.1%.

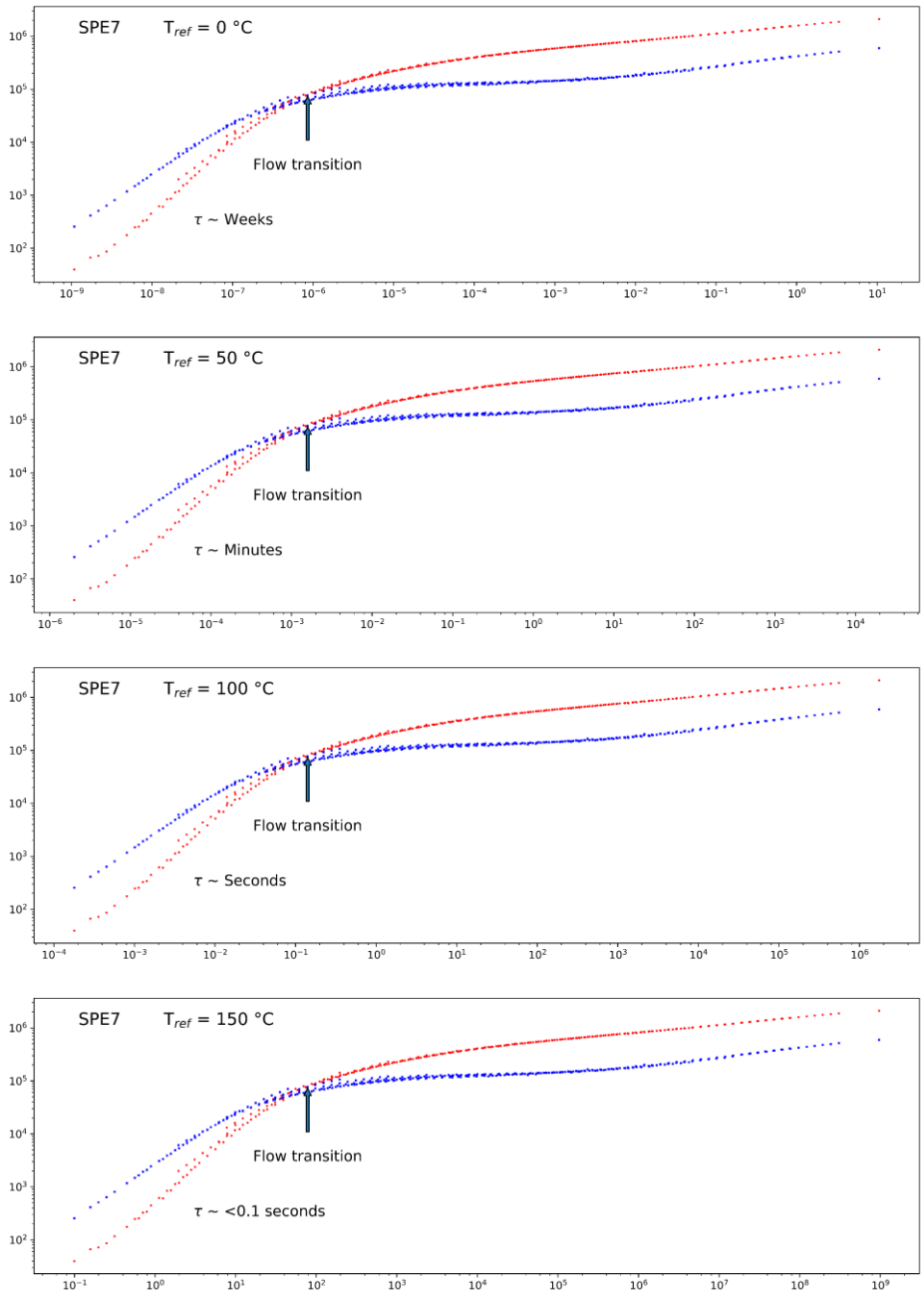

Figure 73. Master curves of **SPE7** at a reference temperature (T_{ref}) of 0, 50, 100, 150 °C, prepared by the TTS for G' and G'' values obtained at from frequency sweeps at 10 °C intervals from 0 to 150 °C, frequency sweeps were performed between 0.1 to 10 Hz at an applied strain of 0.1%.